

How scientists are helping to
bring fallen soldiers home p. 1032

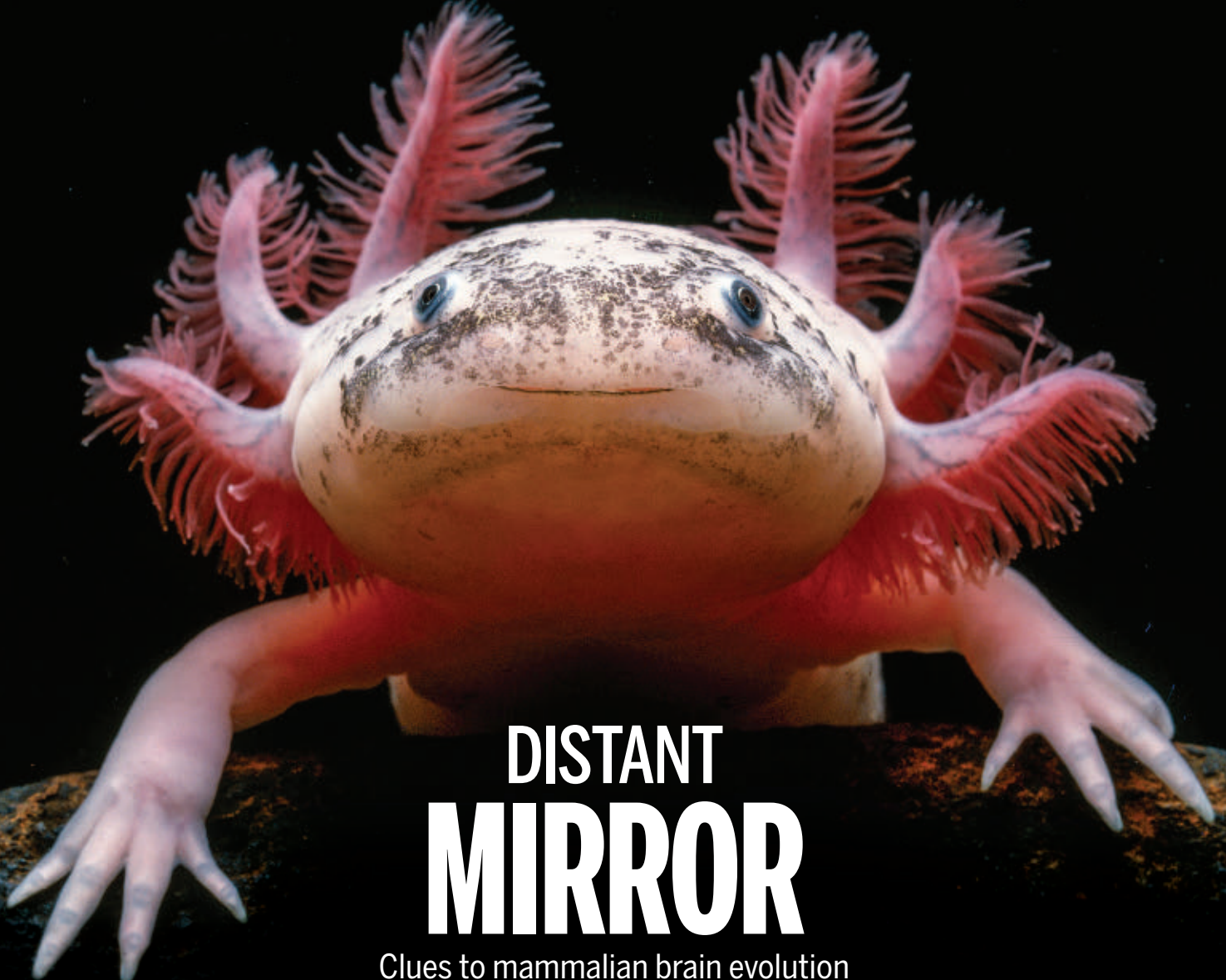
Forthcoming books to
read this fall p. 1036

Assessing the impacts of climate
change on forests p. 1099

Science

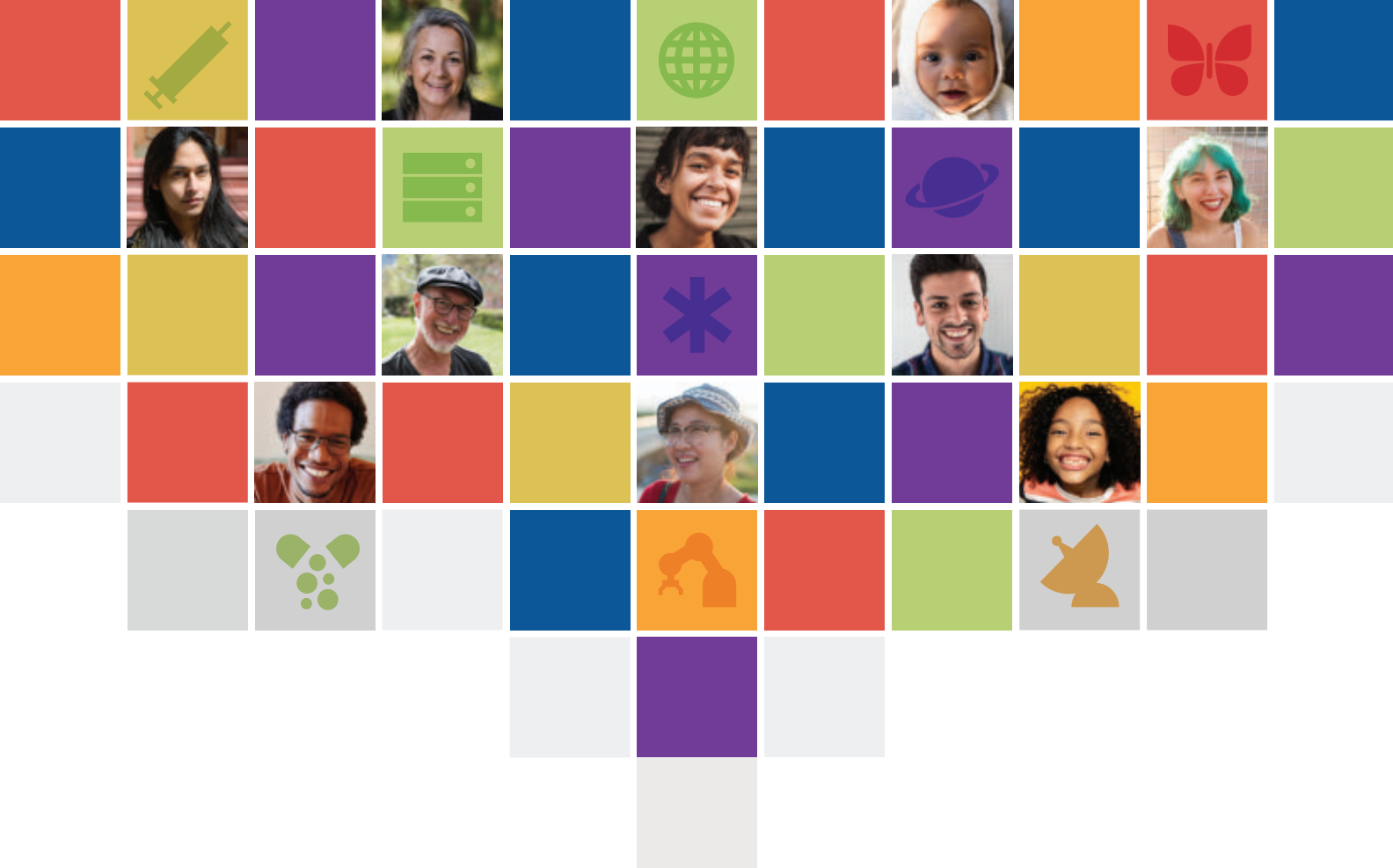
\$15
2 SEPTEMBER 2022
science.org

AAAS



DISTANT MIRROR

Clues to mammalian brain evolution
from salamander and
lizard neurons pp. 1043 & 1060–1063



SCIENCE FOR HUMANITY

AAAS | **ANNUAL MEETING**
Washington, D.C. | March 2–5, 2023

CALLING ALL STEM STUDENTS!

Share your work at the largest general scientific conference and **submit a poster abstract by October 10.**

The 2023 AAAS Annual Meeting will be held online and in Washington, D.C., March 2–5. Program and registration available this fall.

The meeting will highlight groundbreaking multi-disciplinary research that advances knowledge and responds equitably to the needs of humanity.

aaas.org/meetings | [#AAASmtg](https://twitter.com/AAASmtg)

CONTENTS

2 SEPTEMBER 2022 • VOLUME 377 • ISSUE 6610



1032

World War II aviators are among the thousands of U.S. personnel who are missing in action.

NEWS

IN BRIEF

1024 News at a glance

IN DEPTH

1026 U.S. to require free access to papers on all research it funds

The plan, to start at the end of 2025, is a blow to journal paywalls, but its impact on publishing is unclear

By J. Brainard and J. Kaiser

1027 Carbon dioxide detected around alien world for first time

Webb telescope discovery offers clue to planet formation and promises insights on planetary habitability

By D. Clerly

1028 Researchers tackle vexing side effects of potent cancer drugs

Wider use of checkpoint inhibitor therapy spurs efforts to predict and treat immune complications

By J. Couzin-Frankel

1029 Omicron shots are coming—with lots of questions

Decisions on boosters targeting subvariants will be based on limited data

By G. Vogel

1031 Zimbabwe find illuminates dawn of the dinosaurs

Nearly complete specimen shows earliest dinosaurs needed a temperate climate

By A. Reese

FEATURES

1032 A somber search

Can sophisticated research tools, such as plucking environmental DNA from water and the sea floor, speed the recovery of long-missing soldiers?

By T. Joosse

PODCAST

INSIGHTS

BOOKS ET AL.

1036 Readings for a season of reflection

PERSPECTIVES

1042 Boosting cognition with a hormone

A hormone enhances cognition in mouse models of Alzheimer's disease and Down syndrome

By H. M. Hoffmann

RESEARCH ARTICLE p. 1064

1043 A mosaic of new and old cell types

Comparative transcriptomics could reveal patterns of cell type evolution in the tetrapod brain

By D. Z. Faltine-Gonzalez and J. M. Kebschull

RESEARCH ARTICLES pp. 1060, 1061, 1062, & 1063

1045 The “atmosphere” of the human body

A human-occupied indoor space shares many similarities with Earth and its atmosphere

By C. Schoemaeker and N. Carlsaw

RESEARCH ARTICLE p. 1071

1046 3D-printing nanocrystals with light

Nanocrystals are connected to form complex 3D structures by means of two-photon lithography

By J.-A. Pan and D. V. Talapin

REPORT p. 1112

1047 Foreseeing metal failure from its inception

The life span of metals can be inferred from early microscopic deformation events

By M. M. Omar and J. A. El-Awady

RESEARCH ARTICLE p. 1065

1049 Christine Guthrie (1945–2022)

RNA trailblazer who illuminated splicing mechanics

By S. Noble et al.

POLICY FORUM

1051 Toward product-based regulation of crops

Current process-based approaches to regulation are no longer fit for purpose

By F. Gould et al.

LETTERS

1054 Test Patagonia's raptors for rodenticides

By M. D. Saggese et al.

1054 Denmark passes total ban of leaded ammunition

By C. Sonne et al.

1055 Rapid loss of China's pollinator diversity

By F.-Z. Ma et al.

RESEARCH

IN BRIEF

1056 From *Science* and other journals

REVIEW

1059 Heart disease

A coalition to heal—the impact of the cardiac microenvironment

E. Tzahor and S. Dimmeler

REVIEW SUMMARY; FOR FULL TEXT: DOI.ORG/10.1126/SCIENCE.ABM4443

RESEARCH ARTICLES

Neuroevolution

1060 Molecular diversity and evolution of neuron types in the amniote brain
D. Hain et al.

RESEARCH ARTICLE SUMMARY; FOR FULL TEXT: DOI.ORG/10.1126/SCIENCE.ABP8202

1061 Single-cell analyses of axolotl telencephalon organization, neurogenesis, and regeneration
K. Lust et al.

RESEARCH ARTICLE SUMMARY; FOR FULL TEXT: DOI.ORG/10.1126/SCIENCE.ABP9262

1062 Single-cell Stereo-seq reveals induced progenitor cells involved in axolotl brain regeneration
X. Wei et al.

RESEARCH ARTICLE SUMMARY; FOR FULL TEXT: DOI.ORG/10.1126/SCIENCE.ABP9444

1063 Cell-type profiling in salamanders identifies innovations in vertebrate forebrain evolution
J. Woych et al.

RESEARCH ARTICLE SUMMARY; FOR FULL TEXT: DOI.ORG/10.1126/SCIENCE.ABP9186

PERSPECTIVE p. 1043

1064 Neurodevelopment

GnRH replacement rescues cognition in Down syndrome

M. Manfredi-Lozano et al.

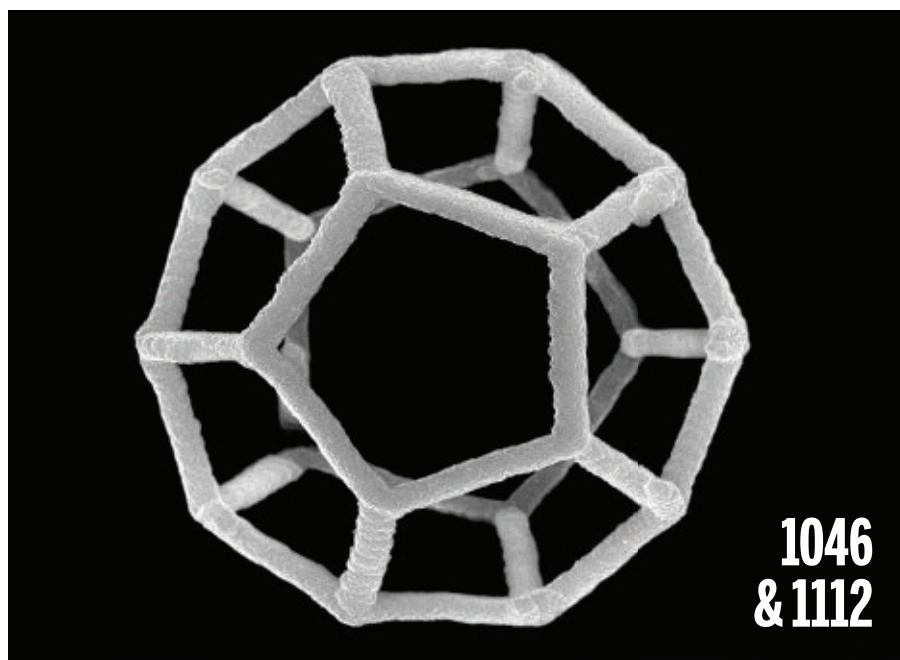
RESEARCH ARTICLE SUMMARY; FOR FULL TEXT: DOI.ORG/10.1126/SCIENCE.ABQ4515
PERSPECTIVE p. 1042

1065 Metallurgy

On the origins of fatigue strength in crystalline metallic materials

J. C. Stinville et al.

PERSPECTIVE P. 1047



1071 Indoor air quality

The human oxidation field
N. Zannoni et al.

PERSPECTIVE P. 1045

1077 Molecular biology

Nested epistasis enhancer networks for robust genome regulation

X. Lin et al.

1085 Cancer immunity

Pituitary hormone α -MSH promotes tumor-induced myelopoiesis and immunosuppression

Y. Xu et al.

1092 Physiology

Insulin signaling in the long-lived reproductive caste of ants

H. Yan et al.

REPORTS

1099 Forest ecology

A climate risk analysis of Earth's forests in the 21st century

W. R. L. Anderegg et al.

1104 Organic chemistry

Late-stage diversification of indole skeletons through nitrogen atom insertion

J. C. Reisenbauer et al.

1109 Multiferroics

Magnetoelectric transfer of a domain pattern

E. Hassanpour et al.

1112 Nanomaterials

3D nanoprnting of semiconductor quantum dots by photoexcitation-induced chemical bonding

S.-F. Liu et al.

PERSPECTIVE p. 1046

DEPARTMENTS

1021 Editorial

Trickle-down climate risk regulation
By A. M. Perrault and G. Giraud

1122 Working Life

Looking for a change *By O. Symes*

ON THE COVER

The axolotl, represented here by the Mexican axolotl *Ambystoma mexicanum*, has the ability to regenerate its brain. In this issue, a group of four papers profiles amphibian and reptile brain neurons with single-cell transcriptomics. Analyses lend insight into why the axolotl



brain retains regenerative capability that the mammalian brain has lost as well as how structural brain innovations arose during evolution. See pages 1043 and 1060 to 1063. Photo: Avalon.red/Alamy Stock Photo

New Products 1117
Science Careers 1118

SCIENCE (ISSN 0036-8075) is published weekly on Friday, except last week in December, by the American Association for the Advancement of Science, 1200 New York Avenue, NW, Washington, DC 20005. Periodicals mail postage (publication No. 484460) paid at Washington, DC, and additional mailing offices. Copyright © 2022 by the American Association for the Advancement of Science. The title SCIENCE is a registered trademark of the AAAS. Domestic individual membership, including subscription (12 months): \$165 (\$74 allocated to subscription). Domestic institutional subscription (51 issues): \$2212; Foreign postage extra: Air assist delivery: \$98. First class, airmail, student, and emeritus rates on request. Canadian rates with GST available upon request. GST #125488122. Publications Mail Agreement Number 1069624. Printed in the U.S.A.

Change of address: Allow 4 weeks, giving old and new addresses and 8-digit account number. Postmaster: Send change of address to AAAS, P.O. Box 96178, Washington, DC 20090-6178. Single-copy sales: \$15 each plus shipping and handling available from backissues.science.org; bulk rate on request. Authorization to reproduce material for internal or personal use under circumstances not falling within the fair use provisions of the Copyright Act can be obtained through the Copyright Clearance Center (CCC), www.copyright.com. The identification code for Science is 0036-8075. Science is indexed in the Reader's Guide to Periodical Literature and in several specialized indexes.

Trickle-down climate risk regulation

Climate change impacts—including flooding, wildfires, and crop failures—are destroying ecosystems, homes, infrastructure, farms, and businesses. Regulators around the globe are paying increasing attention to what these events mean for banks and the financial system, with several attending not only to bank impacts from, but also bank contributions to, climate change. The European Central Bank, for example, is signaling to banks that they must plan and make their transition away from financing of fossil fuels—to respond not only to their own risks but also to the science pointing to the necessity of this transition for the planet and financial system. Yet in the US, the primary regulators of national and community banks are narrowly zeroing in on risks posed to the largest banks—those with over \$100 billion in total consolidated assets—without attention to these banks' role in financing greenhouse gas-emitting activities and what they mean for other important financial actors. Such a “trickle-down” approach to regulation—assuming that protecting big banks will protect other, smaller financial entities and the financial system more broadly—obscures the financial crisis that is already underway and inadequately responds to scientific evidence on distinctive features of climate risk and impacts.

Big banks should be worried about climate risks. Loans for fossil fuel-related activities are at risk of rapidly losing value, causing banks that hold them to suffer major losses. Bank balance sheets will also suffer when property damage creates loan defaults. Still, despite promises by most to reach “net-zero” emissions by 2050, big US banks remain the world's largest fossil fuel financiers, apparently believing they can ditch their fossil assets before the energy transition torpedoes their value and that physical impacts to investments in one location can be offset by safe investments elsewhere.

By focusing on threats to big banks, draft climate risk guidance by the US Office of the Comptroller of the Currency (OCC) and the Federal Deposit Insurance Corporation (FDIC) is treating climate risks like the financial risks that spurred the last global financial crisis. Yet science shows that climate change poses new and substantial risks, requiring greater attention to the interconnectedness of financial and environmental systems and what those relationships imply for other financial actors

and risk management measures. As climate change simultaneously, repeatedly, and often permanently affects natural and human systems across geographic areas—and as borrowers and taxpayers struggle to pay their bills in response—many community banks and municipalities, ignored by the trickle-down approach, could fail. A report to the US Commodity Futures Trading Commission suggests that such repeated “subsystemic” shocks are initiating “a systemic crisis in slow motion.”

Despite having only 15% of total industry loans, community banks are lifelines for rural and underserved communities, representing ~90% of regulated US banks. With lending concentrated in agriculture, mortgages, and commercial real estate, they are especially vulnerable to climate change. As issuers of \$3.8 trillion in bonds, municipalities also play a critical role, their health affecting the financial health of bondholders. A municipality hit hard by a wildfire or hurricane will struggle to make bond payments. The 20 and growing number of lawsuits against fossil fuel companies by municipalities needing financial help to deal with climate-related losses are warnings for municipal bondholders and those dependent on public-sector services. For now, government subsidies, including additional annual federal spending of \$25 to \$128 billion on costs such as disaster relief and insurance, are masking financial harms to these entities.

US banking regulators must reduce threats to bank safety and soundness at every level of the financial system. They should adopt measures that incentivize and require banks to reduce their financed emissions, starting with directing banks to develop science-based plans to accomplish this transition and supporting restrictions on financing of coal and new fossil fuel development. Regulators should also push for disclosure of bank contributions to climate-changing emissions—not just to inform investors as the US Securities and Exchange Commission's recent proposed rule would do, but also to inform regulator efforts to maintain financial system health. In addition to the OCC and FDIC proposals, the Federal Reserve Board will soon issue climate-risk guidance for public comment. As all three finalize their guidance, and prepare follow-up proposals, they have an opportunity to advance just such measures.

—Anne M. Perrault and Gaël Giraud

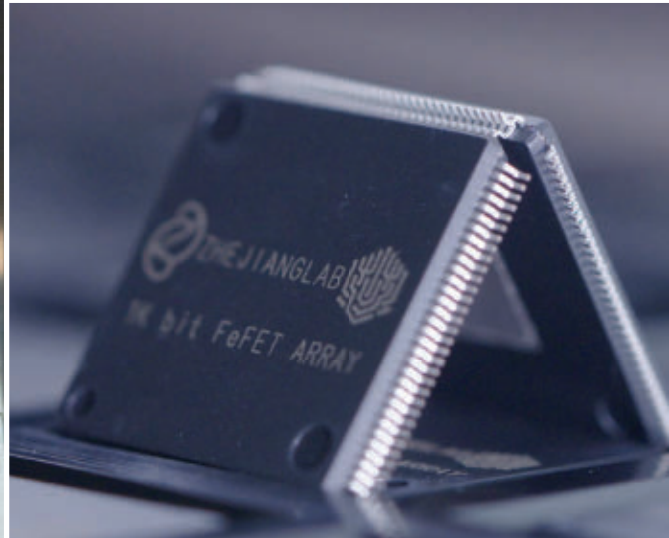
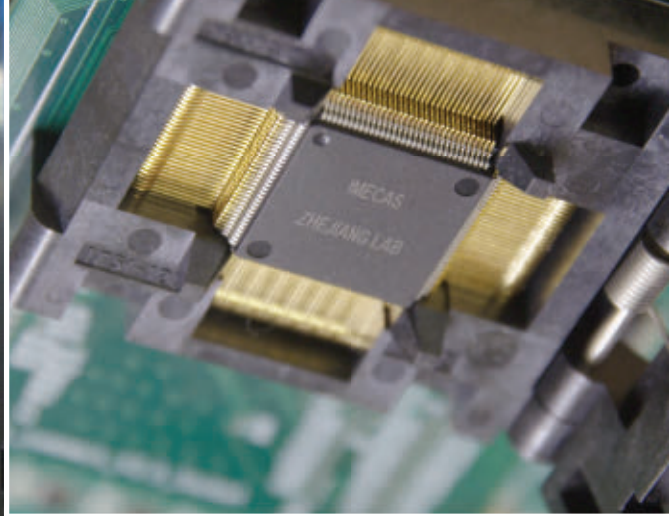
Anne M. Perrault

is a senior climate finance policy counsel at Public Citizen, Washington, DC, USA. aperrault@citizen.org

Gaël Giraud

is founder and director of the Georgetown Environmental Justice Program, McCourt School of Public Policy, Georgetown University, Washington, DC, USA. gg707@georgetown.edu

“...repeated ‘subsystemic’ shocks are initiating ‘a systemic crisis in slow motion.’”



Zhejiang Lab scientists carry out research on intelligent supercomputers (left), computing-in-memory chips (top right), and high-efficiency ferroelectric chips for intelligence edge computing.

The Zhejiang Lab: Using new mechanisms to usher in the next stage of AI development

Five years ago, the Zhejiang Lab, a new type of R&D institution—committed to accelerating the development of artificial intelligence and meeting the computing needs in the age of intelligence—was established in the central area of West Science and Technology Innovation Corridor of Hangzhou, China. The Zhejiang Lab integrates the strengths and operating mechanisms of government, universities, scientific research institutions, and enterprise, and pursue high-quality innovations while promoting cutting-edge basic research and major scientific and technological innovations.

The vision of the Zhejiang Lab is to become an intelligent perception research and experiment center, an AI innovation center, an intelligent science and technology research center, and an intelligent computing hub for basic research and innovation with initial innovation capabilities. Since its establishment the lab has gained several scientific research achievements, including the 2021 Association for Computing Machinery (ACM) Gordon Bell Prize for “Real-Time Simulation of a Random Quantum Circuit Using a New Sunway Supercomputer [SWQSIM],” the publication on fast radio bursts in *Science*, as well as winning the honor of World Leading Internet Scientific and Technological Achievement for the 800G optical transceiver chip and optical engine technology.

Intelligent computing: Cornerstone of a smart society

The Zhejiang Lab focuses on five research disciplines in the field of intelligent science and technology—intelligent perception, AI, intelligent computing, intelligent networks, and intelligent systems—conducting cutting-edge basic research, key technology research, and core systems R&D. Among these research disciplines, the main focus is intelligent computing—what the Zhejiang Lab believes will be the cornerstone of the future development of a smart society. With the development and application of new technologies such as the Internet of Things and AI, human society has entered the era of the three-way intelligent integration of human, machine, and things, which requires strong computing technology support. The intelligent computing that the Zhejiang Lab is working on includes two principal aspects: (1) to form intelligence through computing, and (2) to drive computing in an intelligent way. Its goal is to achieve on-demand access, ubiquitous services, automatic adaptation, and precision and efficiency of computing services, and to make computing accessible everywhere, just as communications, electricity, and water are today.

In order to explore innovative breakthroughs in the field of intelligent computing, the Zhejiang Lab has undertaken a series of major projects focusing on the basic

theory of intelligent computing, novel architectural computing systems, domain-specific platforms, major applications, and intelligent computing standardization. One of these projects, the intelligent computing data reactor, is a major facility. Its core function is to integrate the computing resources of a variety of architectures and to conveniently support various computing needs of the application layer. Its integration and scheduling capacity is enabled by a core system, named the data reactor operating system, which aggregates resources such as brain-like computer, graph computer, and intelligent supercomputer, and dispatches computing tasks. The data reactor can support scientific innovation areas as diverse as computational astronomy, computational genetics, computational materials, computational pharmacology, and computational breeding.

The data reactor works in a way of “focusing more on systematic integration and software engineering, which involve dealing with the complexity caused by incompatible computing power resources,” Intelligent Computing Data Reactor Chief Architect Aimin Pan explains, “as well as the challenge posed by systematic performance optimization integrating computing, storage, and transmission, providing easy and convenient means and tools for upper applications to establish the computing resources that they need.”

Imagine and transform: Breaking new boundaries

The Zhejiang Lab supports the full scientific research work cycle. It encourages researchers to look up at the stars and bravely enter into the “no-man’s land” of scientific research. The Zhejiang Lab also encourages researchers to be down-to-earth; play a central role in major engineering projects; and transform scientific research into cutting-edge technologies that empower economic and social development, support industry, and benefits society. There have been a series of industrialized achievements, such as the Dubhe AI open-source platform serving the development of the AI industry, and the multicenter intelligent medical information platform serving the early screening of chronic diseases. “Under the leadership of Yunhe Pan, academican of the Chinese Academy of Engineering, we are studying dual-driver artificial intelligence with knowledge and data ... with the hope to reach AI 2.0,” says Feng Lin, Executive Dean of the Zhejiang Lab’s AI Research Institute.

One of the major research projects of the Zhejiang Lab in AI is cross-media human-like intelligence. “The project aims to make machines sense, perceive, infer, and decide like humans [do],” says Feng Lin. He adds that the institute will create advanced knowledge-based system of human-like intelligence.

The Zhejiang Lab: Non-traditional scientific research institution

Pursuing innovation, efficiency, and quality, the Zhejiang Lab has been committed from its inception to putting its own stamp on improving scientific research systems and mechanisms. “We don’t want to be the 1,001st traditional scientific research institution. We are always breaking the rules and boundaries, aiming to build a new type of research and development institution with a new mechanism.” points out President Shiqiang Zhu.

The Zhejiang Lab has gathered a team of more than 3,700 people in only 5 years, including more than 2,300 full-time staff and 1,400 part-time personnel. There are about 760 full-time, high-level talents working at the lab, and nearly 240 academic leaders. “We are eager to attract more talent to join the innovative platform of the Zhejiang Lab,” says President Zhu. “Based on the field of intelligent science and technology, we attract more scientists to participate in the scientific research by providing excellent research conditions and carrying out extensive scientific research cooperation, so as to change the world with intelligence and make science and technology benefit mankind.”

Sponsored by



之江实验室
ZHEJIANG LAB

The main campus of the Zhejiang Lab lies in Hangzhou City, one of the seven ancient capitals of China and location of a future Sci-Tech City.



NEWS

“This is very far from a normal monsoon—it is climate dystopia at our doorstep.”

Sherry Rehman, Pakistan's climate change minister, to AFP, about unprecedented flooding that has killed more than 1000 people, a likely impact of climate change despite the country's small carbon footprint.

IN BRIEF

Edited by **Jeffrey Brainard**



A new state policy could make electric charging stations, like this one in San Francisco, a more common sight.

CLIMATE POLICY

California to ban gasoline-only cars

California regulators last week issued the first ban by a U.S. state on the sale of new passenger cars that run only on gasoline. Starting in 2035, nearly all new cars sold in California must be all electric or run on hydrogen fuel cells; 20% can be hybrid-electric vehicles with batteries capable of running at least 80 kilometers. The measure is expected to halve greenhouse gas emissions from passenger cars, pickups, and SUVs in California by 2040. The phased-in mandate from the California Air Resources Board could bolster nationwide efforts to cut greenhouse gas emissions. Up to 40% of all U.S. cars sold may conform to the California rule—if, as expected, some other states adopt the measure, which is stricter than federal rules. But most states will have difficulty meeting the California targets, transportation experts at the University of California, Davis, wrote in an analysis. Today, roughly 15% of new cars sold in California are electric vehicles, and most other states lag far behind in EV sales and installation of charging infrastructure. EU lawmakers voted this year to ban sales of new gasoline-only cars starting in 2035, a measure that requires approval by member states.

High seas treaty delayed

BIODIVERSITY | Nations failed last week to agree on a first-ever treaty to protect high seas biodiversity, after some countries balked at ceding control to a new international regulator. Negotiations had been underway for several years on the pact, which includes provisions on establishing protected marine areas, regulating scientific collection of organisms, improving research capacity of developing nations, and requiring environmental impact assessments for new activities such as mining. The biggest sticking point was over whether environmental impact assessments would be approved by nations themselves or by a new international organization, says Alice Vadrot, a political scientist at the University of Vienna. Another thorny issue is whether countries can be obliged to make payments to a treaty organization so their researchers may collect biological samples in the high seas. A new negotiating session has been scheduled for January 2023.

Gender diversity sparks discovery

PUBLISHING | Mixed-gender research teams produce more novel and highly cited papers than teams composed entirely of men or of women, according to a study of 6.6 million papers published from 2000 to 2019 by 7.6 million medical researchers. Teams with six or more authors of multiple genders—as inferred by a name-matching algorithm—published papers 7% more novel than similar-size, single-gender teams, based on an analysis of novel combinations of journals cited in each paper's bibliography. These teams' papers were also 15% more likely to be among the top 5% most highly cited papers in a given year, according to the study, published this week in the *Proceedings of the National Academy of Sciences* (by a mixed-gender team). More work is needed to understand the reasons for the disparities, it

Walensky eyes CDC reforms

Rochelle Walensky walked into a hot mess when she took the helm of the U.S. Centers for Disease Control and Prevention (CDC) in January 2021. The agency had difficulty keeping up with the fast-moving COVID-19 pandemic. It botched the development and distribution of COVID-19 tests, issued unclear directives about prevention efforts such as social distancing and vaccines, and required several levels of clearance before CDC researchers could publish findings. *Science* spoke with Walensky, a former head of infectious diseases at Massachusetts General Hospital, about preliminary findings of two reviews she commissioned of CDC's COVID-19 response and its policies and processes. (A longer version of this interview is at <https://scim.ag/Walensky>.)

Q: Are you trying to help CDC own its mistakes?

A: I was always a really avid consumer, champion, and cheerleader for CDC before I got here. The people at the CDC are amazing. The issue though is whether the people themselves were responsible or whether many of the things in the structure around them didn't allow them to operate as swiftly as possible and didn't allow them to prioritize. I think it's a little bit of both.

Q: What are you going to prioritize?

A: The clearance process at CDC is too slow. How is it that we get our data out faster? I published enough papers to know that as painful as the review process is, they are generally better after it. So I don't want to get rid of that necessarily. But CDC has been changing. Last week, we put data about monkeypox up on our website, and the [associated] paper hasn't come out yet.

Q: Do you plan to fire or reshuffle staff?

A: We're going to realign incentives for staff so that we move toward promoting people for taking actions that benefit public health. It's not lost on me that changing boxes around on an organizational chart is not going to do anything in and of itself. We haven't spent enough of our time, energy, and resources on our public health infrastructure, our core capabilities of personnel, data modernization, and laboratory infrastructure. And that is the investment that I think we really need to make.



IN FOCUS A photo of eggs from the gliding tree frog (*Agalychnis saltator*) won the Life Close Up category in this year's *BMC Ecology and Evolution* image competition. Brandon André Güell, a Ph.D. student at Boston University, photographed the eggs in Costa Rica. They usually hatch after 6 days of development but can do so prematurely to escape predators and desiccation.

says. The finding is consistent with previous studies that linked research teams that were more diverse racially and culturally to higher creativity.

COVID-19 shot spurs patent fight

INTELLECTUAL PROPERTY | Moderna, which has made billions of dollars from a COVID-19 vaccine based on messenger RNA technology, last week accused its main rival of infringing the company's patents for a similar mRNA shot. Among the allegations in a suit filed in a U.S. court, Moderna says Pfizer and its partner BioNTech made use of its patented strategy of replacing a natural constituent of mRNA with a labmade molecule. But the University of Pennsylvania filed a U.S. patent application for that same molecular substitution 6 years before Moderna did—and filing priority is critical in patent disputes. (Both patents have been issued.) Pfizer and BioNTech say they “will vigorously defend” themselves against Moderna's suit.

Japan reconsiders nuclear power

ENERGY | Japan's government will consider building new nuclear plants while pushing to restart more reactors idled for safety checks after the 2011 Fukushima meltdowns, Prime Minister Fumio Kishida announced last week. The objective is to ensure energy security and cut Japan's greenhouse gas emissions, which are the world's fifth largest. Engineers have restarted 10 of the 54 nuclear reactors shut down after the Fukushima disaster. Twenty-one are being decommissioned, and the rest are still under review, a process Kishida hopes to accelerate. To replace nuclear power, Japan's utilities have burned more coal and natural gas, jeopardizing the country's target of net-zero emissions by 2050. An economy ministry road map unveiled on 29 July suggests new, next-generation light-water reactors could be commercialized by the mid-2030s. Kishida also promised to give greater support to renewable power.



SCIENTIFIC PUBLISHING

U.S. to require free access to papers on all research it funds

The plan, to start at the end of 2025, is a blow to journal paywalls, but its impact on publishing is unclear

By Jeffrey Brainard and Jocelyn Kaiser

A decadeslong battle over how best to provide public access to the fruits of research funded by the U.S. government has taken a major turn.

Last week, President Joe Biden's administration announced that, by the end of 2025, federal agencies must make papers that describe taxpayer-funded work freely available to the public as soon as the final peer-reviewed manuscript is published by a journal. Data underlying those papers should also be made freely available "without delay."

Officials are still working out details of the new policy, including how to pay for publishing costs. But it significantly reshapes and expands fiercely contested rules on free access that have been in place since 2013. Most notably, the White House substantially weakened, but did not end, the ability of journals to keep final versions of federally funded papers behind a subscription paywall for up to 1 year.

Many commercial publishers and non-profit scientific societies have long fought to maintain that 1-year embargo, saying it protects subscription revenues that fund editing, production, and society activities. But critics of paywalls argue they slow the flow of

information, have enabled price gouging by publishers, and force U.S. taxpayers to "pay twice"—once to fund research and again to see the results. Since the late 1990s, the critics have urged policymakers to require immediate "open access" to U.S.-funded research.

The Biden administration heeded those pleas, although the new policy does not expressly embrace the term open access—it uses "public access." But it is "de facto an open-access mandate," says Stefano Bertuzzi, CEO of the American Society for Microbiology (ASM), which publishes 16 journals. And many open-access advocates are applauding it.

"This is an enormous leap forward," says Heather Joseph, executive director of the Scholarly Publishing and Academic Resources Coalition, which promotes open access. "Getting rid of that embargo is huge."

The embargo and related policies "were pure sellouts of the public interest," tweeted biologist Michael Eisen of the University of California, Berkeley, a co-founder of the PLOS journals, which helped pioneer an open-access business model in which authors pay a fee to make their papers free. "The best thing I can say about this new policy is that publishers will hate it."

Many publishers say they support a tran-

sition to immediate public access but criticized the policy. "We would have preferred to chart our own course to open access without a government mandate," Bertuzzi says. (Six ASM journals are open access; the rest will follow by 2027.)

The Association of American Publishers, a leading trade group, complained in a statement that the policy arrived "without formal, meaningful consultation or public input ... on a decision that will have sweeping ramifications, including serious economic impact."

Others took a wait-and-see approach. Sudip Parikh, CEO of AAAS, which publishes the *Science* family of journals, says "it is too soon to tell if this guidance will impact our journals." (AAAS publishes the open-access *Science Advances*, and in 2021 its paywalled journals began to allow authors to place the peer-reviewed, near-final version of papers in institutional repositories on publication.)

The impact of the new policy could vary depending on which of the more than 20 U.S. funding agencies underwrites the research. Each agency is expected to finalize its policy by the end of 2024 and implement it by the end of 2025.

The policy is not intended to mandate any particular business model for publishing, says Alondra Nelson, acting director of the White House Office of Science and Technology Policy (OSTP). For example, it will not require federally funded researchers to publish only in pay-to-publish open-access journals. Researchers who publish in subscription journals might be able to satisfy the policy by depositing the near-final, peer-reviewed, and accepted version into a public repository, leaving journals free to keep their final version of a paper behind a paywall. (Some researchers say only that published version is adequate for scholarly purposes. The not-quite-final, "author-accepted" versions often lack some editing, typesetting, and formatted data tables.)

Nelson says OSTP is acutely aware of concerns about who will pay the costs associated with the policy, especially if publishing in pay-to-publish open-access journals becomes a widespread practice. Some fear the U.S. policy—combined with similar policies adopted in Europe and elsewhere—could accelerate the rise of such journals. That could make publishing more difficult for authors with modest or no grant funding, especially ones who work in underresourced institutions and in developing countries.

OSTP wants "to ensure that public access policies are accompanied by support for more vulnerable members of the research ecosystem," it wrote in a blog post. Agencies could, for example, allow researchers to use grant funds to cover publishing costs—as

some do already—or fund the expansion of public repositories. “We’re not naïve about the challenges we face,” Nelson says. “Implementation on any new policy is key.”

Even if the policy induces publishers to make pay to publish their default business model, the cost to U.S. taxpayers to pay open-access fees for all U.S.-funded authors would be relatively modest, according to an OSTP analysis: not more than \$789 million annually, or a half-percent of total federal spending on R&D.

The policy reflects the profound changes that began rocking academic publishing 3 decades ago. Then, subscription-based print journals were the primary means of disseminating research results, and publishers fiercely resisted any policy that threatened an often highly profitable business model. But pressure from university libraries upset by rising subscription fees and patient groups angry about having to pay to read taxpayer-funded biomedical studies helped catalyze efforts to change policy. At the same time, the rise of the internet led to publishing experiments, such as free online journals and the posting of free “preprints” that have not been peer reviewed.

These shifts prompted both Republicans and Democrats to urge the federal government to revise its access policies. In 2013, then-President Barack Obama attempted to strike a compromise—via the 1-year embargo rule—between publishers and open-access advocates.

But many—including Biden—were not happy with that deal. In a 2016 speech, Biden noted, “The taxpayers fund \$5 billion a year in cancer research, but once it’s published, nearly all of that sits behind [pay] walls. Tell me how this is moving the [scientific] process along more rapidly.”

In recent years, pressure for change grew. In 2018, a group of European science funders called Coalition S unveiled a similar open-access policy, which takes full effect in 2025. (Coalition S requires publishers to give up copyright; the U.S. policy does not.) In 2019, the U.S. National Cancer Institute’s “Cancer Moonshot” program, which Biden helped create, required grantees to make papers it funded open access. And in 2020, publishers made all papers related to COVID-19 free to read, at least temporarily.

The U.S. policy will affect a substantial share of the world’s academic literature. In 2020, OSTP estimates federal funding produced 195,000 to 263,000 articles, or some 7% to 9% of the 2.9 million papers published worldwide that year.

Bertuzzi says the policy is likely to have a global impact that will be hard to ignore, because “the U.S. government is the 800-pound gorilla in the room.” ■

ASTRONOMY

Carbon dioxide detected around alien world for first time

Webb telescope discovery offers clue to planet formation and promises insights on planetary habitability

By **Daniel Clery**

Astronomers have found carbon dioxide (CO₂) in the atmosphere of a Saturn-size planet 700 light-years away. The discovery, made by the James Webb Space Telescope, is the first unambiguous detection of the gas in a planet beyond the Solar System and provides clues to how the planet formed. The result also shows just how quickly Webb could identify a spate of other gases that could hint at a planet’s potential habitability for life.

Webb, which started observing in late June, is “ushering in this new era of the atmospheric science of exoplanets,” says Nikku Madhusudhan of the University of Cambridge, who was not involved in the study. “We’re living in revolutionary times.”

Webb’s sensitivity to infrared wavelengths has already brought the universe’s most distant stars and galaxies into view (*Science*, 12 August, p. 700). But the infrared is also critical for researchers studying worlds much closer to home, in the Milky Way. If an exoplanet’s orbit takes it in front of its star, some of the starlight passes through the planet’s atmosphere and picks up fingerprints of its composition. The atmospheric gases absorb specific wavelengths of light, which show up as dips in brightness when the starlight is spread out into a spectrum.

For many gases of interest, the dips occur at infrared wavelengths, which are mostly blocked by Earth’s atmosphere. The Hubble Space Telescope and its smaller infrared sibling, the Spitzer Space Telescope, have detected water vapor, methane, and carbon monoxide around a few hot, giant exoplanets, but little more. Webb promises to reveal many more gases, and around smaller planets: ones between Neptune and Earth in size, and small rocky Earth-like ones, although it is unlikely to be able to confirm the existence of life.

For its first exoplanet observations, astronomers targeted the hot gas giant WASP-39b, which circles its star every

4 days in an orbit much tighter than Mercury’s. Even in raw data based on a single transit across the star, the spectral dip of CO₂ “just popped out,” says Jacob Bean, a member of Webb’s early science team for transiting exoplanets at the University of Chicago. Previous CO₂ detections had not held up, but Webb’s spectrum is beyond dispute, he says. It is “the right size, the right shape, and in the right position.”

He and his colleagues reported the results last week on the preprint server arXiv and their paper has been accepted by *Nature*. In the coming months the team will identify other dips visible in the planet’s spectrum to “make a complete chemical inventory of its atmosphere,” says team member Laura Kreidberg of the Max Planck Institute for Astronomy.

CO₂ is a clue to a planet’s “metallicity.” The big bang produced hydrogen and helium; anything heavier was forged later in stars. Heavy elements are thought to be crucial for creating giant planets. When planets form out of a disk of material around a new star, heavier elements form solid grains

and pebbles that stick together, eventually forming a solid core that is massive enough to grow into a gas giant by pulling in gases with its own gravity.

From the CO₂ signal of WASP-39b, the team estimates that the planet’s metallicity roughly matches Saturn’s. It is also close to Saturn in mass, even though they have wildly different orbits—perhaps a suggestion that WASP-39b formed farther from its star before drifting inward. “Can we find a common story for these two objects?” Bean says. “I don’t know yet.”

With Webb, finding “important chemicals will be the norm rather than the exception,” Madhusudhan says. He predicts that when the telescope starts to study cooler, smaller planets, it will turn up surprises—perhaps gases that are known to play a role in biological processes on Earth, such as methane, ammonia, and hydrogen cyanide. “It’s anyone’s guess,” he says. “A whole zoo of chemicals is possible.” ■

“A whole zoo of chemicals is possible.”

Nikku Madhusudhan,
University of Cambridge



MEDICINE

Researchers tackle vexing side effects of potent cancer drugs

Wider use of checkpoint inhibitor therapy spurs efforts to predict and treat immune complications

By Jennifer Couzin-Frankel

The patient was a success story, his advanced melanoma erased by a popular new cancer treatment. Known as immune checkpoint inhibitors, the drugs coax the immune system to seek and destroy cancer cells—and in this case, they “worked beautifully,” says Kerry Reynolds, an oncologist at Massachusetts General Hospital (MGH) who helped care for the man.

But about a month after an infusion, without a melanoma cell detectable in his body, the 64-year-old was admitted to the hospital, gravely ill. The drugs were sending his immune system into overdrive, wreaking havoc on his colon and nervous system. Doctors struggled for more than 3 weeks to save him, but “he died of overwhelming toxicity,” Reynolds says. She was haunted by his story. “We felt so hopeless.”

Before he died the man implored Reynolds to learn from his experience, and she promised she would. Soon after, in 2017, Reynolds

founded the Severe Immunotherapy Complications Service at MGH, where immunologist and genomicist Alexandra-Chloé Villani took on a parallel research effort; together they aim to treat and study people with immune complications from these breakthrough cancer drugs. The program is now expanding—part of a larger push by scientists around the world. They are launching clinical trials to test treatments for the side effects, turning to computer algorithms to try to predict who’s at risk, and analyzing single cells to parse the biology of these vexing assaults.

Villani, who came to the field after her mother was saved by checkpoint inhibitors but left with arthritis as a consequence, says wider use of checkpoint treatments is making the research more urgent. “We’re curing patients that were incurable a decade ago,” but side effects limit how the drugs can be used.

About 10% of those who get checkpoint inhibitors are hospitalized with immune toxicities. As many as 1% die. A 2021 study suggested that, like Villani’s mother, about 40% of those taking checkpoint drugs de-

Kerry Reynolds is among the researchers studying immune side effects of checkpoint inhibitors.

velop chronic complications, often arthritis or endocrine dysfunction. “When people have 4 months to live, the risk makes sense,” Reynolds says. For less advanced cancers, “the risk profile changes” and doctors crave more information about who stands to benefit.

Today that tension between the drugs’ risks and benefits is especially acute, because 11 years after the first checkpoint inhibitor was approved in the United States for metastatic melanoma they’re being cleared for earlier stages of several cancers, including melanoma, lung cancer, and breast cancer. More than 40% of cancer patients in the United States are eligible to take the drugs, and they constitute a \$30 billion—and growing—market.

The complications superficially resemble known autoimmune diseases, such as hepatitis or colitis, but “the abrupt development is very different,” says Afreen Shariff, an endocrinologist at Duke University. Colon biopsies of patients with drug-induced colitis suggest a mix of overlapping and distinct features compared with biopsies from patients with ulcerative colitis and Crohn’s disease, says Villani, whose lab is studying this biology.

Some side effects are chronic but manageable. Dysfunction in the adrenal gland or thyroid, for example, may be controlled by medicine once a day, says Douglas Johnson, a melanoma oncologist at Vanderbilt University. Others are devastating: The drugs can cause a myocarditis in which the immune system obliterates heart muscle, for example. Although far rarer than many other immune complications, it’s fatal between one-quarter and half the time.

Most patients with immune complications currently receive steroids, a blunt tool that risks interfering with the cancer-directed attack the checkpoint inhibitors are meant to spur—and that don’t always help patients. So, researchers are seeking better countermeasures. In Paris, Sorbonne University cardiologist Joe-Elie Salem has been investigating an arthritis drug called abatacept, which disrupts the activity of T cells, to treat checkpoint-induced myocarditis. Researchers are still trying to determine whether abatacept interferes with checkpoint therapy’s benefits, but in 2019, Salem and colleagues reported in *The New England Journal of Medicine* that a woman with lung cancer and myocarditis was successfully treated with the arthritis drug without suffering tumor progression. Soon after, Salem was a co-author on another paper that described success with abatacept in a mouse model of checkpoint-induced myocarditis. (The senior author on that pa-

per, published in *Cancer Discovery*, was James Allison of the MD Anderson Cancer Center, one of two scientists awarded a Nobel Prize in 2018 for cancer immunotherapy, including checkpoint inhibitors.)

Salem has launched a clinical trial to test abatacept in more patients. Another trial, funded by Bristol Myers Squibb, the maker of several checkpoint drugs (and abatacept), last month began to enroll myocarditis patients. The preliminary abatacept results are raising hopes for more targeted treatment, and the possibility that the biology driving immune side effects can be “decoupled” from the drugs’ ability to combat cancer. If so, managing their hazards without blunting their effectiveness would be far easier.

This is a major focus of the work at MGH, where Villani and her lab members are running a slew of tests on blood and tissue samples from more than 300 (and counting) patients affected by immune side effects. The team hopes to learn which cell populations and signaling pathways are behind the complications in different patients. “We do have some early results suggesting we can decouple” the good and bad sides of checkpoint drugs, Villani says, but the picture is complex. “It’s not the same immune component that’s upregulated in every patient, not even every patient with the same toxicity.”

Such immune signatures might offer an early warning of looming problems before the patient’s health spirals downward. Immune complications can take weeks or even months after treatment to manifest, and symptoms alone aren’t always a good indicator: Early signs can be vague and common among people with cancer, such as fatigue, weight loss, and loss of appetite, Shariff says.

To refine predictions of who’s careening toward serious illness, Shariff has developed an algorithm based on electronic health records data from 5000 patients treated at Duke for checkpoint inhibitor complications. People on the drugs get blood tests every 3 weeks, and Shariff has noted patterns that seem to anticipate toxicities, such as abrupt changes in lab results like liver function. The algorithm also accounts for risk factors such as taking a combination of checkpoint inhibitors, a popular strategy that is often more effective against cancer. Lesser risks may include a history of autoimmune disease.

In the next month, Shariff hopes to put the algorithm to its first real-world test in some of Duke’s cancer clinics. She wants to see whether it correctly predicts brewing toxicities and influences how doctors care

for patients, perhaps enabling them to prevent hospitalizations by starting immune suppression and other treatments sooner. Initially the algorithm will draw on details from a patient’s medical history and lab results, but she hopes with time to incorporate the kind of molecular detail Villani’s lab is studying.

Pinpointing patients at sky-high risk of immune side effects before they get checkpoint drugs is another frontier. In January researchers reported in *Nature Medicine* that in blood taken from advanced melanoma patients before treatment, high numbers of a certain type of memory T cell, among other features, can signal an up to eightfold increase in the risk of severe immune-related complications. The team now plans to enroll 75 cancer patients getting checkpoint inhibitors and follow them, to validate this crystal ball. Combined with emerging data on who is most likely to benefit from checkpoint drugs, especially in an earlier stage of disease, the information could guide treatment decisions.

But Johnson, who is studying various other markers of immune function to see whether they might anticipate side effects, is cautious. “I’m not so convinced we’re going to find a really

good predictive biomarker” that makes forgoing the therapy worthwhile.

Still, with progress on several fronts, “I think that in the next 4 or 5 years, we will have good answers” on how to counsel people about checkpoint therapy, says Jon McDunn, a biomedical engineer in Cary, North Carolina. McDunn is the executive director of Project Data Sphere, a nonprofit that recently worked with MGH and others to help develop definitions of neurologic side effects, and funded a registry to identify affected patients.

In Boston, meanwhile, Reynolds’s program has expanded to 73 doctors and scientists across specialties who meet regularly. Every morning, a smaller subset that includes Villani and some lab members is notified of potential immune complications in MGH’s cancer patients who have agreed to participate in research studies. Funding has been scarce, Reynolds says: “We have done this by Band-Aid and bootstrap.”

About once a month, with permission from the patient before their death and from the family, an autopsy is performed and tissues collected for Villani’s lab. The man with melanoma was the program’s first autopsy, and Reynolds’s promise to him remains fresh in her mind. “We have to get to the bottom of this,” she says. ■

**“We have to
get to the bottom
of this.”**

Kerry Reynolds,
Massachusetts General Hospital

COVID-19

Omicron shots are coming—with lots of questions

Decisions on boosters targeting subvariants will be based on limited data

By **Gretchen Vogel**

For the first time since the start of the pandemic, COVID-19 vaccines look set to receive an update. Boosters reformulated to protect against the Omicron variant, which has dominated globally since early this year, may get deployed on both sides of the Atlantic Ocean as early as this month.

The United Kingdom has already authorized a shot produced by vaccinemaker Moderna against the Omicron subvariant BA.1 and may start using it soon. This week, after *Science* went to press, the European Medicines Agency (EMA) was set to review applications for Moderna’s BA.1 vaccine and another from the Pfizer-BioNTech collaboration.

But BA.1 is no longer circulating; the BA.4 and BA.5 subvariants eclipsed it in the spring. In June, the U.S. Food and Drug Administration (FDA) asked manufacturers to develop a booster specifically targeting those two subvariants, and last week, both Moderna and the Pfizer-BioNTech collaboration said they have submitted data about their BA.4/BA.5 vaccines to FDA. (Pfizer and BioNTech have also submitted the data to EMA; the European Union could first approve a BA.1-based booster and switch to BA.4/BA.5 vaccines later.)

The data on the updated boosters are limited, however, and the impact they will have if greenlit is unclear. Here are some of the questions surrounding this new generation of vaccines.

What do the new boosters contain?

A bit of the old and a bit of the new. Both the Pfizer-BioNTech collaboration and Moderna make their vaccines from messenger RNA (mRNA) coding for the spike protein of SARS-CoV-2. The new vaccines are bivalent. Half of the mRNA codes for the spike protein of the ancestral virus strain



A nurse administers a regular COVID-19 booster in Los Angeles. Omicron boosters may arrive in September.

that emerged in Wuhan, China, in late 2019, which is also in the original shots; the other half codes for the spike protein in BA.1 or the one in BA.4 and BA.5, which have identical spikes.

What sort of data have the companies collected?

Human data are only available for the companies' boosters targeted to BA.1. At a June meeting of FDA's vaccine advisory committee, both companies showed that the shots had side effects similar to those of the original vaccines—including soreness at the injection site and fatigue—and induced strong antibody responses to both the original strain and Omicron BA.1. The companies also showed that the BA.1 vaccines prompted significant antibody responses to BA.4 and BA.5, although lower than that to BA.1.

For the BA.4/BA.5 boosters, the companies have submitted animal data. They have not released those data publicly, although at the June FDA meeting, Pfizer presented preliminary findings in eight mice given BA.4/BA.5 vaccines as their third dose. Compared with the mice that received the original vaccine as a booster, the animals showed an increased response to all Omicron variants tested: BA.1, BA.2, BA.2.12.1, BA.4, and BA.5.

The companies say clinical trials for the BA.4/BA.5 vaccines will begin next month; they need clinical data both for full approval of the vaccines—their recent submissions are only for emergency use authorization—and to help develop future updates. Presumably they will measure re-

cipients' antibody levels, but not the vaccine's efficacy against infection or severe disease. Such trials are very expensive and were not done for the BA.1 shot either.

How can authorities consider authorizing vaccines without data from human trials?

Influenza vaccines are updated each spring to try to match the strain most likely to circulate in the fall and winter. The reformulated shots don't have to undergo new clinical trials unless the manufacturers significantly change the way they make the vaccine. A similar approach for new COVID-19 variants makes sense, says Leif Erik Sander, an infectious disease expert at the Charité University Hospital in Berlin. The changes to the mRNA are minor and providing updated vaccines as quickly as possible is "an ethical issue," Sander says. "We need to allow people to protect themselves from a virus that we can't fully control."

Why do the new vaccines still contain mRNA targeting the ancestral strain, which is long gone?

It isn't entirely clear. Hana El Sahly, a vaccine development expert at Baylor College of Medicine, says she can't see a biological reason to include both versions of spike. In Pfizer's mouse experiments, an Omicron-only vaccine triggered slightly higher antibody responses against Omicron viruses than a bivalent vaccine did. But the limited human data available show no significant difference between the two formulations. However, Angela Branche of the University of Rochester Medical

Center, who leads a study comparing multiple strain-specific vaccines, notes that the next variant to emerge might be more closely related to the ancestral strain than to Omicron, so the bivalent formula could be a useful hedge.

Will the strain-specific mRNA lead to better protection?

That's hard to predict. It depends in part on how much BA.4 and BA.5 are still circulating by the time the shots are delivered and how closely the next dominant strain matches them. It also depends on how many people have immunity from a recent infection.

In a preprint posted on medRxiv on 26 August, mathematical modeler Deborah Cromer at the Kirby Institute of the University of New South Wales and colleagues attempt to calculate the possible impact of strain-specific vaccines. They combined data from eight clinical trial reports that compared vaccines based on the original spike protein with formulations targeted to the Beta, Delta, and Omicron BA.1 strains. The studies all measured the ability of recipients' serum to neutralize virus variants in the lab.

They found that the biggest effect came from administering any booster: On average, an additional dose of a vaccine coding for the ancestral virus' spike protein resulted in an 11-fold increase in neutralizing antibodies against all variants. "Don't throw out all those ancestral-based boosters!" Cromer says. "They can do a good chunk of the work for you."

But strain-specific vaccines improved things slightly. Recipients of updated vaccines had, on average, antibody levels 1.5 times higher than those who received an ancestral strain vaccine. Even if the vaccine didn't exactly match the viral strain, there was still some benefit.

If the benefits are limited, do we really need the new boosters?

Some scientists don't think we do. Paul Offit, a vaccine researcher at the Children's Hospital of Philadelphia, was one of two members of FDA's committee who voted against asking companies to make Omicron-specific boosters. Offit doesn't dispute that the new vaccines will have some benefit but doubts it's worth the additional resources. Current COVID-19 vaccines still prevent the most severe outcomes, Offit says, and if the goal is to stop infections, even updated vaccines will have little impact. But Branche says the broadened immunity that updated vaccines may confer would pay off if new variants emerge. "We need to cover as much of the map as possible," she says. ■

Zimbabwe find illuminates dawn of the dinosaurs

Nearly complete specimen shows earliest dinosaurs needed a temperate climate

By April Reese

During the late Triassic period, when the terrestrial world was a single sprawling land mass called Pangaea, a dog-size plant-eating dinosaur perished near a river in the southern part of the continent. When the river flooded, its body was buried by sediment, with some bones still articulated as in life.

About 230 million years later, paleontologist Chris Griffin, then a doctoral student at the Virginia Polytechnic Institute and State University, spotted a thigh bone sticking out of a hill in the Cabora Bassa River Basin in what is now Zimbabwe. “I’ve got a dinosaur!” he called to his team.

“As soon as I dug that out, I knew that I was holding Africa’s oldest dinosaur,” says Griffin, now a post-doc at Yale University. “I had to sit down and breathe for a minute, because I thought, ‘There could be a lot more [bones] in there.’”

In the weeks that followed, Griffin and paleontologists Darlington Munyikwa and Michel Zondo of the Natural History Museum of Zimbabwe in Bulawayo unearthed a nearly complete skeleton. It turned out to be a new species of early dinosaur: *Mbiresaurus raathi*, which they describe this week in *Nature*.

Though small by dinosaur standards at 1.8 meters long, the find has outsize implications for the early spread of dinosaurs, says Stephen Brusatte, a vertebrate paleontologist at the University of Edinburgh who was not involved in the study. “We’ve known next to nothing about the earliest dinosaurs in Africa,” Brusatte says. “It is one of the most important recent dinosaur discoveries anywhere in the world.”

Until now, the earliest known dinosaurs, also dating to about 230 million years ago, were found in Argentina and Brazil, with a few partial specimens from India. When the continents were gathered together to form Pangaea, those sites all lay at about 50° south, explains Diego Pol, a paleontologist

at the Egidio Feruglio Paleontology Museum in Argentina who was not part of the team. Earth was warmer at the time, lacking icecaps, and climate models suggest that latitude on Pangaea had a wet, temperate climate with hot summers and cool, rainy winters. Researchers have suspected the first dinosaurs needed this type of climate, and that this limited their spread across the supercontinent. But to confirm that idea, they needed dinosaur fossils from other parts of the same climate belt.

and forelimbs, “was just very amazing and exciting,” Munyikwa says. No bigger than a collie, *M. raathi* is named after Mbire, as the region was called during the 16th century Shona Empire, and a pioneering researcher who found fossils nearby. The dinosaur had a long tail, a smallish head, and small, triangular teeth, suggesting it favored plants.

The team also found fragments of bones from a large carnivorous dinosaur called a herrerasaurid, the first discovered in Africa. And it unearthed an array of other animal fossils, too: cynodonts, which are mammal relatives; armored crocodilian relatives called aetosaurs; and archaic reptiles called rhynchoosaurs. Paleontologists have found similar creatures along the same climate band in South America and India.

Taken together, the fossils are the strongest evidence yet that the earliest dinosaurs and their relatives were constrained to a temperate climate belt bordered by arid ones, Pol says. “The assemblage was very similar to that of South America,” he says. Dinosaurs were restricted to their semihumid oasis for a few million years, until the arid regions to the north and south began to become wetter.

The rare find provides a welcome boost to Zimbabwe’s science that Munyikwa hopes will help attract more research funding. “This new species [shows] we have very important deposits,” he says. The fossils are now on display at the Natural History Museum of Zimbabwe and are a point of pride for the community and nation, he says.

The study notes that other specimens likely await discovery across the same Pangaeian climate belt, offering a road map of sorts for other paleontologists on the hunt for early dinosaurs, says Kristi Curry Rogers, a vertebrate paleontologist at Macalester College. “Now it’s time for all the rest of us working in dinosaur paleobiology to get to work and discover some more early dinosaurs.” ■

April Reese is a journalist based in Aveiro, Portugal.



Mbiresaurus raathi, one of the world’s oldest dinosaurs and about the size of an emu, munched plants along a riverbank in the late Triassic period.

Griffin’s team began its hunt with a geological map, tracing a Pangaeian-era latitude line of 50°. They zeroed in on a shallow drainage in northern Zimbabwe where Munyikwa and Zondo knew other fossils had been found. “If dinosaurs are following this climate, then we should be able to find some of the oldest dinosaurs right here in southern Africa,” Griffin says they reasoned. “And we did.”

The *M. raathi* find, which was almost complete save for portions of the skull

FEATURES

A SOMBER SEARCH

Can sophisticated research tools, such as plucking environmental DNA from water and the sea floor, speed the recovery of long-missing soldiers?

By Tess Joosse



As part of an effort to develop environmental DNA into a forensic tool, diver Evan Kovacs photographs the wreck of a World War II plane off the coast of Saipan.

For 3 weeks in June 1944, bombs rained down on the tiny, lush island of Saipan, then an important Japanese stronghold in the western Pacific Ocean. As part of its World War II campaign, the United States had mounted an assault by sea and air. Amid flaming palm trees and churning seas, a sturdy U.S. Hellcat fighter plane and its lone pilot went down in a harbor west of the island. His body was never found.

Nearly 80 years later, on a calm morning in early March, maritime archaeologist Calvin Mires and underwater imaging expert Evan Kovacs dove off a boat anchored in the harbor and swam 10 meters down through the warm turquoise water toward the wreck of the Hellcat.

Another team of archaeologists would later thoroughly excavate the half-buried wreck, seeking the pilot's remains. Mires and Kovacs had a different job: They circled the wreck, collecting plugs of sediment and 6-liter bottles of seawater. They were exploring whether they could detect human DNA seeping out of the crash site and into the environment.

The work of Mires, of the Woods Hole Oceanographic Institution, and Kovacs, of Marine Imaging Technologies, is part of a new collaboration between the U.S. military and outside scientists to apply the tools of research science to help bring missing service members home. More than 81,500 U.S. soldiers are considered missing in action (MIA); their remains lie buried in untold locations worldwide or are interred as unknowns in military cemeteries (see map, p. 1034). About 41,000 of them were lost over oceans and require underwater recovery.

Mires, Kovacs, and others are working to develop environmental DNA (eDNA) into a forensic tool to hasten these slow, daunting underwater missions. After surveying wrecks in the area for nearly a decade, researchers located the Hellcat in 2018 and are still exploring whether it holds remains. An eDNA tool, if it existed, might have sped the search in this and thousands of similar MIA cases.

"Rather than taking out a full team of divers, scouring the wreck, and excavating the site, we could potentially have a much faster way to tell" whether a soldier's remains are nearby, says Kirstin Meyer-Kaiser, a benthic ecologist at Woods Hole and member of the team.

"We are a force multiplier," says Charles Konsitzke, leader of the University of Wisconsin (UW), Madison's MIA Recovery and Identification Project, which is part of the

eDNA project. He and his team are among dozens of scientists and specialists from outside the U.S. government who have teamed up with an arm of the Department of Defense (DOD) called the Defense POW/MIA Accounting Agency (DPAA) to find soldiers still missing from past wars. In other projects, scientists are surveying the sea floor with instruments normally used for oceanographic research and developing artificial intelligence systems to efficiently pick out the shape of a downed plane from a morass of sonar data. Although methods vary, all the efforts share a common goal, Konsitzke says: "to hasten this process and bring more people home."



Charles and Patricia Krueger in 1943 on his family's farm in Monroe, Wisconsin.

A FEW DAYS BEFORE CHRISTMAS 1944, Patricia Krueger received a telegram from the U.S. Army. She hoped it would contain a belated birthday greeting from her husband, Army flight engineer 1st Lt. Charles Krueger, whom she had not heard from in 2 weeks. Instead, the message said he wasn't coming home: His B-29 had been lost over Mukden, Manchuria, and he was later declared MIA. Their son, John Krueger of Middleton, Wisconsin, now 78, still tears up when he recounts this story.

Decades later, the military continues to work to bring back the remains of soldiers like Charles Krueger. The job of finding them falls to DPAA, created in 2015 after critics charged that the previous MIA search process was slow, burdened by bureaucracy, and behind on innovations in science and technology. Between 1973 and 2014, the remains

of only 1849 missing service members were returned to their families, according to DPAA figures, although the pace has ticked up in recent years; in 2021, the agency accounted for the remains of 141 MIAs.

To accelerate the work, Congress gave DPAA the authority to develop public-private partnerships with scientists and groups outside government. "They tasked us with going out there and leveraging the great expertise and interest in the outside world," says military historian Michael Dolski. He oversees about 200 partnerships at DPAA, which has an annual budget of nearly \$130 million.

Teaming up with academic scientists introduces new ways of thinking, Dolski says.

Academics are more plugged into scientific advances and often have more leeway than the government to be flexible and creative, he explains. "Working with partners allows us to tap into their technologies and capabilities in ways that we just can't maintain."

UW researchers, who work on Wisconsin-based cases independently in addition to partnering with DPAA, took up Charles Krueger's case in 2020. His family welcomed the input: Before then, they had only his 1946 casualty file, which the UW team later found conflicted with other historical documents. "There's a lot of uncertainty with DPAA, and often you get radio silence," John Krueger says. (An agency representative says, "DPAA and our partners work at the speed of science and accuracy.")

Each case involves historical research, finding remains, and then identifying them with DNA and skeletal and dental traits. "It's like detective work," Konsitzke says.

In the case of Charles Krueger, the UW team, which includes historians, archaeologists, geneticists, and others, searched military archives and pored over WWII-era photos and video. They discovered contemporaneous Japanese newsreel footage of Krueger's downed B-29. And, wading through documents, they found evidence that remains matching Krueger's were recovered from Manchuria and buried in an unknowns tomb in Honolulu's National Memorial Cemetery of the Pacific. "We wouldn't have gotten any of this without UW," says John Krueger, who has been in touch with the team for every step.

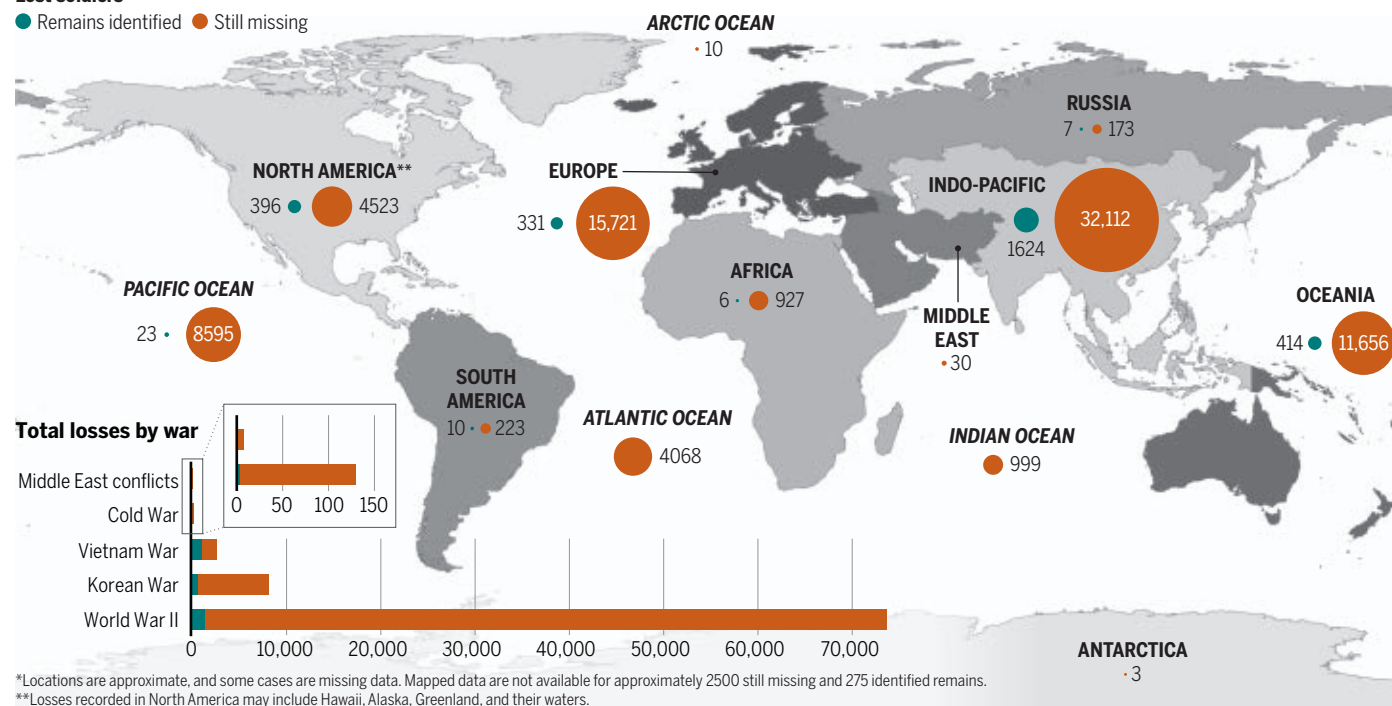
The next move is to exhume and analyze the remains in hopes of making a genetic match to the Krueger family, who have submitted DNA samples. But the unknowns tomb may contain other remains, too, and before disinterment the military requires a means of identifying at least half of all possible people buried in the grave, as well as

Recovering the fallen

More than 81,500 service members from past conflicts around the world are considered missing in action (MIA), most from World War II. To date, the remains of more than 3000 MIAs have been identified by the U.S. government. * Scientists are developing new methods to locate and retrieve others.

Lost soldiers

● Remains identified ● Still missing



approval from a web of federal offices and DOD. UW made the request in late 2021, but the researchers—and the family—are still waiting.

The UW team has had previous successes, for example recovering two WWII soldiers whose aircraft crash sites weren't initially found. Archaeologists walked the French countryside, interviewed eyewitnesses to the crash, and used ground-penetrating radar to find the long-overgrown crash locations. Then they excavated and found the remains.

For the nearly 41,000 U.S. MIAs presumed lost at sea, the historical research is similar. But finding remains underwater requires a specialized suite of scientific tools. For example, in February 2020, scientists from Project Recover—a nonprofit research collaboration between the University of Delaware (UD) and the Scripps Institution of Oceanography—deployed a fleet of torpedo-shaped autonomous underwater vehicles (AUVs), each about as long as a bathtub, off the coast of Vietnam. They were searching for missing Air Force Maj. Paul Avolesse, who had gone down in a B-52 bomber in the region in 1967, according to historical research. The military had searched for his remains since 1993.

The AUVs deployed side-scan

sonar, which shines a “flashlight” of acoustic pulses across the seabed, and magnetometers, which pick up metallic signals. They detected a B-52 wreck and what looked like human remains on the sea floor, and the team's divers and archaeologists brought them up. A DPAA lab later used DNA analysis to confirm they were Avolesse's remains.

Project Recover has found more than 50 other aircraft associated with at least 185 MIAs with these methods, according to the organization's own tallies. “Our ability to locate these is pretty unique,” says Mark Moline, an oceanographer at UD Lewes and Project Recover.

Still, challenges remain. Such underwater

recoveries are logistically challenging and expensive, Dolski says. (A DPAA representative declined to provide an average cost for each mission “as each has unique variables.”) Now, Dolski and others want to use DNA—already vital to identifying remains once found—to more quickly home in on the right spot underwater.

ORGANISMS CONSTANTLY SHED DNA into their surroundings, and a liter of water can yield telltale genetic material from everything from bacteria to blue whales, depending on where the sample was taken. Today, scientists use eDNA extensively to survey biodiversity in rivers, lakes, and oceans, and to detect early clues to invasive species.

“This method is really sensitive and powerful,” says Annette Govindarajan, a biological oceanographer at Woods Hole who uses eDNA to study how organisms migrate up and down the ocean's water column. With eDNA, “we don't even need the animals themselves. It's like ocean forensics.”

In fact, research suggests eDNA could be a useful tool in criminal forensics on dry land. Fungal DNA in dust or plant, insect, and bacterial DNA in soil might reveal where dirt in a suspect's car came from, for example. In 2017, researchers at the



Carrier-based bombers took part in the 1944 invasion of Saipan. Many planes were lost and some of their crews remain unaccounted for.

University of Tennessee found human mitochondrial DNA, which is much more plentiful than nuclear DNA, in the soil beneath four decomposing cadavers, suggesting the method could link a site to a death even if remains have been removed.

But so far, eDNA hasn't been applied extensively to forensic cases, says Kelly Meiklejohn, a forensic scientist at North Carolina State University. "As far as I'm aware, there are no law enforcement labs that do eDNA for casework," she says. And despite eDNA's ubiquity in marine biology, Meyer-Kaiser and Konsitzke say they don't know of any studies using it to detect remains in the ocean.

The team plans to change that. Mires was at an archaeology conference in January 2020 when he ran into his former student Kara Davis, then working at DPAA. They got to talking about the potential of eDNA, with Davis suggesting it could serve as a clue to underwater human remains.

For example, once searchers find the first glimmers of a wreck with sonar, magnetometer, or imaging data from an AUV, scientists could sample nearby water and sediments seeking human DNA. If they get a DNA signal, searchers would have some assurance that remains are present before sending down an expensive and disruptive excavation team. And because wrecks are often partially buried and scattered across the ocean floor, eDNA could help marine archaeologists know where to look.

With eDNA, searchers could impact the environment less. "We also save time and energy [spent] looking in the wrong place," says Hannah Fleming, a maritime archaeologist with DPAA who is coordinating the project.

"It's a really interesting idea," agrees Elena Zavala, a paleogeneticist at the University of California, Berkeley, who has partnered with DPAA on a different challenge: extracting DNA for identification from WWII and Korean War remains coated in DNA-degrading mortuary chemicals. "There's a lot of overlap between ancient DNA and forensic science, and we're just starting to build that bridge," she says.

In her academic research, Zavala and colleagues have detected eDNA from extinct human relatives in cave sediments thousands of years old. By comparison, the decades-old DNA from WWII crash sites seems practically fresh.

But Zavala wonders whether contamination, either from the samplers themselves or a passing scuba diver, could mask the signal of a fallen soldier. She'd also like data on whether human remains in the ocean continue to shed DNA for decades, and whether that DNA is still detectable in water samples.

UW geneticist Joshua Hyman notes that heat and light break down DNA. He says the best bet for preserving it is a cold, dark environment unperturbed by currents—as close to a -80°C freezer as you can get. DNA might degrade beyond recognition in sediment or water from a sunny tropical place such as Saipan. "It would be helpful to do some feasibility testing," Zavala says.

That's why the team visited Saipan's 30°C waters in March. To test detection across environments, they also traveled to the cold, fresh water of Lake Huron in August and will visit milder waters near Palermo, Italy, later this month. At each location they'll sample an area containing confirmed remains, one with possible remains, and one that's empty;

Scientists on the team are also tacking their own research questions onto the work. Meyer-Kaiser, for example, wants to use eDNA to quantify biodiversity at the sampling sites and study how anemones, fish, and other organisms colonize wrecks.

The eDNA work is one part of a "complex toolkit" of underwater innovations DPAA and scientists are working on, Fleming says. Project Recover researchers are pushing the abilities of their AUVs, tinkering with the vehicles and their sensors to survey previously unreachable sites as deep as 600 meters. "Those areas are incredibly difficult to get to, and have not been studied well," Fleming says.

The group is also creating and training a machine learning algorithm they hope will



A 2017 ceremony honored World War II Aviation Radioman Second Class Albert P. "Bud" Rybarczyk, whose crash site in the waters off Palau was located by Project Recover, a collaboration of academic scientists.

together these combinations will help them figure out whether and how eDNA detection works, Fleming says.

In Saipan, UW molecular biologist Bridget Ladell transformed a hotel room into a makeshift lab where the group filtered and packaged the samples on dry ice to ship to Wisconsin, where she extracted the DNA. She'll do the same with sediment and water from Lake Huron and Italy. As of press time, the samples were queued for sequencing on machines nicknamed Bessie, Louise, Valentina, and Willa, in honor of pioneering female aviators. Once the sequence data are available, bioinformaticians will comb through them, looking for human signatures and trying to match them to samples from any remains. The ultimate goal would be to match eDNA data to families and make an immediate identification, but DPAA's Fleming stresses that the research is still exploratory.

be able to sift through the "firehose" of sonar data collected by AUVs to not only identify an aircraft wreck deep on the sea floor, but also discern its make and model. "Within a year we're hoping to have an automated system [that] spits out 20 highlighted areas from an entire mission that we can then examine," Moline says.

For scientists, the work is more than technically satisfying. It's "the most rewarding aspect of my career," Mires says. When diving in Saipan, despite the lagoon's warm water and beautiful scenery, the gravity of the work was top of mind, he says. "In other archaeology sites I've worked on, the history is remote," he says. "Here, you're doing something not for a thing or artifact, but for a person, and all the people they touched." ■

Tess Jooose is a freelance journalist in Madison, Wisconsin.

INSIGHTS

BOOKS *et al.*

FALL BOOKS

Readings for a season of reflection

An evolutionary biologist charts a path toward social justice. A media theorist considers the elites' plans to escape Earth's perils. A bioarchaeologist explores our species' unusually long childhood. An engineer approaches the unseen forces that shape our lives. From a heartfelt homage to cell biology to a vivid history of measurement, the books below invite readers to reconsider how things can and should work. Read on for strategies for better thinking, to challenge your understanding of intelligence, and to learn how parenting changes the brain. —Valerie Thompson

The Song of the Cell

Reviewed by Marie Vodicka¹

Through a series of vignettes peppered with illustrative analogies and vibrant characters, Siddhartha Mukherjee invites readers of his new book, *The Song of the Cell*, on a tour of cell biology from its early origins to its present and future applications. Mukherjee is clear from the start that the book is not a comprehensive history of the field but rather a meandering journey through

selected seminal scientific discoveries.

The book's conversational style draws the reader in, and the text is enlivened by descriptions of major players in the field. We learn, for example, that Frederick Banting—co-winner of the Nobel Prize for the discovery of insulin—devised his key experiment only after experiencing financial difficulties in his medical practice, a broken-down car, and a sleepless night puzzling over a recently published journal article.

While practitioners of biology will recognize many in this cast of characters, from

historical icons to cameos by peers and contemporaries, the book's individual and idiosyncratic descriptions of the scientists and their discoveries are both a strength and a weakness. Such a strategy can help to keep readers engaged, but it can also perpetuate the inaccurate notion of science as a solitary activity, sparked by individual genius.

Traversing millennia and terrain as broad as the 17th-century inventions and observations of Antoni van Leeuwenhoek and Robert Hooke to the 21st-century cells engineered for the treatment of cancer, the book is widely accessible, making ample use of analogies. A signal transduction cascade for cell cycle regulation is described, for example, as a series of molecules bouncing off one another like pinballs. Will nonbiologists grasp every concept presented? Perhaps not, but the book's story line will likely enchant, nonetheless.

The pages sing loudest where Mukherjee's passions evidently lie—blood, the immune system, and cancer treatment. Here, we most intimately understand the author and the joy he has for this subject in reveries to his time spent viewing blood through a microscope: “It is, by far, the favorite time of my day at work,” he writes. “I love looking at cells, in the way that a gardener loves looking at plants—not just the whole but also the parts within the parts: the leaves, the fronds, the precise



smell of loam around a fern, the way the woodpecker has bored into the high branches of a tree. Blood speaks to me—but only if I pay attention.”

Tying together what might otherwise be a disjointed narrative, Mukherjee frequently invokes the patient’s journey. We hear their voices throughout, reminding the reader that however great our knowledge, there is still much to learn.

Near the end of the book, one gets the sense that there is a lot more science crowding in—recent advances and hypotheses—than can be covered. Overall, however, *The Song of the Cell* is a great read with which it is hard not to hum along.

The Song of the Cell: An Exploration of Medicine and the New Human. Siddhartha Mukherjee, Scribner, 2022, 496 pp.

The Mountain in the Sea

Reviewed by Josh Trapani²

David Foster Wallace’s essay “Consider the Lobster” failed to dissuade me from consuming those delicious crustaceans. But

after reading *The Mountain in the Sea*, I may never eat octopus again.

Ray Nayler’s debut is a speculative thriller that engages deeply with ideas about minds and intelligence while balancing great storytelling, complex characters, and lovely writing. The story centers on marine biologist Ha Nguyen, who comes to Vietnam’s isolated Con Dao Archipelago to study its legendary “sea monster”—a large, intelligent, and dangerous species of octopus. Ha’s sponsor, the behemoth artificial intelligence corporation DIANIMA, has purchased the islands, removed the inhabitants, and formed a defensive perimeter to keep outsiders away. The company’s stated motivation is biodiversity protection, but more-mercenary interests—centering on the octopus—soon come to light. Ha’s frustrating first attempts to communicate with the octopuses reminded me of scenes from the movie *Arrival* (itself an adaptation of a Ted Chiang novella). Meanwhile, her only companions on the island are the grim security agent Altantsetseg and the android Evrim, DIANIMA’s crowning and most controversial creation. Other characters’ plotlines intertwine with Ha’s, including those of Rustem, a genius neural net hacker hired by murderous clients, and Eiko, a naïve wannabe DIANIMA employee

who winds up a slave laborer on a giant fishing vessel.

Together, these threads probe themes around the mind. Evrim is blessed—and cursed—with perfect memory, while Eiko creates a memory palace, associating images with places, to protect his own. A variety of intelligences populate the pages. The Con Dao “automonks” exist in meditative semiconsciousness. The “point-fives,” themselves empty vessels, provide emotional support to lonely singles. Even the slave ship’s “Captain Wolf Larsen,” an amoral economic and navigation machine hidden behind armored steel, is intelligent in its own way.

And what of the mysterious octopuses? Using excerpts from Ha’s own (fictional) book, Nayler dives into the concept of “umwelt,” the sensory bubble through which each organism experiences its world. This phenomenon has provided fertile ground for investigation—for example, it was explored by philosopher Thomas Nagel in his 1974 treatise “What Is It Like to Be a Bat?” and by Pulitzer Prize-winning journalist Ed Yong in his 2022 book *An Immense World*.

The octopuses, Ha learns, fashion and use tools—sometimes as weapons to kill people. They create art and symbolic lan-

guage. But Ha's challenge remains daunting. If body and mind are at some level inseparable, how do we communicate with creatures so different from us? The octopus is, as she puts it in one of many beautiful passages, "a mind unbounded by bone—shape-shifting flesh permeated with neural connectivity, exploring its world with liquid curiosity."

As the threads of the story merge, Ha comes to see that only by spurning indifference can she achieve connection and understanding. This fine novel reveals empathy as the lens through which we must consider the octopus—and one another.

The Mountain in the Sea: A Novel, Ray Nayler, MCD, 2022, 464 pp.

Force

Reviewed by **Matthew Diasio**³

In *Force*, engineer Henry Petroski sets out to give a more qualitative, intimate view of physical forces than is typically delivered in an introductory physics or engineering course. Rather than reworking a mechanics class into lessons with less-technical language and fewer formulas, he has created a narrative that reads like a memoir of the physical forces that pervade our lives.

Force is divided into chapters corresponding to different forces and their various applications, with the latter parts of the book generally building on earlier concepts. It begins with simple explanations of individual forces such as gravity, magnetism, and friction and then introduces complex structures, such as buildings, describing the complicated interplay of multiple forces that go into constructing and supporting them. Each chapter presents multiple examples of the phenomenon under discussion, drawn from

Petroski's personal experiences, from relatable instances from everyday life, or from history. These include a recounting of the secret experiments conducted to determine comfort levels in swaying skyscrapers, an analysis of the design of pizza delivery boxes, and an exploration of a theory about the building of the pyramids.

Petroski is a vivid writer who enlivens potentially tedious descriptions of the forces at play in routine activities with sensory detail. For example, when discussing the power of air, he describes how pointing your fingers into the wind can let your hand flex "up and down like a dolphin pacing a boat...in the dry ocean of invisible but sensible wind." However, the book tends to become repetitive when wrapping up a longer discussion, as there are ultimately only so many ways to describe the forces and senses involved.

I also wished the book included more images, which would have helped me to visualize the architecture of buildings with which I was unfamiliar as well as less-routine examples. The book's stock image of a finger trap, for instance, did not add much to the description of its mechanics. And when Petroski described how a similar design is used to align dislocated bones in the thumb, I wondered why this was not shown instead. Similarly, the section on pizza boxes includes an image of the plastic tripods used to stop the lid from collapsing, which (as the book acknowledges) most readers will have seen before, instead of the wilder designs of hybrid pizza utensils.

I generally enjoyed Petroski's descriptions of how things work and that each chapter is a quick, self-contained read. But this brevity can result in strange pacing. The chapter on levers, for example, quickly jumps from scissors to utensils to pencils before settling into a longer discussion on utensils. Earlier chapters may be better for beginners than for someone familiar with mechanics (although I personally loved the friction chapter), but the

breakneck pace of examples may be confusing for some. In the end, however, I admire *Force* for its attempt to immerse readers in the forces shaping our lives.

Force: What It Means to Push and Pull, Slip and Grip, Start and Stop, Henry Petroski, Yale University Press, 2022, 328 pp.

Survival of the Richest

Reviewed by **Carolyn Wong Simpkins**⁴

Having faced a series of increasingly dire existential threats in recent years, we may wonder how the world's wealthiest technology moguls plan to handle the next big crisis. But that would be a mistake, argues Douglas Rushkoff in his new book, *Survival of the Richest*. Not only are they also still working out their own survival plans, most are not planning to help solve climate change, global pandemics, extremist violence, or any other global threat. Quite the opposite, in fact, with many actively engaged in figuring out how to opt out of the next major crisis.

Survival of the Richest reveals fascinating tidbits about the elite tech crowd's post-apocalyptic survival strategies and the niche solutions being marketed to them. We are all familiar with the highly visible race to privately colonize Mars, for example, but do you know where to source, and how best to staff, a high-tech luxury bunker? Or to which social construct you would choose to hitch your free-floating autonomous escape island?

The book's first five chapters may leave the reader with the impression that tech billionaires are knowingly profiting from unspecified activities that accelerate our collective demise, all while inviting experts to help them determine how best to spend their riches to escape from disaster. But beginning in chapter 6, Rushkoff develops a broader thesis, mapping out Western culture's insistence on linear, forward motion, a mindset that dovetails nicely into a financial system structured to require constant, perpetual growth. Our latest technology boom and its leaders are no different from the robber barons of prior eras, he argues, exploiting the latest jump in technology to generate a new burst of growth to feed financial markets, extract the riches, and move on. The next several chapters build on this thesis and illustrate how software achieves a greater escape velocity than previous technologies by decoupling production from physical constraints to a greater extent than ever before possible and by providing the tools through which to live a life largely alienated from others.



Combining art and engineering, Vietnam's Golden Bridge appears to be held up by the hands of a giant.



A rendering of a luxury underground bunker offers a glimpse into the postapocalyptic survival strategies of the elite.

In the book's final chapters, Rushkoff makes an impassioned plea for a more cyclical, steady, and sustainable approach. Here, he introduces the concept of "bounded economics," in which profits are invested back into the community from which they are derived, rather than being extracted to an external entity, as they are when one invests in a stock. This strategy would also remove the option to externalize harms, given that both losses and profits would be accounted for within the system. Groups who find themselves isolated within a larger society, including many Black and immigrant communities, have long practiced such strategies, deploying mutual aid and building circular, cooperative economies to lift up local individuals or enterprises that need financial support.

Rushkoff might consider developing and elaborating on these ideas in his next book. If, that is, the apocalypse doesn't arrive first.

Survival of the Richest: Escape Fantasies of the Tech Billionaires, Douglas Rushkoff, Norton, 2022, 224 pp.

Thinking 101

Reviewed by **Ruthanna Gordon**⁵

Woo-kyoung Ahn's *Thinking 101* offers an accessible explanation of common cognitive biases, how they affect everyday life, and how individuals can mitigate them to improve decision-making. Those already familiar with this area of research will find much to quibble with. Nevertheless, Ahn provides clear explanations of factors that influence cognition and effective shortcuts for enhancing one's mental faculties.

The book's best sections focus on individual errors for which there is rich evidence around solutions. Ahn's discussion

of rumination, for example, lays out simple strategies supported by clinical research.

Ahn is skilled at providing illustrative examples, even while cautioning readers about how example-based thinking can itself be biased. A discussion of overconfidence in perspective-taking is livened by an anecdote about a surprisingly difficult party game wherein couples were asked to verbally describe wines, directing each other to the correct glass using language alone. Most couples waxed poetic and failed miserably. Only Ahn and her husband, aware of their mutual ignorance, succeeded by describing the wines on a scale from least to most sweet.

Ahn tends to overstate the generalizability of her conclusions. The peculiarities of "WEIRD" cultures (Western, educated, industrialized, rich, and democratic populations) go almost unmentioned, and most findings are treated as universal. Optimistic and self-serving biases, for example, certainly deserve the full chapter that is dedicated to them. But such biases are more common in individualist cultures and are subject to variation even there. What should a reader with depression, and its attendant pessimistic biases, take from this chapter? How should a reader from a collectivist culture interpret Ahn's recommendations? Both will learn that humans are "hardwired for optimism." Cultural differences are addressed only toward the end of the book—and only with respect to perspective-taking.

Where the book falls particularly short, however, is in its attempts to address societal problems via individual cognitive limitations. This is not to say that cognitive psychology provides no insight into challenges such as bigotry or climate denial. However, these system-level problems can be addressed only in limited fashion by individuals. The issue is most blatant in the book's discussions of racial prejudice. Although prejudice can in-

deed play out through confirmation bias, suggesting this bias as its primary mechanism is oversimplification verging on insult that does a disservice to research on both cognition and systematic racism.

Four-fifths of the way through the book, Ahn admits that "sometimes the only way to counteract one system is with another—one that is explicitly, consciously, and intentionally designed to protect the greater good." However, this acknowledgment that systemic forces play a role in determining our well-being does not inform the bulk of the text.

Despite these flaws, *Thinking 101* provides evidence-based advice that has real potential to improve lives. Those struggling to make good decisions under the uncertain conditions of a pandemic will find Ahn's references to COVID-19 particularly valuable. However, this is fundamentally a self-help book that is shaped by—and does not mitigate—the individualistic biases to which that genre is prone.

Thinking 101: How to Reason Better to Live Better, Woo-kyoung Ahn, Flatiron Books, 2022, 288 pp.

A Voice in the Wilderness

Reviewed by **Adam R. Shapiro**⁶

In 1988, Joseph L. Graves Jr. became the first Black man to receive a PhD in evolutionary biology. *A Voice in the Wilderness* gives a first-person account of his life, upbringing, education, and activism that reflects a much larger story—concatenating the complex terrains of American racism and working-class poverty, the cultural significance of science, and the network of personal friendships and

relationships that makes survival possible.

By interleaving the personal, political, and scientific, Graves shows that scientific discoveries are inseparable from the social insights that led to them. The effects of caloric restriction on fruit flies, for example, cannot be isolated from concerns over food deserts and access to nutrition that disproportionately affect the impoverished and minoritized in our society. Graves's experiences of racism, whether in the remarks and actions of those who find him in a place they imagine he does not belong or the institutional forms that denied him equal opportunities, are juxtaposed with his explanations of Richard Lewontin's experiments debunking the presumed biological and genetic conception of race and Graves's own subsequent work on the matter.

This serves as a prelude to the second part of the book, in which the man nicknamed "the Black Darwin" turns the full force of his expertise to many of the biological fallacies that continue to pollute political discourse, starting with Graves's refutations of the pseudoscientific racism associated with the 1994 book *The Bell Curve*, which argued that there were essential differences in intelligence between races. Attempts to claim a biological basis for purported differences in intelligence between races have recently been revived under yet further layers of imperial garb. Graves recounts how, decades after his first debates, he has had to delve more deeply into the complexities of biology to unmask the new iterations of pseudoscientific argumentations. Throughout these accounts both personal and political, there is also always the scientific, sometimes lengthy accounts of how genome sequencing works or how algorithms are used to model degrees of genetic difference.

In a chapter on sex and gender, Graves notes Biblical texts about humanity that seem to reinforce a distinct binary. Here, he takes the religious text as uncomplicated evidence of the phenotypical experience of the peoples who created, read, and venerated those texts. There is some reliance on a mythologized history of religious thought that sees the ancients as perhaps more literal and less subtle than they really were. This is largely used to offer contrast to Graves's own understanding of Scripture. He discusses how he went from a childhood belief in the perfection of the Bible to an adolescent atheism to a matured reconciliation of science and religion.

In the culmination of Graves's book is an open acknowledgment of both the possibility and the necessity of social justice. Like some of his own intellectual ancestors, Graves harnesses evolutionary theory to argue that the complexities of multilevel selection make the pursuit of justice "our only hope, not just because it is morally right and long overdue but

because without it our species will die." This is no polemical conclusion but one borne out by all that Graves has shown, in his work in biology and in his own life.

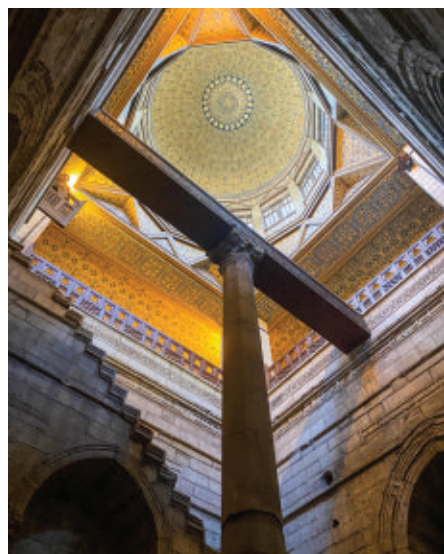
A Voice in the Wilderness: A Pioneering Biologist Explains How Evolution Can Help Us Solve Our Biggest Problems,
Joseph L. Graves Jr., Basic Books, 2022, 384 pp.

Beyond Measure

Reviewed by **David M. Kahler**

In his new book, *Beyond Measure*, James Vincent asks and answers the deceptively complex questions "why is a kilogram a kilogram...Why an inch an inch?" Measurement is so ingrained in our lives, he argues, that most of us do not think about it routinely. Yet measurement is a human invention and thus reflects our priorities and values as well as our blind spots and biases. The success of this book lies in Vincent's ability to connect stories of measurement with human history.

Vincent's journey begins and concludes in Paris with "the" kilogram—*Le Grand K*—"a lump of metal" forged in 1799 and subsequently replaced in 1889 by a platinum-iridium alloy standard. Early standards often took the form of a single object against which all balances were calibrated. Over time, however, the mass of such standards can change as a result of cleaning or handling. By 1988, for example, *Le Grand K* deviated from other standards by as much as 50 micrograms. Thus, in 2019, the International Bureau of Weights and Measures, which oversees the metric system, sought to truly standardize the kilogram, redefining it in terms of the



The Roda nilometer was used by ancient Egyptians to measure the depth of the Nile River.

speed of light and Planck's constant.

Beyond Measure reaches back to ~7500 BCE with the beginning of metrology, the science of measurement, and ends as an expansive treatise on the role of measurement in modern society, approaching the origins of various forms of measurement with regard to their definitions, their utility, and the conflicts that have surrounded them. We learn, for example, that the word "calendar" is derived from the Latin word "calare," which means "to call out," referencing the pronouncements made by early priests announcing new lunar cycles. The "nilometer," meanwhile, was used by ancient Egyptians to measure the flow of the Nile River to judge agricultural water availability. Vincent also introduces readers to historical measurements that were devised for practical purposes, such as units designed to quantify the size of a field on the basis of how long it took to plow, not its area.

Alongside the history of metrology, Vincent presents a chicken-and-egg conundrum: Did writing and measurement enable the establishment of the first governments or were these tools the products of government formation? He reports that the enforcement of verifiable standards has coincided with more cohesive societies in Europe since before the Middle Ages and that the measurement of time became a way for communities to come together in a cohesive unit.

Legal and religious frameworks, such as the Code of Hammurabi, the Talmud, the Mishneh Torah, and the Magna Carta, all acknowledge the importance of measurement and, in some cases, recommend harsh punishments for falsification. However, this has not always stopped those who would deploy measurements to unsavory ends. The intelligence quotient, initially designed to gauge the need for additional attention in school, was given great weight by eugenicists during the early 20th century and was used to justify forced sterilization of humans.

Beyond Measure is a science and technology story, but it also tells a broader tale about humanity's progress and pitfalls throughout history. Measurement, we learn—like art, language, and other forms of human expression—is a powerful tool that reflects how people see and communicate about the world.

Beyond Measure: The Hidden History of Measurement from Cubits to Quantum Constants, *James Vincent*, Norton, 2022, 432 pp.

Mother Brain

Reviewed by **Ilana Goldberg**

Maternal instinct, defined as a rigid, innate sense of how to nurture, is built on a well-

developed narrative that is rarely questioned. This idea, argues Chelsea Conaboy in her book *Mother Brain*, is “about as representative of new motherhood as the someday-your-prince-will-come Disney stories are of dating and marriage.” Science, she argues, tells a different story. Parenting, as evidenced by the data, “is not automatic...instead the parental brain develops through experience.”

In *Mother Brain*, Conaboy delves into the neuroscience of the parental brain, demonstrating that all parents—male and female, biological and nonbiological—experience brain changes associated with caregiving. Mother and baby bonding arises in the responses that they have toward one another as well as through genes and environment. Meanwhile, studies have shown that the brains of fathers who regularly care for their children also change in very similar ways to gestational mothers’ brains.

Conaboy cites research that examined women’s brains before, during, and after childbirth, comparing it with a study that looked for changes in the brains of fathers exposed to infant cues. In both cases, the social and self-referential brain networks were affected. For mothers, a loss of gray matter in specific brain regions was attributed to a fine-tuning of the brain as it adapts to the realities of new motherhood. The study of fathers showed that the superior temporal sulcus is activated, which is implicated in social skills development and the enhancement of predictions. These changes suggest that parenthood helps to extend a caregiver’s sense of self to encompass the child in their care.

Further studies have shown that parental brain changes are permanent alterations and that some may be beneficial to human caregivers. One such study comparing parents and nonparents in midlife found that parenthood was associated with faster response times and better visual memory scores. The performance boosts were greatest for those who had two or three children, and the effect was strongest in fathers.

There is value in researching parenthood, argues Conaboy, who believes that the phenomenon has long been “neglected by science.” This type of work can lead, for example, to science-based social policies that better support families and caregivers.

For new parents who fear they do not have what it takes to succeed, *Mother Brain* offers a science-based reassurance that “unlike a rigid instinct, [parental aptitude] also can be



Parents undergo brain changes associated with bonding and caregiving.

repaired and redirected” by any motivated caregiver. In other words, it is hard work and experience, not an inborn ability, that ultimately makes a good parent.

Mother Brain: How Neuroscience Is Rewriting the Story of Parenthood.

Chelsea Conaboy, Henry Holt, 2022, 368 pp.

Growing Up Human

Reviewed by **Kasra Zarei**⁹

In *Growing Up Human*, bioarchaeologist Brenna Hassett provides a thought-provoking scientific discussion about why humans experience a long childhood, exploring the dynamic evolutionary history of our species, the diversity of ecosystems we inhabit, and parallels that exist between our development and those of other species.

Through the broad lenses of ecology and anthropology, Hassett conveys that raising a child is an investment that requires energetic costs, social capital, and—in the case of recent humans—material wealth. Compared with other animals and with our own ancestors, she notes, modern humans experience a relatively extended childhood, in part because we build the most “expensive” babies we can. One way to buffer the risk of investing so heavily in a single offspring is to ensure that they have sufficient time to prepare for the responsibilities of adulthood.

Hassett writes that childhood is “the long, long intermission between the business of being babies and the business of making

them”—a definition coming from a bioanthropological perspective that understandably does not account for those who cannot or choose not to reproduce—but this length is both changeable and adaptable. Children and their childhoods take different shapes depending on a wide array of factors. Hassett artfully dissects the sometimes-problematic dogma surrounding growth and development, such as whether physical size predicts life span; debunks common myths, such as the idea that the reproductive cycles of women who regularly interact with one another will synchronize; and rejects falsehoods, such as the idea that toxins are produced during the menstrual cycle.

What is the purpose of childhood? In short, argues Hassett, childhood is the period when we learn how to become members of our species. The investments parents make in their offspring are a crucial pillar of our species’ reproductive strategy, and these investments begin in childhood, when we start to cultivate social capital and engage in social learning.

Hassett closes the book with an important question: Does everyone have the same shot at growing up human? Here, she discusses how we live in an unequal world in many respects, noting that nothing says we have to continue living this way. As humans, we have choices, and it is within our power, both individually and collectively, to right the wrongs of our history.

Growing Up Human: The Evolution of Childhood.

Brenna Hassett, Bloomsbury Sigma, 2022, 384 pp.

10.1126/science.ade2368

¹The reviewer is a molecular and cell biologist based in San Jose, CA, USA. Email: mvodicka11@gmail.com ²The reviewer is an editor at *Issues in Science and Technology*, Arizona State University, Washington, DC, USA. Email: jtrapani@asu.edu ³The reviewer is a science policy professional based in Washington, DC, USA. Email: matthew.a.diasio@gmail.com ⁴The reviewer is a physician and molecular biologist based in Washington, DC, USA. Email: carolyndca@gmail.com ⁵The reviewer is at the Applied Research Laboratory for Intelligence and Security, University of Maryland, College Park, MD, USA. Email: rgordon1@umd.edu ⁶The reviewer is a historian of science and religion based in Lancaster, PA, USA. Email: ars45@columbia.edu ⁷The reviewer is at the Center for Environmental Research and Education, Duquesne University, Pittsburgh, PA, USA. Email: kahlerd@duq.edu ⁸The reviewer is a program director based in Bethesda, MD, USA. Email: ilana.goldberg@outlook.com ⁹The reviewer is at the Carver College of Medicine, University of Iowa, Iowa City, IA, USA, and the Department of Global Public Health, Karolinska Institutet, Solna, Stockholm, Sweden. Email: kasra-zarei@uiowa.edu

PERSPECTIVES

MEDICINE

Boosting cognition with a hormone

A hormone enhances cognition in mouse models of Alzheimer's disease and Down syndrome

By **Hanne M. Hoffmann**

As more women conceive later in life, the risk of having a child with a genetic disorder increases (1). Prenatal screening provides the opportunity to discontinue such pregnancies. Despite medical advances that allow early detection of developmental abnormalities in pregnancy, recent changes in abortion access in many US states will soon eliminate this option for millions of women. Combining the reduced access to abortion with the rise in maternal age will undoubtedly lead to more children born with genetic abnormalities, including Down syndrome, which occurs in 1 in 30 pregnancies for women aged 45 (1, 2). Thus, approaches to improve the challenges of living with genetic disorders are needed. On page 1064 of this issue, Manfredi-Lozano *et al.* (3) demonstrate that gonadotropin-releasing hormone (GnRH) improves cognitive function in mouse models of Down syndrome and Alzheimer's disease and in men with Down syndrome.

Down syndrome is characterized by cognitive disability and is often associated with reduced or loss of olfaction. The loss of olfaction in Down syndrome is frequently associated with deficits in fertility, both of which start around puberty. Coexpression of infertility with loss of olfaction is called Kallmann syndrome (4). This is caused by developmental impairments of the olfactory placode, an area in the head that gives rise to the olfactory system and where GnRH-expressing neurons are born. During development, GnRH neurons migrate from the olfactory placode into the brain and locate primarily in the ventral forebrain within the hypothalamus. From the hypothalamus, the majority of GnRH neurons project to the median eminence to release GnRH in a pulsatile pattern, which is re-

quired for GnRH to promote its effects on reproductive function (5).

Throughout life, GnRH release onto the pituitary gland promotes release of the gonadotropin hormones luteinizing hormone and follicle stimulating hormone, which act on the testes in males and on the ovaries in females. Fine-tuning of GnRH release patterns is required throughout life, whereby GnRH release is substantially increased in the pubertal period. After puberty, GnRH continues to promote gonadotropin release, which in adulthood is required for testosterone and sperm production in males and ovarian follicle maturation and ovulation in females. Loss of GnRH or its receptor causes hypogonadism and infertility.

There is also a second population of GnRH neurons in the brain that do not project to the median eminence but in-

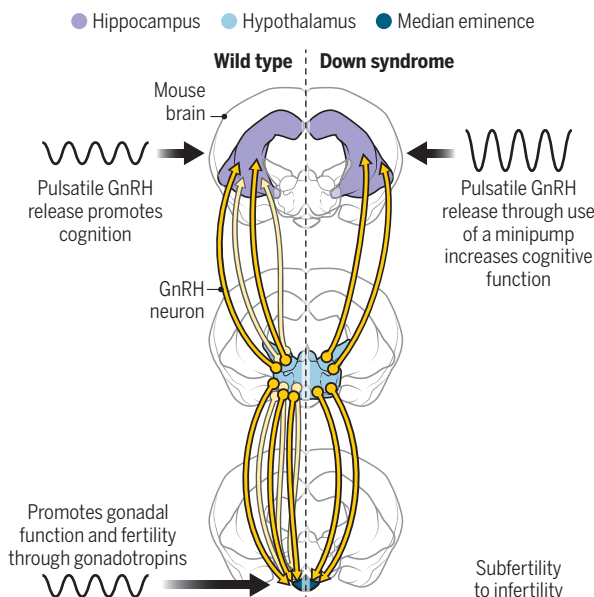
stead project to the hippocampus and cortex, brain structures that are required for learning and memory. The physiological role of this population of GnRH neurons has remained poorly understood (6, 7), but now Manfredi-Lozano *et al.* have found that they are associated with memory and cognition (see the figure). In a mouse model of Down syndrome, giving pulsatile GnRH through a small minipump or restoring the function of the GnRH neuron population that projects to cognitive centers of the brain (such as the hippocampus and the cortex) rescues object recognition memory and olfaction to control levels in both males and females. The treatments also restored luteinizing hormone levels. The value of pulsatile GnRH to enhance cognitive function was not restricted to Down syndrome but was also beneficial in a mouse model of Alzheimer's disease, which also features deregulated GnRH neuron function (8).

Pulsatile GnRH might provide a strategy to enhance cognition. Small minipumps were placed under the skin of seven adult men with Down syndrome. The minipumps allowed timed pulsatile GnRH administration for 6 months, during which time the treatment was well tolerated. Pulsatile GnRH improved working memory, attention, and verbal comprehension. Notably, neuronal connectivity increased in the brain areas that regulate these cognitive skills, including the cortex and hippocampus. However, GnRH treatment did not improve olfaction nor did it change the profile of reproductive hormones, except for a reduction in follicle stimulating hormone, which was close to levels observed in controls after treatment ended. Overall, pulsatile GnRH could be a new treatment to enhance cognitive function for Down syndrome.

The capacity of pulsatile GnRH to enhance cognition in humans was only assessed in men by Manfredi-Lozano *et al.* Owing to

A hormone improves cognition

Most gonadotropin-releasing hormone (GnRH)-positive neurons project from the hypothalamus to the median eminence. They release GnRH in a pulsatile pattern to promote gonadal function and fertility. A subset of GnRH neurons project to the hippocampus where pulsatile GnRH promotes cognitive function, all of which are reduced in Down syndrome. When pulsatile GnRH release is restored, cognitive function, but not fertility, is increased in Down syndrome.



Department of Animal Science, Michigan State University, East Lansing, MI, USA.
Email: hanne@msu.edu

the more complex pulsatile release pattern of GnRH in females, where a burst release of GnRH is required for ovulation, pulsatile GnRH treatment in women of reproductive age might negatively affect their menstrual cycle and ovulation and be incompatible with pregnancy. However, in women who are past reproductive age or who do not want to conceive, pulsatile GnRH is likely to be equally beneficial as it is in men to enhance cognition. To fully establish the value of pulsatile GnRH to enhance cognitive function, a randomized controlled study including both sexes will be required.

These unexpected findings of the cognition-boosting effect of GnRH have broad potential. For example, during menopause, women often report “brain fog,” a symptom caused by changes in the hippocampus associated with the sex steroid estradiol (9). Because estradiol production depends on GnRH regulation of gonadotropin release and menopause slows down GnRH pulse frequency (10), it is possible that the reduced memory and “brain fog” that many women experience during menopause might be prevented by normalizing the pulsatile release of GnRH using implantable minipumps.

Reduced reproductive function later in life is not exclusive to women; men also have altered gonadotropin release with age (11), indicating that GnRH release patterns in aging men might change GnRH pulse amplitude and frequency. If GnRH neurons that project to cognitive centers in the brain lose their capacity to release GnRH at the required level in older adults, pulsatile GnRH might provide unanticipated benefits to slow down cognitive decline. Pulsatile GnRH administration appears to be a promising approach, with few expected side effects, to enhance cognitive function in a broad range of conditions with cognitive decline, which are also characterized by impaired GnRH neuron function. ■

REFERENCES AND NOTES

1. K. T. Jones, S. I. R. Lane, *Development* **140**, 3719 (2013).
2. S. E. Antonarakis *et al.*, *Nat. Rev. Dis. Primers* **6**, 9 (2020).
3. M. Manfredi-Lozano *et al.*, *Science* **377**, eabq4515 (2022).
4. T. S. Han, P. M. G. Bouloux, *Handbook of Neuroendocrinology*, G. Fink *et al.*, Eds. (Academic Press, 2012), p. 597.
5. R. Tsutsumi, N. J. G. Webster, *Endocr. J.* **56**, 729 (2009).
6. A. L. Schang *et al.*, *Endocrinology* **152**, 568 (2011).
7. F. Casoni *et al.*, *Development* **143**, 3969 (2016).
8. S. V. Meethal, M. A. Smith, R. L. Bowen, C. S. Atwood, *Endocr. J.* **26**, 317 (2005).
9. E. G. Jacobs *et al.*, *J. Neurosci.* **36**, 10163 (2016).
10. J. E. Hall, H. B. Lavoie, E. E. Marsh, K. A. Martin, *J. Clin. Endocrinol. Metab.* **85**, 1794 (2000).
11. R. J. Urban, J. D. Veldhuis, R. M. Blizzard, M. L. Dufau, *J. Clin. Invest.* **81**, 1020 (1988).



The amphibian axolotl is known for its regenerative capabilities. Transcriptomic analyses of their brains, and those of salamanders and bearded dragons, are used to understand how tetrapod neuronal cell types evolved.

SINGLE CELL SEQUENCING

A mosaic of new and old cell types

Comparative transcriptomics could reveal patterns of cell type evolution in the tetrapod brain

By Dylan Z. Faltine-Gonzalez and Justus M. Kebschull

Over the past decade, hundreds of cell types have been identified in specialized brain regions of the laboratory mouse. How this staggering diversity of cell types and regions evolved is currently unknown. On pages 1060, 1063, 1061, and 1062 of this issue, Hain *et al.* (1), Woych *et al.* (2), Lust *et al.* (3), and Wei *et al.* (4), respectively, leverage single-cell and spatial transcriptomics in reptiles and amphibians to investigate cell type evolution at the brain scale. Hain *et al.* produce a whole-brain cell atlas of the bearded dragon. Woych *et al.* profile the developing and adult salamander telencephalon. Lust *et al.* and Wei *et al.* tackle the axolotl telencephalon during development and regeneration using complementary single-cell multi-omic and new spatial transcriptomic techniques. Together, these studies reveal that rather than being a set of old and new

regions, vertebrate brains are formed from a mosaic of conserved and new cell types.

Traditionally, brain evolution is studied by identifying homologous brain regions across disparate species on the basis of cytoarchitecture, marker gene expression, and developmental origin. Thus, the brain is often considered a collection of “old” (i.e., shared) and “new” brain regions. The traditional approaches for region comparison do not resolve cell types. Nevertheless, region-level conservation might generalize to the cell type level. Recently, a host of single-cell omics methods have been developed that query gene expression of dissociated single cells and can be applied to any species with an annotated transcriptome or, preferably, an annotated genome. Emerging spatial transcriptomic technologies are also now allowing the interrogation of many genes with high spatial resolution in tissue. These technologies provide the opportunity to systematically compare transcriptomic information across species. Pioneering comparative transcriptomic studies have begun to investigate brain cell type and region evolution in vertebrates outside of the mam-

Department of Biomedical Engineering, Johns Hopkins University, Baltimore, MD, USA. Email: kebschull@jhu.edu

10.1126/science.add9456

malian lineage (5–8), but they have largely focused on individual regions.

Hain *et al.* tested the old versus new brain region and cell type hypothesis by producing a cell type atlas of the brain of the bearded dragon *Pogona vitticeps*, a lizard. When comparing lizard and mouse data, they found that cells from broadly defined brain regions in both species correspond to each other, indicating conserved region-specific gene expression signatures, as expected from traditional methods. These signatures might originate from developmental constraints that are preserved in conserved homeobox transcription factor expression patterns. However, when mapping cell types at higher resolution, the authors observed both similar and very dissimilar cell types across species in almost every brain division investigated (telencephalon, diencephalon, mesencephalon), indicating the intermingling of both highly conserved and species-specific cell types. Although in the telencephalon mostly inhibitory interneurons are conserved, in hypothalamus, tectum, and thalamus excitatory and inhibitory projection and local neurons show evidence of conservation. The existence of conserved and new cell types within conserved brain regions suggests that neuron types are evolutionarily plastic and capable of independently evolving new gene expression signatures and functions within their developmental framework.

These findings resonate with and are extended by the studies of Lust *et al.*, Wei *et al.*, and Woych *et al.*, which focus on the amphibian telencephalon, the part of the brain that in mammals contains the neocortex. They reveal deeply conserved classes of telencephalic inhibitory cells from each of the three developmental origins that have been recognized in mammals. Similar to the findings of Hain *et al.* in bearded dragons and previous findings in turtles (6), conservation of excitatory neurons in the telencephalon is generally lower, suggesting the evolution of new cell types. Nevertheless, broad similarities in gene expression allow both Woych *et al.* and Lust *et al.* to match pallial regions in the amphibian brain to their homologs in reptiles, birds, and mammals.

The intermingling of conserved and new cell types within broad regions challenges the idea of clear-cut old and new regions at the cell type level. Nevertheless, evidence for evolutionary innovation that creates new regions with new cell types and functions is abundant. Woych *et al.* find that salamander (*Pleurodeles waltli*) ventral pallium neurons are homologous to parts of the reptile dorsal ventricular ridge, but no homolog to the excitatory cells of another part of the same structure exists in the salamander.

The mammalian neocortex has no direct match at the level of excitatory cell types in the amphibian. However, cells matching mouse layer 4 neocortical cells seem to emerge with the reptiles. Similarly, Hain *et al.* find evidence of region formation in the amniote thalamus, where medial thalamus appears well conserved between lizard and mouse as is a general mediolateral axis, but specific nuclei and their complement of cell types appear to be evolutionary innovations.

Additionally, the studies of Lust *et al.*, Wei *et al.*, and Woych *et al.* investigate the developmental trajectories of brain regions and cell types observed in the adult. Woych *et al.* note the conservation of transcription factor programs regionally specific to mouse pallium. Similarly, Lust *et al.* identify the gene-regulatory networks underlying the regional diversification of pallial excitatory neurons during postembryonic development in axolotls, and Wei *et al.* examine spatial trajectories during axolotl development. These findings support Hain *et al.*'s proposal that the observed broad region-to-region mapping of neurons across vertebrates is explained by conserved developmental programs. Moreover, Lust *et al.* and Wei *et al.* investigate the ability of axolotls to regenerate their telencephalon after injury. Both identified a distinct wound healing response to damage at the start of regeneration. Subsequently, proliferation and transition to neurogenesis seem to parallel that observed during development, leading to the reestablishment of all previously existing cell types and even long-range connections.

The key to integrating the findings of intermingled old and new cell types and of evolutionary innovation likely rests on two concepts. Regions, like cell types, are thought to be hierarchically organized (9). Therefore, a coarsely defined old region might contain both old and new cell types. When investigated at a finer region resolution, however, these new and old cell types might spatially segregate into evolutionary newer and older subregions that evolved potentially by duplication and divergence of sets of cell types (8). The second concept is that cell classes originating from different developmental niches can have different evolutionary paths and nevertheless intermingle in the adult (6–8). For example, well-conserved telencephalic interneurons migrate during development into divergent regions of the pallium, which results in the intermingling of old and new neurons in the adult.

Like all evolutionary comparisons, comparative transcriptomics must distinguish orthology from convergent evolution. Because transcriptomic space is high dimensional, this is a constant challenge. The

studies of Hain *et al.*, Woych *et al.*, Lust *et al.*, and Wei *et al.* tackle this problem with a remarkable breadth of technology and species comparisons. In particular, Lust *et al.* and Woych *et al.* integrate transcriptomic data with spatial transcriptomics or whole-brain *in situ* hybridization, developmental data, and connectivity data. Wei *et al.* then provide a glimpse into the future of high-spatial resolution comparative transcriptomics by using a new method called Stereo-seq, which allows transcriptome-wide sequencing at subcellular resolution (10). Briefly, thin tissue sections are placed on a special slide with nanoballs of spatially barcoded primers, which are incorporated during reverse transcription and can be used to reconstruct spatial gene expression at micrometer scale after cDNA sequencing. Stereo-seq coverage and depth are sufficient to analyze the spatially collected gene expression data by itself, skipping the usual step of collecting traditional single-cell RNA sequencing in addition to spatially resolved data. This makes the method particularly attractive for nonstandard model systems where animal numbers are limited.

These studies highlight the potential of applying the powerful transcriptomic methods that are usually reserved for mouse to nonstandard models (11). Each of the articles produced massive single-cell and often multimodal datasets and mined publicly available data, showcasing the importance of data sharing and the power of accumulating single-cell data from many species for evolutionary comparisons. They demonstrate that new and old cell types intermingle in broadly defined brain regions. Further studies with increased spatial resolution will be necessary to identify at what level of the cell type hierarchy and region hierarchy this model holds and how evolutionary innovations of brain regions and subregions interface with these findings. Understanding of evolutionary processes is needed both at a level that describes the adult phenotype, which should be most relevant for understanding brain function (12), and at a mechanistic and developmental level. ■

REFERENCES AND NOTES

1. D. Hain *et al.*, *Science* **377**, 1060 (2022).
2. J. Woych *et al.*, *Science* **377**, 1063 (2022).
3. K. Lust *et al.*, *Science* **377**, 1061 (2022).
4. X. Wei *et al.*, *Science* **377**, 1062 (2022).
5. H. Norimoto *et al.*, *Nature* **578**, 413 (2020).
6. M. A. Tosches *et al.*, *Science* **360**, 881 (2018).
7. B. M. Colquitt, D. P. Merullo, G. Konopka, T. F. Roberts, M. S. Brainard, *Science* **371**, eabd9704 (2021).
8. J. M. Keschull *et al.*, *Science* **370**, abd5059 (2020).
9. H. Zeng, *Cell* **185**, 2739 (2022).
10. A. Chen *et al.*, *Cell* **185**, 1777 (2022).
11. J. C. Marioni, D. Arendt, *Annu. Rev. Cell Dev. Biol.* **33**, 537 (2017).
12. N. Jourjine, H. E. Hoekstra, *Neuron* **109**, 1084 (2021).

10.1126/science.add9465



Zannoni *et al.* found that certain chemical reactions that occur in the atmosphere can also be triggered by the human body, albeit at a much smaller scale. These processes may have an outsized impact on the air quality of indoor environments.

AIR CHEMISTRY

The “atmosphere” of the human body

A human-occupied indoor space shares many similarities with Earth and its atmosphere

By **Coralie Schoemaeker**¹
and **Nicola Carslaw**²

The human body is a factory for a variety of chemicals and constantly exchanges molecules with its surroundings. These processes are analogous to what happens in the atmosphere, where chemicals are constantly generated by natural or anthropogenic emissions. In the troposphere during the daytime, emitted gas-phase species such as volatile organic compounds (VOCs) are transformed by reactions that involve the hydroxyl radical ($\cdot\text{OH}$, where the dot denotes an unpaired electron) and generate ozone (O_3). Since the discovery of the role of $\cdot\text{OH}$ in the atmosphere (1), its chemistry has been extensively studied. However, less is known about these reactions on a smaller scale, such as in the air surrounding the human body. On page 1071 of this issue, Zannoni *et al.* (2) report their findings about how the human body generates $\cdot\text{OH}$, with implications for models such as those used to determine indoor air quality.

Understanding the chemistry of indoor air is important because many people spend more time indoors than outdoors and indoor air quality is a public health concern. Chemical processes indoors display similarities to those in the atmosphere but are

subject to enclosed volumes, higher surface-to-volume ratios, lower sunlight levels, and lower exchange rates with air outdoors. Measurements made in indoor environments have shown that indoor air is strongly influenced by human emissions, either from the body (3) or from chemical products (4).

In the atmosphere, $\cdot\text{OH}$ is the key species that drives gas-phase oxidation in the presence of sunlight. It is often called the cleaner of the atmosphere because it breaks down many chemicals. However, there are numerous VOCs that react with $\cdot\text{OH}$ to form a myriad of products, including ozone. In addition, ozone photolysis is one of the main sources of $\cdot\text{OH}$ in the atmosphere. $\cdot\text{OH}$ is also an oxidant, and its reactions with VOCs can lead to the production of even more $\cdot\text{OH}$. Thus, ozone creates $\cdot\text{OH}$, which can then react with VOCs to reform ozone in a nearly endless loop, and the presence of either $\cdot\text{OH}$ or ozone in the atmosphere tends to lead to the other.

To better mitigate and regulate indoor and outdoor air quality, a better understanding of $\cdot\text{OH}$ and its complex chemistry is needed. Since the 1980s, the study of atmospheric $\cdot\text{OH}$ chemistry has progressed through instrumental advances that permit state-of-the-science measurements (5) and atmospheric chemistry modeling (6). The development of instruments that allow the quantification of $\cdot\text{OH}$ in the atmosphere is particularly challenging because of its high reactivity and low atmospheric concentration, and its measurement is prone to in-

terferences from other chemicals that have higher concentrations. However, this challenge has been overcome, partly by including measurements of chemical species involved in the $\cdot\text{OH}$ oxidation cycle and by a better understanding of $\cdot\text{OH}$ reactivity.

In many indoor environments, $\cdot\text{OH}$ formation is dominated by reactions of ozone with alkenes and terpenes, which are emitted by cleaning products (7). The direct measurement of $\cdot\text{OH}$ indoors was reported in 2013, in a study that also highlighted the importance of $\cdot\text{OH}$ formation by photolysis indoors (8). Combining indoor measurements in various conditions with modeling studies has since helped to identify the contribution of different pathways to $\cdot\text{OH}$ formation indoors as well as provide further insight into indoor $\cdot\text{OH}$ chemistry (9, 10).

However, most of these studies share a blind spot—they were performed in the absence of human occupants. Direct human emissions, just like humans, are highly diverse and are influenced by a person's diet, age, activity level, and behavior (11). The human skin itself is a complex matrix of chemical compounds that acts as a reactive surface. For instance, skin oil contains compounds such as squalene and fatty acids that can react with ozone to form a range of carbonyl species (12), some of which are harmful to humans.

Relatively few studies have focused on the role of humans in indoor chemistry (13). Zannoni *et al.* combined measurements and modeling to study $\cdot\text{OH}$ chemistry linked to

¹Université de Lille, CNRS, UMR 8522-PC2A-Physicochimie des Processus de Combustion et de l'Atmosphère, F-59000 Lille, France. ²Department of Environment and Geography, University of York, York, UK.
Email: coralie.schoemaeker@univ-lille.fr

humans in depth. Using a chamber containing occupants and different concentrations of ozone, they measured the reactivity and concentration of $\cdot\text{OH}$ and VOCs inside the chamber. In the absence of ozone, they found that $\cdot\text{OH}$ mainly reacted with the isoprene from human breath, whereas when ozone was present, squalene in skin oil reacted with the ozone to produce species such as 6-methyl-5-hepten-2-one (6-MHO). They also observed that isoprene and products from its reaction with $\cdot\text{OH}$ also react with ozone to produce more $\cdot\text{OH}$. All these observations point to the conclusion that humans are a net source of $\cdot\text{OH}$ indoors. Using a three-dimensional model, the authors simulated the distribution of $\cdot\text{OH}$ around the human body under different indoor conditions. They observed that the human body interacts with the indoor environment in an analogous manner to how Earth interacts with the atmosphere: Both the human body and Earth are chemical reactors, consuming or producing oxidants and oxidized species in their surrounding atmospheres.

Recent research, including that of Zannoni *et al.*, has raised awareness of the need to better understand specific processes that affect indoor air quality. How do human body functions directly influence indoor air, and how does this compare with the activities of humans indoors such as emissions from cooking or cleaning? Furthermore, it is also important to better understand how secondary chemicals and reactions in the indoor environment differ from those that occur in the atmosphere. For instance, it will be interesting to learn whether human emissions indoors interact with chemicals such as the nitrate radical, which is a key atmospheric oxidant during the nighttime outdoors but may be present during the daytime in dimly lit indoor environments (14, 15). These are open questions that need to be answered to better understand indoor air quality to ultimately provide better living and working environments. ■

REFERENCES AND NOTES

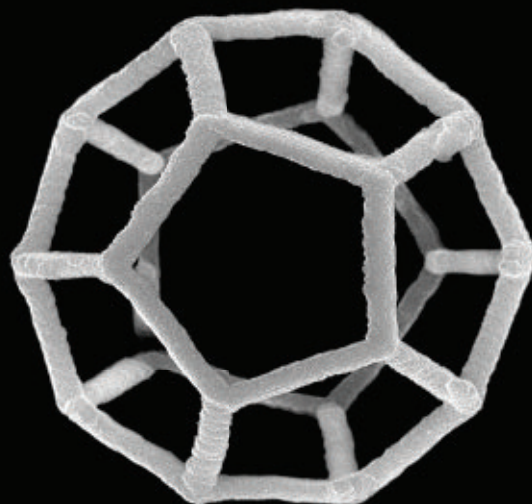
1. H. Levy II, *Science* **173**, 141 (1971).
2. N. Zannoni *et al.*, *Science* **377**, 1071 (2022).
3. N. Wang, L. Ernle, G. Bekö, P. Wargocki, J. Williams, *Environ. Sci. Technol.* **56**, 4838 (2022).
4. A. M. Yeoman *et al.*, *Indoor Air* **30**, 459 (2020).
5. D. E. Heard, M. J. Pilling, *Chem. Rev.* **103**, 5163 (2003).
6. Z. Tan *et al.*, *Atmos. Chem. Phys.* **17**, 663 (2017).
7. C. J. Weschler, H. C. Shields, *Environ. Sci. Technol.* **30**, 3250 (1996).
8. E. Gómez Alvarez *et al.*, *Proc. Natl. Acad. Sci. U.S.A.* **110**, 13294 (2013).
9. M. Mendez *et al.*, *Indoor Air* **27**, 434 (2017).
10. N. Carslaw *et al.*, *Indoor Air* **27**, 1091 (2017).
11. J. Williams *et al.*, *Sci. Rep.* **6**, 25464 (2016).
12. A. Wisthaler, C. J. Weschler, *Proc. Natl. Acad. Sci. U.S.A.* **107**, 6568 (2010).
13. C. J. Weschler, *Indoor Air* **26**, 6 (2016).
14. S. S. Brown, J. Stutz, *Chem. Soc. Rev.* **41**, 6405 (2012).
15. C. Arata *et al.*, *Environ. Sci. Technol. Lett.* **5**, 595 (2018).

10.1126/science.add8461

3D NANOPRINTING

3D-printing nanocrystals with light

Nanocrystals are connected to form complex 3D structures by means of two-photon lithography



By Jia-Ahn Pan and Dmitri V. Talapin

The ability to fabricate custom three-dimensional (3D) objects on demand has revolutionized prototyping and small-scale manufacturing processes. From low-cost filament extruders that a hobbyist can use to replace a plastic battery cover, to laser sintering machines for metal spacecraft parts, the reach of 3D printing technologies in low- and high-end markets continues to broaden. A crucial part of this progress has been the expansion of the library of materials that can be 3D-printed. Nanocrystals have many functional properties, but their integration with 3D printing has been limited, mostly relying on the use of polymer material as a scaffolding. On page 1112 of this issue, Liu *et al.* (1) demonstrate the 3D printing of nanocrystals using a method known as two-photon lithography. The intense beam of an infrared femtosecond laser induces simultaneous absorption of two photons in a very small volume, triggering photochemical reactions at nanocrystal surfaces.

Nanocrystals—nanometer-sized crystals of various inorganic materials—are widely studied as building blocks for functional materials because of their advanced mechanical, electronic, optical, and thermal properties (2). Their surfaces can be made

to repel or attract one another depending on the surface chemistry and external conditions. Thus, they can be suspended in liquids, forming what is known as a colloidal dispersion. Conversely, they can be made to aggregate, precipitating compact solids from the dispersion. This attraction-repulsion property allows for the useful functions of inorganic materials to be combined with the convenience of solution processability. After about three decades of research and development, there are now methods for preparing nanocrystals made of different semiconductors, metals, and many other technologically important materials.

This versatility has enabled nanocrystals to transcend the unfortunate fate of many academically promising nanomaterials that ultimately proved uncompetitive with established technologies in practical applications. For instance, nanocrystals are used as the color component in quantum dot light-emitting diode (QLED) televisions. Nanocrystals have shown impressive performance in optoelectronic components—e.g., in LEDs, infrared sensors, solar cells, smart windows, optical metamaterials, and thermoelectric elements, (3–5). Yet, there still exists a bottleneck for integrating nanocrystals into complex devices. The fabrication of such devices requires precise positioning of nanocrystals with respect to each other, as well as other electronic components.

For planar structures, inkjet printing and direct optical lithography of functional inorganic nanomaterials (6) have

Department of Chemistry, James Franck Institute, and Pritzker School of Molecular Engineering, University of Chicago, Chicago, IL 60637, USA. Email: dvtalapin@uchicago.edu

PHOTO: S.-F. LIU ET AL. (1)

Nanocrystals are 3D printed without the use of a polymer scaffolding.

been used in manufacturing workflows. Optical lithography allows the placing of components with submicrometer resolution, thanks to ideas and tricks borrowed from traditional semiconductor fabrication. However, the arrangement of nanocrystals into arbitrary complex 3D structures has so far been out of reach.

A form of 3D printing of colloidal nanocrystals was demonstrated more than a decade ago (7), but this early approach requires mixing nanocrystals with photocurable organic materials. Exposure to light induces the formation of chemical bonds between the organic components to form the 3D solid while the nanocrystals are simply embedded in the polymer host. Although these hybrids have some useful properties of the organic components (e.g., flexibility), they also inherit less-desirable attributes, such as low electrical conductivity and poor thermal and mechanical stability. The most straightforward route to the fabrication of all-inorganic 3D structures is to use the aforementioned method and then burn off the organic components, as researchers have done through thermal annealing (8). Unfortunately, this high-temperature approach is restricted in chemical scope and induces substantial volume contraction that deforms the printed 3D objects (9). A polymer-free 3D printing approach requires a way to form strong chemical bonds between inorganic components and provide structural integrity without photoactive organic additives.

The study of Liu *et al.* demonstrates a chemical pathway that makes this solidification possible. The authors show that absorption of infrared laser light by cadmium selenide/zinc sulfide core-shell quantum dots or silver nanocrystals leads to the decomposition and detachment of surfactant molecules from the nanocrystal surfaces. This light-induced process triggers a series of chemical transformations that result in the aggregation of the nanocrystals into a densely packed solid with high overall inorganic content. By controlling the path of the focused laser beam, the authors were able to create a fully densified 3D object inside a nanocrystal solution. In their demonstration, sub-100-nm features were successfully printed, which is much smaller than the wavelength of the laser used. Normally, such a high resolution would not be possible because diffraction spreads out even the most tightly focused laser beam into an area comparable in size to the wavelength of the light. To go beyond this limit, the authors use a technique

known as the two-photon absorption process, in which absorption is only possible where the light intensity is at its highest. This shrinks the active volume to a region smaller than the wavelength of the light.

The optoelectronic properties of the quantum dots are preserved during this patterning process. Liu *et al.* also demonstrated the 3D printing of continuous structures made of different material compositions at different points, showing the versatility of this approach. This was achieved by sequential printing with two different nanocrystal solutions.

With a method to 3D print high-quality inorganic structures, future research should explore the patterning mechanism and nuances of the surface chemistry of various nanocrystals. Many questions about the 3D printing of colloidal nanocrystals will need to be answered, such as determining other classes of surface-bound molecules that can similarly detach or decompose upon photo-irradiation. The material properties of these 3D-printed structures, and therefore their utility in fabricating devices with competitive performance, also await characterization. Optimization of the optoelectronic performance of 3D-printed nanocrystals, such as photoluminescence quantum yield and charge mobility, would go a long way in this regard. In a different vein, reducing the minimum light intensity required for 3D patterning would allow this chemistry to be compatible with more cost-efficient 3D printing approaches, such as digital light processing.

The dream of a hobbyist and an engineer alike is a printer that builds complete, fully functional devices with both passive (e.g., casing, wiring, supports) and active components (e.g., sensors, transistors, LEDs) with the press of a button. Liu *et al.* bring this vision one step closer to reality by adding functional inorganic components made of nanocrystals to the library of 3D-printable materials. ■

REFERENCES AND NOTES

1. S.-F. Liu *et al.*, *Science* **377**, 1112 (2022).
2. F. Montanarella, M. V. Kovalenko, *ACS Nano* **16**, 5085 (2022).
3. C. R. Kagan, E. Lifshitz, E. H. Sargent, D. V. Talapin, *Science* **353**, aac5523 (2016).
4. A. Llordés, G. Garcia, J. Gazquez, D. J. Milliron, *Nature* **500**, 323 (2013).
5. P. Losch *et al.*, *Nano Today* **24**, 15 (2019).
6. Y. Wang, I. Fedin, H. Zhang, D. V. Talapin, *Science* **357**, 385 (2017).
7. J.-J. Park *et al.*, *Nano Lett.* **10**, 2310 (2010).
8. F. Kotz *et al.*, *Nature* **544**, 337 (2017).
9. D. W. Yee, J. R. Greer, *Polym. Int.* **70**, 964 (2021).

ACKNOWLEDGMENTS

We thank A. Nelson for helpful suggestions and the National Science Foundation for financial support under award no. CHE-1905290.

METAL FATIGUE

Foreseeing metal failure from its inception

The life span of metals can be inferred from early microscopic deformation events

By Mostafa M. Omar and Jaafar A. El-Awady

In 1842, the axle of a locomotive traveling between Versailles and Paris suddenly snapped, leading to a fiery and fatal crash. Metal fatigue—the weakening and cracking of the material from cyclic loading—was the root cause of this accident. This tragedy likely spurred the first systematic research on this type of material failure (1). Almost two centuries later, metal fatigue remains a constant plague for mechanical systems today. Fatigue can cause failure even if the loads did not result in any macroscopic deformation. This behavior is known to be sensitive to the tiniest defects in the material; hence, an accurate prediction of fatigue failure remains elusive. On page 1065 of this issue, Stinville *et al.* (2) present a physics-informed approach in which the fatigue strength of a metallic material can be predicted from measurements after only a single cycle of loading.

One basic example of metal fatigue is bending a metal paperclip repeatedly until it breaks. If the bent region on the paperclip is carefully inspected before failure, one would notice a change in its surface roughness. This is a manifestation of increased irreversible slip localization on the surface (see the figure), which is induced by the motion of dislocations. In more technical terms, under loading, metals deform by the motion of linear defects known as dislocations, which cause the atoms to slip over each other. Surface slip localizations are stress concentration sites. These locations act as nucleation sites for cracks that can progressively grow with further cyclic loading and eventually lead to failure.

Department of Mechanical Engineering, Johns Hopkins University, Baltimore, MD, USA. Email: jelawady@jhu.edu

10.1126/science.add8382

How metals become fatigued

Stinville *et al.* connect a metal's failure to its first deformation event of a repetitive loading cycle. The results from this study can help better estimate the lifetimes of engineering components. This mechanistic understanding of metal fatigue is visualized here through the repeated bending of a paper clip.

Before loading

Before any loading, the surface of the material is smooth.

First slip localization

After the first loading cycle, atoms slip on each other, and slip bands start to appear on the surface of the metal.

More slip localization

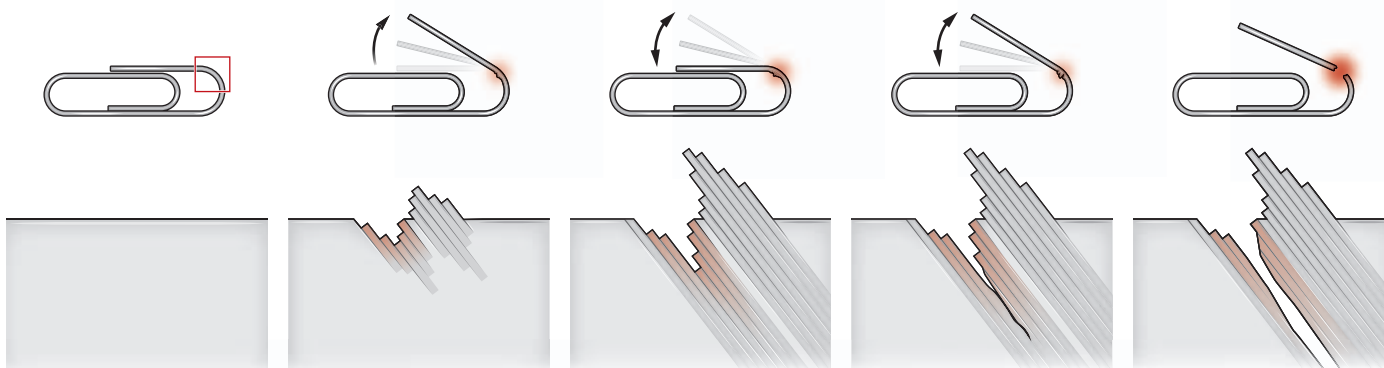
Subsequent loading cycles gradually create a localized concentration of slip bands.

Microcrack propagates

The locations with highest slip band concentration are the most susceptible to separate and form a microcrack.

Total failure

Continuous cyclic loading drives the microcrack to grow and eventually leads to macroscopic structural failure.



Despite this understanding of how metal fatigue happens, most existing approaches for assessing the strength of a specific metal or alloy involve testing samples under different cyclic loading conditions to determine the highest stress the material can withstand for a given number of cycles. This empirical approach is both expensive and time-consuming. Stinville *et al.* tackled the problem from a different perspective. By systematically and experimentally measuring different properties associated with the cyclic loading of metals, they derived a prescriptive theory for metal fatigue. They discovered a correlation between the irreversible slip localization after the first loading cycle and the fatigue strength of different metals. This adds a physical basis to the commonly used empirical laws in the field. The discovered correlation also provides an avenue for predicting the fatigue strength of metals through quantitative and statistical analysis of the localization events that form during early loading cycles.

Although characterizing slip localization during the cyclic loading of metals has been an active research topic for decades (3–6), it has not been quantitatively correlated with fatigue strength. Previous studies have shown that the amplitude of slip localization increases with the number of cycles. After investigating different metallic alloys, Stinville *et al.* showed that the slip amplitude after the first loading cycle is positively and linearly correlated to both the yield strength and the fatigue strength. Yield strength measures how much stress the material can withstand before it permanently deforms, and the fa-

tigue strength measures how many times a certain amount of stress can be applied to the material before it fails. Their observation highlights the impact of these early slip events on the overall fatigue strength. This relationship between slip localization and fatigue damage is also observed in the spatial proximity of slip localization and crack nucleation sites (5, 6). This presents an opportunity for a more accurate and effective pathway for damage mitigation and predicting fatigue life. Extrapolating from what they have discovered, a single loading cycle may be sufficient to meaningfully predict the lifetime of a component.

Several factors can affect the fatigue strength of metals, such as crystal structure, microstructure, processing methods, and intrinsic mechanical properties. The observed correlations by Stinville *et al.* also capture the importance of some of these factors. Specifically, metals with a body-centered cubic structure possess a higher number of possible slip systems compared with that of metals with face-centered cubic or hexagonal-closed pack structures. The structure names are descriptive of how the atoms are stacked inside the metal. Therefore, slip events in body-centered cubic metals tend to be more dispersed but are more localized in face-centered cubic and hexagonal-closed pack metals. Consequently, face-centered cubic and hexagonal-closed pack metals exhibited larger variation in the average slip intensity. This can explain the differences in fatigue life between metals with different crystal structures.

Basquin's law of fatigue has long existed as the standard equation for predicting

the life span of a material under repeated stress, yet it is entirely empirical. The data-driven analysis presented by Stinville *et al.* provides a more mechanistic view of the parameters of Basquin's equation by connecting the fatigue life of metals to both its yield strength and intensity of slip localization. This is a big leap toward a more definite prediction of fatigue strength.

Augmenting statistical and quantitative analysis in studying metal fatigue opens the door to use the advances in machine learning to enhance fatigue prediction capabilities. Furthermore, aerospace engineers tend to set conservative inspection and maintenance schedules to avoid fatigue-related failures; the findings of Stinville *et al.* can act as a blueprint for a new resource-efficient approach for product life estimation. A better understanding of the physics of metal fatigue should lead to more effective safety checks and risk assessments. ■

REFERENCES AND NOTES

1. T. Nicholas, *High Cycle Fatigue: A Mechanics of Materials Perspective* (Elsevier, 2006).
2. J.-C. Stinville *et al.*, *Science* **377**, 1065 (2022).
3. H. Mughrabi, R. Wang, K. Differt, U. Essmann, *Fatigue Mech. Adv. Quant. Meas. Phys. Damage A Conf.* **811**, 1 (1983).
4. H.-S. Ho, M. Risbet, X. Feaugas, *Int. J. Fatigue* **102**, 1 (2017).
5. J. Fathi Sola, R. Kelton, E. I. Meletis, H. Huang, *Int. J. Fatigue* **124**, 70 (2019).
6. S. Lavenstein, Y. Gu, D. Madisetti, J. A. El-Awady, *Science* **370**, eabb2690 (2020).

ACKNOWLEDGMENTS

We acknowledge the support from the Multiscale Structural Mechanics and Prognosis program at the Air Force Office of Scientific Research (AFOSR), grant FA9550-21-1-0028.

Christine Guthrie (1945–2022)

RNA trailblazer who illuminated splicing mechanics

By Suzanne Noble¹, Sean M. Burgess²,
Evelyn Strauss³

Christine Guthrie, molecular geneticist and mentor, died on 1 July at the age of 77. She was a pioneer in the field of RNA splicing, the process by which “nonsense” sequences are removed from eukaryotic messenger RNAs (mRNAs). Christine introduced many fundamental concepts that compose our modern view of this vital cellular activity. Her unerring logic, creative vision, and articulate voice transformed a nascent field and continue to influence the lives of her dozens of trainees.

Born in Brooklyn, New York, on 27 April 1945, Christine was raised by a single mother, writer Irene Kampen. Christine's antics as a young adult inspired several of her mother's comedic novels, including *Life Without George*, which in turn inspired the 1960s television series *The Lucy Show*. Christine earned a bachelor's degree in zoology from the University of Michigan in 1966 and received her PhD in biochemistry from the University of Wisconsin 4 years later. In 1973, she was hired as the first woman and seventh faculty member in the Department of Biochemistry and Biophysics at the University of California, San Francisco (UCSF), where she remained until her retirement in 2014. Christine leaves behind her husband and longtime partner, biochemist John Abelson.

Christine's graduate training with ribosome expert Masayasu Nomura instilled in her a lifelong commitment to drawing the best ideas from across scientific disciplines. Fascinated by a requirement for heat to complete ribosome assembly in the test tube, Christine had a career-defining insight: Perhaps ribosome assembly in cells is also susceptible to getting stuck in the cold. To test this idea, she generated *Escherichia coli* mutants that stopped growing at low temperature and used biochemistry to profile their ribosome assembly. Many mutants accumulated partial ribosomes that

matched the intermediates observed in the test-tube reaction, thereby validating the biological relevance of the pathway inferred from in vitro experiments.

The 1977 discovery of RNA splicing in mammals captured Christine's interest, particularly after it was described in the yeast *Saccharomyces cerevisiae*, a genetically tractable organism. Colleagues doubted that lessons gleaned from a single-celled eukaryote would apply to metazoans, but Christine persevered through years of fruitless experiments to identify yeast versions of the small nuclear RNAs (snRNAs) that are essential for mammalian splicing. Several snRNAs exhibited differences in sequence and size relative to their mammalian counterparts; however, disruption of their genes produced splicing defects and thus demonstrated conservation of function among the evolutionarily distant relatives.

Christine also conducted elegant genetic screens that, paired with rigorous biochemistry, revealed core principles of spliceo-

“Christine energized the entire RNA community with her keen mind and fortitude.”

some function and specific roles of spliceosomal proteins. She discovered that splicing is facilitated by a series of base-pairing interactions among snRNAs and the mRNA substrate, that these interactions occur through massive rearrangements within the spliceosome, and that members of a protein family called DEAH-box RNA helicases ensure that movements occur in the correct order and with high fidelity. This and other work implied that snRNAs serve primarily to catalyze splicing chemistry, whereas proteins safeguard accuracy.

At UCSF, Christine helped to build one of the nation's top biomedical science graduate programs. Her lectures for the foundational course Biological Regulatory Mechanisms captured the power of cross-disciplinary approaches to illuminate the workings of core cellular processes. As her former students dispersed, these lessons worked their way into the practice and pedagogy of modern molecular biology.

We were graduate students in Christine's lab during the mid-1980s and early '90s.

Christine's superpower as a mentor was the ability to trust her trainees, whom she treated as junior colleagues. She demanded independence, diligence, and critical thinking. In return, she offered respect and a safe space to explore unconventional ideas. The result was an uncommonly intellectual and vibrant environment—to the extent that one of us (S.N.) never perceived a lack of support or advice, despite joining the lab while Christine was away on sabbatical. Christine was relentless in attacking scientific problems, and her energy fostered synergistic enthusiasm. One of us (S.M.B.) recalls hours with her at the whiteboard, sketching scheme after scheme until we finally made sense of my puzzling data.

Having contended with overt sexism throughout her career, starting with Nomura's dictum that “girls can't do biochemistry,” Christine resolved to create a nurturing space for students. Many of us were reassured by Christine's acknowledgment of uncertainty and emotional fragility, and she modeled self-care through her attendance at a support group of female scientists that has met for almost 50 years (see the book *Every Other Thursday* by member Ellen Daniell). A cohort of women from our era informally followed her lead. We have retained bonds forged in her lab as we pursue careers in academia, medicine, public health, science writing, and entrepreneurship; true to form, Christine championed scientists' prerogative to take nontraditional paths. In addition to mentoring her own trainees, Christine unofficially “adopted” students and postdocs of other faculty members.

Christine had a droll sense of humor and appreciated absurdity. She merely rolled her eyes, for example, at a mannequin head that we plucked from the street to oversee our warren of tiny rooms, where benchtops overflowed with gel rigs and the crackle of Geiger counters competed with David Bowie. She laughed through viewings of elaborate tribute videos (which included a spoof of Christine set to “She Blinded Me with Science” and a full-length performance of the musical “The Sound of Splicing”). Studying with Christine was serious and seriously fun.

Christine energized the entire RNA community with her keen mind and fortitude. At a gathering to celebrate her retirement, one of us (S.M.B.) led the assembled luminaries and former lab members in a rendition of “Spliceosome” (to the tune of “Edelweiss”). Christine shed tears as she absorbed the warmth and gratitude that rippled through the room. We hope to honor her memory by carrying her example forward. ■

10.1126/science.ade2163

¹Department of Microbiology and Immunology and Division of Infectious Diseases, Department of Medicine, University of California, San Francisco, CA 94143, USA. ²Department of Molecular and Cellular Biology, University of California, Davis, CA 95616, USA. ³Science Communication Program, University of California, Santa Cruz, CA 95064, USA. Email: suzanne.noble@ucsf.edu

An illustration at the top of the page shows four stylized people (two women and two men) working together at a desk. One woman is pointing at a laptop screen. Above them are several speech bubbles and a glowing lightbulb, symbolizing collaboration and ideas. In the center, a large red circle contains the text "Where Science Gets Social." in white.

Where
Science
Gets
Social.

AAAS.ORG/COMMUNITY



AAAS' Member Community is a one-stop destination for scientists and STEM enthusiasts alike. It's "Where Science Gets Social": a community where facts matter, ideas are big and there's always a reason to come hang out, share, discuss and explore.

**Member
COMMUNITY**
AAAS

AMERICAN ASSOCIATION FOR THE ADVANCEMENT OF SCIENCE

POLICY FORUM

AGRICULTURE

Toward product-based regulation of crops

Current process-based approaches to regulation are no longer fit for purpose

By **Fred Gould, Richard M. Amasino, Dominique Brossard, C. Robin Buell, Richard A. Dixon, Jose B. Falck-Zepeda, Michael A. Gallo, Ken E. Giller, Leland L. Glenna, Timothy Griffin, Daniel Magraw, Carol Mallory-Smith, Kevin V. Pixley, Elizabeth P. Ransom, David M. Stelly, C. Neal Stewart Jr.**

Much effort has been expended globally over the past four decades to craft and update country-specific and multinational safety regulations that can be applied to crops developed by genetic engineering processes, while exempting conventionally bred crops. This differentiation made some sense in the 1980s, but in light of technological advances, it is no longer scientifically defensible. In the coming decades, innovations in genetic engineering and modern “conventional” processes of crop development will enable use of these approaches to alter more crops and more traits. Future governance of new plant varieties and foods, regardless of the processes and techniques used to develop them, will require new, scientifically sound assessment methodologies, developed in a manner acceptable to society. Here, we provide a rationale for one governance approach that moves away from current process-based regulation and uses newly developed molecular techniques that enable detailed characterization of the new crops and foods themselves.

CLINGING TO PROCESS

A 2016 report from the US National Academies of Sciences, Engineering, and Medicine (NASEM) on genetically engineered (GE) crops (which we coauthored) stated, “Emerging genetic technologies have blurred the distinction between genetic engineering and conventional plant breeding” [(1), p. 3]. In the past few years, this blurring has increased and resulted in a number of governments struggling to redefine what constitutes a GE plant in need of regulation. Newly enacted and proposed regulations aimed at addressing this problem vary dramatically (2), especially with regard to CRISPR-based genetic changes.

The European Union (EU) considers any crop with a CRISPR-based modification as GE and subject to regulation, whereas other governments, to varying degrees, trigger regulation on the basis of the size of the genetic change and the source of the inserted genetic material (2). A recent EU government study of its regulations for gene editing concluded, “There are strong indications that [EU legislation] is not fit for purpose” and that additional work is needed “in order for the legislation to be resilient, future-proof and uniformly applied as well as contribute to a sustainable agri-food system” [(3), p. 59]. We argue here that the same conclusion is warranted for all current and recently proposed risk assessment systems that use size and source of inserted genetic material to determine the requirement for safety testing.

The recent revision to US government safety regulation of new crop varieties and foods provides an example. Although the United States acknowledges the need to focus on the biological characteristics of new plant products, the reality is that the specific technological approach used to develop the product has generally determined whether a new variety is subject to federal regulation. The 2020 US Department of Agriculture (USDA) rule on plant biotechnology (4) and the proposed rule by the US Environmental Protection Agency (EPA) for pesticidal plants (5) solidify the role of process by exempting from regulation conventionally bred varieties as well as GE plant varieties with new genetic material that could theoretically have been transferred to the variety through conventional breeding (defined broadly to include mutation breeding, embryo rescue, protoplast fusion, and newer techniques).

The assumption is that we have long familiarity with conventional breeding processes and can therefore assume that they are safe. It is noteworthy that the new US rule for labeling GE products (6) does not even define conventional breeding, in part because “attempting to do so may cause confusion in light of the rapid pace of innovation.” That comment makes obvious the logical difficulty with basing regulations on that criterion: There cannot be long famil-

ilarity with something that is rapidly changing. Indeed, major plant breeding corporations are shifting to a new “conventional” approach called genomic selection (7), in which vast, combined, genomic, phenotypic, and environmental databases are used as guides for breeding new varieties with new combinations of genetic materials. Such combinations could not have been produced with conventional breeding approaches that were available when initial regulations to differentiate conventional versus GE crops were developed.

As with conventional breeding, methods for genetic engineering of crops have also changed. The first widely commercialized GE crops in 1996 all involved the transfer of DNA from one or more donor species into a recipient crop (“transgenic”), with the initial placement in the genome being random for the most part. Given the novelty of these crops, there was concern that the engineering would result in unintended changes to the genome that could not be discerned with existing genetic methods but could cause risk to the environment or health. Critics contended that the testing conducted was inadequate to demonstrate that GE foods were safe. At the time, health safety testing for targeted and off-target changes typically involved measurement of approximately 70 plant-produced chemicals and chemical groupings, as well as limited testing on rodents (1). Among the concerns raised were that plants produce thousands of bioactive compounds that were not being monitored, and that unintended changes in these compounds could cause allergies or other illnesses.

Today, genetic engineering technologies based on CRISPR and other site-directed nucleases (SDNs) can substantially alter the properties of a plant by making changes in a single nucleotide in a specific genomic location and by inserting or deleting genetic sequences of varied sizes (2). Arguments have been made that such “gene editing” is in most cases safe and does not require the kind of safety testing that is done with plants developed by using earlier genetic engineering technologies (1). Argentina was one of the first countries to implement legislation that exempts most SDN changes from safety testing (2).

The list of author affiliations is available in the supplementary materials. Email: fred_gould@ncsu.edu

Another factor used by some countries for determining the need for safety testing is whether an inserted DNA sequence comes from a species that could be genetically crossed with the recipient species with natural or advanced laboratory techniques. Such recipient plants would be considered cisgenic, not transgenic. The Canadian regulatory system, which had been strongly focused on the biological properties of the new crop variety and not the process by which it is made, has recently changed course in adopting a new approach in which transgenic origin of the donor DNA is an important criterion (8).

The new USDA rule and those of some other countries assume that a change of one base pair or a deletion of any size could occur naturally and is therefore safe and exempt from regulation. Yet a change could be made in a single base pair to create a stop codon, preventing production of an enzyme that catalyzes a key step in a metabolic pathway. This could result in a desired new trait but also in an unintended metabolic shunt toward greater production of an undesirable metabolite with potentially negative consequences for the environment or human health (9). Under the USDA rule, such a change would categorically be considered less risky than incorporation of a transgene coding for a protein that is metabolically inert in the plant. Thus, a plant rendered nonsusceptible to an herbicide or a plant pathogen through introduction of a transgene is subject to regulation, but a plant made resistant to the same herbicide or plant pathogen by means of a single nucleotide substitution is exempt.

Another assumption of many of the new rules is that genes taken from closely related species are safer to use than those from more distantly related plants. Thus, a genetic sequence for pest resistance moved between two commonly eaten plants (for example, between corn and a cantaloupe) will be considered more of a risk than a pest resistant gene moved into a tomato variety from a wild species of tomato that produces toxic fruits.

These examples illustrate the major contrast between some new and proposed regulations and the 2016 NASEM report finding, “The size and extent of the genetic transformation itself has relatively little relevance to its biological effect and consequently its environmental or food-safety risk” [(1), p. 494]. The changes made

to develop a new cultivar are all aimed at altering a plant’s phenotype through large or small genetic changes. It is unfortunate that these new regulatory policies have synergized with other efforts to characterize CRISPR-based gene editing as safer than approaches that use foreign DNA (transgenics). It is not that CRISPR is inherently unsafe, but rather that this rhetoric contributes to demonization of transgenic methods that could provide us with safer crops and foods if appropriately regulated.

into physical and chemical plant characteristics: (i) genomics, the study of all of an organism’s DNA; (ii) transcriptomics, the measurement of the qualities and quantities of RNAs that are generally translated into proteins; (iii) proteomics, the measurement of the proteins in an organism; (iv) epigenomics, the study of chemical modifications of DNA that affect transcription; and (v) metabolomics, the measurement of the compounds in an organism or tissue that are produced by metabolic processes.

Development of omics technologies for crops has proceeded more slowly than in biomedicine in part because of less funding, the number of species involved, and the large sizes of some plant genomes. Nevertheless, many studies have already been conducted that compare genomes, transcriptomes, proteomes, and metabolomes of GE crop varieties and their non-GE counterparts.

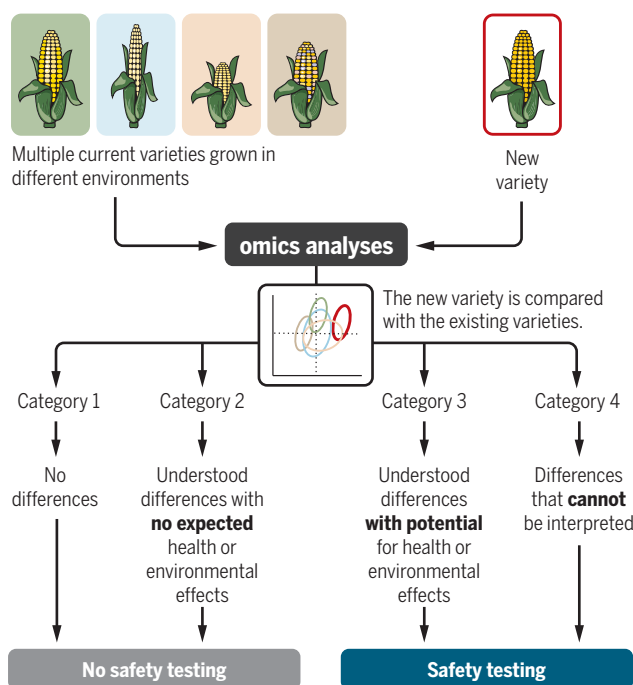
Today, the sample testing costs for off-target changes to the genomes of most major crops are under US\$2000. For another US\$2000 per cultivar, one could generate gene expression profiles of the engineered line with a panel of other existing cultivars. The accuracy and completeness of all omics technologies are advancing rapidly (9, 10). If omics costs continue to fall, 5 to 10 years from now a full omics screen for most crops could cost less than US\$5000.

Genomics could be used to compare the full sequence of a GE plant with that of the specific plant from which it was derived to confirm that no unintended, consequential DNA sequence

changes had occurred. However, as described above, an intended change in a single gene could have unintended impacts on other plant traits, with large and small changes likely to be detected by differences in transcriptomes, proteomes, or metabolomes. The generally accepted approach for these comparisons involves growing, under identical conditions, the GE plant and the plant it was derived from. So, what differences between the pairs of plants would be sufficient to trigger safety testing? Plant genomes are stable when plants are grown in different environments, but other omics measurements are sensitive to environmental conditions. Although a one-on-one test (new variety versus parent) in a single growing environment might demonstrate differences that are of interest

A panel approach, focused on omics

We propose a strategy for evaluating crop varieties using omics technologies [adapted from (1)] to compare a new genetically engineered (GE) or non-GE variety to a set of varieties that are currently in markets.



AN OMICS-BASED APPROACH

As plant breeding technologies evolve, we expect the current regulatory approaches to become even less fit for purpose. A new approach is clearly needed. Here, we outline one path for developing a governance structure for crop and food safety in which the trigger for requiring regulatory testing is based on physical and biological characteristics of new crop varieties and foods that can be measured with the aid of modern molecular technologies.

There have been great advances in GE and non-GE breeding technologies since the first regulations for genetic engineering were developed, but there have been equally important advances in methods for sequencing all of the DNA in a plant and in measuring how that sequence is translated

from an academic perspective, these differences may be within the natural range of variation for varieties within a species, or even for a single variety in multiple environments.

The 2016 NASEM report recognized that the concept of “substantial equivalence” has been used by most regulatory systems to provide assurance to consumers that the composition of the foods from a newly developed variety is equivalent to that of the foods that they had been eating, and so not different in level of risk. Therefore, instead of using omics assessment for one-on-one comparisons, it can be used to determine whether characteristics of the new variety are substantially different from all current varieties, as grown to produce food on grocery shelves across a country. That is, does the new variety have unfamiliar characteristics? This approach could be used for new varieties developed with GE and non-GE methods, and efforts could be focused on the omics of the produce from the varieties.

With this in mind, the 2016 NASEM report proposed an approach in which the omics characteristics of the new variety are compared to a panel of existing commercial varieties (1). The assessment would result in the new variety classified into one of four categories (see the figure). New plants assigned to categories 1 and 2 would be exempt from safety testing, whereas those in categories 3 and 4 would be tested. Here and in the report, we only provide a broad outline of this approach to kindle more detailed conversations about it, and consider other ways to move away from process-based regulation.

ROBUST, TRUSTED STRUCTURE

Researchers understand current technical limitations of omics tools for plants and recognize that new research must be done to overcome these limitations (1, 9–11). Much greater public investment in this area will be needed. Both scientific and societal factors must guide the research. For example, what size and kind of differences between new and existing crop varieties would be substantial enough to trigger regulatory testing? Such questions are not easy to answer but are categorically similar to difficult regulatory questions about what levels of partially understood, environmental pollutants are acceptable.

These types of questions cannot be addressed solely by product developers and regulators, as was done with the first GE crops that resulted in a long-term backlash from members of the public. Diverse members of the public must be included in these deliberations (12). A number of pro-

cesses have been used by social scientists to better involve the public in such deliberations, and all have been found to have limitations (13). Nevertheless, a carefully developed but imperfect process is much more likely to have a positive outcome than one that pays lip service to public consultation. A long-standing issue is that different governments have adopted different approaches. An international process that involves all parties to the Cartagena Protocol on Biosafety (14) would be beneficial, even if difficult.

Recognizing that these new measurement technologies could be used in ways that would over- or underregulate new crops and foods (9–11), we see the need for a multistep process to develop a new, overall approach for governance of new crop varieties and foods. National and international governance bodies are likely to cling to current approaches and legal obligations, so this effort cannot simply

“...national and international governments will need to make decisions that will be unwelcome to some constituencies...”

wait for their leadership. If this process is started now, a structure could be in place before a proliferation of new varieties are ready for commercialization. First, we suggest international workshops of breeders, chemists, and molecular biologists to provide a range of potential options and costs for development of omics methods for major, minor, and orphan crops that would be both accessible and accurate. These options could then be discussed at subsequent workshops that involve policy-makers, regulators, developers, public stakeholders, and natural scientists. Social scientists should be centrally involved in workshop design and implementation (13). In the end, national and international governments will need to make decisions that will be unwelcome to some constituencies, but rigorous and transparent deliberations now can produce new rules with greater public and scientific legitimacy than that of the current rules.

We realize that there are important issues related to the use of GE crops and foods unrelated to health and environmental safety, such as cultural questions about what constitutes naturalness, ethical questions about intellectual property rights, and concerns about corporate control over plant genetics.

In the past, power dynamics caused these societal concerns to become entangled with claims about health and environmental safety (15). Although a robust, trusted structure for assessing safety will not resolve culture- and market-based questions and debates, it should help to disentangle these issues. The omics approach presented here could serve as a basis for developing such a new structure. If instead we continue to maintain scientifically unsupportable regulatory frameworks, we can expect that the status quo of split public and government opinion about the safety and value of GE foods will persist. ■

REFERENCES AND NOTES

1. National Academies of Sciences, Engineering, and Medicine, *Genetically Engineered Crops: Experiences and Prospects* (National Academies Press, 2016).
2. J. Entine *et al.*, *Transgenic Res.* **30**, 551 (2021).
3. European Commission, “Study on the status of new genomic techniques under Union law and in light of the Court of Justice ruling in Case C-528/16” (2021); https://ec.europa.eu/food/system/files/2021-04/gmo_mod-bio_ngt_eu-study.pdf.
4. USDA Animal and Plant Health Inspection Service, *Fed. Regist.* **85**, 29790 (2020).
5. EPA, “Pesticides; Exemptions of certain plant-incorporated protectants (PIPs) derived from newer technologies” (2020); https://www.epa.gov/sites/production/files/2020-09/documents/10014-10-prepub-fr-doc-admin_esignature2020-08-31.pdf.
6. USDA-NMS, *Fed. Regist.* **83**, 65814 (2018).
7. R. K. Varshney *et al.*, *Trends Plant Sci.* **26**, 631 (2021).
8. Canadian Food Inspection Agency, “Draft guidance for determining whether a plant is subject to Part V of the Seeds Regulations” (2021); <https://inspection.canada.ca/about-cfia/transparency/consultations-and-engagement/share-your-thoughts/draft-guidance/eng/1619540046303/1619540212691>.
9. E. M. A. Enfissi *et al.*, *J. Plant Physiol.* **258–259**, 153378 (2021).
10. R. F. Benevenuto, H. J. Venter, C. B. Zanatta, R. O. Nodari, S. Z. Agapito-Tenfen, *Trends Food Sci. Technol.* **120**, 325 (2022).
11. R. A. Herman *et al.*, *GM Crops Food* **12**, 376 (2021).
12. D. R. Gordon *et al.*, *Nat. Biotechnol.* **39**, 1055 (2021).
13. J. S. Dryzek *et al.*, *Science* **363**, 1144 (2019).
14. Cartagena Protocol on Biosafety; <https://bch.cbd.int/protocol/post2020/framework.shtml>.
15. F. H. Buttel, *Env. Polit.* **14**, 309 (2005).

ACKNOWLEDGMENTS

Some of the ideas for this article emerged from discussions during deliberations of the NASEM Committee on Genetically Engineered Crops: Past Experiences and Future Prospects. K.E.G. is a member of the Sustainable Sourcing Advisory Board of Unilever and of the Scientific Advisory Committee of the African Plant Nutrition Institute. R.A.D. holds patents in the field of metabolic engineering for improvement of forage crops and has received funding for research on the above topic from GrasslaNZ Technologies, New Zealand, and Forage Genetics International, USA. C.N.S. and C.R.B. hold patents in plant biotechnology. C.M.-S. has received research funding from agricultural companies and has been retained by counsel for defendants as an expert in litigation related to glyphosate-based herbicides.

SUPPLEMENTARY MATERIALS

science.org/doi/10.1126/science.abo3034

10.1126/science.abo3034

LETTERS



Barn owls (*Tyto alba tuidara*) in Patagonia may be exposed to harmful anticoagulant rodenticides through their prey.

Edited by Jennifer Sills

Test Patagonia's raptors for rodenticides

Thousands of owls and other predators die each year globally after eating rodents that have been poisoned with anticoagulant rodenticides (ARs) (1–3). In Andean Patagonia, where wilderness areas coexist with human settlements (including tourist destinations), ARs are unregulated and routinely used to prevent human contact with rodents (4, 5). This strategy puts raptors in the region at risk and may be the cause of mass mortality events. However, because testing for ARs is difficult, the extent of ARs' effects on raptors and other wildlife remains unknown. Given their potential for harm, it is crucial to test for ARs, especially when raptor mass mortality events occur, and to enact policies that regulate their use.

In Patagonia's forests, the periodic mast seeding of bamboos triggers rapid increases in rodent populations, and owls and other predators are drawn to the affected areas due to increased prey (6, 7). Because the rodents are hosts of the zoonotic ANDV (Sur), a hantavirus lethal for humans (7), local inhabitants fear that the surge in rodents will increase hantavirus transmission. In response, people buy and use massive amounts of ARs without the supervision of any governmental or scientific authorities. At the peak of these rodent influxes, numerous dead owls and other raptors are commonly recorded (7).

The cause of massive owl mortality events in Patagonia is unknown, but secondary poisoning by ARs is one likely explanation given their effects on wildlife elsewhere (1–3). Despite the possible harm caused by

ARs, toxicology laboratories in Argentina do not test for them, and restrictions due to sanitation concerns prevent the exportation of fresh tissue samples to overseas toxicology labs (2). Without a way to identify ARs locally or through international collaboration, no relevant data can be collected to determine whether they are the cause of death.

We urge Argentine and other South American wildlife and health authorities, and the scientific community, to strengthen local capacities to test for ARs. Evidence from both veterinary and human medicine indicates that this problem affects other nontarget subjects in addition to predators, with the same analytical limitations (5, 8). Protecting environmental, wildlife, and human health in the region requires surveillance and well-enforced regulations of AR use.

Miguel D. Saggese¹, Pablo Plaza², Laura Casalins³, Gala Ortiz⁴, Valeria Ojeda^{3*}

¹College of Veterinary Medicine, Western University of Health Sciences, Pomona, CA 91766, USA.

²Grupo de Investigaciones en Biología de la Conservación, Laboratorio Ecotono, Instituto de Investigaciones en Biodiversidad y Medioambiente, Universidad Nacional del Comahue—Consejo Nacional de Investigaciones Científicas y Técnicas (CONICET), Bariloche, Argentina. ³Instituto de Investigaciones en Biodiversidad y Medio Ambiente, Universidad Nacional del Comahue—CONICET, Bariloche, Argentina. ⁴College of Veterinary Sciences, La Plata University, La Plata, Argentina.

*Corresponding author.

Email: valeriaojeda@comahue-conicet.gob.ar

REFERENCES AND NOTES

1. S. M. M. Nakayama *et al.*, *J. Vet. Med. Sci.* **81**, 298 (2019).
2. E. A. Gomez, S. Hindmarch, J. A. Smith, *J. Rap. Res.* **56**, (2022).
3. J. E. Elliott *et al.*, *BioScience* **66**, 401 (2016).
4. "Listado de Insecticidas y Raticidas," Administración Nacional de Medicamentos, Alimentos, y Tecnología Médica (2021); www.argentina.gob.ar/sites/default/files/anmat_listado_de_insecticidas_y_raticidas_actualizado_al_20-9-21.pdf.
5. A. I. Gallardo Ferrada *et al.*, *Acta Tox. Argentina* **23**, 44 (2015).
6. V. Ojeda, L. Chazarreta, *Aust. Ecol.* **43**, 719 (2018).
7. R. D. Sage *et al.*, in *The Quintessential Naturalist: Honoring the Life and Legacy of Oliver P. Pearson*, D. A. Kelt *et al.*, Eds. (University of California, Berkeley, CA, 2007), pp. 177–224.
8. M. F. Lugo, *Acta Tox. Argentina* **27**, 60 (2019).

10.1126/science.ade2357

Denmark passes total ban of leaded ammunition

The use of leaded ammunition has caused collapses of raptor populations worldwide due to secondary lead poisoning (1–3). In Europe, lead kills millions of wild birds each year, and the losses in biodiversity, environmental health, and socio-economic activities are estimated to be more than 1 billion EUR (4). There is no tolerable lead intake for humans (5). In June, Denmark took an important step to address the harm caused by lead: The country will ban the use of all kinds of leaded ammunition for hunting as of April 2024 (6).

Denmark is the first country to enact a total ban on leaded ammunition. The country's previous ban on lead gunshot pellets led to a substantial decline in lead concentrations in game meat over the past 2 decades (7). In contrast, lead in game meat has increased in European countries with no or only partial restrictions on lead ammunition. In these countries, mean concentrations of lead in small game meat between 2011 and 2021 are 14 times higher than the thresholds used in EU-wide risk assessments (7).

Denmark's action should serve as a model. The European Union has proposed a phase-out of leaded gunshot pellets in wetlands by 2023 (EU Regulation 2021/57) and is considering restricting all leaded ammunition in other types of hunting and sport shooting, with a decision expected in

2023 (8, 9). Other countries should do the same. We urge governments, hunters, and conservationist organizations to collaborate and convince their members and industries to phase out the use and production of leaded ammunition worldwide. More public awareness campaigns highlighting the contamination risks from game meat harvested with lead ammunition could help to build the public will to act (10). Only a global One Health approach can mitigate the environmental threats from lead on wildlife and humans (11, 12).

Christian Sonne^{1,2*}, Douglas H. Adams³,
Aage K. O. Alstrup⁴, Su Shiung Lam⁵, Rune Dietz¹,
Niels Kanstrup¹

¹Department of Ecoscience, Aarhus University, Denmark. ²Sustainability Cluster, School of Engineering, University of Petroleum & Energy Studies, Dehradun, Uttarakhand 248007, India. ³Cape Canaveral Scientific, Melbourne Beach, FL 32951, USA. ⁴Aarhus University Hospital, Aarhus University, Aarhus, Denmark. ⁵University Malaysia Terengganu, Terengganu, Malaysia.

*Corresponding author. Email: cs@bios.au.dk

REFERENCES AND NOTES

1. V. A. Slabe *et al.*, *Science* **375**, 779 (2022).
2. D. Méndez *et al.*, *Science* **371**, 1319 (2021).
3. B. Helander *et al.*, *Sci. Tot. Environ.* **795**, 148799 (2021).
4. D. J. Pain, R. Mateo, R. E. Green, *Ambio* **48**, 935 (2019).
5. European Food Safety Authority, "Lead dietary exposure in the European population" (2012); www.efsa.europa.eu/en/efsajournal/pub/2831.
6. Danish Environmental Protection Agency, "Denmark is the first country in the world to ban lead in rifle ammunition for hunting" (2022); <https://mst.dk/service/nyheder/nyhedsarkiv/2022/jun/bly-bliver-forbudt-til-riffeljagt-i-danmark/> [in Danish].
7. D. J. Pain, R. E. Green, M. A. Taggart, N. Kanstrup, *Ambio* **51**, 1772 (2022).
8. European Chemicals Agency, "Lead in shot, bullets and fishing weights" (2022); <https://echa.europa.eu/hot-topics/lead-in-shot-bullets-and-fishing-weights>.
9. G. Treu, W. Drost, W., F. Stock, *Environ. Sci. Eur.* **32**, 68 (2020).
10. V. G. Thomas, D. J. Pain, N. Kanstrup, R. Cromie, *Eur. J. Environ. Public Health* **6**, em0110 (2022).
11. J. M. Arnejo *et al.*, *EcoHealth* **13**, 618 (2016).
12. A. Gerofke *et al.*, *PLoS One* **13**, e0200792 (2018).

10.1126/science.ade3150

Rapid loss of China's pollinator diversity

Pollinators play an irreplaceable role in ensuring food security and maintaining ecosystem stability. Worldwide, 87.5% of angiosperms, more than 70% of crops, and more than 35% of food production depend on animal pollination, primarily by insects (1–3). However, pollinator populations and diversity are declining across the globe (4). The situation is particularly dire in China, where the distribution areas of the two most important indicator species, *Apis cerana* Fabricius and *Bombus chinensis*, are rapidly decreasing (5–8). If China does not take steps to address the threats to pollinators, their

decline could lead to systemic ecological risks and food shortages.

In southwestern China, monoculture planting of rubber trees has caused the total number of bee species in the rubber plantations to drop from 34 to 7, a decrease of 79% (8). In addition, pesticides that seriously threaten bees, such as imidacloprid, have been used intensively throughout the country (9). Several highly invasive nonnative bee species, such as the western honey bee (*Apis mellifera*), risk outcompeting native bees for food (5). Land use changes and climate change pose additional challenges (5).

Only five known pollinator species in China have been included in the List of State Key Protected Wild Animals (10), accounting for less than 2% of the total number of remaining pollinator species in China (11). China's National Forestry and Grassland Administration and its Ministry of Agriculture and Rural Affairs should add all pollinators deemed at risk by the International Union for Conservation of Nature Red List of Threatened Species to the national Key List as soon as possible. Key List recognition would provide government protection and enforcement to the pollinators and their habitats. China should also compile and publish a new Red List of threatened pollinators that could serve as a basis for establishing cross-regional nature reserves and protecting the habitats and migratory passages of migratory species. Finally, policies should be put in place to ensure that nonnative bees do not undermine the protection of native bees.

Fang-Zhou Ma, Chen-Bin Wang, Yan-Jing Zhang,
Peng Cui, Hai-Gen Xu*

Nanjing Institute of Environmental Sciences,
Ministry of Ecology and Environment, Xuanwu,
Nanjing 210042, China.

*Corresponding author. Email: xhg@nies.org

REFERENCES AND NOTES

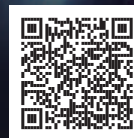
1. R. Aguilar, L. Ashworth, L. Galetto, M. A. Aizen, *Ecol. Lett.* **9**, 968 (2006).
2. J. Ollerton, R. Winfree, S. Tarrant, *Oikos* **120**, 321 (2011).
3. D. Kleijn *et al.*, *Nat. Commun.* **6**, 7414 (2015).
4. Intergovernmental Science-Policy Platform on Biodiversity and Ecosystem Services, "The Assessment Report of the Intergovernmental Science-Policy Platform on Biodiversity and Ecosystem Services on Pollinators, Pollination and Food Production" (2016).
5. J. L. Teichroew *et al.*, *Biol. Conserv.* **210**, 20 (2017).
6. G. H. Yang, *Apic. Chin.* **70**, 18 (2019).
7. D. R. Yang, *Chin. Biodivers.* **7**, 170 (1999).
8. Z. H. Xie, "The effect of anthropogenic disturbance on diversity of bumblebees (*Bombus* spp.) in Sichuan, China," PhD dissertation, Sichuan University, Chengdu (2008).
9. B. B. Li, *Apicult. Chin.* **67**, 31 (2016).
10. National Forestry and Grassland Administration, Ministry of Agriculture and Rural Affairs of the People's Republic of China, *Chin. J. Wildl.* **42**, 605 (2021).
11. J. X. Huang, *Biodiv. Sci.* **26**, 486 (2018).

10.1126/science.ade2089

NEWS FROM Science



Subscribe to **News from Science** for unlimited access to authoritative, up-to-the-minute news on research and science policy.



bit.ly/NewsFromScience

RESEARCH

IN SCIENCE JOURNALS

Edited by Michael Funk



FOREST ECOLOGY Forests at risk

Climate change is having negative effects on forests through extreme heat, drought, and disturbances. Predicting the impact of future climate change on forests is challenging because each approach relies on assumptions and incomplete data. Anderegg *et al.* compared results from three major modeling approaches that provide information on different facets of risk: a global mechanistic

vegetation model, which estimates forest carbon loss; a climate envelope model, which provides information on species shifts; and empirical assessment of forest loss to disturbance using satellite imagery. These approaches provide complementary information but highlight the high overall risk to forests in the southern boreal, dry tropics, and central Europe. —BEL *Science*, abp9723, this issue p. 1099

A climate risk analysis highlights threats to global forests, particularly in the tropics and in boreal forests such as the one pictured above.

CANCER IMMUNITY

Hormone hampers cancer immunity

Cancer immunotherapy has made great progress in recent years, but many tumors do not respond to any of the available immune treatments for reasons that are often unclear. Among other factors, the neuroendocrine system has been emerging as a potential influence on anti-tumor immune responses. Xu *et al.* examined the connections between hypothalamic-pituitary signaling and antitumor immunity, focusing on the role of α -melanocyte-stimulating hormone (α -MSH), which is

produced by the pituitary gland. α -MSH promoted the accumulation of immunosuppressive cells, and its inhibition helped to suppress tumor growth in mouse models, suggesting it as a potential therapeutic approach. —YN

Science, abj2674, this issue p. 1085

PHYSIOLOGY

Long live the queen

A trade-off between reproduction and life span occurs across most living organisms. An exception is insects such as ants, in which reproductive activity is limited to one or a few “queens” that live much longer

than nonreproductive “workers.” Studying a pseudo-queen state of the ant *Harpegnathos saltator*, Yan *et al.* found that the insulin and insulin-like growth factor signaling pathway was activated to promote reproduction, which also shortened life span. The authors propose that one branch of this pathway, mediated by the protein kinase Akt, is suppressed in the fat body and some ovarian tissues. Increased production of a protein that binds insulin-like molecules in the hemolymph might account for the difference that allowed the longer life span of the pseudo-queen. —LBR

Science, abm8767, this issue p. 1092

MULTIFERROICS

Chasing a multiferroic pattern

Multiferroic materials are often characterized by two coupled order parameters, magnetization and electrical polarization, which can be controlled by external fields. Hassanpour *et al.* studied the multiferroic $\text{Dy}_{0.7}\text{Tb}_{0.3}\text{FeO}_3$, which has an additional order parameter stemming from in-plane antiferromagnetic ordering. The researchers created a ferromagnetic multi-domain pattern and applied an external magnetic field, which erased the existing pattern but created one of the same shape

in the system's polarization, minimizing the free energy. The process could be reversed by applying an electric field. —JS
Science, abm3058, this issue p. 1109

ORGANIC CHEMISTRY

Squeezing nitrogen into indole

Numerous pharmaceutical compounds contain five- or six-membered rings composed of carbon and nitrogen. Chemical reactions that interconvert these motifs can therefore be very helpful during drug development research. Reisenbauer *et al.* present a method to insert a nitrogen atom into the five-membered rings of silyl-protected indoles, thereby expanding them into six-membered quinazoline or quinoxaline compounds depending on their substitution pattern at the outset. The chemistry relies on nitrene generation using hypervalent iodine and is compatible with many common functional groups. —JSY

Science, add1383, this issue p. 1104

CANCER THERAPY

Breaking down resistance to degraders

Drugs called PROTACs trigger the degradation of target proteins and have many potential uses, including in the treatment of cancer. However, Kurimchak *et al.* found that cancer cells developed resistance to PROTACs like they do to other anticancer drugs. The drug efflux protein MDR1 mediated resistance to PROTACs that target proteins in the KRAS pathway. In cultured cells and mouse models, drug resistance was prevented by combining PROTACs with lapatinib, which inhibits epidermal growth factor receptors and MDR1. The findings suggest that PROTACs should be explored as a combination therapy with lapatinib, which is already clinically approved for some cancers. —LKF

Sci. Signal. **15**, eabn2707 (2022).

DEVELOPMENTAL BIOLOGY

Foundation for finch flamboyance

Finches have a deeply conserved template of cellular and genetic factors in their skin that underlies their extraordinarily diverse color patterns. Hildago *et al.* investigated the cellular origins and patterns of gene activity in deep layers of the skin in finches with different patterns of plumage coloration. Despite dramatic differences in adult appearance, there are common patterns of gene activity in different parts of the skin. Different species mask or form specific colors in each domain, resulting in the evolutionary diversity seen in finches. These conserved landmarks in early development may serve as the basis for major trends in the evolution of bird plumage. —NS

Sci. Adv. 10.1126/sciadv.abm5800 (2022).

MOLECULAR BIOLOGY

Enhancer network interprets disease risk

Many important genes in human cells have multiple enhancers, noncoding DNA elements that regulate gene expression. It has been a puzzle why many enhancers exist and how they work together over long genomic distances. Combining multiplexed CRISPR interference and machine learning, Lin *et al.* reveal that multiple enhancers form a nested, multilayer architecture that is important to maintain robust gene expression. Enhancers that are far away (more than 1 million bases) cooperate in three-dimensional space and act as synergistic regulators of gene expression when being perturbed. Their long distance reduces co-mutagenesis and confers a mechanism of robustness. The authors built a model to predict enhancer variants that synergistically control disease-relevant genes, which better links multiple noncoding elements to disease risk prediction beyond genome-wide association studies. —DJ

Science, abk3512, this issue p. 1077

IN OTHER JOURNALS

Edited by **Caroline Ash**
and **Jesse Smith**

Jumping spiders, like the one shown here sleeping upside down, display retinal and muscle twitches indicative of a REM sleep-like state.



SLEEP

Do spiders dream?

Anyone who has watched a sleeping dog “chasing rabbits” will be familiar with the characteristic twitching that occurs during rapid eye movement (REM) sleep. Sleep, or a sleep-like state, occurs across many different animal taxa, including arthropods and perhaps even cnidarians, but we do not know whether invertebrates have the capacity to dream. Rößler *et al.* noticed REM-like muscle twitching during what appeared to be sleep in a jumping spider. Further, although spiders cannot move their eyes, they can move their retinas. The authors showed that the muscular twitching movements were associated with retinal eye movements in these spiders, as would be expected in REM sleep, indicating that this sleep stage may be widely distributed among animals. —SNV

Proc. Natl. Acad. Sci. U.S.A. **119**, e2204754119 (2022).

SOIL MICROBIOTA

Little fleas have lesser raptors

If left undisturbed, arid soils develop a surface biocrust of photosynthetic microorganisms. These biocrusts contribute not only to carbon and nitrogen fixation, but also to erosion resistance, and they also moderate surface temperatures. From soil restoration

work, Bethany *et al.* discovered that their cultured cyanobacteria were subject to a devastating predator provisionally named *Candidatus* Cyanoraptor togatus. Evidence of attack by this predator can be seen as plaques of bare soil left after it has infected a biocrust. The organism is a nonmotile bacterium that relies on motile prey species to glide within range of ambush. Then predatory



HUMAN GENETICS

Humans adapted to Peruvian ecoregions

Over the course of 50,000 years, humans left Africa and expanded to many environments around the world. These migrations resulted in exposure and adaptation to selective pressures. Caro-Consuegra *et al.* analyzed genetic data from 196 Peruvian individuals from three ecological regions: the Andean highlands, the arid coast, and the Amazon rainforest. They found that Andean highlanders experienced selection of genes affecting heart function, hypoxia, and other systems affected by living at high altitudes. By contrast, the coastal and rainforest populations both showed population-specific selection in different aspects of the immune system. These findings show the strength of selection toward local adaptation even in populations that are geographically close. —CNS *Mol. Biol. Evol.* **139**, msac158 (2022).

Human populations in the Peruvian Andes (pictured here is Laguna Paron) have accumulated genetic adaptations to high elevation over thousands of years.

cocci dock onto the cyanobacteria surface, invade cells, and develop thread-like structures enveloped by a “cocoon.” Infected cells are stripped of macromolecules and left as ghosts, but not before having traveled and spread the predator in their wake. —CA *Nat. Commun.* **13**, 4835 (2022).

BATTERIES

A temperature problem

“All-solid-state” battery is an umbrella term for a next-generation battery system that does not contain any liquid components. This type of battery has a decisive advantage over the current industry standard, lithium-ion batteries, which are associated with the challenge of safely containing their highly flammable liquid electrolyte.

However, Yoon *et al.* found that one candidate for such an all-solid-state battery, the $\text{Li}_6\text{PS}_5\text{Cl}$ -based system, suffers major degradation after being exposed to elevated temperature ($70^\circ\text{C}/158^\circ\text{F}$) for just a few days. The electrolyte-cathode interface becomes porous during this exposure due to SO_x gas evolution when the battery is charged, which increases the interfacial resistance and lowers battery performance. —YY *Appl. Phys. Rev.* **9**, 031403 (2022).

NEUROETHOLOGY

Sea squirts swim in six styles

Nervous systems process sensory input into behavioral responses. The building blocks of locomotory responses are

organized like the rules that govern language, but we do not understand how they have evolved. Invertebrate chordates are closely related to vertebrates, and Athira *et al.* reasoned that studying the swimming behaviors of the tadpole-like larva of the simple chordate *Ciona intestinalis* could be informative. The tadpole’s nervous system has fewer than 250 neurons to analyze. Most of the postural variance in *Ciona* tadpoles can be explained by six basic shapes that combine in different proportions to produce almost 97% of their postures during swimming. The study provides a new model system with which to identify the evolutionary constraints and flexibility of behavioral organization. —DJ *PLoS Biol.* **20**, e3001744 (2022).

PARENTS AND CHILDREN

Parental competition skews toward sons

Parents’ preference for competition for their children influences children’s pursuit of an academic track in school, with implications for outcomes later in life. Tungodden and Willén integrated administrative data with experimental data from Norwegian students and parents. Before the students performed a task, they and their parents were separately asked whether the child should be paid under a competitive or noncompetitive scheme. Parents chose competition for sons more than daughters, but this parental perspective narrowed the gender gap compared with children’s own perspective. This gender gap was similar for mothers’ and fathers’ choices, although mothers were less likely than fathers to choose competition. —BW

J. Polit. Econ. **10.1086/721801** (2022).

WATER ELECTROLYSIS

 H_2O_2 from water and oxygen

Hydrogen peroxide (H_2O_2) is one of the most important inorganic chemicals and is a well-known oxidizing agent. Its industrial applications include chemical synthesis, detergent production, paper bleaching, textile, pulp, and many others. H_2O_2 is environmentally friendly but its production is not: A lot of carbon dioxide is released when generating molecular hydrogen gas in steam methane reforming, one of the first steps in the auto-oxidation process (also called the Riedl–Pfleiderer process) predominantly used to synthesize H_2O_2 . Huang *et al.* report an alternative, promising H_2O_2 synthesis route based on a hydrogen-permeable gold–palladium membrane reactor that uses electricity to drive the hydrogenation of oxygen and water to H_2O_2 and operates at ambient conditions without using hydrogen gas. —YS

J. Am. Chem. Soc. **144**, 14548 (2022).

ALSO IN *SCIENCE* JOURNALS

Edited by Michael Funk

NEUROEVOLUTION

Lizard traces in the mouse brain

Although lizards and mammals share common evolutionary roots, their pathways to today diverged hundreds of millions of years ago. Using single-cell transcriptomics, Hain *et al.* compared the brain of the lizard *Pogona vitticeps*, known as the Australian dragon, with that of the mouse (see the Perspective by Faltine-Gonzalez and Kebschull). They found that certain neuronal identities, marked by what transcription factors they express, are conserved from lizard to mammal, and others show evidence of evolutionary innovation. Therefore, the mammalian brain is an interwoven tapestry of new and ancestral traces. —PJH

Science, abp8202, this issue p. 1060
see also add9465, p. 1043

HEART DISEASE

A heartfelt collaboration

Historically, researchers trying to understand and treat cardiac diseases have primarily focused on cardiomyocytes and approaches to replace them after injury. However, the heart is also home to multiple other major cell types, such as fibroblasts, endothelial cells, and immune cells, as well as their surrounding extracellular matrix. Tzahor *et al.* reviewed these different components of the cardiac microenvironment, their contributions in a healthy state and in the setting of disease, and their relevance for potential therapeutic interventions. —YN

Science, abm4443, this issue p. 1059

NEUROEVOLUTION

Trade-offs in brain development

Salamander brains share some, but not all, structures with the mammalian brain. They also have greater capacity to regenerate

in response to damage. Three groups now come together with single-cell transcriptomics analyses that set the salamander brain in evolutionary context (see the Perspective by Faltine-Gonzalez and Kebschull). By comparing salamander brains with those of lizard, turtle, and mouse, Woych *et al.* track the evolutionary innovations that gave rise to the mammalian six-layered neocortex, which salamanders do not have. Lust *et al.* take a close look at why the axolotl brain is so much more capable of regeneration than is the mammalian brain. Finally, Wei *et al.* compare the developmental and regenerative processes in the axolotl brain. —PJH

Science, abp9262, abp9444, abp9186, this issue p. 1061, 1062, 1063; see also add9465, p. 1043

NEURODEVELOPMENT
Intervention for Down syndrome

Down syndrome (DS), the result of trisomy of chromosome 21, carries a suite of symptoms including intellectual disability and loss of olfaction. Manfredi-Lozano *et al.* recognized a similarity between some of the DS symptoms and those seen in patients with a deficiency of gonadotropin-releasing hormone (GnRH) (see the Perspective by Hoffmann). Indeed, analysis of a mouse model of DS showed deficits in GnRH expression. Interventions that restored physiological GnRH levels in the mouse DS model also improved cognitive deficits. In a preliminary clinical trial in patients affected by DS, pulsatile GnRH therapy improved cognition. —PJH

Science, abq4515, this issue p. 1064; see also add9456, p. 1042

METALLURGY

Slipping into fatigue

Materials that are cyclically deformed become easier to break due to fatigue. However,

tying fatigue strength to microstructure has been challenging. Stinville *et al.* used nanometer-resolution digital image correlation to observe the slip localization on the surface of a wide range of alloys (see the Perspective by Omar and El-Awady). They found that after one deformation cycle, the amplitude of the early slip localization events determines fatigue strength. This observation helps to provide a physical basis for well-known fatigue laws and paves the way to easily predicting fatigue strength. —BG

Science, abn0392, this issue, p. 1065; see also add8259, p. 1047

INDOOR AIR QUALITY
Radical development

Hydroxyl radicals (OH) are highly reactive species that are responsible for the oxidation of most pollutant gases. Outdoors, OH radicals are formed primarily by the photolysis of ozone by short-wavelength sunlight, but that light is largely filtered out by glass windows, so what is the indoor OH radical environment like? Zannoni *et al.* report that high concentrations of OH radicals were found when people were exposed to ozone in a climate-controlled chamber, and were a product of a reaction with the skin oil squalene (see the Perspective by Schoemaeker and Carslaw). Their finding has implications for indoor air quality and ultimately for human health. —HJS

Science, abn0340, this issue p. 1071; see also add8461, p. 1045

NANOMATERIALS
Photoprinting nanoparticles

Nanoparticle assembly often requires tailored selection of the ligands so that they can selectively bond, as with complementary DNA strands. Alternately, they can be linked together at specified locations

using photopolymerization to connect ligands at the desired places. However, this process adds to the complexity of making the nanoparticles and is limited by the fidelity of the ligand attachment. Liu *et al.* show that light can be used to desorb surface thiolate ligands from cadmium selenide/zinc sulfide core shell quantum dots (see the Perspective by Pan and Talapin). The resulting trapped holes drive bonding between the particles through the remaining surface ligands. The authors reveal photoprinting of arbitrary three-dimensional architectures at a resolution beyond the diffraction limit and for a range of nanocrystals. Printing can be optically selected based on the size and/or bandgap of the quantum dots. —MSL

Science, abo5345, this issue, p. 1112; see also add8382, p. 1046

PAIN

A shared target between cancer and pain

Neuropathic pain is a chronic condition for which safe and effective treatments are lacking. Polymorphisms in the GTP cyclohydrolase 1 (GCH1) gene have been associated with chronic pain severity; however, whether modulation of GCH1 can affect neuropathic pain remains to be seen. Cronin *et al.* screened 1000 US Food & Drug Administration–approved compounds and showed that the antipsychotic fluphenazine hydrochloride reduced GCH1 expression and had analgesic effects in a neuropathic pain model in rodents. Among the hits, epidermal growth factor receptor-KRAS pathway modulators also affected GCH1 expression. The authors identified a common signaling pathway, downstream KRAS, involving GCH1, that affects chronic pain and lung cancer development in mice. The results suggest that targeting this

pathway could alleviate neuropathic pain. —MM

Sci. Transl. Med. **14**, eabj1531 (2022).

TUMOR IMMUNOLOGY

Reinvigorate your CD39⁺ TRM

Immune checkpoint blockade has only displayed efficacy in some subsets of patients with breast cancer, but it is unclear why. Lee *et al.* examined tissue-resident memory T cells (TRMs) in the tumors, lymph nodes, and blood of patients with early breast cancer, finding that tumor-specific CD8⁺ TRMs expressed the cell surface proteins CD39, CD69, and CD103. These CD39⁺ TRMs displayed an exhausted phenotype and overlapping T cell receptor clonality in tumors and lymph nodes. CD39⁺ TRMs were enriched in triple-negative breast cancer (TNBC) samples, correlating with the overall survival of patients with TNBC, and could be reinvigorated from exhaustion with the addition of immune checkpoint blockade *ex vivo*. Together, these data suggest that patients with high CD39⁺ TRM signatures might be good candidates for this treatment. —DAE

Sci. Immunol. **7**, eabn8390 (2022)

BIOCHEMISTRY

A partial TCA cycle in the nucleus

Certain metabolites that are produced within the mitochondrial tricarboxylic acid cycle are also substrates of chromatin-modifying enzymes in the nucleus, but the sources of these nuclear metabolite pools are largely unclear. Kafkia *et al.* demonstrate that portions of the tricarboxylic acid cycle operate within the nuclei of mammalian cells. Tracing of carbon-13–labeled substrates revealed that in purified nuclei, citrate can be metabolized to succinate

and glutamine to fumarate and aspartate. A proximity labeling approach supported the presence of the relevant metabolic enzymes in the nucleus. The data align with mounting evidence that the nucleus is an active metabolic compartment and open questions into the mechanisms regulating these nuclear metabolic pathways and their significance for cell biology. —KEW

Sci. Adv. **10**, 1126/sciadv.abq5206 (2022).

REVIEW SUMMARY

HEART DISEASE

A coalition to heal—the impact of the cardiac microenvironment

Eldad Tzahor* and Stefanie Dimmeler*

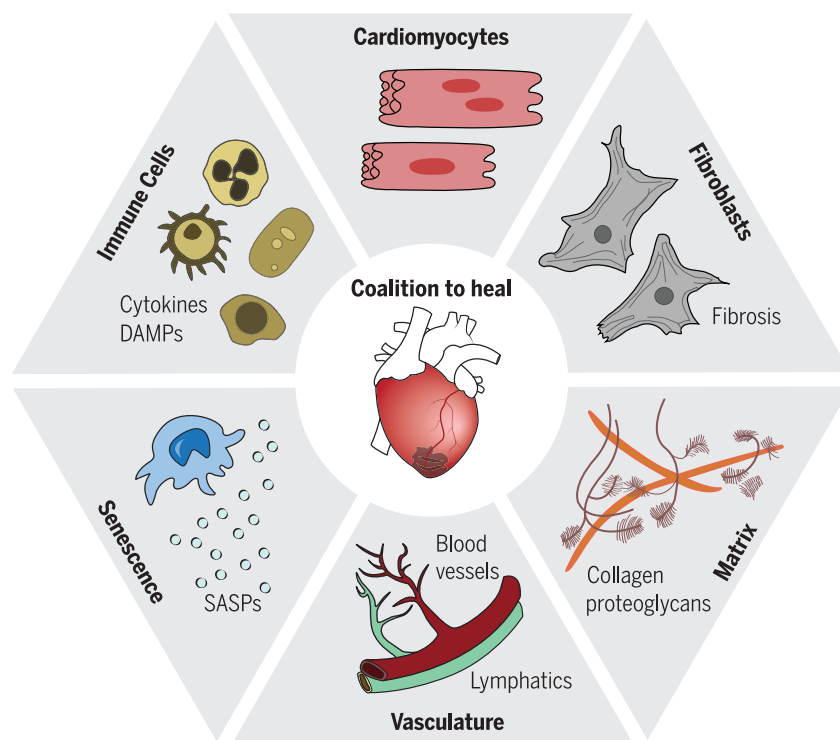
BACKGROUND: Heart regenerative medicine has been gradually evolving from a view of the heart as a nonregenerative organ with terminally differentiated cardiac muscle cells that cannot be renewed in mammals. Cardiomyocytes are the cells responsible for generating contractile force in the heart and were traditionally at the center of interest in the fight against cardiac diseases. Understanding the biology of the heart during homeostasis and in response to injuries had led to the realization that cellular communication between all cardiac cell types holds great promise for treatments. Cellular specialization and interaction between cell types in the heart are essential for the coordinated function of the heart. The complex interplay between cardiomyocytes and the myriad of other cell types such as endothelial, fibroblast, and immune cells of the heart is

necessary for tissue homeostasis and adaptation but can also lead to pathophysiological remodeling. Indeed, nonparenchymal cells outnumber cardiomyocytes; about half of the cells comprise fibroblasts, and one-fourth are endothelial cells. In addition, immune cells have major effects by providing cytokines, which can positively or negatively affect the healing response. Communication between cells changes in response to injury, which could aggravate tissue damage, remodeling, and fibrosis resulting in heart failure. In this review, we aim to characterize the cardiac microenvironment and the dynamic cross-talk between cells under tissue homeostasis and disease.

ADVANCES: Recent studies highlight new disease-reversion concepts in addition to cardiomyocyte renewal, such as matrix- and

vascular-targeted therapies, as well as immunotherapies focusing on inflammation and fibrosis. We will discuss these cellular processes, as well as angiogenesis and senescence, and highlight how specific therapies can target the hostile cardiac milieu under pathological conditions. For example, interfering with cardiac fibroblast activation or depletion of specific activated fibroblast subsets are becoming attractive immunotherapy-based approaches. Furthermore, the vasculature plays a critical role in guaranteeing the supply of oxygen and other substances such as nutrients and metabolites. Because of the high oxygen and metabolic demand of the heart, interfering with these functions directly affects cardiac function and can lead to heart failure. Approaches that can induce a functionally active vasculature would guarantee oxygen and nutrient supply and may assure production of angiocrine factors, which are important for the healing processes. Immunotherapy-based trials include attempts to selectively target maladaptive inflammatory surge, which leads to adverse remodeling, fibrosis, and subsequently heart failure. In addition, lymphatic vessels play key roles in ensuring export of inflammatory cells and tissue repair and are, therefore, also in the spotlight of drug development. We will also discuss how modulation of the extracellular matrix, particularly that of the neonatal heart, may be used to rejuvenate the heart, which could lead to better function and protection from ischemic insults. Finally, we will address how to interfere with cardiac aging and the double-edged roles of senescence.

OUTLOOK: Cellular communication between the different cell types of the heart is essential for cardiac repair and regeneration and can be targeted by various approaches, which we term “coalition to heal.” Although activation of many reparative or regenerative stimuli after injury is generally beneficial for a transient period, overstimulation of these same signals will end up being detrimental, leading to sustained inflammation and fibrosis. Timely application, careful dosing, and combination of therapies, along with selecting the right patient population, are critical for moving forward. Taken together, the therapeutic options and approaches for treatment of heart disease are promising and hopefully will change this devastating pandemic. ■



Cellular communication at the center of cardiac repair: Cardiac cells are dynamically changing under normal and pathological conditions. The interaction (cross-talk) between these populations greatly affects the outcome and function of the heart and is the subject of new therapeutic approaches in combating heart diseases. DAMPS, damage-associated molecular patterns; SASPs, senescence-associated secretory phenotypes.

The list of author affiliations is available in the full article online.

*Corresponding author. Email: eldad.tzahor@weizmann.ac.il (E.T.); dimmeler@em.uni-frankfurt.de (S.D.)

Cite this article as E. Tzahor, S. Dimmeler, *Science* 377, eabm4443 (2022). DOI: 10.1126/science.abm4443

S READ THE FULL ARTICLE AT
<https://doi.org/10.1126/science.abm4443>

REVIEW

HEART DISEASE

A coalition to heal—the impact of the cardiac microenvironment

Eldad Tzahor^{1*} and Stefanie Dimmeler^{2,3,4*}

Heart regenerative medicine has been gradually evolving from a view of the heart as a nonregenerative organ with terminally differentiated cardiac muscle cells. Understanding the biology of the heart during homeostasis and in response to injuries has led to the realization that cellular communication between all cardiac cell types holds great promise for treatments. Indeed, recent studies highlight new disease-reversion concepts in addition to cardiomyocyte renewal, such as matrix- and vascular-targeted therapies, and immunotherapy with a focus on inflammation and fibrosis. In this review, we will discuss the cross-talk within the cardiac microenvironment and how specific therapies aim to target the hostile cardiac milieu under pathological conditions.

Cellular specialization and interaction between cell types in the heart are essential for the coordinated function of the heart. Cardiomyocytes are the cells responsible for generating contractile force in the heart and were traditionally at the center of interest in the fight against cardiac diseases. Eventually, it became clear that the complex interplay between cardiomyocytes and the nonparenchymal endothelial, fibroblast, and immune cells of the heart is necessary for tissue homeostasis and adaptation but can also lead to pathophysiological remodeling. Indeed, nonparenchymal cells outnumber cardiomyocytes; about half of the cells are fibroblasts, and one-fourth are endothelial cells (1–3) (Fig. 1). In addition, small numbers of immune cells, epicardial, and nerve cells can be detected in healthy hearts (1, 2). The assessment of cardiac cellular composition varies between methodologies (4), species, and age, with substantial higher numbers of endothelial cells reported in zebrafish (5) and a higher number of cardiomyocytes observed in postnatal mice (6). Cardiac injury or stress changes the cellular compositions in a spatiotemporal manner. For example, acute myocardial infarction (MI) results in a rapid invasion of immune cells, mainly to the border and infarct zone, which subsequently leads to the local expansion and activation of fibroblasts. In turn, cellular activation results in major changes in the microenvironment dictated by the release of various cytokines and growth factors as well as

matrix proteins (matrikines), which affect cardiomyocyte responses to injury, such as cell death, hypertrophy, or regeneration (Fig. 1).

Changes in cardiomyocyte properties also occur in the uninjured heart, where the early postnatal period is marked by a cardiomyocyte switch from proliferative, hyperplastic growth to nonproliferative, hypertrophic growth in adulthood (7, 8). Additionally, cardiac repair and regeneration are strongly influenced by cues from the microenvironment, although intrinsic properties of cardiomyocytes also contribute to cardiac healing. The idea of targeting cardiomyocyte renewal with potential therapies has been intensively reviewed in recent years (8, 9). Here, we attempt to characterize the cardiac microenvironment and highlight strategies that target it during disease, healing, and aging.

Strategies to therapeutically target the microenvironment niche

The observation of major alterations in cells, matrix, and microenvironmental cues upon acute or chronic injury and aging not only deepens our understanding of the complex interactions that are required to maintain cardiac health but also allows us to identify processes that drive repair and regeneration (Fig. 2). With the advent of single-cell technologies, the heterogeneity within cellular populations is increasingly recognized, and we are beginning to identify subtypes or transition states within cell populations. Whereas harmful cells may be depleted to maintain or restore health, reparative cell populations may be used to improve clinical outcomes. Notably, the communication between all cardiac cell types is crucial for both beneficial and harmful remodeling processes that occur after injury. We will discuss five examples to highlight potential therapeutic interventions targeting cells, paracrine factors, or matrix proteins.

Targeting fibroblasts

Cardiac fibroblasts are a major cell population in the heart and are best known for their capacity to produce extracellular matrix (ECM). Quiescent fibroblasts are important for maintaining structural aspects of the myocardium. After MI, cardiac fibroblasts are activated and expand to stabilize the infarcted area upon cardiomyocyte loss in a process called “replacement fibrosis.” By contrast, cardiometabolic or hypertensive diseases are typically characterized by reactive fibrosis, which occurs throughout the left ventricle. Chronic and pathological activation of the fibroblasts compromises electromechanical coupling of the myocardium and affects paracrine and direct cellular communication with cardiomyocyte, endothelial, and immune cells (10, 11).

Fibroblasts are a plastic cell population that originate from several developmental origins, which do not seem to influence their functions. Single-cell RNA sequencing uncovered previously unknown and dynamic myofibroblast (injury-induced activated fibroblasts) subtypes expressing either profibrotic or antifibrotic signatures, which can vary depending on the genetic background (4, 10, 12, 13). Another cardiac fibroblast subtype, “matrifibrocytes,” which express genes typically observed in tendon, bone, and cartilage (14), was documented at later stages after injury. It will be interesting to explore how these newly identified fibroblast subsets or states affect acute and long-term cardiac function.

The secretome of specific fibroblast cell populations that defines reparative versus fibrotic outcomes in the damaged myocardium may provide promising targets for antifibrotic treatments of heart diseases (Fig. 2). However, many of the fibroblast-secreted proteins have divergent functions. This is, for example, illustrated by the well-characterized ECM protein periostin: Being expressed by activated cardiac fibroblasts after MI, it is required for scar stabilization as deletion of periostin expression, or elimination of periostin-expressing fibroblasts, resulted in cardiac rupture after MI (15, 16). In addition, periostin stimulates cardiomyocyte proliferation and mediates regenerative responses in the postnatal heart (17, 18), although these findings are still controversial (19). By contrast, targeted ablation of periostin-expressing activated fibroblasts prevented cardiac fibrosis upon angiotensin II (Ang II) infusion or MI (20), suggesting a detrimental effect of periostin (or the cell population expressing it) in tissue fibrosis.

Depletion of activated fibroblast subsets that drive cardiac fibrosis recently emerged as a promising strategy to treat cardiac fibrosis: T cell-mediated immunotherapy that specifically targets a population of activated fibroblasts has been introduced as a therapeutic option to treat pathological cardiac fibrosis.

¹Department of Molecular Cell Biology, Weizmann Institute of Science, Rehovot 7610001, Israel. ²Institute of Cardiovascular Regeneration, Center of Molecular Medicine, Goethe University Frankfurt, 60594 Frankfurt, Germany. ³Cardiopulmonary Institute, Goethe University Frankfurt, Frankfurt, Germany. ⁴German Center for Cardiovascular Research, RheinMain, Frankfurt, Germany.

*Corresponding author. Email: eldad.tzahor@weizmann.ac.il (E.T.); dimmeler@em.uni-frankfurt.de (S.D.)

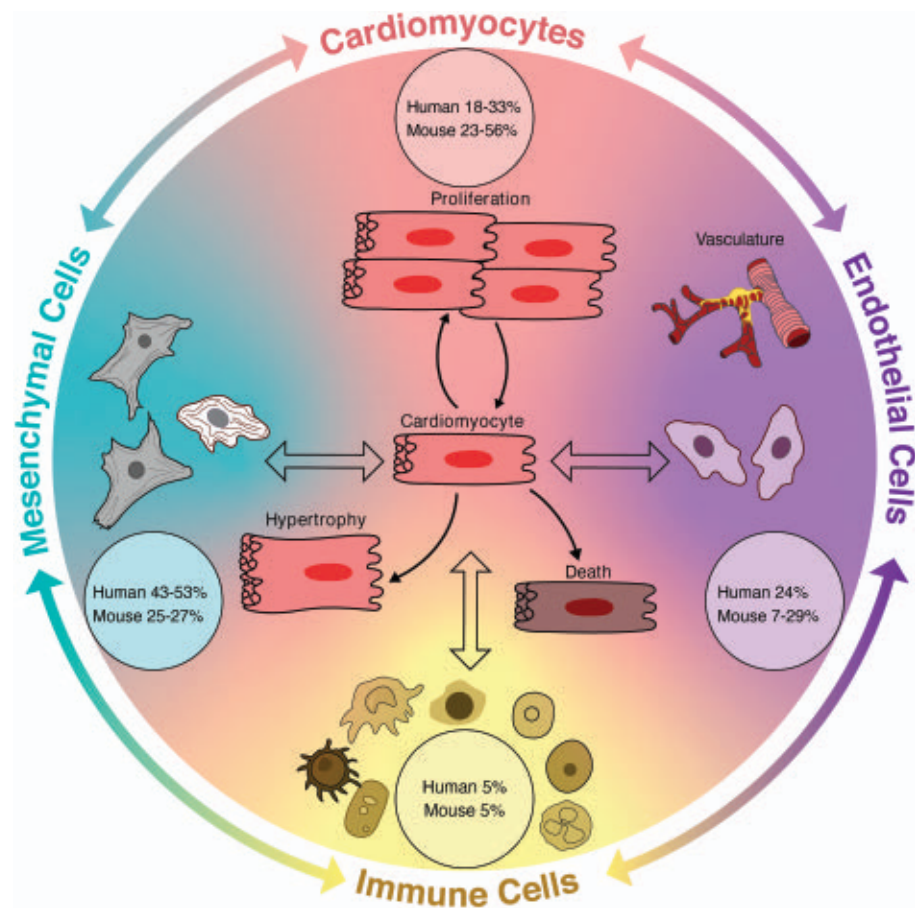


Fig. 1. A summary of cells and regulatory circuits of the cardiac microenvironment. Estimates of cell composition are taken from (1, 2) (human) and (3, 6) (mouse).

The authors used adoptive transfer of antigen-specific CD8⁺ T cells that target the fibroblast activation protein, which is expressed specifically by activated but not quiescent cardiac fibroblasts (27). A subsequent study reported the generation of transient antifibrotic chimeric antigen receptor (CAR) T cells in vivo by delivering modified mRNA targeting T cells to attack activated fibroblasts, which revealed reduced fibrosis and improved cardiac function after injury (22). These results provide a proof of concept for immunotherapeutic approaches to treat cardiac fibrotic disease. Notably, the study used the Ang II-induced hypertension model, which drives reactive fibrosis, hence its therapeutic potential to treat replacement fibrosis as seen after MI is yet unknown.

General approaches to block fibrosis focus on the inhibition of profibrotic factors. Inhibition of transforming growth factor β 1 (TGF β 1), a major driver of fibrosis, is associated with side effects due to its pleiotropic roles. But TGF β 1-induced interleukin-11 (IL-11) acts as an autocrine factor that regulates fibrogenic protein synthesis. Inhibition of IL-11 prevented fibroblast activation in response to several pro-

fibrotic stimuli (23). This mechanism appears not to be conserved in zebrafish, where IL-11 limited scarring and supported regeneration (24). About one-third of all genes involved in TGF β 1-driven fibrosis were shown to be regulated at the translational level, independent of RNA transcript abundance (25). Hence, modulating mRNA degradation or translation by microRNAs might be a promising strategy to prevent cardiac fibrosis (26, 27). Recent studies showed that inhibiting microRNA 21 (miR-21) yielded therapeutic benefits after acute MI in pigs mainly by interfering with immune cell-fibroblast cross-talk (28).

Genetic inactivation of the Hippo pathway in proepicardial cells (one of the origins of cardiac fibroblasts) prevented cardiac fibroblast formation, resulting in a grossly abnormal heart (29). Finally, inhibition of bromodomain and extra-terminal domain (BET) protein prevented fibrosis by regulating an enhancer, which controls fibroblast-to-myofibroblast transition (30). Taken together, cardiac fibroblasts drive ECM secretion and fibrosis following injury. Accurate targeting of specific subpopulations and/or fibroblast-derived

paracrine factors are promising therapeutic strategies.

Vascular therapies

The vasculature plays a critical role in guaranteeing the supply of oxygen and other substances such as nutrients and metabolites (Fig. 3). Because of the high oxygen and metabolic demands of the heart, interfering with these functions affects cardiac function and can lead to heart failure. Although this is obvious upon interfering with the vascular supply of oxygen, detrimental effects were also documented when specifically inhibiting endothelial fatty acid transport (31, 32). Endothelial cells can survive and expand in reduced oxygen environments by switching to glycolytic metabolism. This allows for vessel growth to restore oxygen supply and contribute to wound healing (33). Additionally, endothelial cells act as a barrier against circulating inflammatory cells: Inflammation is limited by the tight endothelial barrier during homeostasis, but proinflammatory conditions lead to an inflamed endothelium and allow the invasion of immune cells. Cardiac sequelae of severe acute respiratory syndrome coronavirus 2 (SARS-CoV-2) infections are recent examples of how an inflamed and activated endothelium together with activated immune cells can lead to microthrombotic events that harm the heart (34).

Controlling the invasion of inflammatory cells is a key feature of endothelial cells, but the vasculature is equally important in the removal of inflammatory cells. Here, lymphatic vessels come into play: Inadequate lymphangiogenesis results in increased interstitial fluid and reduces clearance of inflammatory cells to draining lymph nodes (35). Lymphatic vessels can boost cardiac repair in both zebrafish and mice (36–38). Accordingly, inducing lymphangiogenesis is gaining attention as a therapeutic approach for reducing immune cell persistence, inflammation, and edema to restore heart function.

Endothelial cells additionally produce angiocrine factors, which act in an autocrine or paracrine manner to induce cardiomyocyte proliferation (39, 40). Neuregulin-1 expression is particularly enriched in endothelial cells in proximity to cardiomyocytes and it binds to epidermal growth factor receptor (ErbB) 2 and 4 on cardiomyocytes, contributing to the formation of both endocardial cushions and myocardial trabeculae during development (41, 42). Activation of ErbB2 triggered a robust regenerative response after acute or chronic injuries in mice via the ERK-Yap1 signaling axis (43, 44). In addition, endothelial cells can control cardiomyocyte hypertrophy through ephrin signaling (45).

In addition to proteins, diffusible molecules can affect the cardiac microenvironment. Endothelial-derived nitric oxide (NO) synthase

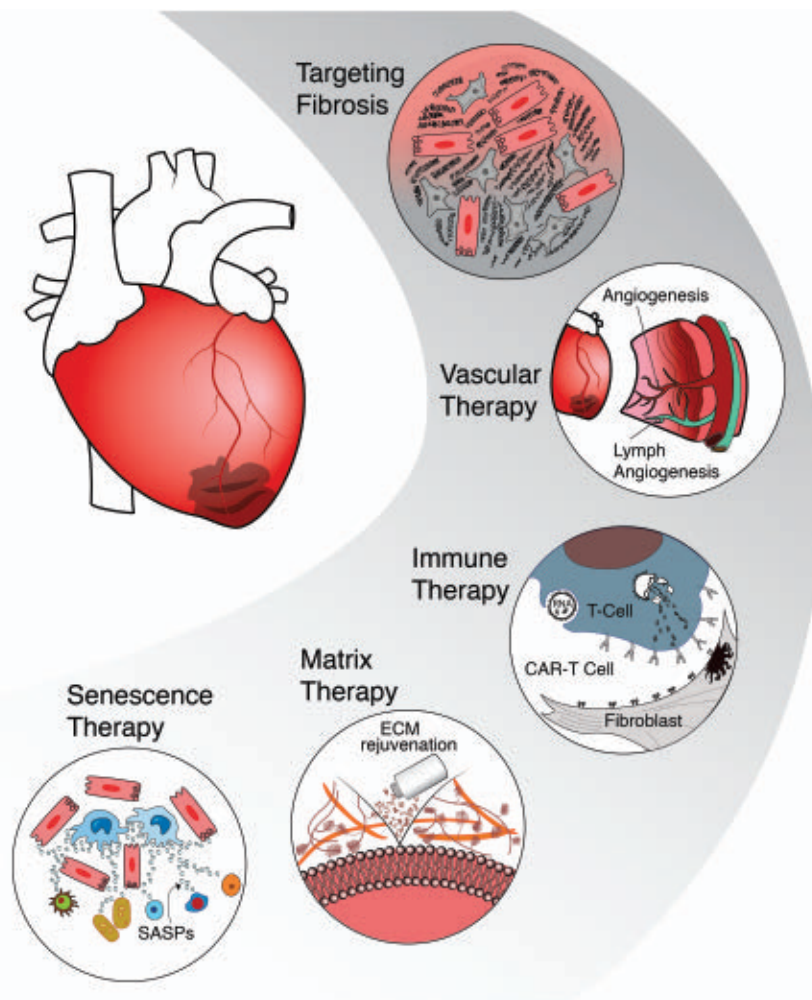


Fig. 2. Therapeutic approaches to targeting autocrine and paracrine cellular communication after injury.

can prevent or enhance cardiac pathologies depending on the redox environment (46). Diffusible molecules such as H_2S , which induces sulfhydrylation of intracellular and extracellular proteins, prevented endothelial dysfunction (47). Furthermore, small metabolites were shown to be involved in the acquisition of a quiescent state in the endothelium (48). Finally, extracellular vesicles originating from different cellular and subcellular sources mediate cellular cross-talk and are attractive therapeutic candidates for cardiovascular diseases (49, 50). Thus, examination of additional endothelial-derived factors that affect the cardiac microenvironment is important.

Given the crucial functions of the micro- and macrovasculature in the heart and the possibility of improving myocardial healing by reactivation of hibernating myocardium, a clinical-relevant state when parts of the myocardium exhibit contractile abnormalities resulting from ischemia, various attempts were made to therapeutically maintain or restore

the vasculature (51, 52). However, various pro-angiogenic strategies did not fulfill their promise, in part because stimulation of excessive angiogenic growth failed to generate functionally mature vasculature. Accordingly, current therapeutic strategies aim at generating healthy and functional vessels, instead of inflamed and leaky ones, which would aggravate heart disease. Recent advances include lowering the doses of proangiogenic factors to amounts that simulate healthy conditions. Thus, low-dose vascular endothelial growth factor A (VEGFA) fully restored microcirculatory function in aged mice and prevented age-associated pathologies in many organs, including skeletal muscle (53). Although the heart has not been specifically investigated in this study (53), such approaches may well be suitable to normalize microcirculation in age-associated cardiac diseases such as heart failure with preserved ejection fraction. Delivery strategies are also improving; for example, modified mRNA of *VEGFA* may have favorable kinetics and effi-

ciency and is being tested in a phase II study (54). Another therapeutic candidate is VEGFB, which increases vessel maturation and cardiac metabolism and seems to be particularly effective in the heart (55). Apelin, an endothelial-derived small secreted peptide, also has a proangiogenic activity in the heart (56).

Monocytes and hematopoietic cell populations are rich sources of angiogenic factors (57, 58), which promote arteriogenesis (59, 60) and could be delivered therapeutically to improve heart function. Recent examples of monocyte-derived factors are VEGFA, myeloid-derived growth factor (MYDGF) (61), and endoplasmic reticulum membrane protein complex unit 10 (ECM10) (62), all of which improve angiogenesis and cardiac repair and could be therapeutic candidates for cardiac ischemia. Whereas VEGF and many proangiogenic growth factors mainly target the microvasculature to rescue its dysfunction, hematopoietic cell-derived factors can induce the formation of macrovessels (a process called arteriogenesis) to promote the perfusion of larger hypoxic regions within hibernating myocardium (59, 60). Although initial attempts to translate these findings failed, enhancing the CXCL12(SDF1)-CXCR4 axis was recently proposed as an alternative option to induce arteriogenesis (63).

Endothelial cells may also be targeted to limit cardiac inflammation. Here, antagonizing angiopoietin-2, which induces vascular leakage and inflammation, can be used to prevent vascular permeability (64). In addition, augmenting lymphangiogenesis by the key driver VEGFC or other factors such as adrenomedullin or apelin can be used to reduce edema formation and support the egress of inflammatory cells (37, 65, 66).

Instead of targeting one pathway, non-coding microRNAs may be useful to interfere with the complex patterns of genes that are required to maintain a functional and healthy endothelium. For example, miR-126 isoforms can prevent endothelial cell inflammation (67), whereas inhibition of miR-92a-3p improved vessel growth and reduced inflammation (68). Anti-miRs directed against miR-92a were tested in initial clinical trials and may represent future options (69). MicroRNAs may also be delivered by cell-derived or engineered extracellular vesicles, to carry a mixture of vasculoprotective RNAs (50). Taken together, a healthy vasculature is a key component in orchestrating cardiac repair processes.

Immune therapies

The immune system plays a critical role during physiological cardiac function and in response to injury (70, 71). The pathogenesis of many heart diseases is intricately related to an incited inflammatory process, though injury types, host, and environmental factors profoundly affect the immune response (71, 72). Briefly,

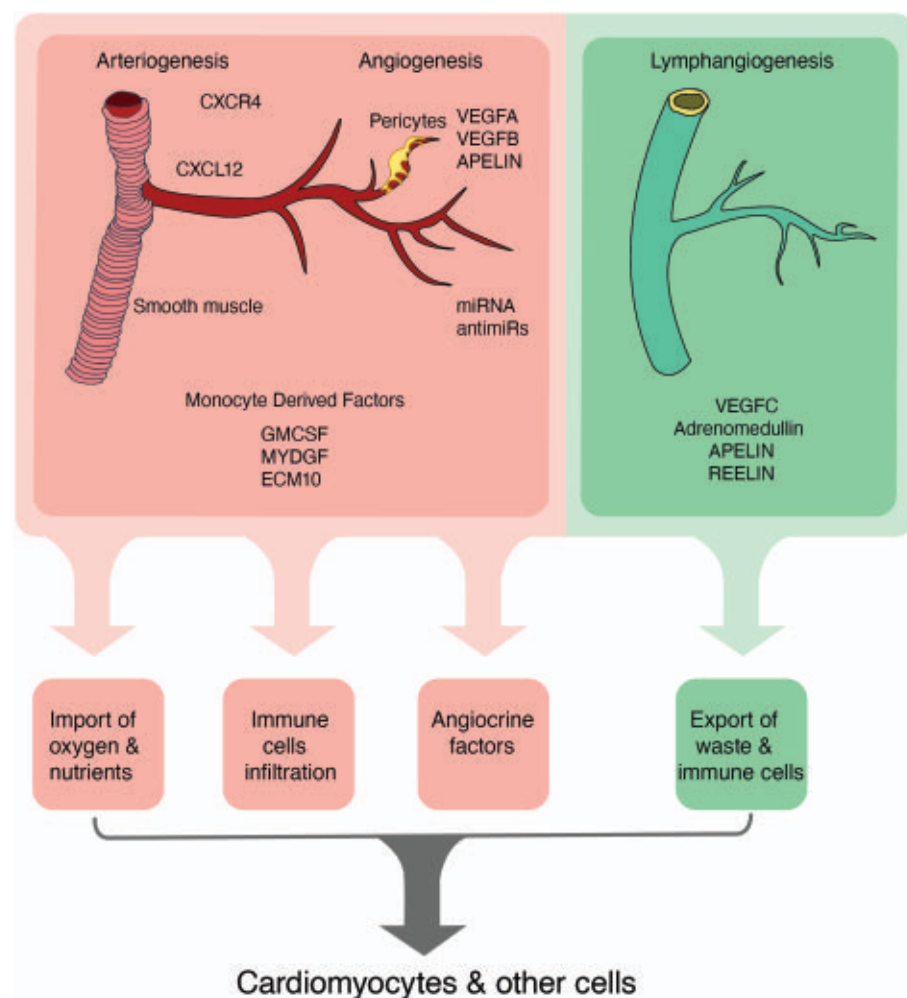


Fig. 3. Approaches to controlling vascular functions for cardiac repair.

ischemic or non-ischemic cardiac injuries activate the innate immune system, which triggers the secretion of proinflammatory cytokines and chemokines that, in turn, further attract immune effector cells into the injured myocardium, as part of a proinflammatory phase. In general, a transient inflammatory response is essential for tissue healing, including cardiac injuries. However, a maladaptive inflammatory surge can drive adverse remodeling and fibrosis that could lead to heart failure. The different types of immune cells communicate with one another and with cardiac fibroblasts, endothelial cells, and cardiomyocytes. This cross-talk is important for driving both repair and pathological processes.

After MI, dying cardiomyocytes release damage-associated molecular patterns (DAMPs), which activate and recruit the innate immune system to the site of injury. For example, dying cardiomyocytes release extracellular adenosine 5'-triphosphate (ATP), which is a DAMP component that disrupt cellular function of macrophages, fibroblasts, endothelial cells, and smooth muscle cells, thereby worsening cardiac

repair (73). DAMPs also activate the complement system, an ancient component of immunity that facilitates the clearance of damaged cells. Therefore, inactivation of the complement system impairs heart function and accelerates development toward heart failure (74). Neutrophils are the major immune cells that infiltrate the infarct region. These cells promote myocardial damage by inducing pro- and anti-inflammatory as well as angiogenic factors (75, 76). Basophils (accounting for 1% of total granulocytes) are important during cardiac injury as their depletion resulted in deteriorated cardiac function and enhanced scarring after MI, likely mediated by the lack of IL-4 and IL-13 (77).

Monocytes and macrophages are of key importance in the mouse and human heart. Resident cardiac macrophages are long-lived cells, primarily of embryonic origin, whereas recruited cardiac macrophages are continually replenished from the bone marrow. Expression of the chemokine receptor CCR2 distinguishes these populations, and CCR2-resident cardiac macrophages are further subdivided

by TIM4 and major histocompatibility complex (MHC) class II expression (78–80). In general, macrophages are essential for cardiac regeneration in zebrafish, salamanders, and mice (9, 79, 81), suggesting that the initial phases of inflammation are critical for heart repair. The functional benefit of cardiac cell therapy was shown to be driven by the acute inflammatory healing response that rejuvenates the injured heart (82). Studies reveal how resident cardiac macrophages regulate adaptive beneficial cardiac remodeling in the failing mouse heart through direct interaction with cardiomyocytes and secretion of insulin-like growth factor 1 (83, 84). Dedifferentiating cardiomyocytes can control macrophage trafficking to the damaged heart by releasing “regenerating islet-derived 3β” (Reg3β). Loss of Reg3β led to a large decrease in the number of macrophages, accompanied by increased ventricular dilatation and insufficient removal of neutrophils (85). Thus, macrophage recruitment is instrumental for myocardial healing.

Cells of the adaptive immune system are increasingly recognized as important regulators not only in myocarditis but also in chronic heart failure (86, 87). T lymphocytes, an important component of the adaptive immune response, are divided into (CD4⁺) T helper (T_H) cells and cytotoxic (CD8⁺) T cells. After MI, CD4⁺ T cells rapidly infiltrate the heart (87, 88). CD4⁺ T cells can be further divided into different subsets, among them, T_H1, T_H2, and T regulatory (T_{reg}) cells according to their phenotype, cytokine production, and function. Experimental evidence suggests a prominent role of CD4⁺ T_H lymphocytes, particularly T_H1 and possibly T_H17 and T_H22 cells, as key players in myocardial remodeling (89). IL-17, mainly expressed by T_H17 cells, exacerbates heart failure (90, 91) and induces cellular senescence in other age-related diseases (92), highlighting a potential link between immune activation and cardiac senescence.

Because T cells are involved in heart failure pathogenesis, they become attractive immunotargets for therapeutic intervention. Abatacept, a US Food and Drug Administration (FDA)-approved drug that selectively inhibits the proinflammatory T cell function, was shown to decrease the severity of cardiac dysfunction in a mouse heart failure model (93). Augmenting or stimulating immunosuppressive T_{reg} cells was beneficial for the heart after MI (94). T_{regs} promote angiogenesis (94) and cardio-protection after MI in mice (95) and zebrafish (96). Thus, T_{regs} facilitate the repair and regeneration of endothelial cells and cardiomyocytes (94–96). Treatment with antibodies against CD28 superagonist resulted in an anti-inflammatory cytokine response and T_{reg} activation, leading to efficacious therapy in many rat and mouse disease models (97). However, in a phase I trial, the same superagonist was highly toxic and

caused a cytokine storm (98), which halted further drug development. Overexpression of protective factors secreted by T_{regs} may be considered as an alternative strategy to more specifically interfere with downstream effector pathways (94). Another immune cytokine, IL-10, was examined as an anti-inflammatory treatment and was shown to improve cardiac function by dampening inflammation after MI in mice (99), whereas IL-10-deficient mice have reduced cardiac function (100). Despite these encouraging data, hints toward the promotion of diastolic dysfunction by cardiac macrophage-derived IL-10 should not be ignored when considering a therapeutic use (101).

Taken together, heart pathologies involve global immune cell activation, which opens up the field of cardioimmunology to further investigation and development of therapies. Intensive investigations of anti-inflammatory strategies for cardiovascular diseases (including allopurinol, methotrexate, salsalate, inhibitors of tumor necrosis factor α (TNF α), IL-6, IL-17, IL-1 β , or IFN- γ) are underway in numerous clinical trials, although most of these trials have failed to provide conclusive results thus far (102). However, reduction of inflammation with low-dose colchicine treatment revealed promising results in patients with coronary artery disease (103), which may be translated to heart failure. One explanation for the lack of established anti-inflammatory treatments for heart failure is that the immune response to injury is complex and includes both beneficial and detrimental effects, which need to be further studied and modulated precisely. Furthermore, although targeting a single immune cell signaling pathway might not be enough, a broad anti-inflammatory

treatment might have numerous side effects. Therefore, selecting heart failure patients with a high inflammatory burden, such as patients with somatic mutations in hematopoietic stem cells leading to clonal hematopoiesis (104), may improve the risk-benefit ratio of anti-inflammatory therapies.

Matrix therapies

All cells of the heart are embedded within a rich ECM microenvironment. The ECM is mainly produced by cardiac fibroblasts, but also by other cells such as endothelial cells, smooth muscle cells, and cardiomyocytes (14). In addition, macrophages contribute directly to cardiac scarring through cell-autonomous deposition of collagen (105). Several studies have revealed roles of the ECM in heart regeneration, suggesting a new therapeutic avenue for “Matrix Medicine” (106–109). The ECM, initially thought of as a tissue structure component or the glue between cells, is emerging as a key signaling player in cellular communication affecting numerous cell behaviors (110). After injury, the cardiac ECM undergoes dynamic changes that involve both synthesis and degradation of the ECM, resulting in ECM remodeling (111). Initial ECM remodeling plays a beneficial role in cellular repair processes and prevention of ventricular rupture, but excessive deposition of ECM has deleterious effects that impair cardiac function. Likewise, chronic inflammation accelerates cardiac fibrosis and vice versa, thereby creating a positive feedback loop between fibrosis and inflammation.

The cardiac ECM is made up of proteins and polysaccharides. Collagen and elastin provide the physical structure. Fibrillar collagen (mostly type I and type III) makes the largest por-

portion of proteins in the ECM of the heart and it changes markedly during ECM remodeling after injury (112). Collagens, along with other matrix components, are increased during cardiac remodeling, leading to scar maturation and fibrosis.

The ECM functions as a reservoir of anchored growth factors, cytokines, chemokines, proteases (such as matrix metalloproteinases (MMPs), protease inhibitors such as tissue inhibitors of metalloproteinases (TIMPs), and noncoding RNAs. Enzymatic degradation of the ECM macromolecules during remodeling generates active peptides or matrilins, which are involved in many processes such as ECM renewal, cellular proliferation and migration, inflammation, angiogenesis, and wound repair. In general, cardiac ECM content and its cross-linking increase with aging (Fig. 4). Along with that, ECM degradation is also augmented by MMPs, predominantly MMP9. Therefore, excessive ECM production and imbalanced ECM degradation are critical processes in many cardiac pathologies and during aging.

The mechanical properties of the ECM also influence cardiac function and repair processes. As cardiac ECM changes during postnatal growth, it affects myocardial stiffness (Fig. 4). The stiffness of the myocardium progressively increases, along with cardiomyocyte maturation and cell cycle arrest. Accordingly, reduced matrix rigidity (or stiffness) induces neonatal cardiomyocyte dedifferentiation and proliferation (113). This and other studies suggest that the increase in cardiac ECM stiffness after birth might dictate the transition from a regenerative to a nonregenerative phase, highlighting the regulatory role of ECM mechanical properties (113, 114). A recent study revealed that collagen V regulates scar size in an integrin-dependent manner. Mice lacking collagen V showed changes in scar stiffness and fibroblasts differentiation, both of which affect scar size (115).

Agrin is an ECM molecule secreted by endothelial cells, which is enriched in the embryonic and neonatal heart, and can promote cardiac regeneration and repair in adult mice and pigs after MI (107, 109). Similarly, other ECM proteins, such as periostin and reelin, which are highly expressed in the neonatal heart, induce cardiomyocyte proliferation and regeneration in mice (17, 38). Reelin is a lymphangiocrine, which promotes cardiomyocyte proliferation and survival, leading to improved cardiac repair (40). Likewise, collagen 15A1, secreted by endothelial cells, can induce cardiomyocyte proliferation (52).

Postnatal cardiac ECM was shown to inhibit cardiomyocyte cytokinesis and, conversely, embryonic ECM proteins, SLIT2 and nephronectin, were able to promote postnatal cardiomyocyte cytokinesis (116). Double knockout of both miR-1 and 133a in cardiomyocytes alters the

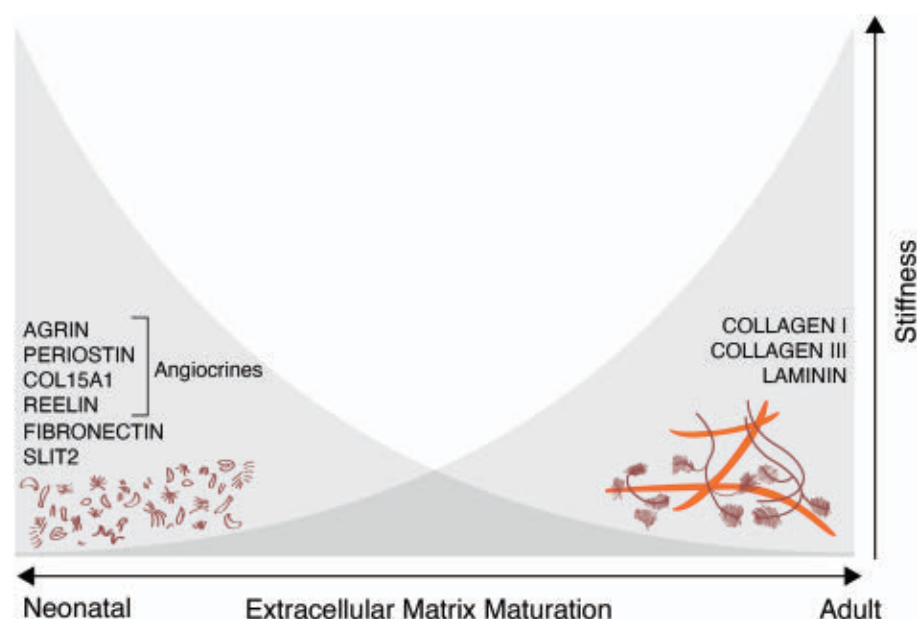


Fig. 4. Regulation of the matrix environment during cardiac development and adulthood.

expression of agrin, periostin, and fibronectin, which are representative for a neonatal-like ECM composition (117). Hence, embryonic and neonatal ECM molecules such as agrin, periostin, reelin, fibronectin, Slit2, and nephronectin and mechanical features (reduced stiffness) can promote cardiomyocyte proliferation and repair, whereas the adult ECM components such as some collagens and laminin, as well as increased stiffness, are associated with organ maturation and fibrosis (Fig. 4). Taken together, the concept of matrix rejuvenation is an attractive therapeutic approach for the treatment of heart disease.

Purified ECM molecules such as collagen, fibrin, and gelatin have been used in preclinical and clinical settings for many heart diseases. These biomaterials can be delivered as hydrogels or as patches on top of the infarcted myocardium either alone or implanted with various stem cells or bioactive drugs (106). Decellularized ECM-based biomaterials, in which cells are removed but the biological and mechanical properties of the ECM are preserved, have also been tested in clinical trials for cardiovascular diseases (106). Hence, ECM-based biomaterials that aim to promote endogenous regenerative mechanisms constitute an emerging therapeutic strategy.

Cardiac senescence

Recent studies began to uncover the key roles played by senescent cells during tissue repair and regeneration, by modulating fibrosis and inflammation (118). Cellular senescence is characterized by an irreversible cell cycle arrest and can be considered as a protective response of the organism that limits the proliferation of nonfunctional aged cells. Senescent cells are metabolically active and release numerous secreted factors, termed senescence-associated secretory phenotype (SASP), which profoundly alters the microenvironment in the aging heart. SASP includes inflammatory cytokines, matrix metalloproteases, and urokinases, or collagens, which act in an autocrine or paracrine fashion on neighboring cardiac cells (119). Depending on the context, cellular senescence and SASP can positively or negatively influence the heart under homeostatic and injury conditions.

The timely accumulation and clearance of senescent cells is a fundamental step for repair processes. Senescent cells can induce a SASP-dependent pro-regenerative microenvironment (ECM remodeling, angiogenesis) and help recruit immune cells, or even promote dedifferentiation and tissue plasticity (120). A transient regenerative senescence was demonstrated in three models of cardiac regeneration (121). Also in adult mice, transient activation of senescence in fibroblasts occurs after MI and limits the expansion of fibroblasts to reduce fibrosis and scar formation (121, 122). Another

study suggested that after neonatal heart injury, CCN1 secretion from cardiomyocytes promotes fibroblast senescence and neonatal heart regeneration (123).

By contrast, persistent accumulation of senescent cells as evident in aging is associated with tissue dysfunction and chronic inflammation, and can promote the onset and progression of cardiovascular diseases (119). Molecules released by pathological senescent cells are often enriched in proinflammatory factors such as IL-1, IL-6, and IL-8 that can aggravate tissue damage and dysfunction. Chronic inflammation or cytokine storm associated with aging—"inflammaging"—acts as a systemic inducer of senescence. T cells with dysfunctional mitochondria instigate multiple age-related features in mice, including senescence and cardiovascular alterations, which together result in premature death (124). In the aging heart, other paracrine factors such as Serpins, which are typically enriched in senescent cells, impair endothelial cell function (11). Along the same lines, telomerase-deficient zebrafish display an aberrant accumulation of senescent cells with failure of heart regeneration (125), and various studies have shown cardioprotective effects of telomerase or telomerase-associated factors (126, 127).

Targeted elimination of senescent cells (senolysis) or neutralization of their undesirable properties (senomorphics) can alleviate some of these pathologies and improve tissue function (128–130). With respect to the heart, treatment with senolytics prevented pathological changes after infarction and during heart failure (130). Also, a genetic senolytic model, which allows the inducible elimination of p16^{INK4a} senescent cells, reduced the size of fibrotic area in the heart of old mice. It may be interesting to further explore the clinical use of senotherapies to treat heart failure.

Injury-induced senescence profoundly affects (through SASP) the cardiac microenvironment by providing mitogenic, protective, and immune recruitment signals, as well as limiting the expansion of fibroblasts. The effects can be beneficial (for example, after transient exposure) or detrimental (prolonged senescence). Hence, eliminating senescent cells by treatment with senolytics should be carefully evaluated considering the fundamental impact of these cells on the reparative milieu of the heart after injury.

Conclusion

Despite a long-standing view that heart disease therapeutics are a graveyard for the industry and big pharma, there seem to be major advances in this huge space. For one, researchers continue to expand the knowledge foundation of cardiovascular biology. The concept that mammals could not regenerate lost myocardium after injury is contrasted by promis-

ing animal studies, some of which are covered here. Nevertheless, there is still a notable gap between preclinical studies and therapies. We postulate that a holistic understanding of the cellular communication between all cardiac cell types and dissection of the dynamics of the microenvironment after injury would identify potential targets for therapies. The field has accumulated insights from models of acute regenerative responses and more chronic scenarios that reveal multiple signaling pathways in different cell types and especially coordinated repair processes such as cardiomyocyte proliferation, angiogenesis, reparative inflammation, senescence, and fibrosis, all of which are critical to the healing of the injured heart.

Overall, activation of any reparative or regenerative stimuli after injury is generally beneficial for a transient period. By contrast, overstimulation of these same signals will end up being detrimental, leading to sustained inflammation and fibrosis. The timely application and careful dosing of therapies in combination with selecting the right patient profile are critical for moving forward. Although the field is evolving toward translational medicine for the treatment of heart diseases, basic research remains vital to elucidating numerous etiologies, mechanisms, and targets for cardiac regeneration and repair.

REFERENCES AND NOTES

- O. Bergmann *et al.*, Dynamics of Cell Generation and Turnover in the Human Heart. *Cell* **161**, 1566–1575 (2015). doi: [10.1016/j.cell.2015.05.026](https://doi.org/10.1016/j.cell.2015.05.026); pmid: 26073943
- M. Litviňuková *et al.*, Cells of the adult human heart. *Nature* **588**, 466–472 (2020). doi: [10.1038/s41586-020-2797-4](https://doi.org/10.1038/s41586-020-2797-4); pmid: 32971526
- M. Wolfien *et al.*, Single nuclei sequencing of entire mammalian hearts: Strain-dependent cell-type composition and velocity. *Cardiovasc. Res.* **116**, 1249–1251 (2020). doi: [10.1093/cvr/cvaa054](https://doi.org/10.1093/cvr/cvaa054); pmid: 32243511
- A. R. Pinto *et al.*, Revisiting Cardiac Cellular Composition. *Circ. Res.* **118**, 400–409 (2016). doi: [10.1161/CIRCRESAHA.115.307778](https://doi.org/10.1161/CIRCRESAHA.115.307778); pmid: 26635390
- C. Patra *et al.*, The zebrafish ventricle: A hub of cardiac endothelial cells for in vitro cell behavior studies. *Sci. Rep.* **7**, 2687 (2017). doi: [10.1038/s41598-017-02461-1](https://doi.org/10.1038/s41598-017-02461-1); pmid: 28578380
- I. Banerjee, J. W. Fuseler, R. L. Price, T. K. Borg, T. A. Baudino, Determination of cell types and numbers during cardiac development in the neonatal and adult rat and mouse. *Am. J. Physiol. Heart Circ. Physiol.* **293**, H1883–H1891 (2007). doi: [10.1152/ajpheart.00514.2007](https://doi.org/10.1152/ajpheart.00514.2007); pmid: 17604329
- E. R. Porrello *et al.*, Transient regenerative potential of the neonatal mouse heart. *Science* **331**, 1078–1080 (2011). doi: [10.1126/science.1200708](https://doi.org/10.1126/science.1200708); pmid: 21350179
- H. Sadek, E. N. Olson, Toward the Goal of Human Heart Regeneration. *Cell Stem Cell* **26**, 7–16 (2020). doi: [10.1016/j.stem.2019.12.004](https://doi.org/10.1016/j.stem.2019.12.004); pmid: 31901252
- E. Tzahor, K. D. Poss, Cardiac regeneration strategies: Staying young at heart. *Science* **356**, 1035–1039 (2017). doi: [10.1126/science.aam5894](https://doi.org/10.1126/science.aam5894); pmid: 28596337
- N. Farbehi *et al.*, Single-cell expression profiling reveals dynamic flux of cardiac stromal, vascular and immune cells in health and injury. *eLife* **8**, e43882 (2019). doi: [10.7554/eLife.43882](https://doi.org/10.7554/eLife.43882); pmid: 30912746
- R. Vidal *et al.*, Transcriptional heterogeneity of fibroblasts is a hallmark of the aging heart. *JCI Insight* **4**, e131092 (2019). doi: [10.1172/jci.insight.131092](https://doi.org/10.1172/jci.insight.131092); pmid: 31723062
- E. Forte *et al.*, Dynamic Interstitial Cell Response during Myocardial Infarction Predicts Resilience to Rupture in

- Genetically Diverse Mice. *Cell Rep.* **30**, 3149–3163.e6 (2020). doi: [10.1016/j.celrep.2020.02.008](#); pmid: [32130914](#)
13. M. M. Gladka *et al.*, Single-Cell Sequencing of the Healthy and Diseased Heart Reveals Cytoskeleton-Associated Protein 4 as a New Modulator of Fibroblasts Activation. *Circulation* **138**, 166–180 (2018). doi: [10.1161/CIRCULATIONAHA.117.030742](#); pmid: [29386203](#)
 14. X. Fu *et al.*, Specialized fibroblast differentiated states underlie scar formation in the infarcted mouse heart. *J. Clin. Invest.* **128**, 2127–2143 (2018). doi: [10.1172/JCI98215](#); pmid: [29664017](#)
 15. M. Shimazaki *et al.*, Periostin is essential for cardiac healing after acute myocardial infarction. *J. Exp. Med.* **205**, 295–303 (2008). doi: [10.1084/jem.20071297](#); pmid: [18208976](#)
 16. O. Kanisicak *et al.*, Genetic lineage tracing defines myofibroblast origin and function in the injured heart. *Nat. Commun.* **7**, 12260 (2016). doi: [10.1038/ncomms12260](#); pmid: [27447449](#)
 17. B. Kühn *et al.*, Periostin induces proliferation of differentiated cardiomyocytes and promotes cardiac repair. *Nat. Med.* **13**, 962–969 (2007). doi: [10.1038/nm1619](#); pmid: [17632525](#)
 18. L. Hortells *et al.*, A specialized population of Periostin-expressing cardiac fibroblasts contributes to postnatal cardiomyocyte maturation and innervation. *Proc. Natl. Acad. Sci. U.S.A.* **117**, 21469–21479 (2020). doi: [10.1073/pnas.2009119117](#); pmid: [32817558](#)
 19. A. Lorts, J. A. Schwaneckamp, J. W. Elrod, M. A. Sargent, J. D. Molkentin, Genetic manipulation of periostin expression in the heart does not affect myocyte content, cell cycle activity, or cardiac repair. *Circ. Res.* **104**, e1–e7 (2009). doi: [10.1161/CIRCRESAHA.108.188649](#); pmid: [19038863](#)
 20. H. Kaur *et al.*, Targeted Ablation of Periostin-Expressing Activated Fibroblasts Prevents Adverse Cardiac Remodeling in Mice. *Circ. Res.* **118**, 1906–1917 (2016). doi: [10.1161/CIRCRESAHA.116.308643](#); pmid: [27140435](#)
 21. H. Aghajanian *et al.*, Targeting cardiac fibrosis with engineered T cells. *Nature* **573**, 430–433 (2019). doi: [10.1038/s41586-019-1546-z](#); pmid: [31511695](#)
 22. J. G. Rurik *et al.*, CAR T cells produced in vivo to treat cardiac injury. *Science* **375**, 91–96 (2022). doi: [10.1126/science.abm0594](#); pmid: [34990237](#)
 23. S. Schafer *et al.*, IL-11 is a crucial determinant of cardiovascular fibrosis. *Nature* **552**, 110–115 (2017). doi: [10.1038/nature24676](#); pmid: [29160304](#)
 24. S. Allanki *et al.*, Interleukin-11 signaling promotes cellular reprogramming and limits fibrotic scarring during tissue regeneration. *Sci. Adv.* **7**, eabg6497 (2021). doi: [10.1126/sciadv.abg6497](#); pmid: [34516874](#)
 25. S. Chothani *et al.*, Widespread Translational Control of Fibrosis in the Human Heart by RNA-Binding Proteins. *Circulation* **140**, 937–951 (2019). doi: [10.1161/CIRCULATIONAHA.119.039596](#); pmid: [31284728](#)
 26. T. Thum, Noncoding RNAs and myocardial fibrosis. *Nat. Rev. Cardiol.* **11**, 655–663 (2014). doi: [10.1038/nrcardio.2014.125](#); pmid: [25200283](#)
 27. R. A. Boon, S. Dimmeler, MicroRNAs in myocardial infarction. *Nat. Rev. Cardiol.* **12**, 135–142 (2015). doi: [10.1038/nrcardio.2014.207](#); pmid: [25511085](#)
 28. R. Hinkel *et al.*, AntimiR-21 Prevents Myocardial Dysfunction in a Pig Model of Ischemia/Reperfusion Injury. *J. Am. Coll. Cardiol.* **75**, 1788–1800 (2020). doi: [10.1016/j.jacc.2020.02.041](#); pmid: [32299591](#)
 29. Y. Xiao *et al.*, Hippo Signaling Plays an Essential Role in Cell State Transitions during Cardiac Fibroblast Development. *Dev. Cell* **45**, 153–169.e6 (2018). doi: [10.1016/j.devcel.2018.03.019](#); pmid: [29689192](#)
 30. M. Alexanian *et al.*, A transcriptional switch governs fibroblast activation in heart disease. *Nature* **595**, 438–443 (2021). doi: [10.1038/s41586-021-03674-1](#); pmid: [34163071](#)
 31. M. Jabs *et al.*, Inhibition of Endothelial Notch Signaling Impairs Fatty Acid Transport and Leads to Metabolic and Vascular Remodeling of the Adult Heart. *Circulation* **137**, 2592–2608 (2018). doi: [10.1161/CIRCULATIONAHA.117.029733](#); pmid: [29353241](#)
 32. G. Luxán *et al.*, Endothelial EphB4 maintains vascular integrity and transport function in adult heart. *eLife* **8**, e45863 (2019). doi: [10.7554/eLife.45863](#); pmid: [31782728](#)
 33. L. S. Tombor *et al.*, Single cell sequencing reveals endothelial plasticity with transient mesenchymal activation after myocardial infarction. *Nat. Commun.* **12**, 681 (2021). doi: [10.1038/s41467-021-20905-1](#); pmid: [33514719](#)
 34. P. Libby, T. Lüscher, COVID-19 is, in the end, an endothelial disease. *Eur. Heart J.* **41**, 3038–3044 (2020). doi: [10.1093/eurheartj/ehaa623](#); pmid: [32882706](#)
 35. K. Klaurakis, J. M. Vieira, P. R. Riley, The evolving cardiac lymphatic vasculature in development, repair and regeneration. *Nat. Rev. Cardiol.* **18**, 368–379 (2021). doi: [10.1038/s41569-020-00489-x](#); pmid: [33462421](#)
 36. D. Gancz *et al.*, Distinct origins and molecular mechanisms contribute to lymphatic formation during cardiac growth and regeneration. *eLife* **8**, e44153 (2019). doi: [10.7554/eLife.44153](#); pmid: [31702554](#)
 37. L. Klotz *et al.*, Cardiac lymphatics are heterogeneous in origin and respond to injury. *Nature* **522**, 62–67 (2015). doi: [10.1038/nature14483](#); pmid: [25992544](#)
 38. X. Liu *et al.*, Lymphoangiocrine signals promote cardiac growth and repair. *Nature* **588**, 705–711 (2020). doi: [10.1038/s41586-020-2998-x](#); pmid: [33299187](#)
 39. B. S. Ding *et al.*, Endothelial-derived angiocrine signals induce and sustain regenerative lung alveolarization. *Cell* **147**, 539–553 (2011). doi: [10.1016/j.cell.2011.10.003](#); pmid: [22036563](#)
 40. J. M. Gomez-Salinerio, T. Itkin, S. Rafii, Developmental angiocrine diversification of endothelial cells for organotypic regeneration. *Dev. Cell* **56**, 3042–3051 (2021). doi: [10.1016/j.devcel.2021.10.020](#); pmid: [34813766](#)
 41. Y. Y. Zhao *et al.*, Neuregulins promote survival and growth of cardiac myocytes. Persistence of ErbB2 and ErbB4 expression in neonatal and adult ventricular myocytes. *J. Biol. Chem.* **273**, 10261–10269 (1998). doi: [10.1074/jbc.273.17.10261](#); pmid: [9553078](#)
 42. K. Bersell, S. Arab, B. Haring, B. Kühn, Neuregulin1/ErbB4 signaling induces cardiomyocyte proliferation and repair of heart injury. *Cell* **138**, 257–270 (2009). doi: [10.1016/j.cell.2009.04.060](#); pmid: [19632177](#)
 43. G. D'Uva *et al.*, ERBB2 triggers mammalian heart regeneration by promoting cardiomyocyte dedifferentiation and proliferation. *Nat. Cell Biol.* **17**, 627–638 (2015). doi: [10.1038/ncb3149](#); pmid: [25848746](#)
 44. A. Aharonov *et al.*, ERBB2 drives YAP activation and EMT-like processes during cardiac regeneration. *Nat. Cell Biol.* **22**, 1346–1356 (2020). doi: [10.1038/s41556-020-00588-4](#); pmid: [33046882](#)
 45. L. Nicin *et al.*, A human cell atlas of the pressure-induced hypertrophic heart. *Nature Cardiovascular Research* **1**, 174–185 (2022). doi: [10.1038/s44161-022-00019-7](#)
 46. H. Otani, The role of nitric oxide in myocardial repair and remodeling. *Antioxid. Redox Signal.* **11**, 1913–1928 (2009). doi: [10.1089/ars.2009.2453](#); pmid: [19203224](#)
 47. S.-I. Bibi *et al.*, Mapping the Endothelial Cell S-Sulphydrome Highlights the Crucial Role of Integrin Sulphydration in Vascular Function. *Circulation* **143**, 935–948 (2021). doi: [10.1161/CIRCULATIONAHA.120.051877](#); pmid: [33307764](#)
 48. J. Andrade *et al.*, Control of endothelial quiescence by FOXO-regulated metabolites. *Nat. Cell Biol.* **23**, 413–423 (2021). doi: [10.1038/s41556-021-00637-6](#); pmid: [33795871](#)
 49. R. R. Smith *et al.*, Regenerative potential of cardiosphere-derived cells expanded from percutaneous endomyocardial biopsy specimens. *Circulation* **115**, 896–908 (2007). doi: [10.1161/CIRCULATIONAHA.106.655209](#); pmid: [17283259](#)
 50. D. Todorova, S. Simoncini, R. Lacroix, F. Sabatier, F. Dignat-George, Extracellular Vesicles in Angiogenesis. *Circ. Res.* **120**, 1658–1673 (2017). doi: [10.1161/CIRCRESAHA.117.309681](#); pmid: [28495996](#)
 51. X. Wu, M. R. Reboll, M. Korf-Klingebiel, K. C. Wollert, Angiogenesis after acute myocardial infarction. *Cardiovasc. Res.* **117**, 1257–1273 (2021). doi: [10.1093/cvr/cvab287](#); pmid: [33063086](#)
 52. G. Luxán, S. Dimmeler, The vasculature: A therapeutic target in heart failure? *Cardiovasc. Res.* **118**, 53–64 (2022). doi: [10.1093/cvr/cvab047](#); pmid: [33620071](#)
 53. M. Grunewald *et al.*, Counteracting age-related VEGF signaling insufficiency promotes healthy aging and extends life span. *Science* **373**, eabc8479 (2021). doi: [10.1126/science.abc8479](#); pmid: [34326210](#)
 54. A. Collén *et al.*, VEGFA mRNA for regenerative treatment of heart failure. *Nat. Rev. Drug Discov.* **21**, 79–80 (2022). pmid: [34873303](#)
 55. M. Räsänen *et al.*, VEGF-B Promotes Endocardium-Derived Coronary Vessel Development and Cardiac Regeneration. *Circulation* **143**, 65–77 (2021). doi: [10.1161/CIRCULATIONAHA.120.050635](#); pmid: [33203221](#)
 56. D. Tempel *et al.*, Apelin enhances cardiac neovascularization after myocardial infarction by recruiting apelin+ circulating cells. *Circ. Res.* **111**, 585–598 (2012). doi: [10.1161/CIRCRESAHA.111.262097](#); pmid: [22753078](#)
 57. C. Urbich *et al.*, Soluble factors released by endothelial progenitor cells promote migration of endothelial cells and cardiac resident progenitor cells. *J. Mol. Cell. Cardiol.* **39**, 733–742 (2005). doi: [10.1016/j.jmcc.2005.07.003](#); pmid: [16199052](#)
 58. J. Rehman, J. Li, C. M. Orschemm, K. L. March, Peripheral blood “endothelial progenitor cells” are derived from monocyte/macrophages and secrete angiogenic growth factors. *Circulation* **107**, 1164–1169 (2003). doi: [10.1161/01.CIR.0000058702.69484.A0](#); pmid: [12615796](#)
 59. M. Arras *et al.*, Monocyte activation in angiogenesis and collateral growth in the rabbit hindlimb. *J. Clin. Invest.* **101**, 40–50 (1998). doi: [10.1172/JCI19877](#); pmid: [9421464](#)
 60. K. Krishnasamy *et al.*, Blood vessel control of macrophage maturation promotes arteriogenesis in ischemia. *Nat. Commun.* **8**, 952 (2017). doi: [10.1038/s41467-017-00953-2](#); pmid: [29038527](#)
 61. M. Korf-Klingebiel *et al.*, Myeloid-derived growth factor (C19orf10) mediates cardiac repair following myocardial infarction. *Nat. Med.* **21**, 140–149 (2015). doi: [10.1038/nm.3778](#); pmid: [25581518](#)
 62. M. R. Reboll *et al.*, EMC10 (Endoplasmic Reticulum Membrane Protein Complex Subunit 10) Is a Bone Marrow-Derived Angiogenic Growth Factor Promoting Tissue Repair After Myocardial Infarction. *Circulation* **136**, 1809–1823 (2017). doi: [10.1161/CIRCULATIONAHA.117.029980](#); pmid: [28931551](#)
 63. S. Das *et al.*, A Unique Collateral Artery Development Program Promotes Neonatal Heart Regeneration. *Cell* **176**, 1128–1142.e18 (2019). doi: [10.1016/j.cell.2018.12.023](#); pmid: [30686582](#)
 64. S.-J. Lee *et al.*, Angiopoietin-2 exacerbates cardiac hypoxia and inflammation after myocardial infarction. *J. Clin. Invest.* **128**, 5018–5033 (2018). doi: [10.1172/JCI96659](#); pmid: [30295643](#)
 65. C. E. Trincot *et al.*, Adrenomedullin Induces Cardiac Lymphangiogenesis After Myocardial Infarction and Regulates Cardiac Edema Via Connexin 43. *Circ. Res.* **124**, 101–113 (2019). doi: [10.1161/CIRCRESAHA.118.313835](#); pmid: [30582443](#)
 66. F. Tatin *et al.*, Apelin modulates pathological remodeling of lymphatic endothelium after myocardial infarction. *JCI Insight* **2**, e93887 (2017). doi: [10.1172/jci.insight.93887](#); pmid: [28614788](#)
 67. A. Schober *et al.*, MicroRNA-126-5p promotes endothelial proliferation and limits atherosclerosis by suppressing Dlk1. *Nat. Med.* **20**, 368–376 (2014). doi: [10.1038/nm.3487](#); pmid: [24584117](#)
 68. A. Bonauer *et al.*, MicroRNA-92a controls angiogenesis and functional recovery of ischemic tissues in mice. *Science* **324**, 1710–1713 (2009). doi: [10.1126/science.1174381](#); pmid: [19460962](#)
 69. W. T. Abplanalp *et al.*, Efficiency and Target Derepression of Anti-miR-92a: Results of a First in Human Study. *Nucleic Acid Ther.* **30**, 335–345 (2020). doi: [10.1089/nat.2020.0871](#); pmid: [32707001](#)
 70. M. Nahrendorf *et al.*, The healing myocardium sequentially mobilizes two monocyte subsets with divergent and complementary functions. *J. Exp. Med.* **204**, 3037–3047 (2007). doi: [10.1084/jem.20070885](#); pmid: [18025128](#)
 71. F. K. Swirski, M. Nahrendorf, Cardioimmunology: The immune system in cardiac homeostasis and disease. *Nat. Rev. Immunol.* **18**, 733–744 (2018). doi: [10.1038/s41577-018-0065-8](#); pmid: [30228378](#)
 72. J. G. Rurik, H. Aghajanian, J. A. Epstein, Immune Cells and Immunotherapy for Cardiac Injury and Repair. *Circ. Res.* **128**, 1766–1779 (2021). doi: [10.1161/CIRCRESAHA.121.318005](#); pmid: [34043424](#)
 73. S. Li *et al.*, Cardiomyocytes disrupt pyrimidine biosynthesis in nonmyocytes to regulate heart repair. *J. Clin. Invest.* **132**, e49711 (2022). doi: [10.1172/JCI149711](#); pmid: [34813507](#)
 74. M. Wyszczynski *et al.*, Complement component 3 is necessary to preserve myocardium and myocardial function in chronic myocardial infarction. *Stem Cells* **32**, 2502–2515 (2014). doi: [10.1002/stem.1743](#); pmid: [24806427](#)
 75. G. Sreejit *et al.*, Neutrophils in cardiovascular disease: Warmongers, peacemakers or both? *Cardiovasc. Res.* **cvab302** (2021). doi: [10.1093/cvr/cvab302](#); pmid: [34534269](#)
 76. J. F. Pruijt *et al.*, Neutrophils are indispensable for hematopoietic stem cell mobilization induced by interleukin-8

- in mice. *Proc. Natl. Acad. Sci. U.S.A.* **99**, 6228–6233 (2002). doi: [10.1073/pnas.092112999](#); pmid: [11983913](#)
77. F. Sicklinger *et al.*, Basophils balance healing after myocardial infarction via IL-4/IL-13. *J. Clin. Invest.* **131**, e136778 (2021). doi: [10.1172/JCI136778](#); pmid: [34196299](#)
 78. G. Bajpai *et al.*, The human heart contains distinct macrophage subsets with divergent origins and functions. *Nat. Med.* **24**, 1234–1245 (2018). doi: [10.1038/s41591-018-0059-x](#); pmid: [29892064](#)
 79. S. A. Dick *et al.*, Self-renewing resident cardiac macrophages limit adverse remodeling following myocardial infarction. *Nat. Immunol.* **20**, 29–39 (2019). doi: [10.1038/s41590-018-0272-2](#); pmid: [30538339](#)
 80. S. Epelman *et al.*, Embryonic and adult-derived resident cardiac macrophages are maintained through distinct mechanisms at steady state and during inflammation. *Immunity* **40**, 91–104 (2014). doi: [10.1016/j.immuni.2013.11.019](#); pmid: [24439267](#)
 81. A. B. Aurora *et al.*, Macrophages are required for neonatal heart regeneration. *J. Clin. Invest.* **124**, 1382–1392 (2014). doi: [10.1172/JCI72181](#); pmid: [24569380](#)
 82. R. J. Vagnozzi *et al.*, An acute immune response underlies the benefit of cardiac stem cell therapy. *Nature* **577**, 405–409 (2020). doi: [10.1038/s41586-019-1802-2](#); pmid: [31775156](#)
 83. R. Zaman *et al.*, Selective loss of resident macrophage-derived insulin-like growth factor-1 abolishes adaptive cardiac growth to stress. *Immunity* **54**, 2057–2071.e6 (2021). doi: [10.1016/j.immuni.2021.07.006](#); pmid: [34363749](#)
 84. N. R. Wong *et al.*, Resident cardiac macrophages mediate adaptive myocardial remodeling. *Immunity* **54**, 2072–2088.e7 (2021). doi: [10.1016/j.immuni.2021.07.003](#); pmid: [34320366](#)
 85. H. Lörchner *et al.*, Myocardial healing requires Reg3 β -dependent accumulation of macrophages in the ischemic heart. *Nat. Med.* **21**, 353–362 (2015). doi: [10.1038/nm.3816](#); pmid: [25751817](#)
 86. S. Epelman, P. P. Liu, D. L. Mann, Role of innate and adaptive immune mechanisms in cardiac injury and repair. *Nat. Rev. Immunol.* **15**, 117–129 (2015). doi: [10.1038/nri3800](#); pmid: [25614321](#)
 87. U. Hofmann, S. Frantz, Role of T-cells in myocardial infarction. *Eur. Heart J.* **37**, 873–879 (2016). doi: [10.1093/eurheartj/ehv639](#); pmid: [26646702](#)
 88. X. Yan *et al.*, Temporal dynamics of cardiac immune cell accumulation following acute myocardial infarction. *J. Mol. Cell. Cardiol.* **62**, 24–35 (2013). doi: [10.1016/j.jymcc.2013.04.023](#); pmid: [23644221](#)
 89. J. Hoffmann *et al.*, Circulating Th17 and Th22 Cells Are Associated With CMR Imaging Biosignatures of Diffuse Myocardial Interstitial Remodeling in Chronic Coronary Artery Disease. *Circ. Res.* **127**, 699–701 (2020). doi: [10.1161/CIRCRESAHA.120.316619](#); pmid: [32576092](#)
 90. M. D. Mora-Ruiz, F. Blanco-Favela, A. K. Chávez Rueda, M. V. Legorreta-Haquet, L. Chávez-Sánchez, Role of interleukin-17 in acute myocardial infarction. *Mol. Immunol.* **107**, 71–78 (2019). doi: [10.1016/j.molimm.2019.01.008](#); pmid: [30660992](#)
 91. G.-L. Xue *et al.*, Interleukin-17 upregulation participates in the pathogenesis of heart failure in mice via NF- κ B-dependent suppression of SERCA2a and Cav1.2 expression. *Acta Pharmacol. Sin.* **42**, 1780–1789 (2021). doi: [10.1038/s41401-020-00580-6](#); pmid: [33589793](#)
 92. H. J. Faust *et al.*, IL-17 and immunologically induced senescence regulate response to injury in osteoarthritis. *J. Clin. Invest.* **130**, 5493–5507 (2020). doi: [10.1172/JCI134091](#); pmid: [32955487](#)
 93. M. Kalikourdis *et al.*, T cell costimulation blockade blunts pressure overload-induced heart failure. *Nat. Commun.* **8**, 14680 (2017). doi: [10.1038/ncomms14680](#); pmid: [28262700](#)
 94. S. Zaccagna *et al.*, Paracrine effect of regulatory T cells promotes cardiomyocyte proliferation during pregnancy and after myocardial infarction. *Nat. Commun.* **9**, 2432 (2018). doi: [10.1038/s41467-018-04908-z](#); pmid: [29946151](#)
 95. T. H. W. Fung, K. Y. Yang, K. O. Lui, An emerging role of regulatory T-cells in cardiovascular repair and regeneration. *Theranostics* **10**, 8924–8938 (2020). doi: [10.7150/thno.47118](#); pmid: [32802172](#)
 96. S. P. Hui *et al.*, Zebrafish Regulatory T Cells Mediate Organ-Specific Regenerative Programs. *Dev. Cell* **43**, 659–672.e5 (2017). doi: [10.1016/j.devcel.2017.11.010](#); pmid: [29257949](#)
 97. D. Eastwood *et al.*, Monoclonal antibody TGN1412 trial failure explained by species differences in CD28 expression on CD4+ effector memory T-cells. *Br. J. Pharmacol.* **161**, 512–526 (2010). doi: [10.1111/j.1476-5381.2010.00922.x](#); pmid: [20880392](#)
 98. G. Suntharalingam *et al.*, Cytokine storm in a phase 1 trial of the anti-CD28 monoclonal antibody TGN1412. *N. Engl. J. Med.* **355**, 1018–1028 (2006). doi: [10.1056/NEJMoa063842](#); pmid: [16908486](#)
 99. J. S. Burchfield *et al.*, Interleukin-10 from transplanted bone marrow mononuclear cells contributes to cardiac protection after myocardial infarction. *Circ. Res.* **103**, 203–211 (2008). doi: [10.1161/CIRCRESAHA.108.178475](#); pmid: [18566343](#)
 100. Z. Yang, B. Zingarelli, C. Szabó, Crucial role of endogenous interleukin-10 production in myocardial ischemia/reperfusion injury. *Circulation* **101**, 1019–1026 (2000). doi: [10.1161/01.CIR.101.9.1019](#); pmid: [10704170](#)
 101. M. Hulsmans *et al.*, Cardiac macrophages promote diastolic dysfunction. *J. Exp. Med.* **215**, 423–440 (2018). doi: [10.1084/jem.20171274](#); pmid: [29339450](#)
 102. Y. Zhang, J. Bauersachs, H. F. Langer, Immune mechanisms in heart failure. *Eur. J. Heart Fail.* **19**, 1379–1389 (2017). doi: [10.1002/ehf.942](#); pmid: [28891154](#)
 103. S. M. Nidorf *et al.*, Colchicine in Patients with Chronic Coronary Disease. *N. Engl. J. Med.* **383**, 1838–1847 (2020). doi: [10.1056/NEJMoa2021372](#); pmid: [32865380](#)
 104. L. Dorsheimer *et al.*, Association of Mutations Contributing to Clonal Hematopoiesis With Prognosis in Chronic Ischemic Heart Failure. *JAMA Cardiol.* **4**, 25–33 (2019). doi: [10.1001/jamacardio.2018.3965](#); pmid: [30566180](#)
 105. F. C. Simões *et al.*, Macrophages directly contribute collagen to scar formation during zebrafish heart regeneration and mouse heart repair. *Nat. Commun.* **11**, 600 (2020). doi: [10.1038/s41467-019-14263-2](#); pmid: [32001677](#)
 106. H. Li, M. Bao, Y. Nie, Extracellular matrix-based biomaterials for cardiac regeneration and repair. *Heart Fail. Rev.* **26**, 1231–1248 (2021). doi: [10.1007/s10741-020-09953-9](#); pmid: [32306220](#)
 107. E. Bassat *et al.*, The extracellular matrix protein agrin promotes heart regeneration in mice. *Nature* **547**, 179–184 (2017). doi: [10.1038/nature22978](#); pmid: [28581497](#)
 108. E. Eroglu, K. R. Chien, Heart Regeneration 4.0: Matrix Medicine. *Dev. Cell* **42**, 7–8 (2017). doi: [10.1016/j.devcel.2017.06.017](#); pmid: [28697334](#)
 109. A. Baehr *et al.*, Agrin Promotes Coordinated Therapeutic Processes Leading to Improved Cardiac Repair in Pigs. *Circulation* **142**, 868–881 (2020). doi: [10.1161/CIRCULATIONAHA.119.045116](#); pmid: [32508131](#)
 110. I. Valiente-Alandi, A. E. Schafer, B. C. Blaxall, Extracellular matrix-mediated cellular communication in the heart. *J. Mol. Cell. Cardiol.* **91**, 228–237 (2016). doi: [10.1016/j.jymcc.2016.01.011](#); pmid: [26778458](#)
 111. N. G. Frangogiannis, The extracellular matrix in myocardial injury, repair, and remodeling. *J. Clin. Invest.* **127**, 1600–1612 (2017). doi: [10.1172/JCI87491](#); pmid: [28459429](#)
 112. A. C. Silva, C. Pereira, A. C. R. G. Fonseca, P. Pinto-do-Ó, D. S. Nascimento, Bearing My Heart: The Role of Extracellular Matrix on Cardiac Development, Homeostasis, and Injury Response. *Front. Cell Dev. Biol.* **8**, 621644 (2021). doi: [10.3389/fcell.2020.621644](#); pmid: [33511134](#)
 113. Y. Yahalom-Ronen, D. Rajchman, R. Sarig, B. Geiger, E. Tzahor, Reduced matrix rigidity promotes neonatal cardiomyocyte dedifferentiation, proliferation and clonal expansion. *eLife* **4**, e07455 (2015). doi: [10.7554/eLife.07455](#); pmid: [26267307](#)
 114. M. Notari *et al.*, The local microenvironment limits the regenerative potential of the mouse neonatal heart. *Sci. Adv.* **4**, eaao5553 (2018). doi: [10.1126/sciadv.aao5553](#); pmid: [29732402](#)
 115. T. Yokota *et al.*, Type V Collagen in Scar Tissue Regulates the Size of Scar after Heart Injury. *Cell* **182**, 545–562.e23 (2020). doi: [10.1016/j.cell.2020.06.030](#); pmid: [32621799](#)
 116. C.-C. Wu, S. Jeratsch, J. Graumann, D. Y. R. Stainier, Modulation of Mammalian Cardiomyocyte Cytokinesis by the Extracellular Matrix. *Circ. Res.* **127**, 896–907 (2020). doi: [10.1161/CIRCRESAHA.119.316303](#); pmid: [32564729](#)
 117. M. Valussi *et al.*, Repression of *Osmr* and *Fgfr1* by *miR-1/133a* prevents cardiomyocyte dedifferentiation and cell cycle entry in the adult heart. *Sci. Adv.* **7**, eabi6648 (2021). doi: [10.1126/sciadv.abi6648](#); pmid: [34644107](#)
 118. H. E. Walters, M. H. Yun, Rising from the ashes: Cellular senescence in regeneration. *Curr. Opin. Genet. Dev.* **64**, 94–100 (2020). doi: [10.1016/j.gde.2020.06.002](#); pmid: [32721584](#)
 119. M. S. Chen, R. T. Lee, J. C. Garbern, Senescence mechanisms and targets in the heart. *Cardiovasc. Res.* **118**, 1173–1187 (2022). doi: [10.1093/cvr/cvab161](#); pmid: [33963378](#)
 120. D. Paramos-de-Carvalho, A. Jacinto, L. Saúde, The right time for senescence. *eLife* **10**, e72449 (2021). doi: [10.7554/eLife.72449](#); pmid: [34756162](#)
 121. R. Sarig *et al.*, Transient p53-Mediated Regenerative Senescence in the Injured Heart. *Circulation* **139**, 2491–2494 (2019). doi: [10.1161/CIRCULATIONAHA.119.040125](#); pmid: [31107623](#)
 122. K. Meyer, B. Hodwin, D. Ramanujam, S. Engelhardt, A. Sarikas, Essential Role for Premature Senescence of Myofibroblasts in Myocardial Fibrosis. *J. Am. Coll. Cardiol.* **67**, 2018–2028 (2016). doi: [10.1016/j.jacc.2016.02.047](#); pmid: [27126529](#)
 123. T. Feng *et al.*, CCN1-Induced Cellular Senescence Promotes Heart Regeneration. *Circulation* **139**, 2495–2498 (2019). doi: [10.1161/CIRCULATIONAHA.119.039530](#); pmid: [31107624](#)
 124. G. Desdin-Micó *et al.*, T cells with dysfunctional mitochondria induce multimorbidity and premature senescence. *Science* **368**, 1371–1376 (2020). doi: [10.1126/science.aaa0860](#); pmid: [32439659](#)
 125. D. Bednarek *et al.*, Telomerase Is Essential for Zebrafish Heart Regeneration. *Cell Rep.* **12**, 1691–1703 (2015). doi: [10.1016/j.celrep.2015.07.064](#); pmid: [26321646](#)
 126. C. Bär *et al.*, Telomerase expression confers cardioprotection in the adult mouse heart after acute myocardial infarction. *Nat. Commun.* **5**, 5863 (2014). doi: [10.1038/ncomms5863](#); pmid: [25519492](#)
 127. H. J. Cho *et al.*, Mobilized endothelial progenitor cells by granulocyte-macrophage colony-stimulating factor accelerate reendothelialization and reduce vascular inflammation after intravascular radiation. *Circulation* **108**, 2918–2925 (2003). doi: [10.1161/01.CIR.0000097001.79750.78](#); pmid: [14568896](#)
 128. Y. Zhu *et al.*, New agents that target senescent cells: The flavone, fisetin, and the BCL-X_L inhibitors, A1331852 and A1155463. *Aging (Albany NY)* **9**, 955–963 (2017). doi: [10.18632/aging.101202](#); pmid: [28273655](#)
 129. D. J. Baker *et al.*, Clearance of p16Ink4a-positive senescent cells delays ageing-associated disorders. *Nature* **479**, 232–236 (2011). doi: [10.1038/nature10600](#); pmid: [22048312](#)
 130. W. A. Owens, A. Walaszczyk, I. Spyridopoulos, E. Dookun, G. D. Richardson, Senescence and senolytics in cardiovascular disease: Promise and potential pitfalls. *Mech. Ageing Dev.* **198**, 111540 (2021). doi: [10.1016/j.jmad.2021.111540](#); pmid: [34237321](#)
 131. O. Bergmann *et al.*, Evidence for cardiomyocyte renewal in humans. *Science* **324**, 98–102 (2009). doi: [10.1126/science.1164680](#); pmid: [19342590](#)

ACKNOWLEDGMENTS

The authors apologize to the many researchers making important contributions to the field, whose work could not be cited owing to space restrictions. We thank members of our laboratories for constructive insights and Maayan Visuals for the art work. **Funding:** S.D. is supported by the Dr. Robert M. Schwiete Foundation, the German Research Foundation (SFB834, SFB1366, TRR267, Exc2026/1), and the European Research Council (ERC AdG 101053352). E.T. is supported by the European Research Council (ERC AdG 788194), the European Union's Horizon 2020 research and innovation program (874764), and the Israel Science Foundation (ISF). **Competing Interests:** S.D. has patents on mRNA therapeutics. E.T. is a founder of a biomedical startup related to Agrin therapy for heart disease and has related patents. **License information:** Copyright © 2022 the authors, some rights reserved; exclusive licensee American Association for the Advancement of Science. No claim to original US government works. <https://www.science.org/about/science-licenses-journal-article-reuse>

Submitted 15 October 2021; accepted 3 August 2022
10.1126/science.abm4443

RESEARCH ARTICLE SUMMARY

NEUROEVOLUTION

Molecular diversity and evolution of neuron types in the amniote brain

David Hain^{†*}, Tatiana Gallego-Flores^{†*}, Michaela Klinkmann, Angeles Macias, Elena Ciirdaeva, Anja Arends, Christina Thum, Georgi Tushev, Friedrich Kretschmer, Maria Antonietta Tosches^{†*}, Gilles Laurent^{†*}

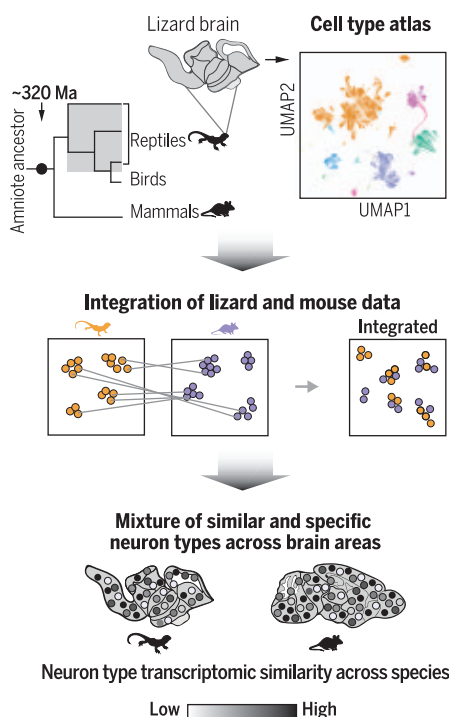
INTRODUCTION: Vertebrate evolution took an important turn before the onset of the Permian, 320 million years ago, with the transition of early tetrapods from water to land, the appearance of amniotes, and, soon thereafter, their bifurcation into sauropsids (future reptiles and birds) and synapsids (future mammals). Despite this branched history, the brains of all tetrapods share the same ancestral architecture defined by brain regions established during embryonic development (pallium, subpallium, thalamus, cerebellum, etc.) and by their long-range connections. Yet how variations on this common organization contributed to lineage- and species-specific adaptations is not clear. A commonly held assumption, for example, is that subcortical regions are ancient and “deeply conserved,” whereas the mammalian cortex is “new,” following profound changes in cortical development in this lineage.

Brain regions, however, do not operate in isolation, raising the possibility that the evolution of interconnected neurons might be correlated. Likewise, areas in reptiles and mammals that derive from a common ancestral structure, such as the cerebral cortex, may have evolved in each lineage in such a way that they now each contain both ancient (thus common) and novel neuron types. Because traditional comparisons of developmental regions and projections may not suffice to reveal these similarities and differences, we investigated these issues using cellular transcriptomic approaches.

RATIONALE: Neurons are the most diverse cell types in the brain; their evolutionary diversification reflects changes in the developmental processes that produce them and, in turn, may drive changes in the neural circuits to which they belong. To the extent that a neuron's transcriptome represents the molecular encoding of its identity, connectivity, and developmental and evolutionary histories, comparing neuronal transcriptomes across species should yield insights into brain evolution. To elucidate the evolution of neuronal diversity across brain regions, we generated a cell type atlas of the brain of a reptile, the Australian bearded

dragon *Pogona vitticeps*, and compared it with existing mouse brain datasets.

RESULTS: We profiled 285,483 single-cell transcriptomes from the brain of *Pogona* and identified and annotated 233 distinct types of neurons. Computational integration of this dataset with publicly available mouse data revealed that lizard and mouse neurons co-cluster according to their regional and neurotransmitter identities. These integrated clusters expressed distinctive combinations of de-



Transcriptomic study of neuronal evolution among amniotes. Reptiles and mammals evolved independently of each other for ~300 million years. We generated a cell type atlas from the brain of a lizard, *Pogona vitticeps*. Computational integration of these data with mouse transcriptomes reveals that telencephalon, diencephalon, and mesencephalon each contain mixtures of similar and divergent neurons, indicating that neuron diversification is ubiquitous in those regions.

velopmental transcription factors (including homeodomain-type) and genes involved in neuronal connectivity (cell junction, synaptic signaling, neuronal projections, synaptic transmission), indicating that both developmental origin and circuit allocation define broad, evolutionarily conserved classes of neurons in the amniote brain.

At a finer level, these broad classes included neuron types with a wide range of transcriptomic variation across species. Certain neuron types could be readily mapped from lizard to mouse, indicating high transcriptomic similarity; others, however, could not be mapped across species unambiguously, owing to transcriptomic divergence. This dichotomy was true for all regions analyzed (telencephalon, diencephalon, and midbrain), indicating that neuronal diversification is ubiquitous in these brain regions.

This was particularly evident in the thalamus, where neurons with high transcriptomic similarity across species (GABAergic reticular thalamic nucleus, glutamatergic “medial thalamus”) are juxtaposed with neuron types with diverging gene expression (glutamatergic “lateral thalamus”). In the lateral thalamus, lizard and mouse neurons from sensory relay nuclei did not co-cluster according to sensory modality, suggesting that these neurons may have diversified extensively, reflecting the different fates of their cortical partners in the reptilian and mammalian lineages.

CONCLUSION: Using comparative single-cell transcriptomics, we identified a core set of neuron types with high transcriptomic similarity between the brains of a lizard and a mammal, despite 320 million years of separate evolution. These neuron types are not restricted to subcortical regions but are found everywhere in the brain, including in the cerebral cortex, challenging the notion that certain brain regions are more ancient than others. Our data suggest that, even if the brain consists of developmental modules defined by ancient and shared molecular determinants, the evolution of the brain acts upon each module by keeping (e.g., reticular thalamic nucleus and medial thalamus) or diversifying (e.g., lateral thalamus) neuron types in a manner that is correlated with local and long-range connectivity. ■

The list of author affiliations is available in the full article online.

*Corresponding author. Email: david.hain@brain.mpg.de (D.H.); maria-tatiana.gallego-flores@brain.mpg.de (T.G.-F.); mt3353@columbia.edu (M.A.T.); gilles.laurent@brain.mpg.de (G.L.)

†These authors contributed equally to this work.

‡These authors contributed equally to this work.

Cite this article as D. Hain et al., *Science* 377, eabp8202 (2022). DOI: 10.1126/science.abp8202

S READ THE FULL ARTICLE AT
https://doi.org/10.1126/science.abp8202

RESEARCH ARTICLE

NEUROEVOLUTION

Molecular diversity and evolution of neuron types in the amniote brain

David Hain^{1,2,*}, Tatiana Gallego-Flores^{1,2,*}, Michaela Klinkmann¹, Angeles Macias¹, Elena Ciirdeaeva¹, Anja Arends¹, Christina Thum¹, Georgi Tushev¹, Friedrich Kretschmer¹, Maria Antonietta Tosches^{1,3,*}, Gilles Laurent^{1,†}

The existence of evolutionarily conserved regions in the vertebrate brain is well established. The rules and constraints underlying the evolution of neuron types, however, remain poorly understood. To compare neuron types across brain regions and species, we generated a cell type atlas of the brain of a bearded dragon and compared it with mouse datasets. Conserved classes of neurons could be identified from the expression of hundreds of genes, including homeodomain-type transcription factors and genes involved in connectivity. Within these classes, however, there are both conserved and divergent neuron types, precluding a simple categorization of the brain into ancestral and novel areas. In the thalamus, neuronal diversification correlates with the evolution of the cortex, suggesting that developmental origin and circuit allocation are drivers of neuronal identity and evolution.

Vertebrates arose during the Cambrian explosion, about half a billion years ago. Despite this long history, their brains share a common basic architecture, including the same identifiable brain divisions: forebrain (telencephalon and diencephalon), midbrain or mesencephalon, and hindbrain or rhombencephalon (metencephalon and myelencephalon). This stability of brain architecture can be contrasted with that in other animal clades, such as mollusks, who, over the same period, evolved a greater variety of nervous system plans and neural circuits (1).

During early vertebrate development, the principal brain divisions are patterned by conserved signaling centers and express similar combinations of developmental transcription factors (2–4). Those divisions develop into brain regions (e.g., pallium, basal ganglia, thalamus, optic tectum, etc.) containing increasingly clade-specific circuits and neuron types. For example, both mammals and nonavian reptiles have a layered cerebral cortex and a thalamus, although with different numbers of cortical layers and thalamic nuclei (5).

Two extreme models could explain the evolution of neuronal diversity in the brain. If neuronal identity were strongly tied to developmental history, then neurons that belong to the same brain region would be expected to evolve in concert and to display similar rates

of molecular divergence from their respective orthologs in other species (Fig. 1A, model 1). By contrast, if the genetic programs that specify brain regions and neuronal identities were, at least in part, independent of one another, then neurons in the same brain region would be free to evolve along distinct paths at different rates. In this case, each brain region would be a mosaic of conserved (i.e., shared across species) and diverging (i.e., specific) neuron types (Fig. 1A, model 2).

To test these models, we quantified and systematically compared neuronal diversity in two amniotes, the mouse and a lizard, the Australian bearded dragon *Pogona vitticeps*, using cellular transcriptomes as proxies for neuronal identities. The common ancestor of mammals and reptiles lived some 320 million years ago, had already fully adapted to life on land, and had a complex brain with a cerebral cortex (6).

Our analysis indicates that brain regional identities are encoded in neuronal transcriptomes by conserved sets of genes, that a core set of deeply conserved neuron classes can be identified in the two species, and that neuronal diversification has occurred in mammals and in reptiles in all the brain divisions that we analyzed in detail (telencephalon, diencephalon, and mesencephalon). This changes and clarifies, at a cellular scale, the simple perspective that certain regions of the vertebrate brain are ancient, while others are new. We propose that most brain regions, in reptiles as in mammals, contain a mixture of ancient and novel neuron types. Within this scheme, we observe interesting local variations, such as across the medial and lateral domains of the thalamus, that parallel the divergent evolution of the cerebral cortex in reptiles and mammals.

A cell type atlas of the lizard brain

To build a cell type atlas of the adult *Pogona* brain, we performed single-cell RNA sequencing (scRNA-seq; 10X Chromium) on 285,483 cells sampled from the telencephalon, diencephalon, mesencephalon, and metencephalon (with the exception of the olfactory bulb and pineal complex, and with a limited sampling of the noncerebellar metencephalon) (figs. S1, S2A, and S3A) (see methods in the supplementary materials). Clustering analysis identified classes of neuronal and non-neuronal cells (Fig. 1B) annotated for the expression of canonical marker genes (Fig. 1C and fig. S2B). For example, neurons were identified by expression of *snap25*, part of the SNARE (soluble *N*-ethylmaleimide-sensitive factor attachment protein receptor) machinery (7); oligodendrocyte precursor cells (OPCs) by *pdgfra*, a receptor for platelet-derived growth factor (8); differentiating oligodendrocytes by *gpr17* (9) and *mag* (10); mature oligodendrocytes by *mag* but not *gpr17*; ependymal cells by *gfap* (11), suggestive of a common origin with mammalian astrocytes (12); a population of ependymoglia in the cerebellum (a putative reptilian homolog of Bergmann glia) by *draxin*, an axon guidance molecule (13); and cells from the sub-commissural organ by *sspo*, involved in the formation of the Reissner's fiber (14).

We focused on the 89,015 neurons in our data, revealing 233 distinct clusters (Fig. 1D and fig. S3C). We assigned each cluster to one of 11 brain regions (Fig. 1D) using several criteria: (i) knowledge of origin by dissection before dissociation (figs. S3, A to C, and S4, and data S1); (ii) expression patterns of cluster-specific marker genes, assayed by *in situ* hybridization; and (iii) expression of known region-specific marker genes described in the literature (data S2 and S3).

An analysis of the expression of gene families across lizard neuron types indicated that, as reported in other systems (15–17), certain gene families, such as G protein-coupled receptors (GPCRs) and transcription factors (especially of the homeodomain type), show cell type-specific expression (Fig. 1E). This supports the hypothesis that homeodomain transcription factors function as selectors of neuronal identity in both vertebrates and invertebrates (17). Because transcription factors, including homeodomain types, are crucial for the early regionalization of the vertebrate nervous system, we sought to determine whether the expression of transcription factors in adult neuron types is sufficient to group them according to the brain regions to which they belong. For this, we performed hierarchical clustering of cluster transcriptomes on the basis of the expression of the 386 transcription factors expressed in the dataset.

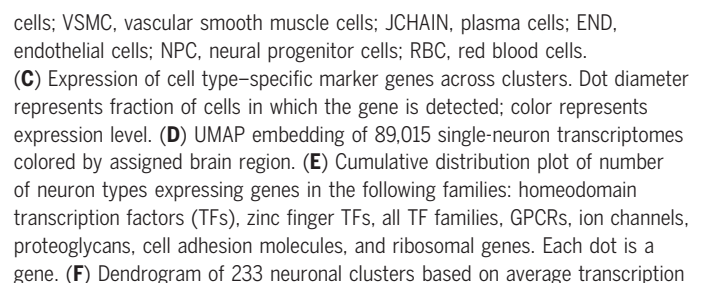
The resulting taxonomy grouped neuronal clusters not only by brain region but also by

¹Max Planck Institute for Brain Research, Frankfurt am Main, Germany. ²Faculty of Biological Sciences, Goethe University, Frankfurt am Main, Germany. ³Department of Biological Sciences, Columbia University, New York, NY, USA.

*Corresponding author. Email: david.hain@brain.mpg.de (D.H.); maria-tatiana.gallego-flores@brain.mpg.de (T.G.-F.); mt3353@columbia.edu (M.A.T.); gilles.laurent@brain.mpg.de (G.L.)

†These authors contributed equally to this work.

‡These authors contributed equally to this work.



cells; VSMC, vascular smooth muscle cells; JCHAIN, plasma cells; END, endothelial cells; NPC, neural progenitor cells; RBC, red blood cells. **(C)** Expression of cell type-specific marker genes across clusters. Dot diameter represents fraction of cells in which the gene is detected; color represents expression level. **(D)** UMAP embedding of 89,015 single-neuron transcriptomes colored by assigned brain region. **(E)** Cumulative distribution plot of number of neuron types expressing genes in the following families: homeodomain transcription factors (TFs), zinc finger TFs, all TF families, GPCRs, ion channels, proteoglycans, cell adhesion molecules, and ribosomal genes. Each dot is a gene. **(F)** Dendrogram of 233 neuronal clusters based on average transcription

factor expression (only 35 of 386 TFs are shown). Colors indicate brain regions (left) and neurotransmitters (right); glutamate, blue: *slc17a6*; GABA, red: *slc32a1*; other, gray: *slc17a6* and *slc32a1*; *chat* and *slc18a3*; *th*, *ddc*, and *slc18a2*; or *tph1/tph2* and *slc18a2*. Cla., claustrum; DLA, dorsolateral amygdala; MGE, medial ganglionic eminence; CGE, caudal ganglionic eminence; LGE, lateral ganglionic eminence; Sept., Septum; VM-Thal., ventromedial thalamic

nucleus; A-Hyp., anterior hypothalamus; VMH-Hyp., ventromedial hypothalamus; PIT, pituitary gland; L-Thal., lateral thalamic nucleus; DM-Thal., dorsomedial thalamic nucleus; MM-Hyp., mammillary hypothalamus; PVN-Hyp., paraventricular hypothalamus; Hb, habenula; CB-GC, cerebellar granule cells; CB-INS, cerebellar interneurons; PGN, pretectal geniculate nucleus; CB-PC, cerebellar Purkinje cells.

neurotransmitter type (Fig. 1F). Brain regions and individual nuclei within them (spatially validated by the criteria listed above) are thus identifiable by the combinatorial expression of sets of transcription factors. For example, telencephalic glutamatergic neurons could be distinguished by the coexpression of *foxg1* and *zbtb18* (18); thalamic glutamatergic neurons by *tcf7l2* and *lhx9* (19, 20); habenular neurons by *tcf7l2*, *zic1*, *lhx9*, and *pou4f1* (19); cerebellar granule cells and interneurons, but not Purkinje cells, by *zic1*, *zbtb18*, and *nfya* (21); medial ganglionic eminence-derived γ -aminobutyric acid-releasing (GABAergic) neurons by *foxg1*, *arx*, *lhx6*, *dlx5*, and *zeb2* (22); lateral ganglionic eminence-derived GABAergic neurons by *foxg1*, *meis2*, and *dlx5* (23); and GABAergic neurons of the tegmentum and tectum express *tal1* and *gata3*, but mostly tegmental neurons express *nr2f2* (24) (Fig. 1F). Using in situ hybridization and data available in the literature (data S2), we identified individual nuclei within these brain regions, such as the claustrum and dorsolateral amygdala in the pallium (25); septum in the subpallium; dorsomedial thalamic nucleus in the thalamus; and paraventricular, ventromedial, and mammillary nuclei in the hypothalamus (Fig. 1F and data S2). All 233 clusters and the expression of some of the transcription factors used for their annotation are shown in Fig. 1F and fig. S3C.

Transcriptomic comparisons reveal shared classes of neuron types

Many region- and neuron type-specific marker genes identified in *Pogona* (Fig. 1F and fig. S3C) corresponded to those described in mammals (3). To examine in detail interspecies similarities and differences of neuron types, we integrated our lizard data with a published mouse brain dataset of comparable size and complexity [70,968 neurons, 181 clusters (26)] (fig. S5A). We used canonical correlation analysis (CCA) (27) to identify vectors of genes with high variance across both datasets and then used the 40 top canonical components for downstream analysis, including clustering on the joint nearest-neighbors graph (“integrated clusters”). Twenty of the 32 integrated clusters obtained (Fig. 2A) included neurons of both species (defined as >10% of neurons from each of the two species), indicating that our analysis captures molecular signatures shared across species. Among the integrated clusters with <10% of lizard neurons, some corresponded to mouse neuron types with no lizard homolog [for in-

stance, mouse neocortical layer 6 neurons, cluster 19 (12)], while others (such as cluster 18, olfactory bulb) were neuron types not included in our lizard tissue selections (Fig. 2A and figs. S3A, S5, and S6A). Most neurons in each integrated cluster originated from the same brain divisions (telencephalon, diencephalon, mesencephalon, and metencephalon) in both species (Fig. 2A and fig. S6A), suggesting that the integrated clusters share molecular signatures that reflect their regional identity. Because the main divisions of the developing brain are evolutionarily conserved among vertebrates (28), we hypothesize that these integrated clusters are evolutionarily conserved classes of neuron types. Integrated clusters include, for example, GABAergic neurons from the lateral (cluster 11), medial (cluster 16), and caudal (cluster 17) ganglionic eminences; habenular neurons (cluster 23); cerebellar inhibitory neurons (cluster 24) and granule cells (cluster 9); and glutamatergic and GABAergic cells from the lizard optic tectum and mouse superior colliculus (clusters 2 and 13, respectively) (Fig. 2A and fig. S6A).

To identify the gene families that underlie the co-clustering of mouse and lizard single neurons, we identified marker genes specific to the integrated clusters and present in neurons of both species (data S4). A gene ontology analysis of these marker genes revealed an enrichment in transcription factors, genes related to neuronal connectivity (cell junction, synaptic signaling, neuronal projections, synaptic transmission) and to neuronal development (fig. S6B). Among the conserved transcription factors, the most represented group belonged to the homeodomain type (fig. S6C; homeodomain-type transcription factors are also the largest category among the one-to-one orthologous transcription factors). To check that transcription factors are expressed in evolutionarily conserved patterns, we performed in situ hybridization with representatives of different transcription factor families, such as *tcf7l2*, member of the high-mobility group (HMG) box (thalamus and habenula); *meis2*, a myocyte-specific enhancer-binding factor 2 gene (pallium and medial and lateral ganglionic eminences); *zic1*, a C2H2 zinc finger protein gene (septum, cerebellar granule cells, and anterior prethalamus and medial thalamus); or *tbr1*, a T-box brain transcription factor (pallium) (Fig. 2B). Taken together, these results indicate that sets of transcription factors and effector genes

common to the lizard and mouse brains can be used to identify not only conserved gene expression territories (3) but, more specifically, classes of neuron types common to both species.

Brain regions include similar and divergent neuron types

Taxonomies are often hierarchical. In a comparative context, it has been observed in mammals that higher levels of a cell type taxonomy (e.g., class and subclass) are more conserved than lower ones (e.g., type and subtype) (29). The integration of mouse and lizard single-cell transcriptomes identified large classes of neurons with high cross-species similarity but proved insufficient to identify similarities at the level of individual neuron types (Fig. 2). We reasoned that, if highly similar lizard and mouse neuron types or subtypes existed, they would be “hidden” within the classes of neurons identified above. To identify similarities at deeper levels of the taxonomy, we used the 181 mouse clusters as references and projected the 89,015 lizard single-neuron transcriptomes onto them (26) on the basis of their distances in their joint-embedding space (Fig. 3A; details in methods). The numbers of neurons in each lizard cluster that projected onto a mouse cluster were used to define “projection scores” (normalized; see methods), reflecting the transcriptomic similarity of cluster pairs across species. One hundred and fifty four of the 181 mouse clusters (26) had lizard cells projecting onto them (Fig. 3A). Projection scores ranged widely (fig. S7, A and B), indicating that neuron types or subtypes can diverge widely at the molecular level, even when they belong to evolutionarily conserved classes of neurons. Many of the neuron types with the highest projection scores (0.4 or above) between lizards and mice were those for which homologies had been suggested on the basis of neuroanatomy and expression of selected marker genes. They include neurons in the claustrum and habenula, striatal medium spiny neurons, cerebellar granule cells, interneurons, and Purkinje cells (Fig. 3A) (25, 30–32). We also discovered previously unknown putatively conserved neuron types, such as certain cortical GABAergic interneurons (e.g., coexpressing *sst*, *nos1*, and *chodl*), glutamatergic neurons in the medial thalamus, and neurons from the mouse reticular thalamic nucleus (Fig. 3A). Neuron types that are thought to have evolved similar transcriptomes by convergence (in the reptilian anterior dorsal ventricular ridge and layer 4 of the mammalian

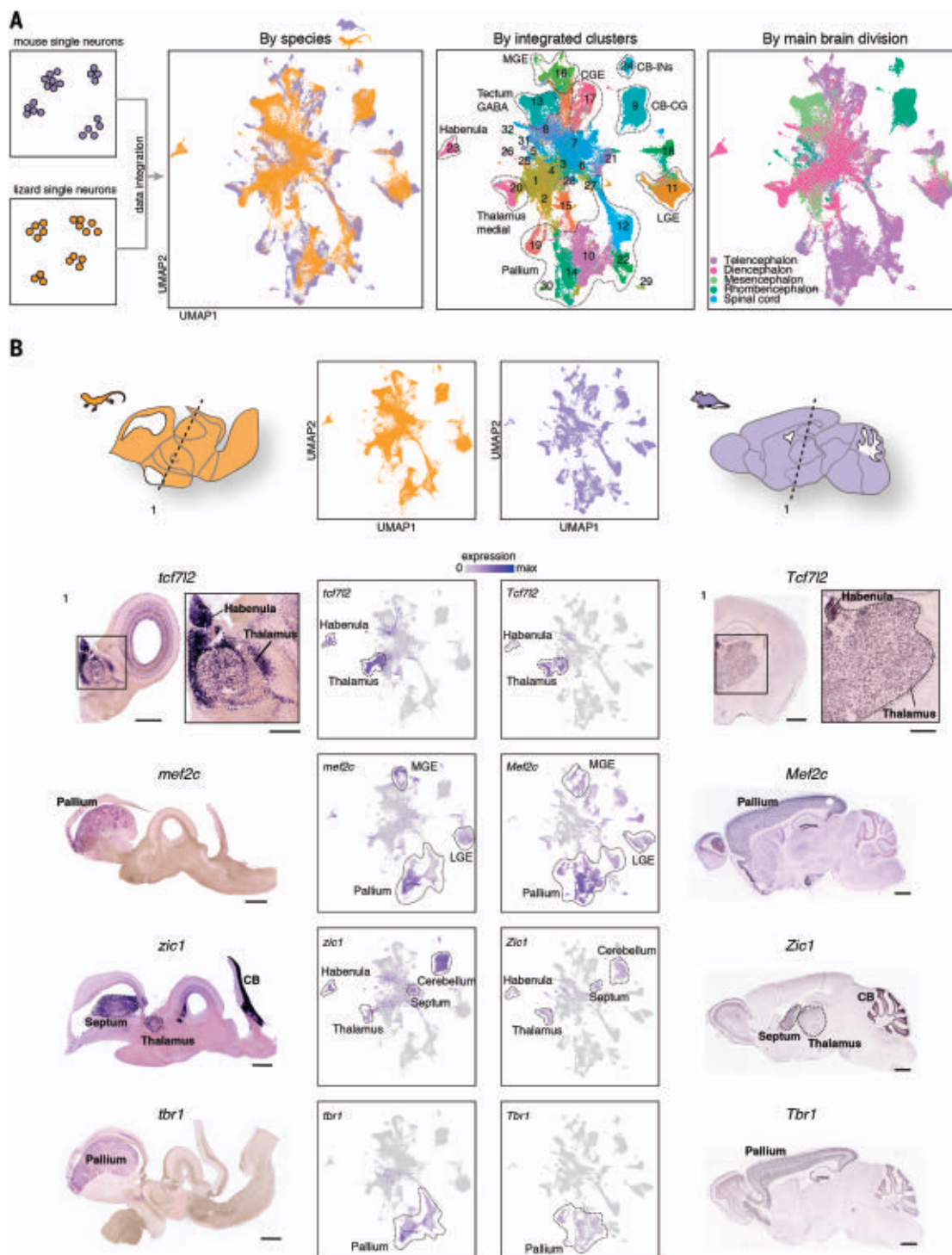


Fig. 2. Comparative analysis of *Pogona* and mouse single-neuron transcriptomes reveals 20 shared neuron-type families. (A) Schematic of CCA-based integration and the UMAP representation of 123,638 integrated single-cell transcriptomes from mouse and *Pogona*. Cells colored by species of origin (left), integrated clusters (1 to 32, middle), and brain division (right). (B) Coronal (top) and sagittal (bottom three) sections of *Pogona* (leftmost column) and mouse

(rightmost column) brain stained by in situ hybridization for the following genes: *tcf7l2*, *mef2c*, *zic1*, and *tbr1*. UMAPs (integrated coordinates, middle two columns) showing the expression of the same genes for cells from *Pogona* (left) and mouse (right). Mouse sections from Allen Mouse Brain Atlas (66). Location of transverse section (labeled “1”) indicated in schematic at top. Scale bars: 1 mm (main images) and 500 μ m (insets).

neocortex (12) also showed high projection scores. We confirmed the localization of some of these neuron types by in situ hybridization [Fig. 3C and fig. S8A; *foxp2* for medial and

dorsal habenula; *gbx2* for medial thalamus (mouse: paraventricular thalamus; lizard: dorso-medial thalamus), *meis2* for prethalamus (mouse: reticular thalamic nucleus; lizard: ventromedial

thalamic nucleus), and *gng13* for cerebellar Purkinje cells].

To assess whether the numbers of transcriptomically similar neuron types differed

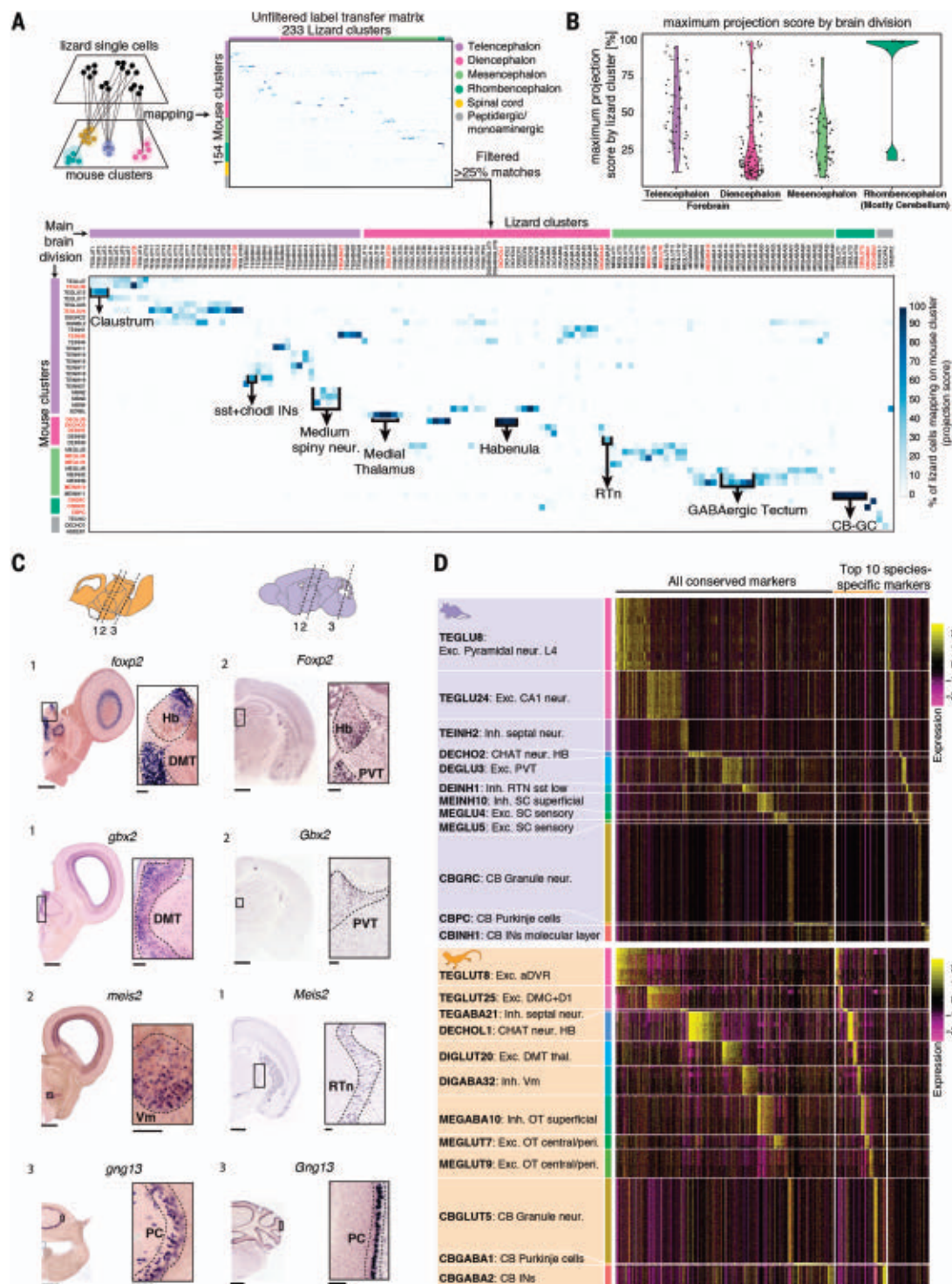


Fig. 3. Comparative analysis reveals a mix of conserved and divergent neuron types in most areas of the forebrain and midbrain. (A) Schematic of label transfer-based integration of lizard and mouse clusters (top left). Unfiltered (top right) and filtered (bottom) matrix (filter for >25% matches of transcriptomic similarity between *Pogona* and mouse clusters). Look-up table: fraction of *Pogona* single-cell transcriptomes from a cluster mapping to a specific mouse cluster (see methods). Selected cluster pairs are shown in red (matrix row and column labels). (B) Maximum projection score for each lizard cluster by brain region. Each dot represents the highest projection score for a lizard

cluster. Note that rhombencephalon samples were mostly from the cerebellum. (C) Coronal sections from adult *Pogona* (left) and mouse (right) brains with in situ staining for *foxp2*, *gbx2*, *meis2*, and *gng13*. Schematic (top) shows approximate section position. Mouse sections from Allen Mouse Brain Atlas (66). Scale bars: 1 mm (main images) and 200 μ m (insets). PVT, paraventricular thalamus; DMT, dorsomedial thalamus; RTn, reticular thalamic nucleus; Vm, ventromedial thalamic nucleus; PC, Purkinje cells. (D) Expression of conserved and top 10 species-specific marker genes for *Pogona* (orange) and mouse (purple) selected cluster pairs. Mouse clusters, top; lizard clusters, bottom.

significantly between main brain divisions (telencephalon, diencephalon, mesencephalon, and metencephalon), we plotted the highest projection score per lizard cluster for each such division (Fig. 3B). These scores were widely distributed within individual divisions. Indeed, all main brain divisions (except for the cerebellum), contained both high and low scores, suggesting that they contain both molecularly similar and divergent cell types (Fig. 3B).

We chose three cell type pairs with high projection scores for each brain division from lizard and mouse and examined the similarities and differences in gene expression between them (Fig. 3D). For each one of these highly similar pairs of neuron types, we identified both common marker genes and mouse- or lizard-specific markers (Fig. 3D and data S5, S6, and S7). Finally, we validated our comparisons of mouse and lizard single-cell transcriptomes—based on Seurat (27)—with SAMap, a method developed specifically to facilitate cross-species single-cell transcriptomic comparisons (33). SAMap and Seurat results were generally consistent, yielding high alignment scores for cell types such as the *sst*⁺, *nos1*⁺, *chodl*⁺ interneurons, medial thalamic cell types, as well as cell types from the reticular thalamic nucleus and septum, cerebellar granule and Purkinje cells, and medium spiny neurons (figs. S9, A to D, S10, and S11).

Hence, even neuron types with considerable transcriptomic overlap between lizard and mouse show specific interspecies differences. This highlights the relevance of comprehensive transcriptomic characterization to identify common marker genes reliably, and the fact that “marker genes” commonly used for cell type identification in one species are not necessarily the most conserved ones. In turtle (12) and lizard, interneurons (INs) homologous to mouse parvalbumin (PV) INs do not express PV; their identification relies on different gene sets. “PV” labels are thus misnomers in reptiles; the terminology is inherited from earlier choices of markers specific to mammalian species. Finally, similar neuron types were not limited to subcortical regions; most brain divisions contained a mixture of similar and divergent neuron types (Fig. 3B).

Transcription factor codes common to lizard and mouse

To corroborate our findings and compare in detail neuron types in mouse and lizard, we selected scRNA-seq datasets with deeper cellular sampling and annotations from specific regions of the mouse brain: telencephalic GABAergic interneurons (34), thalamus (35), hypothalamus (36), and superior colliculus (37). For each of these four datasets, we performed joint CCA embedding on the above mouse cells and corresponding region-specific

subsets in lizard and clustered the joint embedding (Fig. 4), as introduced in Fig. 2A (see methods).

Lizard and mouse neurons were well integrated [see joint uniform manifold approximation and projection (UMAP) representations; Fig. 4, A to D]. For example, among telencephalic interneurons, we identified joint clusters belonging to the different subclasses derived from the medial ganglionic eminence (MGE) (*sst*, *pvalb*, and *chodl* in mouse) or caudal ganglionic eminence (CGE) (*sncg* and *vip* subclasses in mouse) (Fig. 4A and fig. S12, A and B), confirming and extending earlier results (12). In the hypothalamus, we found joint clusters of neurons from the ventromedial hypothalamus (VMH), paraventricular nuclei (PVN), arcuate nucleus, and other tuberal nuclei, as well as two other hypothalamic clusters that split mostly by neurotransmitter type (glutamate and GABA) (Fig. 4B and fig. S13, A and B). In the tectum (lizard optic tectum and mouse superior colliculus), integrated clusters grouped neurons by corresponding strata, or groups of layers (e.g., GABAergic interneurons in the superficial layers of both the superior colliculus and the optic tectum) (Fig. 4C and fig. S14, A and B). In the prethalamus and thalamus, joint clusters grouped the mouse reticular thalamic nucleus (RTn) with the lizard ventromedial thalamic nucleus (Vm), as well as glutamatergic neurons in the medial thalamus of both species, and in the lateral thalamus (Fig. 4D and fig. S15, A and B). These thalamic similarities between mouse and lizard are further examined below.

We next investigated the molecular signatures that underlie these similarities. We identified differentially expressed genes on species-specific datasets and intersected them in a cluster-specific manner across species, to point to common and thus potentially conserved marker genes. From these, we selected transcription factors to test whether integrated clusters can be defined by the combinatorial expression of transcription factors. Such common codes could be identified in many regions and neuronal populations (Fig. 4, E to H). For example, among telencephalic interneurons, mouse and lizard MGE-Sst and MGE-PV were both defined by the coexpression of *zeb2*, *mef2c*, *lhx6*, and *sox6* but differentiated by *pou3f3*, which is expressed only in MGE-Sst. MGE-Chodl cells from mouse and lizard were differentiated from other MGE-derived cell types by expression of *aff2* and lack of expression of *zeb2*; they could be further distinguished from CGE-derived cell types by coexpression of *lhx6*, *satb1*, and *sox6* (Fig. 4E).

In the hypothalamus, neurons from the ventromedial hypothalamus expressed *nr5a1*, *fezf1*, *nr2f2*, and *isl1*, a gene combination common to

lizard and mouse that distinguished these neurons from the rest of the tuberal neurons (Fig. 4F). In the paraventricular hypothalamic nucleus, *nr4a1* differentiated two clusters by its expression (cluster 6) or absence of expression (cluster 5) (Fig. 4, B and F). Similarly shared transcription factor codes were found in the optic tectum/superior colliculus: In both species, GABAergic neurons from central layers were *zfhx4*⁺, *otx2*⁺, and *irx2*⁺, whereas those from superficial layers expressed the same three transcription factors plus *meis2* (Fig. 4G and fig. S16, A to D). Taken together, these examples indicate that evolutionarily conserved classes of neurons can be defined by the expression of a core set of transcription factors. In the thalamus and prethalamus, however, the results proved more complex, prompting us to analyze this region in greater detail (Fig. 4H).

Partial divergence of the thalamus between reptilian and mammalian lineages

The thalamus is a key diencephalic region positioned between the sensory-motor periphery and the cerebral cortex. Because the reptilian cerebral cortex retains ancestral characteristics (e.g., three rather than six layers, absence of sensory topography), examining the molecular organization of the thalamus in a reptile provides a distinctive opportunity to examine the potential coevolution of connected brain areas. Because the growth and complexification of the mammalian neocortex is reflected in a matching growth and complexification of the thalamus (38), we searched for molecular differences between thalamic neuron types in lizard and mouse.

We selected the 7721 lizard single neurons sampled from the thalamus, identified by a combination of dissection region and gene expression (*tcf7l2*, *gbx2*, *lhx9*, or *foxp2* for glutamatergic clusters; *six3*, *meis2*, and *zic1* for GABAergic clusters; fig. S17, A to C). Of these, 4244 were glutamatergic (thalamus proper) neurons and 2617 were GABAergic (prethalamus) neurons (Fig. 5A). These single neurons could be grouped into 37 clusters, distinguished by specific combinations of marker genes (fig. S17A). We assigned each lizard neuron type to a thalamic nucleus by analyzing in situ hybridizations for cluster-specific or area-specific genes (e.g., transcription factors *tcf7l2*, *zic1*, *foxp2*, or *gbx2*; effector genes such as *opn4*, expressed in dorsomedial thalamic neurons; *cbln1* in dorso-lateral thalamic neurons; *vip* in neurons from the nucleus rotundus; and *sst2-like* in the ventromedial thalamic nuclei; 860 transcriptomes could not be assigned confidently to a thalamic nucleus) (Fig. 5B and fig. S17, B and C).

A principal components analysis (PCA) on the transcriptomes of lizard thalamic glutamatergic neurons revealed a clear segregation of medial (DMT1 to DMT4) and lateral

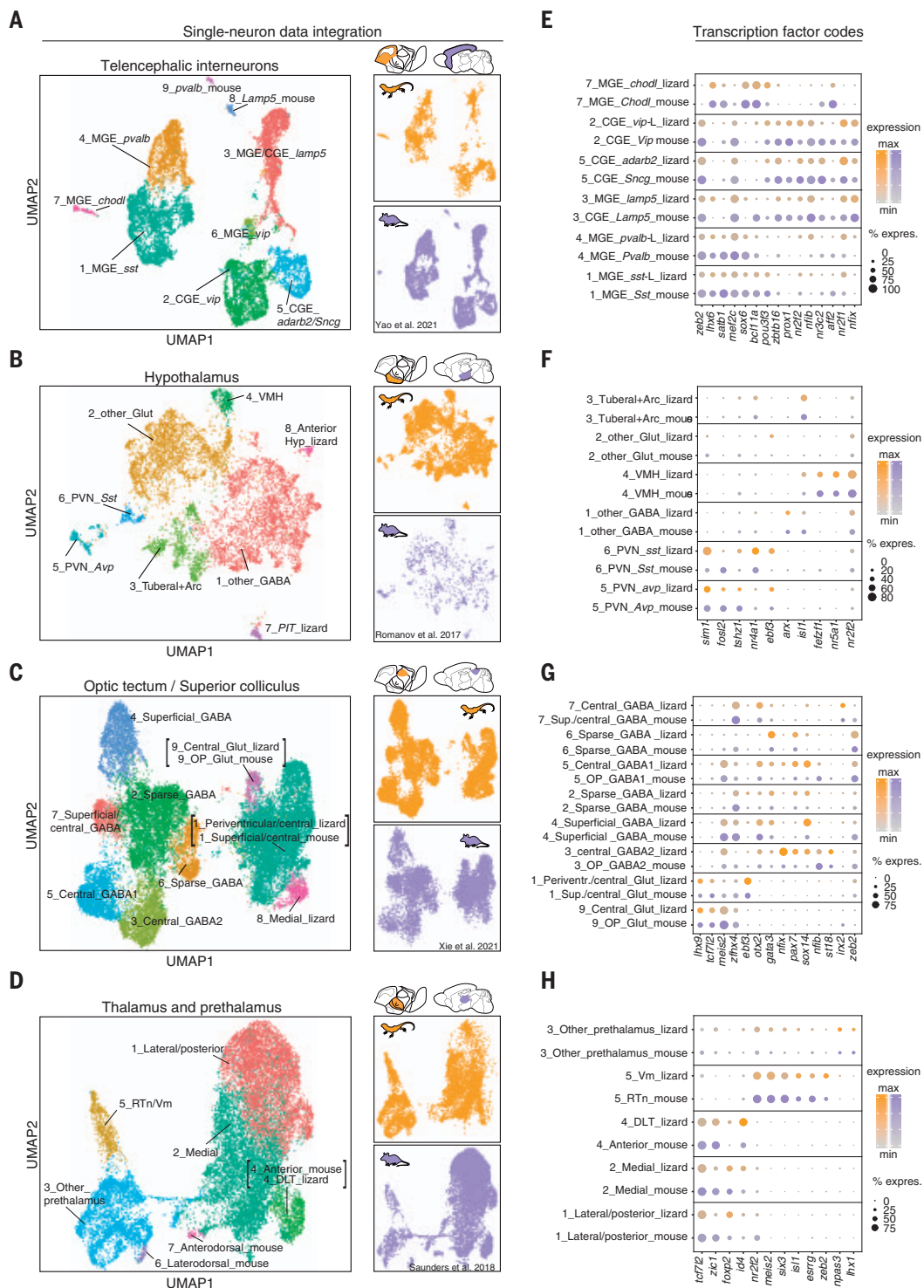


Fig. 4. Common transcription factor codes for identifiable neuron populations in lizard and mouse. (A to D) UMAP representations of integrated single-neuron transcriptomes from *Pogona* (this study) and mouse (34–37) (left), also shown by species of origin (right). Brain schematics show corresponding regions in mouse and lizard. (A) Telencephalic GABAergic interneurons (mouse: 8000 cells; lizard: 2599 cells). (B) Hypothalamic neurons (mouse: 772; lizard: 6221). (C) Optic tectum or superior colliculus (mouse: 8428; lizard: 13278). (D) Thalamic neurons (mouse: 8622; lizard: 6861). (E to H) Dot plots showing shared transcription factor codes for *Pogona* and mouse neuron types. Dot size represents fraction of neurons in a cluster that express the gene, and color intensity represents strength of expression.

thalamic clusters along the first principal component (PC1), confirmed by an analysis of the genes with highest absolute loadings on PC1 (Fig. 5, C and D). A similar finding was reported

in a mouse RNA-seq study of glutamatergic thalamic nuclei (39) and confirmed by joint analysis of mouse thalamic scRNA-seq data (26, 35, 39) (fig. S18A). To identify conserved

genes underlying this spatial segregation, we performed gene ontology analysis on the intersection of the 400 genes with highest absolute loadings on PC1 in each species (112 genes).

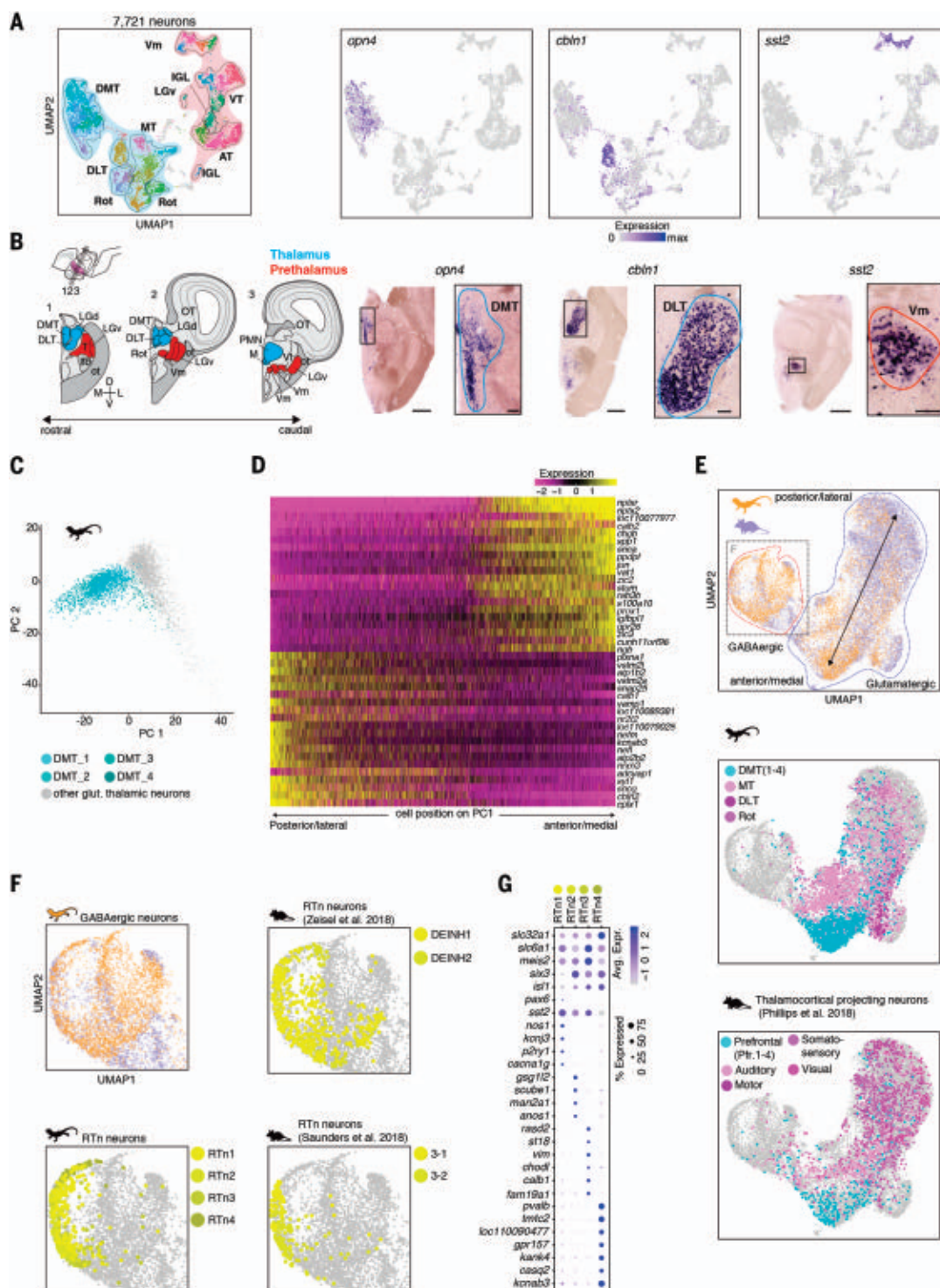


Fig. 5. Partial molecular and anatomical divergence of the thalamus between reptilian and mammalian lineages. (A) UMAP representation of 7,721 neuronal single-neuron transcriptomes from the thalamus of *Pogona* colored by cluster [left; color shades as in (B)] showing the expression of *opn4*, *cbn1*, and *sst2*-like (right). MT, medial thalamic nucleus; DLT, dorsolateral thalamus; IGL, intergeniculate leaflet; Rot, nucleus rotundus; AT, anterior thalamus; VT, ventral thalamic nucleus; Vm, ventromedial thalamic nucleus. (B) Schematic of coronal sections of the lizard thalamus (left) showing glutamatergic (blue) and GABAergic (prethalamus, red) nuclei. Small schematic indicates coronal section planes. (Right) In situ hybridization

for *opn4* (expressed in DMT), *cbn1* (expressed in DLT), and *sst2*-like (expressed in Vm). Scale bar: 1 mm (main images) and 200 μ m (insets). (C) Projections of glutamatergic *Pogona* thalamus neurons in principal components 1 and 2 plane; DMT neurons are highlighted in cyan. (D) Heatmap of the top 40 genes with highest absolute loadings on principal component 1 (PC1); neurons sorted by PC1 score. (E) UMAP representation of 20,490 integrated single-neuron transcriptomes from *Pogona* and mouse thalamic datasets [mouse data from (26, 35, 39)]. Neurons colored by species of origin (top). UMAPs of integrated thalamic objects showing clusters of origin for *Pogona* (middle) and projection regions for mouse

[bottom; data from (39)]. **(F)** UMAP representations of integrated GABAergic neurons from mouse and *Pogona*. Color coded by species (top left: lizard, orange; mouse, purple), and by clusters of RTn neurons in the original datasets (top right, bottom left, and bottom right). **(G)** Dot plot showing

expression of genes defining the four subclusters (RTn1 to RTn4) of the lizard's reticular thalamic nucleus homolog. Dot size represents the fraction of cells in a given cluster that express the gene, and color intensity represents strength of expression.

This analysis revealed gene families related to calcium signaling, neural development, projections, and connectivity (fig. S18B) but only a small number of transcription factors. Taken together, these findings indicate that position along the mediolateral axis is a major correlate of thalamic neuronal diversity in amniotes and that a shared set of effector genes underlies this mediolateral distinction.

These observations were corroborated by an integrated analysis of 6861 lizard transcriptomes with 13,629 mouse single-cell transcriptomes (see methods) from the mouse thalamus and prethalamus (Fig. 5E and fig. S19, A and B). For this analysis, we used the previously mentioned mouse datasets (26, 35, 39), including data from a study where mouse thalamic neurons with distinct projections to cortex were sampled after retrograde tracing from different cortical areas (39). This enabled us to compare these projection types with those of lizard thalamic neurons whose targets have been described (40–44). The cross-species data integration recapitulated our observations from the PCA analysis. Glutamatergic neurons co-clustered in two broad classes, according to their position along the mediolateral axis.

Lizard neurons from the dorsomedial thalamus (DMT), a nucleus that projects to limbic areas in lizards (40, 41), co-clustered with mouse thalamic neurons that project to the prefrontal cortex [Pfr.4 and Pfr.3 from (39)]. On the basis of gene expression and connectivity, these mouse neurons likely originated from the paraventricular nucleus and other medial nuclei that project to prefrontal and limbic areas (45) in mammals (Fig. 5E and fig. S19A).

A second class of thalamic glutamatergic neurons included neurons from sensory relay nuclei, but with an intermingling of sensory modalities (fig. S19A). The lateral or posterior nuclei in lizard include the nucleus rotundus, the dorsolateral thalamic nucleus and, in a more caudal position, the so-called nucleus medialis. The nucleus rotundus is typically compared to the mammalian pulvinar because both relay visual information from the optic tectum/superior colliculus to the pallium (46); the nucleus medialis relays auditory and somatosensory inputs (42, 43), whereas the dorsolateral thalamic nucleus is multimodal (44). In mammals, many of these lateral or posterior thalamic nuclei are connected to topologically ordered sensory areas of the mammalian neocortex that have no clear reptilian equivalent. The absence of co-clustering of lizard and mouse thalamic neurons by modality suggests that the diversification of cell

types in the lateral or posterior thalamus may be related to the divergent fates of the cortex in the mammalian and reptilian lineages, and particularly to the prominent expansion of the cerebral cortex in mammals.

In mammals, the excitatory thalamocortical loops, which reciprocally connect pairs of dorsal thalamic nuclei and cortical regions, rely on the GABAergic neurons of the RTn for inhibitory control and modulation. This negative feedback, connecting reticular thalamic nucleus interneurons to glutamatergic projection neurons within the thalamus, plays important roles in the generation of spindles and slow oscillations during sleep (47–49).

Not much is known about the existence of a reticular thalamic nucleus homolog in reptiles. There is as yet no evidence for sleep spindle oscillations in lizard (50), but immunocytochemical and connectivity studies have suggested that the turtle anterior entopeduncular nucleus (51), the lizard ventromedial thalamic nuclei (52), and the caiman reticular thalamic nucleus (53) could be homologs of the mammalian reticular thalamic nucleus.

Our data revealed that neurons from the lizard ventromedial thalamic nucleus form four separable transcriptomic clusters, and that together they co-cluster with the mouse RTn (Fig. 5F and fig. S19B). In both species, those neuron types had similar transcription factor expression profiles (expression of *six3*, *meis2*, and *isll*, and absence of *pax6*) and shared expression of the ion-channel genes *cacna1i*, *kcnip1*, and other effector genes (54) (Fig. 5G and fig. S19C). In *Pogona* and other reptiles (55), these neurons are close to the lateral forebrain bundle, a position shared with mammals, suggesting a similar relationship with the forebrain. Our data thus suggest that the lizard ventromedial thalamic nucleus is a homolog of the mammalian RTn.

Discussion

The contrast between the conservation of early developmental regions and the diversity of neural cytoarchitectonics and connectivity of vertebrate brains has engendered competing views on brain evolution (56). Our data indicate that neuronal transcriptomes carry molecular signatures of developmental and evolutionary history as well as connectivity, suggesting that a systematic comparison of single-cell transcriptomes across species can bridge earlier types of comparisons in brain evolution studies (57–59). The existence of broad classes of neurons shared by a reptile and a mammal, identified here as joint clus-

ters of lizard and mouse neurons (Figs. 2 and 4), indicates that the broadly defined brain regions of amniotes are organized into smaller units with molecular similarity across species. As suggested by the conserved expression of homeodomain-type transcription factors, these classes might correspond to the adult derivatives of the embryonic prosomeres, units of embryonic progenitors conserved in vertebrate species (3). It has been noticed that the conservation of vertebrate brain regions correlates with the conservation of mesoscale connectivity (60, 61); we suggest that those genes related to connectivity (e.g., axonal pathfinding, surface molecules, etc.) with conserved expression in neuron classes may be functionally implicated in the establishment of evolutionarily conserved patterns of mesoscale connectivity.

At finer resolution, however, the comparison of neuron types challenges the assumption that certain brain regions are more conserved than others. In the telencephalon, diencephalon, and mesencephalon—our sampling of the hind-brain was limited mainly to the cerebellum—we found broad distributions of cell type projection scores (Fig. 3B). While some neuron types could be mapped with confidence from lizard to mouse, many others could not, owing to wide molecular divergence. We interpret these varying degrees of molecular divergence as the results of partial diversification and specialization of neuron types in either or both lineages.

Did common traits link neuron types with similar transcriptomes across the two examined species? Such neuron types were found in the telencephalon, diencephalon, and mesencephalon; they could be local (e.g., reticular thalamic nucleus or pallial GABAergic neurons) or long-range projecting (e.g., striatal medium spiny neurons); and they were not limited to one neurotransmitter type. Thus, the degree of molecular divergence of neuron types could be predicted neither from their developmental origin nor from their phenotypes (neurotransmitter, local versus long-range projection). We propose that, while strong developmental constraints in early embryogenesis underlie the conservation of broad classes of neurons, the development and evolution of specific types and subtypes is more plastic. Neuron types might be deeply conserved if they happen to express genes under stronger pleiotropic constraints, as in the cerebellum (62). Alternatively, neurons could be under strong selective pressure for their singular function in neural circuit motifs. Likewise,

functional constraints may also lead to the convergent evolution of neuronal transcriptomes, as in the case of the reptilian dorsal ventricular ridge and mammalian cerebral cortex (12).

As an extreme example, the thalamic complex provides some indications on the potential drivers of the evolutionary diversification of neurons. The existence of a conserved reticular thalamic nucleus (GABAergic, prethalamic), which occupies a key role in thalamocortical connectivity and dynamics in mammals, suggests that some aspects of the organization of thalamocortical circuits may trace back to amniote ancestors (51, 53). However, similarities between mouse and lizard are less sharp for glutamatergic neurons. On the basis of their shared transcriptomic variation, lizard and mouse thalamic glutamatergic neurons could be grouped into only two large classes, medial and lateral, indicating that other dimensions of thalamic organization (sensory modality, core versus matrix, etc.) are not encoded by the same sets of genes across species. Lizard and mouse neurons that co-clustered as “medial thalamus” both project to limbic areas in the pallium and subpallium, supporting the hypothesis that mammalian medial nuclei (including the paraventricular nucleus) and the reptilian dorsomedial thalamus are homologous (fig. S20) (63–65). In the “lateral thalamus,” lizard and mouse neurons did not co-cluster by sensory modality. This might be explained by transient expression of conserved modality-specific genes only during development. Alternatively, the identity of sensory relay nuclei might not be encoded by conserved transcriptional programs in lizard and mouse, suggesting that modality-specific programs would have evolved independently in reptiles and mammals. Consistent with this, the primary sensory areas in the cerebral cortex that are connected to lateral thalamic relay nuclei underwent, in the evolutionary line leading to mammals, profound changes that are specific to them. The parallel diversification of thalamic and cortical neuron types suggests that thalamocortical circuits evolved in amniotes by duplication and divergence, following a principle similar to that proposed for the evolution of cerebellar nuclei (59).

Hence, even though lizard and mouse diverged more than 300 million years ago, neuron types in their brains can be assigned to conserved classes, reflecting the existence of shared developmental programs that establish vertebrate brain regions. However, further diversity and molecular heterogeneity within each of these classes indicates that neuronal identities evolve under selective pressures that act globally on the brain, regardless of developmental origin. Extending comparative transcriptomics investigations to other species should provide insights about

the processes that enabled the adaptation of vertebrates to different environments over the past 550 million years.

Materials and methods summary

Single-cell RNA sequencing

For single-cell RNA sequencing, cells were prepared by dissociating microdissected brain regions from adult *P. vitticeps* as described previously (25). The single-cell suspension was used to generate scRNA-seq libraries using the 10X Genomics Chromium Single Cell 3' Reagent Kit (v2 and v3 chemistry) and sequenced with Illumina NextSeq 500 according to the manufacturer's protocols. The resulting scRNA-seq data were aligned with Cell Ranger v3.0 and processed using Seurat v3.1. Analysis steps included a first filtering of low-quality cells on the basis of the number of genes expressed per cell (v2: >400 genes per cell; v3: >800 genes per cell) and then normalized, scaled, dimensionality-reduced with PCA and Louvain-clustered. This revealed a cluster of low-quality cells by a combination of features (no. of genes expressed per cell, no. of unique molecular identifiers per cell, percentage of mitochondrial genes per cell, and percentage of rRNAs per cell). A support vector machine (SVM) was then trained to distinguish high- and low-quality cells by these features, and the data were further filtered by removing cells identified as low-quality by the SVM. The remaining high-quality cells (285,483) were processed similarly to reveal major cell classes. We identified neuronal clusters among the major cell classes by their expression of marker genes (e.g., *snap25*), extracted them computationally, filtered further to >1000 genes per cell and, after several rounds of clustering and removal of low-quality clusters (according to the above criteria), ended up with 89,015 neuronal transcriptomes.

Cross-species comparisons

For cross-species comparisons, we used previously published datasets from mice containing cells from the whole brain (26) or region-specific subsets (34–37, 39). For embeddings of specific regions, the lizard data were first subsetted to contain only cells from matching brain regions. We then used Seurat v3.1 for joint CCA embedding of mouse and lizard single cells, using only genes that were annotated as one-to-one orthologs between mouse and *Pogona* by Ensembl. We also validated some of the results obtained by this approach using SAMap (33), a method specifically designed for cross-species integration of scRNA-seq data. For this, we first constructed BLAST maps between the proteomes of *Pogona* and mouse.

Histology

To prepare probes for in situ hybridization, we either PCR-amplified fragments of genes

of interest from *P. vitticeps* cDNA libraries, as previously described (12), or ordered as gene fragments with 31-base pair overhangs on both ends that were overlapping with the pCRII-TOPO vector. Gene fragments were then cloned into the pCRII vector using either the TA Cloning Kit (Invitrogen) or the Gibson Assembly Cloning Kit (New England Biolabs) according to each manufacturer's protocol. Clones were verified by Sanger sequencing, and DIG- or FITC-labeled probes were transcribed in vitro and purified, and a chromogenic in situ hybridization protocol was followed as described previously (12). After mounting, sections were imaged at 20× magnification using an automatic digital slide scanner (Pannoramic MIDI II, 3DHISTECH).

REFERENCES AND NOTES

1. P. S. Katz, Phylogenetic plasticity in the evolution of molluscan neural circuits. *Curr. Opin. Neurobiol.* **41**, 8–16 (2016). doi: 10.1016/j.conb.2016.07.004; pmid: 27455462
2. L. Puelles, M. Harrison, G. Paxinos, C. Watson, A developmental ontology for the mammalian brain based on the prosomeric model. *Trends Neurosci.* **36**, 570–578 (2013). doi: 10.1016/j.tins.2013.06.004; pmid: 23871546
3. L. Puelles, “Plan of the developing vertebrate nervous system: Relating embryology to the adult nervous system (prosomere model, overview of brain organization)” in *Patterning and Cell Type Specification in the Developing CNS and PNS*, J. Rubenstein, P. Rakic, Eds. (Elsevier, 2013), pp. 187–209.
4. R. Nieuwenhuys, Principles of current vertebrate neuromorphology. *Brain Behav. Evol.* **90**, 117–130 (2017). doi: 10.1159/000460237; pmid: 28988231
5. A. B. Butler, The evolution of the dorsal thalamus of jawed vertebrates, including mammals: Cladistic analysis and a new hypothesis. *Brain Res. Brain Res. Rev.* **19**, 29–65 (1994). doi: 10.1016/0165-0173(94)90003-5; pmid: 8167659
6. G. F. Striedter, The telencephalon of tetrapods in evolution. *Brain Behav. Evol.* **49**, 179–194 (1997). doi: 10.1159/000112991; pmid: 9096908
7. E. R. Chapman, S. An, N. Barton, R. Jahn, SNAP-25, a t-SNARE which binds to both syntaxin and synaptobrevin via domains that may form coiled coils. *J. Biol. Chem.* **269**, 27427–27432 (1994). doi: 10.1016/S0021-9258(18)47003-2; pmid: 7961655
8. L. Claesson-Welsh, A. Hammacher, B. Westermark, C. H. Heldin, M. Nistér, Identification and structural analysis of the A type receptor for platelet-derived growth factor. Similarities with the B type receptor. *J. Biol. Chem.* **264**, 1742–1747 (1989). doi: 10.1016/S0021-9258(18)94249-3; pmid: 2536372
9. Y. Chen et al., The oligodendrocyte-specific G protein-coupled receptor GPR17 is a cell-intrinsic timer of myelination. *Nat. Neurosci.* **12**, 1398–1406 (2009). doi: 10.1038/nn.2410; pmid: 19838178
10. R. H. Quarles, Myelin-associated glycoprotein (MAG): Past, present and beyond. *J. Neurochem.* **100**, 1431–1448 (2007). doi: 10.1111/j.1471-4159.2006.04319.x; pmid: 17241126
11. C. Yanes, M. Monzon-Mayor, M. S. Ghandour, J. de Barry, G. Gombos, Radial glia and astrocytes in developing and adult telencephalon of the lizard *Gallotia galloti* as revealed by immunohistochemistry with anti-GFAP and anti-vimentin antibodies. *J. Comp. Neurol.* **295**, 559–568 (1990). doi: 10.1002/cne.902950405; pmid: 2358521
12. M. A. Tosches et al., Evolution of pallium, hippocampus, and cortical cell types revealed by single-cell transcriptomics in reptiles. *Science* **360**, 881–888 (2018). doi: 10.1126/science.aar4237; pmid: 29724907
13. S. M. Islam et al., Draxin, a repulsive guidance protein for spinal cord and forebrain commissures. *Science* **323**, 388–393 (2009). doi: 10.1126/science.1165187; pmid: 19150847
14. S. Gobron et al., SCO-spondin is evolutionarily conserved in the central nervous system of the chordate phylum. *Neuroscience* **88**, 655–664 (1999). doi: 10.1016/S0304-4522(98)00252-8; pmid: 10197783

15. A. Paul *et al.*, Transcriptional architecture of synaptic communication delineates GABAergic neuron identity. *Cell* **171**, 522–539.e20 (2017). doi: [10.1016/j.cell.2017.08.032](https://doi.org/10.1016/j.cell.2017.08.032); pmid: [28942923](https://pubmed.ncbi.nlm.nih.gov/28942923/)
16. S. J. Smith *et al.*, Single-cell transcriptomic evidence for dense intracortical neuropeptide networks. *eLife* **8**, e47889 (2019). doi: [10.7554/eLife.47889](https://doi.org/10.7554/eLife.47889); pmid: [31710287](https://pubmed.ncbi.nlm.nih.gov/31710287/)
17. S. R. Taylor *et al.*, Molecular topography of an entire nervous system. *Cell* **184**, 4329–4347.e23 (2021). doi: [10.1016/j.cell.2021.06.023](https://doi.org/10.1016/j.cell.2021.06.023); pmid: [34237253](https://pubmed.ncbi.nlm.nih.gov/34237253/)
18. T. Kumamoto, C. Hanashima, Evolutionary conservation and conversion of Foxg1 function in brain development. *Dev. Growth Differ.* **59**, 258–269 (2017). doi: [10.1111/dgd.12367](https://doi.org/10.1111/dgd.12367); pmid: [28581027](https://pubmed.ncbi.nlm.nih.gov/28581027/)
19. A. Nagalski *et al.*, Molecular anatomy of the thalamic complex and the underlying transcription factors. *Brain Struct. Funct.* **221**, 2493–2510 (2016). doi: [10.1007/s00429-015-1052-5](https://doi.org/10.1007/s00429-015-1052-5); pmid: [25963709](https://pubmed.ncbi.nlm.nih.gov/25963709/)
20. E. Desfilis, A. Abellán, V. Sentandreu, L. Medina, Expression of regulatory genes in the embryonic brain of a lizard and implications for understanding pallial organization and evolution. *J. Comp. Neurol.* **526**, 166–202 (2018). doi: [10.1002/cne.24329](https://doi.org/10.1002/cne.24329); pmid: [28891227](https://pubmed.ncbi.nlm.nih.gov/28891227/)
21. J. Aruga *et al.*, Mouse *Zic1* is involved in cerebellar development. *J. Neurosci.* **18**, 284–293 (1998). doi: [10.1523/JNEUROSCI.18-01-00284.1998](https://doi.org/10.1523/JNEUROSCI.18-01-00284.1998); pmid: [9412507](https://pubmed.ncbi.nlm.nih.gov/9412507/)
22. I. Bachy, J. Berthou, S. Rétaux, Defining pallial and subpallial divisions in the developing *Xenopus* forebrain. *Mech. Dev.* **117**, 163–172 (2002). doi: [10.1016/S0925-4773\(02\)00199-5](https://doi.org/10.1016/S0925-4773(02)00199-5); pmid: [12204256](https://pubmed.ncbi.nlm.nih.gov/12204256/)
23. R. F. Leung *et al.*, Genetic regulation of vertebrate forebrain development by homeobox genes. *Front. Neurosci.* **16**, 843794 (2022). doi: [10.3389/fnins.2022.843794](https://doi.org/10.3389/fnins.2022.843794); pmid: [35546872](https://pubmed.ncbi.nlm.nih.gov/35546872/)
24. C. E. Love, V. E. Prince, Expression and retinoic acid regulation of the zebrafish *nr2f* orphan nuclear receptor genes. *Dev. Dyn.* **241**, 1603–1615 (2012). doi: [10.1002/dvdy.23838](https://doi.org/10.1002/dvdy.23838); pmid: [22836912](https://pubmed.ncbi.nlm.nih.gov/22836912/)
25. H. Norimoto *et al.*, A claustrum in reptiles and its role in slow-wave sleep. *Nature* **578**, 413–418 (2020). doi: [10.1038/s41586-020-1993-6](https://doi.org/10.1038/s41586-020-1993-6); pmid: [32051589](https://pubmed.ncbi.nlm.nih.gov/32051589/)
26. A. Zeisel *et al.*, Molecular architecture of the mouse nervous system. *Cell* **174**, 999–1014.e22 (2018). doi: [10.1016/j.cell.2018.06.021](https://doi.org/10.1016/j.cell.2018.06.021); pmid: [30096314](https://pubmed.ncbi.nlm.nih.gov/30096314/)
27. T. Stuart *et al.*, Comprehensive integration of single-cell data. *Cell* **177**, 1888–1902.e21 (2019). doi: [10.1016/j.cell.2019.05.031](https://doi.org/10.1016/j.cell.2019.05.031); pmid: [31178118](https://pubmed.ncbi.nlm.nih.gov/31178118/)
28. R. Nieuwenhuys, L. Puelles, *Towards a New Neuromorphology* (Springer International Publishing, Cham, 2016).
29. T. E. Bakken *et al.*, Comparative cellular analysis of motor cortex in human, marmoset and mouse. *Nature* **598**, 111–119 (2021). doi: [10.1038/s41586-021-03465-8](https://doi.org/10.1038/s41586-021-03465-8); pmid: [34616062](https://pubmed.ncbi.nlm.nih.gov/34616062/)
30. E. Rueda-Alaña, F. García-Moreno, Time in neurogenesis: Conservation of the developmental formation of the cerebellar circuitry. *Brain Behav. Evol.* **97**, 33–47 (2022). doi: [10.1159/000519068](https://doi.org/10.1159/000519068); pmid: [34592741](https://pubmed.ncbi.nlm.nih.gov/34592741/)
31. M. Stephenson-Jones, E. Samuelsson, J. Ericsson, B. Robertson, S. Grillner, Evolutionary conservation of the basal ganglia as a common vertebrate mechanism for action selection. *Curr. Biol.* **21**, 1081–1091 (2011). doi: [10.1016/j.cub.2011.05.001](https://doi.org/10.1016/j.cub.2011.05.001); pmid: [21700460](https://pubmed.ncbi.nlm.nih.gov/21700460/)
32. L. Freudenmacher, A. von Twickel, W. Walkowiak, The habenula as an evolutionary conserved link between basal ganglia, limbic, and sensory systems—A phylogenetic comparison based on anuran amphibians. *J. Comp. Neurol.* **528**, 705–728 (2020). doi: [10.1002/cne.24777](https://doi.org/10.1002/cne.24777); pmid: [31566737](https://pubmed.ncbi.nlm.nih.gov/31566737/)
33. A. J. Tarashansky *et al.*, Mapping single-cell atlases throughout Metazoa unravels cell type evolution. *eLife* **10**, e66747 (2021). doi: [10.7554/eLife.66747](https://doi.org/10.7554/eLife.66747); pmid: [33944782](https://pubmed.ncbi.nlm.nih.gov/33944782/)
34. Z. Yao *et al.*, A taxonomy of transcriptomic cell types across the isocortex and hippocampal formation. *Cell* **184**, 3222–3241.e26 (2021). doi: [10.1016/j.cell.2021.04.021](https://doi.org/10.1016/j.cell.2021.04.021); pmid: [34004146](https://pubmed.ncbi.nlm.nih.gov/34004146/)
35. A. Saunders *et al.*, Molecular diversity and specializations among the cells of the adult mouse brain. *Cell* **174**, 1015–1030.e16 (2018). doi: [10.1016/j.cell.2018.07.028](https://doi.org/10.1016/j.cell.2018.07.028); pmid: [30096299](https://pubmed.ncbi.nlm.nih.gov/30096299/)
36. R. A. Romanov *et al.*, Molecular interrogation of hypothalamic organization reveals distinct dopamine neuronal subtypes. *Nat. Neurosci.* **20**, 176–188 (2017). doi: [10.1038/nn.4462](https://doi.org/10.1038/nn.4462); pmid: [27991900](https://pubmed.ncbi.nlm.nih.gov/27991900/)
37. Z. Xie *et al.*, Transcriptomic encoding of sensorimotor transformation in the midbrain. *eLife* **10**, e69825 (2021). doi: [10.7554/eLife.69825](https://doi.org/10.7554/eLife.69825); pmid: [34318750](https://pubmed.ncbi.nlm.nih.gov/34318750/)
38. A. C. Halley, L. Krubitzer, Not all cortical expansions are the same: The coevolution of the neocortex and the dorsal thalamus in mammals. *Curr. Opin. Neurobiol.* **56**, 78–86 (2019). doi: [10.1016/j.conb.2018.12.003](https://doi.org/10.1016/j.conb.2018.12.003); pmid: [30658218](https://pubmed.ncbi.nlm.nih.gov/30658218/)
39. J. W. Phillips *et al.*, A repeated molecular architecture across thalamic pathways. *Nat. Neurosci.* **22**, 1925–1935 (2019). doi: [10.1038/s41593-019-0483-3](https://doi.org/10.1038/s41593-019-0483-3); pmid: [31527803](https://pubmed.ncbi.nlm.nih.gov/31527803/)
40. L. L. Bruce, A. B. Butler, Telencephalic connections in lizards. I. Projections to cortex. *J. Comp. Neurol.* **229**, 585–601 (1984). doi: [10.1002/cne.902290411](https://doi.org/10.1002/cne.902290411); pmid: [6209313](https://pubmed.ncbi.nlm.nih.gov/6209313/)
41. C. Font, A. Martínez-Marcos, E. Lanuza, P. V. Hoogland, F. Martínez-García, Septal complex of the telencephalon of the lizard *Podarcis hispanica*. II. Afferent connections. *J. Comp. Neurol.* **383**, 489–511 (1997). doi: [10.1002/\(SICI\)1096-9861\(19970714\)383:4<489::AID-CNE7>3.0.CO;2-Z](https://doi.org/10.1002/(SICI)1096-9861(19970714)383:4<489::AID-CNE7>3.0.CO;2-Z); pmid: [9208995](https://pubmed.ncbi.nlm.nih.gov/9208995/)
42. R. E. Foster, W. C. Hall, The organization of central auditory pathways in a reptile, *Iguana iguana*. *J. Comp. Neurol.* **178**, 783–831 (1978). doi: [10.1002/cne.901780412](https://doi.org/10.1002/cne.901780412); pmid: [632382](https://pubmed.ncbi.nlm.nih.gov/632382/)
43. M. B. Pritz, M. E. Stritzel, Anatomical identification of a telencephalic somatosensory area in a reptile, *Caiman crocodilus*. *Brain Behav. Evol.* **43**, 107–127 (1994). doi: [10.1159/000113628](https://doi.org/10.1159/000113628); pmid: [8143143](https://pubmed.ncbi.nlm.nih.gov/8143143/)
44. E. Desfilis, E. Font, M. Belekchova, N. Kenigfest, Afferent and efferent projections of the dorsal anterior thalamic nuclei in the lizard *Podarcis hispanica* (Sauria, Lacertidae). *Brain Res. Bull.* **57**, 447–450 (2002). doi: [10.1016/S0361-9230\(01\)00727-4](https://doi.org/10.1016/S0361-9230(01)00727-4); pmid: [11923008](https://pubmed.ncbi.nlm.nih.gov/11923008/)
45. G. J. Kirouac, Placing the paraventricular nucleus of the thalamus within the brain circuits that control behavior. *Neurosci. Biobehav. Rev.* **56**, 315–329 (2015). doi: [10.1016/j.neubiorev.2015.08.005](https://doi.org/10.1016/j.neubiorev.2015.08.005); pmid: [26255593](https://pubmed.ncbi.nlm.nih.gov/26255593/)
46. J. C. Dávila, M. J. Andreu, M. A. Real, L. Puelles, S. Guirado, Mesencephalic and diencephalic afferent connections to the thalamic nucleus rotundus in the lizard, *Psammotromus algerius*. *Eur. J. Neurosci.* **16**, 267–282 (2002). doi: [10.1046/j.1460-9568.2002.02091.x](https://doi.org/10.1046/j.1460-9568.2002.02091.x); pmid: [12169109](https://pubmed.ncbi.nlm.nih.gov/12169109/)
47. D. Contreras, M. Steriade, Cellular basis of EEG slow rhythms: A study of dynamic corticothalamic relationships. *J. Neurosci.* **15**, 604–622 (1995). doi: [10.1523/JNEUROSCI.15-01-00604.1995](https://doi.org/10.1523/JNEUROSCI.15-01-00604.1995); pmid: [7823167](https://pubmed.ncbi.nlm.nih.gov/7823167/)
48. M. Steriade, D. A. McCormick, T. J. Sejnowski, Thalamic oscillations in the sleeping and aroused brain. *Science* **262**, 679–685 (1993). doi: [10.1126/science.8235588](https://doi.org/10.1126/science.8235588); pmid: [8235588](https://pubmed.ncbi.nlm.nih.gov/8235588/)
49. M. Steriade, L. Domich, G. Oakson, M. Deschênes, The deafferented reticular thalamic nucleus generates spindle rhythmicity. *J. Neurophysiol.* **57**, 260–273 (1987). doi: [10.1152/jn.1987.57.1.260](https://doi.org/10.1152/jn.1987.57.1.260); pmid: [3559675](https://pubmed.ncbi.nlm.nih.gov/3559675/)
50. M. Shein-Idelson, J. M. Ondracek, H.-P. Liaw, S. Reiter, G. Laurent, Slow waves, sharp waves, ripples, and REM in sleeping dragons. *Science* **352**, 590–595 (2016). doi: [10.1126/science.1251604](https://doi.org/10.1126/science.1251604); pmid: [27126045](https://pubmed.ncbi.nlm.nih.gov/27126045/)
51. N. Kenigfest *et al.*, The turtle thalamic anterior entopeduncular nucleus shares connectional and neurochemical characteristics with the mammalian thalamic reticular nucleus. *J. Chem. Neuroanat.* **30**, 129–143 (2005). doi: [10.1016/j.jchemneu.2005.07.001](https://doi.org/10.1016/j.jchemneu.2005.07.001); pmid: [16140498](https://pubmed.ncbi.nlm.nih.gov/16140498/)
52. C. Díaz, C. Yanes, C. M. Trujillo, L. Puelles, The lacteridian reticular thalamic nucleus projects topographically upon the dorsal thalamus: Experimental study in *Gallotia galloti*. *J. Comp. Neurol.* **343**, 193–208 (1994). doi: [10.1002/cne.903430202](https://doi.org/10.1002/cne.903430202); pmid: [8027439](https://pubmed.ncbi.nlm.nih.gov/8027439/)
53. M. B. Pritz, M. E. Stritzel, A different type of vertebrate thalamic organization. *Brain Res.* **525**, 330–334 (1990). doi: [10.1016/0006-8993\(90\)90885-F](https://doi.org/10.1016/0006-8993(90)90885-F); pmid: [1701334](https://pubmed.ncbi.nlm.nih.gov/1701334/)
54. Y. Li *et al.*, Distinct subnetworks of the thalamic reticular nucleus. *Nature* **583**, 819–824 (2020). doi: [10.1038/s41586-020-2504-5](https://doi.org/10.1038/s41586-020-2504-5); pmid: [32699411](https://pubmed.ncbi.nlm.nih.gov/32699411/)
55. M. B. Pritz, Thalamic reticular nucleus in *Alligator mississippiensis*: Soma and dendritic morphology. *J. Comp. Neurol.* **529**, 3785–3844 (2021). doi: [10.1002/cne.25194](https://doi.org/10.1002/cne.25194); pmid: [34031891](https://pubmed.ncbi.nlm.nih.gov/34031891/)
56. M. A. Tosches, From cell types to an integrated understanding of brain evolution: The case of the cerebral cortex. *Annu. Rev. Cell Dev. Biol.* **37**, 495–517 (2021). doi: [10.1146/annurev-cellbio-120319-112654](https://doi.org/10.1146/annurev-cellbio-120319-112654); pmid: [34416113](https://pubmed.ncbi.nlm.nih.gov/34416113/)
57. M. E. R. Shafer, A. N. Sawh, A. F. Schier, Gene family evolution underlies cell-type diversification in the hypothalamus of teleosts. *Nat. Ecol. Evol.* **6**, 63–76 (2022). doi: [10.1038/s41559-021-01580-3](https://doi.org/10.1038/s41559-021-01580-3); pmid: [34824389](https://pubmed.ncbi.nlm.nih.gov/34824389/)
58. B. M. Colquitt, D. P. Merullo, G. Konopka, T. F. Roberts, M. S. Brainard, Cellular transcriptomics reveals evolutionary identities of songbird vocal circuits. *Science* **371**, eabd9704 (2021). doi: [10.1126/science.abd9704](https://doi.org/10.1126/science.abd9704); pmid: [33574185](https://pubmed.ncbi.nlm.nih.gov/33574185/)
59. J. M. Kobschall *et al.*, Cerebellar nuclei evolved by repeatedly duplicating a conserved cell-type set. *Science* **370**, eabd5059 (2020). doi: [10.1126/science.abd5059](https://doi.org/10.1126/science.abd5059); pmid: [33335034](https://pubmed.ncbi.nlm.nih.gov/33335034/)
60. S. M. Suryanarayana, J. Pérez-Fernández, B. Robertson, S. Grillner, The lamprey forebrain – evolutionary implications. *Brain Behav. Evol.* **96**, 318–333 (2022). doi: [10.1159/000517492](https://doi.org/10.1159/000517492); pmid: [34192700](https://pubmed.ncbi.nlm.nih.gov/34192700/)
61. R. Nieuwenhuys, L. Puelles, “The ‘wiring’ of the brain” in *Towards a New Neuromorphology* (Springer International Publishing, Cham, 2016), pp. 273–300.
62. I. Sarropoulos *et al.*, Developmental and evolutionary dynamics of cis-regulatory elements in mouse cerebellar cells. *Science* **373**, eabg4696 (2021). doi: [10.1126/science.abg4696](https://doi.org/10.1126/science.abg4696); pmid: [34446581](https://pubmed.ncbi.nlm.nih.gov/34446581/)
63. A. B. Butler, Evolution of the thalamus: A morphological and functional review. *Thalamus Relat. Syst.* **4**, 35–58 (2008). doi: [10.1017/S1472928808000356](https://doi.org/10.1017/S1472928808000356)
64. L. Puelles, Thoughts on the development, structure and evolution of the mammalian and avian telencephalic pallium. *Philos. Trans. R. Soc. Lond. B Biol. Sci.* **356**, 1583–1598 (2001). doi: [10.1098/rstb.2001.0973](https://doi.org/10.1098/rstb.2001.0973); pmid: [11604125](https://pubmed.ncbi.nlm.nih.gov/11604125/)
65. R. Heredia, M. Real, J. Suárez, S. Guirado, J. C. Dávila, A proposed homology between the reptilian dorsomedial thalamic nucleus and the mammalian paraventricular thalamic nucleus. *Brain Res. Bull.* **57**, 443–445 (2002). doi: [10.1016/S0361-9230\(01\)00712-2](https://doi.org/10.1016/S0361-9230(01)00712-2); pmid: [11923007](https://pubmed.ncbi.nlm.nih.gov/11923007/)
66. E. S. Lein *et al.*, Genome-wide atlas of gene expression in the adult mouse brain. *Nature* **445**, 168–176 (2007). doi: [10.1038/nature04543](https://doi.org/10.1038/nature04543); pmid: [17151600](https://pubmed.ncbi.nlm.nih.gov/17151600/)
67. D. Hain, Pogona scRNA-seq analysis, Max Planck Computing and Data Facility GitLab (2022); <https://doi.org/10.17617/1.91>.

ACKNOWLEDGMENTS

We thank H. Winterberg for help with in situ hybridization; E. Northrup, G. Wexel, and N. Vogt for veterinary care; T. Klappich, F. Wagner, M. Wunder, J. Graman C.O.R. Medal, M.d. Vries, and E. Joesten for reptile care; S. Junek, F. Vollrath, and C. Polisseni for help with imaging and microscopy; and E. Morris, F. Baier, and L. Fenk for detailed comments on the manuscript. **Funding:** This work was funded by the Max Planck Society (G.L.), the European Research Council (ERC) under the European Union's Horizon 2020 research and innovation program (grant 834446) (G.L.), the DFG-CRC 1080 (G.L.), the McKnight Foundation (M.A.T.), National Institutes of Health grant NHGRI R01 HG011014 (M.A.T.), and the International Max Planck Research School for Neural Circuits (D.H.). **Author contributions:** scRNA-seq: D.H., T.G.-F., M.A.T., E.C., and M.K. Bioinformatic analysis: D.H., M.A.T., G.T., and F.K. Anatomy and histology: T.G.-F., M.A.T., A.M., A.A., and C.T. Experimental design, data interpretation, and analysis: D.H., T.G.-F., M.A.T., and G.L. Project management and supervision: M.A.T. and G.L. **Competing interests:** The authors declare no competing interests. **Data and materials availability:** Sequencing data have been deposited in the NCBI Sequence Read Archive (<https://www.ncbi.nlm.nih.gov/bioproject/PRJNA812380>) and <https://www.ncbi.nlm.nih.gov/bioproject/PRJNA591493>. Source code can be obtained from the Max Planck Computing and Data Facility (67). All other data are found in the main paper and supplement. **License information:** Copyright © 2022 the authors, some rights reserved; exclusive licensee American Association for the Advancement of Science. No claim to original US government works. <https://www.science.org/about/science-licenses-journal-article-reuse>

SUPPLEMENTARY MATERIALS

science.org/doi/10.1126/science.abp8202

Materials and Methods

Figs. S1 to S20

References (68–74)

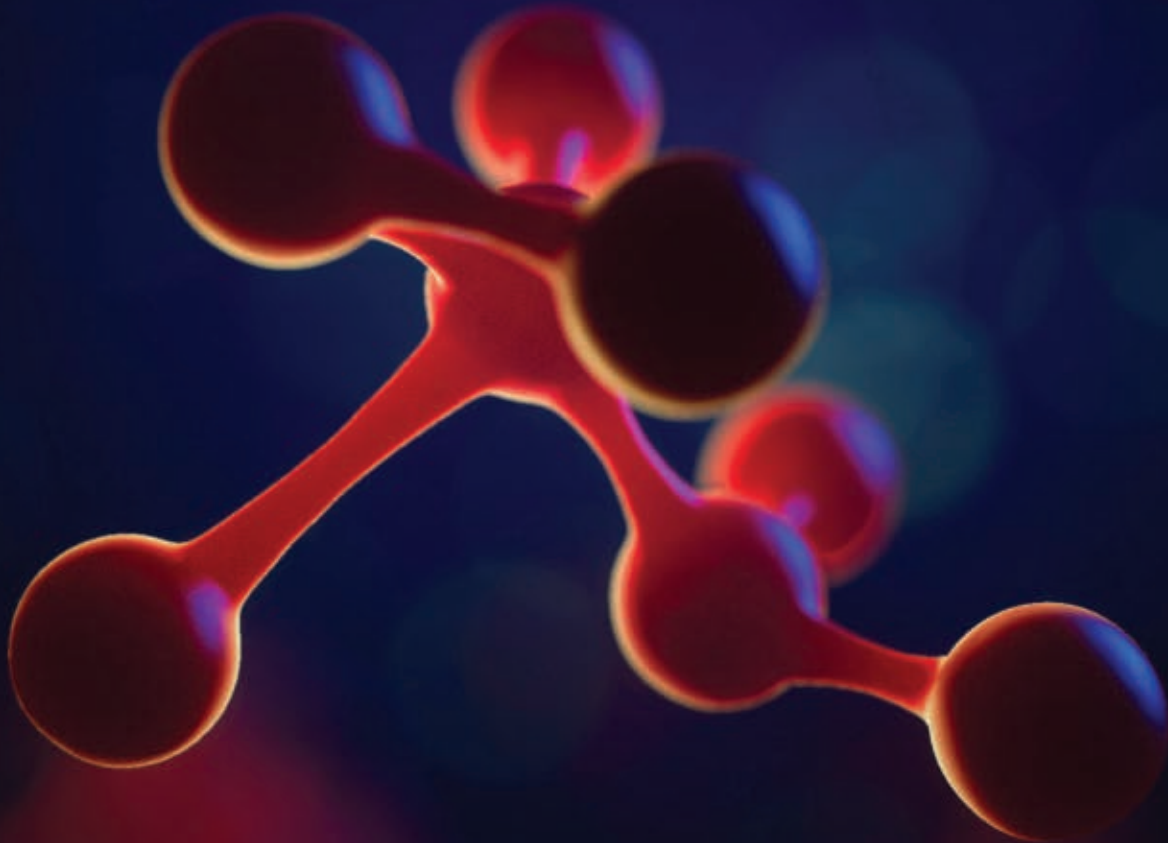
MDAR Reproducibility Checklist

Data S1 to S8

Submitted 28 February 2022; accepted 18 July 2022

[10.1126/science.abp8202](https://doi.org/10.1126/science.abp8202)

Science
JOURNALS 



Publish your research in the *Science* family of journals

The *Science* family of journals (*Science*, *Science Advances*, *Science Immunology*, *Science Robotics*, *Science Signaling*, and *Science Translational Medicine*) are among the most highly-regarded journals in the world for quality and selectivity. Our peer-reviewed journals are committed to publishing cutting-edge research, incisive scientific commentary, and insights on what's important to the scientific world at the highest standards.

Submit your research today!

Learn more at **[Science.org/journals](https://www.science.org/journals)**

RESEARCH ARTICLE SUMMARY

NEUROEVOLUTION

Single-cell analyses of axolotl telencephalon organization, neurogenesis, and regeneration

Katharina Lust^{*†}, Ashley Maynard[‡], Tomás Gomes[‡], Jonas Simon Fleck, J. Gray Camp, Elly M. Tanaka^{*}, Barbara Treutlein^{*}

INTRODUCTION: Salamanders, such as the axolotl (*Ambystoma mexicanum*), play a role in the study of tetrapod-conserved traits. Cell-type diversity in salamander brains and their relation to other vertebrate brains has until now been studied mainly histologically. Axolotl brains grow during postembryonic life, with new neurons generated by proliferating ependymoglia cells. Axolotl brains also regenerate after injury; however, it is still unclear how stem cells regenerate the brain and whether neuronal connections are appropriately recovered.

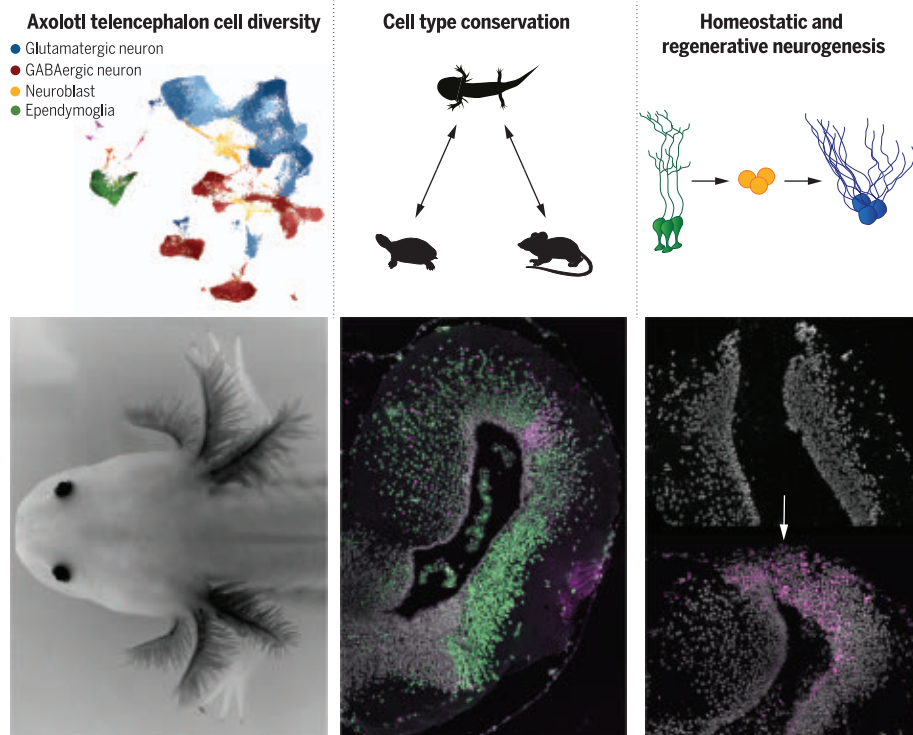
RATIONALE: Single-cell and single-nucleus genomic profiling of the telencephalon has revealed diversity and evolutionary relationships of cell types and brain regions among several amniotes, including reptiles, birds, and mammals. These methods have also revealed molec-

ular trajectories underlying developmental and adult neurogenesis. We molecularly characterized axolotl telencephalon cell types, neurogenesis, and evolutionary conservation. We applied single-nucleus genomic profiling to the axolotl telencephalon in steady state and during regeneration to investigate its cell-type diversity and molecular dynamics of homeostatic neurogenesis. We compared molecular profiles to understand injury-specific features of regenerative neurogenesis.

RESULTS: We determined the cellular diversity of the axolotl telencephalon using single-nucleus RNA sequencing (snRNA-seq) and single-nucleus assay for transposase-accessible chromatin with high-throughput sequencing (snATAC-seq), as well as spatial transcriptomics. We identified regionally distributed

neuron, ependymoglia, and neuroblast populations and determined their conservation with amniotes by using comparative analyses. We found that the axolotl telencephalon contains glutamatergic neurons with transcriptional similarities to neurons of the turtle and mouse hippocampus, dorsal cortex, and olfactory cortex. Olfactory cortex-like neurons also show conserved neuronal input projections from the olfactory bulb. Axolotl γ -aminobutyric acid–releasing (GABAergic) inhibitory neurons show signatures of different subregions of the ganglionic eminence and resemble turtle and mouse GABAergic inhibitory neurons. We used trajectory inference to construct differentiation trajectories of homeostatic neurogenesis and found that ependymoglia largely progress through distinct intermediate neuroblast types and use specific gene regulatory networks to form distinct glutamatergic neuron types. We tracked cycling cells upon injury of the telencephalon and found an injury-specific ependymoglia transcriptional state characterized by up-regulation of wound healing and cell migration genes at the beginning of regenerative neurogenesis. Neurogenesis after injury progresses similarly to homeostatic neurogenesis and results in reestablishment of lost neurons and input projections from the olfactory bulb.

CONCLUSION: Our findings indicate that cell types and gene expression patterns associated with mammalian telencephalon regions are also evident in the amphibian brain. The evolutionary history of cell types clarified the larger divergence in glutamatergic compared with GABAergic neurons that we observed the axolotl, as was also seen in reptiles. We conclude that in the postembryonic axolotl, telencephalon neurogenesis progresses through diverse neuroblast progenitors, which are associated with specific neuron types and dependent on shared as well as specific regulatory programs. We found implementation of these same programs in regenerative neurogenesis, which indicates that brain injury activates neurogenesis through existing pathways after inducing an injury-specific ependymoglia state. Regenerated neurons reestablish their previous connections to distant brain regions, suggesting potential functional recovery. Our insight into how the axolotl brain regenerates may inform studies of brain regeneration in other organisms. ■



Axolotl telencephalon organization, conservation, and neurogenesis. Single-nucleus multiome sequencing provides a comprehensive overview of neuronal and non-neuronal cell types in the axolotl telencephalon and their specific genes and regulatory networks. Cross-species comparison of single-cell data assigned cell populations to reptilian and mammalian brain regions and progenitor types. A snRNA-seq time course after brain injury revealed differences and parallels between regenerative and homeostatic neurogenesis.

The list of author affiliations is available in the full article online.

^{*}Corresponding author. Email: katharina.lust@imp.ac.at (K.L.); elly.tanaka@imp.ac.at (E.M.T.); barbara.treutlein@bsse.ethz.ch (B.T.)

[†]These authors contributed equally to this work.

Cite this article as K. Lust et al., *Science* 377, eabp9262 (2022). DOI: 10.1126/science.abp9262

S READ THE FULL ARTICLE AT
https://doi.org/10.1126/science.abp9262

RESEARCH ARTICLE

NEUROEVOLUTION

Single-cell analyses of axolotl telencephalon organization, neurogenesis, and regeneration

Katharina Lust^{1*†}, Ashley Maynard^{2†}, Tomás Gomes^{2†}, Jonas Simon Fleck², J. Gray Camp^{3,4}, Ely M. Tanaka^{1*}, Barbara Treutlein^{2*}

Salamanders are tetrapod models to study brain organization and regeneration; however, the identity and evolutionary conservation of brain cell types are largely unknown. We delineated the cell populations in the axolotl telencephalon during homeostasis and regeneration using single-cell genomic profiling. We identified glutamatergic neurons with similarities to amniote neurons of hippocampus, dorsal and lateral cortex, and conserved γ -aminobutyric acid–releasing (GABAergic) neuron classes. We inferred transcriptional dynamics and gene regulatory relationships of postembryonic, region-specific neurogenesis and unraveled conserved differentiation signatures. After brain injury, ependymoglia activate an injury-specific state before reestablishing lost neuron populations and axonal connections. Together, our analyses yield insights into the organization, evolution, and regeneration of a tetrapod nervous system.

Comparing brains between animals has been a means to analyze the evolutionary origin and diversification of this structure. Comprehensive single-cell RNA sequencing (scRNA-seq) and single-nucleus RNA sequencing (snRNA-seq) have increased the resolution of cell identity and development of the vertebrate brain. Cell types from the dorsal region of the telencephalon—which in mammals includes the hippocampus, amygdala, claustrum, olfactory (piriform) cortex, and elaborate neocortex—have been resolved and compared between amniotes, including turtle, lizards, birds, mouse, and human (1–4). These studies have revealed evolutionary relationships in cell types and brain regions among amniotes; however, little is known about their conservation in other vertebrates.

The axolotl (*Ambystoma mexicanum*), as an amphibian, represents one of the closest living relatives to amniotes and is therefore suited for comparative studies of brain cell types, neuronal connectivity, and function. The axolotl is also able to regenerate the telencephalon after removal of the dorsal region by activating neurogenesis (5), which is also present during post-embryonic life (6). Neurogenesis can be found in all metazoans with a nervous system (7–9), and in the mouse, cells of the adult subventricular zone (SVZ) undergo continuous

neurogenesis throughout life; however, after brain injury neurogenesis is almost absent (10, 11). The molecular relationship between neurogenesis seen in salamanders and mammals has not been explored. Furthermore, similarities and differences between homeostatic and regenerative neurogenesis in the salamander brain are unclear.

To understand the organizational features of the axolotl telencephalon, we used single-nuclei genomic methods and spatial profiling. We analyzed cell types present in different regions and defined their similarities to amniote telencephalic cell types. To delineate the cellular and molecular dynamics of homeostatic neurogenesis in the axolotl and its relation to adult neurogenesis in mice, we used clonal tracing, trajectory analysis, and multiomic sequencing. Analyzing regenerative neurogenesis, we determined the similarities and differences to homeostatic neurogenesis and found that regenerated neurons reestablish neuronal input from other regions of the telencephalon. Together, our comprehensive analyses of the axolotl telencephalon yielded insights into the organization, evolution, and regeneration of a tetrapod nervous system.

snRNA-seq of the axolotl telencephalon

We used snRNA-seq to generate a comprehensive dataset of the cell types and states from the axolotl telencephalon. We microdissected the telencephalon into medial (containing medial pallium and septum), dorsal (containing dorsal pallium), and lateral (containing lateral pallium, ventral pallium, and dorsal striatum) regions. Additionally, we profiled all of these regions as a whole with single-nucleus multiome sequencing [snRNA-seq and single-nucleus assay for transposase-accessible chromatin with high-

throughput sequencing (snATAC-seq) from the same single nucleus] (Fig. 1A and fig. S1A). We computationally integrated 48,136 nuclei and identified 95 molecularly distinct clusters of neuronal and non-neuronal cells (Fig. 1, B to E, and fig. S1, B to E). We annotated non-neuronal clusters as endothelial cells [*Collagen alpha-1(IV) chain*⁺ (*Col4a1*⁺)] and glial cells, including oligodendrocytes [*Muscle-associated receptor tyrosine kinase*⁺ (*Musk*⁺)], microglia [*Colony-stimulating factor-1*⁺ (*Csf1r*⁺)], and ependymoglia [*GLI family zinc finger 2*⁺ (*Gli2*⁺)]. Neuronal clusters included glutamatergic excitatory neurons [*Solute carrier family 17 member 6/7*⁺ (*Slc17a6/7*⁺)], γ -aminobutyric acid–releasing (GABAergic) inhibitory interneurons [*Glutamate decarboxylase1*⁺ and *2*⁺ (*Gad1*⁺ and *Gad2*⁺)], and a *Mex-3 RNA binding family member A*⁺ (*Mex3a*⁺)/*Gli2*[−] population of cells we termed neuroblasts (fig. S1E). Each cell type was present in each microdissected region (Fig. 1, B and C, and fig. S1A), and we provide a set of marker genes for each cluster identified at this resolution (Fig. 1, D and E, and table S1). We performed immunofluorescence stainings and in situ RNA hybridization chain reaction (HCR) to localize major cell types in the tissue according to marker expression (Fig. 1F). Glial fibrillary acidic protein⁺ (GFAP⁺) ependymoglia line the ventricle of every region, whereas *Mex3a*⁺ neuroblasts are sparsely distributed along the ventricle. GABAergic neurons were sparsely distributed along the medial, dorsal, and lateral region and clustered together densely in the striatum, whereas glutamatergic neurons were located in the medial, dorsal, lateral, and ventral pallium. Small populations of myelin basic protein⁺ (MBP⁺) oligodendrocytes and ionized calcium binding adaptor molecule 1⁺ (IBA1⁺) microglia cells were dispersed throughout all regions.

We next analyzed the abundance of each cell cluster in the sampled pallial regions (Fig. 1G and fig. S1F). Oligodendrocytes, microglia, and endothelial cell clusters originated from each region in similar proportions. By contrast, ependymoglia, neuroblast, glutamatergic, and GABAergic neuron clusters showed variable region contributions, with some cell clusters being completely region-restricted, whereas others could be found throughout the sampled pallium regions. These data provide an overview of cell populations in the axolotl telencephalon and suggest substantial regional specificity in neurogenic programs.

Regional conservation of axolotl glutamatergic neurons

Glutamatergic neurons of the amniote telencephalon show a high degree of transcriptional diversification (1, 2). Our data revealed 29 glutamatergic neuron clusters differentially distributed in medial, dorsal, and lateral regions (Fig. 2, A to C, fig. S2A, and table S1).

¹Research Institute of Molecular Pathology, Vienna Biocenter (VBC), Campus Vienna Biocenter, 1030 Vienna, Austria.

²Department of Biosystems Science and Engineering, ETH Zürich, 4058 Basel, Switzerland. ³Roche Institute for Translational Bioengineering (ITB), Roche Pharma Research and Early Development, Roche Innovation Center Basel, Basel, Switzerland. ⁴University of Basel, 4001 Basel, Switzerland.

*Corresponding author. Email: katharina.lust@imp.ac.at (K.L.); ely.tanaka@imp.ac.at (E.M.T.); barbara.treutlein@bsse.ethz.ch (B.T.)

†These authors contributed equally to this work.

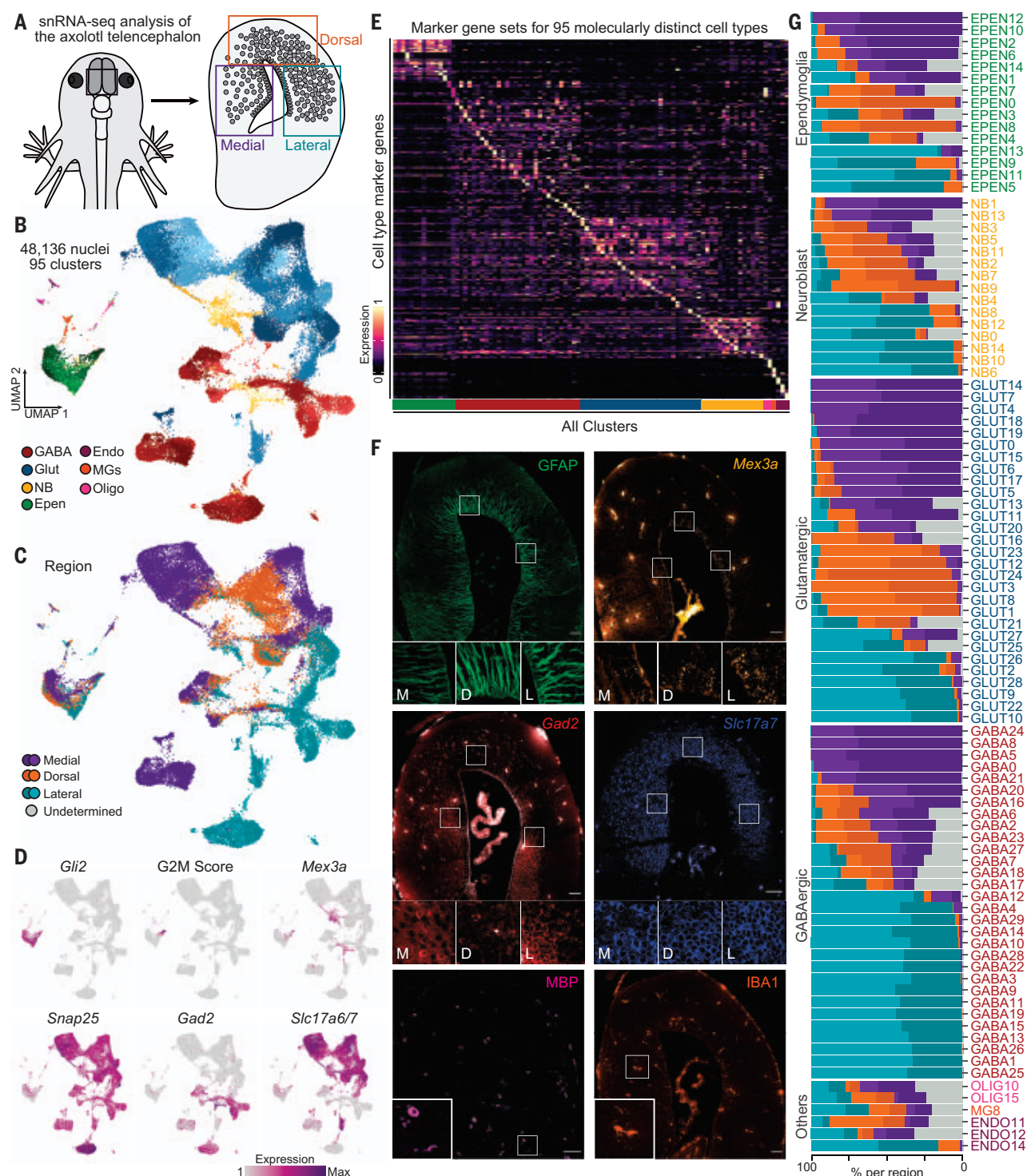
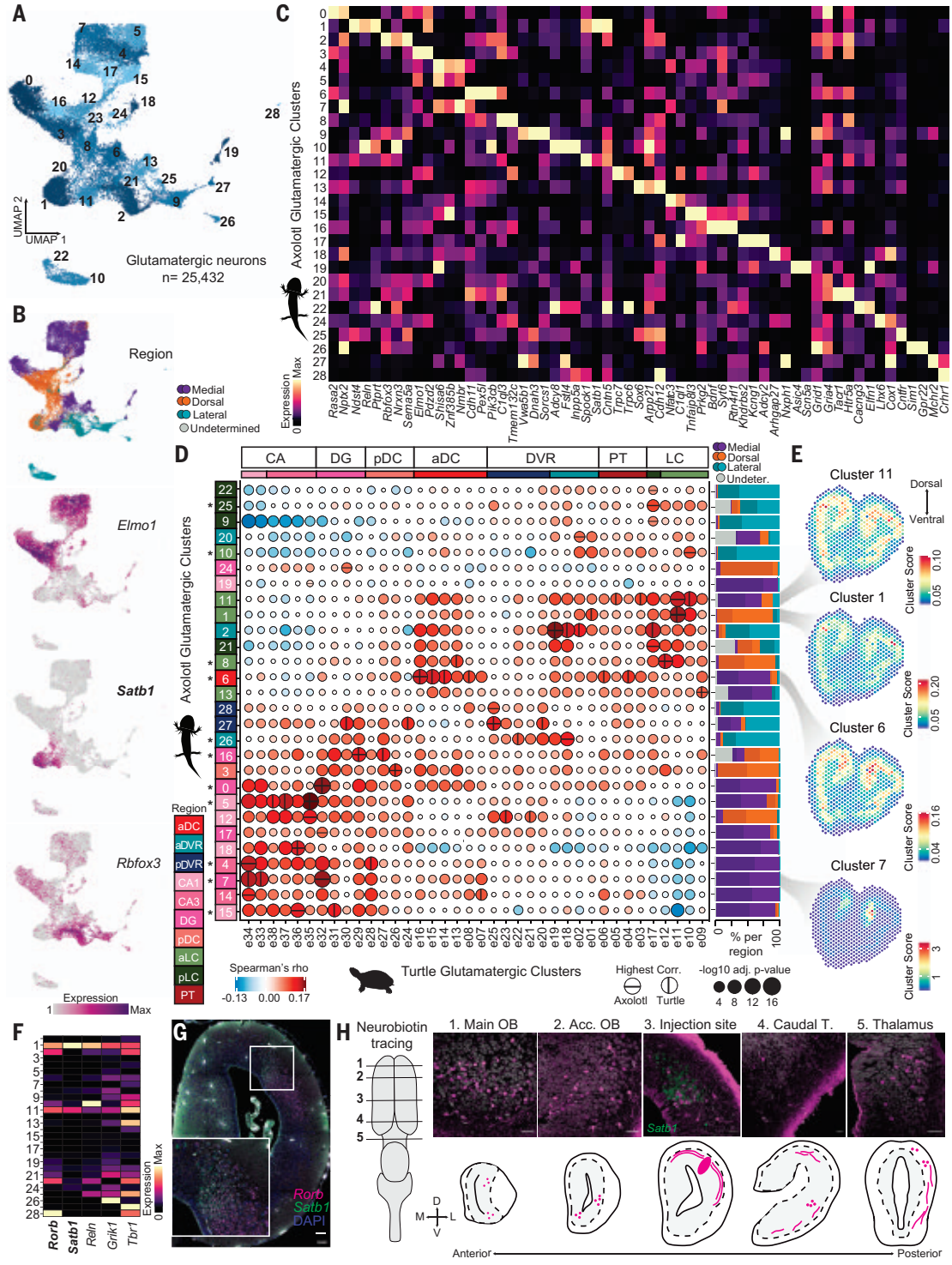


Fig. 1. Cellular diversity of the axolotl telencephalon. (A) Schematic highlighting the regions of the axolotl telencephalon used for snRNA-seq. (B) UMAP of all cell types across all regions colored by cell-type class. Subtypes are shown in different shades. GABA, GABAergic neuron; Glut, glutamatergic neuron; NB, neuroblast; Epen, ependymoglia cell; Endo, endothelial cell; MGs, microglia; and Oligo, oligodendrocyte. (C) UMAP plot of regional distribution of all cell types. Shades indicate true region identity versus predicted regional identity. (D) UMAP plot of the expression of markers for ependymoglia, neuroblast, and neuronal cell types: *Gli2* (ependymoglia), G2M score (active

ependymoglia), *Mex3a* (neuroblasts), *Snap25* (neurons), *Gad2* (GABAergic neurons), and *Slc17a6/7* (glutamatergic neurons). (E) Heatmap illustrates the expression of marker genes (table S1) for the 95 distinct cell types. (F) Antibody stainings and HCR for main cell types: GFAP (ependymoglia), *Mex3a* (neuroblasts), *Gad2* (GABAergic neurons), *Slc17a7* (glutamatergic neurons), MBP (oligodendrocytes), and IBA1 (microglia cells). Scale bars, 100 μ m. (G) Stacked barplots illustrating the regional distribution of the populations of cells. GABA, GABAergic neuron; Glut, Glutamatergic neuron; NB, neuroblast; Epen, ependymoglia cell; Endo, endothelial cell; MGs, microglia; Oligo, oligodendrocyte.

Fig. 2. Diversity of axolotl telencephalic glutamatergic neurons.

(A) UMAP plot of 29 glutamatergic neuron types. **(B)** UMAP plots of the regional distribution of glutamatergic neurons types and the expression of three marker genes: *Elmo1*, *Satb1*, and *Rbfox3*. **(C)** Heatmap illustrating the expression of top markers for each glutamatergic neuron cluster. **(D)** Correlation analysis between expression profiles of axolotl glutamatergic neuron types and turtle glutamatergic neuron types [data are from (2)]. Vertical lines indicate highest correlated cluster to turtle, and horizontal lines indicate highest correlated cluster to axolotl. (Right) Stacked barplots illustrating the regional distribution of the cells from each cluster. Asterisks indicate clusters with agreeing assignments between all genes correlation and integration analysis. CA, cornu ammonis; DG, dentate gyrus; pDC and aDC, posterior and anterior dorsal cortex; DVR, dorsal ventricular ridge; PT, pallial thickening; and LC, lateral cortex. **(E)** Spatial mapping of glutamatergic neuron clusters 11, 1, 6, and 7. **(F)** Heatmap illustrating the expression of *Satb1*, *Rorb*, *Reln*, *Grik1*, and *Tbr1*. **(G)** HCR for *Satb1* and *Rorb*. **(H)** Projection mapping of input into glutamatergic cluster 1 by using Neurobiotin-mediated anterograde and retrograde tracing. Dots indicate locations of cell bodies, and lines indicate locations of fibers. Main OB, main olfactory bulb; Acc. OB, accessory olfactory bulb; and caudal T., caudal telencephalon.



Potential homologies of axolotl glutamatergic neurons to telencephalon neurons were probed with two separate comparisons, by using either species-shared differentially expressed genes or species-shared differentially expressed transcription factors (TFs) to distinguish between convergent evolution versus homology (Fig. 2D; fig. S2, B to F; and tables S2 and S3). We focused then on glutamatergic clusters that have con-

cordant similarities, using both gene sets as indicators of conservation. In parallel, cluster similarities were also assessed through integration of single-cell and single-nuclei datasets from axolotl, turtle pallium (2), and mouse telencephalon (3).

Anatomical and functional evidence suggests that the amphibian medial pallium is homologous to the mammalian hippocampus

(12, 13). We found that the majority of medial glutamatergic clusters (Glut4, -5, -7, -15, and -18) and two dorsal clusters (Glut12 and -16) showed highest correlation to either turtle cornu amonis (CA) or dentate gyrus (DG) clusters (Fig. 2D and fig. S2B). Correlations to the mouse dataset also revealed that medial glutamatergic clusters (Glut5, -7, -14, -17, -24, and -27) correlated most to hippocampus-related

clusters (fig. S2, D to F). Data integration additionally showed co-clustering of a large number of medial glutamatergic clusters to either turtle or mouse hippocampus clusters (fig. S3, A to E). To reveal the locations of hippocampus-correlated glutamatergic clusters and unravel a potential subdivision into CA or DG, we performed spatial transcriptomics using Visium (10x Genomics), resulting in spatial resolution of approximately 1 to 30 cells (Fig. 2E and figs. S4A and S5) (14). We found that all aforementioned clusters except *Glut18* showed exclusive localization in the medial pallium; however, clear subdivisions were not detectable, which was further confirmed by means of HCR for *ETS translocation variant 1* (*Etv1*) (CA), *Prospero homeobox 1* (*Prox1*), and *LIM domain only 3* (*Lmo3*) (DG) (fig. S4B). These data show that neurons of the axolotl medial pallium have transcriptional similarities to amniote hippocampal neurons, but a clear distinction into CA1, CA3, and DG cannot be observed.

One cluster from the medial fraction (*Glut6*) showed highest correlations to clusters of turtle anterior dorsal cortex (aDC) and pallial thickening (PT). The aDC contains the most cell types homologous to mammalian cortical cell types (2). The correlation to mouse showed highest similarity to clusters belonging to cortical cells (fig. S2D), which was also supported by data integration in which *Glut6* was also co-clustered with cortical cell types. We found that this cluster was predicted to be located at the border between the medial and dorsal pallium (Fig. 2E).

One function of the amphibian pallium is the processing of olfactory input (15). One axolotl glutamatergic cluster (*Glut1*) showed co-clustering with a cortical cluster and correlations to both cortical clusters and the turtle anterior LC (aLC), the main olfactory-input recipient region (Fig. 2D and fig. S2B) (16). Neurons in the aLC are homologous to neurons in the mammalian olfactory (piriform) cortex, and *Glut1* also correlated to a mouse piriform cortex cluster (fig. S2, D and E). The piriform cortex contains semilunar cells expressing *RAR-related orphan receptor beta* (*Rorb*), *Reelin* (*Reln*), *Glutamate ionotropic receptor kainate type subunit 1* (*Grik1*), and *T-Box brain transcription factor 1* (*Tbr1*) (17), and these same markers were expressed in *Glut1* (Fig. 2F). Moreover, *Glut1* expressed *Special AT-rich sequence-binding protein-1* (*Satb1*), which we used in combination with *Rorb* expression to define its location in the dorso-lateral region (Fig. 2G), which is consistent with the location in the spatial mapping (Fig. 2E). The mammalian piriform cortex receives input from the olfactory bulb, entorhinal cortex, orbitofrontal cortex, and the amygdala (18). We analyzed axolotl projections by injecting the bidirectional tracer Neurobiotin

into the region containing *Glut1* (Fig. 2H). Labeling of cell bodies in the main and accessory olfactory bulb, caudal pallium (lateral amygdala) (19), and the thalamus indicate that neurons in these regions project into the *Glut1*-containing domain. These data show a strong correspondence between presence of neurons with transcriptional similarity to amniote olfactory cortex neurons and presence of projections consistent with a role in olfactory processing.

Amniote-conserved signatures of axolotl GABAergic neurons

We identified 30 clusters ($n = 15,665$ cells) of GABAergic (*Gad1⁺/Gad2⁺*) neurons (Fig. 3, A to B, and table S1) in the axolotl. In many vertebrates, GABAergic interneurons are born in the lateral, caudal, and medial ganglionic eminences (LGE, CGE, and MGE, respectively) and migrate to the pallium during development (20). Comparative scRNA-seq analyses in mammals, reptiles, and songbirds have revealed strong conservation of GABAergic interneurons (1, 2). To gain an understanding of the conservation of axolotl GABAergic clusters, we performed cross-species comparisons using correlation and integration analysis as for the glutamatergic neurons.

Expression of conserved TFs allowed us to identify putative LGE-derived, CGE-derived, and MGE-derived (hereafter called LGE-like, CGE-like, and MGE-like, respectively) clusters in the axolotl dataset (Fig. 3C). Correlation analysis revealed that 13 out of 14 LGE-like clusters showed high correlations to turtle LGE-derived clusters. Moreover, two out of four CGE-like clusters and five out of seven MGE-like clusters showed similarities to turtle CGE-derived and MGE-derived clusters, respectively. Our analyses additionally identified five axolotl clusters composed of medial cells likely derived from the septum, which showed strong correlations to the turtle GABAergic neurons assigned to septum. These results were additionally supported by data integration in which the majority of axolotl LGE-, CGE-, and MGE-like clusters co-clustered with the respective turtle clusters (fig. S7, A to E).

Turtle LGE-, CGE-, and MGE-derived GABAergic neurons could be further subdivided into different GABAergic classes (2), but their existence in the axolotl was unknown. We found that 11 out of 13 axolotl LGE-like clusters correlated with either turtle striatum or olfactory bulb GABAergic cells (Fig. 3D and fig. S6, A and B), and the majority of these (eight clusters) also correlated to mouse striatum or olfactory bulb GABAergic cells (fig. S6, C to E). By contrast, only one out of four CGE-like clusters (GABA 16) correlated to turtle HTR3A VIP-like neurons. All seven axolotl MGE-like neuron clusters matched to turtle PV-like neurons by TF expression but had similarities to turtle SST neurons at the

level of effector genes, suggesting evolutionary divergence of these cells. Together, these data show that the axolotl telencephalon contains putative LGE-derived, CGE-derived, MGE-derived, and septal GABAergic neurons and that LGE-like striatum and olfactory bulb classes have strong transcriptional similarities between axolotl, turtle, and mouse (tables S2 and S3).

In mammals and turtles, MGE-derived and CGE-derived interneurons are differentially distributed across cortical layers (2, 21). In axolotl, we found MGE-like neurons [*Somatostatin⁺* (*Sst⁺*) and *Satb1⁺*] equally distributed in the medial pallium and enriched in the outer regions of the dorsal and lateral pallium (Fig. 3E and fig. S8A). CGE-like neurons [*Zinc finger and BTB domain containing 16⁺* (*Zbtb16⁺*)] were equally distributed in the medial pallium but closer to the ventricle in the dorsal pallium. LGE-like striatal GABAergic neurons [*Forkhead box P1⁺* (*Foxp1⁺*)] were found exclusively in the striatal region (fig. S8A). Last, we spatially mapped LGE-like, CGE-like, and MGE-like clusters and detected the majority of CGE-like and MGE-like clusters located in all regions of the pallium as well as the striatum (fig. S8B). These data strongly suggest cell migration from putative CGE and MGE regions, whereas LGE clusters are predominantly located in the striatum, as in amniotes.

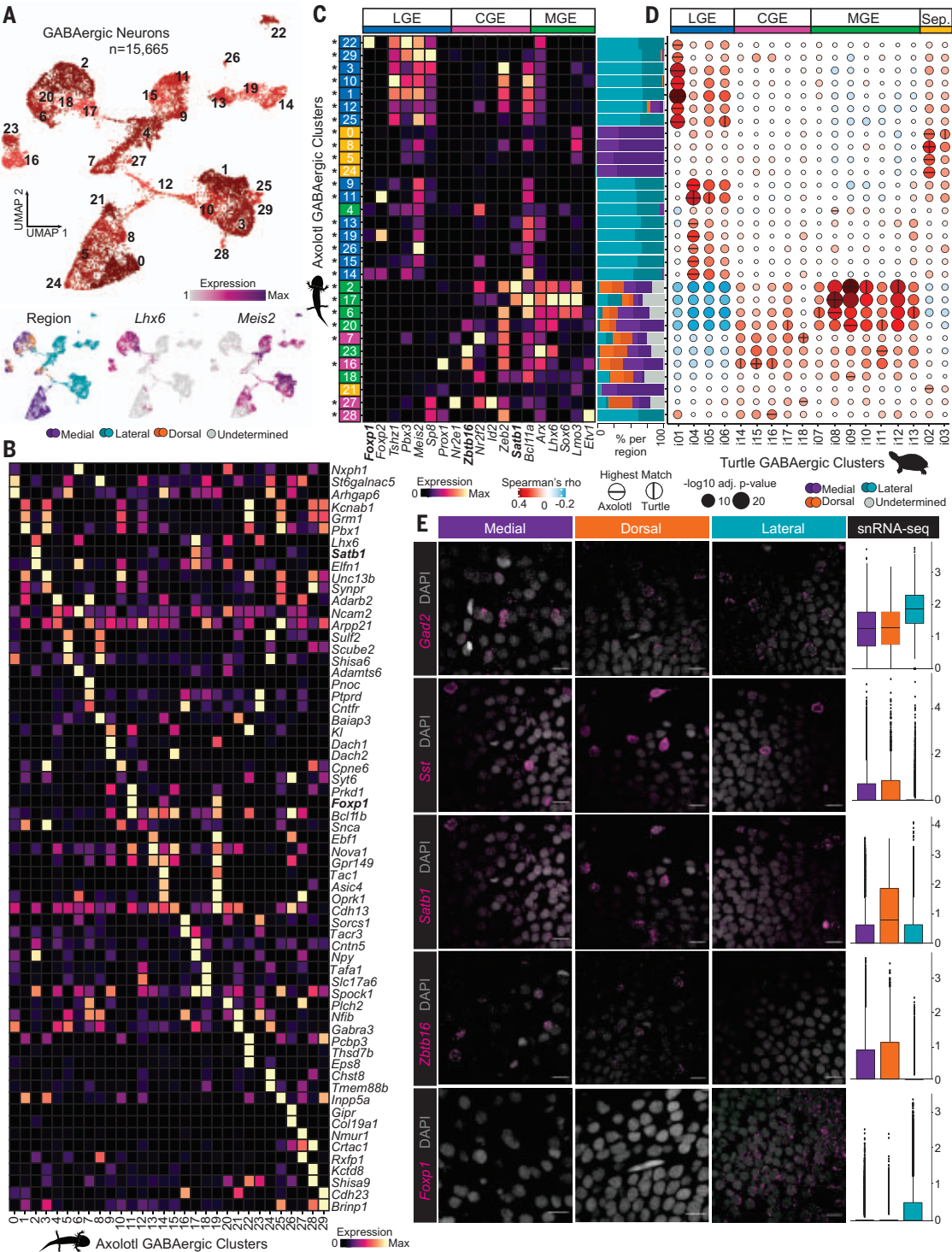
Ependymoglia diversity in the axolotl telencephalon

The predominant glial cells in the salamander central nervous system are ependymoglia, which generate neurons in development, growth, and regeneration (5, 15, 22). In the adult red-spotted newt telencephalon, two ependymoglia types have been identified: quiescent type-1 cells that act as long-term stem cells and proliferative type-2 cells that are progenitor-like (22).

We examined the diversity of axolotl telencephalic ependymoglia (3590 cells) and identified 15 transcriptionally distinct cell clusters (Fig. 4A, fig. S9A, and table S1). These clusters grouped into three types of ependymoglia that were present in all dissected regions: quiescent, active, and a type that we termed pro-neuro ependymoglia (Fig. 4A). Quiescent ependymoglia were noncycling and expressed *Endothelin 3* (*Edn3*), active ependymoglia were characterized by *Notch1* expression and a high cell cycle score, and pro-neuro ependymoglia showed expression of neuron-related genes, such as *Glutamate receptor ionotropic 1* (*Grin1*) (Fig. 4, B and C, and fig. S9, B to D).

We found a clear transcriptional distinction between medial-, dorsal-, and lateral-derived ependymoglia, which was most prominent for signaling pathway components (Fig. 4, C and D, and fig. S9E). A subset of medial quiescent ependymoglia showed strong expression of *Wnt2b*, *Wnt3a*, and *Wnt8b*—genes that are

Fig. 3. Conversation of axolotl GABAergic neuron types. (A) UMAP plots of 30 GABAergic neuron types (top) and regional distribution of GABAergic neurons types, as well as two marker genes, *Lhx6* and *Meis2*. (B) Heatmap illustrating the expression of differential expressed markers for each GABAergic neuron cluster. (C) Heatmap illustrating the expression of TFs known to define GABAergic subtypes (LGE-, CGE-, and MGE-derived) for each axolotl GABAergic neuron type. (Right) Stacked barplots illustrating the regional distribution of the cells from each cluster. (D) Correlation analysis between expression profiles of axolotl GABAergic neuron types and turtle GABAergic neuron types [data are from (2)]. Vertical lines indicate highest correlated cluster to turtle, and horizontal lines indicate highest correlated cluster to turtle. Asterisks indicate clusters with agreeing assignments between all genes correlation and integration analysis. Sep., Septum. (E) HCR and snRNA-seq quantifications for LGE-, CGE-, and MGE-derived GABAergic neurons types (*Gad2*, pan; *Sst* and *Satb1*, MGE; *Zbtb16*, CGE; and *Foxp1*, LGE). Scale bars, 25 μ m.



known to be expressed in the developing medial pallium in human, mouse, and chicken (23). HCR confirmed expression of *Wnt2b*, *Wnt3a*, and β -catenin target gene *Axin2* in a restricted domain of the medial pallium at the border to the septum. Lateral and ventral ependymoglia showed strong expression of *Secreted frizzled-related protein (Sfrp1)*, a gene known to be expressed in the antihem in amniotes (23). Dorsal ependymoglia were

enriched for expression of *Epidermal growth factor receptor kinase substrate 8-like protein 2 (Eps8l2)*. Because Wnt and Sfrp genes have been implicated in patterning of the developing pallium, we performed HCR in embryonic axolotl brains (stage 44). We detected *Wnt3a* in medial ventricular cells and *Sfrp1* lateral and ventral ventricular cells; however, *Eps8l2* was not expressed (Fig. 4E and fig. S9F). These data show that the axolotl telencephalon con-

tains three main ependymoglia types (quiescent, active, and pro-neuro) that divide into regionally distinct subtypes and, barring pro-neuro ependymoglia, continue to express pallial patterning genes in the postembryonic brain.

Identification of glutamatergic and GABAergic neuroblasts

In addition to ependymoglia, we identified cells that we termed neuroblasts because of

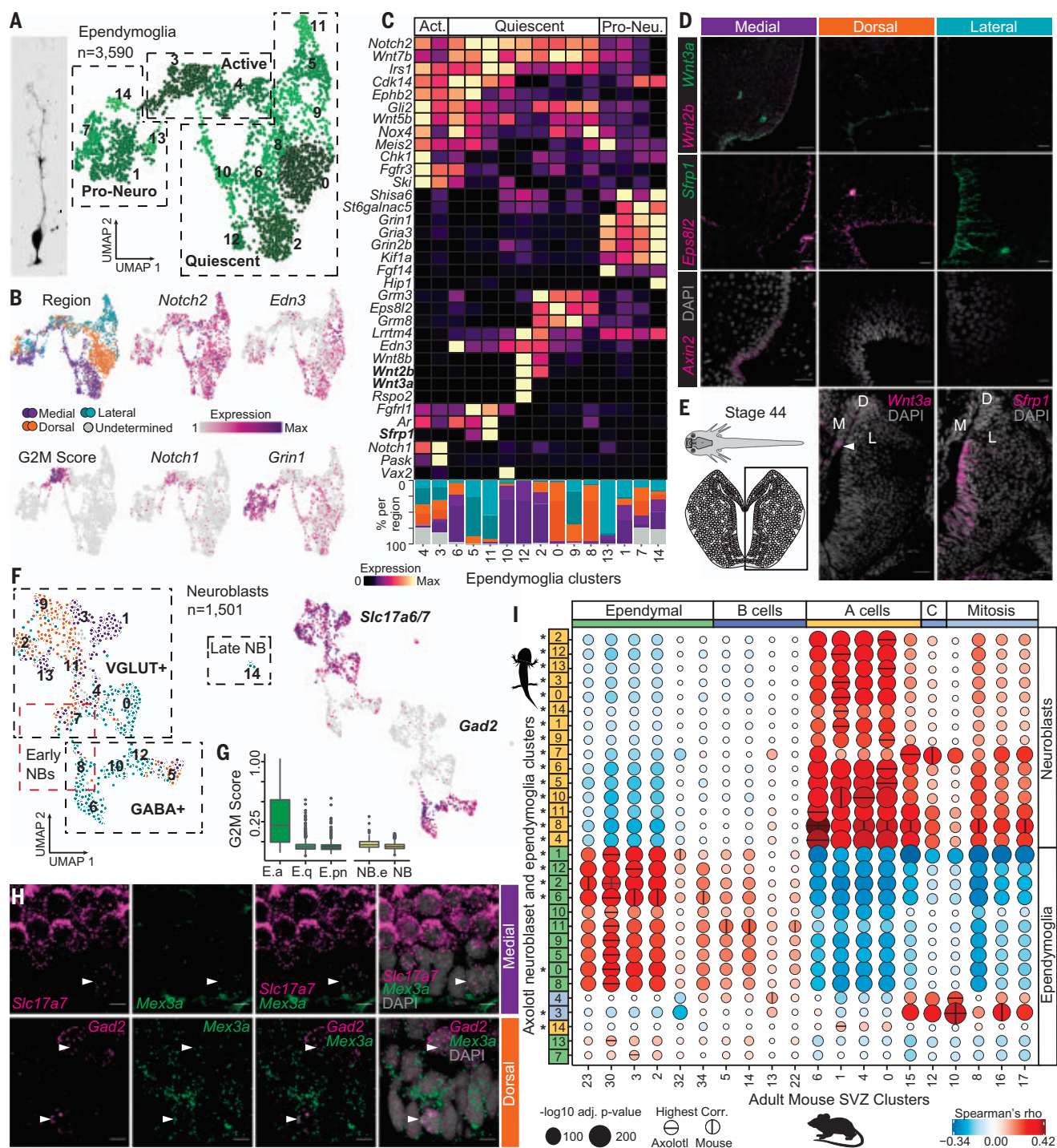


Fig. 4. Axolotl telencephalic ependymoglia and neuroblasts. (A) (Left) Morphology of an axolotl ependymoglia cell and (right) UMAP plot of 15 ependymoglia clusters. Boxes outline the three main cell types: quiescent ependymoglia, active ependymoglia, and pro-neuro ependymoglia. (B) UMAP plot of the regional distribution of ependymoglia and UMAP plots colored by expression for *Notch2* (quiescent and active ependymoglia), *Edn3* (quiescent ependymoglia), G2M score (active ependymoglia), *Notch1* (active ependymoglia), and *Grin1* (pro-neuro ependymoglia). (C) Heatmap illustrating the expression of differentially expressed cell-to-cell communication-related genes in quiescent, active, and pro-neuro ependymoglia. (D) HCR and snRNA-seq quantifications for *Wnt2b*, *Wnt3a*, *Eps8l2*, *Sfrp1*, and *Axin2* in medial, dorsal, and lateral regions. Scale bars, 25 μ m. (E) HCR for *Wnt3a* and *Sfrp1* in the stage 44 developing

telencephalon. Scale bars, 50 μ m. (F) UMAP plots of the regional distribution 15 neuroblast clusters. Black boxes outline the four main cell types: early neuroblasts, VGLUT⁺ and GABA⁺ neuroblasts, as well as late neuroblasts. The red box outlines the early neuroblast population. (G) Boxplot of G2M score for quiescent, active, and pro-neuro ependymoglia as well as neuroblasts. (H) HCR for *Slc17a7*, *Gad2*, and *Mex3a*. Arrows indicate coexpressing cells. Scale bars, 10 μ m. (I) Correlation analysis between expression profiles of axolotl neuroblasts, ependymoglia, and adult mouse SVZ cell types [scRNA-seq data are from (25)]. Vertical lines indicate highest correlated cluster to mouse, and horizontal lines indicate highest correlated cluster to axolotl. Asterisks indicate clusters with agreeing assignments between all genes correlation and integration analysis. C, C cells.

the expression of *Mex3a*, an RNA-binding protein expressed in proliferating neuroblasts in the *Xenopus laevis* central nervous system (24). Additionally, neuroblasts were characterized by the absence of ependymoglia markers such as *Gli2*, *Aquaporin-4* (*Aqp4*), and *Potassium inwardly rectifying channel subfamily J member 10* (*Kcnj10*). We detected 15 neuroblast clusters, which formed two distinct groups that expressed either *Slc17a6/7* (VGLUT⁺) or *Gad1/2* (GABA⁺) (Fig. 4F; fig. S9, G and H; and table S1). In contrast to intermediate progenitors (IPs) found in other vertebrate brains, *Mex3a*⁺ neuroblasts were largely nonproliferative (Fig. 4G and fig. S9I). Two neuroblast clusters (7 and 8) showed an increased G2M score when compared with the rest and were therefore termed early neuroblasts. VGLUT⁺ neuroblasts (except cluster 4) were enriched in medial and dorsal datasets; GABA⁺ neuroblasts (except cluster 5) were mostly found in the lateral dataset. HCR for *Slc17a6* or *Gad2* in combination with *Mex3a* revealed VGLUT⁺ neuroblasts at the ventricle in all pallial regions, whereas GABA⁺ neuroblasts were predominantly present at the striatum ventricle, with the exception of a few cells in the pallium (Fig. 4H and fig. S9J). This pattern was also verified when mapping the neuroblast clusters to our Visium data (fig. S9K).

To define the transcriptional similarities of axolotl ependymoglia and neuroblasts to mouse neural stem and progenitor cells, we performed cluster correlation analysis and cross-species data integration with an adult mouse SVZ dataset (Fig. 4I and figs. S10, A and B, and S11, A to C) (25) and a mouse developmental cortex dataset (figs. S10, C to E, and S11, D to F, and tables S2 and S3) (26). This analysis revealed correlation of quiescent ependymoglia with mouse ependymal cells (adult and development) and B cells (adult), whereas active ependymoglia (clusters 3 and 4) showed strong correlation to mitotic cells (adult), including dividing A cells (cluster 16) and developmental apical radial glia and IPs. Among the pro-neuro ependymoglia, only cluster 1 showed strong correlation to ependymal cells (adult and development), whereas clusters 7 and 13 weakly correlated to ependymal cells (adult) or migrating neurons (development), and cluster 14 weakly correlated to A cells. Data integration revealed co-clustering of ependymoglia with adult ependymal cells or B cells and with apical or IPs in the developmental dataset.

Comparison of axolotl neuroblasts to the adult mouse SVZ dataset revealed strong correlation and co-clustering with A cells, supported by strong correlation and co-clustering with migrating neurons in the developmental dataset (fig. S10, C to E). We found that early neuroblast clusters 7 and 8 correlated also to either C cells or mitotic cells. Furthermore,

these two clusters showed strongest correlation to A cell clusters 6 and 15, which were defined previously as dividing neuroblasts and early A cells, as well as to IP cell clusters in the developmental dataset (Fig. 4I and fig. S10, A and B). Together, these results show that the axolotl telencephalon contains neuroblast populations that already express neurotransmitter signatures of downstream neurons. Moreover, neuroblasts are most similar to mouse progenitor cells and neuroblasts, whereas ependymoglia harbor transcriptional similarities to mouse ependymal cells as well as neural stem cells.

Transcriptional dynamics of postembryonic glutamatergic neurogenesis

We labeled ependymoglia using Cre-loxP-mediated tracing to investigate their self-renewing properties and determine the clonal patterns they generate during post-embryonic neurogenesis (Fig. 5A). This uncovered distinct neurogenesis patterns in medial, dorsal, and lateral regions. Medial and dorsal clones were continuous, spanning from the ventricle to the neuronal layers, indicating a stacking growth mode reminiscent of zebrafish pallial post-embryonic neurogenesis (27). By contrast, lateral clones were dispersed with labeled neurons separated from ependymoglia, indicating neuronal migration.

We used RNA velocity and URD-based trajectory inference (28–30) to explore the cellular and molecular dynamics of post-embryonic neurogenesis (fig. S12, F to T). We focused our analysis on glutamatergic neurons that are known to be generated locally, in contrast to GABAergic neurons that migrate across the pallium from the striatum and for which we likely miss corresponding progenitor populations in our dataset (20). We focused on transitions from active ependymoglia to the most differentiated glutamatergic neurons. To construct trajectories, we first identified the key VGLUT⁺ neuroblast populations that have highest transcriptional similarity to the respective glutamatergic neuronal clusters (fig. S12A) and are therefore able to connect active ependymoglia to neuronal clusters in a trajectory. Using these groups of clusters, we then constructed five trajectories that represent different region-specific neurogenesis (Fig. 5, B and C, and fig. S12, B to E). Although all trajectories were rooted at the active ependymoglia, not all trajectories contained neuroblast intermediates. Hippocampal neuronal clusters, lateral cortex clusters, and laterally derived clusters, including the lateral pallium group and the *Eomesodermin* (*Eomes*) group, all used neuroblast intermediates. By contrast, the dorso-medial neuronal clusters formed a group with lower correlations with the least differentiated neuroblast clusters and were thus inferred to originate through a direct trajectory using pro-neuro ependymoglia as

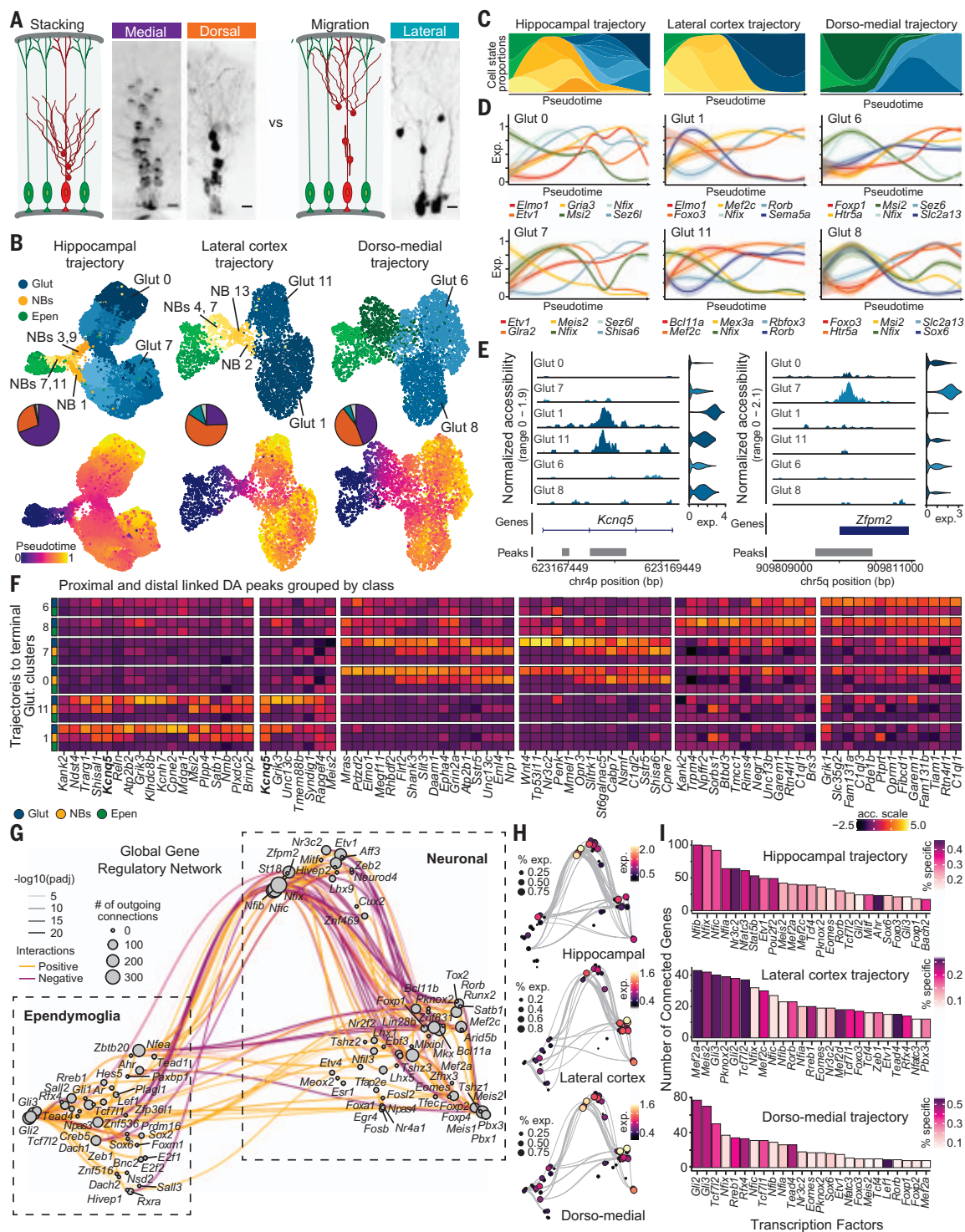
intermediates. We identified many genes with trajectory-specific varying expression along pseudotime, but also some genes with pseudo-temporal expression consistent across trajectories (Fig. 5D).

To resolve the gene regulatory relationships underlying glutamatergic neurogenesis, we leveraged our single-nucleus multiome sequencing of the axolotl whole pallium. We identified proximal and distal candidate regulatory regions differentially accessible in each of the terminal glutamatergic neuron clusters and assessed at which stage in the respective trajectory they become accessible (Fig. 5, E and F; fig. S13, A and B; and table S4). Most elements identified as specific for a given terminal glutamatergic cluster already obtained accessibility in the corresponding neuroblast clusters earlier in the trajectory. We inferred a gene regulatory network (GRN) using Pando (37) by combining gene expression, chromatin accessibility, and TF binding motifs. A uniform manifold approximation and projection (UMAP) embedding of this GRN revealed distinct groups of TFs, corresponding to the transition from ependymoglia to glutamatergic neurons (Fig. 5G and table S5). To better understand how gene regulation differs between neuronal trajectories, we performed differential accessibility analysis and identified regulatory regions enriched within each trajectory. On the basis of these regions, we constructed subnetworks of the GRN that reflect trajectory-specific regulatory features (Fig. 5H, fig. S13C, and table S5). This allowed us to identify the TFs with high centrality in a given trajectory, such as *Nuclear receptor subfamily 3 group C member 2* (*Nr3c2*) in the hippocampus or *Rorb*, *Forkhead box O3* (*Foxo3*), and *Myocyte enhancer factor 2A* (*Mef2a*) in the lateral cortex (Fig. 5I and fig. S13D). Genes differentially expressed between glutamatergic clusters were linked to trajectory-specific TFs with high centrality (fig. S13, E to F). *Nuclear factor 1 X* (*Nfix*) was one of the most central TFs in all subnetworks; however, the regulomes controlled by *Nfix* were distinct for each respective trajectory (fig. S13, G and H, and table S5). Together, these data highlight the regulatory relationships that shape neuronal diversification in the axolotl telencephalon.

Molecular dynamics of axolotl telencephalon regeneration

To study the cellular and molecular dynamics during axolotl telencephalon regeneration, we implemented Div-Seq (32), which combines snRNA-seq with EdU labeling of S-phase cells. We injured the dorso-lateral region of the telencephalon (including the *Satb1*⁺, *Rorb*⁺ domain) by excising a 1- by 1- by 1-mm region and applied Div-Seq throughout regeneration by labeling cells with EdU at 2, 5, 12, 19, and 26 days post injury and collecting EdU⁺ cells

Fig. 5. Gene regulatory programs underlying post-embryonic neurogenesis. (A) Schematic describing the outcomes of Cre-loxP fate mapping performed to assess clonal dynamics and potential clone shapes during homeostatic neurogenesis of the axolotl telencephalon adjacent to measured clonal patterns in medial, dorsal, and lateral pallium. (B) Glutamatergic trajectories reflecting postembryonic neurogenesis of axolotl neurons matched to amniote hippocampus, lateral cortex, and the dorso-medial pallium. UMAPs are colored by cell type (top) and pseudotime (bottom). Pie charts represent the regional composition of neuron clusters. (C) Pseudotemporal cell type progression from ependymoglia to glutamatergic neurons during neurogenesis in the three trajectory groups. (D) Pseudotemporal gene expression changes during neurogenesis for each terminal branch from the trajectories of each group. (E) Representative example peaks associated with (left) *Kcnq5* and (right) *Zfp2m2*. (F) Heatmap of chromatin accessibility changes in distal and proximal elements for glutamatergic clusters 8, 6, 7, 0, 11, and 1. (G) UMAP embedding of the inferred gene modules based on coexpression and inferred interaction strength between TFs. Size represents the number of connections for each TF. (H) Trimmed GRN UMAP embedding of the inferred gene modules based on coexpression and inferred interaction strength between TFs for (top) hippocampal, (middle) lateral cortex, and (bottom) dorso-medial trajectories. (I) Barplot of the top 25 TFs ranked by number of connections for each TF and colored by fraction of trajectory-specific peaks out of total number of peaks in the global module.



at 1, 2, 4, 6, 8, and 12 weeks post injury (Fig. 6A). To visualize the location of EdU⁺ cells during the regeneration process, we fluorescently labeled EdU using click chemistry on regen-

erating brains (Fig. 6B and fig. S14, A and B). At 1 week post injury, the injury site was still open, and EdU⁺ ependymoglia were present in medial and lateral wound-adjacent regions.

Color scale indicates expression, and size indicates the percent of cells expressing. (I) Barplot of the top 25 TFs ranked by number of connections for each TF and colored by fraction of trajectory-specific peaks out of total number of peaks in the global module.

At 2 weeks post injury, the injury site was starting to close from the accumulation of EdU⁺ cells. Throughout the following time points, EdU⁺ cells remained accumulated at

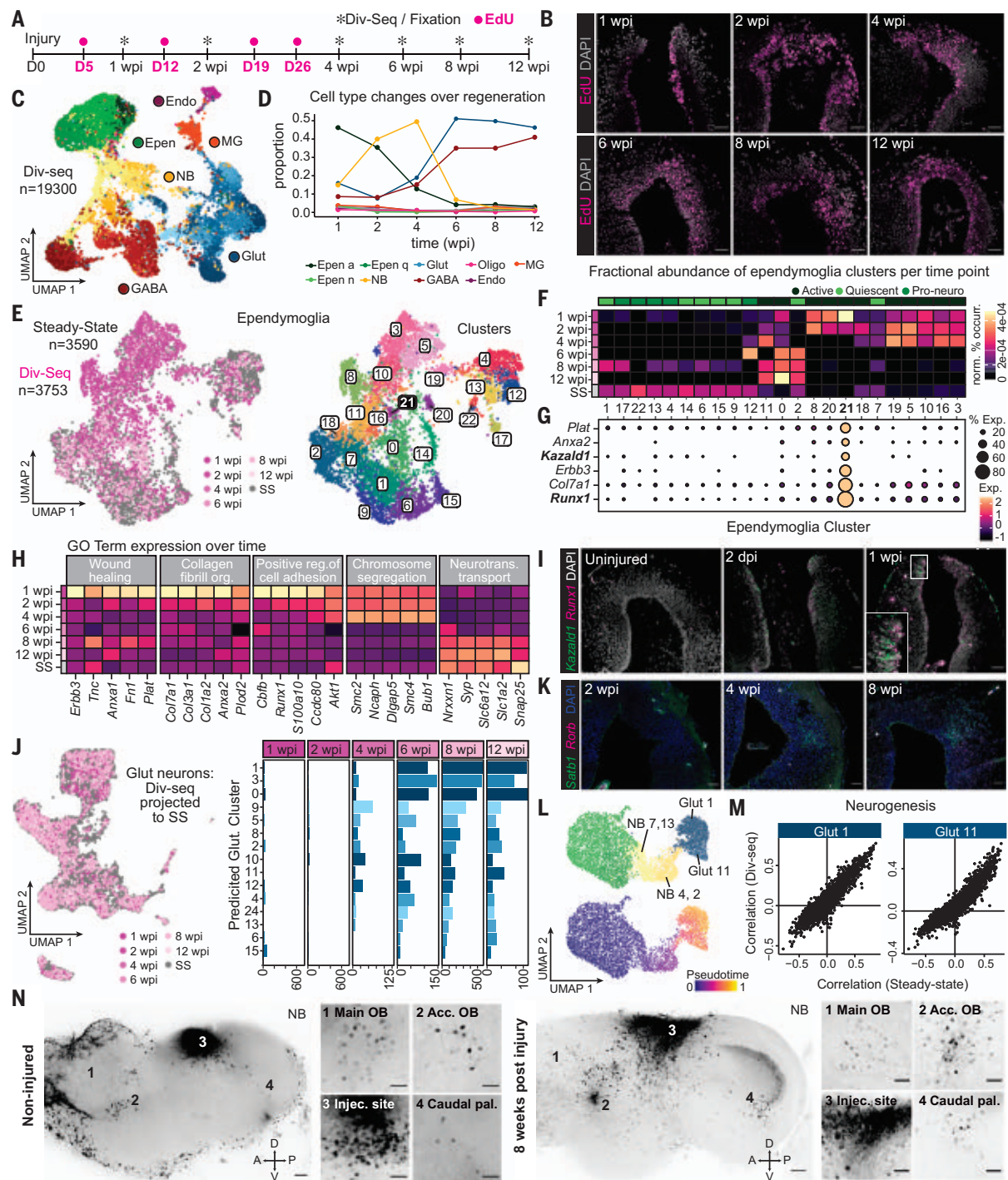


Fig. 6. Axolotl telencephalon regeneration after injury. (A) Schematic describing the Div-Seq protocol used during axolotl telencephalon regeneration. (B) EdU stainings of all regeneration time points. Scale bars, 50 μ m. (C) UMAP plot of all EdU+ cells across all regeneration time points, colored by cell-type class. Predicted cell clusters are shown in different shades. GABA, GABAergic neuron; Glut, Glutamatergic neuron; NB, neuroblast; Epen, ependymoglia cell; Endo, endothelial cell; and MGs, microglia. (D) Change in cell type relative abundance along regeneration time points. (E) (Left) UMAP plot of all Div-Seq ependymoglia (shades of pink indicate different time points) and noninjured brain steady-state (SS) ependymoglia (gray). (Right) UMAP plot of clustering of all ependymoglia. (F) Heatmap of normalized

cluster occurrence per time point. (G) Dotplot of selected ependymoglia cluster 21 differentially expressed genes. (H) Gene average expression change per time point, grouped by GO terms. (I) HCR for *Kazald1* and *Runx1* in steady state, 2 days post injury (dpi) and 1 week post injury (wpi). Scale bars, 50 μ m. (J) (Left) Correlation projection of all Div-Seq glutamatergic neurons (pink) to steady-state glutamatergic neurons (gray). (Right) Barplots of largest glutamatergic neuron clusters recovered throughout regeneration time points. (K) HCR for *Satb1* and *Rorb* throughout regeneration. Scale bars, 50 μ m. (L) Trajectories reflecting regenerative neurogenesis of glutamatergic neuron clusters 1 and 11. UMAPs are colored by (left) cell type and (right) pseudotime. (M) Correlations of lineage driver genes with the

assignment probability for (top) Glut1 and (bottom) Glut11 trajectories, in (y axis) regenerative and (x axis) steady-state neurogenesis. (N) Whole-mount cleared Neurobiotin stainings on (left) noninjured brains and (right) brains 8 weeks post injury. Neurobiotin was injected in the *Satb1*⁺, *Rorb*⁺

domain. (Insets) Labeled cell bodies in the olfactory bulb, accessory olfactory bulb, injection site, and caudal telencephalon. Scale bars, (overviews) 100 μ m; (zooms) 50 μ m. Main OB, main olfactory bulb; Acc. OB, accessory olfactory bulb; and caudal T., caudal telencephalon.

the regeneration site until tissue architecture was largely reestablished.

Next, we investigated the transcriptomes of EdU⁺ cells during the regeneration time course. We used our steady-state data as a reference and identified all major cell types, including ependymoglia, neuroblasts, glutamatergic and GABAergic neurons, as well as endothelial cells and microglia (Fig. 6C). Each cell type was represented in different proportions throughout regeneration (Fig. 6D and fig. S14C), reflecting a wave of neurogenesis induced by the injury. Whereas at 1 week post injury, active ependymoglia constituted the majority of EdU⁺ cells, neuroblasts were the most abundant cell type at 2 and 4 weeks post injury. Starting from 6 weeks post injury, most of the EdU⁺ cells were glutamatergic and GABAergic neurons. In line with the results from the Div-Seq data, HCR and antibody staining for ependymoglia (GFAP⁺, *Eps8l2*⁺, and *Sfrp1*⁺) and neuroblast (*Meis3a*⁺) populations demonstrated that ependymoglia were recovering radial morphology and regional identity, whereas neuroblasts were accumulating at the wound site between 2 and 4 weeks post injury (fig. S14, D and E). We next inferred regional identities of Div-Seq cells by transferring region labels from our steady-state data and found that early cell types (ependymoglia and neuroblasts) largely consisted of dorsal regional transcriptional identities. This predominance of dorsal-like cells was propagated to glutamatergic cells appearing in weeks 6 to 12, whereas GABAergic neuronal populations were dominated by a lateral identity (fig. S14, F to G). This data as well as EdU staining and comparison of EdU⁺ cells between uninjured and regenerating telencephalon (fig. S14H) suggests that our Div-Seq data largely captured cells in the acute injury area of the dorso-lateral pallium but likely also contains a minority of cells derived from homeostatic neurogenesis in areas not associated with the injury site.

Previous studies on axolotl spinal cord regeneration showed that injury-induced ependymoglia activate a transcriptional signature similar to that of embryonic neuroepithelial cells (33). To understand whether telencephalon injury induces injury-specific transcriptomic changes in ependymoglia, we compared Div-Seq and steady-state ependymoglia by integrating and clustering both datasets and assessing differential abundance and expression in each cluster across time points (Fig. 6E). We found three clusters (clusters 8, 20, and 21) strongly enriched at 1 and 2 weeks post injury that were rare or absent at later time points and steady

state (Fig. 6F). Cluster 21 cells differentially expressed genes such as *Kazal type serine peptidase inhibitor domain 1* (*Kazald1*) and *RUNX family transcription factor 1* (*Runx1*) and were enriched in Gene Ontology (GO) terms relating to wound healing and cell adhesion, indicating early response programs to injury (Fig. 6, F to H). Staining for *Kazald1* and *Runx1* confirmed absence of expression in the uninjured telencephalon and strong expression in a subpopulation of cells at 1 week post injury, with an induction of expression as early as 2 days post injury (Fig. 6I). Cluster 8 was enriched for *Lc27* and *Inositol polyphosphate-5-phosphatase* (*Inpp5d*), whereas cluster 21 was enriched for cilia-related genes, which could relate to reestablishment of the ependymoglia layer (table S6).

Projection and classification of Div-Seq neuroblasts and neurons based on steady-state data showed that a majority of steady-state populations had been reestablished during regeneration (Fig. 6J and fig. S14, C, I, and J). Among glutamatergic neurons, all but one steady-state cluster was captured in the Div-Seq data (fig. S14C), with the most expanded clusters predicted to be of dorso-medial origin (fig. S14, C, E, and F). HCR staining demonstrated the recovery of *Satb1*⁺, *Rorb*⁺ glutamatergic neurons between 4 and 8 weeks post injury (Fig. 6K). To explore the dynamics of regenerative glutamatergic neurogenesis, we first determined the correlation of regenerating neuroblasts to regenerating glutamatergic neurons and found a similar correlation pattern as that in homeostatic neurogenesis (fig. S15A). We then constructed trajectories and identified high similarity between regenerative and steady-state neurogenesis trajectories regarding pseudotemporal ordering of cells and correlation of lineage driver genes (Fig. 6, L and M, and fig. S15, B to G). Most TFs were similarly detected in regenerative and steady-state neurogenesis trajectories, with highly correlated timings and high centrality in trajectory-specific GRNs (fig. S16). Despite these similarities, some gene expression differences could also be observed with steady state-specific genes enriched in GO terms related to cell cycle and cell adhesion and regeneration-specific genes enriched in neurogenesis and neuronal activity (fig. S17). Part of the differential expression might have technical origins because of differences in transcriptomic coverage between the samples (fig. S14, A and B).

Last, we set out to determine whether the regenerated *Satb1*⁺, *Rorb*⁺ neuron domain would

reestablish afferent and efferent projections. We injected Neurobiotin into the *Satb1*⁺, *Rorb*⁺ domain in noninjured as well as regenerated brains at 8 weeks post injury and performed whole-mount immunohistochemistry to identify cell bodies and projections. Similarly to noninjured brains, stained cell bodies were located in the olfactory bulb, accessory olfactory bulb, and the caudal telencephalon (amygdala), indicating that the input from these regions is reestablished in the regenerated telencephalon at 8 weeks post injury (Fig. 6N).

Discussion

Using snRNA-seq, multiomic sequencing, and Div-Seq along with spatial transcriptomics, Cre-loxP tracing, HCR, and antibody staining, we have generated a comprehensive single-cell atlas of the axolotl telencephalon during homeostasis and regeneration. Comparative analysis with turtle and mouse datasets allowed us to reveal transcriptional similarities of axolotl telencephalon cell types and their conservation between tetrapods.

Axolotl glutamatergic neurons showed lower pairwise correlations between species compared with those of other cell populations, indicating their evolutionary diversification. Nonetheless, we found glutamatergic neurons similar to amniote hippocampus, turtle aDC, and olfactory cortex. Glut1 cells exhibited transcriptional similarities to the amniote olfactory cortex, and consistently, these neurons also showed olfactory bulb input, indicating a conserved role in olfactory processing. Addressing the functional properties and input-output connectivity will be critical to gain a better understanding of conservation. Our multiomic sequencing analysis has revealed differentially accessible regions in Glut1, which could be used in the future to achieve targeted expression of connectivity and optogenetic and chemogenetic tools.

We identified LGE-like, CGE-like, MGE-like, and septal GABAergic neurons in the axolotl and found conservation of LGE-like striatal and olfactory bulb classes between axolotl and other tetrapods. The LGE and MGE have been found in all studied vertebrates—including anamniotes such as lamprey, fish, and amphibians (34–36)—but the existence of the CGE in anamniotes is unclear. Our identification of putative CGE-derived neurons in this work hints at the existence of a CGE in axolotl. GABAergic neuron migration has not been studied in salamanders, and it will be important to determine the developmental origin and timing of GABAergic neurogenesis in

the putative ganglionic eminences. In axolotl, GABAergic neurogenesis likely continues in the postembryonic brain because we detected GABA⁺ neuroblasts and found one cluster (NB 5) that contains cells from medial and dorsal pallium, which suggests local pallial GABAergic neurogenesis, a phenomenon observed in the developing primate brain (37).

We found that axolotl ependymoglia show transcriptomic signatures of both mouse SVZ ependymal cells and B cells and function as stem cells during homeostatic neurogenesis. Postembryonic ependymoglia in different pallial regions maintained expression of developmental patterning genes thought to regulate dorsal and ventral pallial subdomain size during development in amniotes (23). It is possible that expression of these factors maintains pallial domain proportions during continuous neurogenesis. The mammalian SVZ also contains IPs and migratory neuroblasts that express GABAergic or glutamatergic fate markers (38, 39). The axolotl contains different types of neuroblasts: early, potentially proliferating neuroblasts with high transcriptional similarity to mammalian IPs, and late VGLUT⁺ or GABA⁺ neuroblasts with transcriptional similarities to mammalian neuroblasts. The majority of axolotl VGLUT⁺ neuroblasts could be subdivided depending on their similarity to different glutamatergic neurons, implicating lineage restriction that should be investigated in the future by using genetic barcoding (40).

In contrast to mammalian glial cells, salamander ependymoglia show neurogenic activity after injury. We found that axolotl ependymoglia go through an injury-specific transcriptional state defined by the up-regulation of genes involved in wound healing and cell migration. The early up-regulated gene *Runx1* is also expressed in the mesenchymal limb blastema of axolotl and *X. laevis* (41, 42) and planarian neoblasts after amputation (43), suggesting its involvement in a generic injury response regardless of cell type and species. Apart from the early wound response, regenerative neurogenesis is very similar to homeostatic neurogenesis. We found that *Satb1*⁺/*Rorb*⁺ glutamatergic neurons regenerate after injury and reestablish input connectivity from the olfactory bulb. The conservation of transcriptional profiles, connectivity, and potential function of these neurons makes them suited to study recovery of functional neuronal circuits.

Methods summary

Animal use

White (d/d) axolotls were used for all experiments. Animals of a size of 10 to 11 cm nose to tail were used for all sequencing experiments. All lines were bred and maintained in Research Institute of Molecular Pathology (IMP)

facilities, and each animal is kept individually. All handling and surgical procedures were carried out in accordance with the local ethics committee guidelines. Animal experiments were performed as approved by the Magistrat of Vienna (Genetically Modified Organism Office and MA58, City of Vienna, Austria, license GZ51072/2019/16 and license GZ665226/2019/21).

snRNA-seq library preparation and sequencing

We used snRNA-seq (10x Genomics) to profile medial, dorsal, and lateral regions of the telencephalon. We additionally profiled all these regions as a whole with single-nucleus multiome sequencing (10x Genomics). Libraries were sequenced and then aligned to the axolotl genome.

Data integration and clustering

Datasets from each chemistry were integrated by using harmony integration. Identification of major cell types followed an iterative clustering approach by using the Louvain algorithm. Identities of the clusters were assigned on the basis of the expression of established marker genes. For each major cell type (glutamatergic neurons, GABAergic neurons, ependymoglia, and neuroblasts), the clustering procedure repeated.

Comparison with turtle and mouse datasets

Four single-cell datasets were downloaded for interspecies comparison: mouse brain, mouse development, mouse SVZ, and turtle forebrain. We used two approaches to compare the expression profiles cells between species: (i) pairwise correlations between clusters by using all differentially expressed genes or differentially expressed TFs and (ii) integration of single-cell and single-nuclei datasets.

Region-specific neurogenesis (pseudotime analysis)

Glutamatergic NB progenitors were associated with their corresponding differentiated populations through correlation. For each of the five groups determined, a pseudotemporal trajectory based on RNA velocity was inferred by use of scVelo and CellRank. The resulting trajectories were used to determine lineage driver genes, and gene expression was modeled by using a spline with five degrees of freedom.

GRN construction

The R package Pando was used to infer a GRN from multiome data of cells from all glutamatergic trajectories. To select candidate regions, peaks were linked to genes according to correlation with a distance threshold of 10 megabase. Vertebrate motif annotations were obtained from JASPAR2020. Modules were identified with a significance threshold of false discovery rate (FDR) < 0.05.

Brain regeneration with Div-Seq

Axolotls were injected intraperitoneally with EdU. After the desired pulse-chase period, nuclei were isolated, EdU staining was performed immediately by using Click-iT EdU Flow Cytometry assay Kit (Thermo Fisher Scientific, #C10424), and EdU⁺ nuclei were sorted by means of fluorescence-activated cell sorting (FACS). Nuclei from the Div-Seq dataset were classified into cell types, clusters, and brain regions by using the steady-state data as a reference. Subsequently, ependymoglia were subset from the steady-state and Div-Seq datasets and integrated by using harmony, with the library chemistry as a covariate. Neurogenesis trajectories in regeneration were inferred similarly to steady-state trajectories. Control and regenerated brains were injected with neuronal tracer Neurobiotin, whole-mount stained, and cleared to determine projection patterns.

REFERENCES AND NOTES

1. B. M. Colquitt, D. P. Merullo, G. Konopka, T. F. Roberts, M. S. Brainard, Cellular transcriptomics reveals evolutionary identities of songbird vocal circuits. *Science* **371**, eabd9704 (2021). doi: [10.1126/science.abd9704](https://doi.org/10.1126/science.abd9704); pmid: [33574185](https://pubmed.ncbi.nlm.nih.gov/33574185/)
2. M. A. Tosches et al., Evolution of pallium, hippocampus, and cortical cell types revealed by single-cell transcriptomics in reptiles. *Science* **360**, 881–888 (2018). doi: [10.1126/science.aar4237](https://doi.org/10.1126/science.aar4237); pmid: [29724907](https://pubmed.ncbi.nlm.nih.gov/29724907/)
3. A. Zeisel et al., Molecular architecture of the mouse nervous system. *Cell* **174**, 999–1014.e22 (2018). doi: [10.1016/j.cell.2018.06.021](https://doi.org/10.1016/j.cell.2018.06.021); pmid: [30096314](https://pubmed.ncbi.nlm.nih.gov/30096314/)
4. R. D. Hodge et al., Conserved cell types with divergent features in human versus mouse cortex. *Nature* **573**, 61–68 (2019). doi: [10.1038/s41586-019-1506-7](https://doi.org/10.1038/s41586-019-1506-7); pmid: [31435019](https://pubmed.ncbi.nlm.nih.gov/31435019/)
5. R. Amamoto et al., Adult axolotls can regenerate original neuronal diversity in response to brain injury. *eLife* **5**, el3998 (2016). doi: [10.7554/eLife.13998](https://doi.org/10.7554/eLife.13998); pmid: [27156560](https://pubmed.ncbi.nlm.nih.gov/27156560/)
6. M. Maden, L. A. Marwell, B. K. Ormerod, Proliferation zones in the axolotl brain and regeneration of the telencephalon. *Neural Dev.* **8**, 1 (2013). doi: [10.1186/1749-8104-8-1](https://doi.org/10.1186/1749-8104-8-1); pmid: [23327114](https://pubmed.ncbi.nlm.nih.gov/23327114/)
7. F. Doetsch, J. M. Garcia-Verdugo, A. Alvarez-Buylla, Cellular composition and three-dimensional organization of the subventricular germinal zone in the adult mammalian brain. *J. Neurosci.* **17**, 5046–5061 (1997). doi: [10.1523/JNEUROSCI.17-13-05046.1997](https://doi.org/10.1523/JNEUROSCI.17-13-05046.1997); pmid: [9185542](https://pubmed.ncbi.nlm.nih.gov/9185542/)
8. J. Kaslin, J. Ganz, M. Brand, Proliferation, neurogenesis and regeneration in the non-mammalian vertebrate brain. *Philos. Trans. R. Soc. Lond. B Biol. Sci.* **363**, 101–122 (2008). doi: [10.1098/rstb.2006.2015](https://doi.org/10.1098/rstb.2006.2015); pmid: [17282988](https://pubmed.ncbi.nlm.nih.gov/17282988/)
9. V. Hartenstein, A. Stollenwerk, The evolution of early neurogenesis. *Dev. Cell* **32**, 390–407 (2015). doi: [10.1016/j.devcel.2015.02.004](https://doi.org/10.1016/j.devcel.2015.02.004); pmid: [25710527](https://pubmed.ncbi.nlm.nih.gov/25710527/)
10. M. Faiz et al., Adult neural stem cells from the subventricular zone give rise to reactive astrocytes in the cortex after stroke. *Cell Stem Cell* **17**, 624–634 (2015). doi: [10.1016/j.stem.2015.08.002](https://doi.org/10.1016/j.stem.2015.08.002); pmid: [26456685](https://pubmed.ncbi.nlm.nih.gov/26456685/)
11. A. Arvidsson, T. Collin, D. Kirik, Z. Kokaia, O. Lindvall, Neuronal replacement from endogenous precursors in the adult brain after stroke. *Nat. Med.* **8**, 963–970 (2002). doi: [10.1038/nm747](https://doi.org/10.1038/nm747); pmid: [12161747](https://pubmed.ncbi.nlm.nih.gov/12161747/)
12. G. Roth, G. Westhoff, Cytoarchitecture and connectivity of the amphibian medial pallium. *Eur. J. Morphol.* **37**, 166–171 (1999). doi: [10.1076/0167-2166\(4759](https://doi.org/10.1076/0167-2166(4759); pmid: [10342450](https://pubmed.ncbi.nlm.nih.gov/10342450/)
13. M. I. Sotelo, M. F. Daneri, V. P. Bingman, R. N. Muzio, Telencephalic neuronal activation associated with spatial memory in the terrestrial toad *Rhinella arenarum*: Participation of the medial pallium during navigation by geometry. *Brain Behav. Evol.* **88**, 149–160 (2016). doi: [10.1159/000447441](https://doi.org/10.1159/000447441); pmid: [27889766](https://pubmed.ncbi.nlm.nih.gov/27889766/)
14. E. Zhao et al., Spatial transcriptomics at subspot resolution with BayesSpace. *Nat. Biotechnol.* **39**, 1375–1384 (2021). doi: [10.1038/s41587-021-00935-2](https://doi.org/10.1038/s41587-021-00935-2); pmid: [34083791](https://pubmed.ncbi.nlm.nih.gov/34083791/)

15. A. Joven *et al.*, Cellular basis of brain maturation and acquisition of complex behaviors in salamanders. *Development* **145**, dev.160051 (2018). doi: [10.1242/dev.160051](https://doi.org/10.1242/dev.160051); pmid: 29217751
16. P. S. Ulinski, W. T. Rainey, Intrinsic organization of snake lateral cortex. *J. Morphol.* **165**, 85–116 (1980). doi: [10.1002/jmor.1051650108](https://doi.org/10.1002/jmor.1051650108); pmid: 30180381
17. A. Diodato *et al.*, Molecular signatures of neural connectivity in the olfactory cortex. *Nat. Commun.* **7**, 12238 (2016). doi: [10.1038/ncomms12238](https://doi.org/10.1038/ncomms12238); pmid: 27426965
18. D. M. G. Johnson, K. R. Illig, M. Behan, L. B. Haberly, New features of connectivity in piriform cortex visualized by intracellular injection of pyramidal cells suggest that “primary” olfactory cortex functions like “association” cortex in other sensory systems. *J. Neurosci.* **20**, 6974–6982 (2000). doi: [10.1523/JNEUROSCI.20-18-06974.2000](https://doi.org/10.1523/JNEUROSCI.20-18-06974.2000); pmid: 10995842
19. N. Moreno, A. González, Evolution of the amygdaloid complex in vertebrates, with special reference to the anamniotic transition. *J. Anat.* **211**, 151–163 (2007). doi: [10.1111/j.1469-7580.2007.00780.x](https://doi.org/10.1111/j.1469-7580.2007.00780.x); pmid: 17634058
20. O. Marin, J. L. Rubenstein, A long, remarkable journey: Tangential migration in the telencephalon. *Nat. Rev. Neurosci.* **2**, 780–790 (2001). doi: [10.1038/35097509](https://doi.org/10.1038/35097509); pmid: 11715055
21. Z. Almási, C. Dávid, M. Witte, J. F. Staiger, Distribution patterns of three molecularly defined classes of GABAergic neurons across columnar compartments in mouse barrel cortex. *Front. Neuroanat.* **13**, 45 (2019). doi: [10.3389/fnana.2019.00045](https://doi.org/10.3389/fnana.2019.00045); pmid: 31114486
22. M. Kirkham, L. S. Hameed, D. A. Berg, H. Wang, A. Simon, Progenitor cell dynamics in the Newt Telencephalon during homeostasis and neuronal regeneration. *Stem Cell Reports* **2**, 507–519 (2014). doi: [10.1016/j.stemcr.2014.01.018](https://doi.org/10.1016/j.stemcr.2014.01.018); pmid: 24749074
23. F. García-Moreno, Z. Molnár, Variations of telencephalic development that paved the way for neocortical evolution. *Prog. Neurobiol.* **194**, 101865 (2020). doi: [10.1016/j.pneurobio.2020.101865](https://doi.org/10.1016/j.pneurobio.2020.101865); pmid: 32526253
24. V. Naef *et al.*, The stemness gene Mex3A is a key regulator of neuroblast proliferation during neurogenesis. *Front. Cell Dev. Biol.* **8**, 549533 (2020). doi: [10.3389/fcell.2020.549533](https://doi.org/10.3389/fcell.2020.549533); pmid: 33072742
25. A. Cebrían-Silla *et al.*, Single-cell analysis of the ventricular-subventricular zone reveals signatures of dorsal and ventral adult neurogenesis. *eLife* **10**, e67436 (2021). doi: [10.7554/eLife.67436](https://doi.org/10.7554/eLife.67436); pmid: 34259628
26. D. J. Di Bella *et al.*, Molecular logic of cellular diversification in the mouse cerebral cortex. *Nature* **595**, 554–559 (2021). doi: [10.1038/s41586-021-03670-5](https://doi.org/10.1038/s41586-021-03670-5); pmid: 34163074
27. G. Furlan *et al.*, Life-long neurogenic activity of individual neural stem cells and continuous growth establish an outside-in architecture in the teleost pallium. *Curr. Biol.* **27**, 3288–3301.e3 (2017). doi: [10.1016/j.cub.2017.09.052](https://doi.org/10.1016/j.cub.2017.09.052); pmid: 29107546
28. V. Bergen, M. Lange, S. Peidli, F. A. Wolf, F. J. Theis, Generalizing RNA velocity to transient cell states through dynamical modeling. *Nat. Biotechnol.* **38**, 1408–1414 (2020). doi: [10.1038/s41587-020-0591-3](https://doi.org/10.1038/s41587-020-0591-3); pmid: 32747759
29. M. Lange *et al.*, CellRank for directed single-cell fate mapping. *Nat. Methods* **19**, 159–170 (2020).
30. J. A. Farrell *et al.*, Single-cell reconstruction of developmental trajectories during zebrafish embryogenesis. *Science* **360**, eaar3131 (2018). doi: [10.1126/science.aar3131](https://doi.org/10.1126/science.aar3131); pmid: 29700225
31. J. S. Fleck *et al.*, Inferring and perturbing cell fate regulomes in human cerebral organoids. *bioRxiv* 457460 [Preprint] (2021). doi: [10.1101/2021.08.24.457460](https://doi.org/10.1101/2021.08.24.457460)
32. N. Habib *et al.*, Div-Seq: Single-nucleus RNA-seq reveals dynamics of rare adult newborn neurons. *Science* **353**, 925–928 (2016). doi: [10.1126/science.aad7038](https://doi.org/10.1126/science.aad7038); pmid: 27471252
33. A. Rodrigo Albers *et al.*, Planar cell polarity-mediated induction of neural stem cell expansion during axolotl spinal cord regeneration. *eLife* **4**, e10230 (2015). doi: [10.7554/eLife.10230](https://doi.org/10.7554/eLife.10230); pmid: 26568310
34. F. Sugahara *et al.*, Evidence from cyclostomes for complex regionalization of the ancestral vertebrate brain. *Nature* **531**, 97–100 (2016). doi: [10.1038/nature16518](https://doi.org/10.1038/nature16518); pmid: 26878236
35. I. Carrera, S. Ferreiro-Galve, C. Sueiro, R. Anadón, I. Rodríguez-Moldes, Tangentially migrating GABAergic cells of subpallial origin invade massively the pallium in developing sharks. *Brain Res. Bull.* **75**, 405–409 (2008). doi: [10.1016/j.brainresbull.2007.10.013](https://doi.org/10.1016/j.brainresbull.2007.10.013); pmid: 18331906
36. I. Bachy, J. Berthon, S. Rétaux, Defining pallial and subpallial divisions in the developing *Xenopus* forebrain. *Mech. Dev.* **117**, 163–172 (2002). doi: [10.1016/S0925-4773\(02\)00199-5](https://doi.org/10.1016/S0925-4773(02)00199-5); pmid: 12204256
37. Z. Petanjek, B. Berger, M. Esclapez, Origins of cortical GABAergic neurons in the cynomolgus monkey. *Cereb. Cortex* **19**, 249–262 (2009). doi: [10.1093/cercor/bhn078](https://doi.org/10.1093/cercor/bhn078); pmid: 18477686
38. M. S. Brill *et al.*, A *dlx2*- and *pax6*-dependent transcriptional code for periglomerular neuron specification in the adult olfactory bulb. *J. Neurosci.* **28**, 6439–6452 (2008). doi: [10.1523/JNEUROSCI.0700-08.2008](https://doi.org/10.1523/JNEUROSCI.0700-08.2008); pmid: 18562615
39. M. S. Brill *et al.*, Adult generation of glutamatergic olfactory bulb interneurons. *Nat. Neurosci.* **12**, 1524–1533 (2009). doi: [10.1038/nn.2416](https://doi.org/10.1038/nn.2416); pmid: 19881504
40. R. C. Bandler *et al.*, Single-cell delineation of lineage and genetic identity in the mouse brain. *Nature* **601**, 404–409 (2022). doi: [10.1038/s41586-021-04237-0](https://doi.org/10.1038/s41586-021-04237-0); pmid: 34912118
41. T.-Y. Lin *et al.*, Fibroblast dedifferentiation as a determinant of successful regeneration. *Dev. Cell* **56**, 1541–1551.e6 (2021). doi: [10.1016/j.devcel.2021.04.016](https://doi.org/10.1016/j.devcel.2021.04.016); pmid: 34004152
42. T. Gerber *et al.*, Single-cell analysis uncovers convergence of cell identities during axolotl limb regeneration. *Science* **362**, eaaq0681 (2018). doi: [10.1126/science.aaq0681](https://doi.org/10.1126/science.aaq0681); pmid: 30262634
43. D. Wenemoser, S. W. Lapan, A. W. Wilkinson, G. W. Bell, P. W. Reddien, A molecular wound response program associated with regeneration initiation in planarians. *Genes Dev.* **26**, 988–1002 (2012). doi: [10.1101/gad.187377.112](https://doi.org/10.1101/gad.187377.112); pmid: 22549959
44. A. Maynard, tomasgomes/pallium_evo: Post-revision 1 release. Zenodo (2022); doi: [10.5281/zenodo.6627781](https://doi.org/10.5281/zenodo.6627781)
45. K. Lust *et al.*, Single-cell analyses of axolotl forebrain organization, neurogenesis, and regeneration. Zenodo (2022); doi: [10.5281/zenodo.6390083](https://doi.org/10.5281/zenodo.6390083)

ACKNOWLEDGMENTS

We thank the Treutlein, Camp, and Tanaka laboratories for their discussions, input, and support. FACS support was provided by the single-cell facility at D-BSSE, ETH Zurich. Illumina sequencing was done in the Genomics Facility at D-BSSE, ETH Zurich. We thank the IMP Bio-Optics facility and the animal caretaker team (Vienna Biocenter) for outstanding service. **Funding:** This work was supported by a Long-Term Fellowship from the Human Frontier Science Program LT000605/2018-L (K.L.); EMBO Long-Term Fellowship ALTF 738-2019 (T.G.); European Research Council RegGeneMems 742046 (E.M.T.); Special research program of the Austrian Science Fund project F78 (E.M.T.); European Research Council Organomics 758877 (A.M. and B.T.); European Research Council Braintime 874606 (B.T.); and Swiss National Science Foundation Project Grant 310030_192604 (B.T.). **Author contributions:** Designed study: K.L., A.M., T.G., E.M.T., and B.T. Prepared and collected the samples and performed lineage tracing and staining: K.L. Performed single-nuclei experiments: A.M. Analyzed the sequencing data: T.G., A.M., and J.S.F. Prepared the figures and wrote and approved the manuscript: K.L., A.M., T.G., J.S.F., J.G.C., E.M.T., and B.T. **Competing interests:** The authors declare that they have no competing interests. **Data and materials availability:** Code is available at Github (https://github.com/tomasgomes/pallium_evo) (44). Count tables are deposited at (45). Fastq files have been deposited in ArrayExpress under accession nos. E-MTAB-11638, E-MTAB-11662, E-MTAB-11665, and E-MTAB-11666. All other data are in the main paper or supplementary materials. **License information:** Copyright © 2022 the authors, some rights reserved; exclusive licensee American Association for the Advancement of Science. No claim to original US government works. <https://www.science.org/about/science-licenses-journal-article-reuse>

SUPPLEMENTARY MATERIALS

science.org/doi/10.1126/science.abp9262
Materials and Methods
Figs. S1 to S17
Tables S1 to S7
References (46–71)
MDAR Reproducibility Checklist

Submitted 7 March 2022; accepted 29 June 2022
10.1126/science.abp9262

RESEARCH ARTICLE SUMMARY

NEUROEVOLUTION

Single-cell Stereo-seq reveals induced progenitor cells involved in axolotl brain regeneration

Xiaoyu Wei[†], Sulei Fu[†], Hanbo Li^{*†}, Yang Liu[†], Shuai Wang[†], Weimin Feng[†], Yunzhi Yang[†], Xiawei Liu, Yan-Yun Zeng, Mengnan Cheng, Yiwei Lai, Xiaojie Qiu, Liang Wu, Nannan Zhang, Yujia Jiang, Jiangshan Xu, Xiaoshan Su, Cheng Peng, Lei Han, Wilson Pak-Kin Lou, Chuanyu Liu, Yue Yuan, Kailong Ma, Tao Yang, Xiangyu Pan, Shang Gao, Ao Chen, Miguel A. Esteban, Huanming Yang, Jian Wang, Guangyi Fan, Longqi Liu, Liang Chen^{*}, Xun Xu^{*}, Ji-Feng Fei^{*}, Ying Gu^{*}

INTRODUCTION: Brain regeneration requires the coordination of complex responses in a time- and region-specific manner. Identifying the cell types and molecules involved in this process would advance our understanding of brain regeneration and provide potential targets for regenerative medicine research. However, progress in this field has been hampered by the limited regeneration capacity of the mammalian brain and an incomplete mechanistic understanding of the regeneration process at both the cellular and molecular levels. Axolotls (*Ambystoma mexicanum*) can regenerate damaged appendages and multiple internal organs, including the brain. Therefore, axolotls may serve as a model for studying brain regeneration.

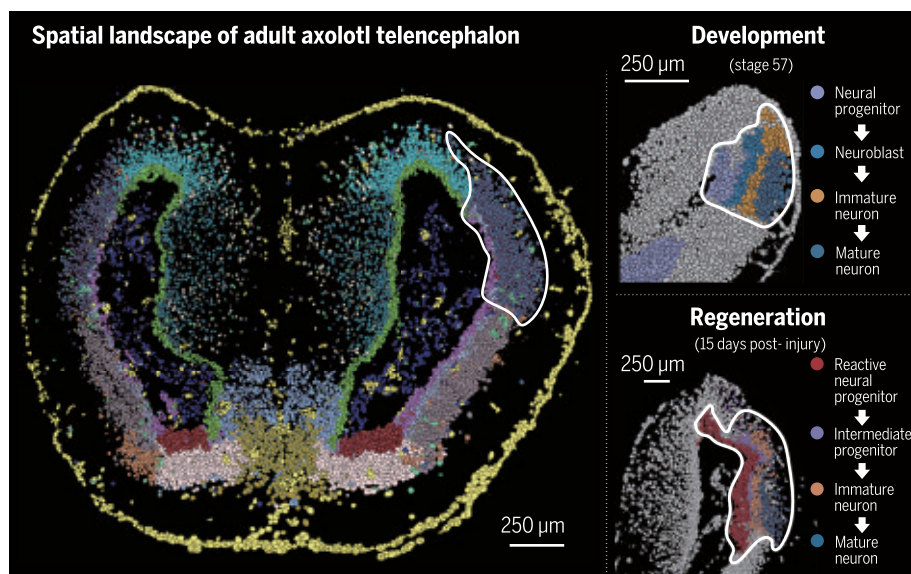
RATIONALE: If we are to understand the mechanism of brain regeneration, we need research tools that can achieve large-scale data acquisition

and analyses to simultaneously decode complex cellular and molecular responses. It also seemed to us that a comparison between brain regeneration and developmental processes would help to provide new insights into the nature of brain regeneration. Accordingly, we removed a small portion of the lateral pallium region of the axolotl left telencephalon and collected tissue samples at multiple stages during regeneration. In parallel, we collected tissue samples of the axolotl telencephalon at multiple developmental stages. We then used high-definition and large-field Stereo-seq (spatial enhanced resolution omics sequencing) technology to generate spatial transcriptomic data from sections that covered both hemispheres of the axolotl telencephalon at single-cell resolution. Analyses of cell type annotation, cell spatial organization, gene activity dynamics, and cell state transition were performed for a mechanistic investigation of injury-induced

regeneration compared to these cell attributes during development.

RESULTS: With the use of Stereo-seq, we generated a group of spatial transcriptomic data of telencephalon sections that covered six developmental and seven injury-induced regenerative stages. The data at single-cell resolution enabled us to identify 33 cell types present during development and 28 cell types involved in regeneration, including different types of excitatory and inhibitory neurons, and several ependymoglia cell subtypes. For development, our data revealed a primitive type of ependymoglia cells that may give rise to three subgroups of adult ependymoglia cells localized in separate areas of the ventricular zone, with different molecular features and potentially different functions. For regeneration, we discovered a subpopulation of ependymoglia cells that may originate from local resident ependymoglia cells activated by injury. This population of progenitor cells may then proliferate to cover the wound area and subsequently replenish lost neurons through a state transition to intermediate progenitors, immature neurons, and eventually mature neurons. When comparing cellular and molecular dynamics of the axolotl telencephalon between development and regeneration, we found that injury-induced ependymoglia cells were similar to developmental-specific ependymoglia cells in terms of their transcriptome state. We also observed that regeneration of the axolotl telencephalon exhibited neurogenesis patterns similar to those seen in development in molecular cascades and the potential cell lineage transition, which suggests that brain regeneration partially recapitulates the development process.

CONCLUSION: Our spatial transcriptomic data highlight the cellular and molecular features of the axolotl telencephalon during development and injury-induced regeneration. Further characterization of the activation and functional regulation of ependymoglia cells may yield insights for improving the regenerative capability of mammalian brains. Our single-cell spatial transcriptome of the axolotl telencephalon, a tetrapod vertebrate, also provides data useful for further research in developmental, regenerative, and evolutionary brain biology. All data are accessible in an interactive database (<https://db.cngb.org/stomics/artista>). ■



Development and regeneration of axolotl telencephalon. The spatially resolved single-cell transcriptome of the adult axolotl telencephalon as determined by Stereo-seq analyses (left). Upon brain injury in the highlighted lateral pallium region of the left hemisphere, a neural progenitor subpopulation at the wound site was rapidly induced and subsequently replenished lost neurons (bottom right) through a process that partially resembles neurogenesis during development (top right).

The list of author affiliations is available in the full article online.

*Corresponding author. Email: guying@genomics.cn (Y.G.); jifengfei@gdph.org.cn (J.-F.F.); xuxun@genomics.cn (X.X.); liang_chen@whu.edu.cn (L.C.); lihanbo@genomics.cn (H.L.)

[†]These authors contributed equally to this work.

Cite this article as X. Wei et al., *Science* 377, eabp9444 (2022). DOI: 10.1126/science.abp9444

READ THE FULL ARTICLE AT
<https://doi.org/10.1126/science.abp9444>

RESEARCH ARTICLE

NEUROEVOLUTION

Single-cell Stereo-seq reveals induced progenitor cells involved in axolotl brain regeneration

Xiaoyu Wei^{1,2,†}, Sulei Fu^{3,4,†}, Hanbo Li^{2,5,6,*}, Yang Liu^{2,†}, Shuai Wang^{2,7,†}, Weimin Feng^{2,7,†}, Yunzhi Yang^{8,†}, Xiawei Liu⁵, Yan-Yun Zeng^{3,4}, Mengnan Cheng^{2,7}, Yiwei Lai⁹, Xiaojie Qiu^{10,11}, Liang Wu^{2,7}, Nannan Zhang⁵, Yujia Jiang^{2,8}, Jiangshan Xu^{2,7}, Xiaoshan Su⁵, Cheng Peng^{3,4}, Lei Han^{2,12,13}, Wilson Pak-Kin Lou^{3,4}, Chuanyu Liu^{2,13}, Yue Yuan^{2,7}, Kailong Ma², Tao Yang², Xiangyu Pan³, Shang Gao⁵, Ao Chen^{2,14}, Miguel A. Esteban^{9,15}, Huanming Yang^{2,16}, Jian Wang^{2,16}, Guangyi Fan², Longqi Liu^{1,2,7,13}, Liang Chen^{17,*}, Xun Xu^{2,18,*}, Ji-Feng Fei^{3,*}, Ying Gu^{1,2,7,18,*}

The molecular mechanism underlying brain regeneration in vertebrates remains elusive. We performed spatial enhanced resolution omics sequencing (Stereo-seq) to capture spatially resolved single-cell transcriptomes of axolotl telencephalon sections during development and regeneration. Annotated cell types exhibited distinct spatial distribution, molecular features, and functions. We identified an injury-induced ependymogial cell cluster at the wound site as a progenitor cell population for the potential replenishment of lost neurons, through a cell state transition process resembling neurogenesis during development. Transcriptome comparisons indicated that these induced cells may originate from local resident ependymogial cells. We further uncovered spatially defined neurons at the lesion site that may regress to an immature neuron-like state. Our work establishes spatial transcriptome profiles of an amniote tetrapod brain and decodes potential neurogenesis from ependymogial cells for development and regeneration, thus providing mechanistic insights into vertebrate brain regeneration.

Mammals face challenges in recovering from brain injury because of their limited regeneration capability (1). In contrast, lower vertebrates, such as teleost fish and salamanders, exhibit regenerative power (2–7). Forebrain regeneration in

axolotls was first observed in larvae (8) and later in adults (4, 9). Lost cortical cell types in the axolotl telencephalon could apparently be restored upon injury (9). Therefore, axolotls may serve as a model for studying brain regeneration, possibly leading to discoveries that could be valuable for understanding the inherent limitations of brain regeneration in mammals and, ultimately, developing regenerative medicine for the central nervous system.

Previous studies in various regenerative species have shown that ependymogial cells (EGCs), equivalent to neural stem cells in mammals, contribute to neurogenesis during brain regeneration (3, 10, 11). Salamander EGCs may give rise to nearly all cell types in the brain during development (12). Unlike mammals, in which neural stem cells are almost consumed once brain development is complete, except those in the subventricular zone and hippocampal dentate gyrus, the adult salamander contains dividing EGCs in the brain (1, 13). EGCs are distributed in the entire ventricular zone (VZ) of adult axolotl brains, as well as in a few confined regions of the VZ in red spotted newts (10). It has been reported that red spotted newts harbor two groups of EGCs: slow-dividing and transient amplifying EGCs (10). The first group is stem cell-like, expressing glial fibrillary acidic protein (GFAP) and glutamine synthetase (3, 14) and showing the stem cell property of long-term 5-bromo-2'-deoxyuridine (BrdU) retention. The second group is located within the proliferative hot spots of the VZ and frequently divides (10). Both EGC groups

can react to injury and can expand to larger areas in the pallium (4, 10).

So far, the role and regulation of EGCs in regeneration have only been partially characterized. A few signaling pathways in EGC activation and brain regeneration have been documented in salamanders and fish, such as Notch, FGF, and Gata3 (10, 15, 16); these are also involved in brain development, indicating that brain regeneration and development may possess similar molecular regulations. However, it remains unknown whether and to what extent brain regeneration recapitulates embryonic development. Therefore, a more systematic characterization of cellular and molecular functions is needed that substantiates the mechanistic understanding of brain regeneration.

Several spatial transcriptomic technologies suitable for dissecting the development and tissue regeneration processes have been developed to resolve gene expression profiles of cells in situ (17). By these approaches, the in situ transcriptome profiles of mouse brain or human cortex have been resolved at resolutions of 100 and 55 μm , respectively, which reflect the average expression profiles of a group of neighboring cells (18, 19). Considering the complexity of brain structures and cell types, improved resolution of transcript capturing is needed to enhance the accuracy of data interpretation. Sequential fluorescence in situ hybridization (FISH) and multiplexed error-robust FISH were developed to profile gene expression in single cells, but their application is limited by low throughput and the requirement for special equipment (20, 21).

Using spatial enhanced resolution omics sequencing (Stereo-seq) (22), we determined spatially resolved single-cell transcriptomes of axolotl telencephalon sections at a series of developmental and regeneration stages. These data enabled us to identify cell types, including EGC subtypes involved in development and regeneration. Further analyses showed that developmental and regenerative neurogenesis shared similarities in cell lineage dynamics from EGCs to mature neurons and related molecular signatures. We also observed a wound-stimulated cell cluster adjacent to EGCs with neuronal regression features. Taken together, our work provides an overview of the cellular dynamics during axolotl brain development and regeneration, the datasets from which may yield insights into the molecular regulation of brain regeneration.

Stereo-seq profiles spatial transcriptomes of axolotl telencephalons

Considering the average size of axolotl cells, we prepared cryosections of the adult axolotl telencephalon at 20- μm thickness to capture roughly a single-cell layer of tissue for Stereo-seq analysis on the entire section (Fig. 1A)

¹BGI-Hangzhou, Hangzhou 310012, China. ²BGI-Shenzhen, Shenzhen 518103, China. ³Department of Pathology, Guangdong Provincial People's Hospital, Guangdong Academy of Medical Sciences, Guangzhou 510080, China.

⁴Key Laboratory of Brain, Cognition and Education Sciences, Ministry of Education, Institute for Brain Research and Rehabilitation, South China Normal University, Guangzhou 510631, China. ⁵BGI-Qingdao, Qingdao 266555, China. ⁶Lars Bolund Institute of Regenerative Medicine, Qingdao-Europe Advanced Institute for Life Sciences, BGI-Qingdao, Qingdao 266555, China. ⁷College of Life Sciences, University of Chinese Academy of Sciences, Beijing 100049, China. ⁸BGI College & Henan Institute of Medical and Pharmaceutical Sciences, Zhengzhou University, Zhengzhou 450000, China.

⁹Laboratory of Integrative Biology, Guangzhou Institutes of Biomedicine and Health, Chinese Academy of Sciences, Guangzhou 510530, China. ¹⁰Whitehead Institute for Biomedical Research, Cambridge, MA 02142, USA. ¹¹Howard Hughes Medical Institute, Massachusetts Institute of Technology, Cambridge, MA 02139, USA. ¹²Shenzhen Key Laboratory of Single-Cell Omics, BGI-Shenzhen, Shenzhen 518120, China. ¹³Shenzhen Bay Laboratory, Shenzhen 518000, China. ¹⁴Department of Biology, University of Copenhagen, Copenhagen DK-2200, Denmark. ¹⁵Institute of Stem Cells and Regeneration, Chinese Academy of Sciences, Beijing 100101, China. ¹⁶James D. Watson Institute of Genome Sciences, Hangzhou 310058, China. ¹⁷Hubei Key Laboratory of Cell Homeostasis, RNA Institute, College of Life Sciences, Wuhan University, Wuhan 430072, China.

¹⁸Guangdong Provincial Key Laboratory of Genome Read and Write, BGI-Shenzhen, Shenzhen 518120, China.

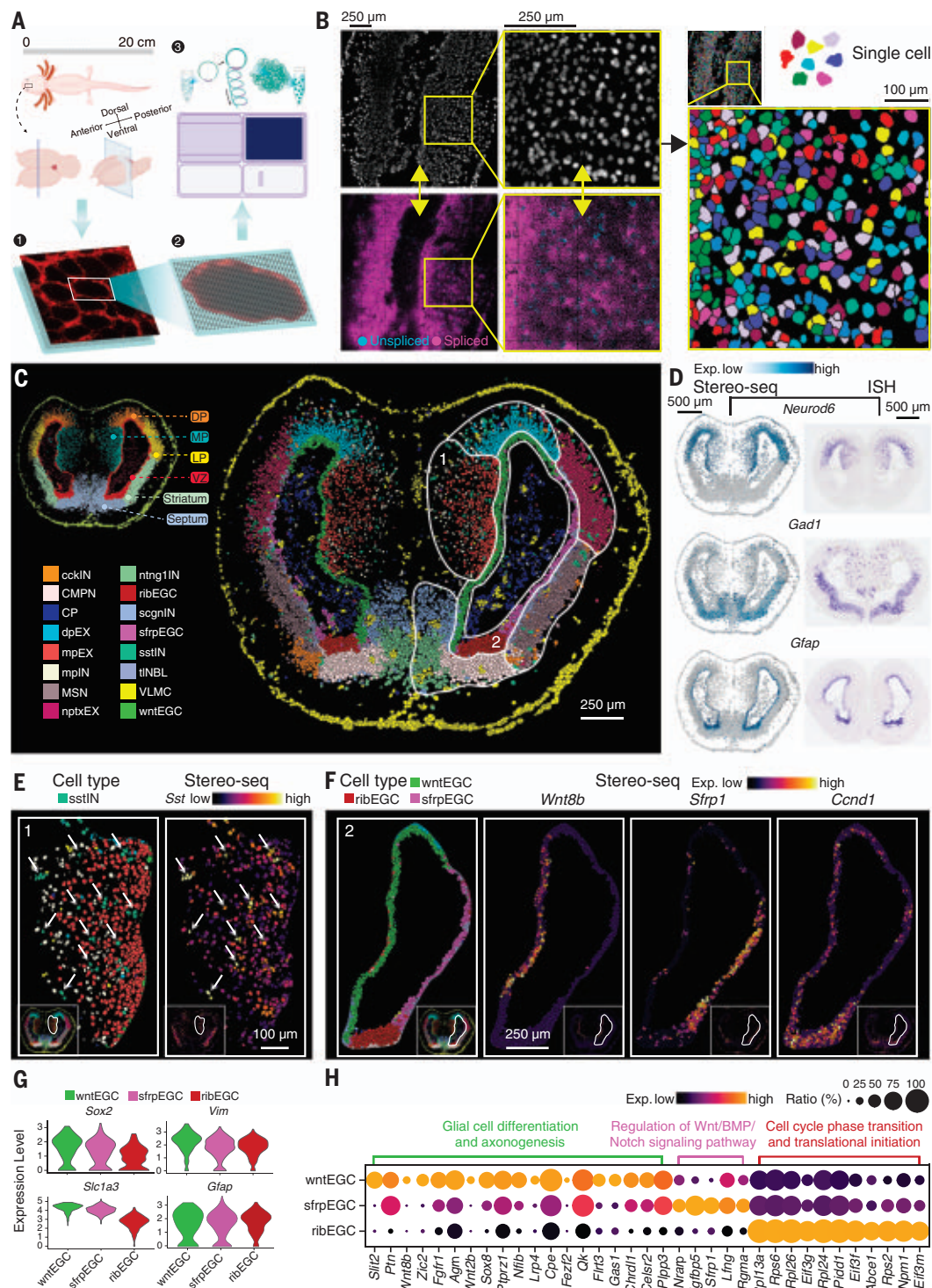
*Corresponding author. Email: guying@genomics.cn (Y.G.); jifengfei@gdph.org.cn (J.-F.); xunxu@genomics.cn (X.X.); liang_chen@whu.edu.cn (L.C.); lihanbo@genomics.cn (H.L.)

†These authors contributed equally to this work.

Fig. 1. Spatial transcriptome of axolotl telencephalon by Stereo-seq.

(A) Schematic diagram of Stereo-seq for the axolotl telencephalon. Step 1: sample collection and frozen section preparation of the adult axolotl telencephalon. Step 2: in situ RNA capture of tissue loaded onto the Stereo-seq chip. Step 3: cDNA amplification, library construction, and sequencing.

(B) Spatially assigned spliced (purple) and unspliced transcripts (blue) (bottom left) and corresponding nucleus areas represented by single-stranded DNA staining (gray) (top left). Single-cell segmentations were performed by watershed algorithm (right). **(C)** Stereo-seq identified anatomical regions (top left) and cell types (right) of axolotl telencephalon. DP, dorsal pallium; MP, medial pallium; LP, lateral pallium; VZ, ventricular zone; cckIN, *Cck*⁺ inhibitory neuron; CMPN, cholinergic, monoaminergic, and peptidergic neuron; CP, choroid plexus; dpEX, dorsal pallium excitatory neuron; mpEX, medial pallium excitatory neuron; mplIN, medial pallium inhibitory neuron; MSN, medium spiny neuron; nptxEX, *Nptx*⁺ lateral pallium excitatory neuron; ntng1IN, *Ntng1*⁺ inhibitory neuron; ribEGC, ribosomal EGC; scgnIN, *Scgn*⁺ inhibitory neuron; sfrpEGC, *Sfrp*⁺ EGC; sstIN, *Sst*⁺ inhibitory neuron; tINBL, telencephalon neuroblast; VLMC, vascular leptomeningeal cell; wntEGC, *Wnt*⁺ EGC. **(D)** Spatial visualization of the expression of selected genes on Stereo-seq maps (left) and corresponding RNA ISH images (right). **(E)** Distribution of the sstIN in the medial pallium region of the adult axolotl telencephalon. Annotated sstIN in green (left) and cells expressing high levels of the *Sst* gene (right) are indicated by white arrows. **(F)** The distribution of three subtypes of EGCs (left). The expression of marker genes for the selected EGC subtype is shown (right). **(G)** Violin plot showing the expression level of neural stem cell markers (*Sox2*, *Vim*, *Slc1a3*, and *Gfap*) in three types of EGCs. **(H)** Bubble plot showing the expression level of specific markers of various biological functions in each EGC subtype.



(22–24). Because Stereo-seq is based on DNA nanoball (DNB) sequencing technology (25), for which each DNB spot on the chip is 220 nm in diameter and the center-to-center distance of two adjacent spots is 500 or 715 nm, we were able to capture transcripts at the sub-cellular level (Fig. 1A and fig. S1A).

To mark the position of individual cells on the section, we performed DNA staining to highlight the nucleus, where newly transcribed pre-mRNAs undergo splicing (Fig. 1B, left panels) (26). Indeed, intron-containing transcripts were observed in nuclear regions and were separated from spliced transcripts (Fig. 1B,

left panels). We then used the watershed algorithm to extract transcripts in each nucleus and its surrounding region, in which both nuclear and cytoplasmic transcript-containing areas were included for cell boundary demarcation. In this way, we were able to assign transcripts to individually defined cell areas,

achieving single-cell resolution (Fig. 1B, right panels, and fig. S1, B and C). Each cell area contained ~850 DNB spots, in which an average of 6291 unique molecular identifiers (UMIs) and 1680 genes were detected (fig. S1, D and E, and table S1).

To acquire a global picture of cell clusters spatially assigned onto the section, we performed the spatially constrained clustering analysis (see Methods). In total, we obtained six clusters of cells separated into previously defined anatomical regions of the axolotl telencephalon, including the VZ, dorsal pallium, medial pallium, lateral pallium, striatum, and septum (Fig. 1C, top left) (3, 13, 27). To dissect cell type composition, we next conducted unsupervised clustering analysis by Seurat based solely on gene expression (28). This analysis identified 16 cell clusters, which were further mapped to the section according to their spatial information (Fig. 1C, right). Referring to established cell marker genes, such as excitatory neuron marker *Neurod6*, inhibitory neuron marker *Gad1*, and EGC marker *Gfap* (Fig. 1D), we determined the identity of each cell cluster (fig. S2A and table S2). We further validated the spatial distribution of Stereo-seq signals for selected marker genes by RNA in situ hybridization (RNA ISH) (figs. S2B and S3).

Different cell types were distributed at distinct locations (Fig. 1C and fig. S4). Excitatory neurons, including dorsal pallium excitatory neurons, medial pallium excitatory neurons, and *Nptx*⁺ lateral pallium excitatory neurons (*nptx*EXs), were enriched in the pallium. In contrast, inhibitory neurons, such as *Cck*⁺ inhibitory neurons, medial pallium inhibitory neurons, medium spiny neurons, *Ntng1*⁺ inhibitory neurons, *Scgn*⁺ inhibitory neurons, and *Sst*⁺ inhibitory neurons, were more abundant in the striatum, medial pallium, and septum regions and were physically separated from excitatory neurons (Fig. 1C and fig. S4).

Similar to other spatial transcriptomic techniques, sample processing for Stereo-seq may cause RNA transcripts to diffuse laterally to neighboring areas (22). We next examined whether this effect would interfere with cell type annotation. We chose *Sst*⁺ inhibitory neurons for demonstration because they are sparsely distributed in the pallium (Fig. 1E and fig. S5A) (9). Although the *Sst* transcript indeed diffused in Stereo-seq data (Fig. 1E, right), its level dropped rapidly beyond cell boundaries (fig. S5B). Statistically, the average transcript levels of *Sst* and *Gad2* (another gene expressed in *Sst*⁺ inhibitory neurons) were significantly lower in neighboring cells than in *Sst*⁺ inhibitory neurons (fig. S5C). Therefore, we were able to achieve identification of *Sst*⁺ inhibitory neurons (fig. S5D). We further evaluated RNA diffusion and cell type identification of Stereo-seq by compar-

ison with RNA ISH. The distribution pattern of *Gad2* and *Sst* transcripts was similar between two methods on two consecutive sections (fig. S5E), as was the estimated percentage of annotated *Sst*⁺ inhibitory neurons (fig. S5, E to G); these findings suggested that Stereo-seq data analysis at the cellular level could be similar to RNA ISH.

EGCs reside in the VZ and are responsible for neurogenesis during development and regeneration (4, 9, 29). We identified three clusters of EGCs located in distinct regions (Fig. 1F). Aside from the commonly expressed radial glia markers *Sox2*, *Gfap*, *Vim*, *Fabp7*, and *Slc1a3*, each EGC cluster was characterized by expression of specific markers such as *Wnt8b*, *Sfrp1*, or ribosome-related genes (Fig. 1, F and G, fig. S2A, and table S2). Accordingly, we named these clusters *wnt*EGC, *sfrp*EGC, and *rib*EGC (Fig. 1, C and F). Gene Ontology analysis (table S3) revealed that cell cycle and translation-related genes were highly expressed in *rib*EGCs (Fig. 1H), suggesting an active proliferation property of *rib*EGC (30–32).

Other identified cell types included cholinergic, monoaminergic, and peptidergic neurons in the septum, neuroblasts near the lateral VZ, and choroid plexus cells and vascular leptomeningeal cells in the outer layer of the telencephalon (Fig. 1C and fig. S4). In this way, our work decodes the spatially resolved transcriptomes at single-cell resolution and cell types of axolotl telencephalon sections. The data can be browsed via the interactive data portal at <https://db.cngb.org/stomics/artista>.

EGC dynamics throughout axolotl telencephalon development

To investigate the cellular and molecular dynamics of axolotl brain development, we applied Stereo-seq to developmental (stage 44, 54, and 57), juvenile, adult, and metamorphosed forebrain sections (Fig. 2A). We collected cross-sections at defined positions (see Methods) to ensure that comparable samples from different developmental stages were used for Stereo-seq analysis. Spatially constrained clustering analysis revealed similar cortex structures on all analyzed sections, except for the section of stage 44, where the dorsal and medial pallia were indistinguishable (fig. S6, A and C), likely reflecting an unfinished brain region specification. Further analysis of the gene expression profiles showed a high correlation of defined regions among all developmental stages (fig. S6, B and D), thus suggesting comparability between sections. We next annotated these sections and identified 33 cell types in total using the unsupervised clustering analysis based on gene expression (Fig. 2A, fig. S7, and table S2). In addition to the cell types identified in Fig. 1, we discovered 13 immature/intermediate cell types, expressing

both progenitor and differentiated cell markers (Fig. 2A and table S2).

We observed a dominant EGC subtype present in the VZ starting at stage 44. This subtype decreased in number from stage 54 and vanished from the juvenile stage (Fig. 2B). It expressed early developmental markers, such as *Fzd5* and *Sox1* (table S2) (33–35), and was thus named as development-related EGCs (*d*EGCs). *sfrp*EGCs and *wnt*EGCs appeared at stage 54 and were gradually restricted to designated locations from the juvenile stage (Fig. 2, A and B). Along with *d*EGCs, immature neurons expressing specific markers, such as *Stmn2*, *Tubb3*, and *Dcx*, were seen at early developmental stages, yet became undetectable from the juvenile stage onward (Fig. 2, A and B, fig. S7, and table S2). The developmental neuroblasts (*d*NBLs) highly expressing marker genes *Nes* and *Cdkn1c* emerged with developmental timing similar to that of *d*EGCs and immature neurons (Fig. 2, A and B, fig. S7, and table S2), indicating a potential lineage transition from EGCs to neuroblasts and immature neurons as previously suggested (29). In contrast, mature neurons started to appear at stage 57, and their spatial distribution at the juvenile stage became similar to that in the adult telencephalon (Fig. 2, A and B, and fig. S7). These results indicate that the cell type and distribution in the axolotl telencephalon were established since the juvenile stage (3).

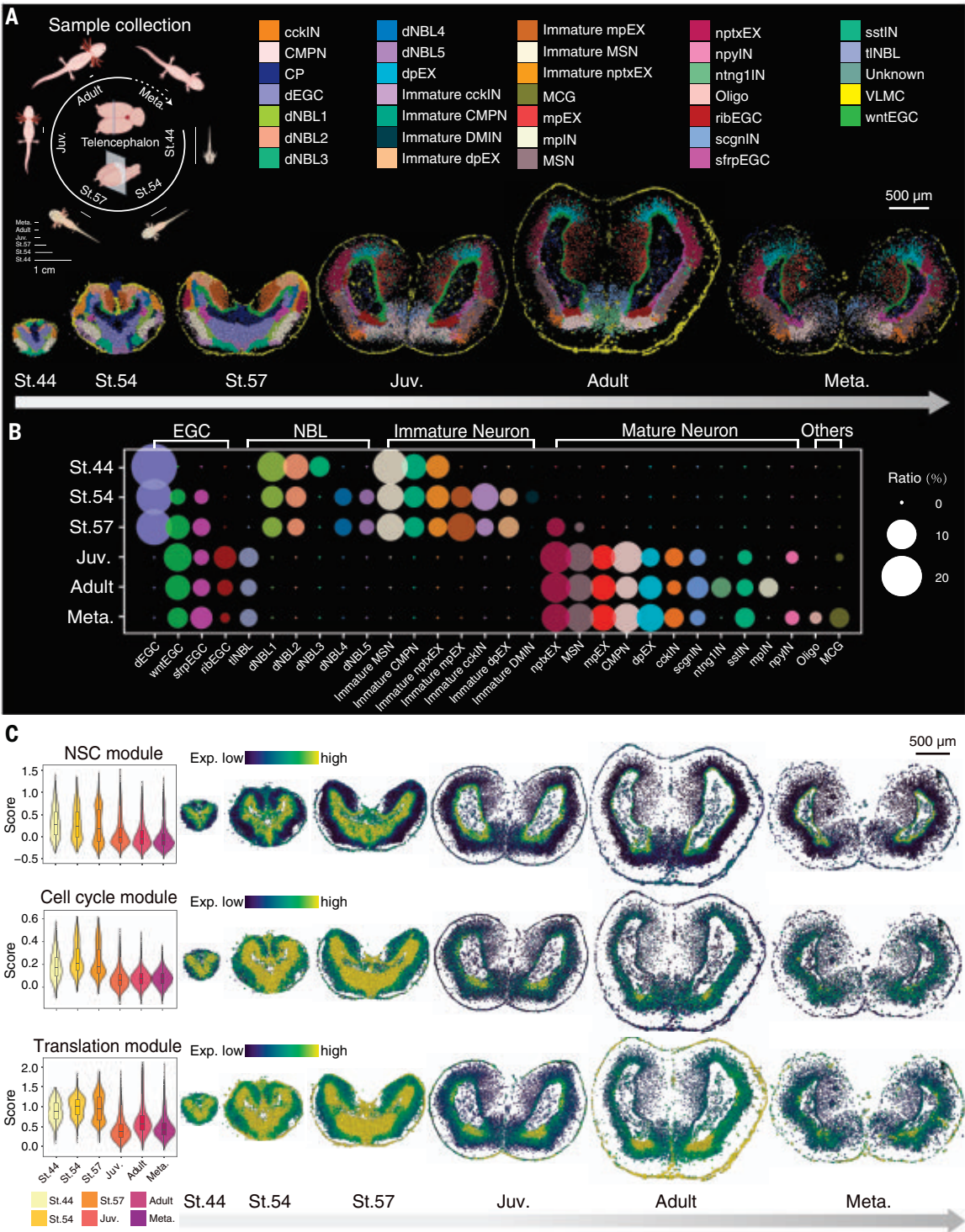
To characterize the molecular dynamics of EGCs during development, we evaluated the expression of composite gene modules defining neural stemness, cell cycle, and translation activity to reveal the proliferative and differentiative potential of EGCs (Methods and table S4) (32, 36). Overall, cells in the expanded VZ at early developmental stages expressed high levels of all three gene modules, in line with active stem cell activities, and showed less neuron maturation during the fast brain expansion phase (Fig. 2C) (37). From the juvenile stage onward, cells positive for these modules dropped in number and became restricted to a thinner ventral area of the VZ (Fig. 2C), where *rib*EGCs were located (Fig. 1H).

Cell dynamics and cell-cell communication during regeneration

Although axolotls are capable of regenerating damaged brains (9), the cell types responsible for regeneration, their origins, and the molecular events that direct regenerative functions of these cells remain elusive. To tackle these questions, we first removed a portion of the dorsal pallium of the left telencephalic hemisphere following an established protocol (9). We then collected sections at 2, 5, 10, 15, 20, 30, and 60 days post-injury (DPI) for Stereo-seq analyses to dissect both immediate wound responses and later regeneration processes (Fig. 3A). We annotated 28 cell types across

Fig. 2. Cell dynamics of axolotl telencephalon during development.

(A) Schematic diagram of sample collection (left). Unsupervised clustering of the axolotl telencephalon sections at stage44 (St.44), stage54 (St.54), stage57 (St.57), juvenile (Juv.), Adult, and metamorphosis (Meta.). dEGC, developmental EGC; dNBL, developmental neuroblast; DMIN, dopa-minergic periglomerular inhibitory neuron; MCG, microglial cell; npyIN, *Npy*⁺ inhibitory neuron; ntng1IN, Oligo, oligodendrocyte. **(B)** Bubble plot showing the ratio of individual cell types in the axolotl telencephalon at different developmental stages, including St.44, St.54, St.57, Juv., Adult, and Meta. **(C)** Violin plot (left) and spatial visualization (right) of gene modules, the expression level of which defines neural stem cell (NSC), cell cycle, and translation captured by Stereo-seq at different developmental stages in the axolotl telencephalon.



sections using established marker genes, eight of which were not previously seen in development (Fig. 3B, fig. S9, A and B, and table S2). To assess the reproducibility of our data, we integrated Stereo-seq data of multiple neighboring sections along the anterior-posterior axis at 2, 5, 10, 15, and 20 DPI. The results showed that both cell type composition and the gene expression profile of each cell type for all sections of same stage were highly consistent with each other, and were therefore integrated for downstream analysis (fig. S8). The series Stereo-seq data revealed that morphological recovery from the injury occurred within 30 days, as previously reported (9). At 60 DPI, we observed that the cell types and their distribution were fully restored (Fig. 3B).

To identify injury-responding cells, we investigated the dynamics of 14 major cell types by calculating the ratio of each cell population in the injured versus uninjured site at seven regeneration stages (Fig. 3C and fig. S10) (see Methods). Two types of cells increased in number from 2 DPI and maintained their population until 15 DPI. One population was microglia cells expressing makers *Ctqb* and *Ctsl*, which likely were recruited to participate in the inflammatory response (Fig. 3, C and D, and table S2) (38). The other population was a type of EGC that expressed higher

sections using established marker genes, eight of which were not previously seen in development (Fig. 3B, fig. S9, A and B, and table S2). To assess the reproducibility of our data, we integrated Stereo-seq data of multiple neighboring sections along the anterior-posterior axis at 2, 5, 10, 15, and 20 DPI. The results showed that both cell type composition and the gene expression profile of each cell type for all sections of same stage were highly consistent with each other, and were therefore integrated for downstream analysis (fig. S8). The series Stereo-seq data revealed that morphological recovery from the injury occurred within 30 days, as previously reported (9). At 60 DPI, we observed that the cell types and their distribution were fully restored (Fig. 3B).

Fig. 3. Spatiotemporal transcriptomics of axolotl brain during regeneration.

(A) Schematic diagram of sample collection (left). Overview of the sampled sections at homeostatic and regenerative stages (right).

(B) Spatial visualization of cell types identified in the axolotl telencephalon sections by Stereo-seq at different stages of regeneration. IMN, immature neuron; obNBL, olfactory bulb neuroblast; reaEGC, reactive EGC; rIPC, regeneration intermediate progenitor cell; WSN, wound-stimulated neuron.

(C) Line graph showing the fold change of the cell ratio in the injured hemisphere compared to the uninjured hemisphere across all stages. We set 4 as the maximum fold-change value for better visualization in the line plot.

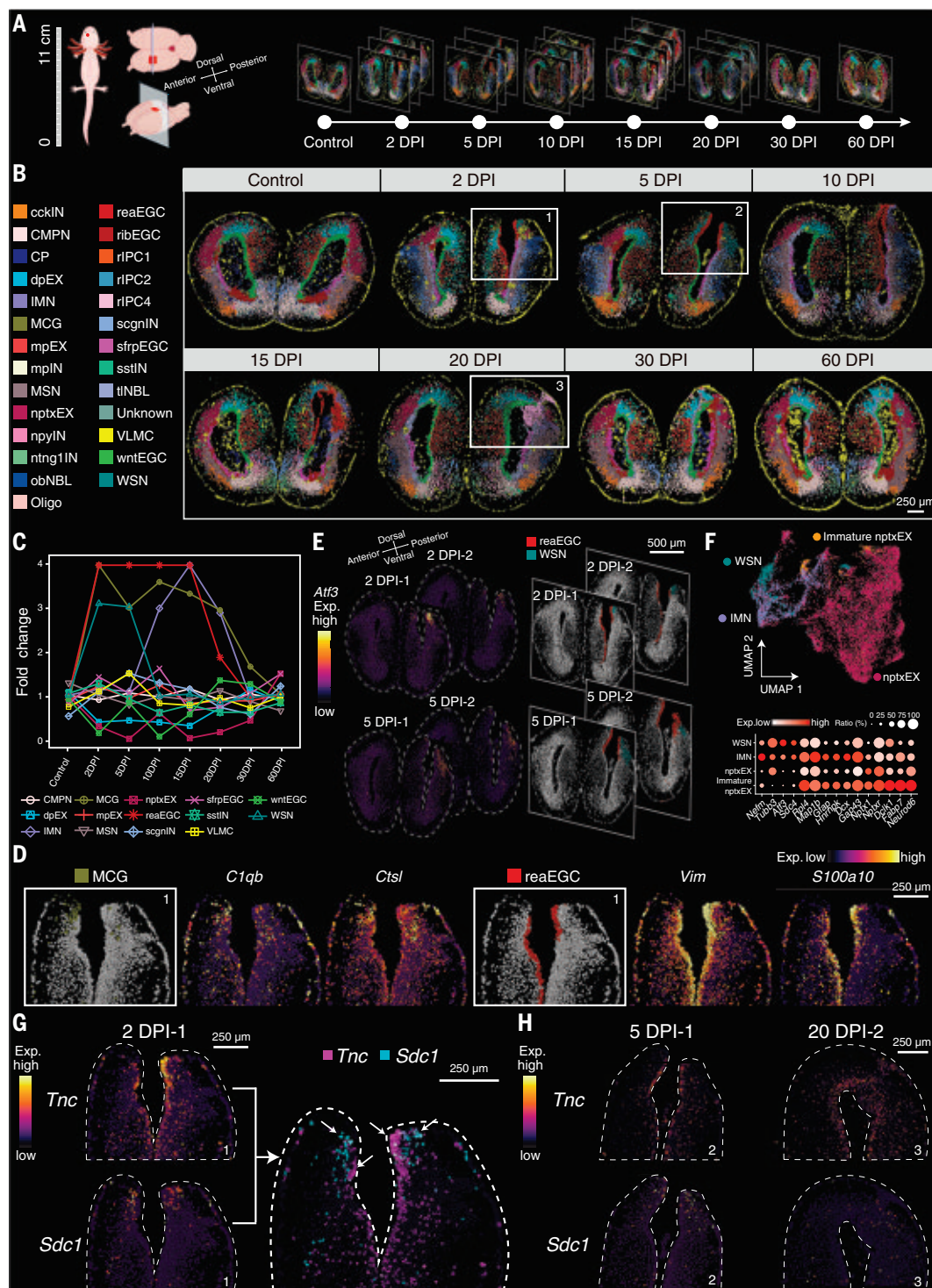
(D) Spatial visualization of marker gene expression in MCGs (left) and reaEGCs (right) on the 2 DPI section.

(E) Spatial visualization of the expression level of *Atf3* and the distribution of reaEGCs and WSNs on the sections of 2 DPI and 5 DPI.

(F) UMAP visualization of the segmented cells from the dorsal regions of developmental stages (St.44, St.54, St.57) and regenerative stages (2 to 20 DPI), including nptxEX from both processes, immature nptxEX from developmental stages, and IMN and WSN from regenerative stages. Cells are colored according to cell type annotation (top).

Bubble plot showing the expression levels of the specific markers of these four cell types (bottom).

(G and H) Spatial visualization of the expression level of a ligand-receptor pair (*Tnc* and *Sdc1*) on the sections of 2, 5, and 20 DPI.



levels of glial cell markers (such as *Vim*) than other EGC subtypes during homeostasis, as well as a unique marker, *S100a10* (Fig. 3D). Thus, it was named as reactive EGCs (reaEGCs) (Fig. 3, C and D, and table S2). Monocle analysis of the sections at 2 DPI indicated that reaEGCs in medial and lateral pallium regions likely originated from local wntEGCs and sfrpEGCs, respectively (fig. S11, A and B).

Further investigation by Monocle2 analysis revealed a group of genes, including several transcription factors, exhibiting patterned expression changes along the pseudotime axis from wntEGCs or sfrpEGCs to reaEGCs (fig. S11, C and D). The predicted regulatory networks and pathways of these transcription factors were related to neural precursor cell proliferation and differentiation (fig. S11D).

Moreover, our WGCNA analysis highlighted four transcription factors specifically coexpressed in reaEGCs (fig. S11E), which are part of regulatory pathways involved in the wound-healing response (fig. S11, F and G). In sum, these results suggest that reaEGCs induced immediately upon injury may have a positive role in regeneration.

In addition, we observed a group of neurons that were transiently induced at 2 and 5 DPI

and highly expressed the neuron growth contributor *Atf3* (Fig. 3, C and E) (39). Their transcriptomic profile was distinct from that of location-matched nptxEXs on the uninjured hemisphere of the telencephalon, but was similar to that of immature neurons (IMN) appearing from 10 to 20 DPI. This group of neurons was thus named as wound-stimulated neurons (WSNs) (Fig. 3F). The genes *Dclk1* and *Gap43* involved in neuron maturation and axonal growth were both up-regulated in expression, whereas genes enriched in mature neurons, such as *Nptx1* and *Neurod6*, were down-regulated in WSNs relative to nptxEXs (Fig. 3F). Considering (i) the identical location of WSNs and nptxEXs before injury, and (ii) the immediate appearance of WSNs at 2 DPI before regenerative neurogenesis (Fig. 3C) (40), we speculated that WSNs were derived from the local nptxEXs via a transcriptomic remodeling response to injury, reminiscent of the observation for corticospinal and somatosensory neurons after nerve injury in rodents (41, 42). Our results indicate that the neuronal identity may be remodeled into a rejuvenated state upon injury in the axolotl brain.

The communication between cells in the local microenvironment is pivotal for coordinated regeneration responses (43). To examine cell-cell communication during the early regeneration period, we divided the 2 DPI section into 10 regions according to spatially constrained clustering analysis and predicted potential ligand-receptor interactions in each region. We found that the majority of detected interacting ligand-receptor pairs were in the VZ and were involved in proliferation, cell migration, and extracellular matrix remodeling, suggesting an active EGC response to injury (fig. S11H). We observed strong expression of *Tnc* and *Sdc1* as well as a high interaction score in adjacent clusters of reaEGCs and WSNs at the wound edge (Fig. 3, G and H, and fig. S11H). TNC is a glycoprotein in adult neurogenic niches required for tissue repair and regeneration (44). SDC1 is also shown to be induced by injury and participate in neurogenesis (45). These data collectively indicate a regulatory role of reaEGCs for injured neurons during regeneration (Fig. 3, B, G, and H).

Cell lineage dynamics during regenerative neurogenesis

The observation of reaEGCs at the wound site elicits a hypothesis that this progenitor cell cluster is responsible for restoring lost neurons, particularly nptxEXs. If so, intermediate cell clusters between reaEGCs and nptxEXs in terms of differentiation state would be expected. To test this idea, we first performed saturated BrdU labeling in the injured brain of axolotls and analyzed sections at 20 DPI to mark all newly generated cells (fig. S12A).

Immature neurons were then immunolabeled using antibody to TUBB3. We found that a layer of cells adjacent to polarized EGCs were positive for both BrdU and TUBB3 (fig. S12B), indicating the presence of newly generated immature neurons in the wounding/regenerating zone next to EGCs.

We then examined the origin of these immature cells by analyzing sections along the anterior-to-posterior direction of the regenerating telencephalon from the same animal at 15 DPI, when the percentage of IMNs reached the peak yet the percentage of reaEGCs started to drop (Fig. 3C). Besides the section from the wound closure area shown in Fig. 3 (15 DPI-3), we included sections from the wound center (15 DPI-1), the wound edge (15 DPI-2), and the remote area (15 DPI-4) (fig. S9B). By integrating data from all four sections, 26 cell types were identified (fig. S9B). A few nptxEXs were seen, whereas reaEGCs appeared to cover the injury site on all sections (fig. S9B). We found a high-to-low spatial gradient of nptxEXs in number from the remote region (section 15 DPI-4) to the center of the wound area (section 15 DPI-1) (fig. S9B), consistent with previous MRI scanning data for axolotl brain regeneration (9). These results suggest that the reconstitution of lost neurons probably occurs along with the conjunction of the injury edge, through a process that may be initiated in the peripheral region and progresses toward the center of the incision.

We noticed on section 15 DPI-4 that nptxEXs were in regions adjacent to IMNs, suggesting a potential transition between them (fig. S9B). We also observed a regeneration-specific cell cluster situated between reaEGCs and IMNs (fig. S9B), expressing markers of both reaEGCs (*Vim*, *Nes*, *Krt18*, and *Sl00a10*) and IMNs (*Ankerd1*, *Stmn4*, and *Nptx1*) (Fig. 4, A and B, and table S2). We therefore named this cell cluster regeneration rIPC1 (intermediate progenitor cells 1). The expression level and signal wave of reaEGC and IMN marker genes across cell layers matched the cell type distribution on the Stereo-seq map, further supporting the four-cell state organization (fig. S13, A to D). In addition, expression of cyclin inhibitors *Cdkn1a* and *Cdkn1c* was sequentially increased from reaEGCs to rIPC1s and immature nptxEXs; this finding suggests that the proliferation potential was reduced along this potential cell state transition axis (Fig. 4A) (46–48).

To further verify this transition, we divided the 15 DPI-4 section into three regions (Fig. 4C), and applied cell type-based and vector field-based RNA Velocity and Monocle pseudotime analyses in these areas (Fig. 4, D and E) (49). The results of both analyses supported the putative lineage transition along the reaEGC-rIPC1-IMN-nptxEX axis. Similar transitions were observed on sections 15 DPI-2 and -3

(fig. S14, A to D and G to J). We then analyzed genes with expression changes along the vector field-based pseudotime axis (Fig. 4F and fig. S14, E and K) and observed matched expression dynamics and gene functions with the potential transition, such as descending expression of stemness marker *Nes* and ascending expression of *Cdkn1c* along the axis (Fig. 4G and fig. S14, F and L).

Next, temporal analysis was performed to verify the above spatial analysis-based findings. The presumed nptxEX regeneration-related cells, including reaEGCs, rIPC1s, IMNs, and nptxEXs (Fig. 4H, left panel), from 2 DPI to 60 DPI were selected to construct a pseudotime trajectory via Monocle3 (Fig. 4H, bottom right panel). The predicted lineage transition of these cells along pseudotime also supported the reaEGC-rIPC1-IMN-nptxEX pattern (Fig. 4H, top right panel). We then coordinated the pseudotime trajectory result with our Stereo-seq sections during regeneration, leading to a match between pseudotime and real-time data (Fig. 4I). In summary, our results depict a scenario in which reaEGCs proliferate to cover the wound, meanwhile converting or differentiating into intermediate and mature neurons for tissue regeneration.

Comparison of developmental and regenerative neurogenesis

We noticed that the cell layer organization in the regenerating telencephalon was similar to that in the developing brain (Fig. 2A). dEGCs, dNBLs (similar to IPCs), and immature nptxEXs arrayed from the VZ to the pallium region were first observed as early as stage 44 (Fig. 5, A and B, and fig. S7). When the mature nptxEXs appeared at stage 57, four cell types of dEGCs, dNBLs, immature nptxEXs, and nptxEXs were arranged in a spatial pattern matching that on the section 15 DPI-4, thus suggesting that nptxEX regeneration may recapitulate the nptxEX development process (Fig. 5, A and B). To test this possibility, we calculated the correlation of EGCs in the dorsal left telencephalon from developmental stages 44, 54, 57, and juvenile, as well as 15 DPI-4 sections. Indeed, relative to other EGC types, the global gene expression signature of reaEGCs was most closely correlated with dEGCs at stage 57 (Fig. 5C); for example, the spatial distribution of markers such as *Nes* and *Nptx1* was similar between 15 DPI-4 and stage 57 (Fig. 4, A and B, and Fig. 5, D and E). Consistently, both RNA velocity and Monocle analyses simulated parallel lineage transition trajectories to generate nptxEXs in both developmental and regenerative processes, from EGCs to IPCs, then to immature and mature neurons (Fig. 5, F to H, fig. S15, A to C, and fig. S16, A to C).

We further assessed the molecular dynamics of these two potential transition processes using data from stage 57 and 15 DPI-4. Differentially

Fig. 4. Putative cell lineage transition during telencephalon regeneration.

(A) Bubble plot reflecting the expression dynamics of marker genes defining reaEGC, rIPC1, and IMN, which are major cell types involved in axolotl telencephalon regeneration.

(B) Spatially visualized heatmap showing the expression pattern of key markers for regeneration-related cells in the injury area of sections, including 15 DPI-2, 15 DPI-3, and 15 DPI-4 cells.

(C) Spatial distribution of cell types around the regenerating site on the section of 15 DPI-4.

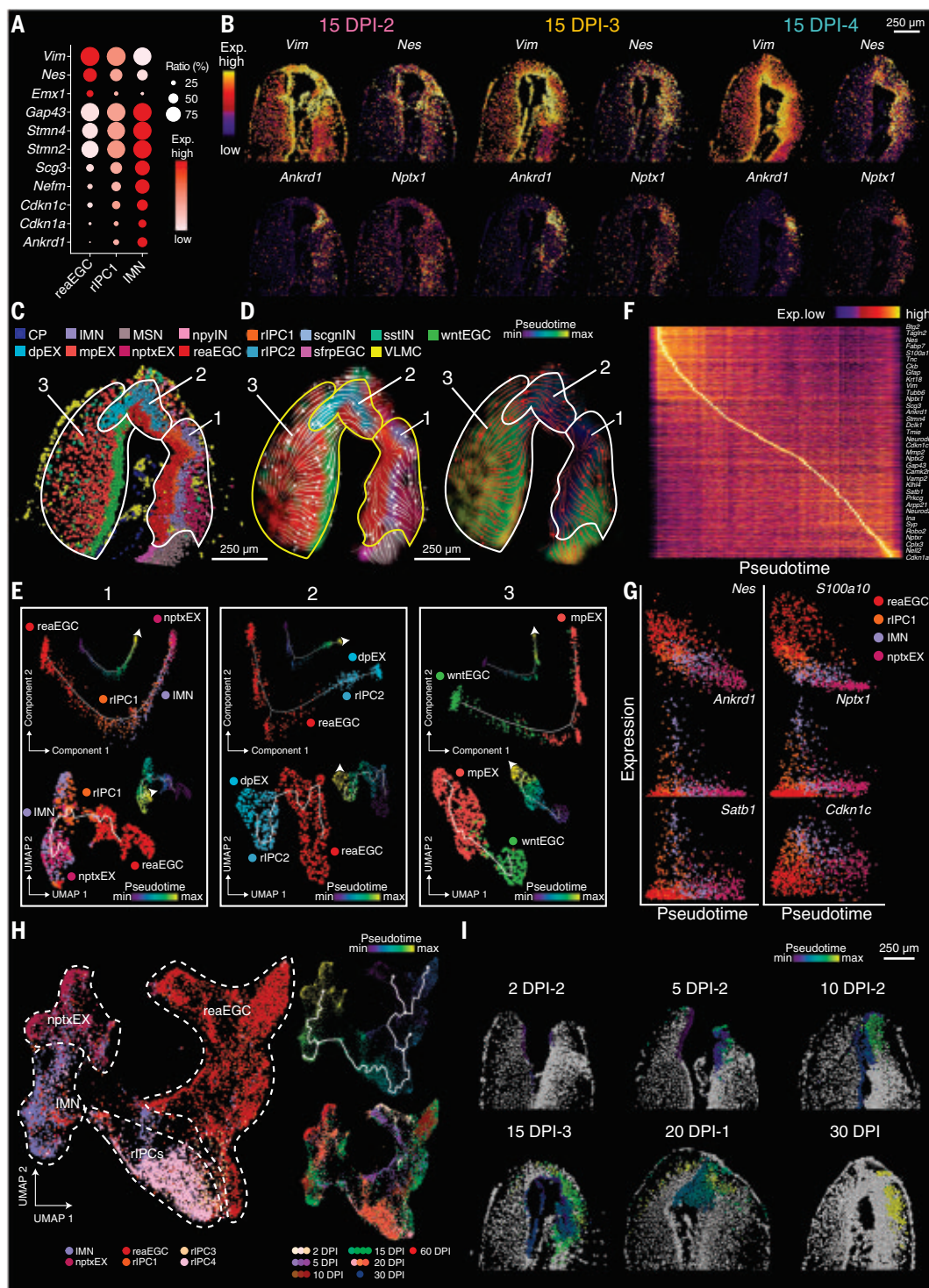
(D) RNA velocity streamline plots showing the predicted trajectory of cell lineage transition in the regenerating region of axolotl telencephalon in 15 DPI-4 cells. Areas are colored by either annotated cell clusters (left) or pseudotime (right).

(E) Pseudotime trajectory analysis corresponding to the three designated areas in (C), via Monocle2 (top) and Monocle3 (bottom). Cells are colored by cell type or pseudotime.

(F) Heatmap showing pseudo-temporal transition of the expression level of representative genes in regeneration.

(G) Scatterplot showing pseudotime dynamics of the expression of *Nes*, *S100a10*, *Ankrd1*, *Nptx1*, *Satb1*, and *Cdkn1c* in clusters of reaEGC, rIPC1, IMN, and nptxEX cells. **(H)** UMAP visualization of the regeneration-related cells across regenerative stages. Cells are colored by cell type annotation (left), pseudotime (top right), and stages (bottom right).

(I) Spatial visualization of cells in (H) with the pseudotime score in the cell lineage transition process. Cells are colored by the pseudotime score.

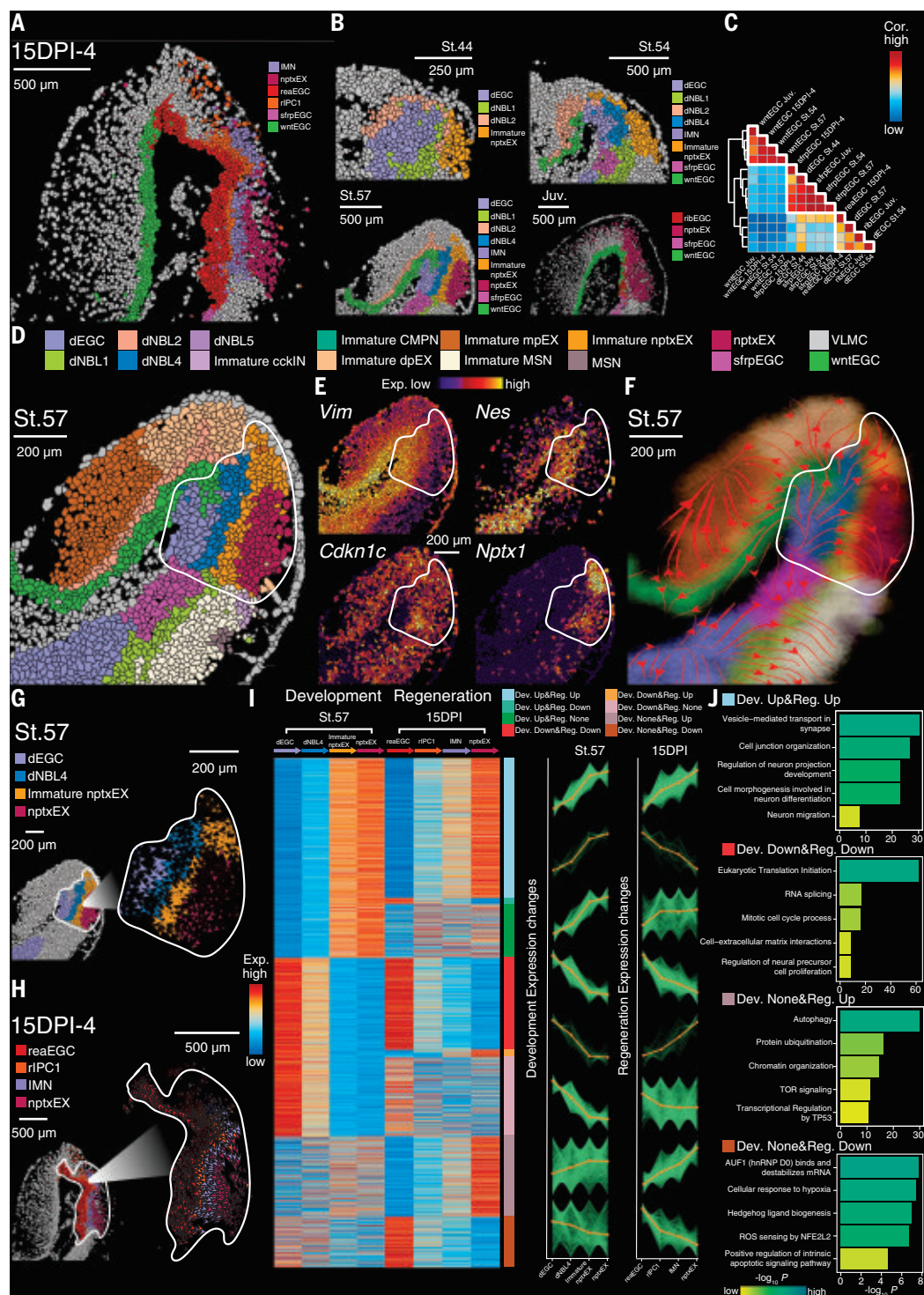


expressed genes were classified into eight groups with either similar or opposite trends along each process (Fig. 5I and table S5). Pathways involved in neuronal differentiation, migration, maturation, communication, and synaptic activities were up-regulated in both processes. In contrast, pathways related to proliferation, cell cycle progression, and related molecular events, such as translation

initiation and RNA splicing, were down-regulated (Fig. 5J). These results agree with the consensus that stemness and proliferation activity decline during neurogenesis (Fig. 5J). Our analysis also showed that chromatin organization, TOR signaling, and transcriptional regulation by TP53 were specifically up-regulated during the transition process in regeneration, suggesting possible metabolic and

genome stability control for the rapid cell growth during regeneration (50, 51). In addition, we observed a regeneration-specific rise of autophagy-related genes and a decline in gene expression related to wound and stress responses (Fig. 5J), possibly reflecting a transition of molecular activities from wound response in reaEGC to neuronal regeneration. In total, hundreds of regenerative-specific

Fig. 5. Comparison of neuro-genesis between development and regeneration. (A and B) Spatial distribution of major cell types in the dorsal pallium of the left hemisphere at 15 DPI-4 (A) and at St.44, St.54, and Juv. (B). (C) Heatmap displaying the correlation between different EGC types at 15 DPI and four developmental stages. (D) Spatial distribution of cell types in the dorsal pallium of the axolotl left telencephalon at St.57. Cells potentially involved in the development of nptxEX are framed by the white line. Cell types are annotated by colored cubes on top. (E) Spatially visualized expression of key markers on the section shown in (D). (F) RNA velocity streamline plot showing the predicted dorsal pallium development trajectory in the left hemisphere of the axolotl telencephalon at St.57. (G and H) RNA velocity streamline plot showing the predicted lineage transition trajectory of dEGC, dNBL, immature nptxEX, and nptxEX at St.57 (G) and reaEGC, rIPC1, IMN, and nptxEX at 15 DPI (H). (I) Left: Heatmap of gene expression during nptxEX development and regeneration. Eight distinct groups of genes were sorted by their dynamic expression pattern. Right: Line plot depicting standardized Stereo-seq signal by fuzzy cluster analysis for eight groups, with green lines representing the expression dynamics of individual genes and the orange line representing the integrated pattern of each group of genes at St.57 or 15 DPI. Dev. Up, up-regulated in development; Dev. Down, down-regulated in development; Reg. Up, up-regulated in regeneration; Reg. Down, down-regulated in regeneration; None, no significant change. (J) Bar plot exhibiting the representative Gene Ontology enrichment pathways of groups in (I).



genes were identified by this comparison (fig. S17 and table S6).

Discussion

How EGCs contribute to brain regeneration in the amphibian remains elusive (10, 11, 14). By identifying the reaEGC subtype and presenting its dynamic functions for regeneration, our work not only supports the injury-specific ac-

tivation and accumulation of EGCs with elevated proliferation capacity around the lesion (9, 10), but also indicates that these cells are the origin of neurogenesis for regeneration (9–11). Moreover, our results show that reaEGCs are similar to dEGCs by whole-transcriptome comparison. As dEGCs appeared from the earliest stage of development sampled in our study, and presumably gave rise to other EGC types

and neurons, they may possess a more pluripotent potential than EGCs in the adult brain. Therefore, as a consequence of the absence of dEGCs in adulthood, our data indicate that reaEGCs may originate from non-dEGC subtypes by reprogramming.

In regard to the cellular origin of reaEGCs, we identified three EGC subtypes in the VZ of the adult telencephalon by whole-transcriptome

analysis and their spatial distribution. These EGC subtypes retained expression of neural stem cell and cell cycle markers, similar to EGCs and radial glial cells previously identified in newts and zebrafish, respectively (2, 10). Our trajectory analysis suggested that reaEGCs were closer to sfrpEGCs and wntEGCs than to ribEGCs. Moreover, we showed that subpopulations of reaEGCs in the medial pallium, lateral pallium, and VZ not only expressed low levels of *Wnt* and *Sfrp*, but also expressed transcription factors that regulate glial cell proliferation and differentiation pathways, suggesting a direct lineage relationship between these EGC populations. In addition, reaEGCs occupied a large area in the VZ of the injured hemisphere at early regeneration stages, where wntEGCs or sfrpEGCs were originally located. Taken together, these findings indicate that reaEGCs may originate mainly from local wntEGCs and sfrpEGCs.

However, we still cannot rule out the possibility that reaEGCs originate from other regions of the axolotl brain and migrate to the wound site. Although we observed few ribEGCs at the dorsal pallium, this type of cell retains active expression of proliferation-related genes. The possibility remains that some ribEGCs proliferate and migrate to the wound area, through which they contribute to the induction of reaEGCs. VZ-specific labeling and functional perturbation assays will be required if we are to elucidate how EGCs in different regions function during regeneration.

Our work has redefined EGC subpopulations and revealed their dynamics and roles in development and regeneration. Injury-induced regeneration also requires collaborative activities of cells in different regions, including cells from the olfactory bulb (4, 9). Therefore, Stereo-seq data from other regions of the brain would help to enable displays of cell activities at the three-dimensional level and to investigate how cellular and molecular cues are polarized to direct regeneration.

Methods summary

In brief, the OCT embedded snap-frozen brain samples from the *d/d* strain of *Ambystoma mexicanum* at different stages of development and regeneration after dorsal telencephalon injury were used for making cryosections, which were then subjected to spatial transcriptomics library construction using Stereo-seq. Brain damage was generated by removing a square-shaped (size 0.5 mm × 0.5 mm) piece of dorsal telencephalon tissue.

Raw sequencing data were processed using the SAW pipeline (<https://github.com/BGIResearch/SAW>). High-quality mapped reads were annotated and calculated to generate a CID-containing expression profile matrix by handleBam (52). To generate the expression matrix at single-cell resolution by Stereo-seq,

the DNB image was first manually registered with nucleic acid staining images. The Scikit-image package was then used to perform single-cell segmentation after removing background and computing Euclidean distances of stained images (53). UMIs from all DNBs in the same putative single cell were aggregated per gene and summed to generate a gene expression matrix for downstream analysis.

Seurat was used for quality control, SCT normalization, dimensionality reduction, clustering, and identification of marker genes (28). Sections along the anterior-posterior axis were integrated by the canonical correlation analysis (CCA) algorithm in the Seurat package. Telencephalon region definition was achieved by combining spatially constrained clustering and morphological information. Cell type identification was performed based on known marker gene sets and verified by in situ hybridization experiments. Newly born neurons were traced by cumulative BrdU labeling and immunohistochemistry.

To capture the cell transition trajectories at the spatial level, the raw count matrix was established according to the annotated bam file and Dynamo was used to perform RNA velocity analysis with unspliced and spliced RNA transcripts (49, 52). For modeling and further clarifying different trajectories on the same section, Monocle2 and Monocle3 were used to perform pseudotime analysis with selected cell types involved in specific developmental or regenerative processes (54, 55). For modeling trajectories across regeneration stages, RPCA with SCT-normalized data was used to integrate regeneration-related cell types across regeneration stages, and Monocle3 analysis was then performed downstream.

See the supplementary materials for further details.

REFERENCES AND NOTES

1. E. M. Tanaka, P. Ferretti, Considering the evolution of regeneration in the central nervous system. *Nat. Rev. Neurosci.* **10**, 713–723 (2009). doi: 10.1038/nrn2707; pmid: 19763104
2. V. Kroehne, D. Freudenreich, S. Hans, J. Kaslin, M. Brand, Regeneration of the adult zebrafish brain from neurogenic radial glia-type progenitors. *Development* **138**, 4831–4841 (2011). doi: 10.1242/dev.072587; pmid: 22007133
3. A. Joven, A. Simon, Homeostatic and regenerative neurogenesis in salamanders. *Prog. Neurobiol.* **170**, 81–98 (2018). doi: 10.1016/j.pneurobio.2018.04.006; pmid: 29654836
4. M. Maden, L. A. Manwell, B. K. Ormerod, Proliferation zones in the axolotl brain and regeneration of the telencephalon. *Neural Dev.* **8**, 1 (2013). doi: 10.1186/1749-8104-8-1; pmid: 23327114
5. K. Lust, E. M. Tanaka, A Comparative Perspective on Brain Regeneration in Amphibians and Teleost Fish. *Dev. Neurobiol.* **79**, 424–436 (2019). doi: 10.1002/dneu.22665; pmid: 30600647
6. T. Gerber et al., Single-cell analysis uncovers convergence of cell identities during axolotl limb regeneration. *Science* **362**, eaq0681 (2018). doi: 10.1126/science.aq0681; pmid: 30262634
7. H. Li et al., Dynamic cell transition and immune response landscapes of axolotl limb regeneration revealed by single-cell analysis. *Protein Cell* **12**, 57–66 (2021). doi: 10.1007/s12338-020-00763-1; pmid: 32748350
8. H. S. Burr, Regeneration in the brain of amblystoma. I. The regeneration of the forebrain. *J. Comp. Neurol.* **26**, 203–211 (1916). doi: 10.1002/cne.900260203
9. R. Amamoto et al., Adult axolotls can regenerate original neuronal diversity in response to brain injury. *eLife* **5**, e13998 (2016). doi: 10.7554/eLife.13998; pmid: 27156560
10. M. Kirkham, L. S. Hameed, D. A. Berg, H. Wang, A. Simon, Progenitor cell dynamics in the Newt Telencephalon during homeostasis and neuronal regeneration. *Stem Cell Rep.* **2**, 507–519 (2014). doi: 10.1016/j.stemcr.2014.01.018; pmid: 24749074
11. D. A. Berg et al., Efficient regeneration by activation of neurogenesis in homeostatically quiescent regions of the adult vertebrate brain. *Development* **137**, 4127–4134 (2010). doi: 10.1242/dev.055541; pmid: 21068061
12. D. Ryczko, A. Simon, A. J. Ijspeert, Walking with Salamanders: From Molecules to Biorobotics. *Trends Neurosci.* **43**, 916–930 (2020). doi: 10.1016/j.tins.2020.08.006; pmid: 33010947
13. A. González, J. M. López, R. Morona, N. Moreno, in *Evolution of Nervous Systems*, J. H. Kaas, Ed. (Academic Press, 2017), vol. 1, chap. 8.
14. A. Joven et al., Cellular basis of brain maturation and acquisition of complex behaviors in salamanders. *Development* **145**, dev160051 (2018). pmid: 29217751
15. N. Kishimoto, K. Shimizu, K. Sawamoto, Neuronal regeneration in a zebrafish model of adult brain injury. *Dis. Model. Mech.* **5**, 200–209 (2012). doi: 10.1242/dmm.007336; pmid: 22028327
16. C. Kizil et al., Regenerative neurogenesis from neural progenitor cells requires injury-induced expression of Gata3. *Dev. Cell* **23**, 1230–1237 (2012). doi: 10.1016/j.devcel.2012.10.014; pmid: 23168169
17. V. Marx, Method of the Year: Spatially resolved transcriptomics. *Nat. Methods* **18**, 9–14 (2021). doi: 10.1038/s41592-020-01033-y; pmid: 33408395
18. C. Ortiz et al., Molecular atlas of the adult mouse brain. *Sci. Adv.* **6**, eabb3446 (2020). doi: 10.1126/sciadv.abb3446; pmid: 32637622
19. K. R. Maynard et al., Transcriptome-scale spatial gene expression in the human dorsolateral prefrontal cortex. *Nat. Neurosci.* **24**, 425–436 (2021). doi: 10.1038/s41593-020-00787-0; pmid: 33558695
20. C. L. Eng et al., Transcriptome-scale super-resolved imaging in tissues by RNA seqFISH. *Nature* **568**, 235–239 (2019). doi: 10.1038/s41586-019-1049-y; pmid: 30911168
21. C. Xia, J. Fan, G. Emanuel, J. Hao, X. Zhuang, Spatial transcriptome profiling by MERFISH reveals subcellular RNA compartmentalization and cell cycle-dependent gene expression. *Proc. Natl. Acad. Sci. U.S.A.* **116**, 19490–19499 (2019). doi: 10.1073/pnas.1912459116; pmid: 31501331
22. A. Chen et al., Spatiotemporal transcriptomic atlas of mouse organogenesis using DNA nanoball-patterned arrays. *Cell* **185**, 1777–1792.e21 (2022). doi: 10.1016/j.cell.2022.04.003; pmid: 35512705
23. G. Roth, W. Walkowiak, The Influence of Genome and Cell Size on Brain Morphology in Amphibians. *Cold Spring Harb. Perspect. Biol.* **7**, a019075 (2015). doi: 10.1101/cshperspect.a019075; pmid: 26261281
24. C. J. Herrick, *The Brain of the Tiger Salamander, Ambystoma tigrinum* (Univ. of Chicago Press, 1948).
25. R. Drmanac et al., Human genome sequencing using unchained base reads on self-assembling DNA nanoarrays. *Science* **327**, 78–81 (2010). doi: 10.1126/science.1181498; pmid: 19892942
26. D. Gaidatzis, L. Burger, M. Florescu, M. B. Stadler, Analysis of intronic and exonic reads in RNA-seq data characterizes transcriptional and post-transcriptional regulation. *Nat. Biotechnol.* **33**, 722–729 (2015). doi: 10.1038/nbt.3269; pmid: 26098447
27. I. Lazcano et al., MRI- and histologically derived neuroanatomical atlas of the *Ambystoma mexicanum* (axolotl). *Sci. Rep.* **11**, 9850 (2021). doi: 10.1038/s41598-021-89357-3; pmid: 33972650
28. Y. Hao et al., Integrated analysis of multimodal single-cell data. *Cell* **184**, 3573–3587.e29 (2021). doi: 10.1016/j.cell.2021.04.048; pmid: 34062119
29. S. C. Nector, A. C. Flint, T. A. Weissman, R. S. Dammerman, A. R. Kriegstein, Neurons derived from radial glial cells establish radial units in neocortex. *Nature* **409**, 714–720 (2001). doi: 10.1038/35055553; pmid: 11217860
30. W. Niu et al., SOX2 reprograms resident astrocytes into neural progenitors in the adult brain. *Stem Cell Rep.* **4**, 780–794 (2015). doi: 10.1016/j.stemcr.2015.03.006; pmid: 25921813
31. M. Barna, Ribosomes take control. *Proc. Natl. Acad. Sci. U.S.A.* **110**, 9–10 (2013). doi: 10.1073/pnas.1218764110; pmid: 23243144

32. S. Temple, The development of neural stem cells. *Nature* **414**, 112–117 (2001). doi: [10.1038/35102174](https://doi.org/10.1038/35102174); pmid: [11689956](https://pubmed.ncbi.nlm.nih.gov/11689956/)
33. C. J. Burns *et al.*, Investigation of Frizzled-5 during embryonic neural development in mouse. *Dev. Dyn.* **237**, 1614–1626 (2008). doi: [10.1002/dvdy.21565](https://doi.org/10.1002/dvdy.21565); pmid: [18489003](https://pubmed.ncbi.nlm.nih.gov/18489003/)
34. D. M. Suter, D. Tirefort, S. Julien, K. H. Krause, A Sox1 to Pax6 switch drives neuroectoderm to radial glia progression during differentiation of mouse embryonic stem cells. *Stem Cells* **27**, 49–58 (2009). doi: [10.1634/stemcells.2008-0319](https://doi.org/10.1634/stemcells.2008-0319); pmid: [18832594](https://pubmed.ncbi.nlm.nih.gov/18832594/)
35. L. H. Pevny, S. Sockanathan, M. Placzek, R. Lovell-Badge, A role for SOX1 in neural determination. *Development* **125**, 1967–1978 (1998). doi: [10.1242/dev.125.10.1967](https://doi.org/10.1242/dev.125.10.1967); pmid: [9550729](https://pubmed.ncbi.nlm.nih.gov/9550729/)
36. J. Fu, A. Warmflash, M. P. Lutolf, Stem-cell-based embryo models for fundamental research and translation. *Nat. Mater.* **20**, 132–144 (2021). doi: [10.1038/s41563-020-00829-9](https://doi.org/10.1038/s41563-020-00829-9); pmid: [33199861](https://pubmed.ncbi.nlm.nih.gov/33199861/)
37. G. M. Schreckenberg, A. G. Jacobson, Normal stages of development of the axolotl, *Ambystoma mexicanum*. *Dev. Biol.* **42**, 391–400 (1975). doi: [10.1016/0012-1606\(75\)90343-7](https://doi.org/10.1016/0012-1606(75)90343-7); pmid: [1167837](https://pubmed.ncbi.nlm.nih.gov/1167837/)
38. Z. Li *et al.*, M-CSF, IL-6, and TGF- β promote generation of a new subset of tissue repair macrophage for traumatic brain injury recovery. *Sci. Adv.* **7**, eabb6260 (2021). doi: [10.1126/sciadv.abb6260](https://doi.org/10.1126/sciadv.abb6260); pmid: [33712456](https://pubmed.ncbi.nlm.nih.gov/33712456/)
39. R. Seijffers, C. D. Mills, C. J. Woolf, ATF3 increases the intrinsic growth state of DRG neurons to enhance peripheral nerve regeneration. *J. Neurosci.* **27**, 7911–7920 (2007). doi: [10.1523/JNEUROSCI.5313-06.2007](https://doi.org/10.1523/JNEUROSCI.5313-06.2007); pmid: [17652582](https://pubmed.ncbi.nlm.nih.gov/17652582/)
40. A. Rodrigo Albors *et al.*, Planar cell polarity-mediated induction of neural stem cell expansion during axolotl spinal cord regeneration. *eLife* **4**, e10230 (2015). doi: [10.7554/eLife.10230](https://doi.org/10.7554/eLife.10230); pmid: [26568310](https://pubmed.ncbi.nlm.nih.gov/26568310/)
41. W. Renthall *et al.*, Transcriptional Reprogramming of Distinct Peripheral Sensory Neuron Subtypes after Axonal Injury. *Neuron* **108**, 128–144.e9 (2020). doi: [10.1016/j.neuron.2020.07.026](https://doi.org/10.1016/j.neuron.2020.07.026); pmid: [32810432](https://pubmed.ncbi.nlm.nih.gov/32810432/)
42. G. H. D. Poplawski *et al.*, Injured adult neurons regress to an embryonic transcriptional growth state. *Nature* **581**, 77–82 (2020). doi: [10.1038/s41586-020-2200-5](https://doi.org/10.1038/s41586-020-2200-5); pmid: [32376949](https://pubmed.ncbi.nlm.nih.gov/32376949/)
43. W. D. Snider, F.-Q. Zhou, J. Zhong, A. Markus, Signaling the pathway to regeneration. *Neuron* **35**, 13–16 (2002). doi: [10.1016/S0896-6273\(02\)00762-6](https://doi.org/10.1016/S0896-6273(02)00762-6); pmid: [12123603](https://pubmed.ncbi.nlm.nih.gov/12123603/)
44. A. Faissner, L. Roll, U. Theodoridis, Tenascin-C in the matrisome of neural stem and progenitor cells. *Mol. Cell. Neurosci.* **81**, 22–31 (2017). doi: [10.1016/j.mcn.2016.11.003](https://doi.org/10.1016/j.mcn.2016.11.003); pmid: [27836730](https://pubmed.ncbi.nlm.nih.gov/27836730/)
45. M. A. Mouthon *et al.*, Syndecan-1 stimulates adult neurogenesis in the mouse ventricular-subventricular zone after injury. *iScience* **23**, 101784 (2020). doi: [10.1016/j.isci.2020.101784](https://doi.org/10.1016/j.isci.2020.101784); pmid: [33294792](https://pubmed.ncbi.nlm.nih.gov/33294792/)
46. I. Dutto, M. Tillhon, O. Cazzalini, L. A. Stivala, E. Prosperi, Biology of the cell cycle inhibitor p21(CDKN1A): Molecular mechanisms and relevance in chemical toxicology. *Arch. Toxicol.* **89**, 155–178 (2015). doi: [10.1007/s00204-014-1430-4](https://doi.org/10.1007/s00204-014-1430-4); pmid: [25514883](https://pubmed.ncbi.nlm.nih.gov/25514883/)
47. D. Mademtoglou *et al.*, Cellular localization of the cell cycle inhibitor Cdkn1c controls growth arrest of adult skeletal muscle stem cells. *eLife* **7**, e33337 (2018). doi: [10.7554/eLife.33337](https://doi.org/10.7554/eLife.33337); pmid: [30284969](https://pubmed.ncbi.nlm.nih.gov/30284969/)
48. F. Calejari, W. Haubensack, C. Haffner, W. B. Huttner, Selective lengthening of the cell cycle in the neurogenic subpopulation of neural progenitor cells during mouse brain development. *J. Neurosci.* **25**, 6533–6538 (2005). doi: [10.1523/JNEUROSCI.0778-05.2005](https://doi.org/10.1523/JNEUROSCI.0778-05.2005); pmid: [16014714](https://pubmed.ncbi.nlm.nih.gov/16014714/)
49. X. Qiu *et al.*, Mapping transcriptomic vector fields of single cells. *Cell* **185**, 690–711.e45 (2022). doi: [10.1016/j.cell.2021.12.045](https://doi.org/10.1016/j.cell.2021.12.045); pmid: [35108499](https://pubmed.ncbi.nlm.nih.gov/35108499/)
50. K. K. Park, K. Liu, Y. Hu, J. L. Kanter, Z. He, PTEN/mTOR and axon regeneration. *Exp. Neurol.* **223**, 45–50 (2010). doi: [10.1016/j.expneurol.2009.12.032](https://doi.org/10.1016/j.expneurol.2009.12.032); pmid: [20079353](https://pubmed.ncbi.nlm.nih.gov/20079353/)
51. M. Charni, R. Aloni-Grinstein, A. Molchadsky, V. Rotter, p53 on the crossroad between regeneration and cancer. *Cell Death Differ.* **24**, 8–14 (2017). doi: [10.1038/cdd.2016.117](https://doi.org/10.1038/cdd.2016.117); pmid: [27768121](https://pubmed.ncbi.nlm.nih.gov/27768121/)
52. G. La Manno *et al.*, RNA velocity of single cells. *Nature* **560**, 494–498 (2018). doi: [10.1038/s41586-018-0414-6](https://doi.org/10.1038/s41586-018-0414-6); pmid: [30089906](https://pubmed.ncbi.nlm.nih.gov/30089906/)
53. F. Pedregosa *et al.*, Scikit-learn: Machine learning in Python. *J. Mach. Learn. Res.* **12**, 2825–2830 (2011).
54. X. Qiu *et al.*, Single-cell mRNA quantification and differential analysis with Census. *Nat. Methods* **14**, 309–315 (2017). doi: [10.1038/nmeth.4150](https://doi.org/10.1038/nmeth.4150); pmid: [28114287](https://pubmed.ncbi.nlm.nih.gov/28114287/)
55. J. Cao *et al.*, The single-cell transcriptional landscape of mammalian organogenesis. *Nature* **566**, 496–502 (2019). doi: [10.1038/s41586-019-0969-x](https://doi.org/10.1038/s41586-019-0969-x); pmid: [30787437](https://pubmed.ncbi.nlm.nih.gov/30787437/)
56. Y. Liu, S. Wang, W. Feng, Y. Yang, X. Wei, Codes for the paper “Single-cell Stereo-seq reveals induced progenitor cells involved in axolotl brain regeneration”. <https://doi.org/10.5281/zenodo.6792037> (2022). doi: [10.5281/zenodo.6792037](https://doi.org/10.5281/zenodo.6792037)

ACKNOWLEDGMENTS

We thank L. Bolund, G. Volpe, and I. Seim for critical reading of the manuscript. **Funding:** This work was supported by the National

Key R&D Program of China (2019YFE0106700, 2021YFA0805000, 2021YFA1100500), Strategic Priority Research Program of the Chinese Academy of Sciences (Grant No. XDA16010000), the Guangdong Provincial Key Laboratory of Genome Read and Write (2017B030301011), the Shenzhen Key Laboratory of Single-Cell Omics (No. ZDSYS20190902093613831), the National Natural Science Foundation of China (32171289, 31970619, 31970782), the Innovative Research Group Program of Hubei Province (2020CFA017), the High-level Hospital Construction Project of Guangdong Provincial People's Hospital (DFJHBF202103, KJ012021012), Project of Department of Education of Guangdong Province (2018KZDXM027), Key-Area Research and Development Program of Guangdong Province (2018B030332001, 2019B030335001), and Guangdong-Hong Kong-Macao-Joint Laboratory Program (2019B121205005). **Author contributions:** X.W., Y.G., J.-F.F., X.X., L.C., and H.L. conceived the idea; Y.G., J.-F.F., X.X., L.C., and H.L. supervised the work; X.W., S.F., H.L., and J.-F.F. designed the experiments; S.F., X.L., and N.Z. performed the majority of the experiments with help from M.C., J.J., J.X., Y.Z., P.L., X.S., and C.P.; X.W., Y.L., S.W., W.F., and Y.Y. performed data analysis; M.K. and T.Y. performed database construction; Y.L., X.Q., L.W., L.H., L.C., Y.Y., X.P., S.G., A.C., M.A.E., H.Y., J.W., G.F., and L.L. gave relevant advice; H.L., Y.G., L.C., J.-F.F., and X.W. wrote the manuscript with input from all authors. **Competing interests:** The authors declare no conflicts of interest. **Data and materials availability:** All data generated in this study are freely accessible in CNGB Nucleotide Sequence Archive under accession code CNP0002068. All other data are in the main paper or the supplementary materials. All code used to analyze the data is available online at <https://github.com/BGI-DEV-REG/ARTISTA> (56). Processed data can be interactively explored and downloaded from <https://db.cngb.org/stomics/artista/>. **License information:** Copyright © 2022 the authors, some rights reserved; exclusive licensee American Association for the Advancement of Science. No claim to original US government works. www.science.org/about/science-licenses-journal-article-reuse

SUPPLEMENTARY MATERIALS

science.org/doi/10.1126/science.abp9444

Materials and Methods

Figs. S1 to S17

Tables S1 to S7

References (57–71)

Submitted 8 March 2022; accepted 6 July 2022

10.1126/science.abp9444

RESEARCH ARTICLE SUMMARY

NEUROEVOLUTION

Cell-type profiling in salamanders identifies innovations in vertebrate forebrain evolution

Jamie Woych[†], Alonso Ortega Gurrola[†], Astrid Deryckere[†], Eliza C. B. Jaeger[†], Elias Gumnit[†], Gianluca Merello, Jiacheng Gu, Alberto Joven Araus, Nicholas D. Leigh, Maximina Yun, Andrés Simon, Maria Antonietta Tosches*

INTRODUCTION: During vertebrate evolution, the first tetrapods transitioning from water to land were confronted with new environmental challenges that required adaptive innovations in the nervous system. These innovations are exemplified in the six-layered neocortex and the dorsal ventricular ridge (DVR) of present-day mammals and sauropsids (reptiles and birds), respectively. The neocortex and DVR bear extensive similarities in terms of gene expression, connectivity, and function and therefore were thought to be homologous. However, recent developmental and adult gene expression data challenge this view, suggesting that similar molecular and functional attributes may instead have arisen through convergent evolution, not a common origin. According to this alternative view, the mammalian neocortex and sauropsid DVR arose from distinct parts of the pallium: the neocortex from the expansion of a simple three-layered cortex in the dorsal pallium of amniote ancestors and the DVR from an expansion of the ventral pallium.

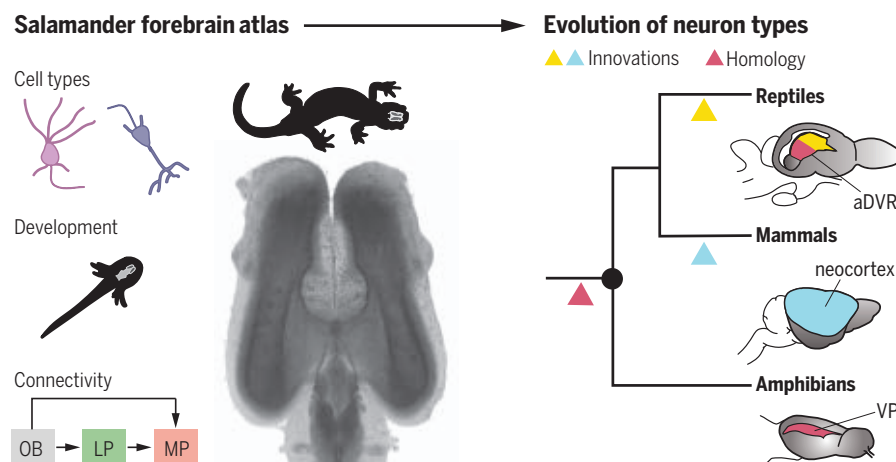
RATIONALE: If the neocortex and DVR have separate evolutionary origins, then they may

trace back to distinct pallial regions that existed in a preamniote ancestor. Amphibians diverged from other tetrapods >350 million years ago and therefore can provide crucial insights into the evolutionary history of the tetrapod brain. The amphibian telencephalon is relatively small and anatomically simple, devoid of obvious nuclei or layering, thus facilitating analysis of the entire structure. Using the salamander *Pleurodeles waltl*, a species with a true postmetamorphic adult stage, we investigated whether amphibian neuron types have transcriptomic similarity to neurons from the neocortex or DVR, probed their developmental trajectories, and characterized broad connectivity patterns.

RESULTS: Using single-cell RNA sequencing (scRNA-seq), we built a cell-type atlas of the salamander telencephalon, revealing 47 clusters of glutamatergic neurons and 67 clusters of GABAergic neurons—a greater degree of complexity and diversity than anticipated. We then mapped the expression of marker genes from select clusters using classic histology and hybridization chain reaction in situ hy-

bridization in cleared brains. This resulted in a three-dimensional molecular map of the salamander brain, displaying the distribution of distinct pallial regions along the mediolateral and radial axes. To characterize the developmental history of these neurons, we performed scRNA-seq on the larval *P. waltl* brain at four developmental stages. We found distinct developmental trajectories for each pallial division, indicating that distinct genetic programs specify the salamander dorsal pallium (DP) and ventral pallium (VP). To compare telencephalic neuron types across tetrapod species, we used manifold integration algorithms on scRNA-seq data from adult salamanders, reptiles (lizards and turtles), and mammals. The salamander VP shows molecular similarity to parts of the reptilian anterior DVR (aDVR), whereas the dorsomedial pallia share molecular similarities with neurons from the mammalian hippocampus, entorhinal cortex, and subiculum, but not the neocortex. This indicates that the salamander DP lacks cellular and molecular characteristics of the mammalian neocortex and is instead more similar to mammalian cortical areas intercalated between the neocortex and hippocampus. Finally, we determined whether these molecular similarities between tetrapod species are reflected in mesoscale connectivity patterns. We confirmed that salamander VP connectivity patterns resemble in part those of the reptilian aDVR and that components of the mammalian olfactory-entorhinal-hippocampal circuit exist in the salamander lateral, dorsal, and medial pallia.

CONCLUSION: These findings suggest that the aDVR in sauropsids is composed of at least two sets of neuron types with distinct evolutionary origins. While one set can be traced back to a specialized region of the anterior ventral pallium in the tetrapod ancestor, the other one is a sauropsid novelty. Additionally, we propose that pyramidal neuron types in the mammalian six-layered neocortex are evolutionary novelties that arose by changes in the gene-regulatory programs specifying ancestral types. These findings corroborate the hypothesis that the functional similarities of the DVR and neocortex are the result of convergence instead of homology. The mammalian olfactory-entorhinal-hippocampal circuit, however, may trace back to a circuit with a simpler architecture that was already present in the last common ancestor of tetrapods. ■



Reconstructing the evolution of neuron types in the vertebrate telencephalon. Amphibians are key to reconstructing the evolution of the vertebrate brain after the transition from water to land. An atlas of the salamander telencephalon, including transcriptomic profiling of cell types, developmental trajectories, and connectivity, offers new insights into the homologies and innovations of the vertebrate brain.

The list of author affiliations is available in the full article online.

*Corresponding author. Email: mt3353@columbia.edu

[†]These authors contributed equally to this work.

Cite this article as J. Woych et al., *Science* 377, eabp9186 (2022). DOI: 10.1126/science.abp9186

S READ THE FULL ARTICLE AT
https://doi.org/10.1126/science.abp9186

RESEARCH ARTICLE

NEUROEVOLUTION

Cell-type profiling in salamanders identifies innovations in vertebrate forebrain evolution

Jamie Woych^{1†}, Alonso Ortega Gurrola^{1,2†}, Astrid Deryckere^{1†}, Eliza C. B. Jaeger^{1†}, Elias Gumnit^{1†}, Gianluca Merello¹, Jiacheng Gu¹, Alberto Joven Arous³, Nicholas D. Leigh⁴, Maximina Yun^{5,6}, Andrés Simon³, Maria Antonietta Tosches^{1*}

The evolution of advanced cognition in vertebrates is associated with two independent innovations in the forebrain: the six-layered neocortex in mammals and the dorsal ventricular ridge (DVR) in sauropsids (reptiles and birds). How these innovations arose in vertebrate ancestors remains unclear. To reconstruct forebrain evolution in tetrapods, we built a cell-type atlas of the telencephalon of the salamander *Pleurodeles waltl*. Our molecular, developmental, and connectivity data indicate that parts of the sauropsid DVR trace back to tetrapod ancestors. By contrast, the salamander dorsal pallium is devoid of cellular and molecular characteristics of the mammalian neocortex yet shares similarities with the entorhinal cortex and subiculum. Our findings chart the series of innovations that resulted in the emergence of the mammalian six-layered neocortex and the sauropsid DVR.

The transition from water to land was a pivotal moment in vertebrate history that exposed the first tetrapods to new environmental and cognitive challenges, which may have accelerated adaptive innovations in the nervous system (1). After the divergence of mammals and sauropsids (reptiles and birds) ~320 million years ago, innovations in the pallium (i.e., the dorsal telencephalon) paved the way for advanced cognition. In mammals, the neocortex, with its characteristic six layers, evolved from a simpler ancestral cortex located in the dorsal pallium (2). In sauropsids, an expansion of the ventral pallium produced a large set of nuclei called the dorsal ventricular ridge (DVR) (Fig. 1A). Although neocortex and DVR develop from different parts of the pallium, they bear extensive similarities in terms of gene expression, connectivity, and function (3–5). A model centered on brain connectivity proposes the homology of neocortex and DVR, implying that differences in neocortex and DVR development and topological positions arose secondarily (6). Developmental studies (2) and adult transcriptomics data (7, 8) challenge this view, suggesting that the DVR and neocortex have separate evolutionary origins in amniote ancestors, and there-

fore similar functions were acquired independently. However, the origin of innovations that led to the DVR and neocortex remains poorly understood at the molecular and cellular levels.

We reasoned that if neocortex and DVR have separate origins, then they may trace back to pallial regions that existed in a pre-amniote ancestor. Amphibians, which diverged from other tetrapods ~350 million years ago, have a seemingly simple telencephalic architecture that is devoid of obvious layering or large brain nuclei (Fig. 1B). Both a dorsal and a ventral pallium exist in amphibians (9), but it is unclear whether they are related in any way to neocortex and DVR. Here, we analyzed the telencephalon of *Pleurodeles waltl*, a salamander species with a true adult (postmetamorphic) stage, to determine the following: (i) Are there neuron types in the amphibian pallium with transcriptomic similarity to neocortical or DVR neurons? (ii) if so, then how do these neurons develop?; and (iii) do these neurons display patterns of connectivity similar to neocortex or DVR?

Results

A cell-type atlas of the salamander telencephalon

To build a cell-type atlas of the salamander telencephalon, we profiled entire brains and microdissected telencephali of adult *P. waltl* (see brain atlas in fig. S1 and movie S1). After single-cell RNA sequencing (scRNA-seq, 10x Genomics), reads were mapped on a new long-read de novo reference transcriptome (see the materials and methods). After quality filtering, we obtained 36,116 single-cell transcriptomes, performed Louvain clustering, and identified 11 major populations of neuronal and non-neuronal cells (Fig. 1C and fig. S2).

We annotated clusters of differentiated neurons, immature neurons, ependymogial cells, microglia, oligodendrocytes, oligodendrocyte precursors, and other non-neuronal cells based on well-established marker genes (Fig. 1D and fig. S2C). Differentiated neurons (29,294 cells), identified by the expression of pan-neuronal markers such as *Snap25*, *Syt1*, and *Rbfox3* (i.e., NeuN), were subclustered to classify neuron types. This revealed 47 clusters of glutamatergic neurons and 67 clusters of γ -aminobutyric acid-releasing (GABAergic) neurons, which we annotated on the basis of marker genes with conserved expression across species, in situ hybridization for cluster-specific markers, and existing amphibian literature [reviewed in (10, 11)] (Fig. 1, E and F, and figs. S3 to S8).

In the salamander telencephalon, hierarchical clustering revealed four distinct groups of glutamatergic clusters (fig. S4A). One expressed *Neurod2* and *Slc17a7* (*Vglut1*) at high levels, and we named this group “cortical pallium” for its molecular similarity to the cerebral cortex of mammals and reptiles (12, 13). The remaining groups included olfactory bulb (OB) mitral and tufted cells expressing the transcription factor *Tbx21* (14), amygdala neurons expressing lower levels of *Slc17a7* and *Neurod2* and high levels of *Slc17a6* (*Vglut2*), and glutamatergic neurons in the septum expressing *Slc17a6*, *Zic2*, and *Isl1* (Fig. 1, E and F, and fig. S4A).

Telencephalic GABAergic neurons express markers of the subpallium, such as *Dlx5*, *Gad1*, and *Gad2*. We found that the amphibian subpallium includes not only neurons from lateral and medial ganglionic eminences (LGE and MGE, respectively), as previously shown (15, 16), but also from the caudal ganglionic eminence (CGE). We identified several types of striatal and septal neurons, nucleus accumbens, bed nucleus of the stria terminalis, and diagonal band neurons, as well as OB LGE-derived GABAergic interneurons (figs. S4A and S5, A to E). Telencephalic GABAergic interneurons, scattered throughout the pallium, included MGE- and CGE-derived cells (fig. S5F). These data indicate that despite its anatomical simplicity, the amphibian telencephalon harbors a greater degree of cell-type diversity than anticipated.

Spatial distribution of pallial glutamatergic neurons

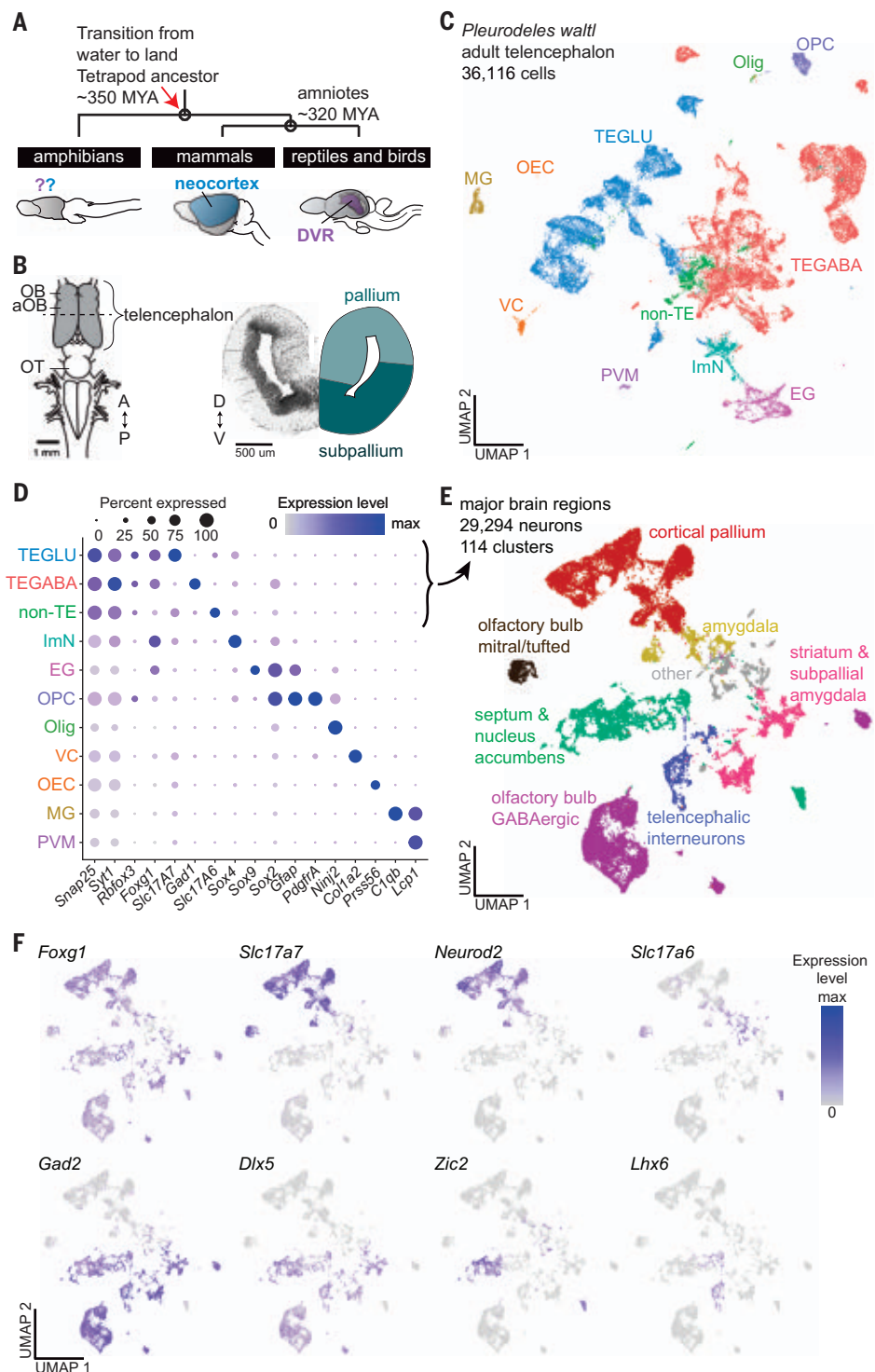
The literature indicates that the amphibian pallium is organized along the mediolateral axis in four regions called the medial, dorsal, lateral, and ventral pallium (MP, DP, LP, and VP, respectively) (9, 17), but precise boundaries and further subdivisions are a matter of dispute (18, 19) (see the supplementary text for a discussion about nomenclature). To clarify the organization of the amphibian telencephalon including the pallium, we associated clusters from scRNA-seq to their spatial

¹Department of Biological Sciences, Columbia University, New York, NY 10027, USA. ²Department of Neuroscience, Columbia University, New York, NY 10027, USA. ³Department of Cell and Molecular Biology, Karolinska Institute, SE-171 77 Stockholm, Sweden. ⁴Molecular Medicine and Gene Therapy, Wallenberg Centre for Molecular Medicine, Lund Stem Cell Center, Lund University, 221 84 Lund, Sweden. ⁵Technische Universität Dresden, CRTD/Center for Regenerative Therapies Dresden, 01307 Dresden, Germany. ⁶Max Planck Institute for Molecular Cell Biology and Genetics, 01307 Dresden, Germany.

*Corresponding author. Email: mt3353@columbia.edu

†These authors contributed equally to this work.

Fig. 1. Neuronal diversity in the *P. waltl* telencephalon. (A) Schematic highlighting the phylogenetic position of amphibians, the mammalian neocortex, and the reptilian DVR. (B) Left: schematic of the *P. waltl* brain (dorsal view). Dotted line indicates the section plane for the coronal slice on the right. (C) Uniform Manifold Approximation and Projection (UMAP) plot of 36,116 salamander single-cell transcriptomes; colors indicate cell classes. (D) Dotplot showing the expression of marker genes used to annotate the telencephalic dataset in (C). (E) UMAP plot of 29,294 single-cell transcriptomes of salamander neurons; colors indicate major brain regions. (F) UMAP plots showing expression of key markers of glutamatergic and GABAergic neurons in the neuronal dataset. A, anterior; aOB, accessory OB; D, dorsal; EG, ependymoglia; GLU, glutamatergic; ImN, immature neurons; MG, microglia; MYA, million years ago; OEC, olfactory ensheathing cells; Olig, oligodendrocytes; OPC, oligodendrocyte precursor cells; OT, optic tectum; P, posterior; PVM, perivascular macrophages; TE, telencephalic; V, ventral; VC, vascular cell.



origin and built a transcriptomics-based map of the telencephalon in *P. waltl*.

Hierarchical clustering of average cluster expression profiles indicates a clear distinction between cortical pallium and amygdala and the existence of four groups of cortical pallium clusters (Fig. 2, A and B, and fig. S4, A and B). As shown by in situ hybridization for specific marker genes (Fig. 2C), the four

groups largely correspond to MP, DP, LP, and VP. In mid-telencephalic sections, the MP, which is comparable to the hippocampus in its position and connectivity, expresses hippocampal transcription factors such as *Foxg2*, *Lhx9*, *Zbtb20*, and *Etv1* (7, 20). The DP, anatomically distinct from the MP, expresses low levels of MP markers but high levels of *Etv1*. The LP, a narrow band of densely packed neurons, ex-

presses *Lhx2*, *Satb1*, *Rorb*, and *Reln*, markers of olfactory-recipient cells in the mammalian piriform cortex (semilunar cells) (21). Most of the VP expresses the transcription factor *Sox6* and is molecularly diverse, which is consistent with its anatomical heterogeneity (9, 22). Subdivisions of VP include a *Nos1*-negative anterior VP (VPa) and a *Nos1*⁺ posterior VP (VPP) [see also (16)]. Along the anterior-posterior

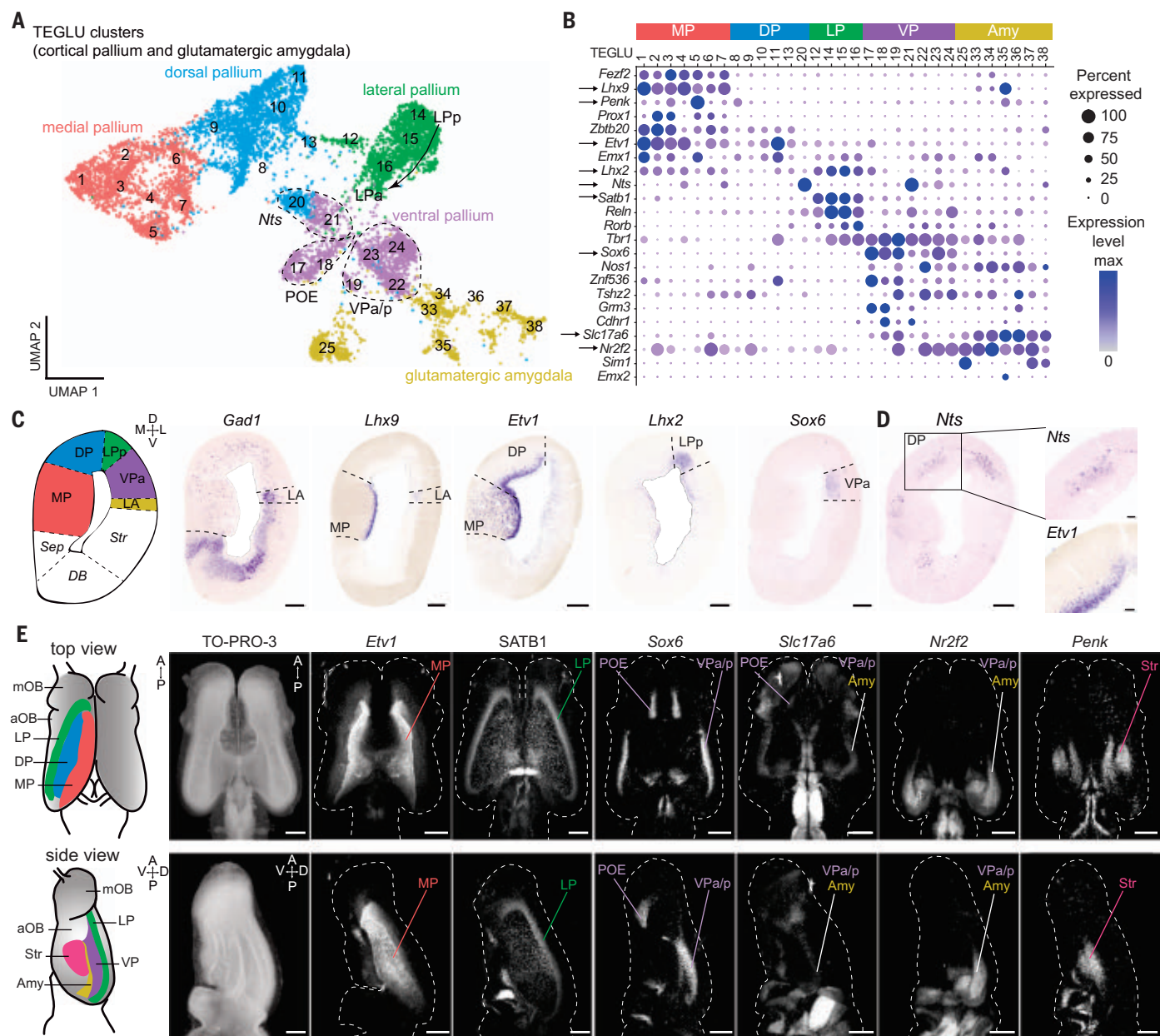


Fig. 2. Spatial mapping of pallial neurons in *P. waltl*. (A) UMAP plot of clusters from cortical pallium and amygdala, annotated by the inferred pallial region. TEGLU, telencephalic glutamatergic. (B) Dotplot showing the expression of key marker genes defining distinct pallial regions. Arrows indicate the genes shown in (C) to (E). (C) Left to right: schematic of a coronal section at the mid-telencephalic level; expression of *Gad1*, a marker of the subpallium, and of transcription factors labeling distinct pallial regions along the mediolateral axis. Scale bars: 200 μ m. (D) Expression

of *Nts* and *Etv1* in layers, boxed areas indicate magnifications on the right. Scale bars in right panels: 50 μ m. (E) Left: schematics of dorsal and lateral surfaces of the salamander telencephalon. Right: dorsal and lateral views of whole-mount immunohistochemistry or HCR stainings for telencephalic markers. Panels show maximum intensity projections of brains after clearing and volumetric light-sheet imaging. Scale bars: 500 μ m. See methods for specifics on SATB1 antibody. Amy, amygdala; for a full list of abbreviations, see fig. S1.

axis, *Slc17a6* is expressed only in the most ventral portion of the VP, suggesting the existence of further diversity along the mediolateral axis; *Slc17a6* is expressed at higher levels in the adjacent amygdala, as described in (23) (figs. S6 to S8 and movies S2 and S3). In addition to these subdivisions of VP, we found expression of *Sox6*, *Znf536*, and *Grm3* in an anterior pallial region, which is not continuous with VP but instead is nested between the OB and the

septum and corresponds to the amphibian postolfactory eminence (POE) (24, 25).

A closer look at *Nts*, a marker expressed at high levels in two clusters (Fig. 2B), revealed differential expression along the radial axis. Visualization of *Nts* expression in tandem with genes expressed in cells closer to the ventricle (e.g., *Etv1* in MP/DP) demonstrates that *Nts* demarcates a discrete, superficial layer of the pallium (Fig. 2D and fig. S6H). These results

suggest that the amphibian pallium contains at least two separate layers of distinct neuron types.

To resolve the three-dimensional (3D) organization of the pallium, we exploited the relatively small size of the salamander brain to combine whole-mount hybridization chain reaction (HCR) in situ hybridization, brain clearing [immunolabeling-enabled 3D imaging of solvent-cleared organs (iDISCO)], and light-sheet

imaging, creating a 3D molecular map (Fig. 2E, fig. S7, and movies S2 and S3). This revealed that the cortical pallium is organized in adjacent longitudinal stripes running the length of the telencephalic vesicle (Fig. 2E). For example, the LP extends from the most rostral tip of the pallium, where it contacts the main OB (mOB) and the POE, to the caudal tip of the telencephalon. The amygdala is localized caudally and is demarcated by the expression of *Slc17a6* and *Nr2f2* and the absence of *Sox6* (Fig. 2E, figs. S7 and S8, and movies S2 and S3). Together, these data represent a transcriptomics-based map of the amphibian pallium and support the existence of distinct regions along the mediolateral axis and distinct layers along the radial axis.

Developmental trajectories of DP and VP

How regions of the amphibian pallium compare with distinct regions of the mammalian and sauropsid pallium, including the hippocampus, olfactory cortex, and amygdala, remains debated (10, 26, 27). Current models postulate that pallial regions are homologous when they develop from homologous progenitor domains (17, 28, 29). To trace the developmental history of *P. waltil* pallial neuron types, we collected scRNA-seq data from stage 36, 41, 46, and 50 larvae (Fig. 3, A and B, and fig. S9A) [see also (30)]. After unsupervised clustering, we identified radial glia and telencephalic glutamatergic and GABAergic developing neurons (Fig. 3, C and D, and fig. S9, B and C). To assign developing neurons to their terminal fate in the adult telencephalon, we mapped adult scRNA-seq data on developmental data using the Seurat label-transfer algorithm (see the materials and methods) (31). This showed that our larval dataset included differentiating neurons from all major pallial and subpallial subdivisions (Fig. 3C and fig. S9C). We then inferred developmental trajectories for differentiation into OB mitral and tufted cells, amygdala, VP, LP, DP, and MP with Slingshot (32) (Fig. 3E). After re-ordering cells according to their pseudotime score, we compared gene expression along the DP and VP trajectories (fig. S9D). Transcription factors up-regulated along the dorsal trajectory included *Lhx2*, *Sox8*, and *Nfix*. Transcription factors up-regulated along the ventral trajectory included *Pbx3* and *Sox6*, which are also expressed in the developing mouse ventral pallium (33) (Fig. 3, F and G). This indicates that neurons in the DP and VP are specified by distinct gene-regulatory cascades, possibly controlled by medial *wnt* signaling and ventrolateral *wnt* antagonists (29). This analysis thus highlights clear differences in the specification of salamander DP and VP neurons, demonstrating that the distinct DP and VP clusters identified in the adult data have their own developmental programs that rely on evolutionarily conserved transcription factor networks.

Comparison of salamander VP and reptilian anterior DVR

To identify neuron types with similar gene expression profiles in salamanders, reptiles, and mammals, we compared scRNA-seq datasets using manifold integration algorithms. We compared several data integration algorithms (fig. S11 and supplementary text) and present here the results obtained using Seurat, an algorithm based on the identification of mutual nearest neighbors across single-cell datasets (see the materials and methods) (31). For consistency and to facilitate data analysis, we limited data integration to single cells sampled from the same brain regions. We integrated our salamander dataset with data from the telencephalon of the agamid lizard *Pogona vitticeps* (34, 35) and from the pallium of the red-eared slider turtle *Trachemys scripta* [which also includes cells from the neighboring subpallium (7)]. Clustering of the Seurat integrated data yielded 65 clusters, which we refer to as integrated clusters. Results from the Seurat integration were largely recapitulated by using alternative parameters in the integration pipeline, as well as alternative integration algorithms (Harmony, SAMap, and scVI; see the supplementary text and figs. S11 and S12). Hierarchical clustering of average gene expression in integrated clusters produced a cross-species taxonomy of telencephalic neuron types (Fig. 4, A to C, and fig. S13).

This kind of analysis is built on molecular similarities of cells that result from either homology or the convergent use of the same effector genes. Here, we observed co-clustering of salamander and reptilian cells from pallial regions that are considered homologous on the basis of independent criteria such as their relative position in the pallium (2, 17). For example, we found co-clustering of salamander MP and the reptilian medial cortex and of salamander LP and the reptilian lateral cortex. The salamander pallial amygdala (23) and reptilian posterior DVR (pDVR), putative homologs of the mammalian pallial amygdala (36), also co-clustered (Fig. 4D and fig. S13). For its position in the pallium and its connectivity, the amphibian VP is a putative homolog of the reptilian ventrolateral pallium, including the anterior DVR (aDVR) (37). We found that reptilian aDVR and salamander VP neurons co-clustered in two distinct neighborhoods, segregating into a total of six clusters (3, 13, 31, 58, 17, and 30). Integrated cluster 13 included salamander cells from the VPa/VPp and turtle and lizard cells from the centromedial aDVR, an area heavily connected with the hypothalamus (Fig. 4E) (7, 37). Integrated cluster 3, in the same neighborhood, included more cells from the lizard and turtle centromedial aDVR. Turtle, lizard, and salamander cells in clusters 13 and 3 shared expression of several transcription factors, including *Tbr1*,

Nr2f2, *Nr2f1*, and *Lmo3* (Fig. 4F), supporting the hypothesis that centromedial aDVR and VP have a shared evolutionary history.

In the second neighborhood, we found cells from the rostral part of the turtle and lizard aDVR (integrated clusters 17 and 30) and from the salamander POE (integrated clusters 58 and 17). The rostral aDVR is an area receiving sensory inputs (visual, somatosensory, and auditory) relayed by the thalamus (7, 37, 38) and expresses the transcription factors *Rorb* and *Satb1* at high levels (7), as well as specific effector genes such as the glutamate receptor *Grm3* and the potassium channel *Kcnh5* (Fig. 4, E and F). The salamander POE is a pallial region primarily involved in olfaction, as suggested by its proximity to and inputs from the OB (24, 25). In *P. waltil*, we found that *Rorb* and *Satb1* are coexpressed in POE (weakly) and LP, both pallial regions with prominent olfactory inputs, but not in the VPa/VPp (Fig. 4, F and G). Furthermore, other transcription factors with specific expression in the salamander POE are not expressed in the lizard or in the turtle rostral aDVR (fig. S14), indicating that the co-clustering of neurons from these regions is driven by effector genes. The lack of transcription factor conservation between these cell types may indicate convergent use of effector genes, because only transcription factors are believed to form core regulatory complexes that track cell types as evolutionary units (39). These results indicate that the salamander ventrolateral pallium comprises neuron types with molecular similarity to reptilian lateral cortex and centromedial aDVR. Furthermore, they suggest that the sensory-recipient neurons in the rostral aDVR may have evolved by recruiting effector genes involved in sensory processing in other pallial areas.

Molecular innovations in dorsal cortex and neocortex

To extend our molecular comparisons to mammals, we computed gene expression correlations between each salamander telencephalic cluster with digitized in situ hybridization data from the Allen Adult Mouse Brain Atlas (40) (Fig. 5A), which confirmed the molecular similarity of salamander subpallial regions with their mouse counterparts. Results for the pallium were more ambiguous. For example, salamander LP clusters correlated with hippocampus, neocortex, piriform cortex, and lateral amygdala; pallial amygdala clusters correlated with the entire mouse pallial amygdala and piriform cortex; and VP clusters correlated with mouse piriform cortex and lateral amygdala (Fig. 5A). This is consistent with the observation that VP expresses transcription factors with specific or enriched expression in the mouse piriform cortex, such as *Znf536* and *Tshz2* (Fig. 2B and fig. S8) (40, 41). Using

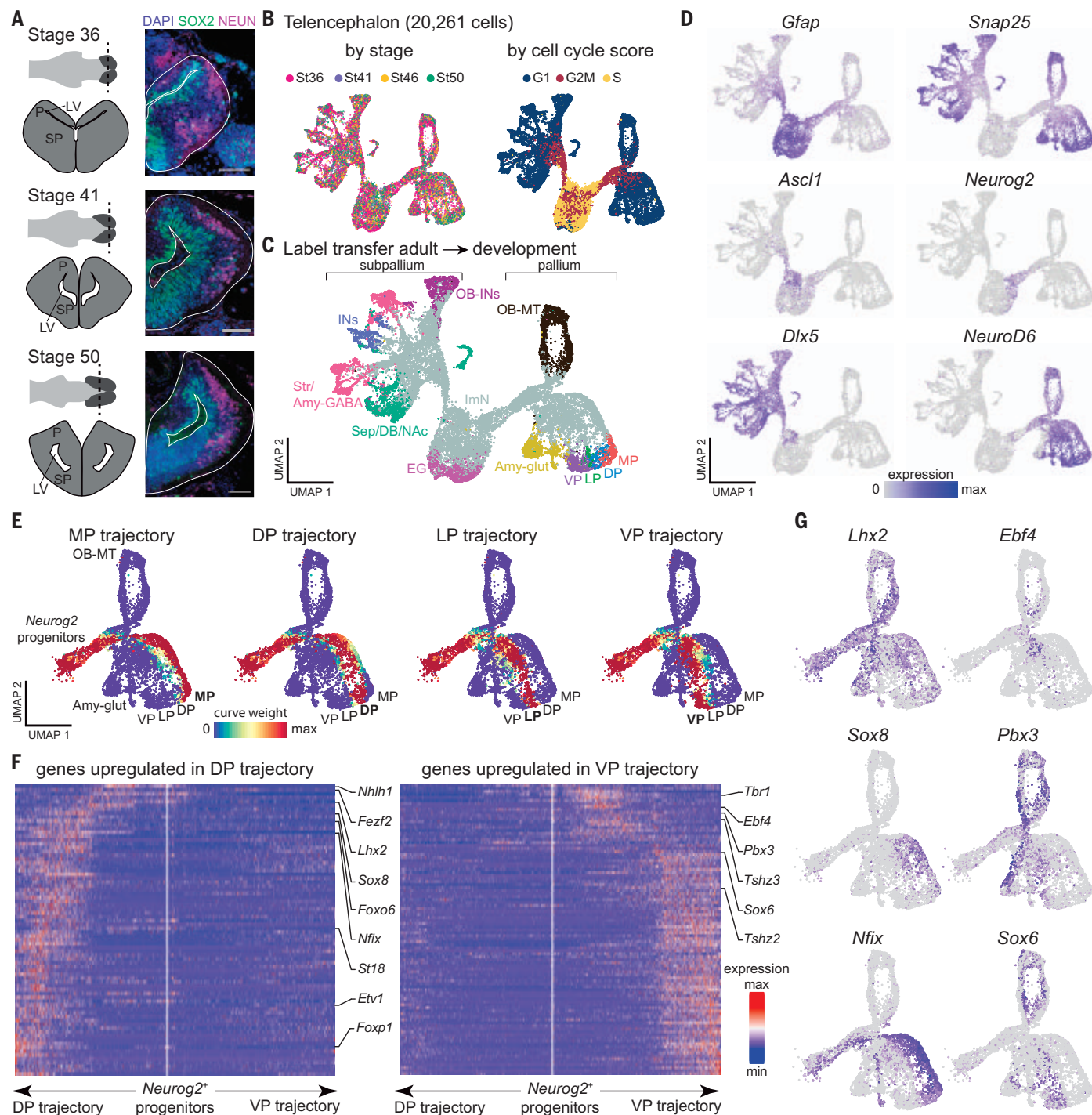


Fig. 3. Developmental trajectories in the *P. waltl* telencephalon. (A) Overview of telencephalic development in *P. waltl*. Right: coronal sections through the telencephalon showing SOX2⁺ radial glia and interneurons and NEUN⁺ differentiated neurons. Scale bars, 100 μ m. (B) UMAP plots of 20,261 telencephalic cells colored by developmental stage (left) and cell cycle score (right). (C) UMAP plot of the developing telencephalon, colored according to cell classes after label transfer from the adult dataset. (D) UMAP plots colored by the expression of *Gfap* (radial glia), *Snap25* (differentiated neurons), *Ascl1* and *Neurog2* (committed subpallial and pallial progenitors), and *Dlx5* and *NeuroD6* (post-mitotic subpallial and pallial neurons). (E) UMAP plots showing the assignment of cells to each of the trajectories on the basis of curve weights, which

represent the likelihood that a cell belongs to a given principal curve calculated by Slingshot. (F) Heatmaps of genes differentially expressed along the trajectories of the DP and VP, with transcription factors highlighted on the side. White line in the middle of each panel indicates the position of the *Neurog2*⁺ progenitors and arrows to the left and right represent the two trajectories. Gene expression levels for each gene are scaled by root mean square ranging from -2 to 6. (G) UMAP plots showing pallial single cells color-coded by expression of transcription factors up-regulated in the dorsal (left) or ventral (right) trajectory. EG, ependymoglia; ImN, immature neuron; LV, lateral ventricle; OB-MT, OB mitral and tufted cell; P, pallium; SP, subpallium; for a full list of abbreviations, see figs. S1 and S3.

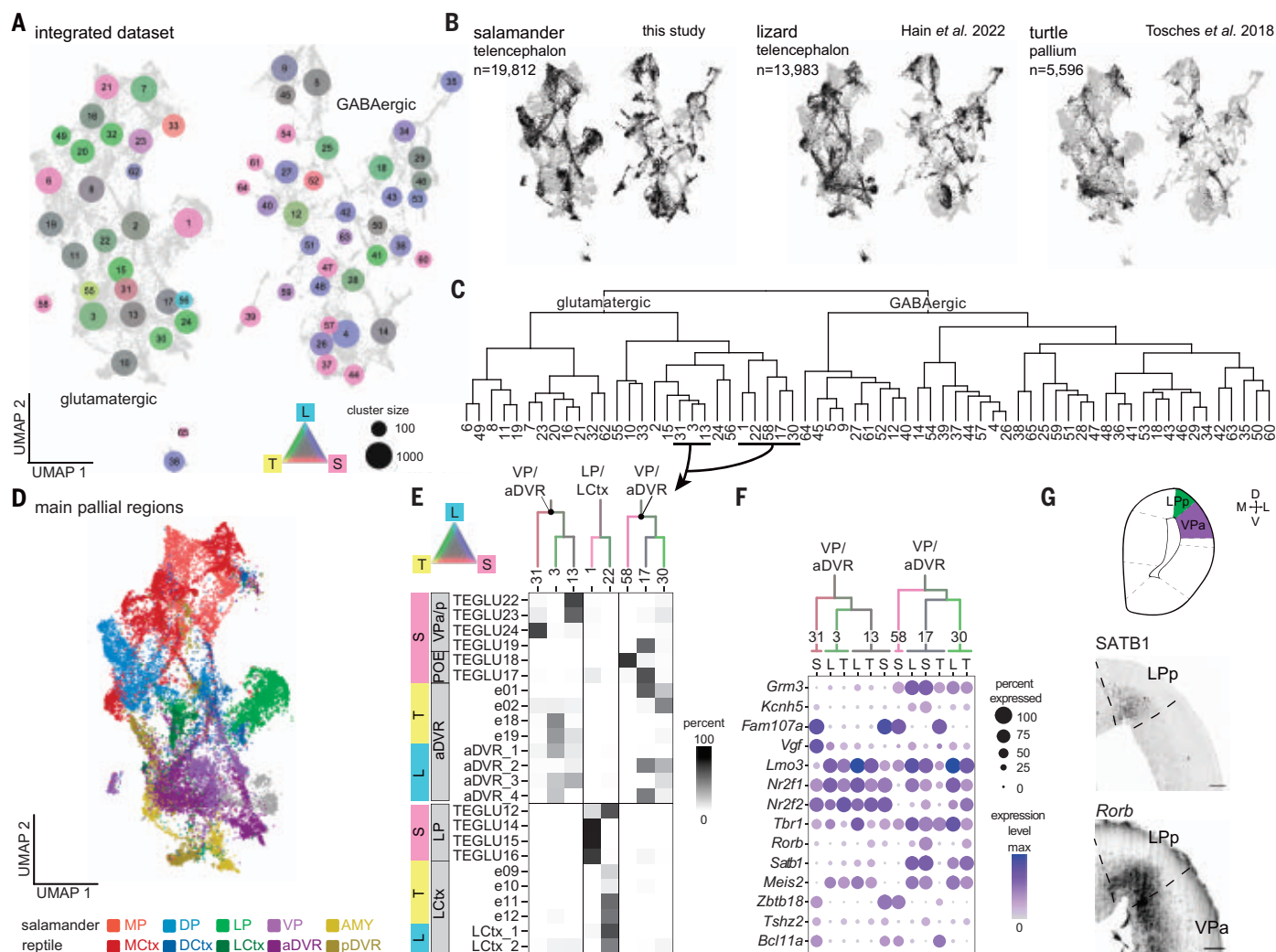


Fig. 4. Salamander and reptile telencephalon cross-species comparison.

(A) UMAP plot after integration of scRNA-seq data from the salamander and lizard telencephalon and from the turtle pallium. Dot colors indicate species mixture in each integrated cluster (gray represents an equal proportion of cells from each species). Dot size indicates the number of cells in each cluster. (B) UMAP plots of the integrated dataset showing cells from each species highlighted in black. (C) Hierarchical clustering of average expression profiles of the integrated clusters shown in (A). (D) UMAP plot of the glutamatergic clusters from the integrated dataset

colored by pallial region. (E) Top: ventrolateral portion of the dendrogram in (C), with branches colored by species mixture. Bottom: percentage of cells from the original species-specific clusters (rows) in the integrated clusters (columns). (F) Dotplot showing the expression of molecular markers in aDVR or VP in the integrated clusters, with cells from each integrated cluster split by species: L, lizard; S, salamander; and T, turtle. (G) Top: schematic of a coronal section at the mid-telencephalic level in the *P. waltl* brain. Bottom: presence of SATB1 and expression of *Rorb* in the salamander LP and VP. Scale bars, 100 μ m.

an alternative approach in which we mapped scRNA-seq data from the mouse telencephalon (42, 43) on our salamander single-cell dataset (see the materials and methods), we also found correspondence between the subpallial and hippocampal regions. However, using this method, mouse cortical pyramidal types could not be mapped to single salamander clusters, suggesting a high degree of transcriptional divergence (fig. S15).

We reasoned that the integration of scRNA-seq data was better suited for the identification of high-level similarities among salamander, reptilian, and mouse neuron types than mapping approaches. However, complete scRNA-seq data from the entire telencephalon of a

mammal are not yet available. In light of our results on development, we decided to focus on the derivatives of the dorsomedial pallium, which in mammals ranges from the hippocampus medially to the insular and entorhinal cortices laterally; complete mouse data are available for all of these cortical areas (43) (Fig. 5B). Telencephalic interneurons (44) were also included in this analysis. Salamander GABAergic interneurons co-clustered with amniote MGE-derived (Pvalb and Sst) and CGE-derived (Lamp5, Sncg, and Vip) interneuron classes (Fig. 5C and fig. S15B), indicating that these interneuron classes trace back to tetrapod ancestors. At deeper levels of interneuron classification, we found interneuron

types conserved in tetrapods, such as long-range projecting Sst Chodl neurons (cluster 13), and mammalian-specific types, such as Pvalb Vipr2 Chandelier cells (cluster 50) (Fig. 5C). Lamp5 interneurons included a nonmammalian subclass (cluster 34), a conserved subclass (cluster 17, Lamp5 Ndnf neurogliaform cells in mouse), and a mouse-specific subclass (cluster 49, Lamp5 Lhx6 cells) (45). The transcription factors that differentiate between mammalian Lamp5 Ndnf and Lamp5 Lhx6 interneurons are coexpressed in nonmammalian Lamp5 cells (cluster 34), suggesting that amniote or mammalian-specific Lamp5 types evolved by diversification of ancestral Lamp5 interneurons (Fig. 5D).

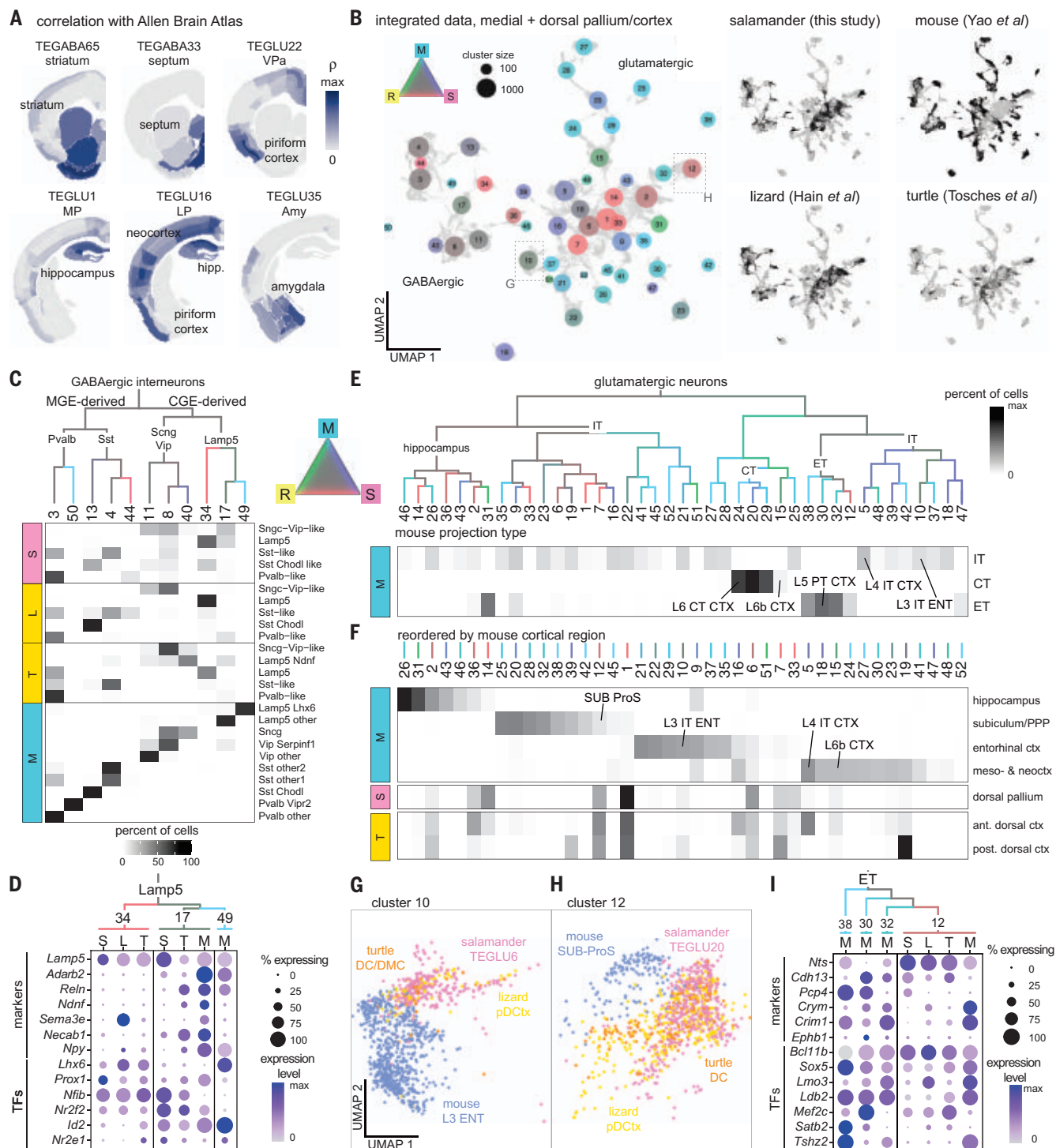


Fig. 5. Salamander, reptile, and mouse cross-species comparison. (A) Correlations of the transcriptome of selected *P. waltl* clusters with in situ hybridization data from the Allen Adult Mouse Brain Atlas. Correlation max is 0.3 for TEGABA33 and 0.2 for all others. (B) Integration of scRNA-seq data from the salamander MP and DP, the turtle and lizard (“reptile”) medial and dorsal cortex, and the mouse hippocampus and cortex. Left: UMAP of the integrated data with dots colored by species mixture; dot size indicates cluster size. Right: UMAP plots of the integrated dataset showing cells from each species highlighted in black. (C) Top: hierarchical clustering of average expression profiles of integrated GABAergic clusters; branches are colored by species mixture (gray represents an equal proportion of cells from each species).

Bottom: percentage of cells from the original species-specific clusters (rows) in the integrated clusters (columns). **(D)** Dotplot showing the expression of differentiation markers and of transcription factors (TFs) in Lamp5 interneurons (integrated clusters 34, 17, and 49). Cells from each integrated cluster are split by species: L, lizard; M, mouse; S, salamander; and T, turtle. **(E)** Top: Hierarchical clustering of the average expression profiles of integrated glutamatergic clusters; branches are colored by species mixture. Bottom: percentage of mouse cells in each integrated cluster (columns); mouse cells are grouped by projection identity (rows). Integrated clusters including selected mouse neuron types are highlighted. ENT, entorhinal cortex; CT, corticothalamic; IT, intratelencephalic; PT, pyramidal tract; ProS, prosubiculum; PPP, pre-

para-, and postsubiculum; SUB, subiculum. **(F)** Top: percentage of mouse cells in each integrated cluster (columns); mouse cells are grouped by cortical area (rows) and columns are reordered by cortical area. Bottom: percentage of salamander DP cells and turtle dorsal cortex cells (rows) in each integrated

cluster (columns). **(G and H)** Magnification of part of the UMAP in (B) showing cells in cluster 10 (G) or cluster 12 (H) colored by species. **(I)** Dotplot showing the expression of differentiation markers and transcription factors in integrated clusters 12, 38, 30, and 32 split by species.

In the cross-species taxonomy of glutamatergic neurons, major splits corresponded to neurons with distinct projection identities in mouse: intratelencephalic neurons, extratelencephalic neurons (including L5 pyramidal tract neurons), and corticothalamic neurons (Fig. 5E and fig. S16). Several integrated clusters included neurons from mouse only, indicating a greater diversity of mouse pyramidal types. These results were largely recapitulated by integration analyses with different algorithms (fig. S17). Among the mouse-specific clusters, we identified neocortical corticothalamic and L5 pyramidal tract neurons, indicating that these neuron types have unique gene expression profiles and suggesting that they are mammalian innovations (46). Consistent with this, the transcription factor combinatorial codes that specify these types are not found in either the turtle dorsal cortex (7) or the *P. waltil* DP (fig. S16B). In Fig. 5F, we plot the same integrated clusters reordered by mouse cortical region and the proportions of salamander DP and turtle dorsal cortex neurons within these clusters. Most salamander MP and DP neurons co-clustered with mammalian neurons from the hippocampus, entorhinal cortex, and subiculum (Fig. 5, F to H, and fig. S16A). The same pattern was observed for neuron types from the reptilian cortex, but with one exception: Reptiles also have neurons that co-cluster with the neocortical thalamorecipient L4 intratelencephalic neurons (Fig. 5F). The analysis of transcription factor expression points to key differences that may underlie the diversity of pyramidal neurons in tetrapods. Some of the transcription factors instructing neuronal identity in the reptilian dorsal cortex and mammalian neocortex, such as *Satb2* and *Rorb* (47, 48), are not expressed at all in the salamander DP (Fig. 2B and fig. S16B). In other cases, there are differences in transcription factor combinatorial codes. For example, we find that mouse L5 pyramidal tract neurons (cluster 30) are grouped together with L5 neurons from the pre-, para-, and postsubiculum (cluster 38) and with other neurons from the prosubiculum and subiculum (clusters 32 and 12). Cluster 12 also includes neuron types from the salamander DP and the reptilian dorsal cortex. All of these neurons share expression of the transcription factors *Bcl11b* and *Sox5* but differ for the expression of others (Fig. 5I), supporting the concept that neuronal diversity evolves through changes of transcription factor regulatory programs. This analysis indicates that the salamander DP lacks the cellular and molecular

characteristics of the mammalian neocortex, and that DP neuron types are molecularly more similar to pyramidal neurons in the mammalian cortical areas intercalated between neocortex and hippocampus (13).

Similarities and innovations in vertebrate telencephalic connectivity

The results of our comparative analysis prompted us to investigate whether neuron types with similar transcriptomes have similar connectivity across species. Expanding on previous findings in salamanders [reviewed in (26)], we conducted retrograde tracing experiments in adult *P. waltil*. We confirmed that both anterior and posterior VP regions project to the putative ventromedial hypothalamus homolog (49) (fig. S18A). The anterior VP receives afferents from mOB, LP, and DP (Fig. 6A and fig. S19), suggesting a function in olfactory processing. Consistent with previous findings (22), VPa also sparsely receives projections from the central thalamus (Fig. 6A). The central thalamus expresses *Slc17a6* and *Calb2* and relays multimodal inputs to the telencephalon. Therefore, it is considered the amphibian homolog of amniote first-order sensory nuclei (50). In reptiles, the aDVR receives inputs from the dorsal cortex, but not from olfactory areas, and is organized in subregions innervated by thalamic visual, auditory, and somatosensory nuclei (4, 37, 51, 52). Although sensory inputs are processed separately by modality in the aDVR, there is no indication that this is the case in the salamander VP. Projections to the aDVR also include the striatum, the pDVR, and the ventromedial hypothalamus (4, 37, 53). The molecular and connectivity data suggest that reptilian aDVR neurons might have evolved from olfactory-recipient VP neurons that lost their connections to the olfactory system and became specialized in the processing of sensory inputs relayed by the thalamus (Fig. 6D and fig. S19B).

We also compared patterns of pallial connectivity in *P. waltil* with mammalian olfactory-entorhinal-hippocampal circuits. In mammals, the primary input to the hippocampal formation is the entorhinal cortex, which includes a lateral region strongly connected to olfactory areas and a medial region that processes spatial and contextual information (54). The subiculum is the primary output region of the hippocampus. Motivated by our molecular data (Fig. 5), we investigated whether the connections between salamander MP and DP are broadly analogous to the connections of mammalian hippocampus, entorhinal cortex, and

subiculum, as suggested by previous literature (9, 22, 26). Retrograde tracer injections confirmed that MP and DP are reciprocally connected (Fig. 6B and fig. S19, A and E). MP and DP also receive direct projections from the *Satb1*⁺/*Reln*⁺ LP region, an area that receives strong mOB inputs; the lateral olfactory tract runs along this region (24) (Fig. 6B and figs. S18C and S19E). Thus, LP neurons are similar to mammalian semilunar cells in the piriform cortex and fan cells in the entorhinal cortex (layer 2), both for their molecular profile [*Satb1*, *Reln*, *Lhx2*, and *Tbr1*; Fig. 2 and (27)] and their connectivity (direct inputs from the mOB and projections to the hippocampus). These findings suggest that components of mammalian olfactory-entorhinal-hippocampal circuits may trace back to tetrapod ancestors (Fig. 6D and fig. S19C).

Discussion

Our molecular data show that despite its anatomical simplicity, the salamander telencephalon harbors a complex repertoire of neuron types. The combined analysis of their molecular identity, development, and connectivity clarifies the evolution of two innovations in amniotes: the sauropsid aDVR and the mammalian neocortex.

The comparison of the reptilian aDVR and the salamander VP reveals similar and species-specific neuron types. The molecular similarities of salamander VPa/VPp neurons and neurons in the centromedial aDVR, together with the origin of these cells from a ventral pallium progenitor domain (distinct from the dorsal pallium) and the partial similarities of their connectivity (e.g., connections with the hypothalamus), suggest that the amphibian VPa/VPp and parts of the reptilian aDVR descend from a common set of neurons in tetrapod ancestors. We also identified reptilian-specific aDVR neurons that do not co-cluster with salamander VP neurons. These rostral aDVR neurons express a unique set of transcription factors (*Rorb* and *Satb1*) and receive thalamic inputs segregated by sensory modality (visual, somatosensory, and auditory, but not olfactory) (38). In light of this, we propose that neuron types in the aDVR that are specialized in processing sensory inputs relayed by the thalamus are an evolutionary innovation in the sauropsid lineage.

The homologs of these ventral pallium neurons in mammals remain ambiguous. Connectivity data point to similarities of the salamander VPa, aDVR, and the mammalian lateral amygdala, a region that receives sensory inputs relayed by the thalamus (37) and expresses some

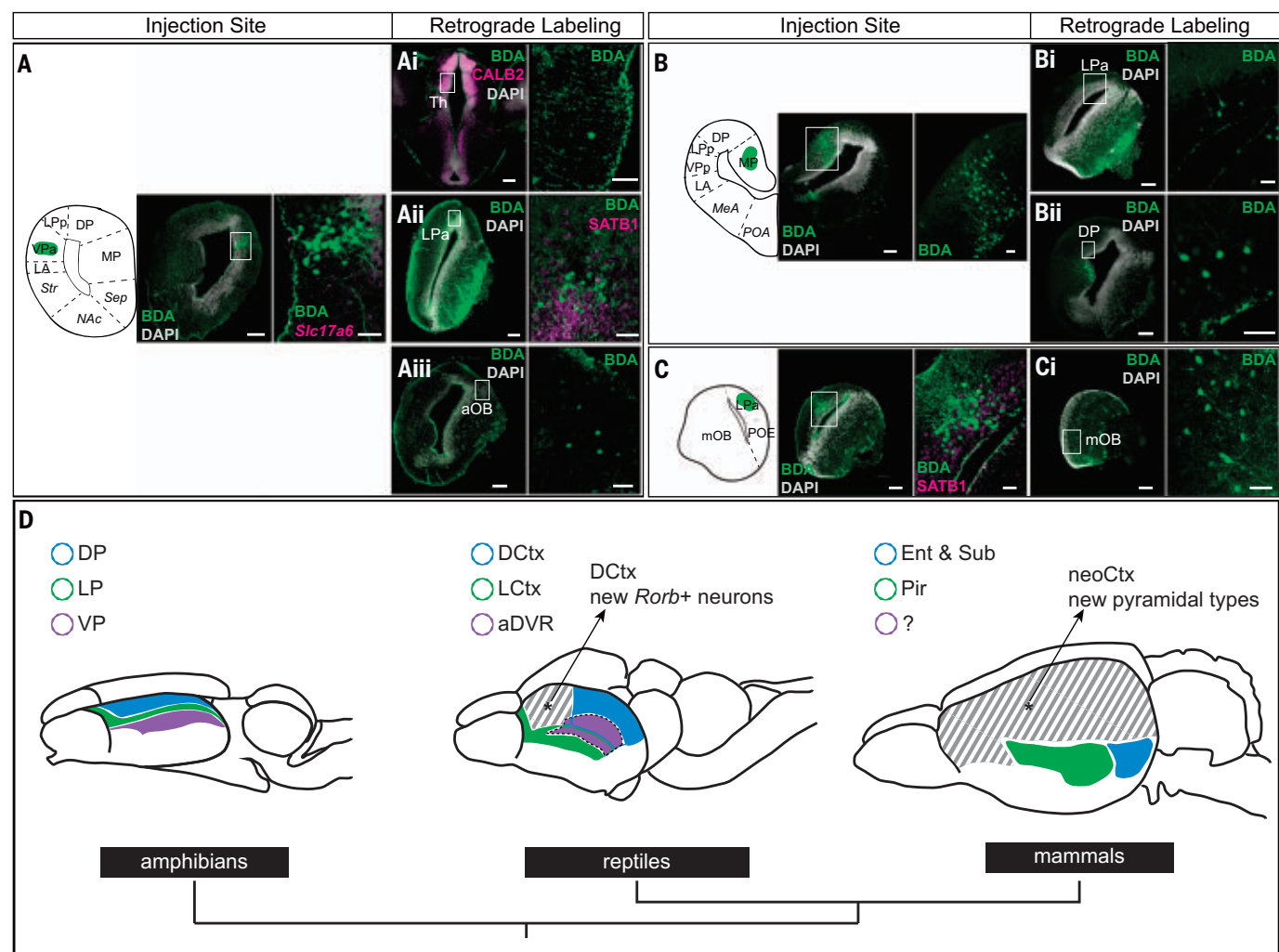


Fig. 6. Connectivity of the *P. waltl* pallium. (A to C) Left: injection sites of the retrograde tracer biotinylated dextran amine (BDA). Scale bars, 200 μ m. BDA (3 kD) was injected into the VP (n = 4) (A), MP (n = 2) (B), and LP (n = 2) (C). Right: magnification of injection site with immunostaining or HCR in situ hybridization of relevant molecular markers. Scale bars, 50 μ m. (Ai, Aii, Aiii, Bi, Bii, and Ci) Left: representative coronal sections in which retrogradely labeled cells were identified with immunostaining or HCR in situ hybridization of relevant molecular markers when applicable. Right: magnification of retrogradely

labeled cells with immunostaining of relevant markers when applicable. (D) Top: schematic representation of amphibian, reptile, and mammalian brains. Colors indicate molecular and connectivity similarities of neuron types across species. Cross-hatching denotes areas with cell-type innovations. MP/medial cortex, hippocampus, and mammalian subiculum are not shown in the drawing. Bottom: phylogenetic tree. DCtx, dorsal cortex; Ent, entorhinal cortex; LCtx, lateral cortex; Pir, piriform cortex; Sub, subiculum; for a full list of abbreviations, see fig. S1.

marker genes found in VP and aDVR, such as *Rorb* (7, 26, 55). However, molecular data also indicate similarities of the salamander VP, bird HVC [part of aDVR (8)], and mammalian piriform cortex (21) (Fig. 5A). A kinship of VP and aDVR with parts of the mammalian piriform cortex is not surprising given that the aDVR and the sauropsid olfactory cortex develop sequentially from the same embryonic progenitors (56). Further molecular and developmental studies on the mammalian piriform cortex and pallial amygdala, the cellular diversity of which remains poorly explored, are needed to clarify their evolutionary relationships with aDVR and VP.

Our data shed light on the nature of the amphibian DP. This region is molecularly dis-

tinct from the MP but does not express many of the markers that define the reptilian dorsal cortex, the area typically compared to the mammalian neocortex for its position, molecular makeup, and connectivity. Our cross-species analysis shows that salamander DP and several reptilian dorsal cortex neurons co-cluster with neurons of the mammalian subiculum and entorhinal cortex. The input-output connectivity of the salamander DP suggests that these molecular similarities may correspond in part to conserved circuit motifs. The *Reln*-expressing neurons in the LP occupy a peculiar position in this circuit, analogous to *Reln* neurons in the reptilian olfactory cortex and mammalian piriform (semilunar cells) and entorhinal cortex (fan cells) (21, 57). We suggest

that mammalian piriform and entorhinal *Reln*-expressing cells are serial homologs [as sister cell types (58)], with the implication that neuron types in layer 2 and in deeper layers of entorhinal cortex may have two distinct evolutionary origins from the lateral and the dorsal pallium of a tetrapod ancestor, respectively (20, 59). This scenario can be tested with molecular data from the mammalian piriform cortex.

In sum, our findings chart the series of innovations that resulted in the emergence of a six-layered neocortex in mammals (Figs. 5 and 6D). We propose that neocortical *L4 Rorb*-expressing neurons receiving sensory inputs from the thalamus evolved first, either in amniote ancestors [if salamanders retained the tetrapod ancestral state (27, 60)] or in earlier

vertebrate ancestors [with secondary loss in salamanders or amphibians (61)]. Neocortical corticothalamic neurons (L6) and pyramidal tract neurons (L5B) emerged later, in mammalian ancestors (46). Expansion of the neocortex led to functional innovations, such as the transition from distributed to columnar information processing (62) and the direct top-down control of locomotion (46). How these molecular and cellular novelties supported such functional innovations within sensory-associative pallial regions remains to be explored.

Methods summary

Animals

Adult *P. waltil* salamanders were obtained from breeding colonies established at Columbia University and Karolinska Institute. All experiments were conducted in accordance with the National Institutes of Health (NIH) guidelines and Columbia University institutional animal care and use committee policies governing animal use and welfare.

scRNA-seq library preparation

Telencephali were dissociated from either adult or larval salamanders and prepared for scRNA-seq using 10X Genomics Chromium Next GEM Single Cell 3' Kit v3.1. Sequenced libraries were aligned to a *P. waltil* reference transcriptome (see the supplementary materials and methods for details).

Analysis of scRNA-seq data

After quality filtering, scRNA-seq datasets were clustered and analyzed using the R package Seurat. For the adult data, high-level neuronal and non-neuronal clusters were first identified. Then, the neuronal dataset was subsetted and re-clustered to identify subclusters. Final clusters were annotated on the basis of the expression of established marker genes.

The quality-filtered developmental data were merged into a single object, and non-neuronal cells were filtered out. These data were regressed for cell cycle score, in addition to RNA count, stage, and percentage of mitochondrial genes, before cluster annotation.

Cross-species comparisons of transcriptomics data

Using Seurat's integration pipeline, we generated two integrated datasets using scRNA-seq data from the turtle pallium (7), the lizard telencephalon (35), and the mouse cortex and hippocampal formation (43). Average cluster expression profiles were computed, distances were computed as $1 - \text{cor}(x)$ (Spearman correlation), and this distance matrix was used for hierarchical clustering with the Ward.D2 method to generate dendrograms (Figs. 4 and 5). Dendrograms were color-coded according to the proportion of each species' cells in the integrated cluster. Additional annotation of the

integrated clusters was performed by analyzing the identities of each species' cells that were contained in each integrated cluster (see the supplementary materials and methods for details).

Trajectory inference

Trajectories were calculated using Slingshot to end points defined by label transfer against adult neurons. Genes that define the dorsal and ventral trajectories were calculated using Seurat's FindMarkers function. Pseudotime values provided by Slingshot were used to generate heatmaps of differentially expressed genes along each trajectory.

Immunohistochemistry and colorimetric and fluorescence in situ hybridization

Immunohistochemistry and colorimetric in situ hybridization were performed on floating sections of the adult brain or frozen sections of larval brains following standard protocols. The hybridization chain reaction protocol from Molecular Instruments was implemented and combined with iDISCO tissue clearing and light sheet imaging to generate 2D and 3D representations of gene expression (see the supplementary materials and methods for details).

Axonal tracing

Dextran amine tracer injections were performed ex vivo and brains were incubated for 24 to 48 hours. The tracer injection site and retrogradely or anterogradely labeled cells were visualized on floating sections and annotated using co-staining for known molecular markers and anatomical landmarks (see the supplementary materials and methods for details).

REFERENCES AND NOTES

- M. A. MacIver, B. L. Finlay, The neuroecology of the water-to-land transition and the evolution of the vertebrate brain. *Philos. Trans. R. Soc. Lond. B Biol. Sci.* **377**, 20200523 (2022). doi: 10.1098/rstb.2020.0523; pmid: 34957852
- G. F. Striedter, The telencephalon of tetrapods in evolution. *Brain Behav. Evol.* **49**, 179–213 (1997). doi: 10.1159/000112991; pmid: 9096908
- A. B. Butler, Z. Molnár, Development and evolution of the collopallium in amniotes: A new hypothesis of field homology. *Brain Res. Bull.* **57**, 475–479 (2002). doi: 10.1016/S0361-9230(01)00679-7; pmid: 11923013
- A. B. Butler, A. Reiner, H. J. Karten, Evolution of the amniote pallium and the origins of mammalian neocortex. *Ann. N. Y. Acad. Sci.* **1225**, 14–27 (2011). doi: 10.1111/j.1749-6632.2011.06006.x; pmid: 21534989
- E. D. Jarvis, "The evolution of vocal learning systems in birds and humans," in *Evolution of Nervous Systems*, J. H. Kaas, Ed. (Elsevier, 2007), pp. 213–227.
- H. J. Karten, Neocortical evolution: Neuronal circuits arise independently of lamination. *Curr. Biol.* **23**, R12–R15 (2013). doi: 10.1016/j.cub.2012.11.013; pmid: 23305661
- M. A. Tosches et al., Evolution of pallium, hippocampus, and cortical cell types revealed by single-cell transcriptomics in reptiles. *Science* **360**, 881–888 (2018). doi: 10.1126/science.aar4237; pmid: 29724907
- B. M. Colquhitt, D. P. Merullo, G. Konopka, T. F. Roberts, M. S. Brainard, Cellular transcriptomics reveals evolutionary identities of songbird vocal circuits. *Science* **371**, eabd9704 (2021). doi: 10.1126/science.abd9704; pmid: 33574185
- R. G. Northcutt, E. Kicliter, "Organization of the amphibian telecephalon," in *Comparative Neurology of the Telencephalon*, S. O. E. Ebesson, Ed. (Springer, 1980), pp. 203–255.
- A. González, J. M. López, R. Morona, N. Moreno, "The organization of the central nervous system of amphibians," in *Evolutionary Neuroscience*, J. H. Kaas, Ed. (Elsevier, 2020), pp. 125–157.
- W. J. Smeets, O. Marin, A. González, Evolution of the basal ganglia: New perspectives through a comparative approach. *J. Anat.* **196**, 501–517 (2000). doi: 10.1046/j.1469-7580.2000.19640501.x; pmid: 10923983
- I. Bormuth et al., Neuronal basic helix-loop-helix proteins Neurod2/6 regulate cortical commissure formation before midline interactions. *J. Neurosci.* **33**, 641–651 (2013). doi: 10.1523/JNEUROSCI.0899-12.2013; pmid: 23303943
- L. Puelles, A. Alonso, E. García-Calero, M. Martínez-de-la-Torre, Concentric ring topology of mammalian cortical sectors and relevance for patterning studies. *J. Comp. Neurol.* **527**, 1731–1752 (2019). doi: 10.1002/cne.24650; pmid: 30737959
- A. Faedo et al., Developmental expression of the T-box transcription factor T-bet/Tbx21 during mouse embryogenesis. *Mech. Dev.* **116**, 157–160 (2002). doi: 10.1016/S0925-4773(02)00114-4; pmid: 12128215
- N. Moreno, A. González, S. Rétaux, Evidences for tangential migrations in *Xenopus* telencephalon: Developmental patterns and cell tracking experiments. *Dev. Neurobiol.* **68**, 504–520 (2008). doi: 10.1002/dneu.20603; pmid: 18214835
- N. Moreno, A. González, Regionalization of the telencephalon in urodele amphibians and its bearing on the identification of the amygdaloid complex. *Front. Neuroanat.* **1**, 1 (2007). doi: 10.3389/neuro.05.001.2007; pmid: 18958195
- A. Brox, L. Puelles, B. Ferreira, L. Medina, Expression of the genes *Emx1*, *Tbr1*, and *Eomes* (*Tbr2*) in the telencephalon of *Xenopus laevis* confirms the existence of a ventral pallial division in all tetrapods. *J. Comp. Neurol.* **474**, 562–577 (2004). doi: 10.1002/cne.20152; pmid: 15174073
- F. Laberge, S. Mühlenbrock-Lenter, W. Grunwald, G. Roth, Evolution of the amygdala: New insights from studies in amphibians. *Brain Behav. Evol.* **67**, 177–187 (2006). doi: 10.1159/000091119; pmid: 16432299
- N. Moreno, A. González, The common organization of the amygdaloid complex in tetrapods: New concepts based on developmental, hodological and neurochemical data in anuran amphibians. *Prog. Neurobiol.* **78**, 61–90 (2006). doi: 10.1016/j.pneurobio.2005.12.005; pmid: 16457938
- A. Abellán, E. Desfilis, L. Medina, Combinatorial expression of *Le1*, *Lhx2*, *Lhx5*, *Lhx9*, *Lmo3*, *Lmo4*, and *Prox1* helps to identify comparable subdivisions in the developing hippocampal formation of mouse and chicken. *Front. Neuroanat.* **8**, 59 (2014). doi: 10.3389/fnana.2014.00059; pmid: 25071464
- A. Diodato et al., Molecular signatures of neural connectivity in the olfactory cortex. *Nat. Commun.* **7**, 12238 (2016). doi: 10.1038/ncomms12238; pmid: 27426965
- T. J. Neary, "The pallium of anuran amphibians," in *Comparative Structure and Evolution of Cerebral Cortex, Part I*, E. G. Jones, A. Peters, Eds. (Springer, 1990), vol. 8A of *Cerebral Cortex*, pp. 107–138.
- A. Deryckere, J. Woych, E. C. B. Jaeger, M. A. Tosches, Glutamatergic neuron types in the amygdala of the urodele amphibian *Pleurodeles waltil*. *BioRxiv* 496313 [Preprint] (2022); doi: 10.1101/2022.06.15.496313
- F. Laberge, G. Roth, Connectivity and cytoarchitecture of the ventral telencephalon in the salamander *Plethodon shermani*. *J. Comp. Neurol.* **482**, 176–200 (2005). doi: 10.1002/cne.20430; pmid: 15611991
- H. Endepols, K. Roden, W. Walkowiak, Hodological characterization of the septum in anuran amphibians: II. Efferent connections. *J. Comp. Neurol.* **483**, 437–457 (2005). doi: 10.1002/cne.20455; pmid: 15700277
- A. Joven, A. Simon, Homeostatic and regenerative neurogenesis in salamanders. *Prog. Neurobiol.* **170**, 81–98 (2018). doi: 10.1016/j.pneurobio.2018.04.006; pmid: 29654836
- G. F. Striedter, R. G. Northcutt, The independent evolution of dorsal pallia in multiple vertebrate lineages. *Brain Behav. Evol.* **96**, 200–211 (2022). doi: 10.1159/000516563; pmid: 34175847
- L. Medina, A. Abellán, E. Desfilis, Evolving views on the pallium. *Brain Behav. Evol.* **96**, 181–199 (2022). doi: 10.1159/000519260; pmid: 34657034
- F. García-Moreno, Z. Molnár, Variations of telencephalic development that paved the way for neocortical evolution. *Prog. Neurobiol.* **194**, 101865 (2020). doi: 10.1016/j.pneurobio.2020.101865; pmid: 32526253

30. A. Joven *et al.*, Cellular basis of brain maturation and acquisition of complex behaviors in salamanders. *Development* **145**, dev.160051 (2018). doi: [10.1242/dev.160051](https://doi.org/10.1242/dev.160051); pmid: 29217751
31. T. Stuart *et al.*, Comprehensive integration of single-cell data. *Cell* **177**, 1888–1902.e21 (2019). doi: [10.1016/j.cell.2019.05.031](https://doi.org/10.1016/j.cell.2019.05.031); pmid: 31178118
32. K. Street *et al.*, Slingshot: Cell lineage and pseudotime inference for single-cell transcriptomics. *BMC Genomics* **19**, 477 (2018). doi: [10.1186/s12864-018-4772-0](https://doi.org/10.1186/s12864-018-4772-0); pmid: 29914354
33. M. X. Moreau, Y. Saillour, A. W. Cwetsch, A. Pierani, F. Causeret, Single-cell transcriptomics of the early developing mouse cerebral cortex disentangle the spatial and temporal components of neuronal fate acquisition. *Development* **148**, dev.197962 (2021). doi: [10.1242/dev.197962](https://doi.org/10.1242/dev.197962); pmid: 34170322
34. H. Norimoto *et al.*, A claustrum in reptiles and its role in slow-wave sleep. *Nature* **578**, 413–418 (2020). doi: [10.1038/s41586-020-1993-6](https://doi.org/10.1038/s41586-020-1993-6); pmid: 32051589
35. D. Hain *et al.*, Molecular diversity and evolution of neuron types in the amniote brain. *Science* **377**, eabp8202 (2022).
36. N. Moreno, A. González, Evolution of the amygdaloid complex in vertebrates, with special reference to the anamnio-amniotic transition. *J. Anat.* **211**, 151–163 (2007). doi: [10.1111/j.1469-7580.2007.00780.x](https://doi.org/10.1111/j.1469-7580.2007.00780.x); pmid: 17634058
37. L. L. Bruce, T. J. Neary, The limbic system of tetrapods: A comparative analysis of cortical and amygdalar populations. *Brain Behav. Evol.* **46**, 224–234 (1995). doi: [10.1159/000113276](https://doi.org/10.1159/000113276); pmid: 8564465
38. P. R. Manger, D. A. Slutsky, Z. Molnár, Visual subdivisions of the dorsal ventricular ridge of the iguana (*Iguana iguana*) as determined by electrophysiologic mapping. *J. Comp. Neurol.* **453**, 226–246 (2002). doi: [10.1002/cne.10373](https://doi.org/10.1002/cne.10373); pmid: 12378585
39. D. Arendt *et al.*, The origin and evolution of cell types. *Nat. Rev. Genet.* **17**, 744–757 (2016). doi: [10.1038/nrg.2016.127](https://doi.org/10.1038/nrg.2016.127); pmid: 27818507
40. E. S. Lein *et al.*, Genome-wide atlas of gene expression in the adult mouse brain. *Nature* **445**, 168–176 (2007). doi: [10.1038/nature05453](https://doi.org/10.1038/nature05453); pmid: 17151600
41. X. Caubit, M.-C. Tiveron, H. Cremer, L. Fasano, Expression patterns of the three Teashirt-related genes define specific boundaries in the developing and postnatal mouse forebrain. *J. Comp. Neurol.* **486**, 76–88 (2005). doi: [10.1002/cne.20500](https://doi.org/10.1002/cne.20500); pmid: 15834955
42. A. Zeisel *et al.*, Cell types in the mouse cortex and hippocampus revealed by single-cell RNA-seq. *Science* **347**, 1138–1142 (2015). doi: [10.1126/science.1234567](https://doi.org/10.1126/science.1234567); pmid: 25700174
43. Z. Yao *et al.*, A taxonomy of transcriptomic cell types across the isocortex and hippocampal formation. *Cell* **184**, 3222–3241.e26 (2021). doi: [10.1016/j.cell.2021.04.021](https://doi.org/10.1016/j.cell.2021.04.021); pmid: 34004146
44. G. Fishell, A. Kepecs, Interneuron types as attractors and controllers. *Annu. Rev. Neurosci.* **43**, 1–30 (2020). doi: [10.1146/annurev-neuro-070918-050421](https://doi.org/10.1146/annurev-neuro-070918-050421); pmid: 31299170
45. N. W. Gouwens *et al.*, Integrated morphoelectric and transcriptomic classification of cortical gabaergic cells. *Cell* **183**, 935–953.e19 (2020). doi: [10.1016/j.cell.2020.09.057](https://doi.org/10.1016/j.cell.2020.09.057); pmid: 33186530
46. S. Shim, K. Y. Kwan, M. Li, V. Lefebvre, N. Sestan, Cis-regulatory control of corticospinal system development and evolution. *Nature* **486**, 74–79 (2012). doi: [10.1038/nature11094](https://doi.org/10.1038/nature11094); pmid: 22678282
47. D. Jabaudon, Fate and freedom in developing neocortical circuits. *Nat. Commun.* **8**, 16042 (2017). doi: [10.1038/ncomms16042](https://doi.org/10.1038/ncomms16042); pmid: 28671189
48. T. Nomura, W. Yamashita, H. Gotoh, K. Ono, Species-specific mechanisms of neuron subtype specification reveal evolutionary plasticity of amniote brain development. *Cell Rep.* **22**, 3142–3151 (2018). doi: [10.1016/j.celrep.2018.02.086](https://doi.org/10.1016/j.celrep.2018.02.086); pmid: 29562171
49. N. Moreno, R. Morona, J. M. López, A. González, in *Evolution of Nervous Systems* (Elsevier, 2017), pp. 409–426.
50. A. Joven, R. Morona, N. Moreno, A. González, Regional distribution of calretinin and calbindin-D28k expression in the brain of the urodele amphibian *Pleurodeles waltl* during embryonic and larval development. *Brain Struct. Funct.* **218**, 969–1003 (2013). doi: [10.1007/s00429-012-0442-1](https://doi.org/10.1007/s00429-012-0442-1); pmid: 22843286
51. E. Lanuza, M. Belekchova, A. Martínez-Marcos, C. Font, F. Martínez-García, Identification of the reptilian basolateral amygdala: An anatomical investigation of the afferents to the posterior dorsal ventricular ridge of the lizard *Podarcis hispanica*. *Eur. J. Neurosci.* **10**, 3517–3534 (1998). doi: [10.1046/j.1460-9568.1998.00363.x](https://doi.org/10.1046/j.1460-9568.1998.00363.x); pmid: 9824465
52. P. Cordery, Z. Molnár, Embryonic development of connections in turtle pallium. *J. Comp. Neurol.* **413**, 26–54 (1999). doi: [10.1002/\(SICI\)1096-9861\(19991011\)413:1<26::AID-CNE2>3.0.CO;2-N](https://doi.org/10.1002/(SICI)1096-9861(19991011)413:1<26::AID-CNE2>3.0.CO;2-N); pmid: 10464368
53. T. J. Voneida, C. M. Sligar, Efferent projections of the dorsal ventricular ridge and the striatum in the Tegu lizard, *Tupinambis nigropunctatus*. *J. Comp. Neurol.* **186**, 43–64 (1979). doi: [10.1002/cne.901860104](https://doi.org/10.1002/cne.901860104); pmid: 457930
54. M. P. Witter, T. P. Doan, B. Jacobsen, E. S. Nilssen, S. Ohara, Architecture of the entorhinal cortex: A review of entorhinal anatomy in rodents with some comparative notes. *Front. Syst. Neurosci.* **11**, 46 (2017). doi: [10.3389/fnsys.2017.00046](https://doi.org/10.3389/fnsys.2017.00046); pmid: 28701931
55. T. P. O'Leary *et al.*, Extensive and spatially variable within-cell-type heterogeneity across the basolateral amygdala. *eLife* **9**, e59003 (2020). doi: [10.7554/eLife.59003](https://doi.org/10.7554/eLife.59003); pmid: 32869744
56. J. B. Johnston, The development of the dorsal ventricular ridge in turtles. *J. Comp. Neurol.* **26**, 481–505 (1916). doi: [10.1002/cne.900260504](https://doi.org/10.1002/cne.900260504)
57. F. C. Leitner *et al.*, Spatially segregated feedforward and feedback neurons support differential odor processing in the lateral entorhinal cortex. *Nat. Neurosci.* **19**, 935–944 (2016). doi: [10.1038/nn.4303](https://doi.org/10.1038/nn.4303); pmid: 27182817
58. M. A. Tosches, From cell types to an integrated understanding of brain evolution: The case of the cerebral cortex. *Annu. Rev. Cell Dev. Biol.* **37**, 495–517 (2021). doi: [10.1146/annurev-cellbio-120319-112654](https://doi.org/10.1146/annurev-cellbio-120319-112654); pmid: 34416113
59. F. Luzzati, A hypothesis for the evolution of the upper layers of the neocortex through co-option of the olfactory cortex developmental program. *Front. Neurosci.* **9**, 162 (2015). doi: [10.3389/fnins.2015.00162](https://doi.org/10.3389/fnins.2015.00162); pmid: 26029038
60. S. Bloch *et al.*, Non-thalamic origin of zebrafish sensory nuclei implies convergent evolution of visual pathways in amniotes and teleosts. *eLife* **9**, e54945 (2020). doi: [10.7554/eLife.54945](https://doi.org/10.7554/eLife.54945); pmid: 32896272
61. S. M. Suryanarayana, B. Robertson, P. Wallén, S. Grillner, The lamprey pallium provides a blueprint of the mammalian layered cortex. *Curr. Biol.* **27**, 3264–3277.e5 (2017). doi: [10.1016/j.cub.2017.09.034](https://doi.org/10.1016/j.cub.2017.09.034); pmid: 29056451
62. J. Fournier, C. M. Müller, I. Schneider, G. Laurent, Spatial information in a non-retinotopic visual cortex. *Neuron* **97**, 164–180.e7 (2018). doi: [10.1016/j.neuron.2017.11.017](https://doi.org/10.1016/j.neuron.2017.11.017); pmid: 29249282
63. Code for: J. Woych, A. Ortega Gurrela, A. Deryckere, E. C. B. Jaeger, E. Gurniit, G. Merello, J. Gu, A. Joven Araus, N. D. Leigh, M. Yun, A. Simon, M. A. Tosches, Cell-type profiling in salamanders identifies innovations in vertebrate forebrain evolution, Zenodo (2022); doi: [10.5281/zenodo.6780577](https://doi.org/10.5281/zenodo.6780577)

ACKNOWLEDGMENTS

We thank J. Barber, S. Cook, and the Columbia University Institute of Comparative Medicine for animal care; B. Jekely for help with cloning; E. Subramanian for contributing to the IsoSeq reference; A. Matheson for the diagram in fig. S19, B and C; and A. Matheson, L. Xu, G. Laurent, O. Hobert, and R. Satija for critical feedback on the manuscript. Light-sheet imaging was performed with support from L. Hammond and the Zuckerman Institute's Cellular Imaging platform (NIH grant 1S100D023587-01). Computing resources were provided by Columbia University's Shared Research Computing Facility (NIH grant 1G20RR030893-01 and NYSTAR contract C090171). The National Genomics Infrastructure (NGI)/Uppsala Genome Center and UPPMAX provided assistance in massive parallel sequencing and computational infrastructure. Work performed at the NGI/Uppsala Genome Center was funded by the Swedish Council for Research Infrastructure and the Science for Life Laboratory (Sweden). Storage and handling of IsoSeq data were enabled by resources provided by the Swedish National Infrastructure for Computing (SNIC) at UPPMAX, which is partially funded by the Swedish Research Council through grant 2018-05973. **Funding:** This work was supported by the McKnight Foundation (M.A.T.), the NIH (grant NHHRI RMIHG011014 to M.A.T.), the National Science Foundation (Graduate Research Fellowship DGE 2036197 to E.C.B.J.), the Knut and Alice Wallenberg Foundation (A.S.), and the European Research Council (A.S.). **Author contributions:** J.W., A.O.G., A.D., and E.G. produced the scRNA-seq data. E.G., A.O.G., M.A.T., and J.G. analyzed the scRNA-seq data. A.J.A., N.D.L., A.S., and M.Y. assembled the IsoSeq transcriptome. J.W., A.D., E.C.B.J., and G.M. analyzed the anatomy and histology. J.W., E.C.B.J., and A.D. produced and analyzed axonal tracing data. M.A.T., A.D., E.C.B.J., A.O.G., J.W., and E.G. wrote the manuscript. A.J.A., A.S., N.D.L., and M.Y. edited the manuscript. M.A.T. provided project management and supervised the study.

Competing interests: The authors declare no competing interests.

Data and materials availability: The scRNA-seq data used in this study have been deposited in the Gene Expression Omnibus (GEO) with accession numbers GSE197701, GSE197722, GSE197796, GSE197807, GSE198363, GSE198364, GSE198366, GSE198367, GSE198365, and GSE206163. The IsoSeq data are accessible on NIH Sequence Read Archive (SRA) with accession number SRX16252717. All other data are included in the main paper or the supplementary materials. Code used for the analysis of scRNA-seq data is available at Zenodo (63). A website to access the data and search genes of interest is available at https://toscheslab.shinyapps.io/salamander_telencephalon/. **License information:** Copyright © 2022 the authors, some rights reserved; exclusive licensee American Association for the Advancement of Science. No claim to original US government works. <https://www.science.org/about/science-licenses-journal-article-reuse>

SUPPLEMENTARY MATERIALS

science.org/doi/10.1126/science.abp9186

Materials and Methods

Supplementary Text

Figs. S1 to S19

References (64–94)

Movies S1 to S3

Data S1

MDAR Reproducibility Checklist

Submitted 7 March 2022; accepted 12 July 2022

10.1126/science.abp9186

Pushing the Boundaries of Knowledge

As AAAS's first multidisciplinary, open access journal, *Science Advances* publishes research that reflects the selectivity of high impact, innovative research you expect from the *Science* family of journals, published in an open access format to serve a vast and growing global audience. Check out the latest findings or learn how to submit your research: [ScienceAdvances.org](https://www.scienceadvances.org)

Science
Advances
AAAS

GOLD OPEN ACCESS, DIGITAL, AND FREE TO ALL READERS

RESEARCH ARTICLE SUMMARY

NEURODEVELOPMENT

GnRH replacement rescues cognition in Down syndrome

Maria Manfredi-Lozano[†], Valerie Leysen[†], Michela Adamo[†], Isabel Paiva, Renaud Rovera, Jean-Michel Pignat, Fatima Ezzahra Timzoura, Michael Candlish, Sabiha Eddarkaoui, Samuel A. Malone, Mauro S. B. Silva, Sara Trova, Monica Imbernon, Laurie Decoster, Ludovica Cotellessa, Manuel Tena-Sempere, Marc Claret, Ariane Paoloni-Giacobino, Damien Plassard, Emmanuelle Paccou, Nathalie Vionnet, James Acierio, Aleksandra Maleska Maceski, Antoine Lutti, Frank Pfrieger, S. Sasika, Federico Santoni, Ulrich Boehm, Philippe Ciofi, Luc Buée, Nasser Haddjeri, Anne-Laurence Boutillier, Jens Kuhle, Andrea Messina, Bogdan Draganski, Paolo Giacobini[‡], Nelly Pitteloud^{*‡}, Vincent Prevot^{*‡}

INTRODUCTION: Patients with Down syndrome (DS), a frequent condition (1 per 800 live births) caused by trisomy of chromosome 21, display a variety of characteristics, including cognitive decline due to an early-onset Alzheimer-like disease along with myelination defects in adulthood, impaired olfaction starting before puberty, and subfertility. No viable treatment exists for the cognitive and olfactory deficits seen in DS patients.

RATIONALE: Gonadotropin-releasing hormone (GnRH), which is secreted in a pulsatile fashion by specialized hypothalamic neurons, is the master molecule that controls reproduction in all mammals. In humans, altered GnRH secretion leads to Kallmann syndrome, which manifests with olfactory defects, gonadal immaturity, and infertility. Hypothalamic GnRH-expressing neurons also project to extrahypothalamic areas, including those involved in intellectual functions. We therefore asked whether the progres-

sive deficits observed in DS bore any temporal correlation to the maturation of the GnRH system; what alterations to this process, if any, could be observed in the brain of animal models of DS; and whether these alterations could be therapeutically reversed in adulthood.

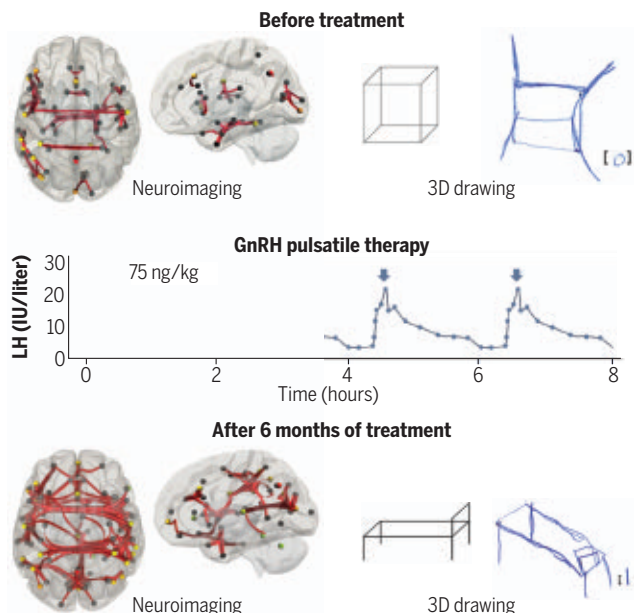
RESULTS: We first further characterized a trisomic mouse model of DS that triplicates regions analogous to human chromosome 21 (Ts65Dn mice) and displays subfertility and progressive cognitive and olfactory impairments similar to that of DS patients. These nonreproductive neurological symptoms closely paralleled a postpubertal loss of GnRH neurons and fibers in the hypothalamus as well as in extrahypothalamic regions, which is reflected by changes in the levels and pattern of release of the gonadotropin luteinizing hormone (LH) in the blood. The decreased GnRH expression in adult mice was accompanied by an imbalance in a complex network of microRNAs (several of

which occur on the trisomic region) and regulatory factors that constitute a “switch” that controls GnRH expression and GnRH neuron maturation in the hypothalamus, starting during the infantile period or “minipuberty.” Indeed, we observed that elements of this switch were dysregulated as far back as the minipubertal period, well before the appearance of cognitive or olfactory deficits. Additionally, this altered expression of microRNAs and transcription factors in the hypothalamus appeared to result in the altered expression of a number of target genes, including several involved in myelination and synaptic transmission, both in the hypothalamus itself and, to a much greater extent, in the hippocampus, as well as in the altered activity of hippocampal neurons. Overexpressing a key microRNA involved in the GnRH developmental switch, miR-200b, in the hypothalamus abolished both the changes in gene expression and the deficits in neuronal activity, olfaction, and cognition in DS mice. Reinduction of miR-200b in adulthood, long after the GnRH switch, increased both the number of GnRH-expressing neurons in the hypothalamus and the proportion of neurons expressing one of its transcriptional activators, *Otx2*, which is known to control the opening and closing of other critical periods in brain maturation. To verify that these improvements were indeed due to the restoration of GnRH, we used cell therapy with normal hypothalamic neurons as well as chemogenetic and pharmacological interventions to produce GnRH at physiological levels and patterns (i.e., pulsatile secretion) in adult DS mice and found that these treatments all abolished olfactory and cognitive defects in the mice. Finally, based on these results, we performed a pilot study in DS patients to assess the effects of pulsatile GnRH therapy on olfaction, cognition, and brain structure and function. This treatment is safe and is presently used to treat GnRH-deficient conditions like Kallmann syndrome. We found that a 6-month pulsatile GnRH treatment improved both cognitive performance and functional brain connectivity in these patients.

CONCLUSION: The maintenance of the GnRH system appears to play a developmental role in brain maturation and higher functions. Pulsatile GnRH therapy holds promise to improve cognitive deficits in DS, paving the way for future clinical trials. ■

Pulsatile GnRH therapy improves cognition in DS.

DS patients show olfactory and cognitive impairments in addition to intellectual disability and reproductive maturation deficits. GnRH neurons, which control reproduction, also project to brain areas involved in cognition such as the hippocampus. In trisomic Ts65Dn mice, which mimic characteristics of DS patients, GnRH expression progressively disappears. Pulsatile GnRH therapy in DS patients improves brain connectivity and function. IU/liter, international units per liter.



The list of author affiliations is available in the full article online.

*Corresponding author. Email: nelly.pitteloud@chuv.ch (N.P.); vincent.prevot@inserm.fr (V.P.)

†These authors contributed equally to this work.

‡These authors contributed equally to this work.

Cite this article as M. Manfredi-Lozano et al., *Science* 377, eabq4515 (2022). DOI: 10.1126/science.abq4515

S READ THE FULL ARTICLE AT
<https://doi.org/10.1126/science.abq4515>

RESEARCH ARTICLE

NEURODEVELOPMENT

GnRH replacement rescues cognition in Down syndrome

Maria Manfredi-Lozano^{1,2,†}, Valerie Leysen^{1,2,†}, Michela Adamo^{3,4,†}, Isabel Paiva⁵, Renaud Rovera⁶, Jean-Michel Pignat⁷, Fatima Ezzahra Timzoura^{1,2}, Michael Candlish^{8,†}, SABIHA Eddarkaoui¹, Samuel A. Malone^{1,2}, Mauro S. B. Silva^{1,2,§}, Sara Trova^{1,2,¶}, Monica Imbernon^{1,2}, Laurine Decoster^{1,2}, Ludovica Cotellessa^{1,2}, Manuel Tena-Sempere⁹, Marc Claret^{10,11}, Ariane Paoloni-Giacobino¹², Damien Plassard¹³, Emmanuelle Paccou³, Nathalie Vionnet³, James Acierno³, Aleksandra Maleska Maceski¹⁴, Antoine Lutti¹⁵, Frank Pfrieger¹⁶, S. Rasika^{1,2}, Federico Santoni⁴, Ulrich Boehm⁸, Philippe Ciofi¹⁷, Luc Buée¹, Nasser Haddjeri⁶, Anne-Laurence Boutillier⁵, Jens Kuhle¹⁴, Andrea Messina^{3,4}, Bogdan Draganski^{15,18}, Paolo Giacobini^{1,2,‡}, Nelly Pitteloud^{3,4,*}, Vincent Prevot^{1,2,*}

At the present time, no viable treatment exists for cognitive and olfactory deficits in Down syndrome (DS). We show in a DS model (Ts65Dn mice) that these progressive nonreproductive neurological symptoms closely parallel a postpubertal decrease in hypothalamic as well as extrahypothalamic expression of a master molecule that controls reproduction—gonadotropin-releasing hormone (GnRH)—and appear related to an imbalance in a microRNA-gene network known to regulate GnRH neuron maturation together with altered hippocampal synaptic transmission. Epigenetic, cellular, chemogenetic, and pharmacological interventions that restore physiological GnRH levels abolish olfactory and cognitive defects in Ts65Dn mice, whereas pulsatile GnRH therapy improves cognition and brain connectivity in adult DS patients. GnRH thus plays a crucial role in olfaction and cognition, and pulsatile GnRH therapy holds promise to improve cognitive deficits in DS.

Down syndrome (DS), or trisomy 21, is the most common genetic cause of intellectual disability, for which treatment options are few and of doubtful efficacy (1, 2). The extra chromosome 21 is associated with increased gene dosage and global alterations of gene expression, disrupting biological homeostasis and contributing to its various clinical and neurological manifestations (3) (4). Among these, adult DS patients present with cognitive decline due to an early-onset Alzheimer's disease (AD)-like pathology (5–11), as well as white matter pathology and hypomyelination (12). A progressive loss of olfaction, which is typical of neurodegenerative diseases, is also prevalent (13) and starts during the prepubertal period (14), and men with DS may display deficits in sexual maturation (15).

The inability to perceive odors, together with infertility, is also characteristic of gonadotropin-releasing hormone (GnRH) deficiency in patients with Kallmann syndrome (16). GnRH, which is essential for reproduction in all mammals (17), is secreted by specialized neurons in the hypothalamus and activates the hypothalamic-pituitary-gonadal (HPG) axis to produce sex steroids (16). However, the first centrally driven gonad-independent activation of the HPG axis occurs well before puberty, during the infantile period in both humans and mice (18, 19), which is a phenomenon known as “minipuberty” that sets in motion the entire process of reproductive maturation (20). Additionally, the expression of GnRH and its cognate receptor GnRHR in extrahypothalamic areas not directly involved

in reproduction suggests a role for GnRH in higher brain functions (21–23). Given these phenotypic and temporal correlations, we used Ts65Dn mice, which overexpress the mouse genomic region orthologous to chromosome 21 (chromosome 16) (24) and recapitulate many of the anatomical, neurobiological, and behavioral phenotypes of human DS (25–27), to examine whether olfactory and cognitive deficits in DS could stem from GnRH abnormalities and be reversed by its replacement in mice and DS patients.

Results

Ts65Dn mice show DS-like olfactory and cognitive deficits

To explore whether olfactory and cognitive deficits, as observed in DS patients, also occurred in Ts65Dn mice and to determine their temporality, we performed habituation-dishabituation tests to assess odor discrimination (28) and a novel object recognition test [also used in DS patients (29)] to assess recognition memory, a hippocampus-dependent task (30), in prepubertal [postnatal day 35 (P35)] and young adult (P90) mice (Fig. 1A). Whereas olfactory performance in Ts65Dn mice was normal at birth (as assessed by milk intake, an olfaction-dependent behavior in newborns) and the infantile period (assessed using the homing test) (fig. S1), olfactory deficits appeared between the second week of life and the juvenile period. Although male and female prepubertal (P35) Ts65Dn mice showed normal habituation (i.e., reduced sniffing time when an odor was reintroduced), once habituated, they were unable to distinguish novel from known odors (Fig. 1B), a deficit that persisted in adulthood (Fig. 1C), phenocopying the prepubertal onset of olfactory deficits in DS patients (14). By contrast, novel object recognition in prepubertal Ts65Dn mice was comparable to that in wild-type (WT) littermates (Fig. 1D) but impaired in young adults (Fig. 1E), revealing an age-dependent cognitive decline reminiscent of DS. Two alternative explanations for age-related cognitive deterioration—neuroinflammation (31) and triplication of the amyloid precursor protein

¹Univ. de Lille, Inserm, CHU Lille, Lille Neuroscience and Cognition, UMR-S 1172, Labex DistAlz, Lille, France. ²Laboratory of Development and Plasticity of the Neuroendocrine Brain, FHU 1000 Days for Health, EGID, Lille, France. ³Department of Endocrinology, Diabetology, and Metabolism, Lausanne University Hospital, Lausanne, Switzerland. ⁴Faculty of Biology and Medicine, University of Lausanne, Lausanne, Switzerland. ⁵Laboratoire de Neurosciences Cognitives et Adaptatives (LNCA), UMR 7364, Université de Strasbourg-CNRS, Strasbourg, France. ⁶Université de Lyon, Université Claude Bernard Lyon 1, Inserm, Stem Cell and Brain Research Institute U1208, Bron, France. ⁷Department of Clinical Neurosciences, Neurorehabilitation Unit, University Hospital CHUV, Lausanne, Switzerland. ⁸Experimental Pharmacology, Center for Molecular Signaling (PZMS), Saarland University School of Medicine, Homburg, Germany. ⁹Universidad de Córdoba, IMIBIC/HURS, CIBER Fisiopatología de la Obesidad y Nutrición, Instituto de Salud Carlos III, Córdoba, Spain. ¹⁰Neuronal Control of Metabolism Laboratory, Institut d'Investigacions Biomèdiques August Pi i Sunyer (IDIBAPS), Barcelona, Spain. ¹¹Centro de Investigación Biomédica en Red (CIBER) de Diabetes y Enfermedades Metabólicas Asociadas (CIBERDEM), Barcelona, Spain. ¹²Department of Genetic Medicine, University Hospitals of Geneva, Genève, Switzerland. ¹³CNRS UMR 7104, INSERM U1258, GenomEast Platform, Institut de Génétique et de Biologie Moléculaire et Cellulaire (IGBMC), Université de Strasbourg, Illkirch, France. ¹⁴Neurologic Clinic and Polyclinic, MS Centre and Research Centre for Clinical Neuroimmunology and Neuroscience Basel, University Hospital Basel, University of Basel, Basel, Switzerland. ¹⁵Laboratory for Research in Neuroimaging (LREN), Centre for Research in Neurosciences, Department of Clinical Neurosciences, Lausanne University Hospital and University of Lausanne, Lausanne, Switzerland. ¹⁶Centre National de la Recherche Scientifique, Université de Strasbourg, Institut des Neurosciences Cellulaires et Intégratives, Strasbourg, France. ¹⁷Université de Bordeaux, Inserm, U1215, Neurocentre Magendie, Bordeaux, France. ¹⁸Neurology Department, Max Planck Institute for Human Cognitive and Brain Sciences, Leipzig, Germany.

*Corresponding author. Email: nelly.pitteloud@chuv.ch (N.P.); vincent.prevot@inserm.fr (V.P.)

†These authors contributed equally to this work. ‡Present address: Institute of Cell Biology and Neuroscience and Buchmann Institute for Molecular Life Sciences (BMLS), University of Frankfurt, Frankfurt am Main, Germany. §Present address: Department of Medicine, Harvard Medical School, Division of Endocrinology, Diabetes, and Hypertension, Brigham and Women's Hospital, Boston, MA 02115, USA. ¶Present address: Istituto Italiano Di Tecnologia, Genoa, Italy. #These authors contributed equally to this work.

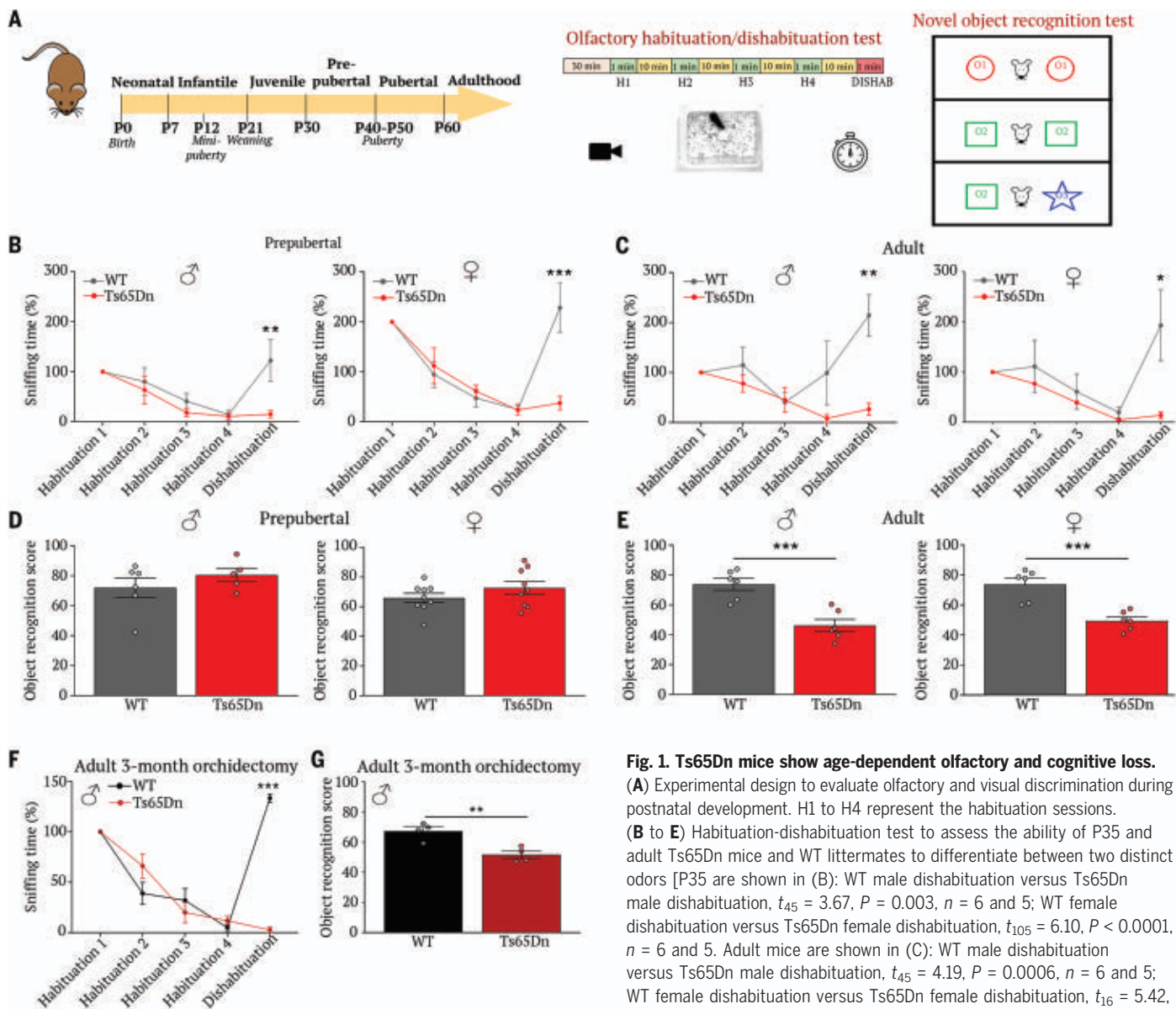


Fig. 1. Ts65Dn mice show age-dependent olfactory and cognitive loss.

(A) Experimental design to evaluate olfactory and visual discrimination during postnatal development. H1 to H4 represent the habituation sessions.

(B to E) Habituation-dishabituation test to assess the ability of P35 and adult Ts65Dn mice and WT littermates to differentiate between two distinct odors [P35 are shown in (B): WT male dishabituation versus Ts65Dn male dishabituation, $t_{45} = 3.67$, $P = 0.003$, $n = 6$ and 5; WT female dishabituation versus Ts65Dn female dishabituation, $t_{105} = 6.10$, $P < 0.0001$, $n = 6$ and 5. Adult mice are shown in (C): WT male dishabituation versus Ts65Dn male dishabituation, $t_{45} = 4.19$, $P = 0.0006$, $n = 6$ and 5; WT female dishabituation versus Ts65Dn female dishabituation, $t_{16} = 5.42$, $P = 0.0002$, $n = 5$ and 5] or recognize new objects in their environment

[P35 mice are shown in (D): WT male versus Ts65Dn male, $t_9 = 1.02$, $P = 0.33$, $n = 6$ and 5; WT female versus Ts65Dn female, $t_{16} = 1.278$, $P = 0.22$, $n = 9$ and 9. Adult mice are shown in (E): WT male versus Ts65Dn male, $t_{10} = 4.8$, $P = 0.0007$, $n = 6$ and 6; WT female versus Ts65Dn female, $t_{10} = 4.93$, $P = 0.0006$, $n = 6$ and 6]. (F and G) Both WT and Ts65Dn littermates behaved similarly to intact animals [(D) and (E)] 3 months after orchidectomy [(F): WT dishabituation versus Ts65Dn dishabituation, $t_{30} = 12.18$, $P < 0.0001$, $n = 4$ and 4; (G): WT versus Ts65Dn, $t_6 = 4.156$, $P = 0.006$, $n = 4$ and 4]. Values represent means \pm SEM. Unpaired Student's t test was used to compare two conditions; two-way repeated-measures analysis of variance (ANOVA) followed by Sidak's post hoc test was used to compare three or more conditions. * $P < 0.05$; ** $P < 0.01$; *** $P < 0.001$.

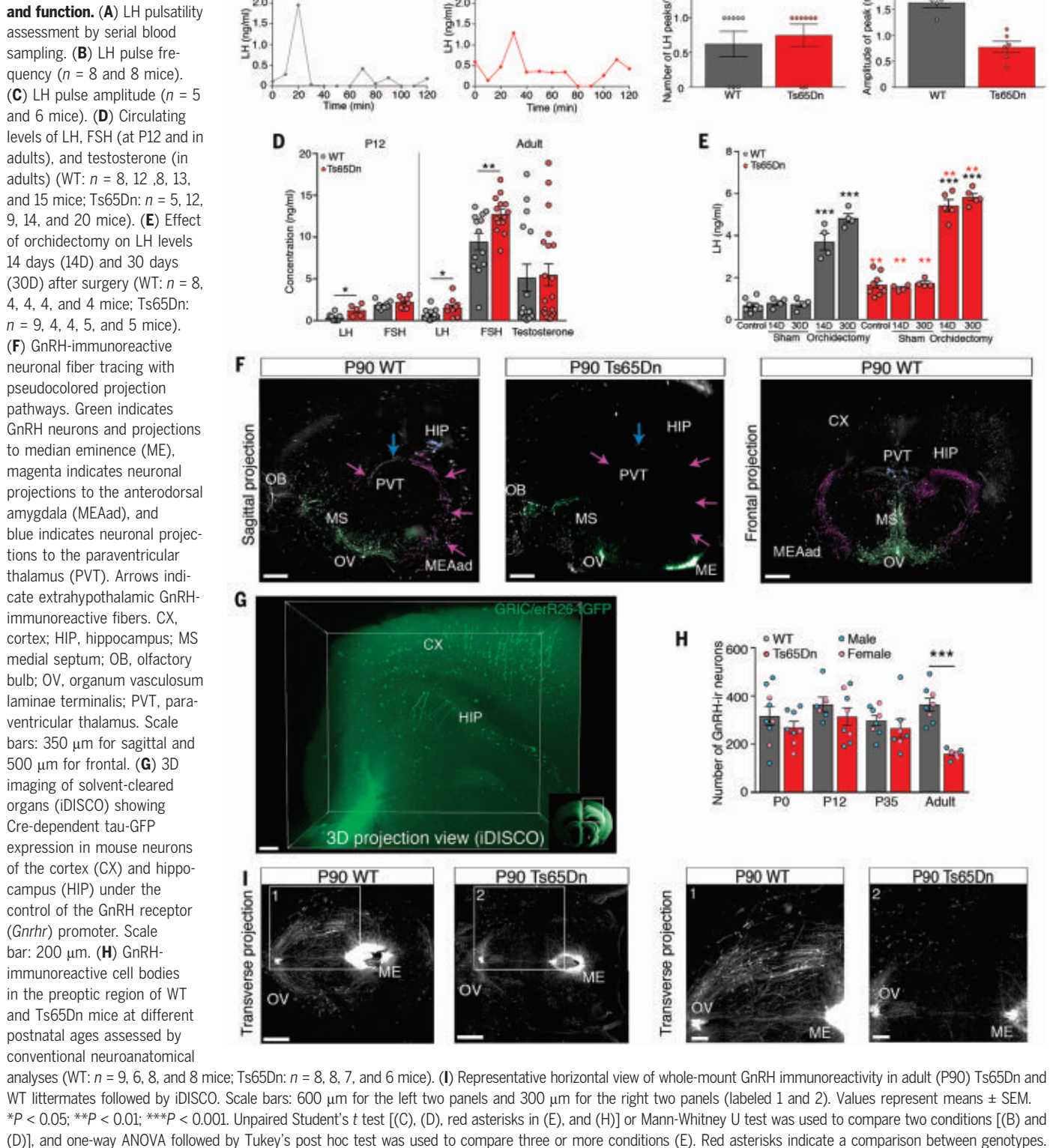
(*App*) gene in both DS patients and Ts65Dn mice (24)—were eliminated because inflammatory markers were comparable between the two genotypes (fig. S2) and any changes in the expression of AD-related proteins occurred in middle-aged (P360) but not young adult (P90) Ts65Dn animals (fig. S3), that is, well after the onset of olfactory and cognitive changes.

With regard to sexual development and reproductive maturation, Ts65Dn mice are known to show abnormalities (24), with males being infertile and females subfertile (32). Additionally, we found that males displayed severe

hypogonadism in adulthood (fig. S4), whereas females showed normal puberty timing and regular estrous cyclicity as young adults but became anovulatory at 12 months of age (fig. S5). These sexually dimorphic phenotypes also resemble those reported in DS patients (15). To understand whether these changes stemmed from alterations to the HPG axis, we measured serum gonadotropin levels. Adult male (Fig. 2, A to C) and female (fig. S5, I to K) Ts65Dn mice showed normal luteinizing hormone (LH) pulse frequency but decreased LH pulse amplitude. However, at P12, during the peak of minipub-

erty, levels of the gonadotropins LH and follicle stimulating hormone (FSH) were not markedly altered in female Ts65Dn mice (fig. S5L). In male Ts65Dn mice at P12, LH but not FSH levels were higher than in WT mice, whereas both gonadotropins were increased in adulthood (Fig. 2D), a phenomenon also seen in DS men (15, 33). Despite this, adult male Ts65Dn mice displayed unaltered testosterone levels (Fig. 2D), similar to DS men (15). However, serum LH levels before and 14 and 30 days after bilateral orchidectomy were comparably increased in both groups (Fig. 2E), indicating

Fig. 2. Ts65Dn mice progressively lose GnRH expression and function. (A) LH pulsatility assessment by serial blood sampling. (B) LH pulse frequency ($n = 8$ and 8 mice). (C) LH pulse amplitude ($n = 5$ and 6 mice). (D) Circulating levels of LH, FSH (at P12 and in adults), and testosterone (in adults) (WT: $n = 8, 12, 8, 13$, and 15 mice; Ts65Dn: $n = 5, 12, 9, 14$, and 20 mice). (E) Effect of orchidectomy on LH levels 14 days (14D) and 30 days (30D) after surgery (WT: $n = 8, 4, 4, 4$, and 4 mice; Ts65Dn: $n = 9, 4, 4, 5$, and 5 mice). (F) GnRH-immunoreactive neuronal fiber tracing with pseudocolored projection pathways. Green indicates GnRH neurons and projections to median eminence (ME), magenta indicates neuronal projections to the anterodorsal amygdala (MEAad), and blue indicates neuronal projections to the paraventricular thalamus (PVT). Arrows indicate extrahypothalamic GnRH-immunoreactive fibers. CX, cortex; HIP, hippocampus; MS, medial septum; OB, olfactory bulb; OV, organum vasculosum laminae terminalis; PVT, paraventricular thalamus. Scale bars: 350 μm for sagittal and 500 μm for frontal. (G) 3D imaging of solvent-cleared organs (iDISCO) showing Cre-dependent tau-GFP expression in mouse neurons of the cortex (CX) and hippocampus (HIP) under the control of the GnRH receptor (*Gnrhr*) promoter. Scale bar: 200 μm . (H) GnRH-immunoreactive cell bodies in the preoptic region of WT and Ts65Dn mice at different postnatal ages assessed by conventional neuroanatomical analyses (WT: $n = 9, 6, 8$, and 8 mice; Ts65Dn: $n = 8, 8, 7$, and 6 mice). (I) Representative horizontal view of whole-mount GnRH immunoreactivity in adult (P90) Ts65Dn and WT littermates followed by iDISCO. Scale bars: 600 μm for the left two panels and 300 μm for the right two panels (labeled 1 and 2). Values represent means \pm SEM.



intact gonadal steroid communication between the testes and the hypothalamus. Similarly, orchidectomy did not affect olfactory or cognitive performance (Fig. 1, F and G), suggesting that any deficits were not due to gonadal steroid deficiency or altered gonad-brain communi-

cation. Together, these results confirm that trisomic Ts65Dn mice also reproduce the olfactory, cognitive, and sexually dimorphic reproductive phenotype of DS patients and implicate HPG axis dysregulation as a putative cause of these deficits.

GnRH is progressively lost in Ts65Dn mice

In keeping with our studies in human fetuses (21), three-dimensional (3D) imaging and analyses of solvent-cleared tissue (iDISCO) from adult WT mice revealed numerous extra-hypothalamic GnRH projections (Fig. 2F),

often in close apposition to the walls of the lateral ventricles (movies S1 and S2). Unilateral stereotaxic injections of adeno-associated viral vectors encoding yellow fluorescent protein (AAV9.EF1a.DIO.eYFP.WPRE.hGH) into the dorsolateral median eminence, where GnRH neuroendocrine terminals are located, in adult WT *Gnrh::Cre* mice (fig. S6A) led to YFP labeling not only of GnRH neuronal cell bodies and processes in the preoptic area (POA) (fig. S6, B and C) but also of processes in the cortex (fig. S6, D and E), hippocampus (fig. S6, D and F), and paraventricular thalamus (fig. S6, D and F). Thus, at least some extrahypothalamic GnRH projections in brain areas that control cognitive and social behaviors actually came from hypophysiotropic GnRH neurons in the hypothalamus (Fig. 2F and fig. S6A). iDISCO analyses of *Gnrhr::Cre;Tau-GFP^{loxP/+}* mice also identified green fluorescent protein (GFP)-labeled neurons expressing the GnRH promoter in the mouse cerebral cortex and hippocampus (Fig. 2G and fig. S7, A to F), supporting a nonreproductive role for GnRH.

Using conventional immunohistochemistry and iDISCO, which provide comparable and accurate counts of GnRH neurons (21, 34), we found no difference in either the distribution or the number of GnRH somata at birth (P0) between Ts65Dn and WT mice regardless of sex but did find a profound loss of both hypothalamic and extrahypothalamic GnRH-immunoreactive somata and fibers starting after puberty onset in Ts65Dn mice (Fig. 2H and fig. S8). In adult (P90) Ts65Dn mice, although GnRH fibers were visible in the median eminence (Fig. 2I), extensive extrahypothalamic GnRH projections were absent (Fig. 2, F and I), mirroring the age-related deterioration of cognitive performance observed in these mice (Fig. 1, D and E).

microRNA-transcription factor imbalances underlie olfactory and cognitive impairments

HPG axis activation through GnRH expression at minipuberty (P12) is regulated by a complex switch consisting of several microRNAs, in particular miR-155 and the miR-200 family, as well as their target transcriptional repressor-activator genes, in particular *Zeb1* and *Cebpb* (Fig. 3A) (18). Human chromosome 21 and murine chromosome 16 code for at least five of these microRNAs (miR-99a, let-7c, miR-125b-2, miR-802, and miR-155), of which all except miR-802 are selectively enriched in GnRH neurons in WT mice around minipuberty (18). Given the peripubertal loss of GnRH immunoreactivity in Ts65Dn mice, we analyzed global microRNA and gene expression in the POA of adult mice and found a down-regulation of miR99a as well as smaller decreases in let-7c, miR-125b-2, miR-802, and miR-155 (Fig. 3B). Despite not being located on chromosome 16, miR-200 family members

were reduced by 50% or more (Fig. 3C) and were accompanied by an up-regulation of *Zeb1* mRNA and a consequent marked decrease in *Gnrhl* expression (Fig. 3D). Real-time polymerase chain reaction (PCR) analyses of cell-sorted GnRH neurons from *Gnrh::gfp*;Ts65Dn mice (Fig. 3E and fig. S9) confirmed that this increase in *Zeb1*, a *Gnrhl* promoter repressor, and a concomitant down-regulation of the *Gnrhl* promoter activators *Otx2* and *Kiss1r* already occurred during the infantile period, that is, minipuberty (Fig. 3F), initiating decreased *Gnrhl* expression (Fig. 3D). Accordingly, the selective overexpression of miR-200b in the POA of adult (P90) Ts65Dn males using stereotaxic injections of AAV9-EF1a-mmu-mir200b-eGFP but not a control vector (Fig. 3, G and H, and fig. S10, A and B), which rescued the capacity to differentiate odors (Fig. 3L) and recognize novel objects (Fig. 3M), also increased the number of neurons expressing *Gnrhl* (Fig. 3, I to K, and fig. S10D) and the *Gnrhl* promoter regulator *Otx2* (Fig. 3I and fig. S10, C and D) in the POA. Conversely, male *Gnrh::Cre;Dicer^{loxP/loxP}* mice, in which microRNA processing (and thus GnRH expression) is selectively knocked out in GnRH neurons, phenocopied Ts65Dn mice, displaying impaired olfactory discrimination and cognition (Fig. 3, N and O).

Hypothalamic miR-200b overexpression rectifies hippocampal gene expression

To further analyze how miR-200 expression in the POA could influence cognitive function, we performed RNA sequencing (RNA-seq) and differential gene expression analyses of the POA and hippocampus dissected from 6- to 8-month-old WT and Ts65Dn littermates injected in the POA with control adeno-associated virus (AAV) and from Ts65Dn mice infected with the vector overexpressing miR-200b (fig. S11A). Whereas eight genes were differentially expressed in the POA of Ts65Dn versus WT littermates (fig. S11B), 91 were differentially expressed in the hippocampus (Fig. 4, A and B), many involved in axon ensheathment, myelination, and oligodendrocyte differentiation, as well as in potassium ion transport (Fig. 4C), in agreement with previous transcriptomic studies of the hippocampus of autopsied DS patients and mouse models (12, 35). Down-regulated genes were involved in G protein-coupled receptor signaling, amino acid transport, and neurotransmission (fig. S11, C and D). miR-200b overexpression for 3 months in the POA of adult Ts65Dn mice reversed the up-regulation of 53 of 72 genes in the hippocampus (Fig. 4D), in particular those involved in the aforementioned biological processes (fig. S11E), and the down-regulation of 6 of 19 genes (fig. S11D). This phenomenon was confirmed by quantitative reverse transcription PCR (qRT-PCR) analyses for key

genes involved in axon ensheathment, myelination, and oligodendrocyte differentiation, including myelin basic protein (*Mbp*) and inhibitor of DNA binding 4 (*Id4*), and potassium ion transport, such as the potassium channel *Kcnj13* and aquaporin 1 (*Aqp1*) (Fig. 4E and fig. S11, F and G). Additionally, seven genes up-regulated in the Ts65Dn hippocampus are known to be similarly altered in DS patients (fig. S12A) (35) and include four that are involved in myelination, of which the up-regulation of three is reversed by miR-200b overexpression in the POA of Ts65Dn mice (fig. S12B). However, although protein levels of two of these, *Kcnj13* and *Mbp*, in the contralateral hippocampus of the same animals showed an effect of miR-200b, there were discrepancies in the direction of change between the two analyses, as might be expected given the complex control mechanisms involved and the concomitant up- or down-regulation of other transcriptional regulators, such as the known *Mbp* transcriptional stabilizer Quaking (*Qk*) (36) (fig. S11, F and G), which can also act as translational repressor depending on the molecular context (37, 38). Similarly, transcripts for the multifunctional homeoprotein *Otx2* (39) were up-regulated in the hippocampal cornu ammonis area 1 (CA1) in Ts65Dn mice, in contrast to the POA (fig. S10, C and D), but normalized by preoptic miR-200b overexpression (fig. S12, C to E). Regardless of the direction of these changes, they provide a putative molecular basis for anomalies of brain structure and composition in DS patients (12), and their reversal by miR-200b infusion in the POA is of both mechanistic and therapeutic interest.

Hypothalamic miR-200b overexpression rectifies hippocampal synaptic transmission

Next, to explore whether the functional basis of recognition memory was altered in Ts65Dn mice, we assessed basal hippocampal synaptic transmission *in vivo* by stimulating commissural fibers from the left hippocampus in anesthetized mice and, for each stimulation site, recording both population spikes and field excitatory postsynaptic potentials (fEPSPs) from CA1 stratum radiatum of the contralateral hippocampus (Fig. 4F). Paired-pulse stimulation (fig. S13A) revealed similar facilitation of fEPSPs in the CA1 pyramidal cell layer of WT and Ts65Dn mice (fig. S13B). However, the stimulus-response curve obtained by recording both fEPSPs and population spikes in the CA1 (Fig. 4G and fig. S13C), as well as the area under the curve (Fig. 4H), were significantly lowered in Ts65Dn compared with WT mice, suggesting lower dendritic excitability. These changes were diminished by miR-200b overexpression in the POA (Fig. 4, G and H, and fig. S13D). To further examine the relationship between synaptic input strength and the amplitude and latency to firing of CA1 pyramidal cells,

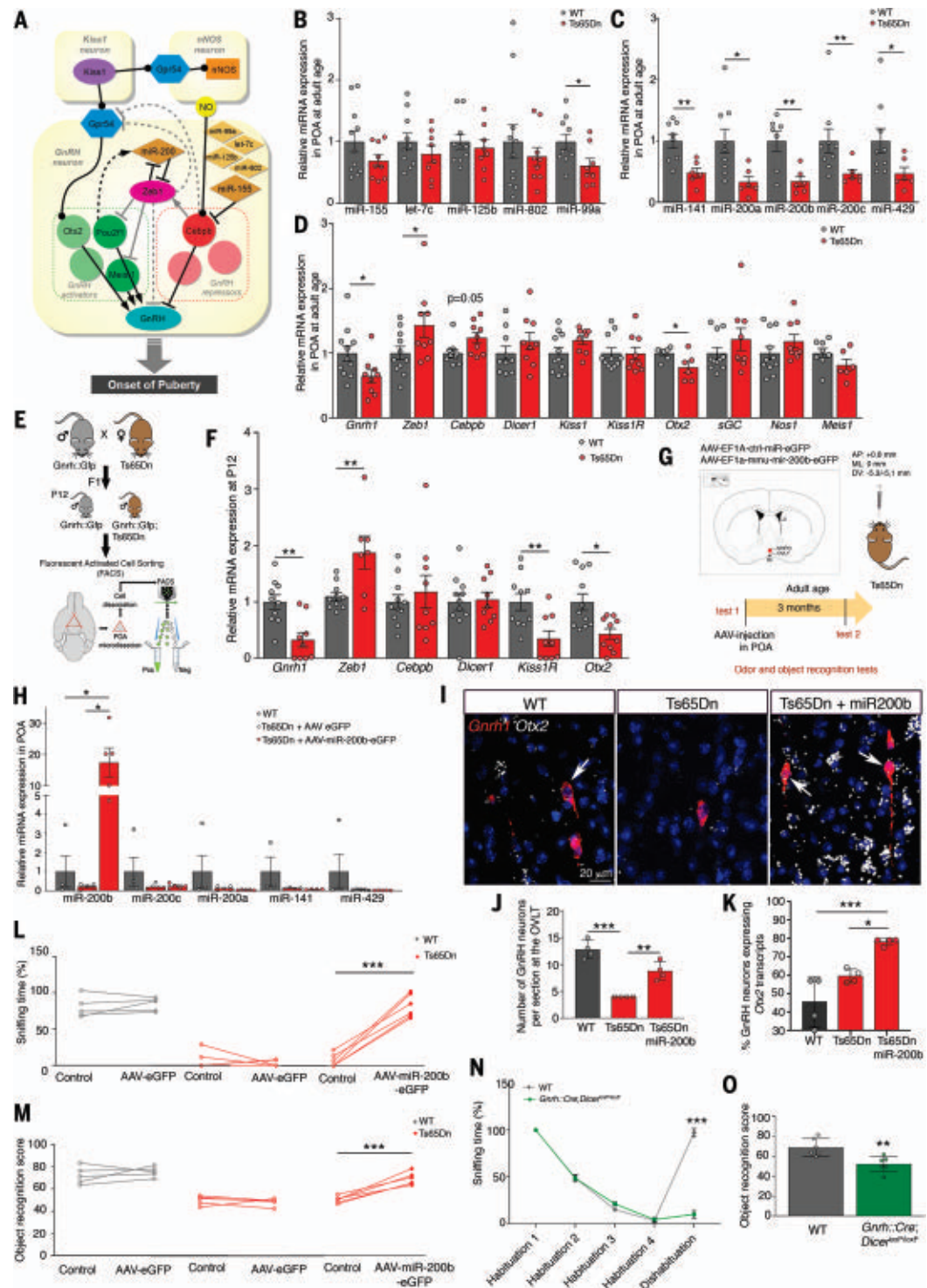
Fig. 3. GnRH transcriptional machinery disequilibrium underlies cognitive impairments.

(A) Putative microRNA–transcription factor network regulating hypothalamic GnRH promoter activation during postnatal development [adapted from (18)]. (B to D) qRT-PCR analysis of expression levels of microRNAs located on chromosome 16 (B) and miR-200 family members (C), as well as hypothalamic GnRH promoter modulators (D) in the POA of adult WT and Ts65Dn littermates [(B): $n = 11, 10, 10, 11$, and 10 WT mice, and $n = 9, 8, 8, 9$, and 8 Ts65Dn mice; (C): $n = 8, 9, 7, 9$, and 9 WT mice, and $n = 6, 6, 6, 6$, and 6 Ts65Dn mice; (D): $n = 11, 11, 9, 10, 11, 11, 7, 11, 11$, and 8 WT mice, and $n = 9, 9, 9, 9, 9, 6, 9, 9$, and 6 Ts65Dn mice]. (E) Generation of *Gnrh::Gfp*/Ts65Dn reporter mice, which express GFP under an ectopic *Gnrh* promoter. GnRH-GFP neurons were isolated by fluorescent activated cell sorting (FACS) from the POA of *Gnrh::Gfp* and *Gnrh::Gfp*/Ts65Dn littermates at P12. (F) qRT-PCR analysis of gene expression in FACS-sorted GnRH-GFP cells ($n = 10, 10, 11, 11, 10$, and 11 WT mice; $n = 9, 7, 9, 9, 9$, and 10 Ts65Dn mice).

(G) Experimental design to evaluate the functional involvement of miR-200 family members in odor discrimination and novel object recognition in Ts65Dn mice. The red dot indicates the viral injection site. LV, lateral ventricle; MePO, median preoptic nucleus; OVLT, organum vasculosum laminae terminalis. (H) Effect of viral overexpression of miR-200b in the POA on miR-200 family member expression ($n = 4, 5$, and 5 mice).

(I to M) Effect of viral miR-200b overexpression in the POA on the number of neurons expressing *Gnrh* transcripts in the OVLT [(I) and (J)] and the proportion expressing *Otx2* [(I) and (K)], as assessed by fluorescent in situ hybridization, as well as odor discrimination (L) and novel object recognition (M) in Ts65Dn mice [(J) and (K): $n = 4, 4$, and 4 mice; (L) and (M): $n = 5, 5$, and 6 mice].

(N and O) Odor discrimination [(N): $n = 6$ mice per group] and novel object recognition [(O): $n = 6$ mice per group] in 12-month-old male mice selectively lacking *Dicer* in GnRH neurons. Values represent means \pm SEM. * $P < 0.05$; ** $P < 0.01$; *** $P < 0.001$. Unpaired Student's *t* test or Mann-Whitney U test [(B) to (D) and (F)], paired Student's *t* test or Wilcoxon matched-pair test [(L) and (M)], and Kruskal-Wallis test (H) were used to compare two conditions, and one-way [(J) and (K)] or two-way repeated measures [(N) and (O)] ANOVA followed by Tukey's and Sidak's post hoc tests was used to compare three or more conditions.



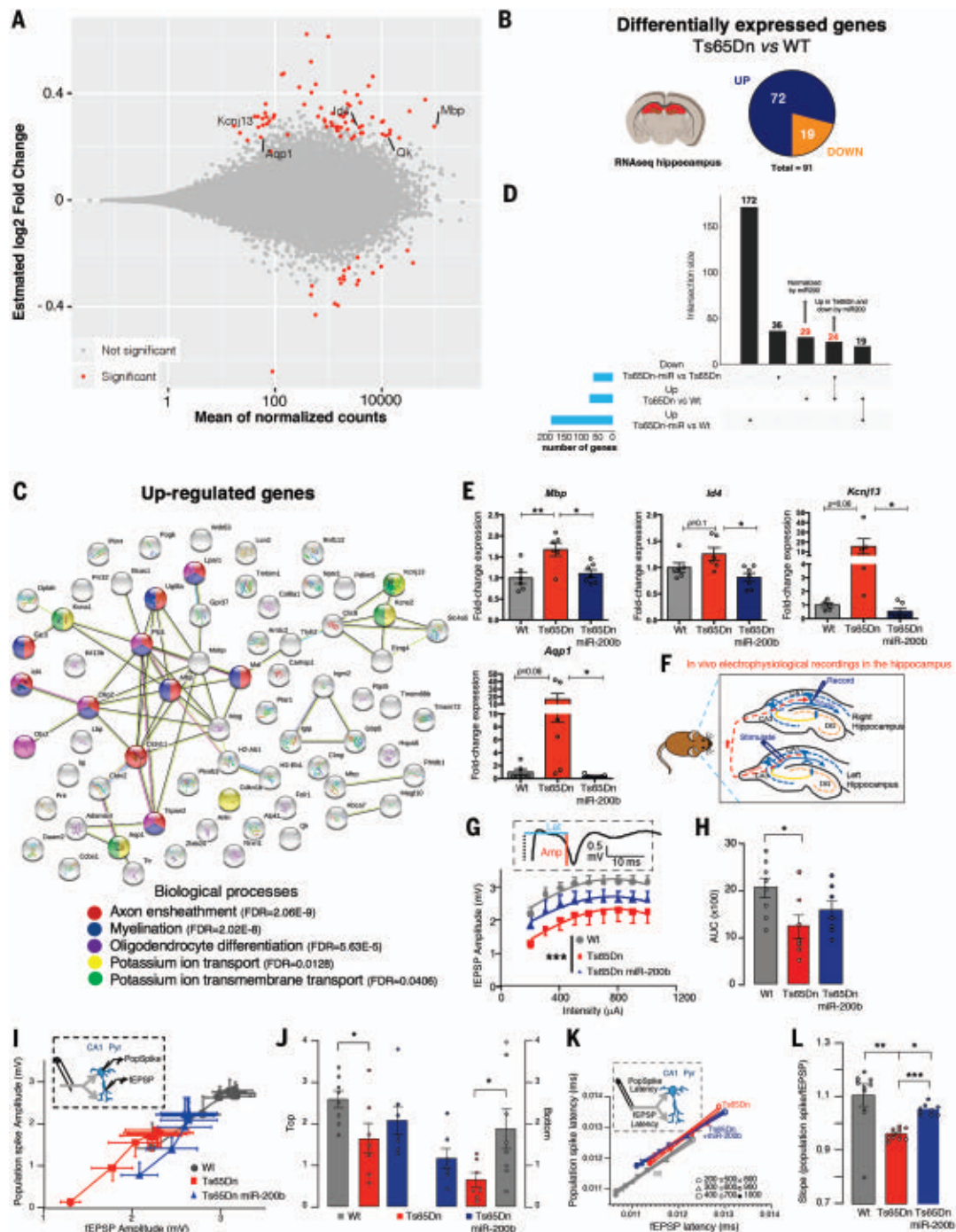
we analyzed population spike–fEPSP coupling at different stimulation intensities (Fig. 4I). The highest and lowest values on the Boltzmann-fitted population spike–fEPSP curve were lower

in Ts65Dn mice than in WT animals, reflecting a lower maximal-minimal spike amplitude in Ts65Dn mice that was rescued by miR-200b overexpression (Fig. 4J). Although latency did

not change (Fig. 4K and fig. S13, E and F), cellular excitability was lowered in Ts65Dn mice and partially reversed by miR-200 overexpression (Fig. 4L). Together, these results

Fig. 4. Hypothalamic miR-200b overexpression rescues hippocampal transcriptome and connectivity. (A) MA plot of gene expression changes (estimated log₂ fold changes as a function of the mean of normalized counts; $P_{adj} < 0.05$) in the hippocampus of adult male (P180) Ts65Dn ($n = 3$) versus WT mice ($n = 4$).

(B) Pie chart of the number of differentially regulated genes between Ts65Dn and WT littermates in the hippocampus ($P_{adj} < 0.05$). (C) STRING protein network analysis of up-regulated genes. (D) UpSet plot showing the intersection between differentially up-regulated genes in the Ts65Dn hippocampus and genes rescued by miR-200b. (E) qRT-PCR confirmation of RNA-seq data. (F) Schematic illustrating in vivo electrophysiological recordings in the dorsal hippocampus of adult WT ($n = 8$), Ts65Dn ($n = 7$), and Ts65Dn mice with miR-200b overexpression ($n = 7$). fEPSPs and population spikes were evoked in the hippocampal CA1 area by stimulating commissural fibers in the contralateral hippocampus. (G) Synaptic input-output curves indicating the relationship between fEPSP amplitude at increasing stimulus intensities (200 to 1000 μ A). The inset shows a representative fEPSP recording with measurement of latency (blue line) and amplitude (red line). (H) Area under the curve (AUC) of fEPSP responses. (I) Boltzmann-fitted fEPSP-population spike coupling. The inset contains a schematic showing both fEPSP and population spike recording in the CA1 pyramidal layer (CA1 pyr) following the same commissural path stimulation. (J) Top and bottom Boltzmann-fitted parameters of fEPSP-population spike coupling as a measure of intrinsic excitability of CA1 pyramidal neurons. (K) Relationship between the mean fEPSP latency and population spike latency at different stimulus intensities (200 to 1000 μ A). The inset contains a schematic showing both fEPSP and population spike recording in the CA1 pyramidal layer (CA1 pyr) following the same commissural path



suggest that miR-200 family expression in the POA alters electrical signal propagation in the hippocampus and that these deficits can be remotely rescued by overexpressing miR-200b in the hypothalamus.

Hypothalamic GnRH compensation reverses olfactory and cognitive deficits

We next attempted to rescue olfactory and cognitive function in adult Ts65Dn mice by GnRH replacement. Stereotactic injection of

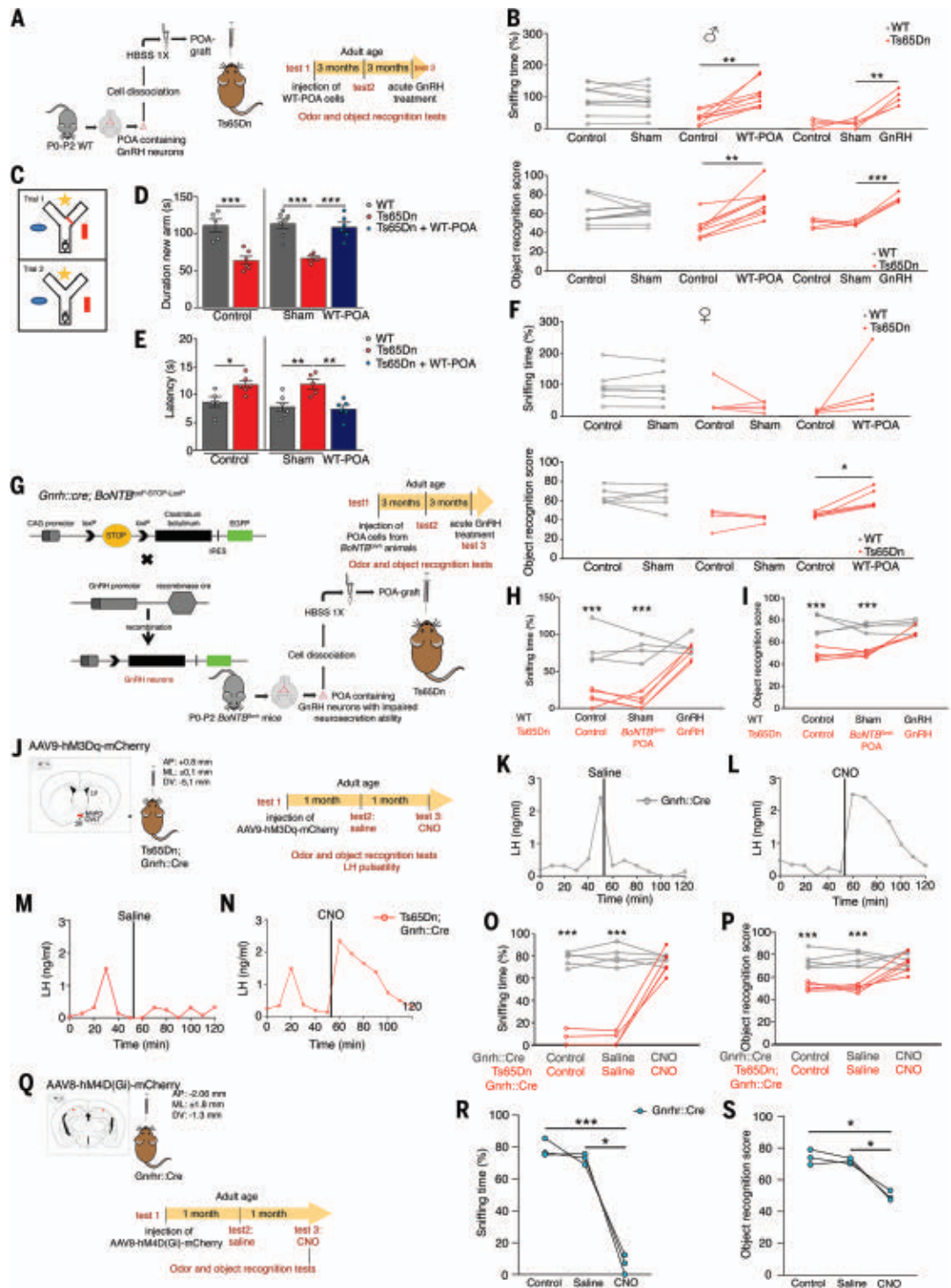
stimulation. (L) Slopes of the fEPSP-population spike relationships. Data represent means \pm SEM. * $P \leq 0.05$; ** $P \leq 0.01$; *** $P \leq 0.001$. Kruskal-Wallis ANOVA and Mann-Whitney U test (G) were used to compare two conditions, and one-way ANOVA followed by Tukey's post hoc test [(E), (H), and (L)] or two-way ANOVA (J) was used to compare three or more conditions.

dissociated cells (18) from the POA of neonatal WT *GnRh::gfp* pups (WT-POA) into the third ventricle (3V) of adult male and female Ts65Dn mice (Fig. 5A and fig. S14) (40) completely reversed both olfactory and cognitive

Fig. 5. Restoring GnRH neuronal function reverses olfactory and cognitive deficits.

(A) Cell therapy by grafting enzymatically dissociated cells from the POA of WT neonatal mice (P0 to P2) into the third ventricle of adult Ts65Dn mice. HBSS, Hanks' balanced salt solution. (B to F) Effect of WT-POA grafts in Ts65Dn mice on olfactory and cognitive performance [(B): $n = 10$, 9, and 5 male mice; (F): $n = 7$, 5, and 5 female mice], and short-term visuospatial memory assessed by the Y-maze test [(C) to (E)] 3 months after surgery [(D): $n = 5$, 6, 7, 5, and 7 male mice; (E): $n = 5$, 6, 7, 5, and 6 male mice]. (G) Experimental design to graft POA cells from neonatal mice with exocytosis-incompetent GnRH neurons (*Gnrh::Cre; BoNTB^{loxP-STOP-loxP}*). (H and I) After a 3-month recovery period, effect of *BoNTB^{Gnrh}* POA grafts and acute intraperitoneal GnRH injection on odor discrimination (H) and object recognition (I) [(H) and (I): $n = 4$ and 5 mice].

(J) Experimental design to study LH pulsatility, cognitive and olfactory performance after the chemogenetic activation of GnRH neurons by injecting adult *Gnrh::Cre* and Ts65Dn;*Gnrh::Cre* mice with an hM3Dq DREADD viral vector followed by CNO (1 mg per kg of body weight) ($n = 5$ and 5 mice). Red dots indicate virus injection sites. 3V, third ventricle; LV, lateral ventricle; MePO, median preoptic nucleus; OVLT, organum vasculosum laminae terminalis. (K to P) Representative graphs for LH pulsatility [(K) to (N)], odor discrimination (O), and novel object recognition (P). (Q) Experimental design to study olfactory and cognitive performance before and after the chemogenetic inhibition of GnRH-R expressing neurons in 6-month-old *Gnrh::Cre* mice by injection of an hM4D(Gi) DREADD viral vector. Red dots indicate virus injection sites. (R and S) Odor discrimination (R) and novel object recognition (S) ($n = 3$ and 3 mice). Values represent means \pm SEM. * $P < 0.05$; ** $P < 0.01$; *** $P < 0.001$. Data were analyzed by unpaired Student's *t* test [(D) and (E)], paired Student's *t* test or Wilcoxon matched-pair test (F), and one-way ANOVA [(D) and (E)] or one-way [(R) and (S)] or two-way [(B), (H), (I), (O), and (P)] repeated-measures ANOVA followed by Tukey's or Sidak's post hoc tests, respectively.



impairments in Ts65Dn males (Fig. 5B) as well as short-term visuospatial memory assessed in a Y-maze test (Fig. 5, C to E). Graft of WT-POA also rescued cognition in adult Ts65Dn females but only partly restored olfactory capacity (Fig. 5F). However, unlike

adult hypogonadal mice (40), WT-POA transplantation did not restore fertility in either Ts65Dn females (fig. S15) or Ts65Dn males (see methods). We next generated *Gnrh::Cre; BoNTB^{loxP-STOP-loxP}* mice in which vesicular GnRH release is selectively silenced by the

GnRH neuron-specific expression of botulinum neurotoxin B (*BoNTB^{Gnrh}*). When neonatal POA cells from these animals were grafted into adult Ts65Dn males (Fig. 5G), no olfactory or cognitive rescue was observed (Fig. 5, H and I). However, intraperitoneal GnRH injection 6 months

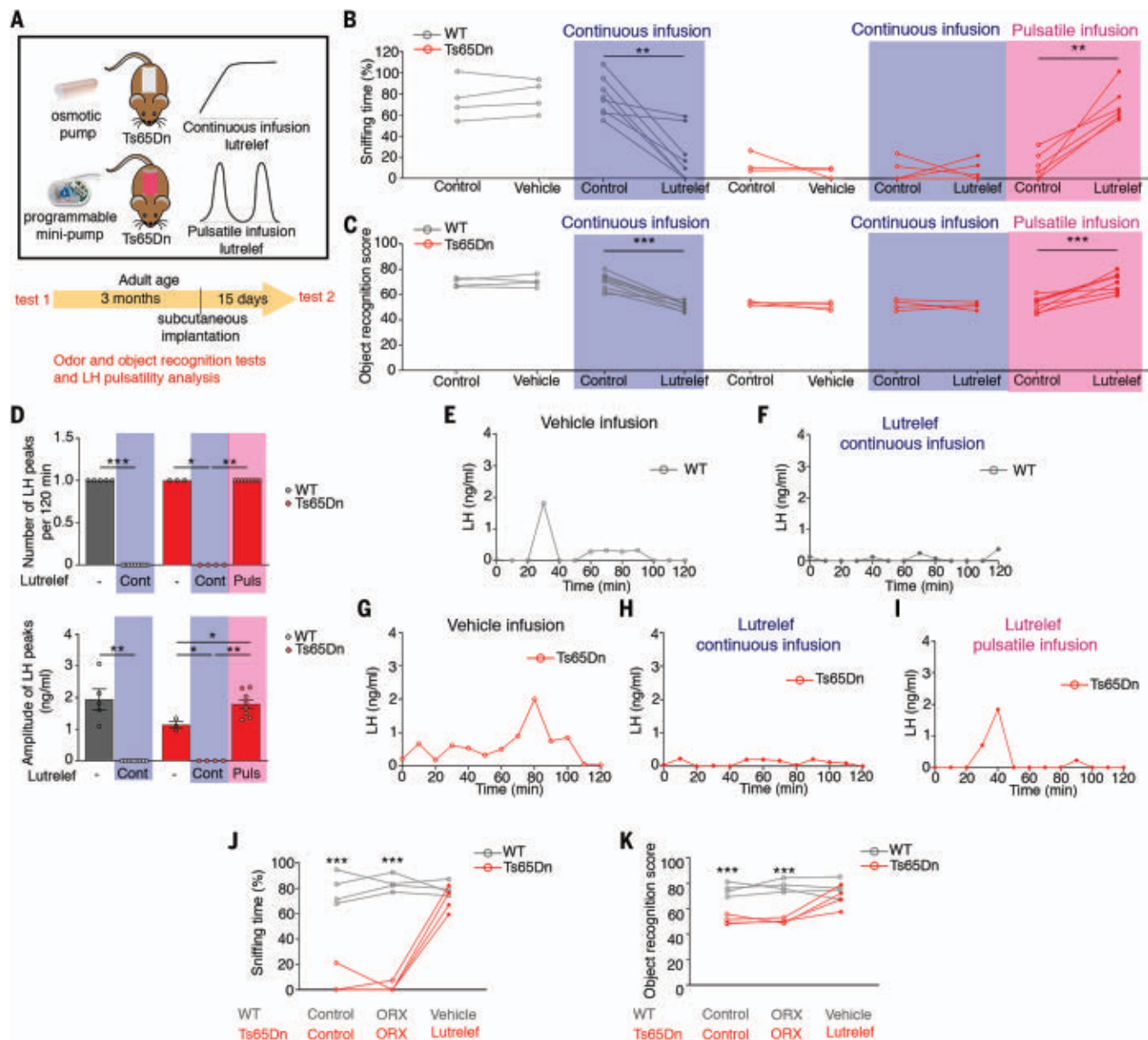


Fig. 6. Olfactory and cognitive deficit reversal requires GnRH pulsatility.

(A) Schematic of pharmacotherapy with Lutrelef, a clinically used GnRH peptide, in adult Ts65Dn mice. Mice were implanted with osmotic pumps to receive a continuous infusion of vehicle or Lutrelef (0.25 μ g over 3 hours for 2 weeks) or with a programmable minipump (iPRECIO) to receive pulsatile Lutrelef infusion (0.25 μ g per pulse over 10 min given every 3 hours over 2 weeks). (B to I) Effect of treatments on odor discrimination (B) ($n = 4, 8, 3, 5$, and 6 mice), object

recognition (C) ($n = 4, 9, 4, 4$, and 8 mice), and LH pulsatility [(D) to (I)] [(D): $n = 4, 9, 3, 4$, and 8 mice; each dot represents one subject]. (J and K) Effects of Lutrelef in orchidectomized (ORX) mice ($n = 4$). Values represent means \pm SEM. * $P < 0.05$; ** $P < 0.01$; *** $P < 0.001$. Data were analyzed by paired Student's t test or Wilcoxon matched-pair test [(B) and (C)], unpaired Student's t test or Mann-Whitney U-test (D), or a two-way repeated-measures ANOVA followed by Sidak's post hoc test [(J) and (K)].

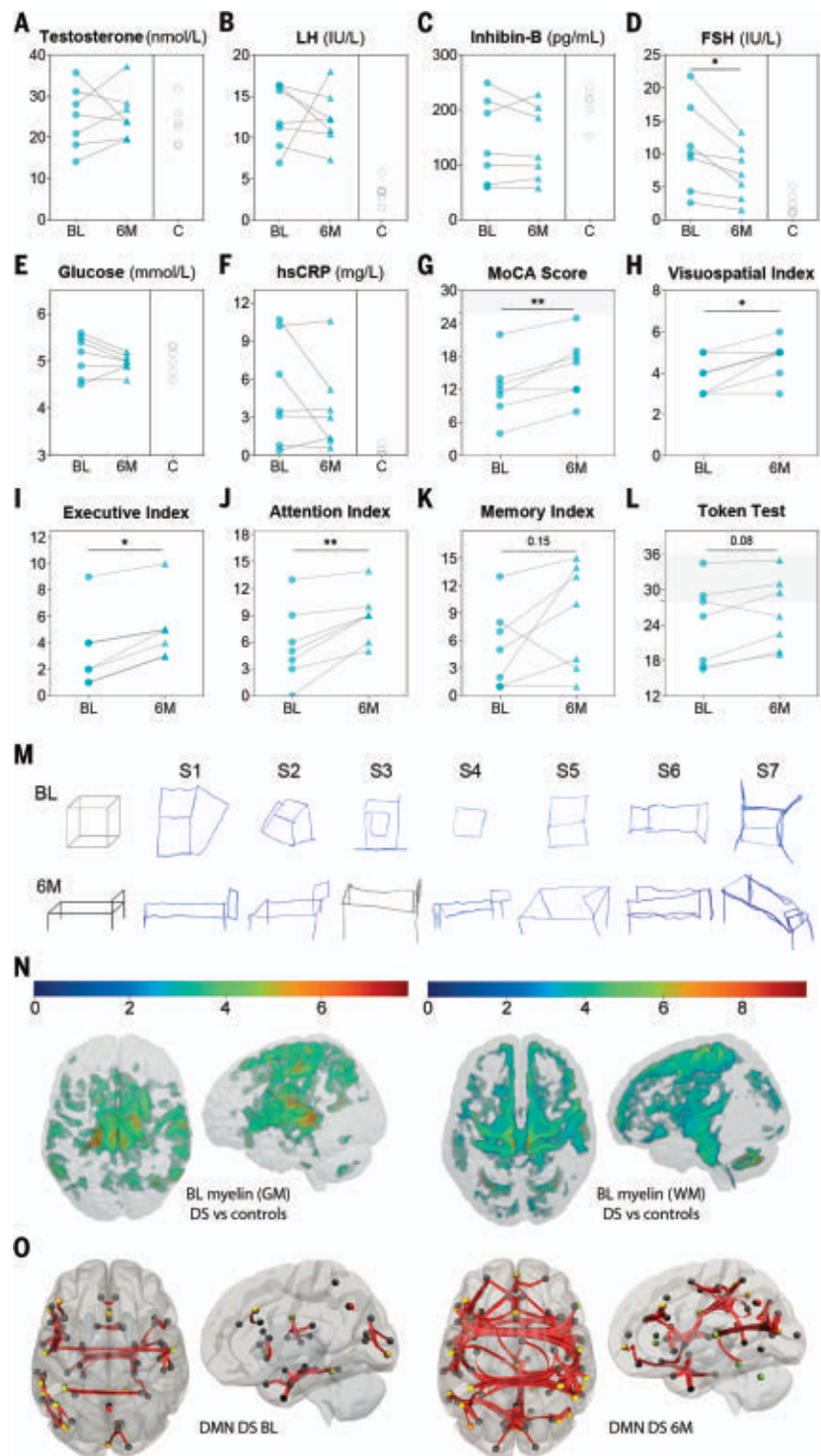
postgraft rescued olfactory and cognitive performance in both sham (Fig. 5B) and *BoNTB^{GnRh}* POA-grafted Ts65Dn mice (Fig. 5, H and I), indicating that the effects of the graft were specifically due to GnRH release.

To determine whether activating endogenous GnRH neuronal activity in Ts65Dn mice could rescue olfactory and cognitive function, we bilaterally injected adult *GnRh::Cre* and Ts65Dn;*GnRh::Cre* mice with a Cre-dependent

neuron-activating hM3Dq-DREADD (designer receptor exclusively activated by designer drugs) vector into the POA (Fig. 5J). Unlike vehicle injection (Fig. 5, K and M), intraperitoneal clozapine *N*-oxide (CNO) injections elicited increased LH levels in both *GnRh::Cre* and Ts65Dn;*GnRh::Cre* males (Fig. 5, L and N), indicating GnRH release. Additionally, they acutely restored olfactory discrimination (Fig. 5O) and cognitive performance (Fig. 5P) in Ts65Dn mice. Conversely, when neurons ex-

pressing GnRHR in the hippocampus of WT *GnRh::Cre* mice were infected with an inhibitory DREADD vector [AAV8-hSYN-DIO-hM4D(Gi)-mCherry] (Fig. 5Q), acute CNO injection (3 mg per kg of body weight) dramatically reduced both cognitive and olfactory performance (Fig. 5, R and S). Together, these data highlight the possibility that normal cognitive and olfactory function depends on extrahypothalamic GnRH neuronal projections and action, which are lost in Ts65Dn mice during

Fig. 7. Pulsatile GnRH improves patient brain connectivity and cognition. (A to F) Biochemical profile at baseline (BL, blue dots, $n = 7$) and after 6-month pulsatile GnRH therapy (6M, blue triangles, $n = 7$) compared with healthy age- and sex-matched controls (C, open circles, $n = 5$ for inhibin-B and $n = 6$ for all the other parameters). (G to L) Results of cognitive tests in male DS patients ($n = 7$) at BL (blue dots) and after 6 months of GnRH therapy (6M, blue triangles): MoCA total score, visuospatial index, executive index, attention index, memory index, and Token test score. (M) 3D drawings representing a cube and a bed, part of the visuospatial index score of the MoCA at BL and 6M for each of the seven subjects (S1 to S7). S2, S3, S5, and S7 improved at 6M. (N) Statistical parametric maps of brain anatomy differences between DS patients ($n = 8$) and age-matched male controls ($n = 44$) after family-wise error $P < 0.05$ correction for multiple comparisons at the whole-brain level. Voxel-based quantification of magnetization transfer (MT) saturation maps reveal volume loss in the cerebellum, anterior cingulate cortex, supplementary motor cortex, substantia nigra, thalamus, insula, and primary motor cortex M1 and loss of myelin content in the thalamus, primary sensorimotor cortex S1/M1, angular gyrus, insula, and superior frontal and temporal gyri bilaterally. GM, gray matter; WM, white matter. (O) Resting-state functional MRI comparison of functional connectivity in DS ($n = 7$) at BL and after 6 months of GnRH therapy (6M) in the visual (including all occipital regions, the lingual gyrus, and the cuneus) and sensorimotor (pre- and postcentral gyri, middle frontal gyrus) DMN, connected to the superior parietal lobule, the superior temporal gyrus, some prefrontal areas, and part of the anterior DMN [increased; false discovery rate (FDR)-corrected $P < 0.0005$] as well as within the hippocampal regions of the ventral DMN linked to the amygdala (reduced; FDR-corrected $P < 0.0005$). * $P < 0.05$; ** $P < 0.01$. IU/L, international units per liter.



postnatal development, leading to their DS-like phenotype.

GnRH pulsatility is essential for deficit reversal

Finally, we tested whether restoring physiological (i.e., pulsatile) GnRH release in Ts65Dn mice could reverse cognitive performance using Lutrelef, the native GnRH used to treat hypogonadotropic infertility (41, 42). Adult Ts65Dn males were implanted with a sub-

cutaneous programmable minipump that delivered either pulsatile Lutrelef (0.25 μg of GnRH per pulse over 10 min given every 3 hours), leading to activation of the GnRH receptor and the reproductive axis, or continuous Lutrelef infusion (0.25 μg over 3 hours), which downregulates the GnRH receptor and blocks the reproductive axis (43), for 15 days (Fig. 6A). Continuous infusion did not improve olfactory or cognitive performance in male Ts65Dn mice

and had a significant deleterious effect in WT mice (Fig. 6, B and C), in addition to blunting LH pulsatility (Fig. 6, D to I). By contrast, pulsatile Lutrelef, which rescued both olfactory discrimination (Fig. 6B) and cognitive function (Fig. 6C), increased LH pulse amplitude to WT levels in Ts65Dn males (Fig. 6D). Neither Lutrelef treatment nor miR-200b overexpression in the POA rescued testicular weight in Ts65Dn mice (fig. S16). Bilateral orchidectomy

did not affect the rescue of olfaction (Fig. 6J) or recognition memory (Fig. 6K) by pulsatile Lutrelief, suggesting that the functional improvements observed were independent of the gonadotropic effects of GnRH and could instead be due to the mobilization of cognitive reserves in Ts65Dn mice.

Pulsatile GnRH improves cognition in DS patients

Based on compelling results in Ts65Dn mice, we conducted an open-label pilot study to assess the effects of pulsatile GnRH therapy on cognition in DS patients. Seven DS men (26.4 ± 2.3 years) who had completed puberty and presented with olfactory defects were enrolled (table S1). Despite normal testosterone and inhibin B levels, patients exhibited mildly increased LH and FSH levels and a mild increase in estradiol levels as compared with controls (Fig. 7, A to D, and fig. S17C) yet normal pituitary sensitivity to a GnRH challenge (fig. S17, A and B). LH pulsatility was not assessed in this vulnerable population. DS patients displayed a normal body mass index and no major alteration in biochemical profile except for increased high-sensitivity C-reactive protein (hsCRP), that is, systemic inflammation (Fig. 7F and table S1). Serum neurofilament light chain, a marker of neuronal damage (44), was within the normal range for age (fig. S17S). The Montreal Cognitive Assessment (MoCA) score was used to assess cognition in DS patients for whom long cognitive battery tests are challenging, given their intellectual disability, attention deficit, and fatigue. All seven DS patients had impaired cognition (Fig. 7, G to K), whereas four had altered verbal comprehension (Token test) (Fig. 7L). Using quantitative relaxometry-based magnetic resonance imaging (MRI), we observed DS-related loss of myelin along the corticospinal tract and thalamus, increased iron in the pallidum, and volume loss in the cingulate gyrus, cerebellum, and thalamus in these patients compared with healthy age-matched controls (Fig. 7N, fig. S17R, and tables S2 and S3) (45). Resting-state functional MRI (rs-fMRI) showed altered default mode network (DMN) in our DS cohort (Fig. 7O), as previously reported (46, 47).

Pulsatile GnRH therapy using a LutrelPulse pump was given for 6 months at a dose of 75 ng per kg body weight per pulse every 2 hours to mimic the LH pulse frequency observed in healthy men (41) and was well tolerated (fig. S17, L and M). The reproductive hormonal profile did not change on GnRH therapy (Fig. 7, A to C, fig. S17C, and table S1) except for a slight decrease in serum FSH (Fig. 7D). Most metabolic parameters showed a trend toward improvement or no change (fig. S17, D to K and S and table S1). Cognitive performance, as assessed by total MoCA score, increased in

six out of seven patients (Fig. 7G), driven by subscores for visuospatial function (Fig. 7, H to M), executive function (Fig. 7I), and attention (Fig. 7J) and a trend for episodic memory (Fig. 7K). GnRH therapy also enhanced verbal comprehension (Fig. 7L). Olfactory performances (fig. S17, N to Q) and brain anatomical features did not change (fig. S18, A to D, and tables S2 and S3). However, functional connectivity as assessed by rs-fMRI increased mainly within a broad network encompassing visual and sensorimotor DMN regions, whereas connectivity within the hippocampal regions (ventral DMN) linked to the amygdala decreased (Fig. 7O), approaching control values (46, 48, 49).

Discussion

Our study demonstrates an unexpected role for GnRH in olfactory and cognitive performance, consistent with the expression of GnRH and its cognate receptor GnRHR in extra-hypothalamic areas (21–23). The progressive loss of GnRH expression during postnatal development precedes the onset of cognitive and olfactory impairments in a mouse model of DS, which can be reversed by replacing GnRH. Furthermore, in our pilot study of DS patients, pulsatile GnRH therapy improved cognition, consistent with improved connectivity in the relevant brain regions. This is particularly important given that translational studies in DS have fallen short and no pharmacological therapy to date has appreciably improved cognition (1, 50–53).

In DS patients, a deviation from neurotypical developmental trajectories leads to reduced cognitive abilities (54) and AD-like neurodegenerative changes in their 40s after a long preclinical phase (5, 6, 11, 55). Olfactory deficits of prepubertal onset worsen in adulthood concomitant with the acceleration of cognitive decline (14). In our trisomic model, which faithfully phenocopies several clinical aspects of DS, cognitive and olfactory deficits parallel a gradual loss in GnRH expression beginning in childhood and culminating in adulthood, well before any AD-like changes. The loss of GnRH itself can be traced even further back to the perturbation of the minipubertal microRNA–transcription factor switch in *Gnrh1* promoter activity during the infantile period, which integrates multiple feedback loops (18) and is partially localized on the triplicated region of both the human and mouse chromosome. Overexpressing miR-200b, one of the effectors of this switch, in the hypothalamic POA, where most GnRH neuronal cell bodies reside, not only rescues other genes of the GnRH transcriptional regulation network but also remotely normalizes olfaction and hippocampal synaptic transmission. miR-200 members have multiple targets, but although an action through other pathways cannot be ruled

out, similar effects can be obtained by directly replacing physiologically relevant GnRH levels. The improvement in cognitive function induced by pulsatile GnRH infusion is independent of changes in the sex steroid milieu in both DS patients and Ts65Dn mice. Similarly, in patients with congenital GnRH deficiency, who show a marked impairment of spatial ability while verbal abilities remain unchanged, these deficits are not rescued by exogenous androgen therapy (56). Conversely, inhibiting GnRHR-expressing cells in extrahypothalamic target regions, to which hypothalamic GnRH neurons also project, leads to DS-like changes, indicating that GnRH neurons have two or more sites of action, for reproductive and nonreproductive functions separately.

Although gonadotropin-induced gonadal function is not necessary for the cognitive or olfactory functions of GnRH, its pulsatility, which is necessary to regulate gonadotropin release, does appear necessary for these other functions also and may even regulate age-related cognitive decline (57). Thus, LH serum concentration and pulsatility, although not measurable in our study, may still be a useful marker for DS-like changes (58). Similarly, in a mouse model of AD, FSH, which is increased in DS patients and reduced by pulsatile GnRH treatment, acts directly on hippocampal neurons to mediate the AD phenotype, supporting a similar mechanism in DS (59). In that study, the effects of reducing FSH were mediated by inhibiting C/EBP β , the product of the *Cebpb* gene, a part of the minipubertal GnRH switch that both directly and indirectly, through *Zeb1*, controls GnRH expression (18) (Fig. 3A), and whose expression was also increased in our adult trisomic mice.

Other than those genes involved in *Gnrh* expression, several genes involved in oligodendrocyte differentiation or myelination, including some that show age-related dysregulation in human DS brains, were also differentially expressed in Ts65Dn mice (12). This may explain the myelin loss observed, even though decreased brain volume and hypocellularity in DS are often attributed to a neurogenesis deficit (60). During human brain development, myelin content increases during adolescence in the cortical gray matter and to some extent in white matter (61), concomitant with improved cognition (62). Given that miR-200 in the POA normalizes the expression of myelination-related genes in the Ts65Dn mouse hippocampus, it is tempting to suggest that pulsatile GnRH secretion at puberty, a crucial hypothalamic event, could also be a signal for overall brain maturation. Some animal models of dementia, including AD, also show an up-regulation of myelination genes (63) that overlap with those found in Ts65Dn mice (fig. S19A), whereas genes involved in GnRH signaling are among the most down-regulated in discrete cortical

areas of postmortem AD patient brains (64), and are also dysregulated in the hippocampus of the *THY::TAU22* mouse AD model (65), which progressively develop a hippocampal tau pathology in parallel with cognitive deficits (66, 67). Like adult Ts65Dn mice (Fig. 2, A to C), 12-month-old male *THY::TAU22* mice showed normal LH pulse frequency (fig. S19B) but decreased LH pulse amplitudes (fig. S12C). Pulsatile Lutrelef infusion rescued odor discrimination (fig. S12, D and E) and object recognition memory (fig. S12F) in these mice, confirming that olfactory and cognitive deficits in other neurodegenerative disorders could also be caused by the loss of GnRH and reversed by its replacement, perhaps through the same molecular pathways. Strengthening the parallels between DS and AD, *Afg3l2*, a mitochondrial gene down-regulated in the Ts65Dn hippocampus, prevents both demyelination and tau hyperphosphorylation, linking it to the AD-like phenotype observed in DS (68, 69). Additionally, mutations in *DUSP6* have been identified in patients with hypogonadotropic hypogonadism (70), but it is also hypermethylated in AD and prevents tau hyperphosphorylation (71, 72). The differentially modulated genes identified in Ts65Dn mice thus lie at the interface between reproductive dysfunction and AD-like cognitive and neurodegenerative alterations, much like the phenotype of DS patients themselves, making these mice a valuable DS model.

In terms of neuronal activity, cognitive deficits in Ts65Dn mice could result from alterations of synaptic plasticity and neurotransmission (73). Aberrant γ -aminobutyric acid (GABA)-mediated (GABAergic) signaling has been previously observed in Ts65Dn mice (74), as has altered long-term potentiation associated with increased hippocampal GABA release (75) and GABAergic inhibition (76, 77). Synaptic transmission in the hippocampus of our Ts65Dn mice was partly normalized by miR-200b overexpression in the septal POA, with which it is reciprocally connected (78) and which is a source of hippocampal GABAergic neurons during embryogenesis (79). GABA is known to activate CA1 pyramidal cells in adult Ts65Dn mice, accompanied by a positive shift in the reversal potential of GABA type A (GABA_A) receptor-driven Cl⁻ currents and increased hippocampal expression of the cation-Cl⁻ cotransporter NKCC1 in both Ts65Dn mice and DS individuals (80). This suggests that the excitation-inhibition balance of hippocampal or other neuronal circuits may be perturbed in DS, resulting in impaired cognition, and that restoring physiological GnRH signaling somehow reestablishes this balance, even after the end of the developmental period. One possible molecular player underlying this mechanism is the homeoprotein *Otx2*, which acts as a microRNA-regulated *Gnrhl1* promoter acti-

vator in the POA (18), and it has long been suspected to play a role in maintaining GnRH expression in the adult hypothalamus as well (81). *Otx2* has also been described to modulate the opening and closure of critical developmental windows for cortical GABAergic neurons at the end of the infantile period (39), raising the possibility that POA-derived *Otx2* during the minipubertal GnRH switch could influence neocortical development and function. Our results provide the rationale to launch a randomized multicentric study to confirm the efficacy of pulsatile GnRH therapy in correcting the neurodevelopmental trajectory and age-related cognitive decline seen in DS and other conditions, such as AD, that share similar molecular or functional underpinnings.

Methods summary

Animals

Male and female Ts65Dn mice (P9-P360) and their WT littermates were housed under specific pathogen-free conditions in a temperature-controlled room (20° to 21°C) with a 12-hour light-dark cycle and ad libitum standard chow and water. Several additional transgenic mouse lines were used in this study. Animal studies were approved by the Institutional Ethics Committees for the Care and Use of Experimental Animals of the Universities of Lille and Lyon 1 and the French Ministry of National Education, Higher Education and Research (APAFIS# 29172-2020121811279767 v5 and APAFIS#10164-2017060710541958 v4).

Ts65Dn mouse phenotyping

Sexual maturation and postnatal acquisition of reproductive, olfactory, and cognitive impairments were assessed throughout life using external signs of puberty, hormonal profiling, olfactory discrimination, novel object recognition, visuospatial memory tests, and so on.

Imaging

The distribution of GnRH-immunoreactive neuronal cell bodies and projections in the brain as well as the neocortical distribution of cells expressing the GnRH receptor promoter were assessed using both classical neuroanatomical approaches (immunofluorescence and multiplex fluorescent in situ hybridization) and advanced 3D imaging and analysis of solvent-cleared tissue (iDISCO) methods.

Functional studies

Pharmacological (intraperitoneal administration of GnRH or CNO), viral (stereotaxic infection of the preoptic region or the hippocampus with AAV vectors expressing Cre-dependent activatory or inhibitory DREADDs, or untargeted miR-200b), and cellular approaches (grafting dissociated newborn preoptic region cells into the hypothalamus of adult mice) were used to characterize the role of GnRH neu-

rons and secretion in the postnatal acquisition of olfactory and cognitive deficits in Ts65Dn mice. RNA-seq, qRT-PCR, fluorescent in situ hybridization, Western blotting, and in vivo CA1 field recordings in anesthetized mice were used to further investigate the molecular and cellular mechanisms underlying these processes.

Pulsatile GnRH treatment

Ts65Dn mice were subjected to LH pulsatile release evaluation, olfactory habituation-dishabituation, and object recognition tests 1 month before and after 2 weeks of pulsatile GnRH therapy (Lutrelef, Ferring SA, Switzerland) via a programmable subcutaneous microinfusion pump at a rate of 0.25 μ g at 3-hour intervals to mimic the LH pulse frequency seen in male WT mice (SMP-300, iPRECIO, Japan).

Patients

Seven French-speaking men with Down syndrome (20 to 50 years of age) were enrolled in an open-label pilot study at Lausanne University Hospital (CHUV, Switzerland) to assess the effect of 6-month pulsatile GnRH therapy on cognitive and olfactory function (clinicaltrials.gov, NCT04390646). Written informed consent was obtained from all participants and their legal representatives before inclusion (Ethics Committee of Vaud, 2020-00270). Patients were subjected to baseline clinical evaluation (detailed history, physical examination, hormonal and cognitive profiling, MRI analyses) before and after 6-month pulsatile GnRH therapy via a subcutaneous pump at a rate of 75 ng per kg of body weight per pulse at 2-hour intervals (Lutrepulse manager and Lutrepod, Ferring SA, Switzerland) to mimic LH pulse frequency in normal men. Six age-matched healthy male controls were also recruited to compare baseline parameters.

Imaging studies comprised structural MRI and rs-fMRI using a 3T whole-body MRI system using a 64-channel radiofrequency head and body coil for transmission (Magnetom Prisma, Siemens Medical Systems, Germany).

Statistics

Data were assessed for normality and statistical differences and evaluated using appropriate parametric or nonparametric tests for two or more groups.

REFERENCES AND NOTES

1. S. E. Antonarakis et al., Down syndrome. *Nat. Rev. Dis. Primers* **6**, 9 (2020). doi: 10.1038/s41572-019-0143-7; pmid: 32029743
2. R. de la Torre et al., Safety and efficacy of cognitive training plus epigallocatechin-3-gallate in young adults with Down's syndrome (TESDAD): A double-blind, randomised, placebo-controlled, phase 2 trial. *Lancet Neurol.* **15**, 801–810 (2016). doi: 10.1016/S1474-4422(16)30034-5; pmid: 27302362
3. B. L. Shapiro, J. Hermann, J. M. Opitz, Down syndrome—A disruption of homeostasis. *Am. J. Med. Genet.* **14**, 241–269 (1983). doi: 10.1002/ajmg.1320140206; pmid: 6220605
4. A. A. Baburamani, P. A. Patkee, T. Arichi, M. A. Rutherford, New approaches to studying early brain development

- in Down syndrome. *Dev. Med. Child Neurol.* **61**, 867–879 (2019). doi: [10.1111/dmcn.14260](#); pmid: [31102269](#)
5. M. J. Bull, Down Syndrome. *N. Engl. J. Med.* **382**, 2344–2352 (2020). doi: [10.1056/NEJMr1706537](#); pmid: [32521135](#)
 6. J. Fortea *et al.*, Clinical and biomarker changes of Alzheimer's disease in adults with Down syndrome: A cross-sectional study. *Lancet* **395**, 1988–1997 (2020). doi: [10.1016/S0140-6736\(20\)30689-9](#); pmid: [32593336](#)
 7. E. Bayen, K. L. Possin, Y. Chen, L. Cleret de Langavant, K. Yaffe, Prevalence of aging, dementia, and multimorbidity in older adults with Down syndrome. *JAMA Neurol.* **75**, 1399–1406 (2018). doi: [10.1001/jamaneurol.2018.2210](#); pmid: [30032260](#)
 8. S. E. Antonarakis, Down syndrome and the complexity of genome dosage imbalance. *Nat. Rev. Genet.* **18**, 147–163 (2017). doi: [10.1038/nrg.2016.154](#); pmid: [28029161](#)
 9. M. Dierssen, Down syndrome: The brain in trisomic mode. *Nat. Rev. Neurosci.* **13**, 844–858 (2012). doi: [10.1038/nrn3314](#); pmid: [23165261](#)
 10. The Lancet Neurology, Strengthening connections between Down syndrome and AD. *Lancet Neurol.* **12**, 931 (2013). doi: [10.1016/S1474-4422\(13\)70228-X](#); pmid: [24050729](#)
 11. I. T. Lott, E. Head, Dementia in Down syndrome: Unique insights for Alzheimer disease research. *Nat. Rev. Neurol.* **15**, 135–147 (2019). doi: [10.1038/s41582-018-0132-6](#); pmid: [30733618](#)
 12. J. L. Olmos-Serrano *et al.*, Down syndrome developmental brain transcriptome reveals defective oligodendrocyte differentiation and myelination. *Neuron* **89**, 1208–1222 (2016). doi: [10.1016/j.neuron.2016.01.042](#); pmid: [26924435](#)
 13. R. L. Doty, Olfactory dysfunction in Parkinson disease. *Nat. Rev. Neurol.* **8**, 329–339 (2012). doi: [10.1038/nrneuro.2012.80](#); pmid: [22584158](#)
 14. R. K. Nijjar, C. Murphy, Olfactory impairment increases as a function of age in persons with Down syndrome. *Neurobiol. Aging* **23**, 65–73 (2002). doi: [10.1016/S0197-4580\(01\)00263-9](#); pmid: [11755021](#)
 15. Y.-H. H. Hsiang *et al.*, Gonadal function in patients with Down syndrome. *Am. J. Med. Genet.* **27**, 449–458 (1987). doi: [10.1002/ajmg.1320270223](#); pmid: [2955699](#)
 16. U. Boehm *et al.*, European Consensus Statement on congenital hypogonadotropic hypogonadism—pathogenesis, diagnosis and treatment. *Nat. Rev. Endocrinol.* **11**, 547–564 (2015). doi: [10.1038/nrendo.2015.112](#); pmid: [26194704](#)
 17. E. Knobil, The GnRH pulse generator. *Am. J. Obstet. Gynecol.* **163**, 1721–1727 (1990). doi: [10.1016/0002-9378\(90\)91435-F](#); pmid: [2122728](#)
 18. A. Messina *et al.*, A microRNA switch regulates the rise in hypothalamic GnRH production before puberty. *Nat. Neurosci.* **19**, 835–844 (2016). doi: [10.1038/nn.4298](#); pmid: [27135215](#)
 19. G. Pellegrino *et al.*, GnRH neurons recruit astrocytes in infancy to facilitate network integration and sexual maturation. *Nat. Neurosci.* **24**, 1660–1672 (2021). doi: [10.1038/s41593-021-00960-z](#); pmid: [34795451](#)
 20. L. Lanciotti, M. Cofini, A. Leonardi, L. Penta, S. Esposito, Up-to-date review about minipuberty and overview on hypothalamic-pituitary-gonadal axis activation in fetal and neonatal life. *Front. Endocrinol.* **9**, 410 (2018). doi: [10.3389/fendo.2018.00410](#); pmid: [30093882](#)
 21. F. Casoni *et al.*, Development of the neurons controlling fertility in humans: New insights from 3D imaging and transparent fetal brains. *Development* **143**, 3969–3981 (2016). doi: [10.1242/dev.139444](#); pmid: [27803058](#)
 22. K. Skrapits *et al.*, The cryptic gonadotropin-releasing hormone neuronal system of human basal ganglia. *eLife* **10**, e67714 (2021). doi: [10.7554/eLife.67714](#); pmid: [34128468](#)
 23. A. L. Schang *et al.*, GnRH receptor gene expression in the developing rat hippocampus: Transcriptional regulation and potential roles in neuronal plasticity. *Endocrinology* **152**, 568–580 (2011). doi: [10.1210/en.2010-0840](#); pmid: [21123436](#)
 24. R. H. Reeves *et al.*, A mouse model for Down syndrome exhibits learning and behaviour deficits. *Nat. Genet.* **11**, 177–184 (1995). doi: [10.1038/ng1095-177](#); pmid: [7550346](#)
 25. I. Kola, P. J. Hertzog, Down syndrome and mouse models. *Curr. Opin. Genet. Dev.* **8**, 316–321 (1998). doi: [10.1016/S0959-437X\(98\)80088-9](#); pmid: [9690992](#)
 26. C. J. Epstein *et al.*, Protocols to establish genotype-phenotype correlations in Down syndrome. *Am. J. Hum. Genet.* **49**, 207–235 (1991). pmid: [1829580](#)
 27. P. Bianchi *et al.*, Age-related impairment of olfactory bulb neurogenesis in the Ts65Dn mouse model of Down syndrome. *Exp. Neurol.* **251**, 1–11 (2014). doi: [10.1016/j.expneurol.2013.10.018](#); pmid: [24192151](#)
 28. V. Breton-Provencher, M. Lemasson, M. R. Peralta III, A. Saghatelian, Interneurons produced in adulthood are required for the normal functioning of the olfactory bulb network and for the execution of selected olfactory behaviors. *J. Neurosci.* **29**, 15245–15257 (2009). doi: [10.1523/JNEUROSCI.3606-09.2009](#); pmid: [19955377](#)
 29. L. Nelson *et al.*, Learning and memory as a function of age in Down syndrome: A study using animal-based tasks. *Prog. Neuropsychopharmacol. Biol. Psychiatry* **29**, 443–453 (2005). doi: [10.1016/j.pnpbp.2004.12.009](#); pmid: [15795053](#)
 30. S. J. Cohen *et al.*, The rodent hippocampus is essential for nonspatial object memory. *Curr. Biol.* **23**, 1685–1690 (2013). doi: [10.1016/j.cub.2013.07.002](#); pmid: [23954431](#)
 31. G. Zhang *et al.*, Hypothalamic programming of systemic ageing involving IKK- β , NF- κ B and GnRH. *Nature* **497**, 211–216 (2013). doi: [10.1038/nature12143](#); pmid: [23636330](#)
 32. C. S. Moore *et al.*, Increased male reproductive success in Ts65Dn “Down syndrome” mice. *Mamm. Genome* **21**, 543–549 (2010). doi: [10.1007/s00335-010-9300-8](#); pmid: [21110029](#)
 33. R. P. Grinspon *et al.*, Early onset of primary hypogonadism revealed by serum anti-Müllerian hormone determination during infancy and childhood in trisomy 21. *Int. J. Androl.* **34**, e487–e498 (2011). doi: [10.1111/j.1365-2605.2011.02120.x](#); pmid: [21831236](#)
 34. M. Belle *et al.*, Tridimensional visualization and analysis of early human development. *Cell* **169**, 161–173.e12 (2017). doi: [10.1016/j.cell.2017.03.008](#); pmid: [28340341](#)
 35. B. Pinto *et al.*, Rescuing over-activated microglia restores cognitive performance in juvenile animals of the Dp(16) mouse model of Down syndrome. *Neuron* **108**, 887–904.e12 (2020). doi: [10.1016/j.neuron.2020.09.010](#); pmid: [33027640](#)
 36. Z. Li, Y. Zhang, D. Li, Y. Feng, Destabilization and mislocalization of myelin basic protein mRNAs in quaking dysmyelination lacking the QKI RNA-binding proteins. *J. Neurosci.* **20**, 4944–4953 (2000). doi: [10.1523/JNEUROSCI.20-13-04944.2000](#); pmid: [10864952](#)
 37. S. Schafer *et al.*, Translational regulation shapes the molecular landscape of complex disease phenotypes. *Nat. Commun.* **6**, 7200 (2015). doi: [10.1038/ncomms8200](#); pmid: [26007203](#)
 38. S. Chothani *et al.*, Widespread translational control of fibrosis in the human heart by RNA-binding proteins. *Circulation* **140**, 937–951 (2019). doi: [10.1161/CIRCULATIONAHA.119.039596](#); pmid: [31284728](#)
 39. J. Spatzza *et al.*, Homeoprotein signaling in development, health, and disease: A shaking of dogmas offers challenges and promises from bench to bed. *Pharmacol. Rev.* **65**, 90–104 (2013). doi: [10.1124/pr.112.006577](#); pmid: [23300132](#)
 40. D. T. Krieger *et al.*, Brain grafts reverse hypogonadism of gonadotropin-releasing hormone deficiency. *Nature* **298**, 468–471 (1982). doi: [10.1038/298468a0](#); pmid: [7045700](#)
 41. A. R. Hoffman, W. F. Crowley Jr., Induction of puberty in men by long-term pulsatile administration of low-dose gonadotropin-releasing hormone. *N. Engl. J. Med.* **307**, 1237–1241 (1982). doi: [10.1056/NEJM19821113072003](#); pmid: [6183732](#)
 42. D. M. Hurley *et al.*, Induction of ovulation and fertility in amenorrheic women by pulsatile low-dose gonadotropin-releasing hormone. *N. Engl. J. Med.* **310**, 1069–1074 (1984). doi: [10.1056/NEJM198404263101702](#); pmid: [6424012](#)
 43. P. E. Belchetz, T. M. Plant, Y. Nakai, E. J. Keogh, E. Knobil, Hypophyseal responses to continuous and intermittent delivery of hypothalamic gonadotropin-releasing hormone. *Science* **202**, 631–633 (1978). doi: [10.1126/science.100883](#); pmid: [100883](#)
 44. P. Benkert *et al.*, Serum neurofilament light chain for individual prognostication of disease activity in people with multiple sclerosis: A retrospective modelling and validation study. *Lancet Neurol.* **21**, 246–257 (2022). doi: [10.1016/S1474-4422\(22\)00099-6](#); pmid: [35182510](#)
 45. N. R. Lee *et al.*, Hypoplasia of cerebellar afferent networks in Down syndrome revealed by DTI-driven tensor based morphometry. *Sci. Rep.* **10**, 5447 (2020). doi: [10.1038/s41598-020-61799-1](#); pmid: [32214129](#)
 46. M. D. Figueroa-Jimenez *et al.*, Resting-state default mode network connectivity in young individuals with Down syndrome. *Brain Behav.* **11**, e01905 (2021). doi: [10.1002/brb3.1905](#); pmid: [33179859](#)
 47. M. D. Figueroa-Jimenez *et al.*, Complexity analysis of the default mode network using resting-state fMRI in Down syndrome: Relationships highlighted by a neuropsychological assessment. *Brain Sci.* **11**, 311 (2021). doi: [10.3390/brainsci11030311](#); pmid: [33801471](#)
 48. C. C. Huang *et al.*, Age-related changes in resting-state networks of a large sample size of healthy elderly. *CNS Neurosci. Ther.* **21**, 817–825 (2015). doi: [10.1111/cns.12396](#); pmid: [25864728](#)
 49. J. Pujol *et al.*, Anomalous brain functional connectivity contributing to poor adaptive behavior in Down syndrome. *Cortex* **64**, 148–156 (2015). doi: [10.1016/j.cortex.2014.10.012](#); pmid: [25461715](#)
 50. C. Goeldner *et al.*, A randomized, double-blind, placebo-controlled phase II trial to explore the effects of a GABA $_A$ - α 5 NAM (basmisnil) on intellectual disability associated with Down syndrome. *J. Neurodev. Disord.* **14**, 10 (2022). doi: [10.1186/s11689-022-09418-0](#); pmid: [35123401](#)
 51. M. Hanney *et al.*, Memantine for dementia in adults older than 40 years with Down's syndrome (MEADOWS): A randomised, double-blind, placebo-controlled trial. *Lancet* **379**, 528–536 (2012). doi: [10.1016/S0140-6736\(11\)61676-0](#); pmid: [22236802](#)
 52. R. McShane, A. Areosa Sastre, N. Minakaran, Memantine for dementia. *Cochrane Database Syst. Rev.* **2006**, CD003154 (2006). doi: [10.1002/14651858.CD003154.pub5](#); pmid: [16625572](#)
 53. R. Boada *et al.*, Antagonism of NMDA receptors as a potential treatment for Down syndrome: A pilot randomized controlled trial. *Transl. Psychiatry* **2**, e141 (2012). doi: [10.1038/tp.2012.66](#); pmid: [22806212](#)
 54. J. Carr, Stability and change in cognitive ability over the life span: A comparison of populations with and without Down's syndrome. *J. Intellect. Disabil. Res.* **49**, 915–928 (2005). doi: [10.1111/j.1365-2788.2005.00735.x](#); pmid: [16287480](#)
 55. C. Ballard, W. Mobley, J. Hardy, G. Williams, A. Corbett, Dementia in Down's syndrome. *Lancet Neurol.* **15**, 622–636 (2016). doi: [10.1016/S1474-4422\(16\)00063-6](#); pmid: [27302127](#)
 56. D. B. Hier, W. F. Crowley Jr., Spatial ability in androgen-deficient men. *N. Engl. J. Med.* **306**, 1202–1205 (1982). doi: [10.1056/NEJM198205203062003](#); pmid: [7070432](#)
 57. Z. Wang, W. Wu, S. K. Kim, D. Cai, GnRH pulse frequency and irregularity play a role in male aging. *Nature Aging* **1**, 904–918 (2021). doi: [10.1038/s43587-021-00116-5](#)
 58. S. M. Moenter, N. P. Evans, Gonadotropin-releasing hormone (GnRH) measurements in pituitary portal blood: A history. *J. Neuroendocrinol.* **34**, e13065 (2021). doi: [10.1111/jne.13065](#); pmid: [34918405](#)
 59. J. Xiong *et al.*, FSH blockade improves cognition in mice with Alzheimer's disease. *Nature* **603**, 470–476 (2022). doi: [10.1038/s41586-022-04463-0](#); pmid: [35236988](#)
 60. S. Guidi, E. Ciani, P. Bonasoni, D. Santini, R. Bartesaghi, Widespread proliferation impairment and hypocellularity in the cerebellum of fetuses with down syndrome. *Brain Pathol.* **21**, 361–373 (2011). doi: [10.1111/j.1750-3639.2010.00459.x](#); pmid: [21040072](#)
 61. N. M. Corrigan *et al.*, Myelin development in cerebral gray and white matter during adolescence and late childhood. *Neuroimage* **227**, 117678 (2021). doi: [10.1016/j.neuroimage.2020.117678](#); pmid: [33359342](#)
 62. D. Kwon, A. Pfefferbaum, E. V. Sullivan, K. M. Pohl, Regional growth trajectories of cortical myelination in adolescents and young adults: Longitudinal validation and functional correlates. *Brain Imaging Behav.* **14**, 242–266 (2020). doi: [10.1007/s11682-018-9980-3](#); pmid: [30406353](#)
 63. E. Benito *et al.*, HDAC inhibitor-dependent transcriptome and memory reinstatement in cognitive decline models. *J. Clin. Invest.* **125**, 3572–3584 (2015). doi: [10.1172/JCI79942](#); pmid: [26280576](#)
 64. M. Wang *et al.*, Integrative network analysis of nineteen brain regions identifies molecular signatures and networks underlying selective regional vulnerability to Alzheimer's disease. *Genome Med.* **8**, 104 (2016). doi: [10.1186/s13073-016-0355-3](#); pmid: [27799057](#)
 65. S. Chatterjee *et al.*, Reinstating plasticity and memory in a tauopathy mouse model with an acetyltransferase activator. *EMBO Mol. Med.* **10**, e8587 (2018). doi: [10.15252/emmm.201708587](#); pmid: [30275019](#)
 66. K. Schindowski *et al.*, Alzheimer's disease-like tau neuropathology leads to memory deficits and loss of functional synapses in a novel mutated tau transgenic mouse without any motor deficits. *Am. J. Pathol.* **169**, 599–616 (2006). doi: [10.2353/ajpath.2006.060002](#); pmid: [16877359](#)
 67. A. Van der Jeugd *et al.*, Progressive age-related cognitive decline in tau mice. *J. Alzheimers Dis.* **37**, 777–788 (2013). doi: [10.3233/JAD-130110](#); pmid: [23948912](#)
 68. A. K. Kondadi *et al.*, Loss of the m-AAA protease subunit AFG3L2 causes mitochondrial transport defects and tau

- hyperphosphorylation. *EMBO J.* **33**, 1011–1026 (2014). doi: [10.1002/emboj.201387009](https://doi.org/10.1002/emboj.201387009); pmid: [24681487](https://pubmed.ncbi.nlm.nih.gov/24681487/)
69. S. Wang *et al.*, The mitochondrial m-AAA protease prevents demyelination and hair greying. *PLOS Genet.* **12**, e1006463 (2016). doi: [10.1371/journal.pgen.1006463](https://doi.org/10.1371/journal.pgen.1006463); pmid: [27911893](https://pubmed.ncbi.nlm.nih.gov/27911893/)
 70. H. Miraoui *et al.*, Mutations in *FGF17*, *IL17RD*, *DUSP6*, *SPRY4*, and *FLT3* are identified in individuals with congenital hypogonadotropic hypogonadism. *Am. J. Hum. Genet.* **92**, 725–743 (2013). doi: [10.1016/j.ajhg.2013.04.008](https://doi.org/10.1016/j.ajhg.2013.04.008); pmid: [23643382](https://pubmed.ncbi.nlm.nih.gov/23643382/)
 71. Y. Liu, M. Wang, E. M. Marcora, B. Zhang, A. M. Goate, Promoter DNA hypermethylation—Implications for Alzheimer's disease. *Neurosci. Lett.* **711**, 134403 (2019). doi: [10.1016/j.neulet.2019.134403](https://doi.org/10.1016/j.neulet.2019.134403); pmid: [31351091](https://pubmed.ncbi.nlm.nih.gov/31351091/)
 72. J. Banzhaf-Strathmann *et al.*, MicroRNA-125b induces tau hyperphosphorylation and cognitive deficits in Alzheimer's disease. *EMBO J.* **33**, 1667–1680 (2014). doi: [10.1525/emboj.201387576](https://doi.org/10.1525/emboj.201387576); pmid: [25001178](https://pubmed.ncbi.nlm.nih.gov/25001178/)
 73. N. Cramer, Z. Galdzicki, From abnormal hippocampal synaptic plasticity in down syndrome mouse models to cognitive disability in down syndrome. *Neural Plast.* **2012**, 101542 (2012). doi: [10.1155/2012/101542](https://doi.org/10.1155/2012/101542); pmid: [22848844](https://pubmed.ncbi.nlm.nih.gov/22848844/)
 74. G. Deidda *et al.*, Reversing excitatory GABAAR signaling restores synaptic plasticity and memory in a mouse model of Down syndrome. *Nat. Med.* **21**, 318–326 (2015). doi: [10.1038/nm.3827](https://doi.org/10.1038/nm.3827); pmid: [25774849](https://pubmed.ncbi.nlm.nih.gov/25774849/)
 75. T. Begenisic *et al.*, Fluoxetine in adulthood normalizes GABA release and rescues hippocampal synaptic plasticity and spatial memory in a mouse model of Down syndrome. *Neurobiol. Dis.* **63**, 12–19 (2014). doi: [10.1016/j.nbd.2013.11.010](https://doi.org/10.1016/j.nbd.2013.11.010); pmid: [24269730](https://pubmed.ncbi.nlm.nih.gov/24269730/)
 76. J. M. Schulz, F. Knoflach, M. C. Hernandez, J. Bischofberger, Enhanced dendritic inhibition and impaired NMDAR activation in a mouse model of Down syndrome. *J. Neurosci.* **39**, 5210–5221 (2019). doi: [10.1523/JNEUROSCI.2723-18.2019](https://doi.org/10.1523/JNEUROSCI.2723-18.2019); pmid: [31000585](https://pubmed.ncbi.nlm.nih.gov/31000585/)
 77. A. Freeburn, R. G. K. Munn, Signalling pathways contributing to learning and memory deficits in the Ts65Dn mouse model of Down syndrome. *Neuronal Signal.* **5**, NS20200011 (2021). doi: [10.1042/NS20200011](https://doi.org/10.1042/NS20200011); pmid: [33763235](https://pubmed.ncbi.nlm.nih.gov/33763235/)
 78. L. W. Swanson, W. M. Cowan, The connections of the septal region in the rat. *J. Comp. Neurol.* **186**, 621–655 (1979). doi: [10.1002/cne.901860408](https://doi.org/10.1002/cne.901860408); pmid: [15116692](https://pubmed.ncbi.nlm.nih.gov/15116692/)
 79. D. M. Gelman *et al.*, The embryonic preoptic area is a novel source of cortical GABAergic interneurons. *J. Neurosci.* **29**, 9380–9389 (2009). doi: [10.1523/JNEUROSCI.0604-09.2009](https://doi.org/10.1523/JNEUROSCI.0604-09.2009); pmid: [19625528](https://pubmed.ncbi.nlm.nih.gov/19625528/)
 80. G. Deidda *et al.*, Early depolarizing GABA controls critical-period plasticity in the rat visual cortex. *Nat. Neurosci.* **18**, 87–96 (2015). doi: [10.1038/nn.3890](https://doi.org/10.1038/nn.3890); pmid: [25485756](https://pubmed.ncbi.nlm.nih.gov/25485756/)
 81. C. G. Kelley, G. Lavgorgna, M. E. Clark, E. Boncinelli, P. L. Mellon, The Otx2 homeoprotein regulates expression from the gonadotropin-releasing hormone proximal promoter. *Mol. Endocrinol.* **14**, 1246–1256 (2000). doi: [10.1210/mend.14.8.0509](https://doi.org/10.1210/mend.14.8.0509); pmid: [10935548](https://pubmed.ncbi.nlm.nih.gov/10935548/)
 82. V. Prevot, A. Messina, P. Giacobini, V. Laysen, M. Manfredi-Lozano, Patent WO/2020/221821 (2020).

ACKNOWLEDGMENTS

We thank PLBS UAR 2014 – US41 (<https://urns-plbs.univ-lille.fr/>) with its different platforms and staff for expert technical assistance: C. Laloux (behavioral exploration platform for rodents), N. Jouy (cell sorting facility, BiCel), M. Tardivel and A. Bongiovanni (microscopy core facility, BiCel), and J. Devassine (animal house) of the UMS2014-US41. For technical expertise during the clinical study, we also thank B. Landis (Olfactology Unit, HUG), A.-S. Boulin and P. Cazin D'Honinchtun (neuropsychological tests, Neurorehabilitation Unit, CHUV), G. Di Domenicantonio (Department of Neuroclinical Sciences, LREN - CHUV), A. Stojkai (Department of Endocrinology, CHUV), and P. Benkert (Department of Neuroimmunology and Neuroscience, Basel). GnRH therapy was kindly provided by Ferring SA, Switzerland. **Funding:** This work has been supported by the European Research Council COST action BM1105 for the study of GnRH deficiency (to U.B., P.C., P.G., N.P., V.P., and M.T.-S.), Agence Nationale de la Recherche grants ANR-17-CE16-0015 (to V.P., P.C., and L.B.), DistAlz (ANR-11-LABEX-0009 to V.P. and L.B.), I-SITE ULNE (ANR-16-IDEX-0004), and the Région Rhône-Alpes- SCUSI 2018- #R18119CC and Swiss National Fund 310030B_201275 (to N.P.). M.M.-L. received a postdoctoral fellowship from the European commission (H2020-MSCA-IF-2014, no. 656730) and V.L. a doctoral fellowship from Inserm and the Region Hauts de France. P.G. is supported by the European Union's Horizon 2020 Research and Innovation Programme under grant agreement no. 874741. B.D. is supported by the Swiss National Science Foundation (project grant numbers 32003B_135679, 32003B_159780, 324730_192755, and CRSK-3_190185), the ERA-NET iSEE project, the UNIL-EPFL CLIMACT program, and the SPHN-SACR project. A.L. is supported by the Swiss National Science Foundation (project grant number 320030_184784) and the ROGER DE SPOELBERCH Foundation. The members of the Laboratory for Research in Neuroimaging (LREN) are grateful to the ROGER DE SPOELBERCH and Partridge Foundations for their generous financial support. **Author contributions:** V.P. designed the preclinical studies, analyzed data, prepared the figures, and wrote the manuscript along with U.B., M.C., and N.P. M.M.-L. and V.L. designed and performed the experiments in mice and were involved in all aspects of study design, interpretation of results,

manuscript preparation, and preparation of the figures. N.P. designed the clinical study, analyzed the data, interpreted the results, and, along with M.A. and E.P., performed the clinical study. M.A. analyzed the data, prepared the figures, and contributed to manuscript preparation. N.V. and F.S. contributed to the data analysis and manuscript preparation. A.P.-G. contributed to the recruitment of the subjects for the clinical study. B.D. analyzed structural MRI data and J.-M.P. analyzed the functional MRI data. A.L. contributed to MRI data acquisition using prospective motion correction. S.R. and J.A. contributed to the preparation of the manuscript. A.M.M. and J.K. performed and analyzed the neurofilament light-chain analyses. N.H. and R.R. designed and performed in vivo electrophysiology experiments. S.E., F.E.T., and M.I. performed the Western blot analyses; I.P., D.P., and A.-L.B. performed transcriptomic analyses; M.S.B.S. performed the viral tracing injections; S.T. performed GnRHR image analyses; S.A.M. performed tissue-clearing experiments and analyzed the data; L.D., L.C., F.E.T., and P.G. conducted the fluorescent in situ hybridization analyses; M.T.-S., U.B., L.B., M.Ca., M.Cl., and F.P. contributed material; and A.M., L.B., U.B., P.C., N.P., and P.G. were involved in the study design, interpretation of the results, and preparation of the manuscript. **Competing interests:** M.M.-L., V.L., A.M., P.G., and V.P. disclose that they are inventors of a patent covering the treatment of cognitive disorder and dementia with pulsatile GnRH (82). All other authors have no competing interests. **Data and code availability:** The accession number for the RNA-seq data reported in this paper is GEO: GSE199974. All other data supporting the findings of this study are present in the paper or the supplementary materials. The AAV8-hSyn-DIO-hM4D-mCherry was obtained from Addgene. **License information:** Copyright © 2022 the authors, some rights reserved; exclusive licensee American Association for the Advancement of Science. No claim to original US government works. <https://www.science.org/about/science-licenses-journal-article-reuse>

SUPPLEMENTARY MATERIALS

science.org/doi/10.1126/science.abq4515

Materials and Methods

Figs. S1 to S19

Tables S1 to S7

References (83–138)

MDAR Reproducibility Checklist

Movies S1 and S2

Submitted 9 April 2022; accepted 13 July 2022
10.1126/science.abq4515

Your Legacy to Science

AN ESTATE GIFT TO THE
AMERICAN ASSOCIATION FOR THE ADVANCEMENT OF SCIENCE



Since 1848, our founding year, the American Association for the Advancement of Science (AAAS) has been deeply committed to advancing science, engineering and innovation around the world for the benefit of all people.

By making AAAS a beneficiary of your will, trust, retirement plan or life insurance policy, you become a member of our 1848 Society, joining Thomas Edison, Alexander Graham Bell and the many distinguished individuals whose vision led to the creation of AAAS and our world-renowned journal, *Science*, so many years ago.

Unlike many of its peers, *Science* is not for-profit. Your estate gift would provide long-term financial stability and durable annual income that will support operations and competitive innovation for years to come. **This support is vital.**

"As a teacher and instructor, I bear responsibility for the younger generations. If you have extra resources, concentrate them on organizations, like AAAS, that are doing work for all."

—Prof. Elisabeth Ervin-Blankenheim, 1848 Society member

If you intend to include AAAS in your estate plans, provide this information to your lawyer or financial adviser:

Legal Name: American Association for the Advancement of Science

Federal Tax ID Number: 53-0196568

Address: 1200 New York Avenue, NW, Washington, DC 20005

If you would like more information on making an estate gift to AAAS, cut out and return the form below or send an email to philanthropy@aaas.org. Additional details are also available online at www.aaas.org/1848Society.

cut here ✂

Yes, I would like more information about joining the AAAS 1848 Society.

PLEASE CONTACT ME AT:

Name: _____

Address: _____

City: _____ State: _____ Zip code: _____ Country: _____

Email: _____ Phone: _____

RETURN THIS FORM TO:

AAAS Office of Philanthropy and Strategic Partnerships • 1200 New York Avenue, NW • Washington, DC 20005 USA



RESEARCH ARTICLES

METALLURGY

On the origins of fatigue strength in crystalline metallic materials

J. C. Stinville^{1,2*}, M. A. Charpagne^{1,2}, A. Cervellon^{2†}, S. Hemery³, F. Wang^{2‡},
P. G. Callahan^{2§}, V. Valle³, T. M. Pollock²

Metallic materials experience irreversible deformation with increasing applied stress, manifested in localized slip events that result in fatigue failure upon repeated cycling. We discerned the physical origins of fatigue strength in a large set of face-centered cubic, hexagonal close-packed, and body-centered cubic metallic materials by considering cyclic deformation processes at nanometer resolution over large volumes of individual materials at the earliest stages of cycling. We identified quantitative relations between the yield strength and the ultimate tensile strength, fatigue strength, and physical characteristics of early slip localization events. The fatigue strength of metallic alloys that deform by slip could be predicted by the amplitude of slip localization during the first cycle of loading. Our observations provide a physical basis for well-known empirical fatigue laws and enable a rapid method of predicting fatigue strength as reflected by measurement of slip localization amplitude.

Cyclic fatigue is the root cause of many catastrophic failures in engineering systems, with notable examples in aircraft, artificial heart valves, prosthetic devices, electronics packages, railways, bridges, offshore platforms, and conventional and nuclear power plants. The weakening of the metallic materials caused by cyclic loading ultimately results in fracture at stresses that are often substantially lower than that necessary to cause fracture under monotonic loading (1). Such failures often occur after millions or even billions of cycles, complicating the ability to predict when failure will occur.

The design of safety-critical components for survival beyond a critical number of cycles requires knowledge of the fatigue strength of the material for the required number of cycles. In measurements of fatigue strength, samples are typically cycled between a minimum and maximum stress (σ_{\min} , σ_{\max}) to failure in a servohydraulic testing machine at a frequency near 1 Hz. At this frequency, ~278 hours are required to apply a million cycles or 278,000 hours (~32 years) for a billion cycles. With the development of ultrasonic fatigue testing approaches (2, 3), fatigue testing can be performed at 20 kHz, allowing cycling to a billion cycles in ~14 hours. This accelerated approach to testing enables rapid fatigue characterization of a broader set of materials at very high cycles and

enables more tests of a given material, which is essential for capturing the variability in fatigue behavior. Fatigue life variability may be attributable to the presence of rare flaws

that are introduced during material processing or component fabrication, or if these flaws are absent, from intrinsic features of the material itself (1, 4, 5).

Correlations between fatigue strength in the high or very high cycle fatigue regimes and the intrinsic mechanical properties of metallic materials, including yield strength, ultimate tensile strength, and hardness, have been widely reported in the literature (4, 6–9). Of most interest is the observation that fatigue strength increases with increasing yield strength or ultimate tensile strength. However, plotting normalized fatigue strength as a fraction of the yield strength or ultimate tensile strength of the metal (the fatigue efficiency; Fig. 1) shows that metallic materials with high strengths in many cases fail by fatigue at stresses as low as 25% of their yield strength, indicating a markedly low fatigue efficiency. The physical processes and parameters at the microstructure scale that link the tensile and yield strengths to fatigue strength are not yet fully understood. Moreover, it is unclear why metals and alloys with high tensile strength possess such a low fatigue efficiency. Substantial efforts on fatigue modeling that fit constitutive models to large amounts of fatigue test data, or

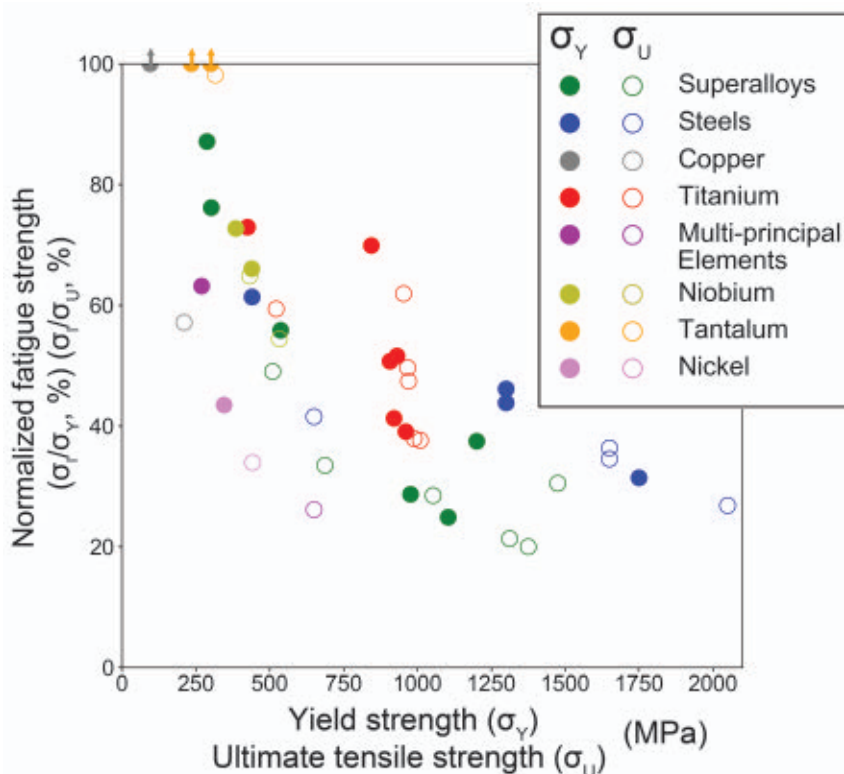


Fig. 1. Relationship between tensile properties and fatigue strength. σ_y and σ_u refer to yield and ultimate tensile strengths, respectively. The fatigue strength, σ_f , is reported as a percentage of the yield strength (dots) and tensile strength (open circles). Fatigue tests were performed in the VHCF regime (frequency of 20 kHz, tension-compression cycling at room temperature to 10^9 cycles with $R = \sigma_{\min}/\sigma_{\max} = -1.0$) [steels (41–44), Ti alloys (45–47), superalloys (48–51), high-entropy alloy (fcc) CrMnFeCoNi (52), Cu, Ni, Ta, and Nb alloys (49, 53–55)]. The fatigue data are restricted to materials that deform by slip and contain a minimum content of extrinsic defects (e.g., inclusions or pores).

¹University of Illinois at Urbana-Champaign, Urbana, IL, USA.

²University of California, Santa Barbara, CA, USA. ³Institut PPRIME, Université de Poitiers, CNRS, ISAE-ENSMA, UPR 3346, 86962 Chasseneuil Cedex, France.

*Corresponding author. Email: jstinville@illinois.edu

†Present address: Safran Aircraft Engines, Chatelleraut, France.

‡Present address: Shanghai Jiao Tong University, Shanghai, China.

§Present address: US Naval Research Laboratory, Washington, DC, USA.

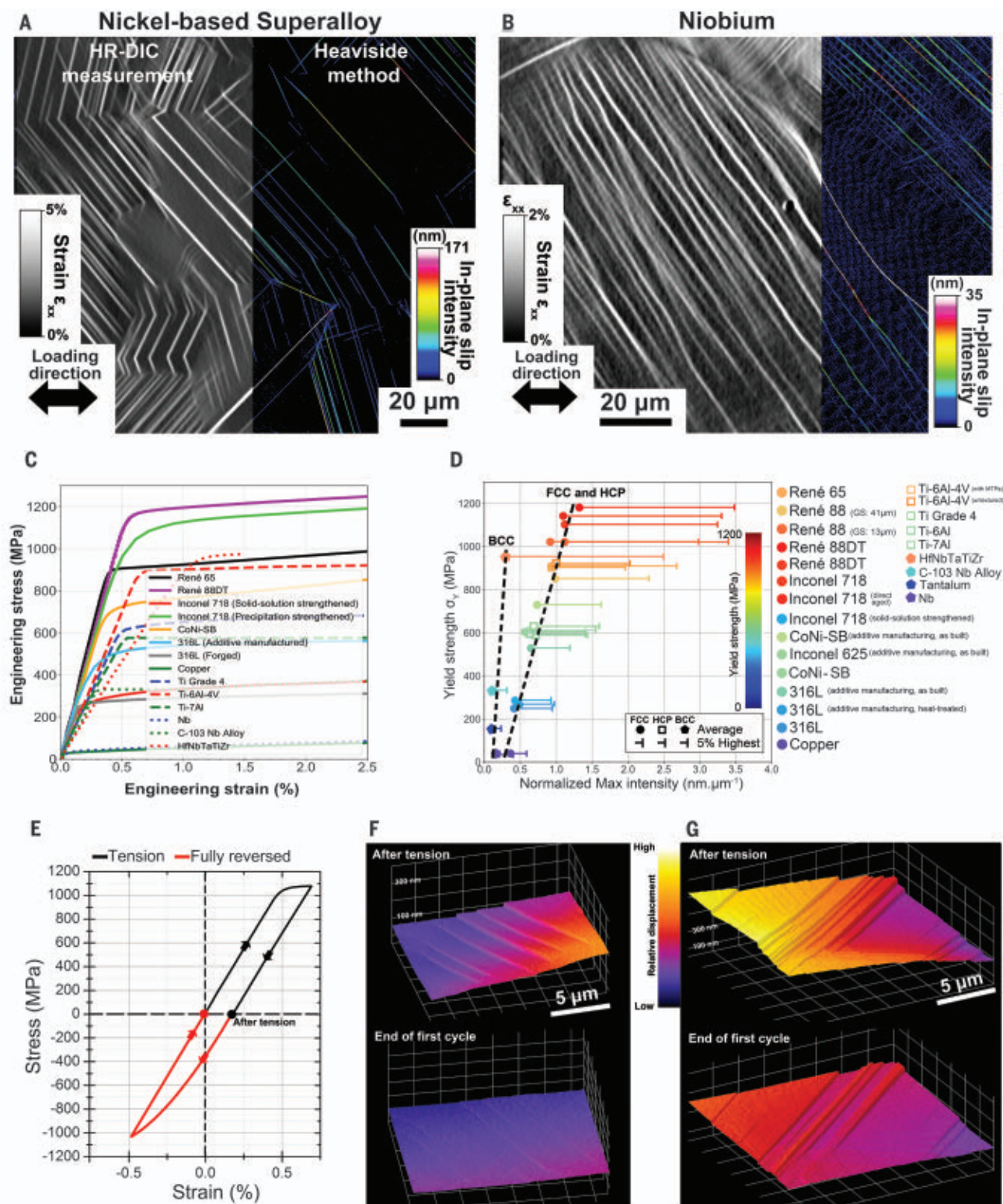


Fig. 2. Quantitative measurement of the surface slip localization. (A) Left: Conventional strain field obtained by HR-DIC measurement under a SEM. Right: The discontinuity-tolerant Heaviside-DIC method provides quantitative measurement of each single-slip event that develops at the surface of the specimen during deformation. The displacement induced along the slip event is reported in nanometers. (B) Surface slip localization induced by monotonic loading at the surface of a nickel-based superalloy and pure niobium polycrystalline materials. (C) Engineering stress-strain curves of some of the

investigated polycrystalline metals for monotonic deformation at quasi-static strain rate. (D) Average and 5% highest maximum slip intensity at 0.2% applied macroscopic plastic strain as a function of the yield strength of the metal. The maximum slip intensity for each single-slip event is normalized by the length of the slip event to capture the effect of grain size. (E) Reversed loading to investigate reversibility of slip. (F and G) Regions in a nickel-based superalloy that display complete and partial reversibility during reversed loading. The 3D representation on the displacement field was obtained by HR-DIC.

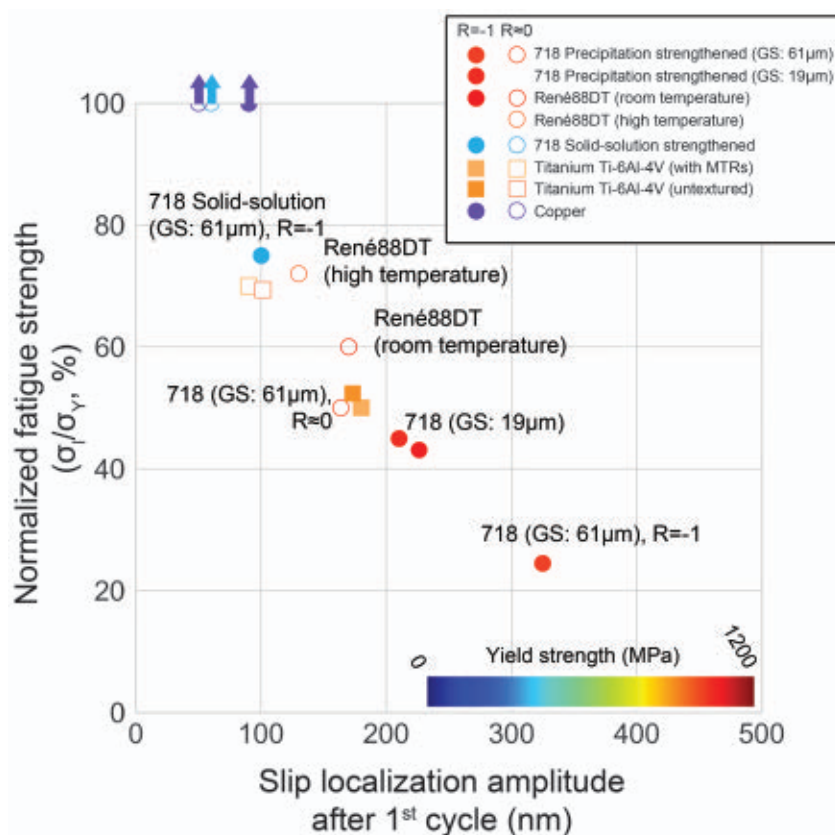


Fig. 3. Fatigue strength as a function of slip amplitude. Fatigue strength, σ_f , is determined for different metallic materials by VHCF loading. The amplitude of the localization by slip is evaluated during monotonic loading at 0.2% strain and compared to the fatigue strength for a ratio near zero (tension), or evaluated after fully reversed loading and compared to the fatigue strength for a ratio of -1 (tension-compression). Points are color-coded according to yield strength.

that make use of damage or fatigue indicator parameters, have led to considerable improvement of our predictive capabilities (10–14). However, such models rely on parameters that are not universal to all metallic materials.

Fatigue failure occurs by a complex series of processes that include cyclic plastic deformation, crack nucleation, and crack propagation to a critical size that results in fracture (15, 16). The cyclic deformation process occurs by glide of crystalline defects, so-called dislocations, that develop into complex structures such as persistent slip bands with ladder structure (5), deformation bands (17), or fatigue shear bands (18). Fatigue crack nucleation is thought to be a consequence of a phenomenon known as cyclic irreversibility (5), in which dislocations glide along slip planes as the sample is loaded, but do not return to their original positions during unloading or reversed loading into compression. This results in a heterogeneous accumulation of plastic strain along with roughening of the sample surface, which occurs when some of the defects exit the surface of the crystal. In many instances, this

results in fatigue crack nucleation at the free surface of a material. We hypothesize that a more quantitative and statistical understanding of the plastic localization processes that occur in near-surface regions would improve our ability to predict the fatigue strength of a given material. Further, such understanding could guide the development of fatigue-resistant materials.

Quantification of plastic localization at the microstructure scale—that is, at the scale of individual crystals (grains) across a polycrystalline aggregate—is challenging for both monotonic and cyclic loading. Experimental observation of slip events requires nanometer-scale spatial resolution. Conversely, capturing the material response over statistically representative populations of microstructural configurations requires millimeter-scale fields. However, recent advances in testing devices that operate in situ in the scanning electron microscope (SEM), combined with high-resolution digital image correlation and automated multimodal data analysis, provide opportunities to quantify the character of discrete slip events and slip activity over large fields of view (19–22).

We integrated these experimental capabilities to study slip localization during monotonic and fully reversed loading on a large collection of alloys with face-centered cubic (fcc), hexagonal close-packed (hcp), and body-centered cubic (bcc) crystal structures. We performed measurements over statistically significant regions of interest, and we used multimodal data-merging approaches to quantitatively study the relationship between microstructure and individual slip localization events, including their location, intensity, and degree of reversibility. We found that fatigue strength as a fraction of yield strength is directly correlated with the slip amplitude observed during the first cycle of loading. This observation offers insights into cyclic irreversibility, provides physical insights into well-known fatigue laws, and suggests a more efficient approach to designing fatigue-resistant materials.

Quantitative and representative measurements of slip localization

We studied a large collection of polycrystalline metals with varied crystallographic structure and processing paths (see table S1 and supplementary materials). The engineering stress-strain curves exhibited a large spectrum of yield strengths (Fig. 2C), ranging from 39 to 1183 MPa. We performed high-resolution digital image correlation (HR-DIC) measurements during monotonic and fully reversed loading in the early plastic regime to investigate the displacements associated with discrete slip events that occur at the surface. We performed measurements in the SEM that provided displacement resolutions down to 10 nm and spatial resolution of a few tens of nanometers. In Fig. 2, A and B, we show typical HR-DIC maps for a reduced field of view for a nickel-based alloy and pure niobium during monotonic loading. Bands of highly localized deformation develop from sequential slip of groups of dislocations along crystallographic planes. Combining HR-DIC measurements with a discontinuity-tolerant Heaviside-DIC method (23) enables a quantitative measurement of the slip intensity along each individual band during deformation over large regions of each material (Fig. 2A, right). We can track the evolution of the slip intensity during monotonic and cyclic deformation, and this evolution is highly dependent on the material type and loading condition. When reverse loading is involved (Fig. 2E), the evolution of slip intensity is complex, with certain regions displaying complete reversibility of slip (Fig. 2F) while others display a certain amount of irreversibility (Fig. 2G). This irreversibility is indicative of the development of extrusions (displacement above the initial surface) or intrusions (displacement below the initial surface) that may later serve as a crack nucleation site.

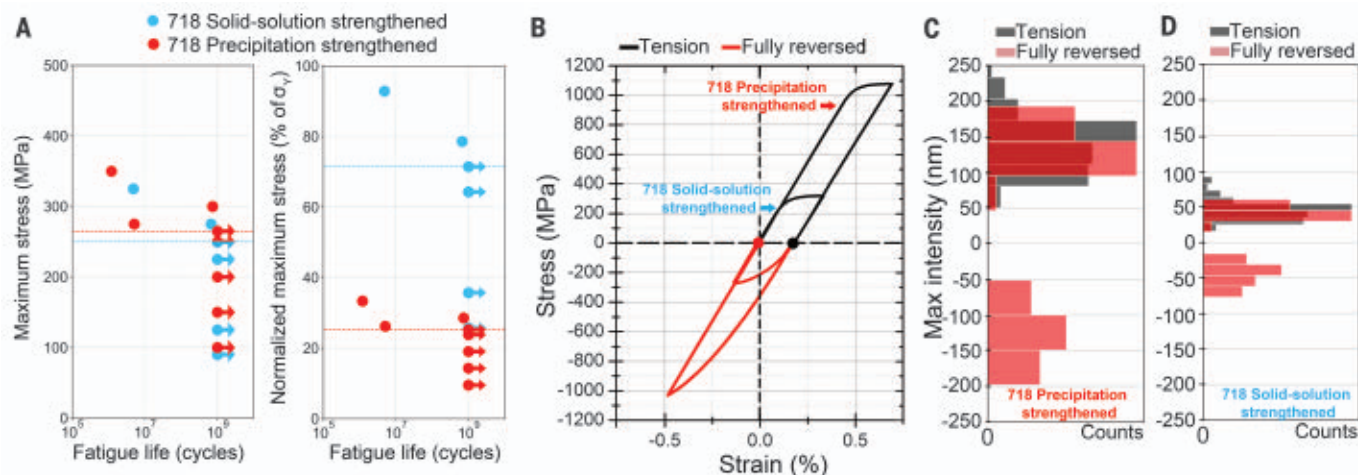


Fig. 4. Measurement of fatigue strength and amplitude of localization by slip of metallic materials. (A) Fatigue curves for nickel-based superalloy Inconel 718 strengthened by precipitation and by solid solution, tested in the VHCF regime at a ratio of -1 . Maximum stress is displayed in MPa (left) and as a percentage of the yield strength (right). (B) Associated engineering stress-strain curves of Inconel 718 strengthened by precipitation and by solid solution

under fully reversed loading. (C) Distribution of the highest slip intensity for Inconel 718 strengthened by precipitation after tensile part (black) and fully reversed loading (red). Negative values are indicative of slip events that display an intrusion character; positive values are associated with extrusion character. The horizontal axis (count) for the distribution after compression was adjusted for better comparison. (D) Same as (C) for Inconel 718 strengthened by solid solution.

We performed statistical analyses on the experimental materials for $>20,000$ individual slip events. We identified each slip event (see fig. S1 and supplementary materials) and extracted its maximum intensity along its surface trace. We normalized the maximum intensity by the length of the slip event to capture grain size effects. We obtained the distributions of the normalized maximum intensity and slip trace spacings for each material and subsequently related these values to the microstructure of the material. In Fig. 2D, we show the average and highest 5% of the distribution after an applied plastic strain of 0.2% for all materials we investigated as a function of yield strength. Interestingly, the average and 5% highest values of the distribution of the maximum slip intensity and average of the slip trace spacing (fig. S2B) display a linear dependence on the yield strength across the large set of materials examined. Materials with higher yield strength, such as the precipitation-strengthened superalloys, exhibit substantially higher slip intensity during monotonic loading. Surprisingly, both the fcc and hcp materials show the same dependence. However, this linear relationship is distinctly different for bcc materials, with less variation in average slip intensity and slip trace spacing with yield strength. Also, differences in slip localization characteristics arise from processing along different paths (i.e., 316L processed along wrought and additive manufacturing paths, and nickel alloy 718 in solid solution-strengthened and precipitation-strengthened forms).

Relationship between fatigue strength and slip localization

We measured the fatigue strengths of several of the materials using very high cycle fatigue (VHCF) testing to 10^9 cycles. Fatigue tests were performed at a fatigue stress ratio of either -1 (tension-compression) or near 0 (tension). The fatigue efficiency (fatigue strength as a function of yield strength) is displayed for the investigated materials as a function of the maximum slip amplitude (highest 5%) after a single cycle (tension or tension-compression) to a maximum plastic strain of 0.2% (macroscopic yield) (Fig. 3). Remarkably, a linear dependence of fatigue strength on slip amplitude measured after the first cycle of fatigue is apparent. Further, this relationship captures the effect of the loading conditions (temperature and stress ratio), grain size, crystal structure, and yield strength and explicitly links the monotonic properties to the cyclic fatigue strength, through the physical characteristics of the slip that occurs in the first cycle.

Polycrystalline metallic materials, as a consequence of their processing paths, naturally contain variations in many features of material structure, including grain structure, chemical distribution of solute, and strengthening precipitates if present. As a result, as the material is loaded, plastic deformation does not occur uniformly, but instead initially occurs by localized slip in regions where dislocations first overcome the obstacles to deformation. The intensity of the slip displacements is highly dependent on the intrinsic properties of the material (crystal structure and microstructure) and testing conditions (temperature, strain rate,

and loading). Dislocations can be pinned for many reasons—lattice friction, the presence of solute atoms, segregation, preexisting dislocations within the material, obstacles such as precipitates, low- and high-angle boundaries or cell walls—and can escape when the resolved shear stress on the slip plane is greater than the strengths of the forces pinning them. This results in the collective motion of multiple dislocations along individual planes, producing a heterogeneous pattern of plasticity. Thus, slip amplitudes in early cycling should vary with the presence of solute and precipitates and depend also on grain size (Fig. 2D). We clearly illustrate this dependence on microstructure in two variants of a model material, nickel-based Inconel 718: precipitation-strengthened with high yield strength, and solid solution-strengthened with lower yield strength. Both of these materials originated from the same forged disk and initial heat treatment, resulting in an identical chemistry and grain structure in both variants. We obtained the precipitation strengthening by an additional aging treatment that does not affect the grain structure. These two variants of material exhibit different slip intensities, with the higher-strength precipitate-containing material subject to slip intensities that are a factor of >2 higher than for the solid solution-strengthened version. Another striking example in the literature is slip in neutron irradiated and nonirradiated zirconium alloys (24), where an increase of yield strength by a factor of 2 due to neutron irradiation results in a substantial increase in slip intensity (25).

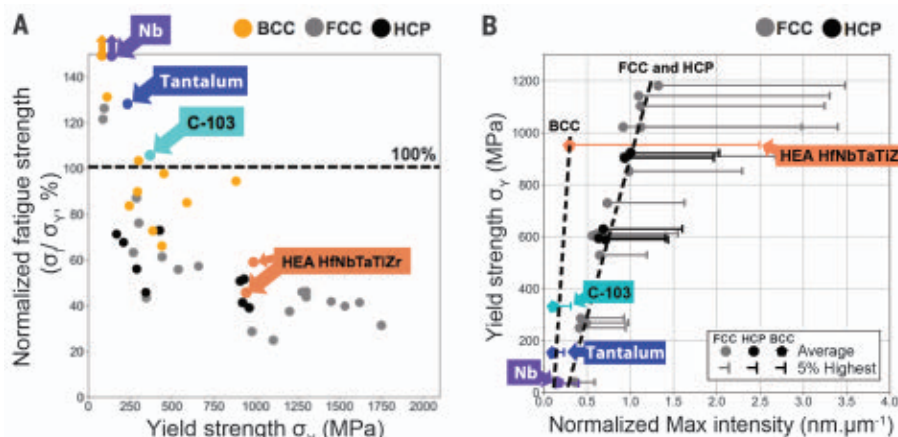


Fig. 5. Fatigue and localization for body-centered cubic metals. (A) The fatigue strength of various metals is reported as a percentage of the yield strength. Fatigue tests were performed at room temperature in the VHCF regime [steels (41–44); Ti alloys (45–47); superalloys (48–51); high-entropy alloy (fcc) CrMnFeCoNi (52); Cu, Ni, Ta, and Nb alloys (49, 53–55)] and in the high cycle fatigue regime [Mo, W, Ta, Nb, Fe, and Co alloys (39); HfNbTaTiZr alloy (40, 56); steels (57); aluminum (16, 58); magnesium (59, 60)]. (B) Average and 5% highest maximum slip intensity for various metals at 0.2% applied macroscopic plastic strain as a function of the yield strength of the metal. The maximum slip intensity for each single-slip event is normalized by the length of the slip event to capture the effect of grain size.

We found the collective dislocation glide and slip localization processes at room temperature in hcp/fcc structures to be substantially different from those in bcc structures. In general, the higher number of available slip systems in the bcc crystal structure results in a less well defined band structure relative to the fcc and hcp structures. As a consequence, slip is well dispersed in bcc alloys but more highly localized in fcc and hcp alloys. In addition, plasticity in bcc metals is usually controlled by screw dislocation motion, resulting in some ambiguity as to the nature of the slip planes (26), because screw dislocations easily cross-slip and glide on multiple planes. In the dislocation dynamics simulations of Cui *et al.* (27), screw dislocations were found to contribute to frequent cross-slip and jog multiplication, inducing more spatially homogeneous plastic deformation with less pronounced slip localization in bcc metals.

Our measurement of slip events over large fields of view (encompassing many thousands of grains) provides statistical information and also reveals the effect of the microstructure on slip localization. The development of data-merging tools (19, 21) allows for direct correlation of slip events with specific features of microstructure. For example, particular grain configurations that develop during processing of metallic materials (“special” boundaries or “annealing twins”) have been known to promote intense slip localization parallel to them (fig. S3) during deformation of steels (28), nickel-based superalloys (18, 29, 30), and titanium alloys (31, 32). Intragranular slip localization may also vary substantially from

grain to grain. The variation in slip localization intensity is especially pronounced in some of the high-strength bcc alloys and the additively manufactured alloys. In the case of bcc alloys, the localization process is highly dependent on crystallographic orientation. High dispersion in slip intensity and slip band spacing observed in the bcc high-entropy alloy HfNbTaTiZr in comparison to other fcc materials is an example (fig. S4). To a lesser degree, high dispersion is also observed in the additively manufactured materials, which can be attributed to heterogeneity in the fine-scale printed structure (low-angle boundaries and cell structure).

The location of the highest slip amplitude events during monotonic and reverse loading correlates well with the location of the crack nucleation site in the high cycle fatigue and VHCF regimes (table S2), indicating again the close relation between slip localization and crack nucleation. Because fatigue often involves loading in tension to a specific stress level and then reverse loading into compression to the same magnitude of stress (R ratio = -1), the factors that influence the reverse motion of dislocations as the load goes into compression are important to the evolution of slip amplitude. In Fig. 4B, we show how this behavior varies with stress-strain behavior for the two model variants of the nickel-based Inconel 718 alloy. The first variant (red curve) is the precipitation-strengthened version; the second variant is the solid solution-strengthened material (blue). Despite the large difference in their yield strength, we observed similar fatigue strengths for the two variants. The solid solution-strengthened

variant displayed a substantially higher fatigue efficiency, defined as the fatigue strength as a percentage of the yield strength. We evaluated the tendency of the two variants to localize deformation by slip after monotonic loading and unloading from a maximum applied plastic strain of 0.2% (Fig. 4B, black curves) and after a fully reversed loading (Fig. 4B, black plus red curves) to bring the macroscopic plastic strain near zero after compressive load. Some of the high-intensity slip events did not recover their displacements during the compressive part of the cycle, indicating substantial plastic irreversibility. In addition, slip events with intrusion character formed during the compressive loading part of the cycle, displayed as negative values in the distributions. More details can be found elsewhere (20) regarding quantitative measurements of irreversibility during reverse loading at the scale of individual slip bands by HR-DIC. Whereas the average macroscopic plastic strain is near zero, the slip amplitude, defined as the absolute difference between the average negative and positive values of the maximum slip intensity, is substantial. We can explain the substantially higher fatigue efficiency of the solid solution-strengthened material with its lower residual slip displacement (slip amplitude) relative to the precipitation-strengthened material (Fig. 4, C and D).

The intensity of the slip localization is clearly predictive of the fatigue strength in the large material set we investigated (Fig. 3). Monotonic properties such as yield strength, tensile strength, or hardness have long been known to be related to cyclic fatigue strength (4, 6–9). Our data make clear that slip localization is the physical origin of this observation. This relationship may come as a surprise, considering that fatigue life is controlled by cyclic processes that involve complex plastic deformation structures (5, 17, 18, 33, 34) and fatigue life is governed by a combination of crack nucleation, early propagation, and crack growth. For tests we performed in the high cycle fatigue regime ($>10^6$ cycles) and especially in the VHCF regime ($\sim 10^9$ cycles) that we used to determine fatigue strength, the cyclic peak stress is usually lower than the monotonic yield strength; consequently, most of the lifetime is consumed by plastic localization and the initiation of a critically sized fatigue crack (15, 16). In addition, the nucleation of cracks is directly related to the amplitude of the extrusion/intrusion phenomenon that originates from slip localization (35) or to dislocation pile-ups at grain boundaries that result from intense slip. Moreover, it has been previously observed that the dislocation structures that form during cyclic loading are dependent on the propensity of the material to easily cross-slip or develop highly planar slip.

Labyrinths, cells, deformation band walls, persistent slip band ladders, dipole arrays, and stacking fault bands are dislocation patterns that develop during fatigue; the types of dislocation patterns that form are highly dependent on the slip character (36, 37). These phenomena are evidently all reflected in the tendency of the material to localize the plastic deformation.

Finally, our experiments yield the observation that fatigue strength as a fraction of yield strength (at 10^9 cycles) can be predicted by the slip amplitude after the first cycle of loading. From the data plotted in Fig. 3, we found the following relation:

$$\frac{\sigma_1}{\sigma_Y} = 1 - \lambda\delta \quad (1)$$

where σ_1 is fatigue strength at 10^9 cycles, σ_Y is yield strength, λ is the localization parameter [which depends only on crystal structure (fcc/hcp or bcc)], and δ is the slip amplitude in a single cycle that is representative of the loading ratio (after tensile loading for $R = 0$ and after fully reversed loading for $R = -1$). This expression describes the behavior of a wide range of fcc and hcp materials, with the possible exception of materials with very low yield strength (such as Cu) where the barriers to dislocation glide are very low. Only for high-purity metals is the value of δ very low, and as a consequence the fatigue strength approaches or is above the yield strength of the material. The precise normalized fatigue strength where this relationship breaks down is an interesting subject for future investigation.

The expression in Eq. 1 is applicable to fatigue strengths that are in the high cycle fatigue or VHCF regimes, where fatigue data are represented by the well-known empirical Basquin law:

$$\sigma_a = \sigma_f' (N_f)^c \quad (2)$$

where σ_a is the stress amplitude, σ_f' is the fatigue strength coefficient, N_f is the number of cycles to failure, and c is the fatigue life coefficient. The stress amplitude σ_a can be expressed as

$$\sigma_a = \frac{\sigma_{\max}(1 - R)}{2} \quad (3)$$

where R is the stress ratio and σ_{\max} is the maximum applied stress. Considering the previous equations and the fatigue strength at 10^9 cycles, the fatigue strength coefficient for all investigated materials that deform by slip is expressed as

$$\sigma_f' = \frac{1 - R}{2(10^9)^c} \sigma_Y (1 - \lambda\delta) \quad (4)$$

Our analysis provides insights on the physical origins of the fatigue strength coefficient

σ_f' , which has generally been treated as a fit parameter. Increasing the yield strength of a material might be expected to increase its fatigue strength by increasing the fatigue strength coefficient. However, with the tendency for higher-strength materials to localize more intensely, this potential benefit is offset, as demonstrated by the $\lambda\delta$ term in Eq. 4. As such, we link the low fatigue efficiency of the strongest materials directly to the localization process.

Another important consideration revealed by HR-DIC measurements during fatigue loading (20) is that the highest-amplitude slip events that develop in tension also have a tendency to have the highest level of irreversibility during the compressive part of the cycle (negative R ratio). Although many high-intensity slip events do not reverse completely during compressive loading (Fig. 4), the resulting effect is that new slip events with intrusion character develop during the compressive phase, giving rise to local combined intrusion-extrusion events that are captured by the slip amplitude δ . The degree of irreversibility can be different from one material to another.

Slip localization for fatigue strength prediction

The investigation of the slip activity and amplitude of localization during monotonic and reversed loading provides an opportunity to rapidly evaluate the fatigue strength and fatigue efficiency of materials and their different microstructural variants that develop along different processing paths. This approach not only provides new insights into the role of crystal structure and microstructure in determining fatigue strength, it also provides guidance for alloy and microstructure design. Alloy deformation is often characterized in terms of slip character (37), with slip bands described qualitatively as wavy, planar, coarse, or fine. However, the further quantitative assessment of slip amplitude provides unique information linking the crystal structure and microstructure to mechanical properties. The propensity of high-strength fcc/hcp materials to produce high slip amplitudes results in a low fatigue efficiency. Thus, monotonic strength and cyclic fatigue strength must be balanced in recognition of the specific engineering application of a material and with consideration of which of these properties is life-limiting. Beyond this, the statistical measurements of the slip character in relation to the microstructure point to different pathways for the design of alloys and processing paths that control microstructure in order to minimize the localization of the plasticity, and as a consequence increase the fatigue strength.

The high-yield strength, high-entropy alloy HfNbTaTiZr displays unusual behavior among

all the bcc alloys (Fig. 5). The fatigue ratio is known to usually be substantially higher for bcc metals relative to fcc or hcp metals. The fatigue strengths of bcc metals usually approach their yield strengths, even for relatively high-yield strength materials. As an example, bcc steels and eutectoid steels are known to display high fatigue strength (38) in addition to their high yield or tensile strength. The fatigue properties we report for a list of bcc alloys and metals (39, 40) (Fig. 5A) overlap with literature results (Fig. 1). We investigated some of the reported bcc alloys such as pure Nb, pure tantalum, C-103, and HfNbTaTiZr using HR-DIC; their propensities to localize the deformation are shown in Fig. 5B. Our data indicate that in comparison to fcc and hcp metals, bcc metals tend to distribute strain in a more spatially homogeneous fashion. Relatively low average slip intensities develop during monotonic loading of the pure Nb, pure tantalum, and C-103 alloys. As a consequence, they display very high fatigue efficiency, in some cases demonstrating fatigue strengths higher than their yield strengths. The particular example of HfNbTaTiZr is an interesting exception because it displays the highest intensities of slip localization, with levels similar to fcc and hcp materials. The most intense slip traces in this alloy are associated with particular crystallographic orientations that inhibit cross-slip. This observation is further highlighted by the high dispersion in slip intensities and slip band spacing observed in the bcc HfNbTaTiZr in comparison to other bcc and fcc materials (fig. S4). These results suggest that control of the crystallographic texture in this class of alloys may be critical for achieving exceptional properties. A deeper physical understanding of the dislocation mechanisms that result in intense localization in high-yield strength bcc alloys may also provide guidance for the design of alloys within this class of materials.

We observed a linear relationship between the amplitude of slip localization that develops during the first cycle and the fatigue strength of the material. We have directly quantified this interrelationship among slip amplitude, irreversibility, and fatigue life for materials that deform by slip. Our observations suggest that the plastic localization that occurs during the first cycle naturally reflects the propensity of the material for cyclic irreversibility. Our analyses also capture global differences in the behavior of fcc and hcp materials compared to bcc and the tendency for more homogeneous deformation in the bcc alloys. The slip analysis is also very useful for identification of alloys that exhibit exceptional/unusual behavior, as exhibited by the bcc multi-principal element alloy HfNbTaTiZr, and provides a different approach for focusing the search for fatigue-resistant alloys.

REFERENCES AND NOTES

- H. Mughrabi, *Procedia Eng.* **55**, 636–644 (2013).
- H. Mayer, *Int. Mater. Rev.* **44**, 1–34 (1999).
- C. Bathias, *Fatigue Fract. Eng. Mater. Struct.* **22**, 559–565 (1999).
- N. Fleck, K. J. Kang, M. F. Ashby, *Acta Metall. Mater.* **42**, 365–381 (1994).
- H. Mughrabi, *Metall. Mater. Trans. A* **40**, 1257–1279 (2009).
- J. Pang, S. X. Li, Z. G. Wang, Z. F. Zhang, *Mater. Sci. Eng. A* **564**, 331–341 (2013).
- Z. Li, Q. Wang, A. A. Luo, P. Fu, L. Peng, *Int. J. Fatigue* **80**, 468–476 (2015).
- Y. Murakami, *Metal Fatigue: Effects of Small Defects and Nonmetallic Inclusions* (Elsevier, 2019).
- C. Bathias, P. C. Paris, *Gigacycle Fatigue in Mechanical Practice* (CRC Press, 2004).
- J.-H. Park, J.-H. Song, *Int. J. Fatigue* **17**, 365–373 (1995).
- A. Karolczuk, D. Skibicki, Ł. Pejkowski, *Fatigue Fract. Eng. Mater. Struct.* **42**, 197–208 (2019).
- M. Yaghooobi et al., *Npj Comp. Mater.* **7**, 38 (2021).
- J. Polák, J. Man, *Procedia Eng.* **101**, 386–394 (2015).
- A. Fatemi, D. F. Socie, *Fatigue Fract. Eng. Mater. Struct.* **11**, 149–165 (1988).
- H. Mughrabi, *Philos. Trans. R. Soc. A* **373**, 2014.0132 (2015).
- Q. Zhang, Y. Zhu, X. Gao, Y. Wu, C. Hutchinson, *Nat. Commun.* **11**, 5198 (2020).
- H. Ho, M. Risbet, X. Feaugas, *Acta Mater.* **85**, 155–167 (2015).
- J. C. Stinville et al., *Acta Mater.* **152**, 16–33 (2018).
- M. A. Charpagne, F. Strub, T. M. Pollock, *Mater. Charact.* **150**, 184–198 (2019).
- J. C. Stinville et al., *Acta Mater.* **186**, 172–189 (2020).
- M. A. Charpagne et al., *Mater. Charact.* **163**, 110245 (2020).
- J. C. Stinville et al., *Exp. Mech.* **56**, 197–216 (2016).
- F. Bourdin et al., *Acta Mater.* **157**, 307–325 (2018).
- L. Coge, W. Li, O. T. Woo, *CNL Nuc. Rev.* **6**, 221–230 (2017).
- R. Thomas et al., *Materialia* **5**, 100248 (2019).
- C. R. Weinberger, B. L. Boyce, C. C. Battaile, *Int. Mater. Rev.* **58**, 296–314 (2013).
- Y. Cui et al., *Int. J. Plast.* **124**, 117–132 (2020).
- A. Heinz, P. Neumann, *Acta Metall. Mater.* **38**, 1933–1940 (1990).
- M. A. Charpagne et al., *Acta Mater.* **215**, 117037 (2021).
- J. Miao et al., in *Superalloys 2008* (Minerals, Metals & Materials Society, 2008), pp. 589–597.
- C. Lavogiez, S. Hémerly, P. Villechaise, *Scr. Mater.* **183**, 117–121 (2020).
- S. Hémerly et al., *Acta Mater.* **219**, 117227 (2021).
- D. Khireddine, M.-H. Khireddine, *Int. J. Fatigue* **22**, 585–591 (2000).
- Y. Brechet, F. Louchet, *Acta Metall.* **37**, 2469–2473 (1989).
- P. Lukáš, L. Kunz, *Philos. Mag.* **84**, 317–330 (2004).
- P. Li, S. X. Li, Z. G. Wang, Z. F. Zhang, *Acta Mater.* **129**, 98–111 (2017).
- J. C. Williams, A. W. Thompson, R. G. Baggerly, *Scr. Metall.* **8**, 625–630 (1974).
- M. P. Nascimento, H. J. C. Voorwald, J. C. Payão Filho, *J. Mater. Process. Technol.* **211**, 1126–1135 (2011).
- A. Ferro, P. Mazzetti, G. Montalenti, *Philos. Mag.* **12**, 867–875 (1965).
- B. Guennec et al., *Materialia* **4**, 348–360 (2018).
- G. Chai, T. Forsman, F. Gustavsson, C. Wang, *Fatigue Fract. Eng. Mater. Struct.* **38**, 1315–1323 (2015).
- P. Zhao et al., *Mater. Sci. Eng. A* **712**, 406–413 (2018).
- N. Torabian et al., *Acta Mater.* **134**, 40–52 (2017).
- C. Wang, Y. Liu, A. Nikitin, Q. Wang, M. Zhou, *Fatigue Fract. Eng. Mater. Struct.* **42**, 2183–2194 (2019).
- A. Nikitin, T. Palin-Luc, A. Shanyavskiy, *Int. J. Fatigue* **93**, 318–325 (2016).
- S. Heinz, D. Eifler, *Int. J. Fatigue* **93**, 301–308 (2016).
- J. Zuo, Z. G. Wang, E. H. Han, *Mater. Sci. Eng. A* **473**, 147–152 (2008).
- Q. Chen et al., *Int. J. Fatigue* **27**, 1227–1232 (2005).
- C. Stocker, M. Zimmermann, H.-J. Christ, *Int. J. Fatigue* **33**, 2–9 (2011).
- A. Kolyshekin, M. Zimmermann, E. Kaufmann, H.-J. Christ, *Int. J. Fatigue* **93**, 272–280 (2016).
- C. Stocker, M. Zimmermann, H.-J. Christ, *Acta Mater.* **59**, 5288–5304 (2011).
- M. Z. Ghomsheh et al., *Mater. Sci. Eng. A* **777**, 139034 (2020).
- N. Marti, V. Favier, F. Gregori, N. Saintier, *Mater. Sci. Eng. A* **772**, 138619 (2020).
- S. E. Stanzl-Tschegg, B. Schönbauer, *Int. J. Fatigue* **32**, 886–893 (2010).
- M. Papakyriacou, H. Mayer, C. Pypen, H. Plenk Jr., S. Stanzl-Tschegg, *Mater. Sci. Eng. A* **308**, 143–152 (2001).
- S. Chen et al., *J. Mater. Sci. Technol.* **114**, 191–205 (2022).
- J. C. Pang, S. X. Li, Z. G. Wang, Z. F. Zhang, *Fatigue Fract. Eng. Mater. Struct.* **37**, 958–976 (2014).
- M. Gazizov, R. Kaibyshev, *Trans. Nonferrous Met. Soc. China* **27**, 1215–1223 (2017).
- D. Yu et al., *Mater. Sci. Eng. A* **711**, 624–632 (2018).
- Z. Xu et al., *Int. J. Fatigue* **95**, 156–167 (2017).

ACKNOWLEDGMENTS

We thank a number of colleagues for providing experimental materials, including N. Philips (C-103 and HfNbTaTiZr alloys), D. Banerjee (titanium grade 4 and Ti 6Al), A. Pilchak (Ti-7Al), S. Agnew (additive 316L), P. Villechaise (forged 316L), D. Texier and J. Cormier (Inconel 718 materials), General Electric (René 88DT), and N. Zhou and S. Forsik (cobalt-based superalloy). We also thank L. Mills for preparation of the HfNbTaTiZr sample and C. Torbet for experimental support. **Funding:** Supported by a Vannevar Bush DoD Faculty Fellowship, ONR grant N00014-18-1-3031; the Naval Research Laboratory under the auspices of the Office of Naval Research (P.G.C.); and startup funds from the Department of Materials Science and Engineering, University of Illinois at Urbana-Champaign (J.C.S.). **Author contributions:** The concept was developed by J.C.S. and T.M.P.; J.C.S. designed

the experimental program. J.C.S. performed the experimental measurements. J.C.S., A.C., and C.J.T. performed the VHCF tests. S.H. processed the titanium alloys. J.C.S. and P.G.C. performed the EBSD and HR-DIC measurements for the titanium alloys. J.C.S. and F.W. performed the EBSD and HR-DIC measurements for the 316L materials. M.A.C. performed the dataset merging and alignment. J.C.S. and V.V. performed the H-DIC calculations. J.C.S. and T.M.P. analyzed the experimental data and prepared the manuscript. All authors contributed to the discussion and revision of the manuscript. **Competing interests:** The authors declare no competing interests. **Data and materials availability:** All data are available in the manuscript or the supplementary materials. **License information:** Copyright © 2022 the authors, some rights reserved; exclusive licensee American Association for the Advancement of Science. No claim to original US government works. www.science.org/about/science-licenses-journal-article-reuse

SUPPLEMENTARY MATERIALS

science.org/doi/10.1126/science.abn0392

Materials and Methods

Figs. S1 to S10

Tables S1 to S3

References (61–83)

Submitted 29 October 2021; accepted 7 July 2022
10.1126/science.abn0392

INDOOR AIR QUALITY

The human oxidation field

Nora Zannoni^{1*†}, Pascale S. J. Lakey², Youngbo Won³, Manabu Shiraiwa^{2*}, Donghyun Rim^{3*}, Charles J. Weschler^{4,5}, Nijing Wang¹, Lisa Ernlé¹, Mengze Li[†], Gabriel Bekó⁴, Pawel Wargocki⁴, Jonathan Williams^{1,6*}

Hydroxyl (OH) radicals are highly reactive species that can oxidize most pollutant gases. In this study, high concentrations of OH radicals were found when people were exposed to ozone in a climate-controlled chamber. OH concentrations calculated by two methods using measurements of total OH reactivity, speciated alkenes, and oxidation products were consistent with those obtained from a chemically explicit model. Key to establishing this human-induced oxidation field is 6-methyl-5-hepten-2-one (6-MHO), which forms when ozone reacts with the skin-oil squalene and subsequently generates OH efficiently through gas-phase reaction with ozone. A dynamic model was used to show the spatial extent of the human-generated OH oxidation field and its dependency on ozone influx through ventilation. This finding has implications for the oxidation, lifetime, and perception of chemicals indoors and, ultimately, human health.

North Americans and Europeans spend, on average, ~90% of their time indoors (including home, workplace, and transport) (1, 2). Within this enclosed space, occupants are exposed to a multitude of chemicals from various sources, including

outdoor pollutants that penetrate indoors, gaseous emissions from building materials and furnishings, and products of human activities such as cooking and cleaning (3). In addition, the occupants themselves are a potent mobile source of gaseous emissions from breath and skin (human bioeffluents) as well as primary and secondary particles (4). Characterization of these indoor sources and the main indoor removal mechanisms are key to understanding indoor air quality (5).

Chemical removal of gas-phase species in outside air during daytime is mostly initiated by hydroxyl (OH) radicals, which are formed when a short-wavelength photolysis product of ozone (O₃) [an excited oxygen atom, O (¹D)] reacts with water. Longer-wavelength photolysis of nitrous acid (HONO) and formaldehyde (HCHO) also provides small additional OH sources outside, as does the light-independent

ozonolysis of alkenes via Criegee intermediate formation (6). By contrast, the indoor environment is less influenced by direct sunlight, in particular ultraviolet light, which is largely filtered out by glass windows, so that primary production of OH indoors via O (¹D) is negligible. Although some OH can be generated by longer-wavelength artificial light by photolysis with natural light of formaldehyde and HONO if present, O₃ entering the building from outside is generally considered to be the principal oxidant indoors (7). Nevertheless, previous studies have highlighted the potential importance of alkene ozonolysis (8–11) in generating OH via Criegee intermediates in indoor environments, particularly when reactive molecules such as limonene from air fresheners or cooking are abundant. Previous estimates and measurements of indoor OH concentrations have ranged from 10⁵ to 10⁷ molecules cm^{−3}, which is substantially higher than outdoor nighttime concentrations and comparable to daytime atmospheric OH concentration levels in some regions (8–15).

None of the aforementioned model or measurement studies considered occupied indoor environments and therefore the underlying chemical influence of humans. Yet with every breath, humans exhale reactive alkenes such as isoprene, which can oxidize to further alkenes such as methyl vinyl ketone (MVK) and methacrolein (MACR) (16). Moreover, O₃ reacting at the skin surface with the skin-oil squalene (C₃₀H₅₀), a triterpene responsible for almost 50% of the unsaturated carbon atoms on human skin, releases a host of alkene-containing compounds to the air, including geranyl acetone, 6-methyl-5-hepten-2-one (6-MHO), OH-6-methyl-5-hepten-2-one (OH-6-MHO), 4-methyl-8-oxo-4-nonenal (4-MON),

4-methyl-4-octene-1,8-dial (4-MOD), and *trans*-2-nonenal (17). These species have the potential to react further in the gas phase, either to generate OH through reaction with O₃ or to deplete OH through direct reaction with the alkene. Therefore, humans have the potential to profoundly affect the oxidative environment indoors, particularly in areas of high occupancy (18), larger exposed body surface, and higher air temperature and humidity (19).

In this study, measurements were conducted in a climate-controlled stainless-steel chamber (see Fig. 1) with three different groups of four adult subjects on four separate days (including two replicates from the same group) (20). The air change rate (ACR) (3.2 hour^{−1}) and O₃ concentration [100 parts per billion (ppb) at the inlet and 35 ppb indoors] used in this experiment were chosen for reproducing a realistic scenario based on the expected O₃ decrease due to occupancy (21). (ACR is the number of times that the total air volume in a room or space is completely replaced by outdoor air in an hour.) From this data, we have determined the indoor concentrations and spatial distribution of OH radicals generated by humans upon exposure to O₃. This oxidative field is produced in isolation from other indoor sources or sinks of OH. A steady-state approach was applied, combining measured total OH reactivity (OH loss frequency in s^{−1}), measured concentrations of compounds containing an alkene double bond, and available literature values of OH yields from O₃ with alkene reactions. For comparison, the OH levels were also determined by an independent method using isoprene and its oxidation products. In the final step, the empirically derived OH levels and measurements were compared with those

obtained from a detailed multiphase chemical kinetic model, and these results were used to simulate high spatial and time-resolved OH distributions in a room using a computational fluid dynamics (CFD) model. To investigate the existence and variability of spatial concentration gradients, we tested four scenarios: (i) an evaluation of the experimental results using the same underfloor air distribution from a perforated floor along with intensive air mixing at the average indoor O₃ concentration of 35 ppb as in the experiment, (ii) the same ventilation condition of the experiment without any mixing fans at an indoor O₃ concentration of 35 ppb to simulate a residential condition, (iii) air jets supplied at ceiling height and an indoor O₃ concentration of 35 ppb to simulate an office condition, and (iv) same as (iii) except the indoor O₃ concentration was 5 ppb.

Results
Total OH reactivity of human emissions

Figure 2 shows the OH loss frequency (total OH reactivity) measured directly in the chamber. The total OH reactivity of the gas-phase human bioeffluents was, on average, 8 ± 4 s^{−1} in the absence of O₃ and 34 ± 16 s^{−1} when O₃ was present (mean value ± measurement error; determined at equilibrium in the last 15 min before volunteers left the chamber). In the absence of O₃, the dominant OH sinks were reactive compounds in human breath (e.g., isoprene 64%), whereas in the presence of O₃, the dominant OH sinks were reactive compounds generated by O₃ reactions with skin lipids such as 6-MHO (31%), 4-oxopentanal (4-OPA) (6%), and the sum of other aldehydes (29%) (19, 22). Figure S1 shows the fractional contributions to OH reactivity for the various measured species. A comparison between the measured and calculated reactivities from the individually measured volatile organic compounds (VOCs) (Fig. 2) showed that the main reactive VOCs present in the chamber were quantified within the method uncertainties (total uncertainty for the measured OH reactivity is 48%; total uncertainty for the calculated OH reactivity is 30%) (19, 22). This was a prerequisite for applying the steady-state method to determine OH using total OH reactivity and the combined OH sources.

OH radical concentration from the steady-state method

Table 1 reports the predominant alkenes of human origin measured in the presence of O₃, their OH production rates, and the resulting OH concentrations at steady state (see methods eq. S5). The empirically determined OH concentration from the four experiments involving three different groups of four adult human subjects was, on average, (7.1 ± 2) × 10⁵ molecules cm^{−3}, whereas replicate experiments on the same group of subjects yielded

Table 1. OH production rates of the measured alkenes and OH concentrations. OH radical production rates of isoprene, 6-MHO, OH-6-MHO, limonene, MVK plus MACR, 4-MON, 4-MOD, geranyl acetone, and *trans*-2-nonenal (in units of molecules cm^{−3} s^{−1}) and OH concentrations (in units of molecules cm^{−3}) obtained with the steady-state method from measurements of alkenes and OH reactivity of four adult volunteers. The data reported in each column were obtained from experiments on separate days, under the same conditions, and within the same campaign. A1, A2, and A3 indicate different groups of subjects. A2(1) and A2(2) were replicates of the same experiment with the same group of volunteers. LOD, limit of detection.

Compound <i>i</i>	A1	A2(1)	A2(2)	A3
Isoprene	3.61 × 10 ⁵	3.06 × 10 ⁵	3.07 × 10 ⁵	4.10 × 10 ⁵
6-MHO	1.22 × 10 ⁷	1.57 × 10 ⁷	1.66 × 10 ⁷	1.82 × 10 ⁷
OH-6-MHO	1.67 × 10 ⁶	1.72 × 10 ⁶	2.35 × 10 ⁶	2.72 × 10 ⁶
Limonene	7.52 × 10 ⁵	below LOD	8.78 × 10 ⁵	7.28 × 10 ⁵
MVK plus MACR	7.59 × 10 ³	5.46 × 10 ³	8.34 × 10 ³	1.17 × 10 ⁴
4-MON	below LOD	5.25 × 10 ⁴	5.61 × 10 ⁵	2.87 × 10 ⁵
4-MOD	below LOD	below LOD	6.05 × 10 ⁵	3.40 × 10 ⁵
Geranyl acetone	1.96 × 10 ⁶	2.13 × 10 ⁶	2.44 × 10 ⁶	2.07 × 10 ⁶
<i>trans</i> -2-nonenal	1.17 × 10 ⁵	9.39 × 10 ⁴	1.76 × 10 ⁵	1.42 × 10 ⁵
OH	(4.2 ± 1) × 10 ⁵	(7.2 ± 2) × 10 ⁵	(7.1 ± 2) × 10 ⁵	(9.7 ± 3) × 10 ⁵

$(7.16 \pm 0.07) \times 10^5$ molecules cm^{-3} (mean value $\pm 1\sigma$). The values assume that the room is uniformly well mixed; therefore, the result represents the mean OH concentration within the chamber under the prevailing conditions: ventilation rate of 3.2 ± 0.11 hour $^{-1}$ and O_3 of 35 ppb with four people present. [Note that O_3 was equal to 100 ppb at the inlet and 95 ppb in the chamber before people entered (20).] For one of the four experimental days, Fig. 2 shows a time series of the calculated OH concentration from the onset of its generation (when O_3 is introduced into the chamber) to when the human bioeffluents reached steady-state conditions. Detailed information on the measured alkene concentrations, their reaction rate coefficients, and OH yields for the same experiment are provided in table S1, whereas fig. S2 shows the simplified reaction scheme of 6-MHO ozonolysis and respective product yields. The most important alkene for generating OH was found to be 6-MHO, followed by geranyl acetone, OH-6-MHO, limonene, 4-MON, and 4-MOD (fig. S3). By contrast, isoprene (OH yield 0.27) and the products resulting from isoprene reacting with OH (MVK plus MACR) made a negligible contribution. Most of the alkenes responsible for generating OH result from the ozonolysis of skin lipids. Notably, the same molecule, 6-MHO, is both the strongest chemical source of OH radicals (fig. S3) and the predominant sink for OH under these conditions (fig. S1).

OH radical concentration from the precursor-product method

Figure 2 also shows the concentration of OH determined by an alternative approach (see methods eq. S6), namely, using a precursor (isoprene) and product [mass-to-charge ratio (m/z) 71.049, here reported as m/z 71, which represents the sum of the products generated from the reaction between isoprene and OH and which is considered here as solely MVK plus MACR; see methods and supplementary text and (23)]. In the presence of O_3 , a ~ 4 -fold increase of the m/z 71 mixing ratio was observed (fig. S4), which is primarily due to isoprene oxidation by OH (isoprene fractional loss of 0.16%) with a small contribution from gas-phase ozonolysis (isoprene fractional loss of 0.012%). The mean OH concentration obtained is 1.2×10^6 molecules cm^{-3} , which is close to, but higher than, the value obtained from eq. S5 (Fig. 2). The agreement between the measured and calculated OH reactivities reported in Fig. 2 precludes the possibility that an unmeasured alkene is the cause. A second possibility is that the OH yields and rate coefficients used in eq. S6 overestimate the OH radicals generated from human emissions. A sensitivity test (table S2) was therefore conducted on the result from eq. S6, where each input variable was varied within its confidence interval. This indicated that the vari-

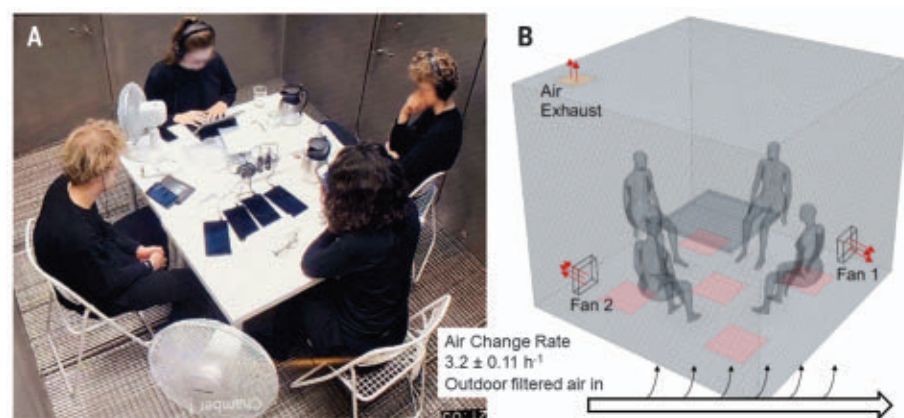


Fig. 1. Photo of one experiment and CFD model framework. (A) Photograph of the occupied stainless-steel climate chamber at the Technical University of Denmark (DTU). (B) Framework of the experiment used for the CFD modeling. Ambient air is introduced through the entire floor and exhausted via one air outlet in the ceiling.

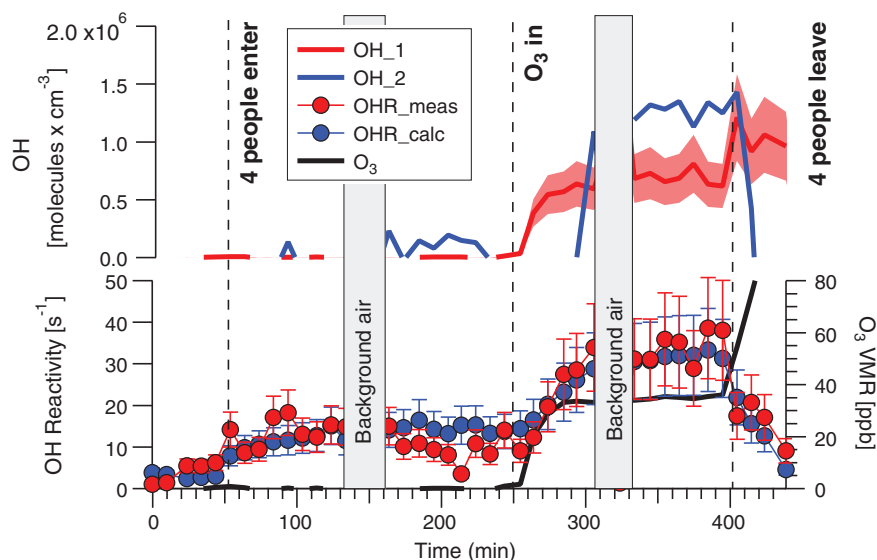


Fig. 2. Time series of OH concentration, OH reactivity, and O_3 concentrations. Time series of OH concentration (top) and measured OH reactivity (OHR_meas), calculated OH reactivity (OHR_calc), and O_3 (bottom) for one selected experiment. OH concentration was determined by two independent methods: (i) OH_1 (steady-state method), from the OH production rate through ozonolysis of alkenes and the measured total OH reactivity and (ii) OH_2 (precursor-product), using the lifetime of isoprene. VMR, volume mixing ratio.

ables that most influence the OH concentration are the isoprene oxidation product yields (relative change 19 to 31%) and the ratio between isoprene oxidation products and isoprene concentrations (relative change 19%). Therefore, any fragment interfering in the measurement of m/z 71 would result in a higher OH concentration as determined through eq. S6. However, in a separate experiment, it was noted that some m/z 71 signal was generated from the O_3 exposure of four clean shirts (without people). Detailed results on the OH reactivity of people wearing short and long clothing and of solely clothing were discussed in Zannoni *et al.* (19). We therefore deduce that the precursor-product method overestimated the OH radical

abundance because of interfering emissions of the product from the clothing. Nevertheless, it should be noted that there is broad agreement between the two OH estimates and that the values derived for human-generated OH are substantial and highly meaningful in the indoor environment.

Modeled OH radical field in the occupied environment

The measured alkene concentrations, OH concentration, and OH reactivity were simulated with the detailed kinetic model KM-SUB-Skin-Clothing (24, 25) (figs. S5 and S6). Outputs from the kinetic model were then used in a CFD model to simulate the human OH radical

field (26, 27). The OH radical field in the chamber due to the presence of the people within was determined for four different conditions. The results of OH reactivity and OH concentration under steady-state conditions with O₃ present (before the occupants left the chamber, at 360 min elapsed time from the beginning of the experiment) are reported in Fig. 3 for all four simulations.

The first condition (Fig. 3A) allows direct comparison with the measured results: air and O₃ are supplied from a simulated perforated floor, and two virtual fans mix the air inside the chamber (as represented in Fig. 1). The maximum air velocity occurs at the chamber walls, and the maximum air temperature occurs at the human-body surface, whereas around the subjects, the air velocity and temperature are uniformly distributed (fig. S7). With O₃ present, the largest source of OH reactivity is the human-body surface (Fig. 3Ai), with O₃-squalene-generated carbonyls such as 6-MHO being the predominant contributors to the OH reactivity. The maximum modeled OH reactivity is 50 s⁻¹, whereas the mean chamber value is ~35 s⁻¹, in good agreement with the measured value. The spatial distribution of the OH radicals generated by the occupants has the opposite distribution to the OH reactivity; their concentration is highest in the room air and lowest at the body surface (Fig. 3Aii). The mean OH concentration under steady-state conditions is 1 × 10⁶ molecules cm⁻³, which agrees

well with the values inferred from the two independent empirical methods described in the prior sections “OH radical concentration from the steady-state method” and “OH radical concentration from the precursor-product method.”

The second condition investigates the impact of the reduced air mixing by suppressing the virtual fans and simulating a more realistic scenario of a typical residence without active mixing (Fig. 3B). A buoyancy-driven flow pattern then developed because of the low-momentum air supply from the floor level and convective flow generated by the heat of the seated occupants. In this case, air movement is mainly driven by temperature gradients associated with indoor heat sources, as seen in fig. S9, which shows the corresponding air temperature and velocity distributions. Without active air mixing, both air temperature and velocity have a clear vertical gradient, with the room air temperature being highest near the chamber ceiling and with the maximum air speed around the body surface of the occupants (fig. S9). Therefore, a strong vertical gradient of OH reactivity is generated from the floor (low) to ceiling (high), as shown in Fig. 3B. Air temperature, velocity, and airflow pattern determine the evolution of the OH reactivity field shape, forming a reactive cloud around and above the mouth of the occupants that prolongates above the head of the occupants (Fig. 3Bi) in the convectively rising air plume. Accordingly,

the vertical profile of OH radical concentration is opposite to that of OH reactivity, showing a maximum at the chamber floor (Fig. 3Bii). The maximum modeled OH reactivity and OH concentration values were 50 s⁻¹ and 2 × 10⁶ molecules cm⁻³, respectively. Under such conditions, the lifetime of the OH radical is 20 ms above a person’s head, increasing to 100 ms toward the floor.

The third condition investigates how the vertical gradient is affected by the location of the incoming air and O₃ source. Air and O₃ are supplied from a jet diffuser at ceiling height, as in a realistic scenario of a typical office. In this case, the maximum OH reactivity is again reached at the body surface and above people’s heads, with minimum levels close to the air-O₃ inlet (Fig. 3Ci). The maximum OH concentration is now displaced to the air-O₃ inlet, although still caused by the interaction of O₃ with 6-MHO (Fig. 3Cii).

The fourth case investigates the spatial gradient using the conditions applied in the third case but with lower indoor O₃ concentration (5 ppb). This is the median reported O₃ indoor concentration from a number of residences, schools, and offices during occupancy (28). As shown in Fig. 3D, the OH reactivity (Fig. 3Di) and OH concentrations (Fig. 3Dii) are reduced to ~20 s⁻¹ and ~3 × 10⁴ molecules cm⁻³, respectively, whereas the spatial gradients are qualitatively very similar to those of the original simulations with higher O₃. In all the

Table 2. Comparison between this study and previous direct and indirect measurements and estimates of OH concentration in indoor environments. FAGE, fluorescence assay by gas expansion; MCM, master chemical mechanism.				
OH concentration (molecules cm ⁻³)	O ₃ concentration (ppb)*	Method	Notes	Reference
(7.1 ± 2) × 10 ⁵	35, 100	Measured OH reactivity	Four adult occupants	This study
4 × 10 ⁶ to 2 × 10 ⁷	20, 40	OH direct measurements with FAGE	No occupants	Carslaw <i>et al.</i> (43)
3 × 10 ⁵ to 3.5 × 10 ⁶	5, 180	OH direct measurements with FAGE	No occupants, cleaning products and maximum O ₃ present	Bloquet <i>et al.</i> (14)
1.8 × 10 ⁶	5, 30	OH direct measurements with FAGE	No occupants, daytime maximum level	Gómez Alvarez <i>et al.</i> (12)
6.5 × 10 ⁴ to 3.7 × 10 ⁵	1.6, 4.8	Tracer decay measurement	No occupants	White <i>et al.</i> (15)
4.6 × 10 ⁵	60, 120	Constant emission of a tracer measurement	No occupants, detergents present	Singer <i>et al.</i> (10)
4 × 10 ⁵	12, 37	Estimate from detailed chemical model based on the MCM	No occupants	Carslaw (13)
1.2 × 10 ⁵	20, 200	Estimate based on SAPRC-99 chemistry model	No occupants	Sarwar <i>et al.</i> (11)
(7.1 ± 0.8) × 10 ⁵	62, 192	Constant emission of a tracer measurement	No occupants	Weschler and Shields (9)
1.7 × 10 ⁵	20†	Estimate based on steady-state mass-balance model	No occupants	Weschler and Shields (8)

*Values represent O₃ indoor concentration followed by O₃ outdoor concentration †O₃ indoor concentration

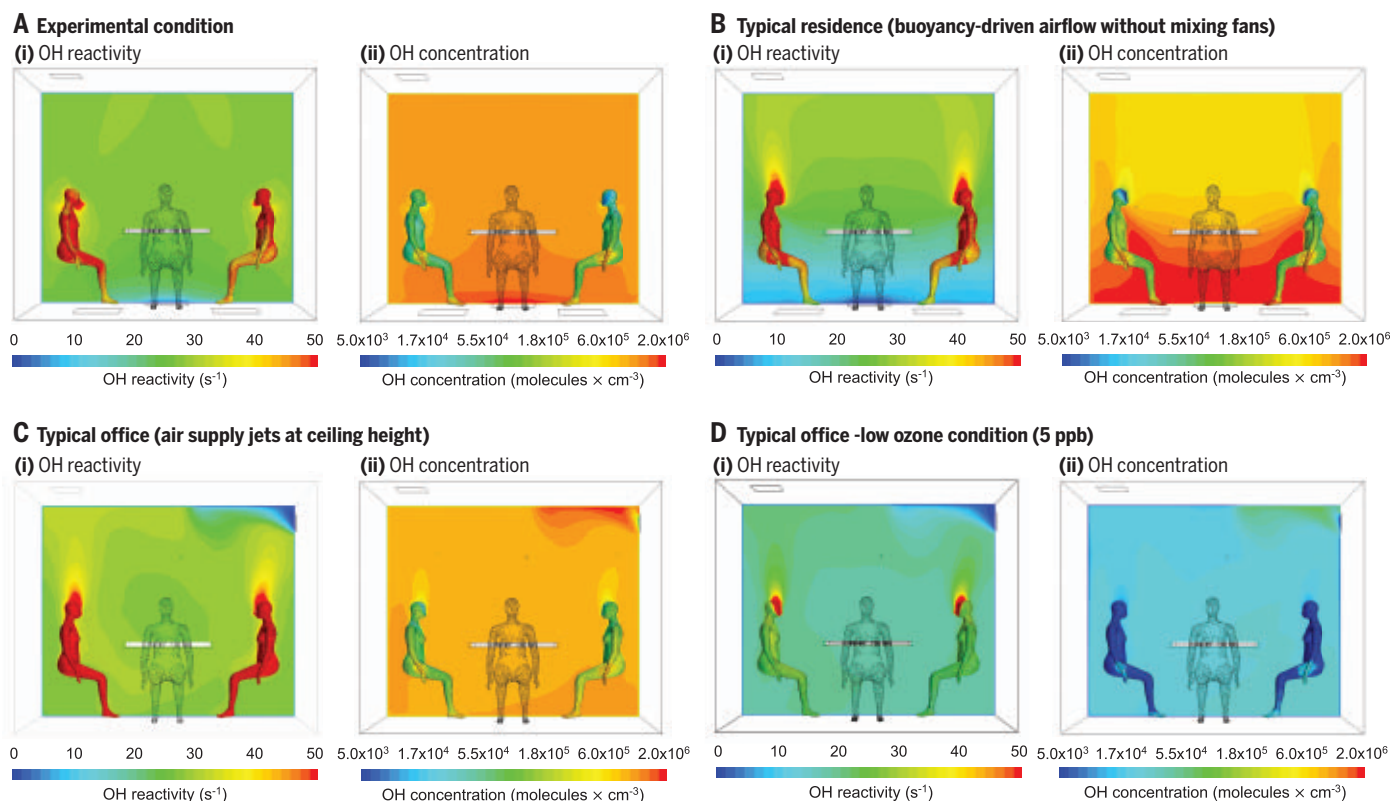


Fig. 3. Spatial distribution of OH reactivity and OH concentration at elapsed time 360 min (before people left the chamber). (A) Simulation of the experiment with two indoor mixing fans and inflow through the floor to match the experimental conditions. (B) Simulation with no virtual mixing by fans for typical conditions. (C) Simulation of inflow from an upper supply inlet of a wall. (D) Simulation with lower (5 ppb) O_3 from an upper supply inlet.

investigated conditions, humans exposed to O_3 generated an indoor OH oxidation field around them.

Discussion

This study has experimentally and theoretically determined with consistent results that substantial OH concentrations are generated in indoor environments owing to the presence of humans and O_3 . Using an OH production rate based on measured alkenes and simultaneous direct measurements of OH reactivity, the steady-state approach yielded OH concentrations under equilibrium conditions of $(7.1 \pm 2) \times 10^5$ molecules cm^{-3} , whereas the precursor-product yielded 1.2×10^6 molecules cm^{-3} . Under the conditions of the bare chamber experiments (ACR of 3.2 ± 0.11 hour $^{-1}$ and O_3 of ~ 35 ppb), the oxidation field generated by one adult is $\sim 1.8 \times 10^5$ molecules cm^{-3} .

These results show that humans exposed to O_3 generate a substantial OH oxidizing field around them. The OH radical levels are sufficiently high to outcompete the more abundant but slower O_3 reactions that are now assumed to dominate organic compound oxidation in the indoor environment. Isoprene, for example, under this chamber's experimental conditions, is predominantly oxidized by OH.

Notably, the OH concentrations derived in this study are of the same order of magnitude as the OH concentrations measured or modeled in previous indoor studies (8–15) that were conducted without people present (Table 2). This suggests that the OH oxidizing field strength generated by human occupants is comparable to that resulting from all other indoor sources of alkenes. In this context, it is important to note that humans are mobile and so represent a displaceable chemical source and oxidation field indoors. Furthermore, it is shown that within indoor environments, strong spatial gradients in OH concentration can develop, with the direction depending on the location of the O_3 source and ventilation. Such pronounced spatial gradients have been reported in indoor experiments previously, with OH levels varying with degree of illumination (12), with trace gases showing strong gradients around the breathing zone (29), and, during cooking, with markedly different VOC levels occurring between floor and ceiling (30). Under real-world conditions, the occupied space can be influenced by additional heat sources such as those from incoming light or hot cooking surfaces that will further affect the spatial gradients observed. Spatial and temporal scales of indoor constituents are modulated by rates of

chemical reactions, surface interactions, and building ventilation; short-lived compounds, including OH radicals, can exhibit sharp spatial gradients because their temporal scales are determined mainly by reaction rates and are only marginally affected by deposition and ventilation rates (31).

Key to the generation of OH around humans is the presence of reactive alkenes generated from the reaction of O_3 with various components of skin oil (e.g., squalene), particularly 6-MHO but also geranyl acetone, OH-6-MHO, 4-MON, and 4-MOD. Because of its extremely rapid reaction with OH [rate coefficient of the reaction 6-MHO with OH ($k_{6-MHO+OH}$) = 1.57×10^{-10} cm^3 molecules $^{-1}$ s $^{-1}$, which is faster than that of isoprene] and its high measured yield of OH upon ozonolysis [0.75 (32)], 6-MHO was found to be the most important OH source and OH sink. As such, it should be included in future modeling and measurement studies of indoor environments. Previous studies have measured or estimated the indoor OH concentration based on OH generated from the ozonolysis of alkenes from nonhuman sources (8–10) and OH produced from HONO photolysis (12, 14). Weschler and Shields focused on the importance of terpenes from scented products to generate OH in an indoor environment

(8, 9), and Carslaw calculated that typically ~90% of OH indoors is produced from alkene ozonolysis, whereas only ~10% is generated from HONO photolysis (13). Gómez Alvarez *et al.* showed that when sunlight shines directly into an unoccupied classroom, HONO photolysis is the main source of OH indoors, measuring peaks of OH up to 1.8×10^6 molecules cm^{-3} during the highest photolysis period (12). The relative importance of these human- and nonhuman-related OH sources will depend critically on the conditions of the specific indoor environment, including lighting, outdoor and indoor sources, temperature, humidity, and, as demonstrated here, people. The human-induced OH field will also interact with other indoor sources and surfaces, including emissions from floors, walls, furnishings, and scented products (which were excluded on purpose in our study). In real-world environments, O_3 can also react with squalene in settled dust, on skin flakes, and on skin oil-soiled surfaces such as clothes, generating 6-MHO and further influencing the OH oxidation field, even without people being present. Liu *et al.* (18) showed that such reactions are still detectable after 5 days without occupancy by measuring squalene oxidation products. Zhang *et al.* (33) estimated the “off-body” skin-oil contribution from the aforementioned experiment. Collectively, squalene and three squalene-derived oxidation products (which can be a source of secondary 6-MHO) contributed 2.7 μmol of double bonds per square meter of surface in this residence.

Previous studies have shown that exposure to natural light indoors has a large effect on OH generation (12). Carslaw simulated an OH concentration of 9×10^4 molecules cm^{-3} for indoor winter conditions in a home environment with artificial light (13), which is similar to the value obtained from our study when O_3 was absent. However, such levels are small in comparison to the human-induced concentrations found in our study when O_3 was present. The indoor O_3 concentration is therefore a critical parameter in determining the strength of the human-generated oxidation field (8–10). This in turn is dependent on the outdoor O_3 concentration and ventilation rates of the indoor space. Real-world indoor environments, including offices and homes, typically have lower ventilation rates (21) than that of our study. Moreover, the availability of multiple surfaces for O_3 reactions provided by furnishings will further lower indoor O_3 concentrations below those used here (7). At an ACR of 3 hour^{-1} , one would expect indoor O_3 concentrations that are roughly 50% of outdoor values. At an ACR of 1 hour^{-1} , one would expect indoor O_3 concentrations that are roughly 25% of outdoor values (21). Hence, although an indoor O_3 level of 40 ppb is high, it does occur when outdoor levels are

high and the ACR is moderate to high. Median O_3 levels for residences, offices, and classrooms are ~5 ppb (28), and this scenario is represented by the simulation of Fig. 3D, i and ii. Therefore, the OH concentrations associated with the human oxidation field reported from our experimental case (Fig. 3A, i and ii) likely represent upper limits. However, even with lower O_3 concentrations, substantial OH fields will establish wherever humans are exposed to O_3 , which is virtually all indoor and outdoor environments. In addition to generating OH radicals, the reaction of O_3 with skin-surface lipids also produces nanocluster aerosols (34).

The human OH radical oxidation field may play an important role in the detection of chemical cues because oxidation gradients near the body surface can attenuate and transform odor signals, affecting odor perception. Indeed, it was recently shown that molecules that react rapidly with the OH radical are generally more sensitively detected by the human nose (35). Growing research is reporting the role of chemical signals in human communication (36).

In indoor environments, O_3 reacts primarily with organic compounds that contain carbon-carbon double bonds. This is typically about 10% of the total number of organics detected in indoor air. The OH radical is a less-discriminating oxidant and reacts rapidly with almost all organics present in indoor air. A number of the measured products cannot be explained by O_3 chemistry; they can only be explained by OH radical chemistry. In essence, this study reveals a cascade of oxidation pathways that lead to many more oxidation products (present at higher concentrations) than would be present if O_3 were the sole oxidant.

The chemistry revealed in this study has health implications. These include the acute and chronic health impacts of certain OH-oxidation products whose toxicities have been evaluated [e.g., methacrolein (37)]. However, there exists a large set of reaction products with unevaluated toxicities. Knowledge about this underlying chemistry and its products can guide us toward selecting compounds for which toxicity data should be generated. This group may include compounds that adversely affect human health. The fact that products are generated in the vicinity of the breathing zone (see Fig. 3) amplifies these concerns. Over the past decade, there have been considerable advances in our knowledge of the products derived from indoor O_3 chemistry (38).

Products of such chemistry include short-lived species such as stabilized Criegee intermediates, OH radicals, hydroperoxyl radicals, and alkylperoxy radicals, as well as more stable products such as hydrogen peroxide, organic hydroperoxides, peroxy acids, organic nitrates, and secondary organic aerosols (39–41) (see extended discussion in the supplementary

materials). The interactions among the human oxidation field, the convective heat transfer (thermal plume), the chemical mass transfer around a human body, and the generation of a personal reactive cloud (42) warrant further research regarding the human health implications. The different conditions simulated in this study can be particularly useful to evaluate potential mitigation strategies. This study shows that in the presence of O_3 , humans both emit and oxidize chemical compounds in their immediate environment, a process that affects all indoor environments.

REFERENCES AND NOTES

- N. E. Klepeis *et al.*, *J. Expo. Anal. Environ. Epidemiol.* **11**, 231–252 (2001).
- European Commission, Press corner; <https://ec.europa.eu/commission/presscorner/home/en>.
- D. K. Farmer *et al.*, *Environ. Sci. Process. Impacts* **21**, 1280–1300 (2019).
- C. J. Weschler, *Indoor Air* **26**, 6–24 (2016).
- W. W. Nazaroff, A. H. Goldstein, *Indoor Air* **25**, 357–361 (2015).
- B. J. Finlayson-Pitts, J. N. Pitts, *Chemistry of the Upper and Lower Atmosphere* (Elsevier, 2000).
- A. P. Ault *et al.*, *Chem* **6**, 3203–3218 (2020).
- C. J. Weschler, H. C. Shields, *Environ. Sci. Technol.* **30**, 3250–3258 (1996).
- C. J. Weschler, H. C. Shields, *Environ. Sci. Technol.* **31**, 3719–3722 (1997).
- B. C. Singer *et al.*, *Atmos. Environ.* **40**, 6696–6710 (2006).
- G. Sarwar, R. Corsi, Y. Kimura, D. Allen, C. J. Weschler, *Atmos. Environ.* **36**, 3973–3988 (2002).
- E. Gómez Alvarez *et al.*, *Proc. Natl. Acad. Sci. U.S.A.* **110**, 13294–13299 (2013).
- N. Carslaw, *Atmos. Environ.* **41**, 1164–1179 (2007).
- M. Blocquet *et al.*, in vol. 1 of *14th International Conference on Indoor Air Quality and Climate (INDOOR AIR 2016)* (International Society of Indoor Air Quality and Climate, 2016), pp. 1310–1317.
- I. R. White *et al.*, *Environ. Sci. Technol.* **44**, 6269–6274 (2010).
- A. Amann *et al.*, *J. Breath Res.* **8**, 034001 (2014).
- A. Wisthaler, C. J. Weschler, *Proc. Natl. Acad. Sci. U.S.A.* **107**, 6568–6575 (2010).
- Y. Liu *et al.*, *Proc. Natl. Acad. Sci. U.S.A.* **118**, e2018140118 (2021).
- N. Zannoni *et al.*, *Environ. Sci. Technol.* **55**, 13614–13624 (2021).
- G. Bekö *et al.*, *Indoor Air* **30**, 1213–1228 (2020).
- W. W. Nazaroff, *Indoor Air* **31**, 282–313 (2021).
- N. Wang *et al.*, *Environ. Sci. Technol.* **55**, 149–159 (2021).
- J. C. Rivera-Rios *et al.*, *Geophys. Res. Lett.* **41**, 2014GL061919 (2014).
- P. S. J. Lakey *et al.*, *Indoor Air* **27**, 816–828 (2017).
- P. S. J. Lakey *et al.*, *Commun. Chem.* **2**, 56 (2019).
- D. Rim, E. T. Gall, S. Ananth, Y. Won, *Build. Environ.* **130**, 40–48 (2018).
- Y. Won, P. S. J. Lakey, G. Morrison, M. Shiraiwa, D. Rim, *Indoor Air* **30**, 1229–1240 (2020).
- W. W. Nazaroff, C. J. Weschler, *Indoor Air* **32**, e12942 (2022).
- P. V. Nielsen, C. Xu, *Indoor Built Environ.* **31**, 1420326X2110485 (2021).
- G. Shen *et al.*, *Environ. Pollut.* **267**, 115493 (2020).
- P. S. J. Lakey *et al.*, *Commun. Chem.* **4**, 110 (2021).
- A. M. Smith, E. Rigler, E. S. C. Kwok, R. Atkinson, *Environ. Sci. Technol.* **30**, 1781–1785 (1996).
- M. Zhang, Y. Gao, J. Xiong, *Chemosphere* **291**, 132772 (2022).
- S. Yang *et al.*, *Environ. Sci. Technol.* **55**, 14536–14545 (2021).
- J. Williams, A. Ringsdorf, *Philos. Trans. R. Soc. London Ser. B* **375**, 20190274 (2020).
- S. C. Roberts, J. Havlíček, B. Schaal, *Philos. Trans. R. Soc. London Ser. B* **375**, 20190258 (2020).
- New Jersey Department of Health, Workplace health and safety: Hazardous substances; <https://www.nj.gov/health/workplacehealthandsafety/right-to-know/hazardous-substances/>.
- Committee on Emerging Science on Indoor Chemistry, Board on Chemical Sciences and Technology, Division on Earth and Life Studies, National Academies of Sciences, Engineering, and Medicine, *Why Indoor Chemistry Matters* (National Academies Press, 2022).

39. C. J. Weschler, *Environ. Health Perspect.* **114**, 1489–1496 (2006).
40. C. J. Weschler, N. Carslaw, *Environ. Sci. Technol.* **52**, 2419–2428 (2018).
41. J. P. D. Abbatt, C. Wang, *Environ. Sci. Process. Impacts* **22**, 25–48 (2020).
42. R. L. Corsi, J. Siegel, A. Karamalegos, H. Simon, G. C. Morrison, *Atmos. Environ.* **41**, 3161–3165 (2007).
43. N. Carslaw, L. Fletcher, D. Heard, T. Ingham, H. Walker, *Indoor Air* **27**, 1091–1100 (2017).

ACKNOWLEDGMENTS

We thank S. Langer for measuring NO₂. N. Ziersen, T. Klüpfel, and R. Hofmann are acknowledged for their support. We thank the volunteers for participating in the study. **Funding:** This work was

funded by Alfred P. Sloan Foundation grants G-2018-11233 (J.W., G.B., and P.W.), G-2019-12306 (M.S. and D.R.), and G-2020-13912 (M.S. and D.R.). **Author contributions:** Conceptualization: J.W., G.B., P.W., C.J.W., N.Z.; Methodology: J.W., N.Z., C.J.W., M.S., P.S.J.L., D.R., Y.W., G.B., P.W.; Investigation: N.Z., J.W., P.S.J.L., M.S., Y.W., D.R., C.J.W., N.W., L.E., M.L., G.B., P.W.; Visualization: N.Z., J.W., P.S.J.L., M.S., Y.W., D.R.; Funding acquisition: J.W., G.B., P.W., M.S., D.R.; Project administration: J.W., G.B., P.W., M.S., D.R.; Supervision: N.Z., J.W., M.S., D.R.; Writing – original draft: N.Z., J.W.; Writing – review and editing: All authors. **Competing interests:** The authors declare that they have no competing interests. **Data and materials availability:** All data are available in the main text or the supplementary materials. **License information:** Copyright © 2022 the authors, some rights reserved; exclusive licensee American

Association for the Advancement of Science. No claim to original US government works. <https://www.science.org/about/science-licenses-journal-article-reuse>

SUPPLEMENTARY MATERIALS

science.org/doi/10.1126/science.abn0340

Materials and Methods
Supplementary Text

Figs. S1 to S9
Tables S1 to S5
References (44–62)
Data S1

Submitted 7 November 2021; accepted 7 July 2022
10.1126/science.abn0340

MOLECULAR BIOLOGY

Nested epistasis enhancer networks for robust genome regulation

Xueqiu Lin^{1†}, Yanxia Liu^{1†}, Shuai Liu^{2†}, Xiang Zhu^{3,4,5}, Lingling Wu¹, Yanyu Zhu¹, Dehua Zhao¹, Xiaoshu Xu¹, Augustine Chemparathy⁶, Haifeng Wang¹, Yaqiang Cao², Muneaki Nakamura¹, Jasprina N. Noordermeer¹, Marie La Russa¹, Wing Hung Wong^{3,7}, Keji Zhao², Lei S. Qi^{1,8,9*}

Mammalian genomes have multiple enhancers spanning an ultralong distance (>megabases) to modulate important genes, but it is unclear how these enhancers coordinate to achieve this task. We combine multiplexed CRISPRi screening with machine learning to define quantitative enhancer-enhancer interactions. We find that the ultralong distance enhancer network has a nested multilayer architecture that confers functional robustness of gene expression. Experimental characterization reveals that enhancer epistasis is maintained by three-dimensional chromosomal interactions and BRD4 condensation. Machine learning prediction of synergistic enhancers provides an effective strategy to identify noncoding variant pairs associated with pathogenic genes in diseases beyond genome-wide association studies analysis. Our work unveils nested epistasis enhancer networks, which can better explain enhancer functions within cells and in diseases.

Disease-associated genes, including oncogenes, are frequently associated with many remote enhancers spanning across a long genomic distance [>megabases (Mb)] (1–4). Genome-wide association studies (GWAS) reveal that noncoding variants of the regulatory elements, including enhancers, account for >90% of variants in diseases and can spread over a long distance (5–8). Although individual enhancer variants may present modest clinical risks (9) there are examples showing that a combination of multiple variants may greatly amplify the effects in traits and diseases (10–12). Similar

to gene interactions (13), these enhancers may interact as an epistatic network wherein the effect of an enhancer is dependent on other enhancers to regulate gene dosage and confer robustness. Aside from these observations it remains largely unknown why multiple ultralong-distance enhancers exist for important genes and how their interactions modulate gene regulation and diseases.

Enhancer interactions were previously studied within a single enhancer cluster. For example, super enhancers were defined as a dense cluster, which contains adjacent enhancers within tens of kilobases (kb) (14–16). Other enhancer clusters similar to super enhancers were also reported including stretch enhancers and enhancer clusters (17, 18). A few examples by perturbing local enhancers within these enhancer clusters showed they may interact additively or synergistically for regulatory roles (19–25). However, these short-range enhancers organized in a cluster cannot explain the prevalence of ultralong-distance enhancers in the human genome.

It remains unknown how multiple enhancers interact with one another over long genomic distances to confer regulatory roles in gene

expression and disease risks. We hypothesize that by using ultralong-distance enhancers (>1 Mb), disease-associated genes have evolved high robustness to disruptive effects from genetic variations. These interactions likely occur through an elaborate network on the three-dimensional (3D) genome organization level.

High-resolution multiplexed perturbation of enhancers reveals a nested two-layer epistasis network

To gain insights into the ultralong-distance enhancer network for disease-relevant genes, we adopted a high-resolution approach to quantitatively analyze enhancer interactions in gene regulation. We chose the endogenous *MYC* locus as a model system. As an important oncogene governing cancer cell proliferation, the *MYC* locus encompasses seven enhancers (e1 to e7) spanning a 1.9-Mb region in K562 erythroleukemia cells (26). The reported linear correlation between *MYC* expression and cellular growth supports its use as a model system to quantitatively dissect the enhancer epistatic network over ultralong distances (26, 27). We conducted a multiplexed CRISPR interference (CRISPRi) screen (28–30), using a pooled library consisting of 87,025 pairs of single guide RNAs (sgRNAs) tiling all single and pairwise combinations of seven enhancers (Fig. 1A, fig. S1, A and B, and table S1). We transduced the pooled sgRNA library into K562 cells stably expressing a doxycycline-inducible nuclease-dead dCas9-KRAB fusion and cultured cells for 30 doublings.

We calculated the depletion score of each sgRNA pair by comparing the relative abundance before and after cell culture (Fig. 1A, fig. S2, A and B, and table S2; see Methods). Using the depletion scores to fit a linear additive model we calculated enhancer interaction scores to identify epistasis interactions and generated a high-density quantitative epistasis map of enhancer-targeting sgRNAs (Fig. 1B and fig. S2, C to E; see Methods). We confirmed the epistasis interaction scores were reproducible across biological replicates and different sgRNA pairs targeting the same enhancer pair

¹Department of Bioengineering, Stanford University, Stanford, CA 94305, USA. ²Laboratory of Epigenome Biology, Systems Biology Center, National Heart, Lung and Blood Institute NIH, Bethesda, MD 20892, USA. ³Department of Statistics, Stanford University, Stanford, CA 94305, USA. ⁴Department of Statistics, The Pennsylvania State University, University Park, PA 16802, USA. ⁵Huck Institutes of the Life Sciences, The Pennsylvania State University, University Park, PA 16802, USA. ⁶School of Medicine, Stanford University, Stanford, CA 94305, USA. ⁷Department of Biomedical Data Science, Stanford University, Stanford, CA 94305, USA. ⁸Sarafan ChEM-H, Stanford University, Stanford, CA 94305, USA. ⁹Chan Zuckerberg BioHub, San Francisco, CA 94158, USA.

*Corresponding author. Email: stanley.qi@stanford.edu

†These authors contributed equally to this work.

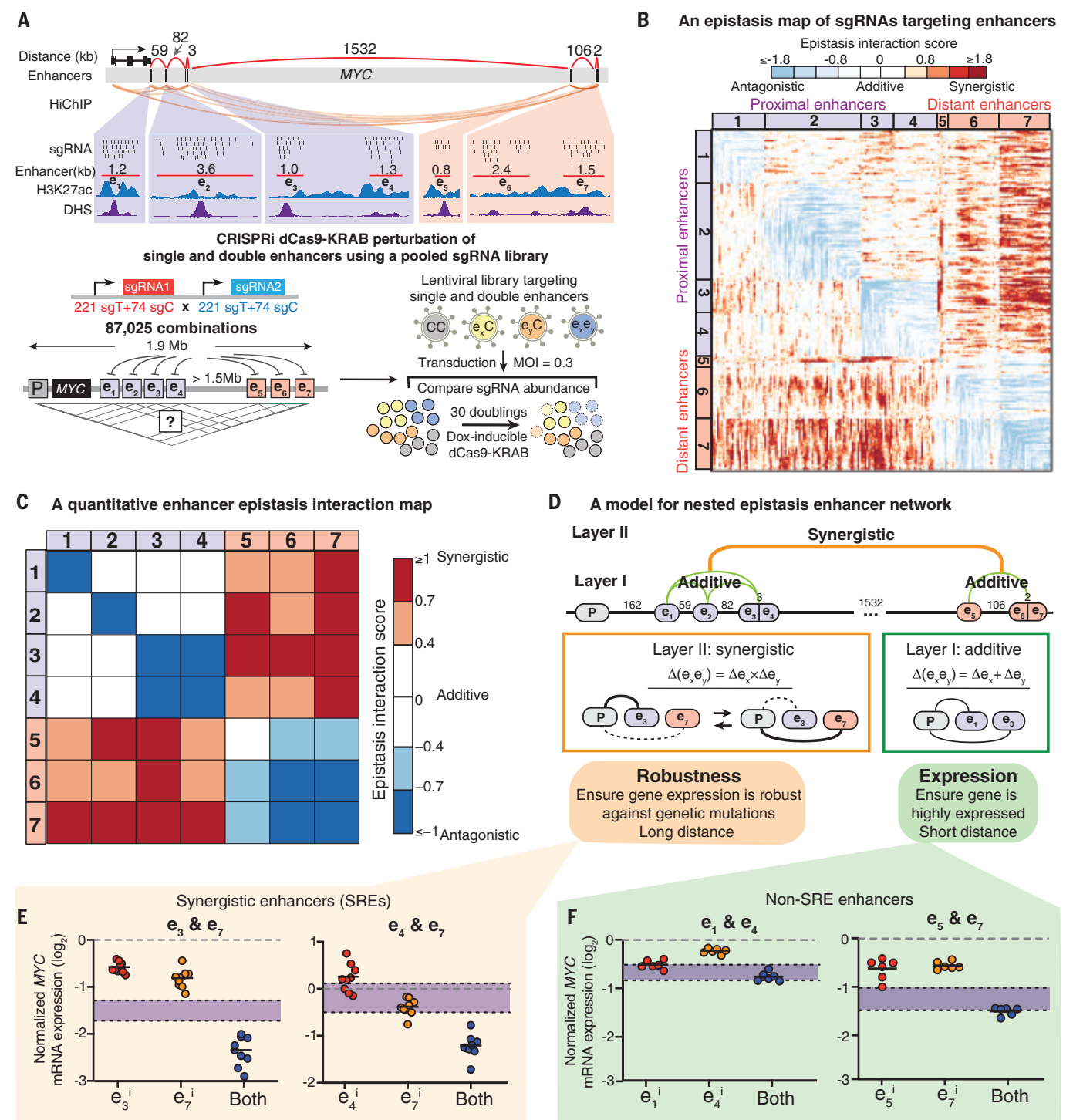


Fig. 1. High-resolution multiplexed CRISPRi perturbation of ultralong-distance enhancers at the MYC locus reveals a nested two-layer epistasis network. (A) (Top) The MYC locus regulated by multiple enhancers distributed over an ultralong distance (~1.9 Mb). (Bottom) Diagram showing the multiplexed CRISPRi screening for high-resolution dissection of enhancer interactions. K562 cells expressing the doxycycline (Dox)-inducible dCas9-KRAB are transduced by a pooled sgRNA library targeting single or double MYC enhancers. Cells are harvested to sequence the pairwise sgRNA enrichment before and after 30 doublings. sgT, targeting sgRNA; sgC, control sgRNA. (B) A quantitative epistasis map of sgRNA pairs targeting all enhancer

combinations in the MYC locus. Each dot represents the epistasis interaction score of a pair of sgRNAs smoothed by adjacent sgRNAs. (C) A quantitative enhancer epistasis map at the MYC locus. (D) A nested two-layer model for the enhancer epistasis network. (E and F) qRT-PCR of MYC mRNA expression for perturbing SREs e3 and e7 or e4 and e7 (E), or non-SREs e1 and e4 or e5 and e7 (F). $P = 0.02, 1.13 \times 10^5, 0.13, 0.61$, for e3 and e7, e4 and e7, e1 and e4, e5 and e7, respectively. Data are represented as individual biological replicates (dots) and the mean value (black bar). The purple area indicates the expected additive effect by plotting mean \pm one standard derivation. P values are calculated by t test.

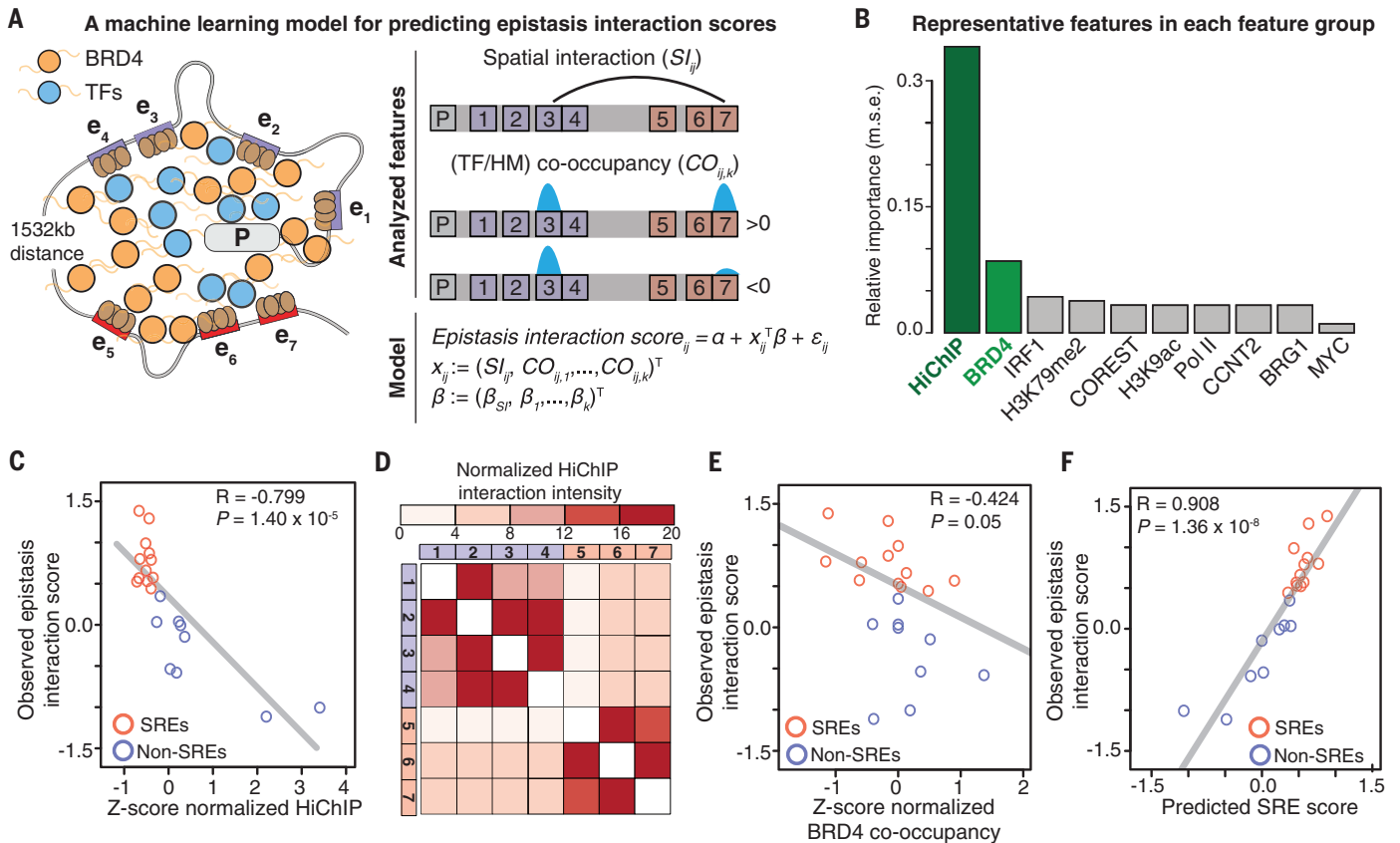


Fig. 2. A machine learning model for analyzing determinants of the SRE synergy. (A) An elastic net regularized linear regression model for predicting epistasis interaction scores. We selected features including the chromatin spatial interaction (SI_{ij}) and co-occupancy ($CO_{ij,k}$) of 38 TFs and 8 HM profiles. (B) The relative importance of each feature group for predicting epistasis interaction scores. The representative feature has the highest correlation in that group

(fig. S8A). m.s.e., mean squared error. (C to F) Correlation between epistasis interaction scores and Z-scores normalized spatial contact (C) and BRD4 co-occupancy (E). (D) Heatmap of normalized HiChIP interaction intensity between enhancers. (F) Correlation between predicted SRE scores and observed epistasis interaction scores. In (C), (D), and (F), red, SREs; blue, non-SREs. The Pearson correlation coefficient (R) and P value are shown.

(fig. S2, F to I). We observed clusters of sgRNAs targeting the same pairs of enhancers showing similar patterns of synergistic or additive interactions, suggesting an epistatic interaction relationship between enhancer pairs (Fig. 1B and figs. S2E and S3A).

We computed the epistasis interaction scores for each enhancer pair by averaging the epistasis interaction scores of the top 25% sgRNA pairs (Fig. 1C and fig. S3B; see Methods). We observed synergistic epistasis when perturbing distant enhancer pairs (>1 Mb), with all four proximal enhancers (e1 to e4) showing strong synergistic interactions with the other three distant enhancers (e5 to e7) upon perturbation. By contrast, perturbation of enhancer pairs within the proximal or distant group mostly showed additive interactions (Fig. 1C).

Our data suggested a nested two-layer architecture of the enhancer epistasis network in regulating genes with large-scale landscapes (Fig. 1D). In the first layer (layer I), enhancer pairs (<100 kb at the *MYC* locus) behave additively after perturbation, suggesting that indi-

vidual enhancers contribute independently to gene expression. In the second layer (layer II), distant enhancer pairs showed nonlinear synergistic effects after perturbation, which are speculated to function as compensatory regulatory elements for one another to maintain the robustness of gene expression upon perturbation. These synergistic enhancers are distributed over long genomic distances, which likely reduces the chance of co-mutation and thus confers robustness of gene expression against mutations or chromosome perturbations. We define synergistic regulatory enhancers (SREs) as a pair of distant enhancers with synergistic effects on gene expression upon perturbation.

We experimentally validated SREs and non-SRE pairs by examining whether they can combinatorially perturb *MYC* expression and cellular growth. Using different sgRNA pairs targeting the same SREs (e3 and e7; e4 and e7), we observed synergistically decreased *MYC* expression as well as cell proliferation (Fig. 1E, fig. S4, A to C, and table S1). In comparison,

inhibiting enhancers within the same proximal or distant groups led to additive repression effects (Fig. 1F and table S1).

We performed H3K9me3 and H3K27ac chromatin immunoprecipitation sequencing (ChIP-seq) to characterize the resolution of using dCas9-KRAB for enhancer perturbation. We confirmed no spreading effects of KRAB on adjacent enhancers (fig. S5, A and B, and fig. S6, A and B). We also knocked out pairs of enhancers by transducing sgRNAs to K562 cells that stably expressed the nuclease Cas9 (see Methods). We confirmed consistent synergistic and additive interactions between e3 and e7 and e1 and e4, respectively (fig. S7, A and B). However, we also observed deletions of large chromatin regions when knocking out pairs of enhancers (fig. S7, C to F). This observation was consistent with reports that gene editing at multiple sites on the same DNA can induce megabase-scale chromosome deletions, which potentially confounds the study of enhancer interactions (31, 32). These results together confirm that dCas9-KRAB is a

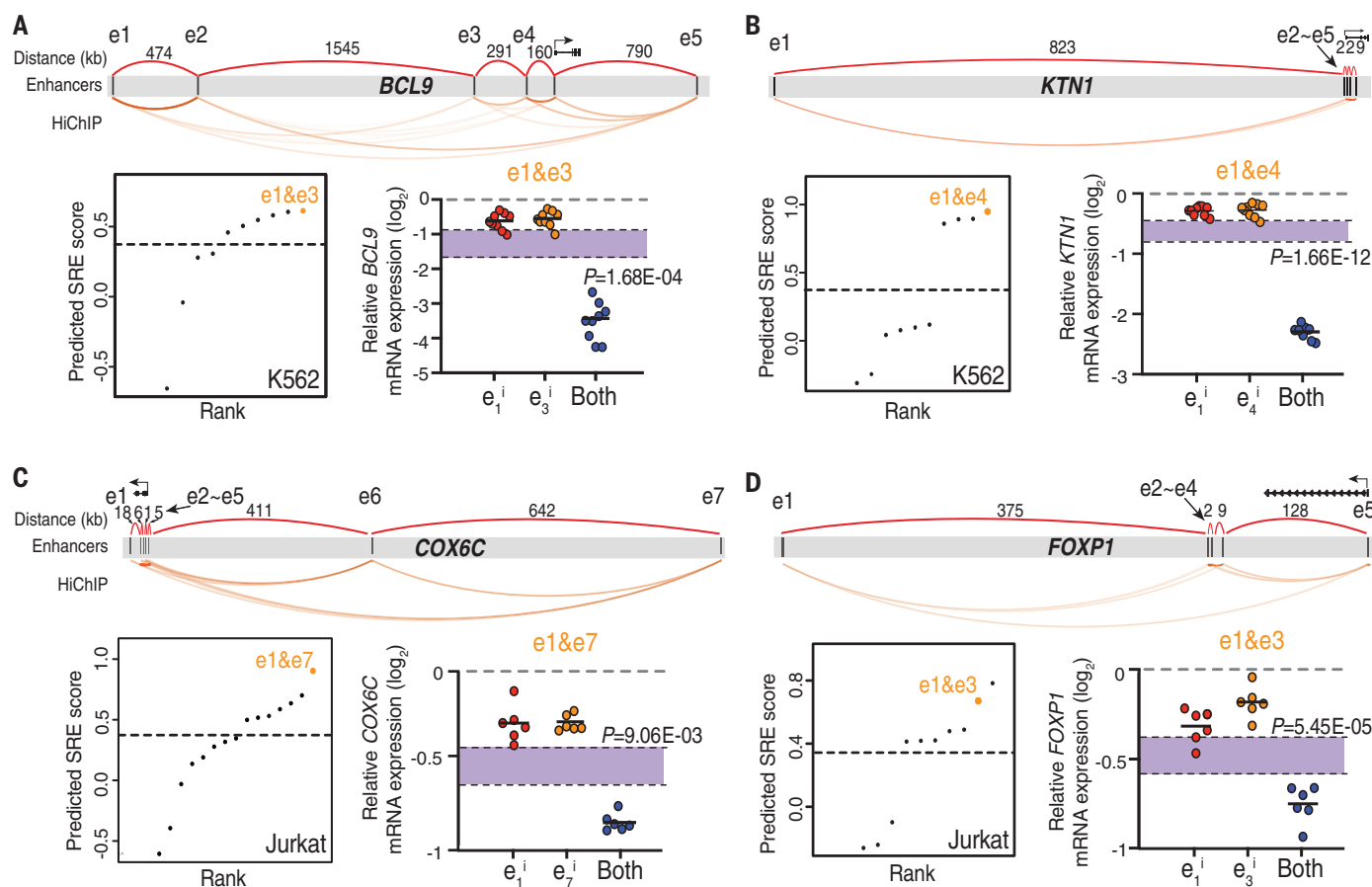


Fig. 3. Experimental validation of predicted SREs at other genomic loci in different cell types. (A to D) Prediction and validation of SREs at *BCL9* (A) and *KTN1* loci (B) in K562 cells, and *COX6C* (C) and *FOXP1* loci (D) in Jurkat cells. (Top) Diagram showing multiple enhancers spanning an ultralong distance at each genomic locus. (Bottom left) Rank of predicted SREs using the model. Dashed line represents the empirical threshold

from the *MYC* locus. Orange dots indicate the validated SREs. (Bottom right) qRT-PCR of mRNA expression for each gene when perturbing the predicted SREs. Data are represented as individual biological replicates (dots) and the mean value (black bar). The purple area indicates the expected additive effect by plotting mean \pm one standard deviation. *P* values are calculated by *t* test.

high-resolution approach for studying multiple enhancer interactions without unwanted large DNA deletions.

Machine learning modeling reveals determinants of SRE synergy

We next developed a machine learning model based on an elastic-net regularized generalized linear model to analyze the determinants of SRE synergy (33) (Fig. 2A). We examined publicly available transcription factor (TF) binding profiles, histone modification (HM) profiles, and H3K27ac HiChIP datasets that capture DNA-DNA spatial contacts in K562 cells (table S3; see Methods) (5). Among all features spatial DNA contact is the most relevant feature and was inversely correlated with calculated epistasis interaction scores (Fig. 2, B and C, and fig. S8A). We found that the spatial contacts between SREs were weaker than non-SREs, which displayed an inverse pattern with the enhancer epistasis map (Fig. 2D versus Fig. 1C). In addition, the co-occupancy of bromodomain-containing protein 4 (BRD4), a

key chromatin-associated coactivator, showed a strong anticorrelation with epistasis interaction scores (Fig. 2, B and E, and fig. S8, A and B).

The elastic net regression model performed better for predicting SREs compared with simple linear models using individual representative features (fig. S8, C and D). Predicted scores of all enhancer pairs were correlated with observed epistasis interaction scores assessed from the CRISPRi screen (Fig. 2F). Altogether, our machine learning model suggests that spatial DNA contacts and BRD4 co-occupancy are two major determinants for predicting SREs.

The SRE model can predict synergistic enhancer interactions at other genomic loci

We next verified whether the SRE prediction model can be generalized to study other genes that have multiple enhancers spanning an ultralong distance in different cell types (fig. S9A; see Methods). We examined the enhancer profiles of four disease-relevant genes: *BCL9* and *KTN1* in K562 cells and *COX6C* and *FOXP1*

in Jurkat cells, all of which have multiple enhancers spreading over a large genomic distance (3.3, 0.8, 1.1, and 0.5 Mb, respectively) (Fig. 3, A to D; see Methods). We used the SRE prediction model to calculate putative SREs and non-SREs and designed sgRNA pairs to target each SRE and non-SRE.

We observed synergistic changes in gene expression when targeting the predicted SRE pairs (Fig. 3, A to D and fig. S9, B to E), as well as additive effects when targeting the non-SRE pairs (fig. S9, B and C). These data suggested that our machine learning model can predict functional interaction between enhancers (SRE or non-SRE) that regulate different genes spanning an ultralong distance in different cell types. We further developed a website (<http://enhancer.stanford.edu/>) by exploring all 4835 putative networks of ultralong distance enhancers (≥ 5 enhancers; >200 kb interdistance) across six cell types (GM12878, K562, Jurkat, A549, HUVEC, and HCT116), which reports many predicted SREs and associated epistasis interaction scores.

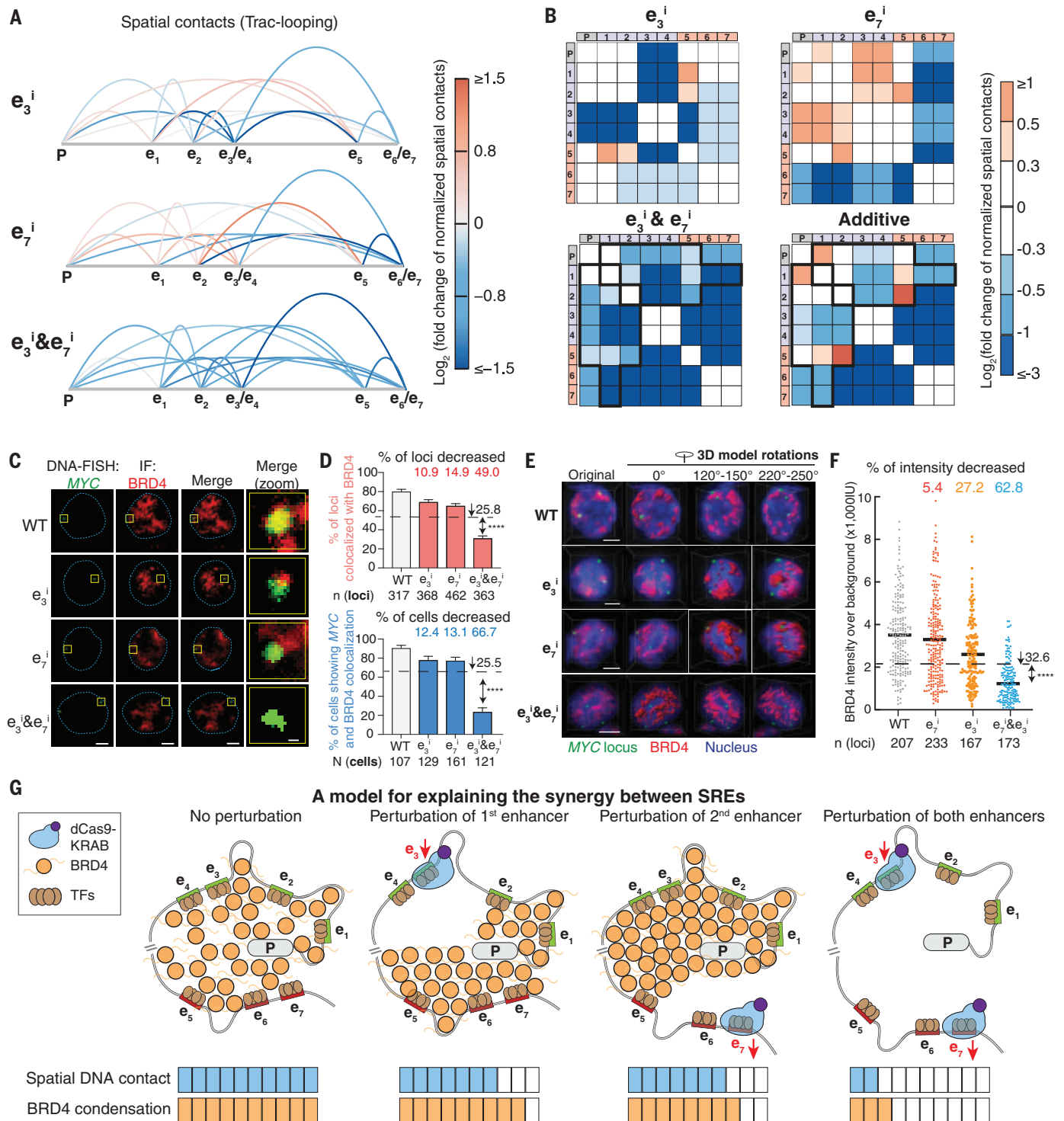


Fig. 4. Perturbation of SREs leads to synergistic reduction of spatial contacts and BRD4 condensation at the genomic locus. (A and B) Spatial contacts between the promoter and enhancers measured by Trac-looping for the MYC locus upon perturbation of e_3 , e_7 , and e_3 and e_7 . Colors represent the \log_2 fold change of spatial contacts normalized to the wildtype cells. Black boxes in (B) indicate synergistically decreased (more than additive) spatial contacts of e_3 and e_7 pair perturbation. (C to F) DNA-FISH colocalization between BRD4 and the MYC locus of representative K562 cells for 2D (C) and (D) and 3D image analysis (E) and (F) upon perturbation of e_3 , e_7 , and e_3 and e_7 . In (C) and (E), red, BRD4 immunofluorescence (IF) staining; green, DNA-FISH at the MYC

locus; blue dashed line, nuclear periphery determined by DAPI staining (not shown); scale bars, 5 μm . The rightmost column in (C) shows insets in the yellow boxes. Scale bars, 500 nm. Quantification of BRD4 and the MYC colocalization are shown for 2D (D) and 3D image analysis (F) upon perturbation of e_3 , e_7 , and e_3 and e_7 . In (D), percentage of loci with colocalization is shown on the top and percentage of cells (≥ 2 colocalization loci) is shown on the bottom; data are represented as mean \pm standard error of the mean. In (F), each dot represents an individual locus. n = total loci, N = total cells. **** $P < 0.0001$ in Fisher's exact test (D) or t test (F) versus the expected additive effect (dashed line). (G) A model to explain the synergy between SREs.

Inhibition of SREs leads to synergistic reduction of local spatial contacts and BRD4 condensation

To experimentally examine the predicted determinants of the SRE model, we performed Trac-

looping assays on CRISPRi-perturbed samples targeting an SRE pair e3 and e7 to measure both spatial contacts and chromatin accessibility (fig. S10A) (34). We observed that inhibition of individual enhancers decreased spatial

contacts only between the targeted enhancer and other elements whereas simultaneous inhibition of e3 and e7 led to synergistic reduction of the spatial contacts at the MYC locus (Fig. 4, A and B), which is consistent with the

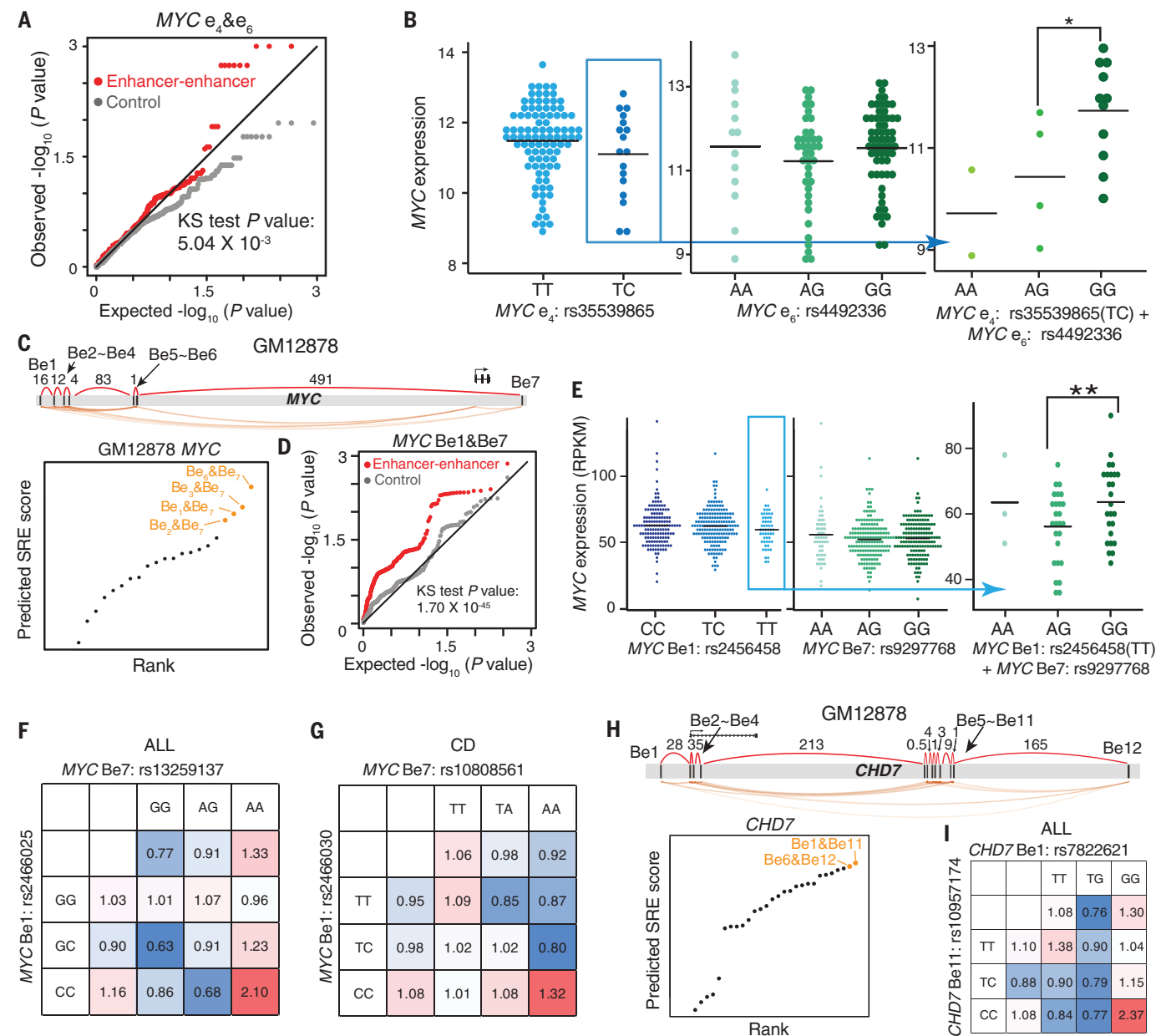


Fig. 5. Synergistic interactions between predicted SRE variants influence gene expression and disease risk in an epistatic manner. (A and B) Analysis of predicted SRE variants at the *MYC* locus in K562 cells for influence on gene expression. (A) quantile-quantile (QQ) plot showing the distribution of P values for the epistasis influence on *MYC* expression between e4 and e6 variants (red) in LAML patients, compared with random permutations (gray); P value in Kolmogorov-Smirnov (KS) test. (B) *MYC* expression in LAML patients stratified by e4 and e6 SRE variants. $*P < 0.05$ in Wilcoxon test. (C to G) Analysis of predicted SRE variants at the *MYC* locus in GM12878 cells for influence on gene expression and associated disease risk. (C) Diagram showing the rank of predicted SREs; orange dots show top SREs. (D) QQ plot showing the distribution of P values for the epistasis influence of Be1 and Be7 variants

(red) on *MYC* expression in the B lymphoblasts of 373 European individuals, compared with random permutations (gray). P value in KS test. (E) *MYC* expression in the B lymphoblasts from individuals stratified by Be1 and Be7 variants. $**P < 0.01$ in Wilcoxon test. (F) and (G) Calculated odds ratio on the relapse risk in acute lymphoblastic leukemia (ALL) (F) and Crohn's disease (CD) (G). Odds ratios are calculated by considering the genotypes of individual variants or both SRE variants. Colors represent the odds ratios. (H and I) Analysis of predicted SRE variants at the *CHD7* locus in GM12878 cells for influence on ALL. (H) Diagram showing the rank of predicted SREs; orange dots show top SREs. (I) Calculated odds ratio on the relapse risk in ALL. Odds ratios are calculated by considering the genotypes of individual variants or both SRE variants. Colors represent the odds ratios.

observed epistatic effects on *MYC* expression and cell growth (Fig. 1E and fig. S4, A and B). By contrast simultaneous inhibition of a non-SRE pair e1 and e4 led to additive reduction of spatial contacts (fig. S10B). We also observed that inhibition of SREs showed no substantial difference from the additive effects on chromatin accessibility (fig. S10, C to E), suggesting that chromatin accessibility is less involved in synergistic interactions.

Perturbation of the distant enhancer e7 increased spatial contacts among the proximal enhancers and the promoter (e.g., e1-e3, e1-e4, e2-e3, e2-e4, e3-promoter, and e4-promoter) (Fig. 4, A and B). Similarly, perturbing e3 or e4 led to increased spatial contacts among the distant enhancers (Fig. 4, A and B, and fig. S10B). These observations imply a possible compensation mechanism on the spatial DNA contact between the SREs, which likely confers robustness of gene expression upon genome disruption (e.g., mutations or loss of DNA-TF interactions).

We next investigated the relationship between enhancer interactions and BRD4 localization. Clustered coactivator condensates mediated by BRD4 can assemble the transcription apparatus at enhancers to drive robust gene expression (35–37). Our machine learning model predicted that the SREs were associated with distinct BRD4 clusters (Fig. 2E and fig. S11A). We examined this relationship by studying BRD4 colocalization at the *MYC* locus through immunostaining and fluorescence in situ hybridization (FISH) confocal imaging.

Compared with wildtype K562 cells, inhibiting individual enhancers (e3 or e7) resulted in a small reduction in colocalization between BRD4 and *MYC* loci, whereas simultaneous inhibition of e3 and e7 synergistically decreased colocalization (49.0%) and the percentage of

cells showing colocalization (66.7%) (Fig. 4, C and D). Similar results were observed for another SRE pair e4 and e7 (fig. S11, B and C). We also performed 3D FISH to better quantify the fluorescent intensity of the BRD4 condensate at the *MYC* locus. Whereas individual enhancer perturbation slightly decreased the BRD4 intensity (27.2% and 5.4% for e3 and e7, respectively), simultaneous perturbation led to synergistic BRD4 reduction (62.8%) (Fig. 4, E and F, and movies S1 to S4). By contrast, simultaneous inhibition of non-SRE e1 and e4 led to additive decrease of colocalization between BRD4 and *MYC* loci (fig. S11D). We further used a BRD4 inhibitor, JQ1, to investigate whether BRD4 condensation was involved in maintaining the synergistic interaction of SRE (38). Consistently, with increasing JQ1 concentrations the synergistic effects from SRE perturbation decreased and then disappeared, implying the importance of BRD4 condensation for enhancer synergy (fig. S11, E and F).

These results together confirmed that SRE perturbation synergistically reduced spatial DNA contact and BRD4 condensation at the target genomic locus, which led to synergistic changes in gene expression (Fig. 4, A to F, and Fig. 1E). Based on computational and experimental analysis, we propose a speculative model (Fig. 4G): while perturbing individual enhancers modestly reduces spatial contacts and BRD4 condensation, perturbation of two distant enhancers considerably alters the 3D chromosome organization and BRD4 condensation to confer synergistic regulatory roles.

Synergistic interactions between predicted SRE variants influence gene expression and disease risk

We evaluated whether SRE genetic variants spanning the ultralong distance can alter gene

regulation and disease risks in an epistatic manner (fig. S12A). We examined the effect of our validated SREs within the *MYC* locus using an acute myeloid leukemia (AML) patient database containing genomic and transcriptomic data. In AML patients, we observed that e4 and e6 SRE variants interacted more frequently to alter *MYC* expression than that expected by chance, additive effects, and non-SRE variants (Fig. 5A and fig. S12, B to D; see Methods and Supplementary Text). A large difference in *MYC* expression levels was observed in two patient groups stratified by the genotype combinations of e4 and e6 SRE variants, whereas there were no dynamic changes when considering the genotypes of individual SRE variants (Fig. 5B).

We further examined the epistatic effect of *MYC* SRE variants on gene regulation in B lymphoblastic cells. We named the enhancers in GM12878 B lymphoblastoid cells as Be and used the SRE model to predict the interaction network among seven enhancers and rank SREs (Fig. 5C). We examined the interactions of variants across predicted SREs in a database of B lymphoblast genomic variants and transcriptomes (39). Although no difference in *MYC* expression was seen when looking at the genotypes of single enhancer variants a significant difference in *MYC* expression was observed when combinatorically considering the genotypes of SRE variants at Be1 and Be7 (Fig. 5, D and E, and fig. S12, E to G; Supplementary Text), or Be6 and Be7 (fig. S12, H and I).

Next, we applied the predicted SREs to investigate the association of *MYC* SRE variants in B cell-associated diseases, acute lymphoblastic leukemia (ALL), and Crohn's disease (CD) (40–44). In the top four predicted SRE pairs, we identified two SRE instances—Be1

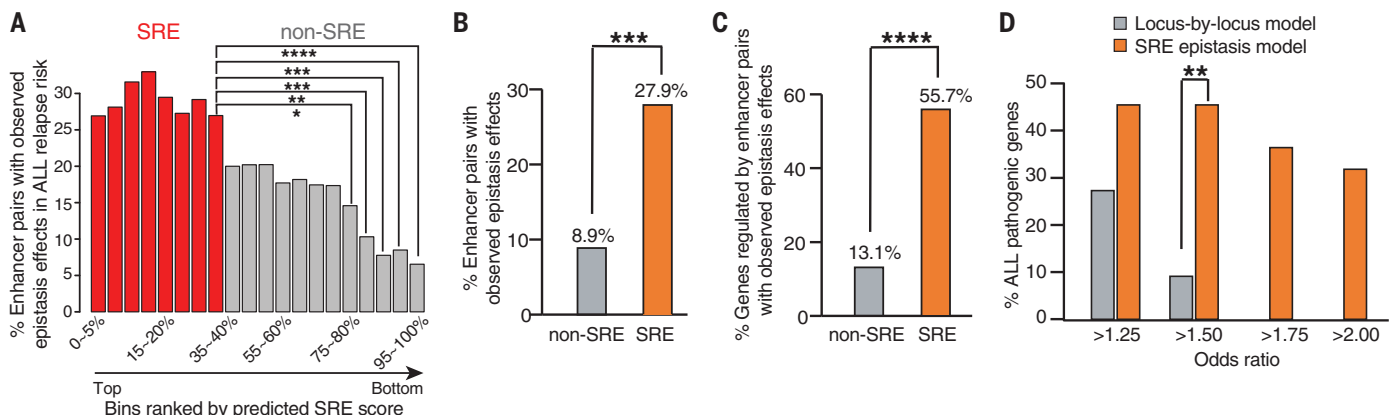


Fig. 6. Genome-wide analysis of epistatic influence of SRE variants on disease risk. (A) Percentage of enhancer pairs with observed epistatic effects on ALL relapse risk for predicted SREs and non-SREs. (B and C) Percentage of enhancer pairs (B) and genes (C) exhibiting interactive effects on ALL relapse risk. SRE pairs: enhancer pairs with top 40% SRE

predicted score; non-SRE pairs: enhancer pairs with bottom 10% SRE predicted score. (D) Comparison of identified ALL pathogenic genes between the SRE model and the traditional locus-by-locus model at different odds ratio levels. In all figures, * $P < 0.05$; ** $P < 0.01$; *** $P < 0.001$; **** $P < 0.0001$ in Fisher's exact test.

and Be7 and Be2 and Be7—where the SRE variant pairs can synergistically influence the clinical risk, including ALL relapse risk and CD disease risk (fig. S13, A to E; Supplementary Text). Particularly, when we stratified case and control population based on SRE variants the odds ratio was significantly higher than that of the odds ratio determined by individual SRE variants alone or additively (Fig. 5, F and G, and fig. S13, F and G; Supplementary Text).

We also predicted SREs in other gene loci in GM12878 cells and observed the epistatic influence of SRE variants in gene expression and clinical risks, including the leukemogenesis-associated *CHD7* locus and B cell antigen *CD180* locus (45) (Fig. 5, H and I, and figs. S13G, S14, and S15; see Methods), which both have enhancer networks spreading ultralong genomic distance (0.4 Mb and 1.2 Mb, respectively).

The SRE model better identifies epistatic influence of genome-wide noncoding variants on disease risk

Finally, we applied the SRE prediction model to the genome-wide analysis in GM12878 cells to link multiple enhancer variants to disease risk. Among more than 900 genes containing ultralong distance enhancer networks, we focused on 70 immune- or cancer-related and highly expressed genes (fig. S16, A and B, and fig. S17; Supplementary Text). Notably, the predicted SRE scores correlated well with the epistatic effects of noncoding variants on the clinical risk for ALL relapse patients (Fig. 6A; Supplementary Text). Specifically, 27.9% of predicted SREs targeting 55.7% of genes showed epistatic effects on ALL relapse risk through our SRE model, which is significantly higher than the non-SRE pairs (Fig. 6, B and C). Furthermore, the SRE model also identified significantly more ALL-associated pathogenic genes compared with the traditional locus-by-locus model (Fig. 6D). For example, among 22 literature-reported ALL-associated pathogenic genes (table S4; Supplementary Text), our SRE model recovered 10 genes, whereas the locus-by-locus model showed only two genes (Fig. 6D; Supplementary Text). Therefore, the SRE prediction model can effectively elucidate the epistatic influence of multiple noncoding variants on associated clinical risk.

Discussion

Our work differs from previous studies on interactions (<100 kb) within enhancer clusters (e.g., super enhancers) (19–25, 46). Although small-scale perturbations revealed additive (21, 22, 46) or synergistic (23, 25) interactions within these enhancer clusters, it remains unknown whether enhancers distributed on a very large scale (>1 Mb) play interactive roles for gene regulation. Our results demonstrate that the observed nested synergistic inter-

actions over the long distance and additive interactions in the short distance are important for an integrated function in the enhancer network; whereas the additive effects ensure a high expression level, the synergistic effects confer robustness against perturbations. Additional quantitative interaction mapping at more genomic loci in more cell types (e.g., diploid cells to rule out aneuploidy effects) should allow for the derivation of distance requirements for ultralong distance enhancer networks and a universal prediction model for enhancer networks. It should also help elucidate whether strong versus weak inhibition effects of individual enhancers determine whether they are SREs or non-SREs.

Our analysis showed that SREs are prevalent in the mammalian genome. The identification of SREs is consistent with evidence from studies in the 1000 Genomes Project, which showed that enhancer regions can be deleted without obvious phenotypic alterations (47, 48). Theoretically, long-distance enhancers are less likely to be mutated at the same time, which avoids co-mutagenesis and thus provide compensation effects on important gene expression against mutations. Our website—which comprehensively explores genome-wide SREs—provides a resource to study enhancer interactions for gene regulation and multiple noncoding variants for diseases.

Because perturbations of individual enhancers may exhibit modest effects on gene expression, multiplexed perturbation of enhancers in the native chromatin context is crucial to fully elucidate their roles. We observed clusters of sgRNA pairs showing similar patterns of synergistic or additive interactions within an enhancer (fig. S3A), suggesting a high-resolution (~300 bp) subenhancer interaction mapping capability. We note that as a result of dCas9-KRAB spreading effects (500 bp~1 kb estimated by H3K9me3 peaks) (fig. S5, A and B), results from dCas9-KRAB should be validated with the Cas9 nuclease knockout for very close enhancers (<1 kb). Nevertheless, our analysis among 15 cell lines showed that >90% of enhancers have an inter-distance of >1 kb. By contrast, because the Cas9 nuclease may induce unwanted DNA deletions when perturbing multiple enhancers (fig. S7, C to F) (31, 32), dCas9-KRAB offers technology for high-throughput study of enhancer interactions with high resolution and minimal side effects.

We provided a speculative model that links the 3D genome and BRD4 interaction to the ultralong distance enhancer network (Fig. 4G). In this model, large BRD4 condensates are formed by smaller distinct BRD4 clusters at individual enhancers (49), which connects these enhancers across ultralong distances to create weak 3D spatial contacts (50). This model is consistent with our quantitative map-

ping of enhancer networks that showed an inverse correlation between spatial contacts and synergistic interactions. Although the inverse correlation may be partly derived from the genomic distance, our experimental validation demonstrated that the 3D genome organization at SREs is casually linked to the synergistic interactions.

With more whole genome DNA sequencing data available in patients, the SRE model can be applied to infer the biological roles of SRE variants in cancer and other diseases and interpret the interactive influence of non-coding elements on disease risk to aid diagnosis and therapy.

REFERENCES AND NOTES

1. P. A. Northcott et al., *Nature* **511**, 428–434 (2014).
2. M. J. Fullwood et al., *Nature* **462**, 58–64 (2009).
3. X. Han et al., *Nat. Commun.* **9**, 2138 (2018).
4. X. Wang, D. B. Goldstein, *Am. J. Hum. Genet.* **106**, 215–233 (2020).
5. ENCODE Project Consortium, *Nature* **489**, 57–74 (2012).
6. Roadmap Epigenomics Consortium et al., *Nature* **518**, 317–330 (2015).
7. M. T. Maurano et al., *Science* **337**, 1190–1195 (2012).
8. M. Kellis et al., *Proc. Natl. Acad. Sci. U.S.A.* **111**, 6131–6138 (2014).
9. T. A. Manolio et al., *Nature* **461**, 747–753 (2009).
10. S. Chatterjee et al., *Cell* **167**, 355–368.e10 (2016).
11. O. Corradin et al., *Nat. Genet.* **48**, 1313–1320 (2016).
12. D. C. Factor et al., *Cell* **181**, 382–395.e21 (2020).
13. P. C. Phillips, *Nat. Rev. Genet.* **9**, 855–867 (2008).
14. W. A. Whyte et al., *Cell* **153**, 307–319 (2013).
15. J. Lovén et al., *Cell* **153**, 320–334 (2013).
16. D. Hnisz et al., *Cell* **155**, 934–947 (2013).
17. S. C. J. Parker et al., *Proc. Natl. Acad. Sci. U.S.A.* **110**, 17921–17926 (2013).
18. L. Pasquali et al., *Nat. Genet.* **46**, 136–143 (2014).
19. D. Hnisz et al., *Mol. Cell* **58**, 362–370 (2015).
20. J. Huang et al., *Dev. Cell* **36**, 9–23 (2016).
21. D. Hay et al., *Nat. Genet.* **48**, 895–903 (2016).
22. C. Bahr et al., *Nature* **553**, 515–520 (2018).
23. H. Y. Shin et al., *Nat. Genet.* **48**, 904–911 (2016).
24. J. Huang et al., *Nat. Commun.* **9**, 943 (2018).
25. M. W. Perry, A. N. Boettiger, M. Levine, *Proc. Natl. Acad. Sci. U.S.A.* **108**, 13570–13575 (2011).
26. C. P. Fulco et al., *Science* **354**, 769–773 (2016).
27. T. Wang et al., *Science* **350**, 1096–1101 (2015).
28. L. S. Qi et al., *Cell* **152**, 1173–1183 (2013).
29. P. I. Thakore et al., *Nat. Methods* **12**, 1143–1149 (2015).
30. L. A. Gilbert et al., *Cell* **159**, 647–661 (2014).
31. M. Kosicki, K. Tornberg, A. Bradley, *Nat. Biotechnol.* **36**, 765–771 (2018).
32. H. Y. Shin et al., *Nat. Commun.* **8**, 15464 (2017).
33. J. Friedman, T. Hastie, R. Tibshirani, *J. Stat. Softw.* **33**, 1–22 (2010).
34. B. Lai et al., *Nat. Methods* **15**, 741–747 (2018).
35. D. Hnisz, K. Shrinivas, R. A. Young, A. K. Chakraborty, P. A. Sharp, *Cell* **169**, 13–23 (2017).
36. W.-K. Cho et al., *Science* **361**, 412–415 (2018).
37. B. R. Sabari et al., *Science* **361**, eaar3958 (2018).
38. P. Filippakopoulos et al., *Nature* **468**, 1067–1073 (2010).
39. T. Lappalainen et al., *Nature* **501**, 506–511 (2013).
40. Wellcome Trust Case Control Consortium, *Nature* **447**, 661–678 (2007).
41. J. J. Yang et al., *Nat. Genet.* **43**, 237–241 (2011).
42. J. J. Yang et al., *Blood* **120**, 4197–4204 (2012).
43. J. Vijayakrishnan et al., *Leukemia* **31**, 573–579 (2017).
44. J. Vijayakrishnan et al., *Nat. Commun.* **10**, 5348 (2019).
45. T. Zhen et al., *Blood* **130**, 2431–2442 (2017).
46. D. D. Lam et al., *PLOS Genet.* **11**, e1004935 (2015).
47. D. Xu, O. Gokcumen, E. Khurana, *PLOS Genet.* **16**, e1008663 (2020).
48. M. Osterwalder et al., *Nature* **554**, 239–243 (2018).
49. K. Shrinivas et al., *Mol. Cell* **75**, 549–561.e7 (2019).
50. N. S. Benabdallah et al., *Mol. Cell* **76**, 473–484.e7 (2019).
51. X. Lin, L. S. Qi, Code and processed data for: Nested Epistasis Enhancer Networks for Robust Genome Regulation, Zenodo (2022); <https://zenodo.org/record/6823833#.YuwiTxhMI2w>.

52. X. Lin, L. S. Qi, SRE predictor for: Nested Epistasis Enhancer Networks for Robust Genome Regulation, Zenodo (2022); <https://zenodo.org/record/6823807#yuiw63bm2w>.

ACKNOWLEDGMENTS

The authors thank all members from the Lei Stanley Qi laboratory for useful comments and help on experiments and manuscript preparation. S. Shang and X. Chen for helping with the fluorescence-activated cell sorting, M. Han for helping with the imaging, and J. Magnusson for comments. We thank Y. Ye and L. Han from UTHealth Houston for helping with the LAML linear model. We thank W. Li and J. Zhang from the University of California, Irvine; Y. Ruan and M. Kim from the Jackson laboratory; and F. Ye from Northwestern University for helpful comments. We thank Z. Duren, S. Ma, and S. Wang for helpful discussion. We thank F. Wang and C. Yu for experimental assistance. We acknowledge the data generated by the TCGA Research Network (<https://www.cancer.gov/tcga>), which allowed us to generate the results of variant interaction. We acknowledge the CD GWAS dataset generated by the Wellcome Trust Case Control Consortium. The ALL Relapse GWAS dataset used for the analyses described in this manuscript were obtained from dbGaP at phs000638.v1.p1. The ALL Relapse GWAS dataset was generated at St. Jude Children's Research Hospital and by the Children's Oncology Group, supported by NIH grants CA142665, CA21765, CA158568, CA156449, CA36401, CA98543, CA114766, CA140729, and UO1GM92666, Jeffrey Pridmore Foundation, the National Childhood Cancer Foundation, and by ALSAC. **Funding:** X.Z. acknowledges supports by the Stein Fellowship from Stanford University and Institute for Computational and Data Sciences Seed Grant from the Pennsylvania State University. W.H.W. acknowledges support from NIH R01 HG010359. L.S.Q. acknowledges support from the Li Ka Shing Foundation and National Science Foundation. The project is supported by the Li Ka Shing Foundation, the National Cancer Institute of the National Institutes of Health under award no. R01CA266470, and a National Science Foundation CAREER award (L.S.Q., award 2046650). L.S.Q. is a Chan Zuckerberg Biohub investigator. **Author contributions:** X.L., Y.L., and L.S.Q. conceived of the concept. Y.L., X.L., S.L., and L.S.Q. planned and designed the experiments. Y.L. and X.L. designed the sgRNA library. Y.L. and L.W. constructed the double sgRNA library. Y.L. performed the CRISPRi screens. D.Z. cloned 192 plasmids in the library and helped with deep sequencing. X.X. cloned 96 plasmids in the library and helped with deep sequencing. X.L. analyzed the CRISPRi screen data and built the SRE model. X.L. applied the model to predict SREs of other genes and designed sgRNAs. Y.L. generated sgRNAs and performed qPCR experiments. S.L. performed Trac-looping, ATAC-seq, and ChIP-seq. X.L. and Y.C. analyzed Trac-looping, ATAC-seq, and ChIP-seq data. Y.L. and Y.Z. performed imaging experiments and 2D image analysis. H.W. performed the 3D image analysis and generated supplementary movies. Y.L. performed the JQ1 experiment. X.Z. mentored X.L. on the SRE variant analysis. A.C. and X.L. developed the enhancer website. X.L., Y.L., and L.S.Q. wrote the manuscript. M.N., H.W., M.L.R., and J.N.N. provided critical comments on the manuscript. L.S.Q. initiated the project. W.H.W., K.Z., and L.S.Q. supervised the project. **Competing interests:** L.S.Q. is a founder and scientific advisor of Epicrispr Biotechnologies, and a scientific advisor of Laboratory of Genomics Research. The roles are unrelated to this study. **Data and materials availability:** The CRISPRi functional tiling screen, Trac-looping data, ChIP-seq data, and ATAC-seq data have been deposited in the Gene Expression Omnibus under the accession ID GSE160768. The codes for the analysis of CRISPRi screen and the SRE prediction model are publicly accessible at Zenodo (51, 52). The CRISPRi double sgRNA library and key plasmids will be available on Addgene (https://www.addgene.org/Stanley_Qi/). **License information:** Copyright © 2022 the authors. some rights reserved; exclusive licensee American Association for the Advancement of Science. No claim to original US government works. <https://www.sciencemag.org/about/science-licenses-journal-article-reuse>

SUPPLEMENTARY MATERIALS

science.org/doi/10.1126/science.abk3512

Materials and Methods

Supplementary Text

Figs. S1 to S17

Tables S1 to S4

References (53–72)

MDAR Reproducibility Checklist

Movies S1 to S4

Submitted 7 July 2021; resubmitted 24 March 2022

Accepted 28 July 2022

Published online 11 August 2022

10.1126/science.abk3512

CANCER IMMUNITY

Pituitary hormone α -MSH promotes tumor-induced myelopoiesis and immunosuppression

Yueli Xu^{1†}, Jiaxian Yan^{1†}, Ye Tao², Xiaojun Qian³, Chi Zhang¹, Libei Yin¹, Pengying Gu⁴, Yehai Liu², Yueyin Pan³, Renhong Tang^{5*}, Wei Jiang^{1*}, Rongbin Zhou^{1,6*}

The hypothalamic–pituitary (HP) unit can produce various hormones to regulate immune responses, and some of its downstream hormones or effectors are elevated in cancer patients. We show that the HP unit can promote myelopoiesis and immunosuppression to accelerate tumor growth. Subcutaneous implantation of tumors induced hypothalamus activation and pituitary α -melanocyte-stimulating hormone (α -MSH) production in mice. α -MSH acted on bone marrow progenitors to promote myelopoiesis, myeloid cell accumulation, immunosuppression, and tumor growth through its melanocortin receptor MC5R. MC5R peptide antagonist boosted antitumor immunity and anti-programmed cell death protein 1 (anti-PD-1) immunotherapy. Serum α -MSH concentration was elevated and correlated with circulating myeloid-derived suppressor cells in cancer patients. Our results reveal a neuroendocrine pathway that suppresses tumor immunity and suggest MC5R as a potential target for cancer immunotherapy.

Tumor-induced immune suppression is the main reason for cancer's evasion of immune surveillance and immune attack (1, 2). Immune checkpoint therapy (ICT) has achieved great results in the clinical treatment of some cancers, including melanoma and non-small cell lung cancer (NSCLC), by targeting inhibitory immune receptors such as cytotoxic T-lymphocyte-associated antigen 4 (CTLA-4) and programmed cell death protein 1 (PD-1) to reverse T cell immunosuppression (3–5). However, ~70% of cancer patients do not respond to this treatment (6, 7), suggesting that it is necessary to further clarify the mechanism of tumor-induced immunosuppression and find additional immunotherapy targets.

Emerging evidence from both experimental and epidemiologic studies indicates that the central nervous system (CNS) can regulate both cancer progression and the activity of the immune system (8, 9). The neuroendocrine system is a major pathway of the CNS that can regulate immune responses (10). The hypothalamic–pituitary (HP) unit is the “command center” of the neuroendocrine system and has been re-

ported to regulate immune responses by producing hormones, such as adrenocorticotrophic hormone (ACTH), thyroid stimulating hormone (TSH), and prolactin (8, 10). Moreover, previous studies have reported that some downstream hormones or effectors of the HP unit, such as glucocorticoids, estrogen, and progesterone, are elevated in cancer patients and can regulate the function of immune cells in the tumor microenvironment (TME) (11–14), suggesting that the neuroendocrine system and HP unit might modulate tumor immunity.

Tumor bearing in mice promotes hypothalamus activation and pituitary α -MSH production

To investigate the role of the HP unit in tumor immunity, we examined pituitary hormones in mice bearing different subcutaneous tumors, including both ICT-resistant [LLC (Lewis lung carcinoma) and B16F10-GMCSF (granulocyte-macrophage colony-stimulating factor)] and ICT-sensitive tumors (MC38 and MCA205) (15–18). We found that the production of α -melanocyte-stimulating hormone (α -MSH) was increased in serum of these tumor-bearing mice (Fig. 1, A and B, and fig. S1, A and B). α -MSH is an endogenous peptide hormone and neuropeptide of the melanocortin family encoded by proopiomelanocortin (POMC), a gene highly expressed in the pituitary gland (19) (Fig. 1C). In some mammals, such as mice, α -MSH is believed to be produced by the melanotrophs in the intermediate lobe (IL) of the pituitary gland (20). We found that tumor transplantation increased POMC expression in the IL of the pituitary gland (Fig. 1, D and E, and fig. S1, C and D).

In addition to α -MSH, POMC can give rise to other peptide hormones, such as ACTH in the anterior pituitary (20). Consistent with previous results (11, 12, 14), we found that the production of ACTH, a pituitary hormone that

¹Hefei National Research Center for Physical Sciences at the Microscale, The CAS Key Laboratory of Innate Immunity and Chronic Disease, School of Basic Medical Sciences, Division of Life Sciences and Medicine, University of Science and Technology of China, Hefei 230027, China. ²Department of Otolaryngology–Head and Neck Surgery, The First Affiliated Hospital of Anhui Medical University, Hefei 230022, China.

³Department of Oncology, The First Affiliated Hospital of University of Science and Technology of China, Division of Life Sciences and Medicine, University of Science and Technology of China, Hefei 230001, China. ⁴Department of Geriatrics, Gerontology Institute of Anhui Province, The First Affiliated Hospital of University of Science and Technology of China, Division of Life Sciences and Medicine, University of Science and Technology of China, Hefei 230001, China.

⁵State Key Laboratory of Translational Medicine and Innovative Drug Development, Nanjing 210000, China.

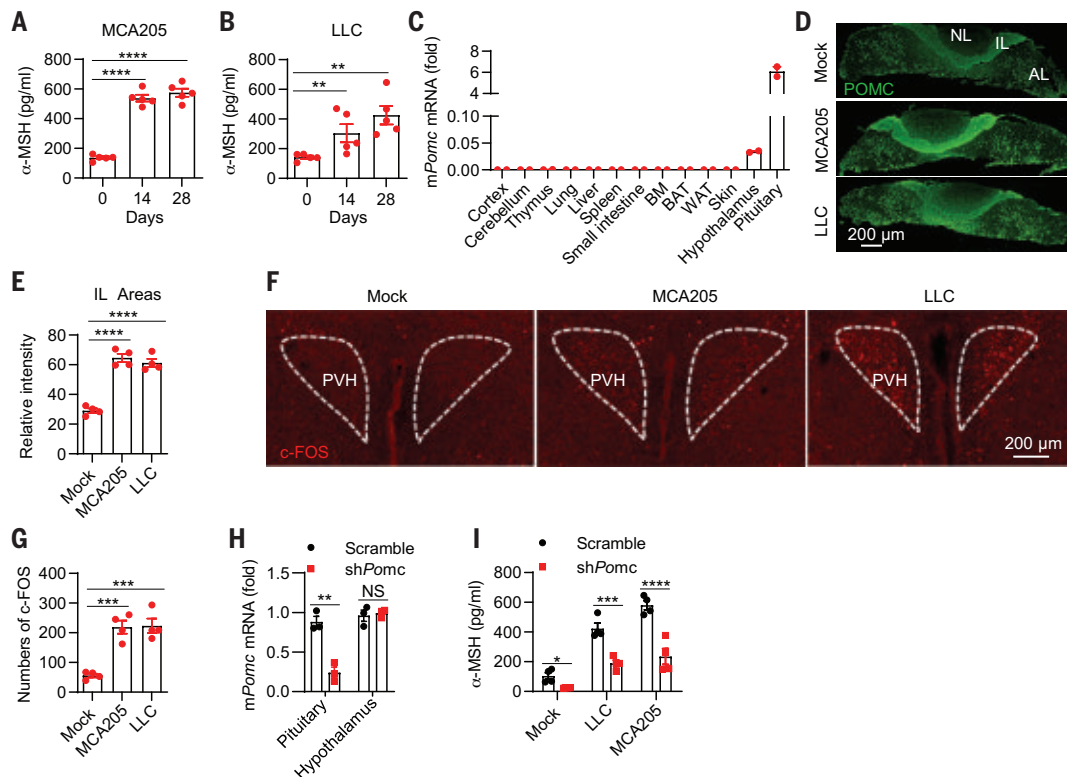
⁶Institute of Health and Medicine, Hefei Comprehensive National Science Center, Hefei 230601 China.

*Corresponding author. Email: zrb1980@ustc.edu.cn (R.Z.); ustcqw@ustc.edu.cn (W.J.); renhong.tang@simcergroup.com (R.T.)

†These authors contributed equally to this work.

Fig. 1. Hypothalamus activation and pituitary α -MSH production in tumor models. (A and B)

Serum α -MSH concentration of MCA205 (A) or LLC (B) tumor-bearing mice on day 0, day 14 (~150 mm³), and day 28 (~1000 mm³) was determined by enzyme-linked immunosorbent assay (ELISA; $n = 5$ mice per group). (C) Quantitative PCR (qPCR) analysis to determine the *Pomc* mRNA expression in different tissues. BAT, brown adipose tissue; WAT, white adipose tissue. (D to G) Representative POMC staining (D) and quantification of the intermediate lobe (IL) in the pituitary (E), and representative c-FOS staining (F) and quantification of the paraventricular hypothalamic nucleus (PVH) (G) on day 10 (~100 mm³) after injection of MCA205 or LLC tumor cells ($n = 4$ mice per group). NL, neural lobe; AL, anterior lobe. (H) qPCR analysis to determine the *Pomc* mRNA expression in the pituitary or hypothalamus of mice infected with AAV-sh*Pomc* on day 30 after stereotaxic injection into the pituitary (sh*Pomc*^{pituitary} mice). (I) ELISA assay of serum α -MSH of control and sh*Pomc*^{pituitary} mice on day 30 after implantation of LLC or MCA205 tumor cells (tumor volume in control mice was ~1000 mm³) ($n = 4$ mice per group). All data are mean \pm SEM or typical photographs of one representative experiment.



The P values were determined by two-way analysis of variance (ANOVA) with Sidak's multiple comparisons test [(A), (B), (E), and (G)] or unpaired two-tailed Student's t test [(H) and (I)]. * $P < 0.05$, ** $P < 0.01$, *** $P < 0.001$, **** $P < 0.0001$. NS, not significant. Data are representative of two [(A) to (C), (H), and (I)] or three [(E) and (G)] independent experiments.

is essential for stress-induced hypothalamic-pituitary-adrenal (HPA) axis activation and glucocorticoid production (21), was normal (LLC, MCA205, or MC38) or slightly elevated (B16F10-GMCSF) in tumor-bearing mice (fig. S2). These results suggest that the HPA axis is not involved in tumor-induced immune suppression and that elevated glucocorticoid production in cancer patients may be HP independent (22). The production of other pituitary hormones, including β -endorphin, TSH, prolactin, follicle-stimulating hormone, and luteinizing hormone, was normal in tumor-bearing mice (fig. S2).

The production of α -MSH by the pituitary gland is under the control of the hypothalamus (23). We found that tumor transplantation resulted in the activation of neurons in the paraventricular nucleus of the hypothalamus (PVH) (Fig. 1, F and G, and fig. S3, A and B), a main hypothalamic nucleus involved in the regulation of pituitary hormone production (24, 25). Moreover, knockdown of pituitary *Pomc* expression by short hairpin RNA reduced α -MSH production in the serum of tumor-bearing mice (Fig. 1, H and I, and fig. S3C). Thus, these results indicate that tumor-bearing

in mice can promote hypothalamus activation and α -MSH production by the pituitary.

α -MSH suppresses antitumor immunity by regulating myelopoiesis

We then investigated the role of pituitary-derived α -MSH in tumor growth. Inhibition of POMC expression in the pituitary showed no obvious toxicity but suppressed the growth of LLC tumors (Fig. 2, A and B, and figs. S4 and S5A). Moreover, inhibition of POMC expression in the pituitary increased the infiltration of cytotoxic lymphocytes, including CD8⁺ T, CD4⁺ T, natural killer (NK), and NKT cells, in LLC tumors (Fig. 2C). The expression of interferon- γ (IFN- γ) in tumor-infiltrating CD8⁺ T, CD4⁺ T, or NK cells was also enhanced by POMC inhibition (Fig. 2D and fig. S5, B to F). Furthermore, POMC inhibition decreased the percentages of regulatory T cells or CD8⁺PD-1⁺ T cells in LLC tumors (fig. S5, G to I). The same results were also observed in MCA205, B16F10-GMCSF, and MC38 tumors (fig. S6). Moreover, the effects of POMC inhibition on tumor growth and antitumor immunity could be reversed by α -MSH supplementation (Fig. 2, A to D, and fig. S5). These results indicate that pituitary-

derived α -MSH promotes tumor growth and immune suppression.

We further investigated whether the tumor suppression induced by POMC inhibition was attributable to the enhanced immune response. After subcutaneous transplantation of LLC tumors, we treated mice with both anti-CD4 and anti-CD8 antibodies from day 7, with one dose given every 7 days (fig. S7A). The antibody treatments effectively depleted T cells, as evidenced by the loss of CD4⁺ and CD8⁺ T cell populations in spleen, lymph node (LN), and tumor, and abrogated the difference in tumor growth between *Pomc*-knockdown and control mice (Fig. 2E and fig. S7, B and C). Thus, these results indicate that inhibition of POMC expression in the pituitary suppresses tumor growth by enhancing antitumor immunity.

We next investigated how POMC inhibition potentiates antitumor immunity. Tumor-associated myeloid cells (TAMCs), such as tumor-associated macrophages (TAMs) and myeloid-derived suppressor cells (MDSCs), play vital roles in tumor-induced immune suppression (26–28). We analyzed TAMCs in LLC tumors and found that POMC inhibition decreased the accumulation of TAMs,

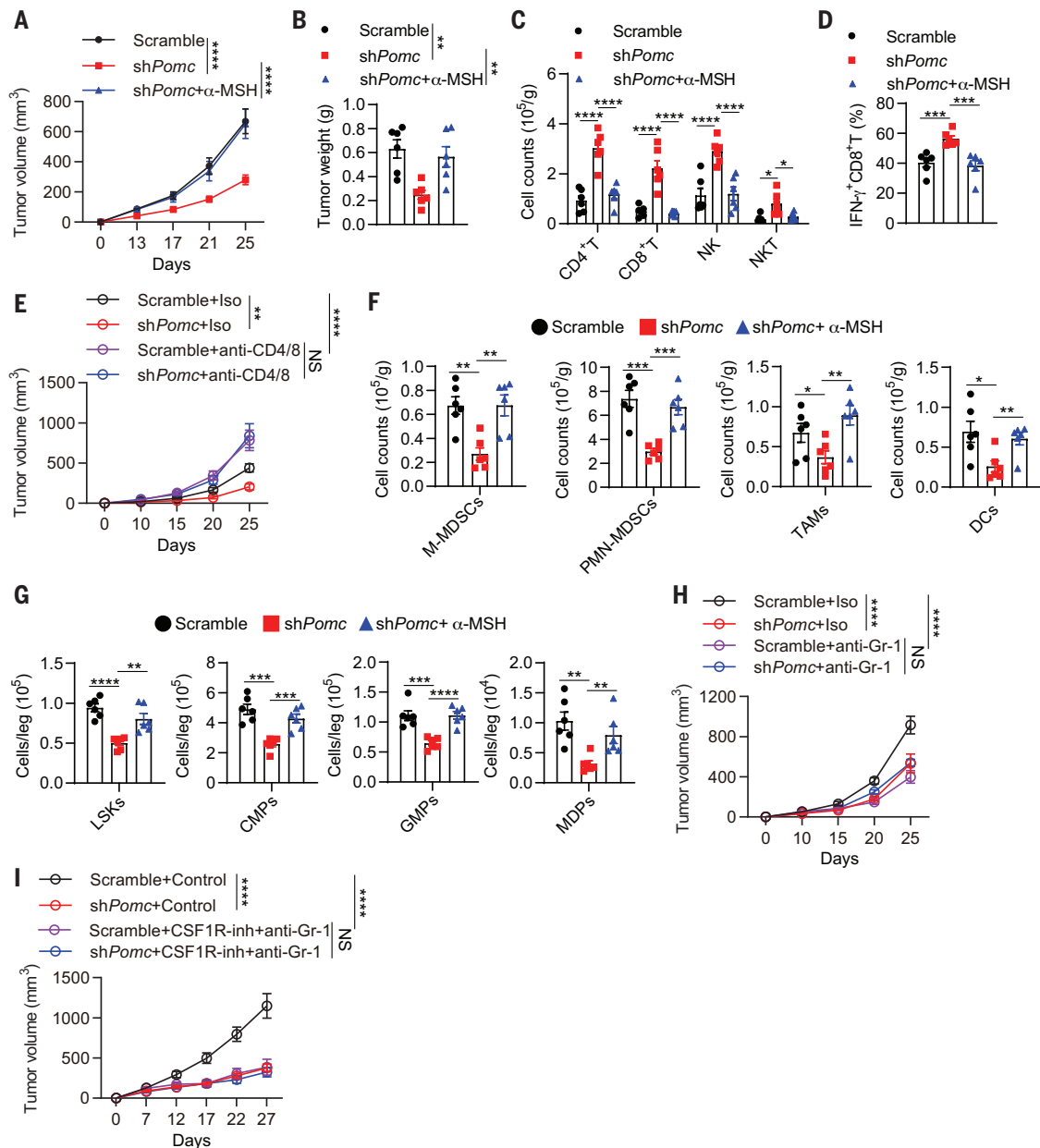


Fig. 2. Role of pituitary α -MSH in tumor-induced myelopoiesis and immunosuppression. (A to D) LLC tumor growth (A), weight (B), and quantification of tumor-infiltrating lymphocytes (C) and IFN- γ ⁺CD8⁺ T cells (D) of tumors on day 25 in control mice, shPomc^{pituitary} mice, or shPomc^{pituitary} mice with α -MSH supplementation ($n = 6$). (E) LLC tumor growth in control mice and shPomc^{pituitary} mice treated with either isotype antibody (Iso) or anti-CD4/8 antibodies ($n = 5$). (F and G) Quantification of myeloid cells from tumors (F) and hematopoietic stem cells (LSKs) and myeloid progenitors (CMPs, GMPs, and MDPs) in the bone marrow (BM) (G) from the mice, as

in (B) ($n = 6$). (H) LLC tumor growth in control mice and shPomc^{pituitary} mice treated with either Iso or anti-Gr-1 antibody (anti-Gr-1) ($n = 5$). (I) MC38 tumor growth in control mice and shPomc^{pituitary} mice treated with either Iso, CSF1R inhibitor, or anti-Gr-1 ($n = 6$). All data are mean \pm SEM. The P values were determined by two-way ANOVA with Sidak's multiple comparisons test (A), unpaired two-tailed Student's t test [(B) to (D), (F), and (G)], or two-way ANOVA with Tukey's multiple comparisons test [(E), (H), and (I)]. * $P < 0.05$, ** $P < 0.01$, *** $P < 0.001$, **** $P < 0.0001$. Data are representative of two independent experiments.

granulocytic (polymorphonuclear) MDSCs (PMN-MDSCs), monocytic MDSCs (M-MDSCs), and dendritic cells (DCs) (Fig. 2F and fig. S8A). Moreover, LLC transplantation-induced expansion of MDSCs in spleen and blood was also impaired by POMC inhibition (fig. S8B). Consistent with these findings, LLC transplantation induced expansion of Lineage⁻ (Lin⁻) cKit⁺ Sca1⁺ (LSK) hematopoietic progenitors,

multipotent common myeloid progenitors (CMPs), granulocyte-monocyte progenitors (GMPs), or monocyte-dendritic cell progenitors (MDPs) in bone marrow (BM), but not expansion of common lymphoid progenitors (CLPs) (fig. S8, C to E). Similar results were also observed in MCA205, B16F10-GMCSF, or MC38 tumor-bearing mice (fig. S9). Moreover, POMC inhibition-induced impaired TAMC

expansion and myelopoiesis in tumor-bearing mice could be rescued by α -MSH supplementation (Fig. 2, F and G). In addition, POMC inhibition had no impact on MDSC- or TAM-mediated suppression of T cell proliferation or DC-mediated antigen presentation to T cells (fig. S10). These results indicate that pituitary-derived α -MSH can enhance tumor-induced myelopoiesis.

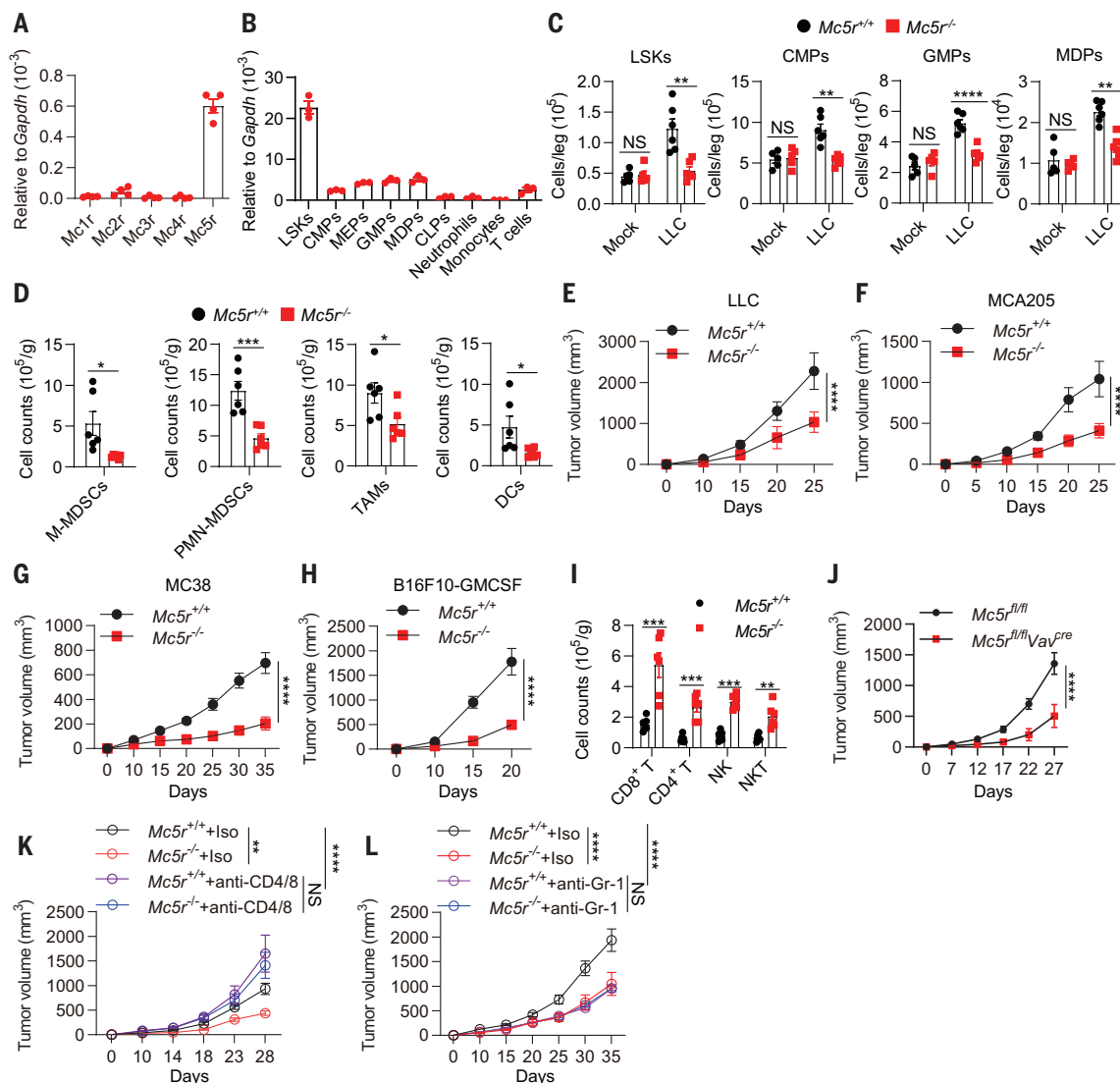


Fig. 3. Role of MC5R in tumor-induced myelopoiesis and immunosuppression.

(A and B) qPCR analysis to determine the relative mRNA expression of the indicated genes (A) and *Mc5r* mRNA expression of the indicated cells (B) in BM. (C) Quantification of LSKs and myeloid progenitors in the BM of control ($n = 5$) or LLC tumor-bearing *Mc5r*^{+/+} and *Mc5r*^{-/-} mice ($n = 6$) on day 25. (D) Flow cytometry analysis and quantification of myeloid cells from tumors in *Mc5r*^{+/+} and *Mc5r*^{-/-} mice on day 25 after LLC tumor implantation ($n = 6$). (E to H) Tumor growth in *Mc5r*^{+/+} and *Mc5r*^{-/-} mice injected subcutaneously (s.c.) with LLC cells (E), MCA205 cells (F), MC38 cells (G), or B16F10-GMCSF cells (H) ($n = 5$).

(I) Same as (D) but for lymphocytes ($n = 6$). (J) Tumor growth in *Mc5r*^{fl/fl} and *Mc5r*^{fl/fl}Vav^{cre} mice injected s.c. with LLC cells ($n = 5$). (K and L) LLC tumor growth in *Mc5r*^{+/+} and *Mc5r*^{-/-} mice treated with either Iso or anti-CD4/8 antibodies (K) or anti-Gr-1 (L) ($n = 5$). All data are mean \pm SEM. The P values were determined by two-way ANOVA with Sidak's multiple comparisons test [(E) to (H) and (J)], unpaired two-tailed Student's t test [(C), (D), and (I)], or two-way ANOVA with Tukey's multiple comparisons test [(K) and (L)]. * $P < 0.05$, ** $P < 0.01$, *** $P < 0.001$, **** $P < 0.0001$. Data are representative of two [(A), (B), (G), (H), and (J) to (L)] or three [(C) to (F) and (I)] independent experiments.

We further investigated whether TAMCs contribute to POMC inhibition-induced tumor suppression. Consistent with previous results (29), depletion of MDSCs with anti-granulocyte receptor-1 (anti-Gr-1) antibody delayed LLC tumor growth, but depletion of TAMs with colony-stimulating factor 1 receptor (CSF1R) inhibitor did not (Fig. 2H and fig. S11, A to G), suggesting that MDSCs are the major TAMCs in LLC tumors. Moreover, knockdown of *Pomc* expression could not inhibit LLC tumor growth or enhance antitumor immunity when

MDSCs were depleted by anti-Gr-1 antibody (Fig. 2H and fig. S11, G to I). Similar results were also observed when MDSCs were eliminated by anti-DR5 antibody (fig. S12). In MC38 tumors, both TAMs and MDSCs contributed to immunosuppression (18). Knockdown of *Pomc* expression could not inhibit MC38 tumor growth or enhance antitumor immunity when both TAMs and MDSCs were eliminated (Fig. 2I and fig. S13). These results indicate that pituitary-derived α -MSH suppresses antitumor immunity by enhancing myelopoiesis.

α -MSH promotes tumor-induced myelopoiesis and immunosuppression through MC5R

Next, we investigated the mechanism by which α -MSH promotes myelopoiesis. The biological function of α -MSH is mediated by five melanocortin receptors (MC1R to MC5R) (30). We examined the expression of these receptors in BM cells and found that only MC5R was highly expressed on Lin⁻ BM cells, especially LSK cells (Fig. 3, A and B, and fig. S14, A to C). In contrast, *Mc5r* mRNA was not expressed on tumor cells (fig. S14D).

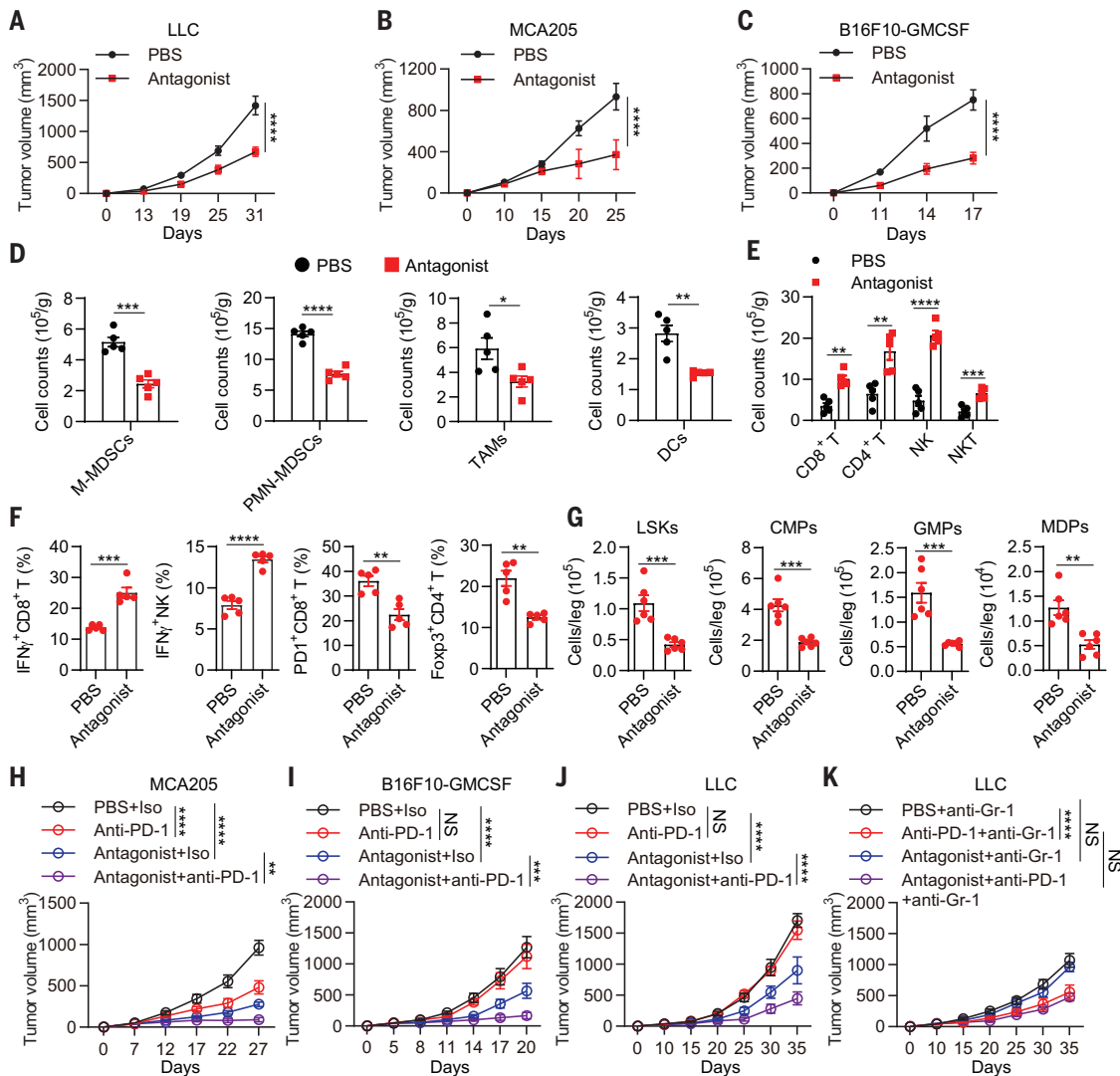


Fig. 4. The immunotherapeutic effects of MC5R antagonist. (A to C) Tumor growth in mice with or without MC5R antagonist ("antagonist") treatment. LLC (A) ($n = 5$), MCA205 (B) ($n = 5$), or B16F10-GMCSF (C) ($n = 6$). (D to G) Quantification of myeloid cells (D); lymphocytes (E); IFN- γ ⁺ CD8⁺ T, IFN- γ ⁺ NK, PD-1⁺ CD8⁺ T, or Fopx3⁺ CD4⁺ T cells (F) in the tumors ($n = 5$); and LSK and myeloid progenitors in the BM (G) ($n = 6$) from LLC tumor-bearing mice that have been treated with or without antagonist on day 31. (H and I) MCA205 (H) ($n = 8$) and B16F10-GMCSF (I) ($n = 10$) tumor growth in mice treated with Iso, anti-PD-1, antagonist, or

antagonist plus anti-PD-1 antibody. (J) LLC tumor growth in mice treated with Iso, anti-PD-1, antagonist, or antagonist plus anti-PD-1 antibody ($n = 7$ or 8). (K) Same as (J), but in the presence of anti-Gr-1 ($n = 7$ or 8). All data are mean \pm SEM. The P values were determined by two-way ANOVA with Sidak's multiple comparisons test [(A) to (C)], unpaired two-tailed Student's t test [(D) to (G)], or two-way ANOVA with Tukey's multiple comparisons test [(H) to (K)]. * $P < 0.05$, ** $P < 0.01$, *** $P < 0.001$, **** $P < 0.0001$. Data represent two [(C) and (H) to (K)] or three [(A), (B), and (D) to (G)] independent experiments.

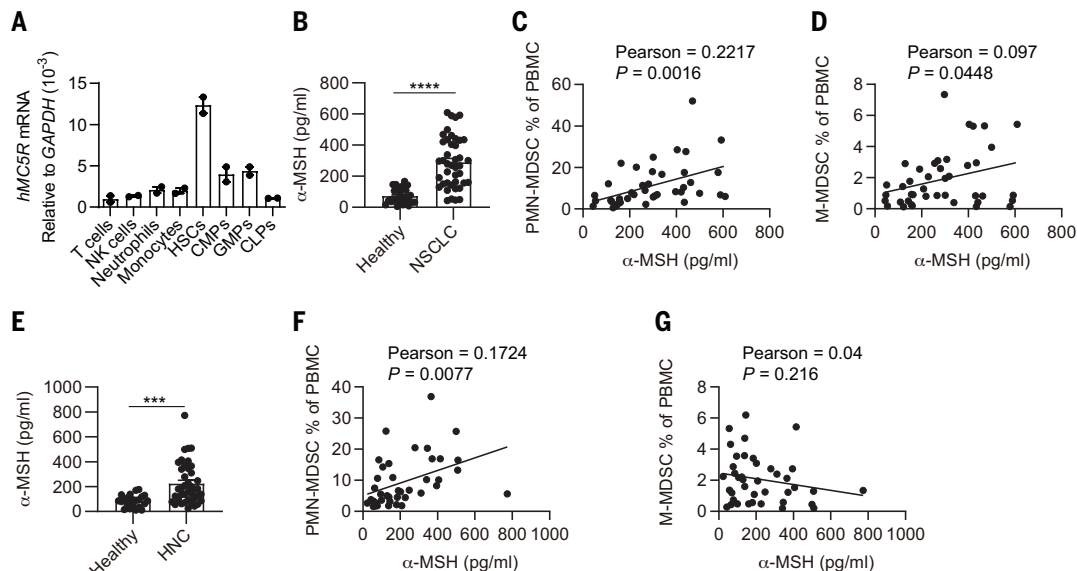
To study the role of MC5R, we generated an *Mc5r*^{-/-} mice line using CRISPR-Cas9 technology (fig. S14, E to G). LLC transplantation-induced LSK proliferation and the expansion of myeloid progenitor cells, such as CMPs, GMPs, and MDPs, were abrogated in *Mc5r*^{-/-} mice (Fig. 3C and fig. S15, A and B). Moreover, the accumulation of TAMCs in LLC tumor-bearing mice was also reduced in *Mc5r*^{-/-} mice (Fig. 3D and fig. S15C). Similarly, MCA205 transplantation-induced myelopoiesis and MDSC expansion also relied on MC5R (fig. S15, D to F). In addition, we found that the immunosuppressive functions of MDSCs or TAMs and the antigen-presenting capacity of DCs were

not changed in *Mc5r*^{-/-} mice (fig. S16). Moreover, we found that α -MSH alone could promote the expansion of myeloid progenitors, monocytes, and neutrophils by means of MC5R (fig. S17, A and B). However, the CD11b⁺Gr-1⁺ myeloid cells from α -MSH-treated mice showed comparable immunosuppressive capacity to those from control mice (fig. S17, C and D). These results indicate that MC5R signaling is required for tumor-induced myelopoiesis.

We then studied the mechanism of how α -MSH-MC5R regulated myelopoiesis. α -MSH stimulation could promote the proliferation of LSK cells in vitro, and this effect was dependent on MC5R (fig. S18, A and B). We further

found that α -MSH treatment in Lin⁻ BM cells induced the activation of signal transducer and activator of transcription 3 (STAT3) (fig. S18, C and D), which is an essential transcription factor for myeloid progenitor proliferation (37). Consistent with the expression of MC5R, α -MSH treatment induced STAT3 activation in Lin⁻ BM cells but not Lin⁺ BM cells (fig. S18E). Moreover, ACTH could not induce STAT3 activation in Lin⁻ BM cells (fig. S18F). α -MSH-induced STAT3 activation was inhibited in *Mc5r*^{-/-} Lin⁻ BM cells (fig. S18G), suggesting that α -MSH activates STAT3 through MC5R. MC5R activation results in the activation of the phosphatidylinositol 3-kinase-AKT (PI3K-AKT)

Fig. 5. Correlation of serum α -MSH concentration with circulation MDSC percentages in cancer patients. (A) qPCR analysis to determine *MC5R* mRNA expression in cells sorted from human PBMCs. (B) Serum concentration of α -MSH in healthy volunteers ($n = 30$) or patients with non-small cell lung cancer (NSCLC, $n = 42$) was determined by ELISA. (C and D) The correlation of serum α -MSH with the percentage of PMN-MDSCs (C) or M-MDSCs (D) in PBMCs from NSCLC ($n = 42$) was analyzed by Pearson's correlation coefficient assay with the indicated P values. (E) Serum concentration of α -MSH in healthy volunteers ($n = 23$) or patients with head and neck cancer (HNC, $n = 40$) was determined by ELISA. (F and G) The correlation of serum α -MSH with the percentage of PMN-MDSCs (F) or M-MDSCs (G) in PBMCs from HNC ($n = 40$) was analyzed by Pearson's correlation coefficient assay with the indicated P values. All data are mean \pm SEM. The P values were determined by unpaired two-tailed Student's t test [(B) and (E)] or Pearson's correlation coefficient assay [(C), (D), (F), and (G)]. *** $P < 0.001$, **** $P < 0.0001$.



and extracellular signal-regulated kinase (ERK) pathways (32). We then found that inhibition of ERK suppressed α -MSH-induced STAT3 activation, but inhibition of PI3K-AKT pathway could not (fig. S18H), suggesting that α -MSH-MC5R activates STAT3 in an ERK-dependent manner. Notably, α -MSH-induced proliferation of LSK cells was suppressed by STAT3 inhibitor (fig. S18, I and J). Because STAT3 has been reported to promote myelopoiesis through CCAAT/enhancer-binding protein beta (CEBP β), we also examined whether α -MSH could affect the expression of CEBP β and other transcription factors involved in myelopoiesis (31, 33) and found that α -MSH could up-regulate the expression of *Cebpb* and *Spil* (encoding PU.1) in Lin[−] BM cells in an MC5R, ERK, and STAT3-dependent manner (fig. S19). Thus, these results indicate that α -MSH-MC5R can promote the proliferation of BM LSK cells through the ERK-STAT3 pathway.

We next investigated the role of MC5R in tumor growth and antitumor immunity. In comparison with control mice, the growth of LLC, MCA205, MC38, or B16F10-GMCSF tumors was substantially reduced in *Mc5r*^{−/−} mice (Fig. 3, E to H, and fig. S20, A to D). Moreover, *Mc5r*^{−/−} mice showed enhanced antitumor immunity in tumor tissues (Fig. 3I and fig. S20E). We also found that *Mc5r*^{−/−} mice showed delayed tumor growth and enhanced antitumor immunity in an orthotopic model of lung cancer established by LLC cells (fig. S20, F to K). To study the role of MC5R expressed on hematopoietic progenitors in tumor immunity, we generated *Mc5r*^{fl/fl}*Vav*^{cre} mice in which *Mc5r* expression was ablated in the hematopoietic system (fig. S21, A to C). Similar to *Mc5r*^{−/−}

mice, *Mc5r*^{fl/fl}*Vav*^{cre} mice showed reduced tumor growth and impaired myelopoiesis and antitumor immunity (Fig. 3J and fig. S21, D to I). Moreover, we found that T cell or MDSC depletion abrogated the tumor suppression observed in *Mc5r*^{−/−} mice (Fig. 3, K and L, and fig. S22). Taken together, these results indicate that α -MSH promotes tumor-induced myelopoiesis and immune suppression by means of MC5R.

Antagonizing MC5R promotes antitumor immunity and enhances anti-PD-1 immunotherapy

We next investigated the possibility of targeting MC5R in cancer therapy. A cyclic peptide has been reported to antagonize human MC5R (34). Using a cyclic adenosine monophosphate assay, we found this peptide had antagonist activity for mMC5R but not for other α -MSH receptors, including mouse MC1R (mMC1R), mMC3R, and mMC4R (fig. S23, A and B). This antagonist also inhibited α -MSH-induced STAT3 activation in Lin[−] BM cells (fig. S23C). We then treated tumor-bearing mice with this antagonist from day 7, with one dose every 2 days, and found that this treatment had no obvious toxicity but could delay the growth of ICT-sensitive MCA205 tumors and ICT-resistant LLC or B16F10-GMCSF tumors (Fig. 4, A to C, and figs. S24 and S25, A to C). Moreover, treatment of LLC tumor-bearing mice with MC5R antagonist inhibited tumor growth in *Mc5r*^{+/+} mice but not *Mc5r*^{−/−} mice (fig. S25, D and E). Consistent with the antitumor effects, MC5R antagonist could reverse tumor-induced immune suppression and suppresses myelopoiesis in LLC tumor-bearing mice

(Fig. 4, D to G). Thus, these results indicate that antagonizing MC5R can enhance tumor immunity and has potential antitumor effects, even in anti-PD-1-resistant tumors.

High infiltration of immune-suppressive myeloid cells correlates with poor prognosis and ICT resistance, and myeloid cells have a major role in limiting the efficiency of ICT (35–37). We thus investigated whether inhibition of MC5R-dependent myelopoiesis improved the efficiency of ICT or overcame ICT resistance. In MCA205 tumor-bearing mice, anti-PD-1 antibody or MC5R antagonist treatment could inhibit tumor growth, but a combination of these two treatments had much better efficacy (Fig. 4H and fig. S25F). In LLC or B16F10-GMCSF tumor-bearing mice, anti-PD-1 antibody treatment alone had no effects but in combination with MC5R antagonist could restore the sensitivity of anti-PD-1 antibody and showed strong antitumor effects (Fig. 4, I and J, and fig. S25, G and H). Moreover, the suppressive effects of anti-PD-1 antibody on LLC tumor growth in the presence of MC5R antagonist were abrogated when MDSCs were depleted by anti-Gr-1 antibody (Fig. 4, J and K, and fig. S25H). Thus, these results indicate that antagonizing MC5R provides an opportunity to improve the efficacy of ICT or overcome ICT resistance.

Serum α -MSH concentration is elevated and correlates with circulating MDSCs in cancer patients

Lastly, we investigated the clinical relevance of the α -MSH-MC5R axis in cancer patients. First, we found that the *MC5R* gene was highly expressed in hematopoietic stem cells (HSCs,

Lin[−]CD34⁺CD38[−]CD90⁺CD45RA[−]) from human peripheral blood mononuclear cells (PBMCs) (Fig. 5A and fig. S26A). Increased myelopoiesis and MDSC expansion have been observed in various types of cancers, such as NSCLC and head and neck cancers (HNCs) (38). Consistent with previous reports, we found that both PMN-MDSCs and M-MDSCs were increased in the blood of NSCLC patients (fig. S26, B to E). We analyzed α -MSH concentrations in the serum of NSCLC patients and found that α -MSH concentrations were higher than in healthy volunteers (Fig. 5B). Moreover, the circulating α -MSH concentrations were positively correlated with the percentages of PMN-MDSCs or M-MDSCs in PBMCs (Fig. 5, C and D). In patients with malignant HNC, PMN-MDSCs, but not M-MDSCs, were increased in the blood (fig. S26F), consistent with a previous report (39). Circulating α -MSH concentrations were also increased in HNC patients compared with healthy controls and positively associated with the percentages of PMN-MDSCs, but not M-MDSCs, in PBMCs (Fig. 5, E to G). Thus, these results suggest that α -MSH concentration is increased and correlates with circulating MDSCs in cancer patients.

Discussion

Cancer-induced myelopoiesis leads to the accumulation of TAMCs that can dampen anti-tumor immunity and limit the efficiency of ICT (26, 27, 35–37), therefore, elucidating the mechanism of cancer-induced myelopoiesis can help explain the mechanism of tumor-induced immunosuppression. We demonstrate that tumor bearing in mice can promote hypothalamus activation and pituitary-derived α -MSH production, which then acts on BM LSK cells and boosts myelopoiesis and TAMC expansion by means of MC5R. Genetic or pharmacological inhibition of MC5R can reverse tumor-induced immunosuppression. Moreover, antagonizing MC5R can improve the efficacy of ICT or overcome ICT resistance when combined with anti-PD-1 therapy.

Our results demonstrate that pituitary-derived α -MSH can promote tumor-induced myelopoiesis and the expansion of TAMCs, such as MDSCs. MDSC development in cancer can be roughly divided into two stages: expansion and activation (40). We found that α -MSH signaling promoted the expansion of myeloid progenitors and MDSCs but had no impact on their suppressive activity, suggesting that α -MSH-MC5R signaling only affects the expansion stage of MDSCs. Unlike α -MSH, other tumor- or TME-derived MDSC-inducing factors, including GM-CSF, granulocyte colony-stimulating factor (G-CSF), interleukin-6 (IL-6), IL-1 β , and adenosine, have been reported to promote both expansion and activation of MDSCs (41, 42). A possible reason for this difference is that MC5R is highly specifically ex-

pressed on LSK cells, according to our results, whereas the receptors for other factors are widely expressed on different progenitors and myeloid cells. Some factors, such as GM-CSF and G-CSF, are important for myelopoiesis in steady state (43), but we found that MC5R deficiency had no effects on myeloid cells and progenitors, suggesting that α -MSH-MC5R is functional only in disease conditions, such as cancer.

Our results indicate that tumor transplantation can activate the HP unit to produce α -MSH, but the mechanism needs to be further investigated. One possible mechanism is that tumor cells or immune cells in the TME can produce some cytokines or other factors that can enter the brain and then activate the HP unit directly or indirectly. It has been reported that IL-1 β and IL-6 can cross the blood-brain barrier or act at the level of circumventricular organs and then modulate neuronal activity and behavioral processes (44, 45). Another possible mechanism is that tumor- or TME-derived cytokines or other factors can act on sensory neurons and then communicate information to the HP unit. Indeed, nerves have been found in different tumors and are associated with tumor progression and poor outcomes (9, 46).

Our results reveal the hypothalamic-pituitary-bone marrow (HPB) axis as a neuroendocrine pathway that contributes to cancer-induced myelopoiesis and immunosuppression. Moreover, these results also suggest MC5R as a target for cancer immunotherapy, especially for ICT-resistant cancers.

REFERENCES AND NOTES

- J. A. Joyce, D. T. Fearon, *Science* **348**, 74–80 (2015).
- K. Shimizu, T. Iyoda, M. Okada, S. Yamasaki, S. I. Fujii, *Int. Immunol.* **30**, 445–455 (2018).
- F. S. Hodi et al., *N. Engl. J. Med.* **363**, 711–723 (2010).
- J. R. Brahmer et al., *N. Engl. J. Med.* **366**, 2455–2465 (2012).
- P. Sharma, J. P. Allison, *Science* **348**, 56–61 (2015).
- A. Kalbasi, A. Ribas, *Nat. Rev. Immunol.* **20**, 25–39 (2020).
- S. Bagchi, R. Yuan, E. G. Engleman, *Annu. Rev. Pathol.* **16**, 223–249 (2021).
- M. Schiller, T. L. Ben-Shaanan, A. Rolls, *Nat. Rev. Immunol.* **21**, 20–36 (2021).
- S. Gillespie, M. Monje, *Annu. Rev. Cancer Biol.* **4**, 371–390 (2020).
- J. I. Webster, L. Tonelli, E. M. Sternberg, *Annu. Rev. Immunol.* **20**, 125–163 (2002).
- G. van der Pompe, M. H. Antoni, C. J. Heijnen, *Psychoneuroendocrinology* **21**, 361–374 (1996).
- H. Yang et al., *Nat. Med.* **25**, 1428–1441 (2019).
- B. C. Özdemir, G. P. Dotto, *Clin. Cancer Res.* **25**, 4603–4610 (2019).
- M. M. S. Obradović et al., *Nature* **567**, 540–544 (2019).
- O. De Henau et al., *Nature* **539**, 443–447 (2016).
- H. Y. Li et al., *Cancer Immunol. Res.* **5**, 767–777 (2017).
- B. Routy et al., *Science* **359**, 91–97 (2018).
- H. Tang et al., *J. Clin. Invest.* **128**, 580–588 (2018).
- P. Lowry, *J. Mol. Endocrinol.* **56**, T1–T12 (2016).
- A. Takahashi, in *Handbook of Hormones: Comparative Endocrinology for Basic and Clinical Research*, Y. Takei, H. Ando, K. Tsutsui, Eds. (Elsevier, ed. 1, 2016), chap. 16.
- P. E. Stokes, C. R. Sikes, *Annu. Rev. Med.* **42**, 519–531 (1991).
- S. R. Bornstein, G. P. Chrousos, *J. Clin. Endocrinol. Metab.* **84**, 1729–1736 (1999).

- R. Vazquez-Martinez et al., *Am. J. Physiol. Endocrinol. Metab.* **285**, E1039–E1046 (2003).
- C. Qin, J. Li, K. Tang, *Endocrinology* **159**, 3458–3472 (2018).
- A. K. Sutton, M. G. Myers Jr., D. P. Olson, *Annu. Rev. Physiol.* **78**, 207–221 (2016).
- F. Veglia, E. Sanssevier, D. I. Gabrilovich, *Nat. Rev. Immunol.* **21**, 485–498 (2021).
- B. Z. Qian, J. W. Pollard, *Cell* **141**, 39–51 (2010).
- S. Ostrand-Rosenberg, *Annu. Rev. Immunol.* **5**, 17–38 (2017).
- V. Kumar et al., *Cancer Cell* **32**, 654–668.e5 (2017).
- A. J. Clark, L. A. Metherell, *Nat. Clin. Pract. Endocrinol. Metab.* **2**, 282–290 (2006).
- H. Zhang et al., *Blood* **116**, 2462–2471 (2010).
- A. R. Rodrigues, H. Almeida, A. M. Gouveia, *Cell. Mol. Life Sci.* **72**, 1331–1345 (2015).
- F. Rosenbauer, D. G. Tenen, *Nat. Rev. Immunol.* **7**, 105–117 (2007).
- P. Balse-Srinivasan, P. Grieco, M. Cai, D. Trivedi, V. J. Hruby, *J. Med. Chem.* **46**, 3728–3733 (2003).
- C. M. Diaz-Montero, J. Finke, A. J. Montero, *Semin. Oncol.* **41**, 174–184 (2014).
- L. M. Coussens, L. Zitvogel, A. K. Palucka, *Science* **339**, 286–291 (2013).
- T. F. Gajewski, H. Schreiber, Y. X. Fu, *Nat. Immunol.* **14**, 1014–1022 (2013).
- Z. Hao et al., *Biomark. Res.* **9**, 77 (2021).
- L. Cassetta et al., *J. Immunother. Cancer* **8**, e001223 (2020).
- T. Condamine, D. I. Gabrilovich, *Trends Immunol.* **32**, 19–25 (2011).
- N. Karin, *Front. Immunol.* **11**, 557586 (2020).
- T. Condamine, J. Mastio, D. I. Gabrilovich, *J. Leukoc. Biol.* **98**, 913–922 (2015).
- M. G. Manz, S. Boettcher, *Nat. Rev. Immunol.* **14**, 302–314 (2014).
- L. Vitkovic et al., *Mol. Psychiatry* **5**, 604–615 (2000).
- J. R. Huh, H. Veiga-Fernandes, *Nat. Rev. Immunol.* **20**, 217–228 (2020).
- H. Wang et al., *Cell Death Discov.* **7**, 76 (2021).

ACKNOWLEDGMENTS

We thank Y. Ma and S. Zhu for providing cell lines. We thank L. Zong, M. Ma, and B. Lin for technical support and all other members in the Zhou lab for helpful discussions. **Funding:** This research was supported by the National Key Research and Development Program of China (grants 2019YFA0508503 and 2020YFA0509101), the Strategic Priority Research Program of the Chinese Academy of Sciences (grant XDB29030102), the National Natural Science Foundation of China (grants 81821001 and 82130107), the CAS Project for Young Scientists in Basic Research (YSBR-074), and the Fundamental Research Funds for the Central Universities and the University Synergy Innovation Program of Anhui Province (GXXT-2019-026). **Author contributions:** Y.X., J.Y., Y.T., C.Z., L.Y., and X.Q. performed the experiments of this work. Y.X., J.Y., P.G., Y.L., Y.P., R.T., W.J., and R.Z. designed the research. Y.X., J.Y., R.T., W.J., and R.Z. wrote the manuscript. W.J. and R.Z. supervised the project. **Competing interests:** R.T. is an employee of Jiangsu Sincere Pharmaceutical Company, Ltd. Y.X., J.Y., W.J., and R.Z. are co-inventors of a pending patent application (202110566828.3) submitted by University of Science and Technology of China that covers the function of MC5R and the antitumor effect of MC5R antagonist. All other authors declare that they have no competing interests. **Data and materials availability:** All data are available in the main text or the supplementary materials. All the cell lines generated in this study are available from the authors. **License information:** Copyright © 2022 the authors, some rights reserved; exclusive licensee American Association for the Advancement of Science. No claim to original US government works. <https://www.science.org/about/science-licenses-journal-article-reuse>

SUPPLEMENTARY MATERIALS

science.org/doi/10.1126/science.abj2674
Materials and Methods
Figs. S1 to S26
Tables S1 and S2
References (47–58)
MDAR Reproducibility Checklist

Submitted 30 April 2021; resubmitted 13 June 2022

Accepted 22 July 2022

Published online 4 August 2022

10.1126/science.abj2674

PHYSIOLOGY

Insulin signaling in the long-lived reproductive caste of ants

Hua Yan^{1,2,3}†, Comzit Opachaloemphan¹†, Francisco Carmona-Aldana¹†, Giacomo Mancini⁴, Jakub Mlejnek⁴, Nicolas Descostes¹†, Bogdan Sieriebriennikov^{1,4}, Alexandra Leibholz⁴, Xiaofan Zhou⁵, Long Ding⁴, Maria Traficante⁴, Claude Desplan^{4*}, Danny Reinberg^{1,2*}

In most organisms, reproduction is correlated with shorter life span. However, the reproductive queen in eusocial insects exhibits a much longer life span than that of workers. In *Harpegnathos* ants, when the queen dies, workers can undergo an adult caste switch to reproductive pseudo-queens (gamergates), exhibiting a five-times prolonged life span. To explore the relation between reproduction and longevity, we compared gene expression during caste switching. Insulin expression is increased in the gamergate brain that correlates with increased lipid synthesis and production of vitellogenin in the fat body, both transported to the egg. This results from activation of the mitogen-activated protein kinase (MAPK) branch of the insulin signaling pathway. By contrast, the production in the gamergate developing ovary of anti-insulin Imp-L2 leads to decreased signaling of the AKT/forkhead box O (FOXO) branch in the fat body, which is consistent with their extended longevity.

Differences in life span within a species offer an opportunity to investigate the regulatory processes involved in aging. Reproduction has an important influence on longevity: Genes that favor reproductive fitness normally shorten life span because animals allocate nutritional and metabolic resources for reproduction at the cost of longevity (1–3). Adaptive responses to dietary restriction in various species include reduced reproductive capability and prolonged life span (1, 2). The functional anticorrelation between reproduction and longevity involves the insulin/insulin-like growth factor (IGF) signaling pathway (IIS) because increased IIS activity required for reproduction leads to shorter life span in most animals (2, 4, 5).

Studies in *Caenorhabditis elegans*, *Drosophila*, mouse, and other model organisms have analyzed the effects of signaling pathways, particularly those of the IIS pathway, in regulating longevity (2, 3). In insects, the brain, fat body (the metabolic organ that is similar to the vertebrate liver and adipose tissue), and ovary are the primary tissues that regulate longevity and reproduction (3, 6). Ablation at the larval stages of the insulin-producing cells (IPCs) in the *Drosophila* brain causes lower female fecun-

dity, increased storage of lipid, and extended life span (3, 7). The fat body mainly contains adipocytes and oenocytes (hepatocyte-like cells), which have essential roles in energy storage and utilization, pheromone synthesis, reproduction, and longevity (3, 6, 8). Up-regulation of the forkhead box O (FOXO) transcription factor, a negative effector of IIS, in the *Drosophila* fat body or adipose tissue in mice extends life span but reduces fecundity (2, 7). The ovary also has a role in the regulation of life span in some species: Removal of germline cells extends life span in *Drosophila* and *C. elegans* (7). However, in eusocial insects—such as ants, bees, wasps, and termites—the complete reproductive function of a colony depends on one or very few female individuals that have increased longevity [up to 30 times longer compared with their nonreproductive female nestmates (workers)] (9–11), despite sharing a similar genome. Although IIS has been widely studied in eusocial insects [for example, (12)], it is not clear yet how this reproduction-associated longevity is regulated at the cellular and molecular levels.

Extended longevity upon caste switching from worker to pseudo-queen

In the ant *Harpegnathos saltator* (Hs), when the queen in a colony dies or is removed, non-reproductive workers start dueling with each other. The winners gradually transition to becoming gamergates (pseudo-queens) that continue dueling, develop queen-like behavior, begin laying eggs, and exhibit a five-times life span extension (Fig. 1A) (10, 13, 14). Gamergates can also be reverted back to workers (“revertants”) when they are placed in a colony with an established reproductive caste, returning to a shortened life span (15). Although the median life span of regular workers (W) was 217 days (Fig. 1B and fig. S1A), the median

life span of gamergates (G) was ~1100 days (10). The median life span of revertants (R) was 188 days, which was comparable with 184 days found in their worker nestmates (W^R) (Fig. 1B and fig. S1A). This was shorter than the 217-day life span of regular workers, possibly because the harsh policing of gamergates by workers during the reversion induces colony stress.

To determine the reproductive potential of the castes, we inspected the ovaries of workers, gamergates, and revertants. Fertile gamergates had eight ovarioles (four on each side) that contained chains of four to six egg chambers, including some with fully developed oocytes (stage 6) (Fig. 1, C and D). By contrast, workers had ovaries with very small, partially developed ovarioles that each contained the germarium where stem cells are located, with zero to two early-stage egg chambers (stages 1 or 2) and no fully developed oocytes. Thus, ovary growth is blocked at the early stage of egg formation in workers but is activated in gamergates (Fig. 1, C and D). The ovaries of revertants also had zero to two immature egg chambers per ovariole (Fig. 1, C to E), which correlated with their loss of reproduction (15). We sought to address how life span could be increased during active reproduction in this species.

Insulin expression is increased in the brain of the reproductive caste

We performed bulk RNA sequencing from tissues that are important for reproduction and metabolism (brain, ovary, and fat body) from workers, gamergates, and revertants. The results confirmed the expression profile of previously characterized differentially expressed genes (DEGs), such as the gene encoding the neuropeptide Corazonin (Crz), which is highly expressed in the worker brain, and the egg yolk precursor *vitellogenin* (Vg) gene, which is increased in the gamergate fat body (Fig. 2, A and B, and table S1) (16). Additionally, we compared worker versus gamergate DEGs with gamergate versus revertant DEGs and found that the majority (>60%) of fat body and ovary genes with altered expression during the transition to gamergates returned to their worker expression in the revertants (fig. S1B). Several top Gene Ontology (GO) terms that were enriched among the DEGs up-regulated in the gamergate fat body were associated with fatty acid synthesis (fig. S1C and table S2). Fat body and ovary DEGs were also enriched in gamergates for terms associated with the IIS pathway, such as phosphatidylinositol 3-kinase (PI3K) signaling and insulin catabolic process (table S2). These results suggested that IIS-regulated metabolism is altered during the transition and reversion processes.

The IIS pathway has a central role in metabolism and, in particular, female reproduction: In most species studied, mutants in the

¹Department of Biochemistry and Molecular Pharmacology, New York University School of Medicine, New York, NY 10016, USA.

²Howard Hughes Medical Institute, New York University School of Medicine, New York, NY 10016, USA.

³Department of Biology, Center for Smell and Taste, University of Florida, Gainesville, FL 32611, USA.

⁴Department of Biology, New York University, New York, NY 10003, USA. ⁵Guangdong Province Key Laboratory of Microbial Signals and Disease Control, South China Agricultural University, Guangzhou 510642, China.

*Corresponding author. Emails: cd38@nyu.edu (C.D.); danny.reinberg@nyulangone.org (D.R.)

†These authors contributed equally to this work.

‡Present address: European Molecular Biology Laboratories, 00015 Monterotondo, Italy.

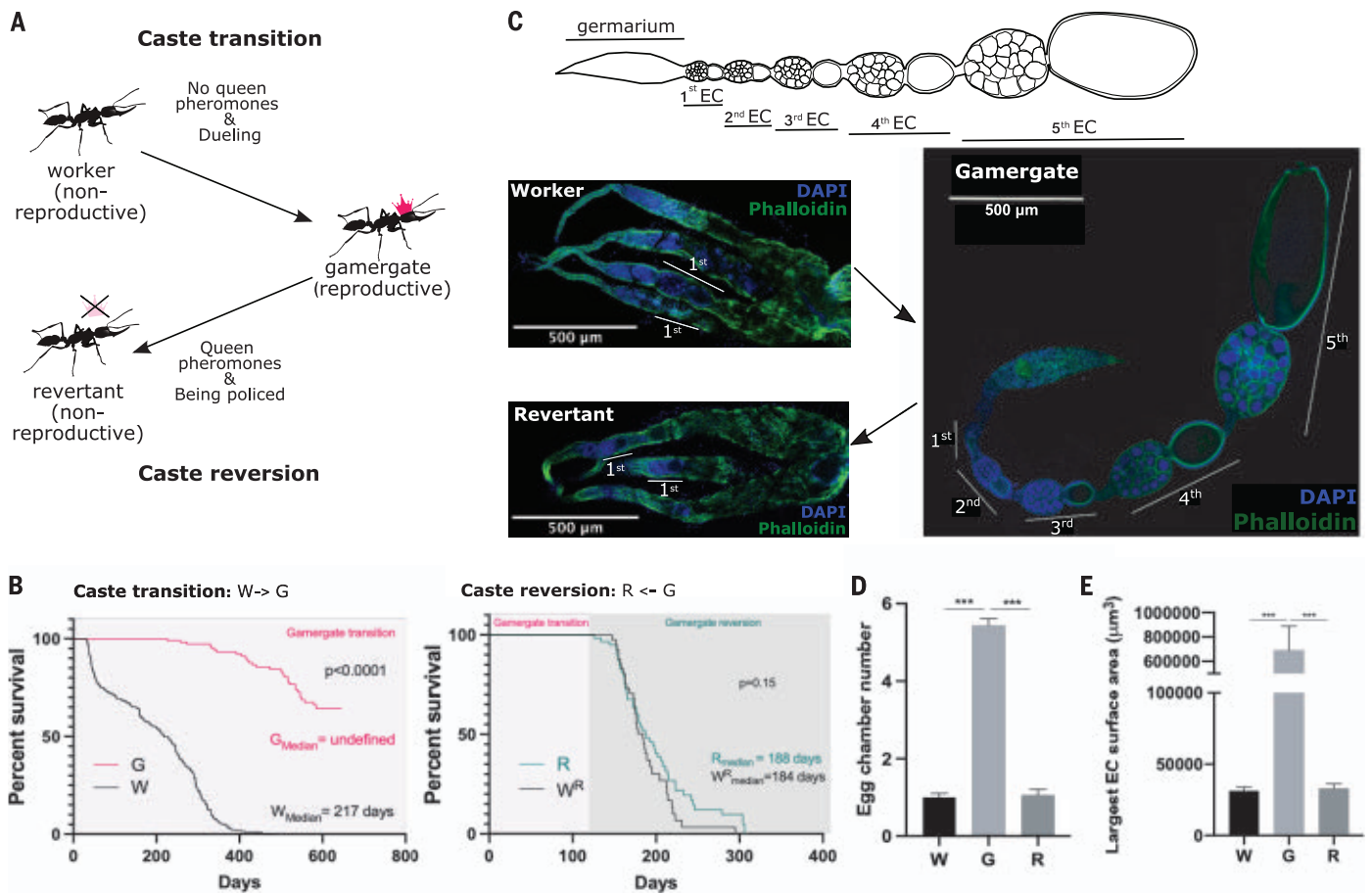


Fig. 1. Phenotypic plasticity in the ant *Harpegnathos*. (A) *Harpegnathos* female workers retain reproductive potential, which is suppressed by the queen pheromone. Removal of the queen pheromone drives some nonreproductive workers to start dueling and become reproductive pseudo-queens, called gamergates (caste transition). The gamergates can transition anew to nonreproductive revertants in the presence of queen pheromones (policing and caste reversion). (B) Life span of ants during the caste transition and reversion. (Left) Survival curves of nonreproductive workers (W, black; $n = 291$) versus reproductive gamergates (G, pink; $n = 40$) during the W-to-G transition. (Right) Survival curves of revertants (R, green; $n = 47$) versus worker nestmates (W^R , black; $n = 36$) during the G-to-R reversion. Gamergates derived from 3 months of transition (pink box) were subsequently subjected to reversion (green box). P values from Log-rank

(Mantel-Cox) test are indicated in the plots. (C) Ovary development during the caste transition and reversion. (Top) Schematic of an ovariole within a gamergate ovary comprising a germarium and different stages of developing egg chambers (ECs). The sixth EC, which only contains a large oocyte without nurse cells, is not shown. (Bottom) Immunofluorescence (IF) staining of (top left) ovaries of worker and (bottom left) revertant and (right) a single ovariole of a gamergate with Phalloidin (green) and 4',6-diamidino-2-phenylindole (DAPI) (blue). The numbers of developing ECs are indicated in the gamergate panel. (D and E) Quantifications of (D) the average number of developing ECs per ovariole and (E) the surface area of the largest EC in each ovariole of worker (W), gamergate (G), and revertant (R). P values are from Kruskal-Wallis test and multiple comparisons ($***P < 0.001$, $n = 5$ individuals). Bars and error bars represent mean \pm SEM.

IIS pathway exhibit extended life span and reduced reproduction (2, 3). We performed a phylogenetic analysis of genes related to insulin signaling of 71 Hymenopteran species (ants, bees, wasps, and sawflies) in the National Center for Biotechnology Information (NCBI) RefSeq database. In almost all species, including *Harpegnathos* but not in the ant *Camponotus floridanus*, there are two insulin-like peptides (ILPs): an insulin homolog (Ins) and an insulin-like growth factor homolog (IGF) (fig. S2). Ins contains A and B chains, whereas IGF has A and B and retains the C chain. Both ILPs can form three disulfide bonds, a structure that is essential for the interactions with their receptors (fig. S3, B and C).

We identified several genes differentially expressed between *Harpegnathos* gamergates and workers that were related to the IIS pathway: *Ins* mRNA was more abundant in the gamergate brain (ranking fifth among the gamergate-biased DEGs), whereas *IGF* mRNA was increased in the mature gamergate ovary (Fig. 2, A and C, and fig. S3A). By contrast, expression of the two genes encoding insulin receptors (InR1 and InR2) was decreased in the gamergate fat body and ovary (Fig. 2, B and C) but was unchanged in the brain. We generated mRNA probes and antibodies against *Hs-Ins* and *Hs-IGF* and examined their distribution by means of in situ hybridization (ISH) and immunofluorescence staining. As in *Drosophila*, the main source of

Ins in the brain is the IPCs (Fig. 2D and fig. S4A) (17). *Ins* mRNA was more abundant in the cell body of IPCs in gamergates than in those of workers (Fig. 2D), whereas the Ins protein accumulated in both the cell body and the axons of the IPCs (fig. S4A). Increased *IGF* mRNA and protein were mainly detected in nurse cells and the follicle cells of the gamergate ovary (fig. S4B). This increase in ILPs in gamergates is consistent with the high metabolic requirement for egg production. However, high IIS activity should also lead to decreased life span.

Altered metabolism in gamergates

Because IIS regulates metabolism and the gamergate-biased genes in the fat body were

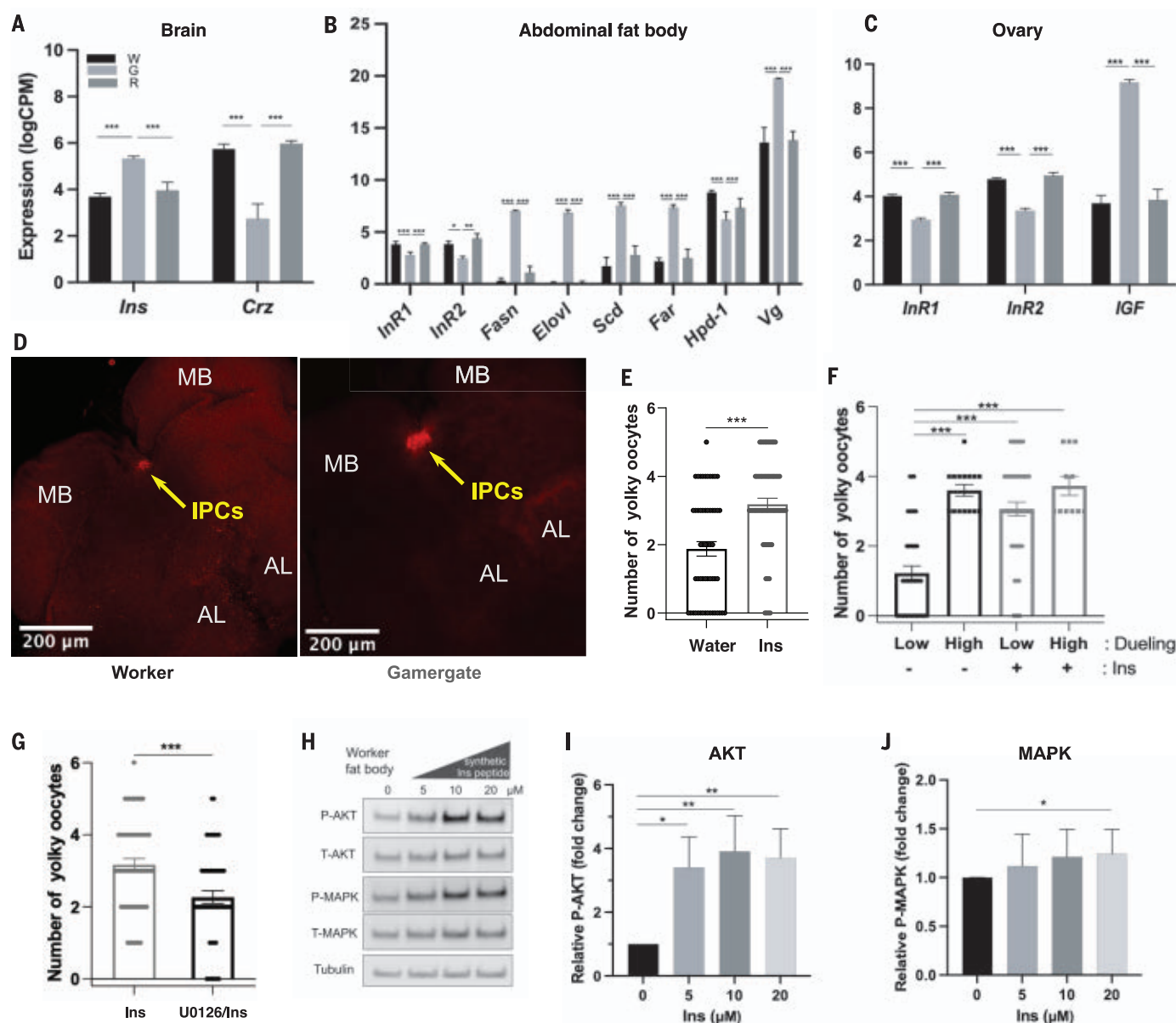


Fig. 2. Ins-related gene expression in different castes and its induction of oogenesis through IIS-MAPK pathways. (A to C) RNA abundance of DEGs in the (A) central brain, (B) abdominal fat body, and (C) ovary in workers (W; black), gamergates (G; light gray), and revertants (R; dark gray). Data are from four biological replicates per caste. *P* values from EdgeR are indicated. *Hpd-1*, 4-hydroxyphenylpyruvate dioxygenase; *Fasn*, fatty acid synthase; *Elovl1*, fatty acid elongase; *Scd*, desaturase; *Far*, fatty acyl-CoA reductase; *Vg*, vitellogenin; LogCPM, log counts per million. (D) Localization of (left) *Ins* mRNA in the worker and (right) gamergate brains by means of ISH. *Ins* mRNA is located in the IPCs (indicated with yellow arrows) located between mushroom bodies (MB). AL, antennal lobe. (E to G) Yolk oocyte production in (E) water- versus Ins-injected ants, (F) low- versus high-

dueling ants, and (G) Ins-injected versus Ins and U0126 co-injected ants. In (E) and (G), ovary development is represented by the number of yolk oocytes per individual in all workers regardless of their dueling activity. Bars and error bars represent mean \pm SEM (* P < 0.05, ** P < 0.01, *** P < 0.001). (H) Western blot analysis of phosphorylated AKT (P-AKT), total AKT (T-AKT), phosphorylated MAPK (P-MAPK), total MAPK (T-MAPK), and tubulin levels in the worker fat body treated with different concentrations of synthetic Ins peptide (0, 5, 10, and 20 μ M). (I and J) Quantification of fold changes in (I) relative P-AKT/T-AKT and (J) P-MAPK/T-MAPK. Relative levels of AKT and MAPK phosphorylation were normalized to the control fat body. n = 8 individuals; *P* values are from Kruskal-Wallis test with multiple comparisons. Bars and error bars represent mean \pm SEM.

enriched in the GO terms associated with fatty acid synthesis, we analyzed metabolic changes in gamergates. The gamergate fat body exhibited increased expression of genes related to lipid metabolism and modifying enzymes—such as *fatty acid synthase* (*Fasn*), *fatty acid elongase* (*Elovl1*), *desaturase* (*Scd*), and *fatty*

acyl-CoA reductase (*Far*)—suggesting an active synthesis of lipids either for the production of the egg yolk or of cuticular hydrocarbons (CHCs), which are made up of long-chain hydrocarbons and constitute the queen pheromones (Fig. 2B) (14, 15, 18, 19). Thus, the fat body of gamergates exhibits transcriptional

signatures of increased lipid production. The fat body of workers in the abdomen was large and white-colored, whereas it was reduced in size and had a yellowish color in the gamergate abdomen that was mainly occupied by the developed ovarioles (fig. S5A). We measured the lipid contents of the fat body [tri- and

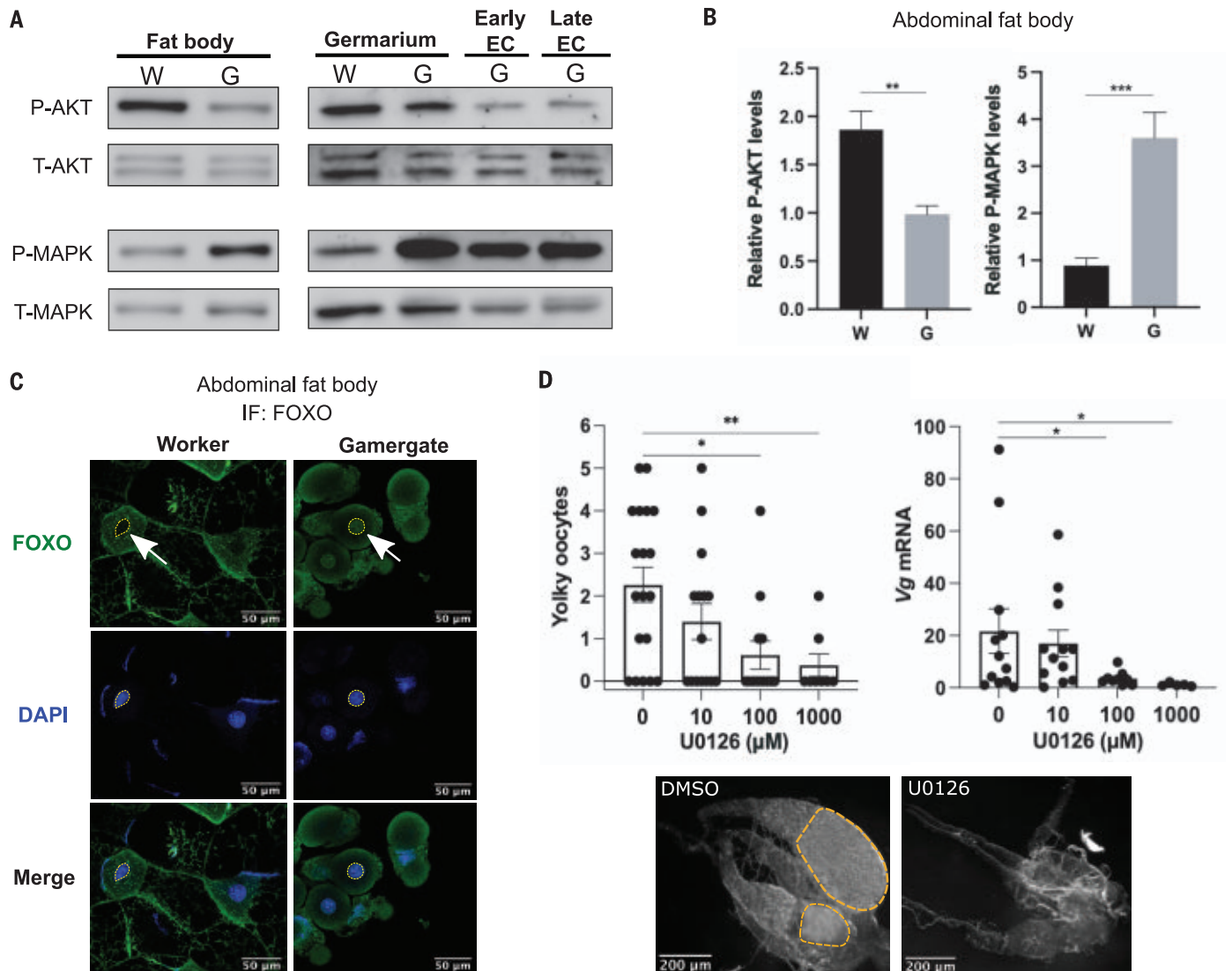


Fig. 3. Activity of the IIS-AKT and IIS-MAPK pathways in different tissues and the requirement of MAPK activity for reproduction. (A to C) IIS activity is represented by phosphorylation of AKT and MAPK (P-AKT and P-MAPK, respectively), normalized by total AKT and MAPK (T-AKT and T-MAPK, respectively). (A) Western blot analysis of P-AKT, T-AKT, P-MAPK, and T-MAPK in (left) the fat body and (right) different parts of the dissected ovary [germarium, early egg chamber (EC), and late EC tissues from worker (W) versus gamergate (G)]. (B) Quantification of the relative P-AKT and P-MAPK levels in the fat body of W and G described in (A). *P* values are from unpaired Student's *t* test (***P* < 0.01, ****P* < 0.001, *n* = 6 individuals). Bars and error bars represent mean \pm SEM. (C) Immunofluorescence (IF) staining of transcription factor FOXO in

the fat body as detected by *Hs*-FOXO antibody (green) and DNA staining with DAPI (blue). (Left) FOXO localization in the cytoplasm of worker fat body. (Right) FOXO localization in the nucleus of gamergate fat body. Nuclei were identified with DAPI and are indicated with arrows in the FOXO staining. (D) (Top) Averages of the yolk oocyte number per workers and quantitative RT-PCRs for *vitellogenin* (*Vg*) mRNA in abdominal fat body of workers 7 days after injection with either dimethyl sulfoxide (DMSO) or U0126 at different dosages (10, 100, and 1000 μ M). (Bottom) Representative bright-field images of dissected ovaries. Data are from more than 10 biological replicates per condition. Bars and error bars indicate mean \pm SEM. *P* values are from Kruskal-Wallis test with multiple comparisons. *Rpl32* is used as a reference gene for data normalization.

diacylglycerol (TAG and DAG, respectively)] using an enzymatic conversion of glycerides into glycerol. Lipids were significantly decreased in the gamergate fat body compared with that of workers (fig. S5C), which is consistent with the observation that the dissected worker fat body floated in saline solution [1X phosphate-buffered saline (PBS)], whereas that of gamergate sank (fig. S5B). However, circulating lipids were increased in the

hemolymph of gamergates, pointing to lower lipid storage and greater lipid mobilization in the reproductive gamergates (fig. S5, D and E). Moreover, Nile Red staining in the fat body revealed that lipid droplets were abundant in the enlarged adipocytes of workers but rarely detected in the smaller adipocytes of gamergates. Unlike in workers, lipids were mainly found in gamergate oenocytes (fig. S5, F to H). This result is consistent with the increased

production of queen pheromone in gamergates because oenocytes are the main source for CHC pheromone synthesis in the abdomen (8, 18). We also measured carbohydrate abundance in dissected fat body tissue and in the hemolymph, including glycogen, trehalose, and glucose [supplementary materials (SM), materials and methods]. The abundance of carbohydrates, notably glycogen, was decreased in the fat body after the transition to gamergate,

whereas the circulating trehalose and glucose in the hemolymph were unchanged (fig. S5, I and J).

Insulin promotes oogenesis in workers but does not induce dueling

Ins and IGF activate ovary growth in multiple invertebrate and vertebrate species, and Ins induces reproduction in clonal raider ants (20). To test the role of IIS in *Harpegnathos* reproduction, we synthesized *Hs*-Ins. We injected the Ins peptide into the abdomen of ~2-week-old workers in queenless colonies (13, 14); 2 days after the setup of three independent colonies, half of the members (20 individuals) of each colony were injected with the Ins peptide, and the others were injected with water as a control. We scored the dueling behavior 5 days after dueling initiation and measured the development of the ovary. Ins injection did not induce dueling behavior in workers (27% of workers dueled in control colonies, whereas 19% of workers dueled in the Ins group; $n = 3$ colonies, $P = 0.75$) (fig. S6A). However, Ins-injected individuals developed ovarioles with an average of 3.2 egg chambers as compared with 1.9 in control ants (Fig. 2E). By contrast, an inactive form of Ins (B chain) (SM materials and methods) did not promote ovariole development (fig. S6B). Normally, in this experimental context, high dueling activity positively correlates with the probability of transitioning to a gamergate, and workers do not have developed ovaries. However, after injection of the Ins peptide, the number of yolky oocytes was increased by ~2.3 times in the workers that did not duel (3.0 versus 1.3; $P < 0.001$), but Ins injection in individuals that already dueled often had little further effect on ovarian development (3.8 versus 3.6) (Fig. 2F). Dueling and oocyte numbers were positively correlated in control workers [coefficient of determination (R^2) = 0.54] but were not correlated in Ins-injected workers ($R^2 = 0.02$) (fig. S6C). We also injected Ins into workers in colonies with established reproductive individuals, in which any worker that attempted to become a gamergate was subject to policing by other workers that detected its increased CHC profile (15, 18). Ins-injected ants were not policed while they developed ovarioles (Fig. S6D), suggesting that Ins is able to induce oogenesis but not dueling or production of queen pheromones. In clonal raider ants, Ins injections also promote egg production, although in a different context (20).

Insulin can activate AKT and MAPK, but AKT is down-regulated in the gamergate fat body

We tested how Ins regulates the distinct downstream branches of the IIS pathway, IIS-AKT and IIS-MAPK (mitogen-activated protein kinase). ILPs can induce phosphorylation of the protein kinase AKT that prevents nuclear

localization of the FOXO transcription factor. Thus, nuclear FOXO that promotes longevity is negatively regulated by IIS. ILPs can also induce phosphorylation of MAPK/ERK (extracellular signal-regulated kinase) to increase cell proliferation (21). We treated dissected fat bodies from workers with the synthetic *Hs*-Ins peptide. Ins activated phosphorylation of AKT (~3.5 times increase after Ins treatment; $P < 0.01$, $n = 8$ individuals) (Fig. 2, H and I), whereas the MAPK pathway was only mildly activated (~1.3 times increase after treatment; $P < 0.05$, $n = 8$ individuals) (Fig. 2, H and J).

Because Ins leads to activation of both AKT and MAPK (Fig. 2, H to J, and fig. S3C), we expected to see globally increased activity of both IIS pathways in vivo in gamergates. To test this, we dissected multiple tissues, including the fat body and ovary, and analyzed the phosphorylation of MAPK. Consistent with the increased production of Ins in gamergates, MAPK phosphorylation was increased in the gamergate fat body (approximately four times increase; $n = 6$ individuals, $P < 0.001$) (Fig. 3, A and B) and in the ovary, including the germarium and the early- and late-stage egg chambers, and in the malpighian vesicle, the tissue equivalent to the vertebrate kidney (Fig. 3A and fig. S6E). However, MAPK phosphorylation was unchanged in the brain and the postpharyngeal gland (PPG), a tissue implicated in the synthesis and storage of cuticular CHC pheromones (fig. S6E) (22). Although MAPK can also be activated by the epidermal growth factor receptor tyrosine kinase (Egfr) (23), our transcriptome indicated that *Egfr* and its ligands, *Spitz* and *Vein* mRNAs, were less abundant in the gamergate fat body (fig. S3D), suggesting that the epidermal growth factor (EGF) pathway does not play a major role in activating MAPK in the fat body.

We also measured phosphorylation of AKT in multiple tissues in gamergates versus workers. Phosphorylation of AKT was significantly lower in gamergate fat bodies than in those of workers (approximately one half; $n = 6$ individuals, $P < 0.01$) (Fig. 3, A and B). This is consistent with evidence that reducing the AKT branch of insulin signaling in the fat body and adipose tissue lengthens the life span of other species (3). Phosphorylation of AKT was increased in the PPG of gamergates compared with that in workers but was at similar levels in the brain and the malpighian vesicle of workers and gamergates (fig. S6E) as well as in the germarium (Gm), the ovarian region that contains the germline stem cells in workers and gamergates (Fig. 3A). However, AKT phosphorylation was low in the ovary in early- and in late-stage egg chambers that are only present in gamergates (Fig. 3A). We analyzed the subcellular localization of FOXO in these tissues. If IIS-AKT was inactivated, unphosphorylated FOXO should be localized to the nucleus (24).

FOXO was localized in the nucleus in the gamergate fat body, whereas it was localized in the cytoplasm of workers (Fig. 3C). mRNA for one of the target genes that are transcriptionally repressed by FOXO, *4-hydroxyphenylpyruvate dioxygenase* (*Hpd-1*) (25), was less abundant in the fat body of gamergates than in those of workers (Fig. 2B). *Hpd-1* encodes an enzyme that functions in the degradation of tyrosine, the precursor for biogenic amines, and dopamine is in greater abundance in gamergates than in workers (26). In the gamergate ovary, FOXO was localized in the nucleus in all follicle cells and in the nurse cells of egg chambers up to stage 4, whereas at stage 5, FOXO was localized to the cytoplasm in nurse cells (fig. S6F), suggesting that AKT activity is higher in late-stage nurse cells.

We conclude that increased Ins production in the gamergate brain leads to the activation of the MAPK pathway in the fat body and ovary. However, AKT activity is low in the fat body and part of the ovary of gamergates. How decreased AKT (but not MAPK) phosphorylation is achieved in gamergates is unclear.

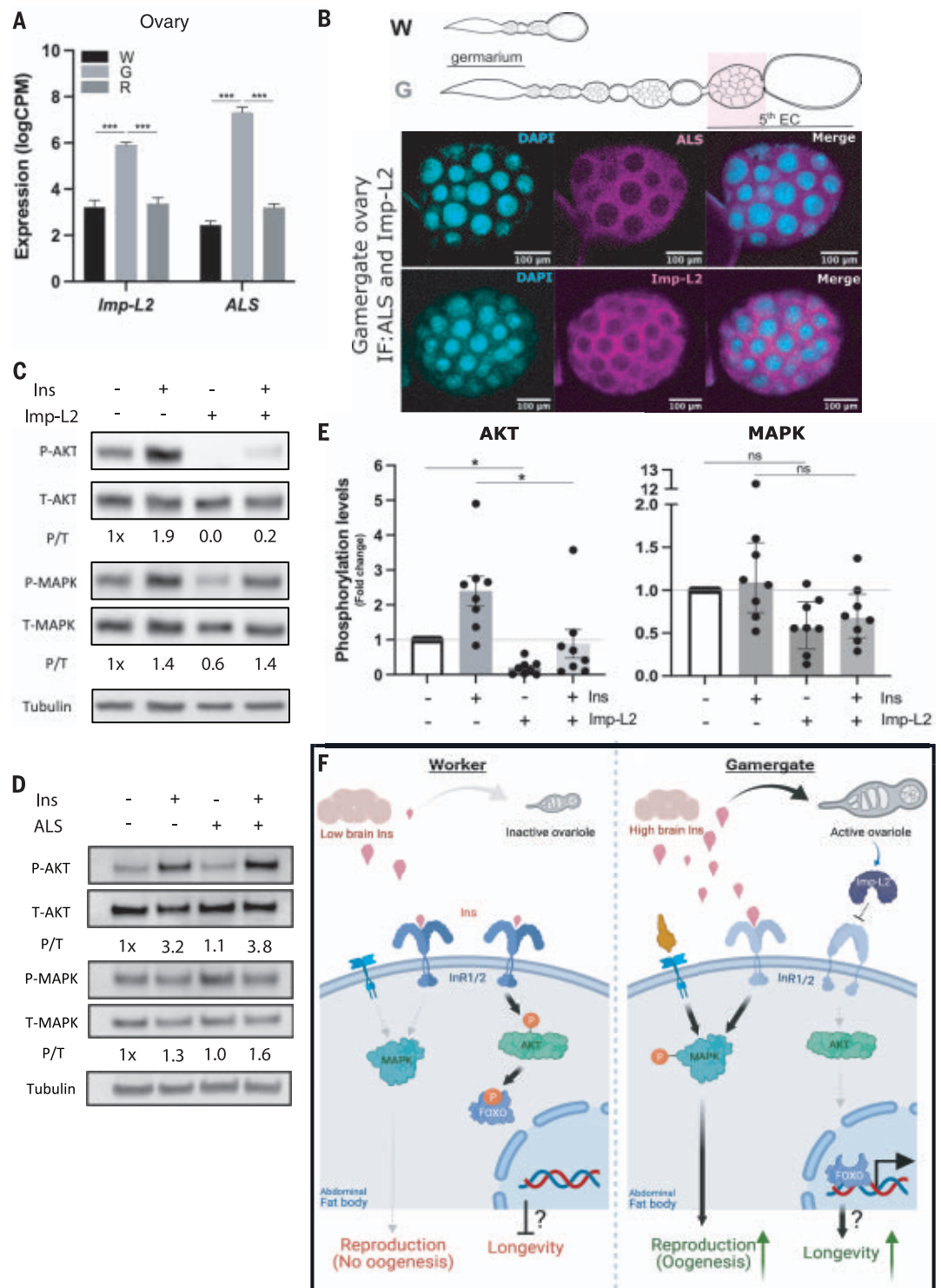
Pharmacological inhibition of MAPK activity affects ovary growth

Similar to what was observed in the clonal raider ants (20), Ins induces reproduction in *Harpegnathos* (Fig. 2, E and F). Because MAPK, but not AKT, appeared to be active in the gamergate fat body and ovary, we tested the effect of U0126 (a MAPK/ERK kinase inhibitor that prevents MAPK phosphorylation) on caste transition and ovary activation. U0126 inhibited MAPK phosphorylation in the dissected fat bodies of workers (to one-third of that of fat bodies from control ants) but only reduced AKT phosphorylation by 20%. In worker fat bodies exposed to both Ins and U0126, MAPK phosphorylation was reduced by one-half, and AKT phosphorylation was decreased by ~10% (fig. S6G).

We injected U0126 in workers during their transition to gamergates and measured *vitellogenin* expression as a molecular marker for egg production, then scored ovary growth 6 days after injection. U0126 treatment led to a concentration-dependent decreased expression of *vitellogenin* in the fat body as well as a decreased number of yolky oocytes in dueling individuals (Fig. 3D). Although oogenesis was promoted by Ins injection to workers (Fig. 2, E and F), U0126 impeded this effect (Fig. 2G). The germarium remained intact, suggesting that the inhibitor did not cause atrophy of the germline stem cell niche, which is present in both workers and gamergates.

We concluded that Ins from the brain can activate the MAPK pathway in the fat body and ovary and induces the production of

Fig. 4. Imp-L2 produced from gamergate ovaries preferentially antagonizes the IIS-AKT pathway. (A) RNA abundance of ovarian *Imp-L2* and *ALS* in workers (W), gamergates (G), and reverts (R). Bars and error bars represent mean \pm SEM. LogCPM, log counts per million. (B) IF staining of insulin/IGF-binding proteins (ALS and Imp-L2) in the late stages of the egg chambers of a gamergate ovary as indicated with a pink box in the schematic at top. Magenta indicates ALS and Imp-L2 at top and bottom, respectively. DAPI is shown in cyan. (C and D) Western blot analyses showing the effects of recombinant Imp-L2 or ALS (produced in Sf9 cells) on IIS-AKT and IIS-MAPK pathways in the abdominal fat body tissue dissected from workers. Levels of P-AKT, T-AKT, P-MAPK, T-MAPK, and tubulin detected in the fat body as a function of treatment with Ins peptide minus/plus recombinant (C) Imp-L2 or (D) ALS protein. (E) A quantitative plot of phosphorylation levels of AKT and MAPK from the worker fat body incubated with or without Imp-L2 in the presence and absence of Ins peptide. Bars and error bars indicate median with interquartile range. *P* values are from Mann-Whitney test (**P* < 0.05, *n* = 8 individuals). (F) Proposed models of reproduction-associated longevity in ants. (Left) A short-lived worker. (Right) A long-lived gamergate. The basal level of insulin (Ins) secreted from the worker brain is sufficient to activate the IIS-AKT pathway through insulin receptors (InRs) in the abdominal fat body, resulting in FOXO phosphorylation and a normal life span in workers. By contrast, the high level of Ins in the gamergate brain promotes ovary maturation and contributes to MAPK activation in the fat body.



mature egg chambers. MAPK activation seems to be necessary to promote *vitellogenin* expression in the fat body, ovary growth, and the transition to being reproductive. By contrast, AKT phosphorylation was decreased in

the fat body and the developed ovaries of gamergates but remained comparable in the germarium of workers and gamergates. AKT activity in the germarium of both castes may function in germline stem cell maintenance

and early differentiation, as it does in *Drosophila* (27). In this manner, workers can retain a functioning germ line that will allow them to reactivate oogenesis if they ever become gamergates.

The IIS inhibitors Imp-L2 and ALS are up-regulated in the ovary, whereas InRs are decreased in the fat body

To explain the paradox of increased MAPK phosphorylation and decreased AKT phosphorylation in gamergates, we searched for candidate genes that could mediate the decreased IIS-AKT activity in the fat body and some ovarian tissues. In our differential expression analysis, *insulin receptor 1 and 2 (InR1/2)* mRNAs were decreased in the gamergate fat body and whole ovary (Fig. 2B). However, this decrease was not sufficient to prevent MAPK phosphorylation in response to Ins treatment. Expression of two genes encoding secretory proteins that inhibit the IIS pathway was increased in the ovary of gamergates: *Imaginal morphogenesis protein-Late 2 (Imp-L2)* and *Acid-labile Subunit (ALS)* (Fig. 4A). In *Drosophila*, Imp-L2 and ALS bind to circulating Dilp2 and Dilp5, the Ins homologs produced in brain IPCs. They are secreted into the hemolymph and antagonize IIS in peripheral tissues (28). Likewise, reduced expression of ILPs and increased expression of Imp-L2 appear to increase survival of mosquitoes (29). In mammals, ALS and IGF-binding protein 7 (IGFBP7), a homolog of Imp-L2, both bind plasma insulin and IGF in the circulation and subsequently restrain their interaction with their receptors (30, 31). IGFBP7 displays higher binding affinity to insulin than to IGF (30). Our expression analysis, paired with the evidence in insects and mammals, suggested that the elevated expression of *Imp-L2* and *ALS* genes in gamergate ovaries and their secretion into the hemolymph may antagonize insulin receptor activation in both mature ovarioles and the fat body.

The major sources of ALS in mammals are the liver and kidney (32), whereas *Imp-L2* mRNA is found in ovarian follicle cells (33). Quantitative reverse transcription polymerase chain reaction (RT-PCR) on multiple *Harpegnathos* tissues showed that *Imp-L2* and *ALS* mRNA were mainly expressed in ovaries, especially in late-stage egg chambers and yolk oocytes that were only present in gamergates but absent in workers. By contrast, their abundance was relatively low in other tissues, such as the brain, fat body, gut, and early-stage egg chambers (fig. S7A). We generated antibodies to Imp-L2 and ALS proteins. Proteins were only detected in late-stage egg chambers (Fig. 4B and fig. S7, B and C). Thus, Imp-L2 and ALS are predominantly expressed in gamergate ovaries, particularly in well-developed egg chambers from which they are secreted, and may act on abdominal tissues, including the fat body.

Imp-L2 specifically blocks AKT in the fat body

Imp-L2 and *ALS* expressed in the ovary may act as inhibitors that contribute to decreased

AKT phosphorylation in the fat body and ovary of gamergates and thus increase life span. To test whether these proteins affect IIS in ants, we generated FLAG-tagged versions of *Hs-Imp-L2* and *Hs-ALS* in baculovirus and purified the proteins from lysates of transfected Sf9 insect cells using FLAG-based affinity purification (fig. S7D). We used purified proteins to treat dissected abdominal fat body tissues from workers. To minimize individual variations, the dissected fat body tissue from the same individual was separated for incubation with Ins, with or without Imp-L2 or ALS. Because of limited amounts of Imp-L2 purified from the baculovirus expression system, we used low doses of Ins (1 μ M) to keep equal stoichiometry with Imp-L2 and ALS (1 μ M). Although this dose of Ins significantly activated AKT, it was not sufficient to activate MAPK (Fig. 4, C to E).

Imp-L2 inhibited AKT phosphorylation: Even without Ins treatment, the baseline of AKT phosphorylation was strongly inhibited by Imp-L2 (to one-fifth of that of control tissue; $P < 0.05$, $n = 8$ individuals) (Fig. 4, C and E), whereas it did not significantly affect MAPK phosphorylation. Strong AKT phosphorylation after Ins treatment was completely suppressed by Imp-L2 (to one-third of that of control tissue; $P < 0.05$, $n = 8$ individuals) (Fig. 4, C to E), whereas MAPK phosphorylation was still not affected (Fig. 4, C and E), suggesting that Imp-L2 can specifically inhibit phosphorylation of AKT in gamergates. By contrast, ALS had no effect on AKT and MAPK phosphorylation (Fig. 4D). In support of our results, a study of human IGFBP7, a homolog of Imp-L2, was shown to inhibit IGF-induced phosphorylation of AKT in vitro but had less effect on MAPK phosphorylation, although this selectivity is not well understood [figure 1C in (34)].

Thus, we speculate that Imp-L2 produced by the ovary of gamergates acts as an Ins inhibitor to specifically reduce AKT activity in the fat body and ovary that might play a role in extending life span in gamergates. MAPK activity might be less affected and appears to be the primary regulator for initiating and sustaining the reproductive function of the ovary, in particular by producing vitellogenin and mobilizing lipids from the fat body that will accumulate in the egg. Therefore, phosphorylation of MAPK and inhibition of AKT phosphorylation in response to Ins could offer an effective solution to the discrepancy between increased insulin and reproduction and prolonged life span (Fig. 4F).

Discussion

The traits that favor reproduction have particular importance in eusocial insects because the reproductive duty of the whole colony is placed on one or very few queens that are highly prolific. Such individuals are difficult

or impossible to replace without disrupting the colony, so they must have a very long life span to allow the colony to thrive beyond the individual life of its workers (9, 35). Natural selection has thus resulted in increased life span in queens.

In *Harpegnathos*, production of Ins in the brain facilitates active reproduction through MAPK, but AKT phosphorylation in the fat body and developing ovary appears to be inhibited, which might contribute to extension of life span in gamergates. This local effect correlates with lower expression of InRs in the fat body and ovary and might result from the inhibitory effect of Imp-L2 secreted from the reproductive ovary.

The altered metabolism in the fat body of gamergates might lead to newly synthesized lipids to be directed through the hemolymph to the ovary to promote egg production. Because gamergates feed constantly, energy storage through lipid is less important. Although our work analyzed gamergates, *Harpegnathos* queens display even higher fecundity and longer life span than that of gamergates (35, 36), and higher expression of Ins has been found in queens in multiple ant species (20). Therefore, it is likely that our findings in gamergates apply to queens. In accordance, the queens of higher termites *Macrotermes natalensis* display higher Ins expression and lower fat storage compared with those of workers (37).

As in raider ants (20), the regulation of reproduction in *Harpegnathos* gamergates is achieved through increased insulin production. However, the peculiar lifestyle of raider ants (20) does not require an extended life span. To foster the extended life span of gamergates, the increased insulin in *Harpegnathos* does not stimulate the IIS-AKT pathway but instead only the IIS-MAPK branch. Our data demonstrate that Ins only mildly activates MAPK activation, although MAPK activity in the gamergate fat body is approximately four times greater than in workers; other ligands, in addition to Ins, may be responsible for MAPK activation in gamergates. We propose a model in which the transition of workers to gamergates is accompanied by the activation of IIS-MAPK, which might activate TOR (target of rapamycin) and its downstream transcription factor SREBP (sterol regulatory-element binding protein), a conserved pathway that might turn on expression of the *Fasn* and *vitellogenin* in the fat body and reactivates ovary growth (1). This is similar to what has been argued in *Drosophila*, in which vitellogenesis is regulated through the IIS-MAPK branch but not by IIS-AKT/FOXO (21, 38).

Reduced IIS-AKT activity in the fat body and early-stage egg chambers (stages 1 to 4) leads to the nuclear localization of FOXO and to reduced expression of a FOXO-negative target gene *Hpd-1* that functions in the degradation

of tyrosine, the amino acid precursor for biogenic amines. In *C. elegans* and *Drosophila*, depletion of *Hpd-1* leads to extended life span, which was attributed to increased levels of dopamine and octopamine, which have a protective role in neuromuscular functions (39). Dopamine is greater in *Harpegnathos* gamergates than in workers (26). Thus, *Hpd-1* down-regulation might contribute to the extended longevity of reproductive gamergates.

Reduced IIS-AKT activity might be related to the production of Imp-L2 from the mature ovary, which is secreted into the hemolymph and might inhibit Ins-induced AKT phosphorylation in the fat body as observed ex vivo. This finding may offer a mechanism to slow down the aging process during active reproduction. By staying in the nest, queen ants are much better protected from extrinsic mortality for a longer life span (9, 40). However, intrinsic senescence that contributes to aging is also affected in *Harpegnathos* gamergates, and our findings could explain why higher fecundity promotes higher longevity: Imp-L2 is produced in the egg chambers of the mature ovary, and as more egg chambers are produced, this might further lower AKT signaling in the fat body, leading to a longer life span.

Our study in *Harpegnathos* gamergates reveals selectivity in the response of AKT and MAPK to insulin production. Activated MAPK and AKT differentially regulate metabolism, ovary growth, germline maintenance, and life span. Ants appear to restrict IIS hyperactivity throughout their very long reproductive life through selective inhibition of IIS-AKT possibly by Imp-L2 and through decreased expression of *InRs*, thus retarding aging and achieving longevity in the reproductive caste. This interplay, which evolved in ants and perhaps in other eusocial insects, may contribute to the unusual longevity associated with high reproduction observed in reproductive ants.

REFERENCES AND NOTES

1. S. C. Johnson, P. S. Rabinovitch, M. Kaeblerlein, *Nature* **493**, 338–345 (2013).
2. L. Fontana, L. Partridge, V. D. Longo, *Science* **328**, 321–326 (2010).
3. M. Tatar, A. Bartke, A. Antebi, *Science* **299**, 1346–1351 (2003).
4. M. Tatar, *Exp. Gerontol.* **46**, 363–368 (2011).
5. R. G. J. Westendorp, T. B. L. Kirkwood, *Nature* **396**, 743–746 (1998).
6. L. Partridge, N. Alic, I. Bjedov, M. D. Piper, *Exp. Gerontol.* **46**, 376–381 (2011).
7. M. Tatar, *Ann. N.Y. Acad. Sci.* **1204**, 149–155 (2010).
8. E. L. Arrese, J. L. Soulages, *Annu. Rev. Entomol.* **55**, 207–225 (2010).
9. L. Keller, M. Genoud, *Nature* **389**, 958–960 (1997).
10. M. Ghaninia et al., *Sci. Rep.* **7**, 3732 (2017).
11. B. Hölldobler, E. O. Wilson, *The Ants* (Belknap Press, 1990).
12. S. A. Ament, M. Corona, H. S. Pollock, G. E. Robinson, *Proc. Natl. Acad. Sci. U.S.A.* **105**, 4226–4231 (2008).
13. C. Opachaloemphan, H. Yan, A. Leibholz, C. Desplan, D. Reinberg, *Annu. Rev. Genet.* **52**, 489–510 (2018).
14. C. Opachaloemphan et al., *Genes Dev.* **35**, 410–424 (2021).
15. C. A. Penick et al., *Proc. Biol. Sci.* **288**, 20210141 (2021).
16. J. Gospocic et al., *Cell* **170**, 748–759.e12 (2017).
17. W. Brogiolo et al., *Curr. Biol.* **11**, 213–221 (2001).

18. J. Liebig, C. Peeters, N. J. Oldham, C. Markstädter, B. Hölldobler, *Proc. Natl. Acad. Sci. U.S.A.* **97**, 4124–4131 (2000).
19. H. Yan, J. Liebig, *Genes Dev.* **35**, 470–482 (2021).
20. V. Chandra et al., *Science* **361**, 398–402 (2018).
21. C. Slack et al., *Cell* **162**, 72–83 (2015).
22. P. Decio, A. S. Vieira, N. B. Dias, M. S. Palma, O. C. Bueno, *PLOS ONE* **11**, e0154891 (2016).
23. K. E. Brown, M. Kerr, M. Freeman, *Dev. Biol.* **307**, 105–113 (2007).
24. A. E. Webb, A. Brunet, *Trends Biochem. Sci.* **39**, 159–169 (2014).
25. S. S. Lee, S. Kennedy, A. C. Tolonen, G. Ruvkun, *Science* **300**, 644–647 (2003).
26. C. A. Penick, C. S. Brent, K. Dolezal, J. Liebig, *J. Exp. Biol.* **217**, 1496–1503 (2014).
27. H. J. Hsu, D. Drummond-Barbosa, *Proc. Natl. Acad. Sci. U.S.A.* **106**, 1117–1121 (2009).
28. N. Arquier et al., *Cell Metab.* **7**, 333–338 (2008).
29. L. V. Hun, S. Luckhart, M. A. Riehle, *J. Insect Physiol.* **118**, 103932 (2019).
30. Y. Yamanaka, E. M. Wilson, R. G. Rosenfeld, Y. Oh, *J. Biol. Chem.* **272**, 30729–30734 (1997).
31. I. Ueki et al., *Proc. Natl. Acad. Sci. U.S.A.* **97**, 6868–6873 (2000).
32. E. Chin, J. Zhou, J. Dai, R. C. Baxter, C. A. Bondy, *Endocrinology* **134**, 2498–2504 (1994).
33. L. Manning et al., *Mech. Dev.* **148**, 56–68 (2017).
34. V. Evdokimova et al., *Sci. Signal.* **5**, ra92 (2012).
35. J. Liebig, H.-J. Poethke, *Ecol. Entomol.* **29**, 203–207 (2004).
36. C. Peeters, J. Liebig, B. Hölldobler, *Insectes Soc.* **47**, 325–332 (2000).
37. S. Séité et al., *Commun. Biol.* **5**, 44 (2022).
38. A. R. Armstrong, D. Drummond-Barbosa, *Dev. Biol.* **440**, 31–39 (2018).
39. A. A. Parkhitko et al., *eLife* **9**, e58053 (2020).
40. M. A. Negroni, E. Jongepier, B. Feldmeyer, B. H. Kramer, S. Foitzik, *Curr. Opin. Insect Sci.* **16**, 51–57 (2016).

ACKNOWLEDGMENTS

We thank the New York Langone Health (NYULH) Genome Technology Center for sequencing; Y. Deng and the NYULH Microscopy Core for help with confocal imaging; H. Yang, J. Gospocic, K. Glastad, C. Penick, K. Haight, R. Bonasio, and J. Liebig for their insightful suggestions and technical support; the entire Desplan and Reinberg laboratories for

helpful discussions; and L. Vales for help with manuscript preparation.

Funding: This work was supported by Howard Hughes Medical Institute (HHMI) Collaborative Innovation Award (CIA) 2009005 and HCIA 2009005 to D.R. and C.D.; NIH grants R21GM114457 (to D.R.), R01EY13010 (to C.D.), and R01AG058762 (to D.R. and C.D.); NIH Ruth L. Kirschstein NRSA postdoctoral fellowship F32AG044971 and NSF I/UCRC CAMTech grant IIP1821914 to H.Y.; and Human Frontier Science Program long-term fellowship LT000010/2020-L to B.S. **Author contributions:** H.Y., C.O., F.C.-A., G.M., C.D., and D.R. designed the study; H.Y., C.O., and G.M. performed transition experiments, life-span monitoring, and sample collection; C.O., N.D., and B.S. performed bioinformatic analyses; H.Y., C.O., G.M., A.L., and B.S. performed ISH/IF staining; C.O. and J.M. injected ants; H.Y., C.O., F.C.-A., J.M., and L.D. performed insulin and pharmacological experiments; X.Z. performed phylogenetic analysis; H.Y., C.O., F.C.-A., J.M., and M.T. quantified IIS activities; F.C.-A. performed ALS and Imp-L2 assays; H.Y., C.O., F.C.-A., and C.D. wrote the manuscript with feedback from all authors; C.D. and D.R. supervised the project.

Competing interests: The authors declare no competing interests.

Data and materials availability: All data that support the conclusions in this manuscript can be found in the main text or in the supplemental materials. Raw sequence data are available through NCBI (accession no. GSE209617). Newly created materials from this study may be requested from the corresponding authors. **License information:** Copyright © 2022 the authors, some rights reserved; exclusive licensee American Association for the Advancement of Science. No claim to original US government works. <https://www.science.org/about/science-licenses-journal-article-reuse>

SUPPLEMENTARY MATERIALS

science.org/doi/10.1126/science.abm8767

Materials and methods

Figs. S1 to S7

References (41, 42)

MDAR Reproducibility Checklist

Tables S1 to S5

Submitted 26 October 2021; accepted 28 July 2022
10.1126/science.abm8767

REPORTS

FOREST ECOLOGY

A climate risk analysis of Earth's forests in the 21st century

William R. L. Anderegg^{1,2*}, Chao Wu^{1,2}, Nezha Acil^{3,4}, Nuno Carvalhais^{5,6}, Thomas A. M. Pugh^{3,4,7}, Jon P. Sadler^{3,4}, Rupert Seidl^{8,9}

Earth's forests harbor extensive biodiversity and are currently a major carbon sink. Forest conservation and restoration can help mitigate climate change; however, climate change could fundamentally imperil forests in many regions and undermine their ability to provide such mitigation. The extent of climate risks facing forests has not been synthesized globally nor have different approaches to quantifying forest climate risks been systematically compared. We combine outputs from multiple mechanistic and empirical approaches to modeling carbon, biodiversity, and disturbance risks to conduct a synthetic climate risk analysis for Earth's forests in the 21st century. Despite large uncertainty in most regions we find that some forests are consistently at higher risk, including southern boreal forests and those in western North America and parts of the Amazon.

Earth's forests store carbon, support enormous terrestrial biodiversity, and provide trillions of dollars each year in ecosystem goods and services to society (1, 2). Because of their potential carbon sequestration capacity and cobenefits there is wide-

spread and growing interest in leveraging forests for climate mitigation through nature-based climate solutions (3, 4). However, the future of forests globally is uncertain as a result of both land use decisions and climate change (5–7). Forests face substantial climate

risks that could trigger carbon cycle feedbacks which would accelerate climate change and fundamentally undermine their role in climate mitigation (7–9). Critical climate-sensitive risks to forest stability, biodiversity, and long-term carbon storage include disturbance triggered by extreme weather (e.g., fire, drought, hurricanes), biotic agents and invasive species, and large-scale demographic shifts (e.g., elevated mortality rates, species turnover, and/or physiological limits to growth or regeneration) (7, 10–12).

The large-scale and cross-biome patterns of climate risks to forests are not well understood. With respect to ecosystems, the Intergovernmental Panel on Climate Change (IPCC) defines risk as the potential for adverse consequences for ecological systems and highlights that risk results from the dynamic interaction of climate-related hazards, exposure, susceptibility, and (lack of) adaptive capacity of a system (5, 13). Three major approaches have been

used to examine key determinants of forests' climate risk, each considering different processes and having distinct uncertainties and limitations: First, global mechanistic vegetation models, such as those included in Earth system models, simulate forest carbon fluxes and pools, climate impacts on those processes, some key climate-sensitive disturbances such as fire, and dynamic growth and recovery after disturbances (14, 15). Second, “climate envelope” approaches use empirical models based on relationships between observed climate patterns and forest attributes such as biomass, species presence/abundance, or ecoregion/life zone presence (16–18). Third, empirical assessments of climatic controls on stand-replacing disturbances, typically based on satellite data of forest loss or meta-analyses of field studies, are also common (11, 19). These major approaches roughly capture different axes of forest climate risk to: (i) carbon stocks or storage (hereafter, C risk), (ii) species composition changes (species risk), and (iii) disturbance regime change (disturbance risk). These approaches have different inherent strengths and weaknesses, but a synthesis of approaches at a global scale is lacking. A multimethod analysis to quantify risks spatially and estimate which regions may be particularly vulnerable under future climate conditions is urgently needed to inform land management, conservation, and climate mitigation efforts.

We compare results from these three types of approaches to provide a global assessment

of climate risks facing Earth's forests in the 21st century and ask the following: (i) what is the mean and uncertainty in projections of forest carbon storage and potential forest carbon losses in mechanistic vegetation models included in Earth system models (e.g., C risk); (ii) what do empirical climate envelope and climate-sensitive disturbance approaches estimate for spatial and temporal climate risks to forests (e.g., species and disturbance risks); and (iii) what broader risk patterns emerge from the synthesis and comparisons of these three different axes of risks?

We first examined simulations of the live carbon in vegetation in forested areas (C risk) from mechanistic vegetation models from the Coupled Model Intercomparison Project Phase 6 (CMIP6: 23 models total, 13 with prognostic fire and 6 with dynamic vegetation; table S1), removing the direct influences of human land use change to contextualize overall forest carbon changes (20). Comparing 2081 to 2100 with 1995 to 2014, these models on average show carbon gains in currently forested areas in both high- and low-emissions scenarios (Fig. 1 and fig. S1). The multimodel mean was positive across most of the world but there was very high variation and uncertainty across models, particularly in the tropics and swaths of the boreal forests (Fig. 1, A and B, and fig. S1). We examined relative agreement in spatial patterns of carbon gains and losses across models and found that spatial correlations across models for carbon changes were

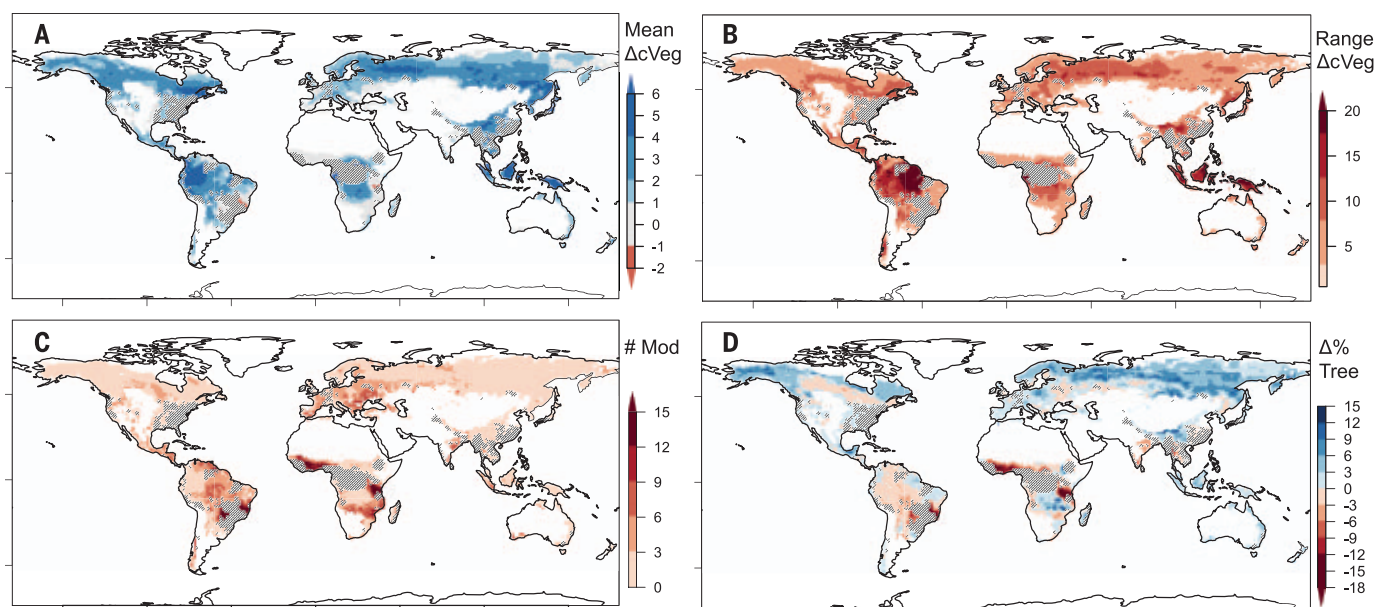


Fig. 1. Future forest carbon and climate risk projections from mechanistic vegetation models. All panels analyze the change between 2081 to 2100 in Shared Socioeconomic Pathway 5-8.5 (SSP585) compared with 1995 to 2014 historical simulations and are masked by present forested areas. (A) Multimodel mean and (B) range of the change in live carbon mass in vegetation (kilograms per square meter) across 23 models. (C) Number of models projecting vegetation carbon losses in a grid cell over the same time period. (D) Multimodel mean spatial patterns of the percent change in fraction of tree plant functional types in a grid cell. Gray hatched areas indicate grid cells removed from analysis due to land use-driven forest loss.

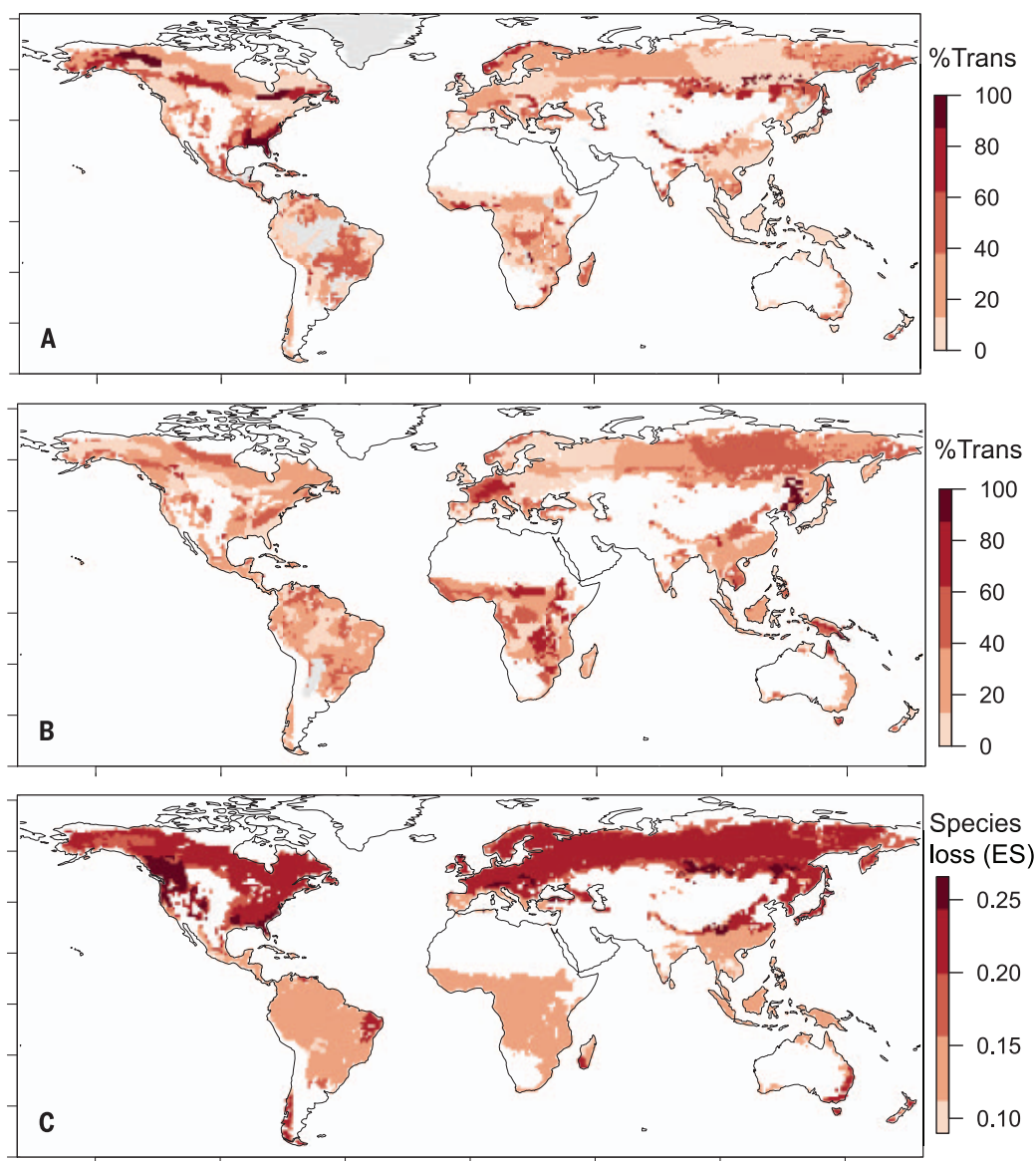


Fig. 2. Global forest risk estimates from climate envelope approaches. (A) Projected percent transition (%Trans) of ecoregions to another ecoregion with a warming of +2°C above preindustrial from Dobrowski *et al.* 2021 (17). (B) Projected percent transition of climate life zones between 1979 to 2013 and 2061 to 2080 in a moderate (RCP 4.5) climate scenario from Elsen *et al.* 2021 (22). (C) Risk of loss in species richness [quantified as an effect size (ES) of $-1 \times \log(\Delta\text{SpeciesRichness}_{\text{highcc-mitigation}}/\Delta\text{SR}_{\text{baseline}})$] where higher numbers indicate more risk of species loss in the 2070s in a high climate change (RCP 8.5) scenario from Mori *et al.* 2021 (21).

modest with an average of $r = 0.30$ across the 23 models considered (fig. S2).

We calculated two complementary metrics of potential climate C risk from these models as follows: (i) the number of models with carbon losses by 2081 to 2100 compared with 1995 to 2014 and (ii) the percent change from tree functional types to other vegetation in a grid cell between those two periods for the subset of models ($n = 14$) that reported data on vegetation change (20). The first metric uses the inherent variability in the model ensemble and assumes that the higher the number of models with C loss, the greater the risk; by contrast, the second metric directly calculates forest loss in models where it is represented. With the first metric, large areas of the Neotropics, the Mediterranean region and eastern Europe, and southwestern North America show notable risk (Fig. 1C). With the second metric, sub-

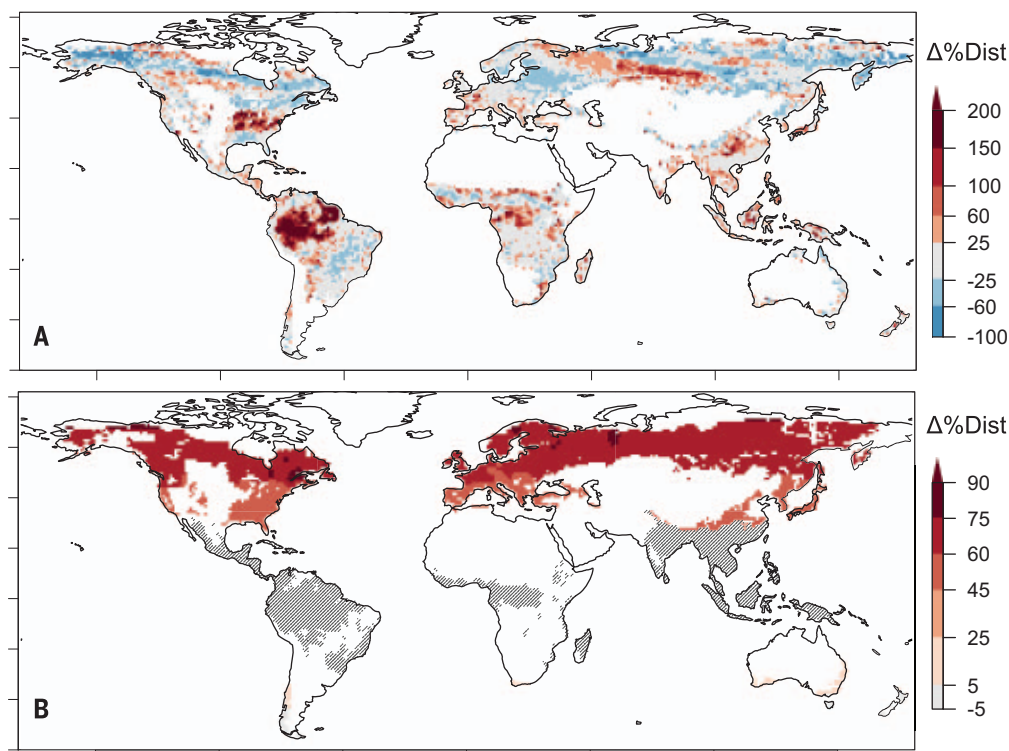
tropical and southern boreal regions were more likely to lose tree functional types (Fig. 1D). We further found that these two metrics showed similar patterns of higher projected risk in southern boreal and drier regions in the Amazon and African tropics. Spatial patterns of carbon changes and climate risks were broadly similar between emissions scenarios (Fig. 1 and fig. S1) and between models with versus without prognostic fire simulated (fig. S3).

We then examined forest species risk, estimated through empirical climate envelope models in three recently published papers. Using observed climate relationships at global scales, two papers estimated ecoregion/life zone transitions (i.e., shifts from one ecoregion/life zone to another), while the third modeled changes in forest species richness within a biome (17, 21, 22). Ecoregion transitions were

projected to most likely occur at current biome boundaries (subtropical-temperate, temperate-boreal, and tropical-subtropical biomes; Fig. 2, A and B). We note that there could be similarly large transitions in terms of species composition within individual biomes but that by their inherent ecoregion-focused structure the underlying analyses in Fig. 2, A and B would not capture community-level changes. Considering the third paper's analyses, risk of species loss estimates were highest in boreal regions and western North America and generally lower in tropical regions (Fig. 2C).

To quantify climate-sensitive disturbance risk we used two complementary methods: (i) an empirical random forest model linking observed climate to stand-replacing disturbance estimates based on satellite data from 2002 to 2014 with human land-use conversion removed (but harvest included) (20) and (ii)

Fig. 3. Projected change in climate-sensitive disturbance risks. (A) Average change in percent disturbed in a grid cell from random forest model projections of Landsat-based stand-replacing disturbances for 2081 to 2100 in a moderate climate change scenario [Shared Socioeconomic Pathway 2-4.5 (SSP245)] compared with 1995 to 2014. (B) Average change in percent disturbed in a grid cell from protected area disturbance models for only temperate and boreal ecosystems in 2081 to 2100 in a moderate climate change scenario (SSP245) compared with 1995 to 2014. Gray hatching in grid cells indicates no data from this data source.



upscaled climate-dependent rates of disturbance in 103 protected areas from temperate and boreal biomes (19). For both methods, the models were built with observed relationships in the historical period. We estimated the change in stand-replacing disturbance rates with a climate model output from the same 23 climate models we used for C risk for 2081 to 2100, with a moderate climate scenario (SSP2-4.5). The model of stand-replacing disturbances indicated that if current forests were exposed to projected future temperatures and precipitation, the largest increases of disturbance would be expected to occur in the tropics and southern boreal forests (Fig. 3, A and B), whereas upscaled relationships from protected areas indicated high disturbance vulnerability broadly across boreal forests, although this dataset did not include tropical forests (Fig. 3B).

We emphasize that these three distinct axes of risk are capturing different aspects and dimensions of climate risks to forests, all of which are generally considered important responses of forests to climate change (20). The spatial and cross-biome relative risk patterns within each approach are likely what is most insightful and important in these comparisons, rather than the absolute values. Thus, we compared the spatial correlations in relative projected risk patterns with a correlation matrix and computed spatial covariation of risk percentiles across all metrics. Notably, none of the different metrics were significantly spatially correlated with each other ($P > 0.05$), leading to high variability across risk metrics in many regions (fig. S4),

and the mechanistic vegetation model projections tended to be slightly negatively correlated with the other approaches (Fig. 4B). Despite this broad-scale disagreement, identification of regions that are at relatively higher or lower risk in most approaches can still provide useful information for risk management. Aggregating risk metrics by the average percentile across all metrics with data in a given grid cell, southern boreal regions (e.g., central Canada) and drier regions of the tropics (e.g., southeast Amazonia) emerged as regions with higher-than-average risk across metrics, consistent with multiple observational studies (e.g., 23, 24). By contrast, eastern North America, western Amazonia, and southeast Asia exhibited lower than average risk (Fig. 4A and fig. S5); a recent pantropical study also observed lower vulnerability in southeast Asian tropics (25). These regional patterns were generally robust in a sensitivity analysis that sequentially excluded individual risk maps (fig. S6). Considering biome-wide patterns, tropical forests had slightly higher average median risk percentiles (51%ile and 62%ile for tropical moist broadleaf and tropical/subtropical dry broadleaf forests, respectively) than boreal (44%ile) or temperate (35%ile and 42%ile for broadleaf and coniferous, respectively) forests (fig. S7).

All of the different approaches to estimating forest climate risk have limitations and different uncertainties that are worth noting. Mechanistic model projections (C risk axis) include the benefits of rising atmospheric CO_2 concentrations on forest productivity (i.e., CO_2

fertilization) as well as coarse estimates of climate sensitivities of plant functional types and fire disturbance. However, these models are generally thought to be lacking a substantial range of key impacts of climate on tree mortality and other disturbances, making it likely that risk estimates from this approach are overly conservative and that carbon gains may be overestimated (26). Furthermore, these models do not realistically capture current tropical forest carbon dynamics (27) and the potential for biome shifts remains very uncertain in these models (14, 28) in part because they frequently neglect processes of tree regeneration (29).

The empirical species distribution and ecoregion biome transition models (species risk axis) are correlative in nature and do not directly include mechanistic processes of growth, mortality, CO_2 -related effects, or disturbance. They are nevertheless widely used across the globe for conservation planning efforts (16, 30) as they provide a powerful approach to estimate the species pool under given climatic conditions. Empirical disturbance models (disturbance risk axis) capture only one key component of forest carbon cycling and do not account for regrowth, species turnover, and other dynamics. Nonetheless, a broad body of literature has demonstrated that changes in disturbance regimes have strong leverage on forest carbon cycling in many ecosystems globally (9, 12, 28). Finally, all of these approaches treat direct human impacts of land-use change and management distinctly. Forest management—as a key disturbance and

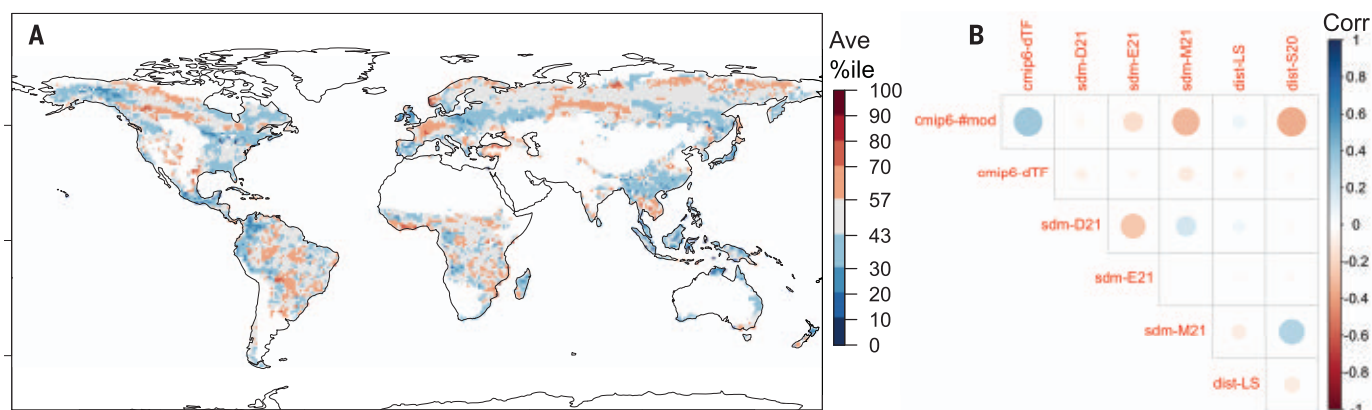


Fig. 4. Comparisons and syntheses across different climate risk axes.

(A) Average percentile of risk combined across all metrics where 0%ile is lowest climate risk and 100%ile is highest climate risk, averaged across all datasets that covered a given grid cell. (B) Correlation matrix between different climate risk axes and metrics where the size and color are proportionate to correlation strength and magnitude (all correlations not significant). Risk axes and metrics: number of models showing carbon losses in forested regions in Coupled Model Intercomparison Project Phase 6 data (cmip6-#mod), change in tree

fraction in the subset of CMIP6 models (cmip6-dTF), species distribution/climate niche models of ecoregion percent changes from Dobrowski *et al.* (2021) (sdm-D21), species distribution/climate niche models of life-zone percent changes from Elsen *et al.* (2021) (sdm-E21), species distribution models of loss of species richness from Mori *et al.* (2021) (sdm-M21), random forest based projections of Landsat-detected stand-replacing disturbances (dist-LS), and change in percent disturbed in a grid cell from protected area disturbance models from Seidl *et al.* (2020) (dist-S20).

arbiter of forest risk—is included implicitly or explicitly in all methods here. Although we have made extensive efforts to screen out changes resulting from land conversion (20), land management remains an important uncertainty and caveat in these analyses. A previous global risk analysis for forest loss with a single, older mechanistic vegetation model (31) projected the highest forest loss in the eastern Amazon, eastern North American boreal, and broad areas of the European and Asian boreal forests, which is partially consistent with the species turnover and biome transition estimates presented here (e.g., Fig. 2A) and the multimethod aggregate map.

Ultimately, our analysis reveals a notably divergent set of projections when comparing across a wide range of methods and approaches to examine the vulnerability of Earth's forests to climate risks. If forests are tapped to play an important role in climate mitigation, an enormous scientific effort is needed to better shed light on when and where forests will be resilient to climate change in the 21st century. These results highlight an urgent need for more detailed treatment of climate-sensitive disturbances in mechanistic vegetation models, more extensive benchmarking of those models against disturbance and mortality datasets, and better identification of agents of change in observational datasets to underlie more nuanced empirical approaches. Continuing the long-term monitoring efforts that enable such work will be fundamental to improving such models. Our results also underscore key needs to focus on climate-driven biome transitions. Currently, enormous uncertainty remains regarding the spatial and temporal patterns

of forest vulnerability to climate change. They further emphasize that the effectiveness of nature-based climate solutions currently under discussion (3, 4) faces great uncertainty given the profound climate impacts on forests expected in the 21st century.

REFERENCES AND NOTES

- G. B. Bonan, *Science* **320**, 1444–1449 (2008).
- FAO and UNEP, *The State of the World's Forests 2020*. Forests, biodiversity and people (FAO, 2020).
- B. W. Griscom *et al.*, *Proc. Natl. Acad. Sci. U.S.A.* **114**, 11645–11650 (2017).
- S. Roe *et al.*, *Nat. Clim. Chang* **9**, 817–828 (2019).
- IPCC, "Managing the Risks of Extreme Events and Disasters to Advance Climate Change Adaptation. A Special Report of Working Groups I and II of the Intergovernmental Panel on Climate Change" C.B. Field *et al.*, Eds. (Cambridge Univ. Press, 2012).
- T. J. Brodrick, J. Powers, H. Cochard, B. Choat, *Science* **368**, 261–266 (2020).
- W. R. L. Anderegg *et al.*, *Science* **368**, eaaz7005 (2020).
- P. Friedlingstein *et al.*, *J. Clim.* **27**, 511–526 (2014).
- W. A. Kurz *et al.*, *Nature* **452**, 987–990 (2008).
- C. D. Allen *et al.*, *For. Ecol. Manage.* **259**, 660–684 (2010).
- R. Seidl *et al.*, *Nat. Clim. Chang* **7**, 395–402 (2017).
- J. A. Wang, A. Baccini, M. Farina, J. T. Randerson, M. A. Friedl, *Nat. Clim. Chang* **11**, 435–441 (2021).
- J. Lecina-Diaz *et al.*, *Front. Ecol. Environ.* **19**, 126–133 (2021).
- R. A. Fisher *et al.*, *Glob. Change Biol.* **24**, 35–54 (2018).
- S. Hantson *et al.*, *Geosci. Model Dev.* **13**, 3299–3318 (2020).
- J. Elith *et al.*, *Ecography* **29**, 129–151 (2006).
- S. Z. Dobrowski *et al.*, *Commun. Earth Environ.* **2**, 198 (2021).
- S. R. Coffield, K. S. Hemes, C. D. Koven, M. L. Goulden, J. T. Randerson, *AGU Adv.* **2**, 2021AV000384 (2021).
- R. Seidl *et al.*, *Ecography* **43**, 967–978 (2020).
- Materials and methods are available as supplementary materials.
- A. S. Mori *et al.*, *Nat. Clim. Chang* **11**, 543–550 (2021).
- P. R. Elsen *et al.*, *Glob. Change Biol.* **28**, 918–935 (2022).
- M. Michaelian, E. H. Hogg, R. J. Hall, E. Arseneault, *Glob. Change Biol.* **17**, 2084–2094 (2011).
- L. V. Gatti *et al.*, *Nature* **595**, 388–393 (2021).
- S. Saatchi *et al.*, *One Earth* **4**, 988–1003 (2021).
- B. M. Sanderson, R. A. Fisher, *Nat. Clim. Chang* **10**, 175–177 (2020).
- A. Koch, W. Hubau, S. L. Lewis, *Earth's Future* **9**, 2020EF001874 (2021).

- T. A. M. Pugh, A. Arneeth, M. Kautz, B. Poulter, B. Smith, *Nat. Geosci.* **12**, 730–735 (2019).
- K. Albrich *et al.*, *Glob. Ecol. Biogeogr.* **29**, 2082–2096 (2020).
- L. L. Porfiri *et al.*, *PLOS ONE* **9**, e113749 (2014).
- M. Scholze, W. Knorr, N. W. Arnell, I. C. Prentice, *Proc. Natl. Acad. Sci. U.S.A.* **103**, 13116–13120 (2006).

ACKNOWLEDGMENTS

Funding: W.R.L.A. acknowledges support from the David and Lucille Packard Foundation, US National Science Foundation grants 1802880, 2003017, and 2044937, and USDA National Institute of Food and Agriculture, Agricultural and Food Research Initiative Competitive Programme, Ecosystem Services and Agro-Ecosystem Management, grant 2018-67019-27850. C.W. acknowledges support from the David and Lucille Packard Foundation. R.S., N.A., and T.P. acknowledge support from the European Research Council (ERC) under the European Union's Horizon 2020 research and innovation programme (grant agreement 101001905, FORWARD, to R.S.; grant agreement 758873, TreeMort, to N.A. and T.P.) This study contributes to the strategic research areas BECC and MERGE. **Author contributions:** W.R.L.A. designed the study with input from all co-authors. W.R.L.A., C.W., and N.A. analyzed the data. W.R.L.A. wrote an initial draft and C.W., N.A., N.C., T.A.M.P., J.P.S., and R.S. provided extensive comments and revisions. **Competing interests:** The authors declare no competing interests. **Data and materials availability:** Analysis code and processed data underlying the paper analyses can be found at doi:10.6084/m9.figshare.19755568. Google Earth Engine code for disturbance analysis can be found at: https://code.earthengine.google.com/?accept_repo=users/NXA807/ForestGlobalClimateRisks. All CMIP6 data and datasets underlying the empirical model analysis are publicly available from the CMIP6 data portal or published article reference. **License information:** Copyright © 2022 the authors, some rights reserved; exclusive licensee American Association for the Advancement of Science. No claim to original US government works. <https://www.sciencemag.org/about/science-licenses-journal-article-reuse>

SUPPLEMENTARY MATERIALS

science.org/doi/10.1126/science.abp9723

Materials and Methods

Figs. S1 to S10

Table S1

References (32–88)

MDAR Reproducibility Checklist

Submitted 9 March 2022; accepted 20 July 2022
10.1126/science.abp9723

ORGANIC CHEMISTRY

Late-stage diversification of indole skeletons through nitrogen atom insertion

Julia C. Reisenbauer[†], Ori Green[†], Allegra Franchino, Patrick Finkelstein, Bill Morandi*

Compared with peripheral late-stage transformations mainly focusing on carbon–hydrogen functionalizations, reliable strategies to directly edit the core skeleton of pharmaceutical lead compounds still remain scarce despite the recent flurry of activity in this area. Herein, we report the skeletal editing of indoles through nitrogen atom insertion, accessing the corresponding quinazoline or quinoxaline bioisosteres by trapping of an electrophilic nitrene species generated from ammonium carbamate and hypervalent iodine. This reactivity relies on the strategic use of a silyl group as a labile protecting group that can facilitate subsequent product release. The utility of this highly functional group-compatible methodology in the context of late-stage skeletal editing of several commercial drugs is demonstrated.

Major advances in the field of late-stage functionalization have recently unlocked extraordinary structural diversity from common synthetic scaffolds, obviating the resource and time-consuming *de novo* synthesis of a library of derivatives (1). The development of numerous, versatile, late-stage C–H functionalization strategies to modify target molecules has been a core tenet of this paradigm shift (2, 3), allowing the introduction of key peripheral modifications. By contrast, complementary approaches that can directly modify the underlying core skeleton of a molecule are less common despite their

potential to expand the accessible chemical space (4–11). Formal single-atom insertion reactions to modify aromatic moieties have proven to be especially challenging given the inherent inertness of aromatic carbon-based skeleton toward cleavage of a C–C bond (12). Despite this formidable challenge, a limited number of carbon (13–16) or oxygen (17, 18) insertion or deletion reactions to reshape molecular architectures have been developed. Given the prevalence of nitrogen atoms in biologically active molecules, the direct modification of valuable core structures through single-nitrogen-atom manipulation is of parti-

cular significance (19) and is especially interesting in the context of evaluating structure–activity relationships in medicinal chemistry settings. Although broad-scope methods to delete a nitrogen atom in molecular scaffolds have been recently disclosed (20–23), methods to insert a single nitrogen atom have remained limited despite their immense potential for the synthesis of ubiquitous *N*-heterocycles. Apart from the classical Beckmann rearrangement of carbonyl derivatives (24), these methods are currently either restricted to structural motifs that are not commonly found in nature (e.g., indene and 2-arylindoles) or do not exhibit broad functional group compatibility, preventing their application to late-stage functionalization (25–32).

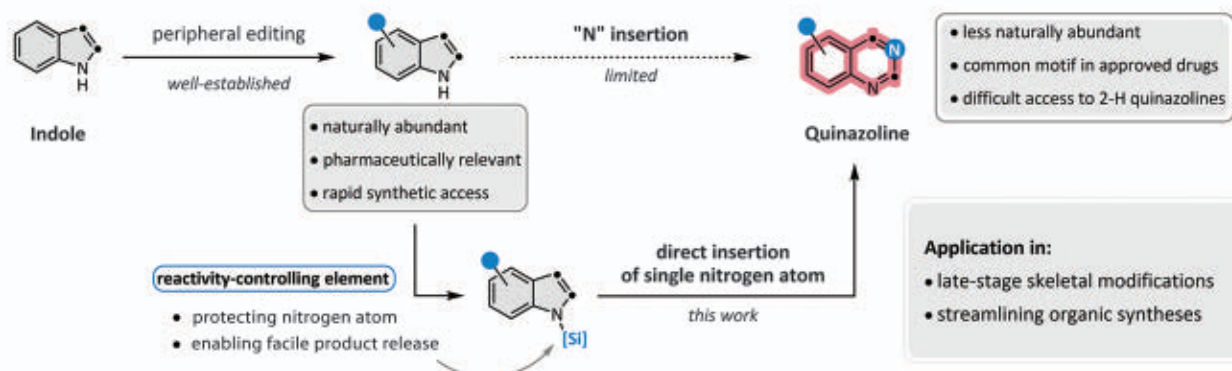
Indoles are among the most widespread nitrogen-containing heterocycles in medicinal chemistry compounds and natural products (33) and thus represent an ideal substrate class for the development of late-stage skeletal editing reactions (6). Such an approach is particularly attractive if less naturally abundant, yet pharmaceutically interesting, scaffolds could be rapidly accessed (Fig. 1A). Direct insertion of a nitrogen atom into the indole scaffold would enable straightforward access to *N,N*-heterocycles without changing the substitution pattern on the starting indole. This

Laboratorium für Organische Chemie, ETH Zürich, 8093 Zürich, Switzerland.

*Corresponding author. Email: bill.morandi@org.chem.ethz.ch

[†]These authors contributed equally to this work.

A Conceptual outline



B Mechanistic design

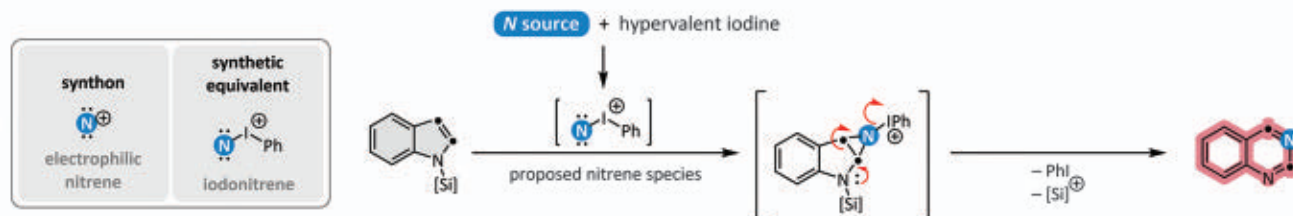


Fig. 1. Core derivatization of indoles. (A) Diversification of indoles to access pharmaceutically interesting quinazoline motifs. (B) Mechanistic design for the transformation of indole skeletons into the corresponding quinazoline scaffold.

transformation of the indole core into such bioisosteric motifs (34, 35), which are not commonly found as building blocks in medicinal chemistry libraries (36) but are widely recognized as privileged pharmacophores in modern drug discovery (33, 37), could have a transformative impact on the field of late-stage diversification, facilitating the discovery and optimization of drug candidates.

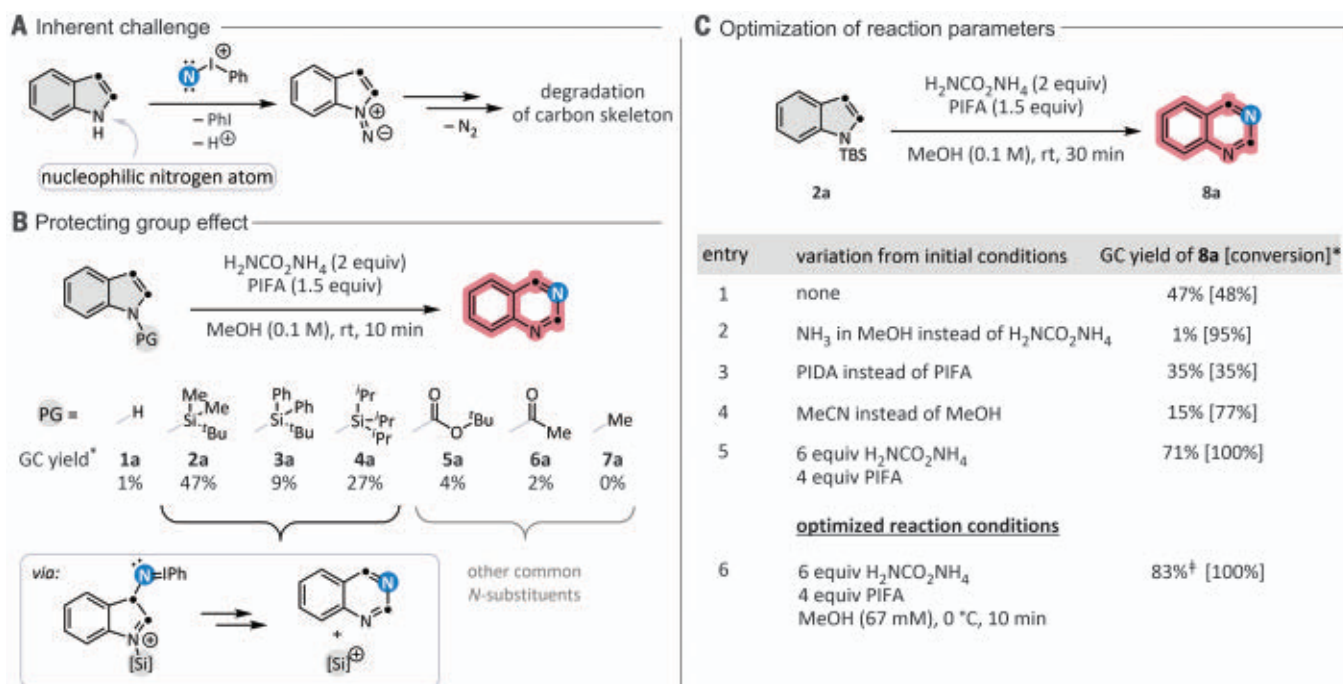
Here, we introduce a method for the insertion of a nitrogen atom into indoles affording *N,N*-heterocycles. Depending on the substitution pattern of the parent indole structure, either quinazolines or quinoxalines can be selectively accessed. This practical reaction tolerates a broad range of functional groups so that a wide set of natural products and commercial drugs can be transformed into their corresponding bioisosteric analogs.

To transform indole scaffolds into the corresponding quinazoline motifs, we needed to identify a suitable reagent to act as an electrophilic nitrogen atom donor. We chose to investigate in situ-generated electrophilic iodonitrenes that were accessed by combining commercially available hypervalent iodine with nitrogen sources (Fig. 1B). In the context of skeletal editing, these reagents have already been harnessed in nitrogen deletion rather than insertion reactions (22), in addition to exhibiting other unique reactivity patterns (38–40). In our design, a stepwise (2+1) cycloaddition would initially provide an aziridine intermediate. Sub-

sequent elimination of iodobenzene, followed by aromatization of the reaction intermediate, would facilitate the desired ring expansion reactions toward the quinazoline product (15).

A key challenge in the overall design is the inherent reactivity of the unprotected indole nitrogen, which could directly react with the electrophilic iodonitrene species. This would lead to the generation of a labile isodiazene intermediate that could ultimately promote the degradation of the underlying carbon skeleton (Fig. 2A) (22). Our design overcomes this intrinsic challenge through the strategic use of a protecting group that is capable of both suppressing the reactivity of the nitrogen and acting as a sufficiently labile electrofuge to release the product. We investigated silyl-based groups because of their aptitude for stabilizing positively charged intermediates and their potency as electrofuges (41). Additionally, the silyl group's susceptibility to hydrolysis can be appropriately adjusted by changing the substituents on the silicon atom (42). Indoles bearing silyl-based and other commonly used protecting groups, such as *tert*-butyloxycarbonyl, acetyl, and methyl, were evaluated under the initial reaction conditions. As might be expected based on the proposed mechanism, only silyl groups were effective in providing the desired quinazoline product **8a** (Fig. 2B), with *tert*-butyldimethyl (TBS)-protected indoles undergoing the desired transformation most efficiently.

In addition to the choice of labile protecting group, the reaction conditions were further optimized by investigating the effect of the other reaction parameters (Fig. 2C). Commercially available [bis(trifluoroacetoxy)iodo]benzene (PIFA) in methanol, in combination with ammonium carbamate as the nitrogen source, proved to be the preferred reagent mixture to suppress undesired oxidative decomposition of the indole core and obtain the product in high yield. With the optimized reaction conditions in hand, the scope of the iodonitrene-enabled skeletal ring expansion was explored using this operationally simple protocol (Fig. 3). The compatibility of the nitrogen atom insertion method with diverse substitution patterns and common functional groups on the TBS-protected indole precursors was evaluated. Quinazoline products featuring electron-withdrawing substituents, such as halogens (**8b** to **8f**), esters (**8g** and **8h**), nitriles (**8i** and **8j**), and sulfones (**8k**), as well as electron-donating groups such as ethers (**8m** to **8o**) and silyl ethers (**8p**), were obtained in moderate to good yields from the corresponding TBS-protected indole precursors. In most cases, except for nitrile-bearing indole precursors, full conversion of the starting materials was observed. Likewise, carboxylic acids (**8l**), alkenes (**8q**), and alkynes (**8r**) were compatible under the optimized reaction conditions. An unprotected piperidine-substituted indole could be transformed into the corresponding product (**8s**), although in



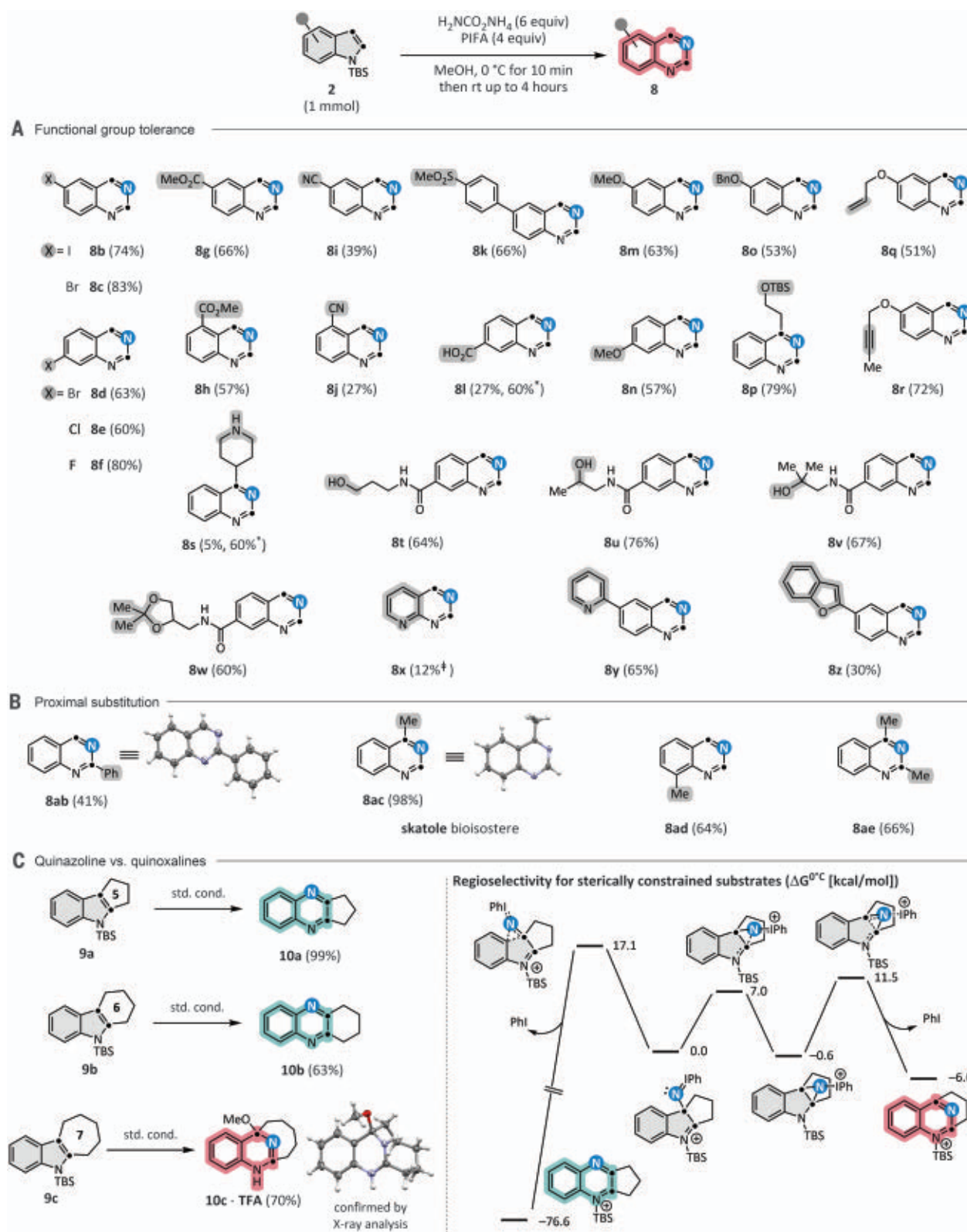


Fig. 3. Substrate scope for the single-nitrogen-atom insertion. Yields are given for isolated products. Reaction conditions: TBS-indole (1 mmol, 67 mM), ammonium carbamate (6 equiv), and PIFA (4 equiv) in MeOH at 0 °C for 10 min, then at room temperature (rt) for up to 4 hours. **(A)** Investigation of the functional group compatibility of the reaction. **(B)** Effect of proximal substitutions on the reaction outcome. **(C)** Investigating the dependence of the reaction outcome on sterically constrained

substrates. Shown are DFT calculations for the regioselective preference of substrate **9a**. Gibbs free energies are indicated in kilocalories per mole at 0 °C. *Yield determined by ^1H nuclear magnetic resonance analysis of the crude reaction mixture using 1,1,2,2-tetrachloroethane or mesitylene as an internal standard. ‡The reaction was performed on 0.2-mmol scale and the product was co-isolated with a side product in ~1:1 ratio (for more details, see the supplementary materials). TFA, trifluoroacetic acid.

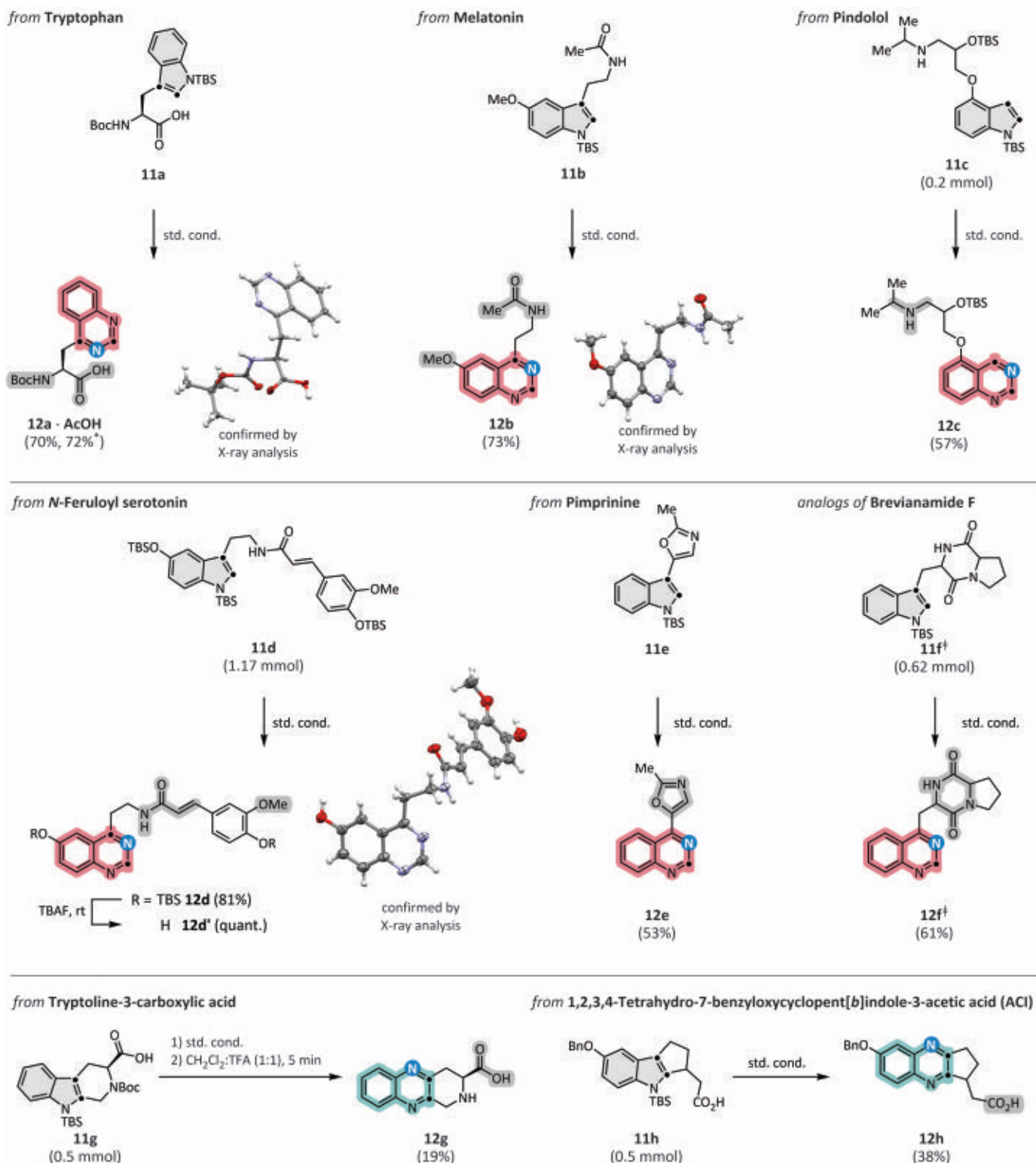


Fig. 4. Late-stage skeletal editing to access quinazoline and quinoxaline scaffolds. Enantiomeric excess was not determined. Reactions were performed on 1.0-mmol scale unless otherwise stated. Standard reaction conditions: TBS-indole (1 equiv, 67 mM), $\text{H}_2\text{NCO}_2\text{NH}_4$ (6 equiv), and

PIFA (4 equiv) in MeOH at 0°C for 10 min, then at room temperature for up to 4 hours. *The reaction was performed on 8.0-mmol scale. ‡Diastereoisomeric ratio = 7:3. AcOH, acetic acid; TBAF, tetra-*n*-butylammonium fluoride; TFA, trifluoroacetic acid.

lower yield, likely because of the propensity of the secondary amine to form isodiazenes, leading to degradation. Indole substrates bearing acetals and primary, secondary, or tertiary alcohol groups performed comparably well under the reaction conditions, leading to the desired quinazoline products (**8t** to **8w**). This strategy also accessed the 1,3,8-triazanaphthalene core (**8x**) from the TBS-protected *aza*-indole in moderate yield (for more details, see the supplementary materials). Additionally, indoles bearing adjacent pyridine and benzofuran motifs, common heterocyclic handles, were efficiently transformed into the corresponding quinazoline moieties (**8y** and **8z**). Despite their structural simplicity, synthetic protocols to access most of these quinazolines are unreported because existing methods do not allow easy access to the 2-H quinazoline products (**43**). TBS-protected indoles featuring substituents on the 2-, 3-, or 7-position, as well as 2,3-disubstituted indoles, were successfully converted to the corresponding quinazoline motifs (**8ab**, **8ac**, **8ad**, and **8ae**, respectively) in good yields, showing the reaction's compatibility with proximal substituents (Fig. 3B). The identities of products **8ab** and **8ac** were further confirmed by x-ray analysis. This is an important result because most biologically active indole derivatives are substituted at the 2- and/or 3-position of the indole scaffold (**33**).

Evaluation of a diverse set of indole cores revealed pathways to either quinazoline or quinoxaline scaffolds, depending on the reactant's substituents (Fig. 3C). 2,3-Disubstituted TBS-protected indoles bearing five- or six-membered fused rings (**9a** and **9b**) exclusively afforded the corresponding quinoxaline products (**10a** and **10b**) in good to excellent yields. This result further extends the utility of the protocol because five- and six-membered polycyclic indole scaffolds are prevalent in nature. Thus, straightforward access to less naturally abundant quinoxaline motifs could be streamlined synthetically. To gain deeper insight into the parameters influencing selectivity, a seven-membered ring-fused indole substrate (**9c**) was also tested, which rearranged to the quinazoline-like scaffold. However, because of the inherent ring strain, the reactive intermediate was attacked by the nucleophilic solvent, leading to the corresponding methanol adduct (**10c**), as confirmed by single-crystal x-ray analysis, preventing rearrangement toward the aromatic quinazoline product. The regioselectivity for the fused five-membered, 2,3-disubstituted indole scaffold (**9a**) was further rationalized by density functional theory (DFT) calculations. These results suggested that a rearrangement to the quinoxaline product is most likely explained by thermodynamic considerations because the transformation into the corresponding quinazoline would result in the formation of a highly strained, energetically unfavored

product (computational details can be found fig. S14) (**44**).

To illustrate the reaction's potential for expanding accessible chemical space, we applied it to naturally occurring amino acids and commercially available drug molecules (Fig. 4) (**45**). Protected tryptophan (**11a**) was transformed into the corresponding quinazoline product (**12a**) in good yields. Moreover, the reaction could be performed on 8-mmol scale, demonstrating the scalability of this process. The synthesis of this previously unexplored unnatural amino acid (**12a**) allows for the investigation of its effect on protein and peptide properties (**46**). The skeletal cores of both melatonin (**11b**), a widely encountered neurohormone (**47**), and pindolol (**11c**), a β -adrenoceptor antagonist used for high blood pressure treatments (**48**), were remodeled to afford the corresponding quinazolines **12b** and **12c**, demonstrating the compatibility with secondary amines and amides. Similarly, the molecular scaffold of *N*-feruloyl serotonin (**11d**), bearing an α,β -unsaturated amide, was transformed into the quinazoline derivative (**12d**) in excellent yield. Pimpridine-derived substrate (**11e**), as well as analogs of brevianamide F (**11f**), which both exhibited diverse biological activities such as fungicidal activities (**49**, **50**), were transformed into the corresponding quinazoline products **12e** and **12f**. Alongside natural products featuring variable functional handles attached to the core indole scaffold, widely encountered polycyclic indole derivatives have also been shown to have diverse biological activities and interesting pharmacologically relevant properties (**51**). Tricyclic tryptoline-3-carboxylic acid (**11g**) was successfully transformed into lycoperoxidine-1-derived quinoxaline **12g**. Similarly, 1,2,3,4-tetrahydro-7-methoxycyclopent[*b*]indole-3-acetic acid (**11h**), a key intermediate in the synthesis of APD334, a drug candidate for the treatment of autoimmune diseases (**52**), was transformed into the corresponding quinoxaline core structure **12h**.

Because indoles are widely encountered, pharmaceutically relevant substrates, we believe that this highly efficient protocol will enable the adoption of more skeletal editing steps in late-stage diversification strategies.

REFERENCES AND NOTES

- D. C. Blakemore *et al.*, *Nat. Chem.* **10**, 383–394 (2018).
- L. Guillemard, N. Kaplaneris, L. Ackermann, M. J. Johansson, *Nat. Rev. Chem.* **5**, 522–545 (2021).
- T. Cernak, K. D. Dykstra, S. Tyagarajan, P. Vachal, S. W. Kraska, *Chem. Soc. Rev.* **45**, 546–576 (2016).
- Y. Hu, D. Stumpfe, J. Bajorath, *J. Med. Chem.* **60**, 1238–1246 (2017).
- H. Lyu, I. Kevlishvili, X. Yu, P. Liu, G. Dong, *Science* **372**, 175–182 (2021).
- J. Jurczyk *et al.*, *Nat. Synth.* **1**, 352–364 (2022).
- J. B. Roque, Y. Kuroda, L. T. Göttemann, R. Sarpong, *Nature* **564**, 244–248 (2018).
- Y. Xia, S. Ochi, G. Dong, *J. Am. Chem. Soc.* **141**, 13038–13042 (2019).

- Y. Xu *et al.*, *Nature* **567**, 373–378 (2019).
- A. J. Smaligo *et al.*, *Science* **364**, 681–685 (2019).
- J. Jurczyk *et al.*, *Science* **373**, 1004–1012 (2021).
- A. Sattler, G. Parkin, *Nature* **463**, 523–526 (2010).
- H. Wynberg, E. W. Meijer, in *Organic Reactions* (Wiley, 1982), pp. 1–36; <https://onlinelibrary.wiley.com/doi/10.1002/0471264180.or028.01>.
- Z. Wang, L. Jiang, P. Sarro, M. G. Suero, *J. Am. Chem. Soc.* **141**, 15509–15514 (2019).
- B. D. Dherange, P. Q. Kelly, J. P. Liles, M. S. Sigman, M. D. Levin, *J. Am. Chem. Soc.* **143**, 11337–11344 (2021).
- J. Woo *et al.*, *Science* **376**, 527–532 (2022).
- Z.-C. Cao, Z.-J. Shi, *J. Am. Chem. Soc.* **139**, 6546–6549 (2017).
- A. Baeyer, V. Villiger, *Ber. Dtsch. Chem. Ges.* **32**, 3625–3633 (1899).
- M. M. Heravi, V. Zadsirjan, *RSC Advances* **10**, 44247–44311 (2020).
- H. Qin *et al.*, *Angew. Chem. Int. Ed.* **60**, 20678–20683 (2021).
- S. H. Kennedy, B. D. Dherange, K. J. Berger, M. D. Levin, *Nature* **593**, 223–227 (2021).
- C. Hui, L. Brieger, C. Strohmann, A. P. Antonchick, *J. Am. Chem. Soc.* **143**, 18864–18870 (2021).
- J. K. Im *et al.*, *Synthesis* **53**, 1760–1770 (2021).
- E. Beckmann, *Ber. Dtsch. Chem. Ges.* **19**, 988–993 (1886).
- S. Liu, X. Cheng, *Nat. Commun.* **13**, 425 (2022).
- M. Somei, Y. Kurizuka, *Chem. Lett.* **8**, 127–128 (1979).
- W. E. Noland, D. A. Jones, *J. Org. Chem.* **27**, 341–342 (1962).
- E. J. Moriconi, F. J. Creggan, C. K. Donovan, F. A. Spano, *J. Org. Chem.* **28**, 2215–2217 (1963).
- K. Maeda, T. Mishima, T. Hayashi, *Bull. Chem. Soc. Jpn.* **47**, 334–338 (1974).
- Y. Feng, Y. Li, G. Cheng, L. Wang, X. Cui, *J. Org. Chem.* **80**, 7099–7107 (2015).
- M.-M. Xu, W.-B. Cao, X.-P. Xu, S.-J. Ji, *Chem. Commun.* **54**, 12602–12605 (2018).
- P. R. Kumar, *Heterocycles* **26**, 1257–1262 (1987).
- E. Vitaku, D. T. Smith, J. T. Njardarson, *J. Med. Chem.* **57**, 10257–10274 (2014).
- R. A. Smits *et al.*, *J. Med. Chem.* **51**, 7855–7865 (2008).
- G. Bouz *et al.*, *Pharmaceuticals (Basel)* **14**, 768 (2021).
- Y. Wang, I. Haight, R. Gupta, A. Vasudevan, *J. Med. Chem.* **64**, 17115–17122 (2021).
- V. Alagarsamy *et al.*, *Eur. J. Med. Chem.* **151**, 628–685 (2018).
- M. Zenzola, R. Doran, L. Degennaro, R. Luisi, J. A. Bull, *Angew. Chem. Int. Ed.* **55**, 7203–7207 (2016).
- S. Chaabouni *et al.*, *Chem. Eur. J.* **24**, 17006–17010 (2018).
- T. Glachet *et al.*, *J. Am. Chem. Soc.* **141**, 13689–13696 (2019).
- H. F. T. Klare *et al.*, *Chem. Rev.* **121**, 5889–5985 (2021).
- M. Bols, C. M. Pedersen, *Beilstein J. Org. Chem.* **13**, 93–105 (2017).
- M. Faisal, A. Saeed, *Front Chem.* **8**, 594717 (2021).
- F. Neese, *Wiley Interdiscip. Rev. Comput. Mol. Sci.* **12**, e1606 (2022).
- G. W. Gribble, in *Indole Ring Synthesis: From Natural Products to Drug Discovery* (Wiley, 2016), pp. 1–38; <https://onlinelibrary.wiley.com/doi/full/10.1002/9781118695692.ch1>.
- T. Narancic, S. A. Almaboub, K. E. O'Connor, *World J. Microbiol. Biotechnol.* **35**, 67 (2019).
- R. Boileau *et al.*, *Eur. J. Med. Chem.* **189**, 112078 (2020).
- W. H. Aellig, *Br. J. Clin. Pharmacol.* **13**, 187S–192S (1982).
- B. Liu *et al.*, *J. Agric. Food Chem.* **67**, 1795–1806 (2019).
- S. N. Kumar, V. S. Nath, R. P. Chandran, B. Nambisan, *World J. Microbiol. Biotechnol.* **30**, 439–449 (2014).
- W. Chen *et al.*, *Nat. Commun.* **13**, 908 (2022).
- A. Garrido Montalban, Y.-A. Ma, S. Johannsen, S. Tandel, M. J. Martinelli, *Tetrahedron Lett.* **56**, 378–381 (2015).

ACKNOWLEDGMENTS

We thank the NMR and x-ray service (SMoCC) and the Molecular and Biomolecular Analysis Service (MoBiAS) of ETH Zürich for technical assistance and the Morandi group for critical proofreading. **Funding:** This work was supported by the European Research Council under the European Union's Horizon 2020 research and innovation program (Shuttle Cat, project ID: 757608) and by ETH Zürich. J.C.R. acknowledges a fellowship from the Stipendiatfonds der Schweizerischen Chemischen Industrie (SSCI). O.G. acknowledges a fellowship from the International Human Frontier Science Program Organization (grant LT000861/2020-L). **Author contributions:** J.C.R. conceived the project. J.C.R., O.G., and A.F. performed the experiments. P.F. performed the DFT studies. B.M. supervised the research. J.C.R., O.G., and B.M. wrote the manuscript. All authors revised and approved the manuscript. **Competing interests:** The authors declare no

competing interests. **Data and materials availability:** X-ray data for compounds **8n**[†], **8ab**, **8ac**, **10c-TFA**, **12a**, **12b**, and **12d**[†] are freely available at the Cambridge Crystallographic Data Centre under deposition numbers 2173003, 2173004, 2171863, 2171881, 2171882, 2172251, and 2174296, respectively. **License information:** Copyright © 2022 the authors, some rights reserved; exclusive licensee American Association for the Advancement of Science. No

claim to original US government works. <https://www.sciencemag.org/about/science-licenses-journal-article-reuse>

SUPPLEMENTARY MATERIALS

science.org/doi/10.1126/science.add1383
Materials and Methods

Figs. S1 to S23
Tables S1 to S15
References (53–100)
Data S1

Submitted 23 May 2022; accepted 27 July 2022
10.1126/science.add1383

MULTIFERROICS

Magnetoelectric transfer of a domain pattern

Ehsan Hassanpour^{1,2†}, Yannik Zemp¹, Yusuke Tokunaga³, Yasujiro Taguchi⁴, Yoshinori Tokura^{4,5}, Thomas Lottermoser¹, Manfred Fiebig^{1,4*}, Mads C. Weber^{1,6}

The utility of ferroic materials is determined by the formation of domains and their poling behavior under externally applied fields. For multiferroics, which exhibit several types of ferroic order at once, it is also relevant how the domains of the coexisting ferroic states couple and what kind of functionality this might involve. In this work, we demonstrate the reversible transfer of a domain pattern between magnetization and electric-polarization space in the multiferroic Dy_{0.7}Tb_{0.3}FeO₃. A magnetic field transfers a ferromagnetic domain pattern into an identical ferroelectric domain pattern while erasing it at its magnetic origin. Reverse transfer completes the cycle. To assess the generality of our experiment, we elaborate on its conceptual origin and aspects of application.

The functionality of a material is determined not only by its static properties but also by its response to alterations of the external conditions. For example, the utility of a ferromagnet depends on how its magnetization reacts to an external magnetic field. How easily do its magnetized areas—the domains—form and move, and how magnetically hard or soft is the material?

In composite systems assembled from several ferroic materials, it is also of interest how the domains of the respective ordered states interact. This can be a source of coupling effects that systems with a single ferroic order cannot exhibit. For example, strain can mediate a correlation between electric and magnetic domains in heterostructures, where the piezoelectric deformation of one constituent modifies the magnetic anisotropy of the other (*1*). The spatial correlation between ferromagnetic and antiferromagnetic domains in a heterostructure can lead to exchange bias (*2*). Domains can also be imprinted from a ferromagnetic to an antiferromagnetic thin film by making use of thermomagnetic coupling (*3*).

Multiferroics, materials that exhibit both magnetic and electric long-range order, are of particular interest. The magnetoelectric

coupling between the coexisting orders may be used to manipulate the magnetic state with electric fields, which could provide an energy-saving way to switch magnetization (*4–7*). Since the discovery of multiferroics in the late 1950s, followed by an enormous increase in research activity from the year 2000 (*8*), a variety of multiferroics exhibiting pronounced magnetoelectric coupling have been found. However, these studies have primarily focused

on the coupling of single-domain states. By contrast, the correlation of magnetic and electric domains, which are inevitably formed during the switching between these single-domain states, is little understood. Consequently, phenomena resulting from the coupling of the magnetic and electric domains remain unrecognized.

As a notable example of such a phenomenon, we demonstrate the reversible transfer of a spatial domain pattern between magnetization (spin) and electric-polarization (charge) space in a multiferroic exhibiting both a ferromagnetic and a ferroelectric component. The transfer of the domain patterns in our model system, Dy_{0.7}Tb_{0.3}FeO₃ (DTFO), is mediated by applied magnetic or electric fields. The creation of the domain configuration at the target location depends on its erasure at the place of origin. This transfer is fundamentally different from the process of duplication in the composite systems discussed above (*1–3*, *9*).

We begin by explaining the conceptual basis of such a process. To do so, we use the principle of free-energy minimization as the framework guiding the transfer between magnetization and polarization space. For a free energy of

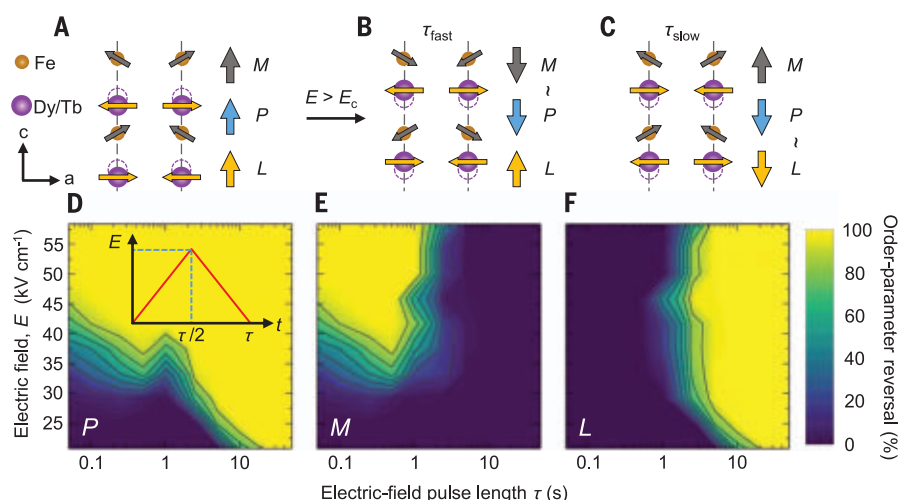


Fig. 1. Three-order-parameter coupling in multiferroic DTFO. (A) Sketch of the arrangement of the transition metal (Fe³⁺) and rare-earth (Dy³⁺/Tb³⁺) ions and spins along with the associated order parameters for Dzyaloshinskii-Moriya-type ferromagnetism (M), antiferromagnetism (L), and magnetostrictively induced electric polarization (P) (*10*). (B and C) Joint P-M or P-L reversal upon application of a fast or slow electric field pulse, in accordance with (D) to (F). (D to F) Switching behavior of P, M, and L in a DTFO sample at 2.5 K under a triangular electric field pulse [inset to (D)] applied along the c axis. The color scale represents the volume fraction of the sample where an order-parameter reversal in response to the poling pulse was observed.

¹Department of Materials, ETH Zurich, 8093 Zurich, Switzerland. ²Department of Physics, ETH Zurich, 8093 Zurich, Switzerland. ³Department of Advanced Materials Science, The University of Tokyo, Chiba 277-8561, Japan. ⁴RIKEN Center for Emergent Matter Science (CEMS), Saitama 351-0198, Japan. ⁵Department of Applied Physics and Tokyo College, The University of Tokyo, Tokyo 113-8656, Japan. ⁶Institut des Molécules et Matériaux du Mans, UMR 6283 CNRS, Le Mans Université, 72085 Le Mans, France. *Corresponding author. Email: manfred.fiebig@mat.ethz.ch †Present address: Department of Diabetes, Endocrinology, Nutritional Medicine and Metabolism, Bern University Hospital, University of Bern, 3010 Bern, Switzerland.

the form $F_2 \propto -O_1O_2$, where $O_{1,2}$ are order parameters or fields, a reversal of O_1 promotes simultaneous reversal of O_2 to retain the negative value of F_2 . If, for example, O_1 and O_2 relate to a spontaneous magnetization M and an electric polarization P of a multiferroic, the contribution $F_2 \propto -MP$ promotes coupled domain configurations for M and P . Magnetization and polarization space are then merely copies of each other. A different yet similarly rigid correlation holds in multiferroics, where the noncentrosymmetric order of a magnetic sublattice directly drives the electric polarization (4).

Multiferroics with three linearly coupled order parameters have more freedom. With a free-energy contribution $F_3 \propto -O_1O_2O_3$, any change in O_1 demands a compensating change in the product of O_2 and O_3 . In the general case, the individual factors within this product are not specifically determined; however, they can be controlled and determined by the experimental conditions.

A multiferroic material exhibiting this kind of three-order-parameter coupling is DTFO (10). Below 2.65 K (Fig. 1A), the Fe^{3+} sublattice exhibits a Dzyaloshinskii-Moria-type magnetization M along the c axis on top of its antiferromagnetic order. The $\text{Dy}^{3+}/\text{Tb}^{3+}$ sublattice is purely antiferromagnetic, parametrized by the order parameter L . Symmetric 3d-4f exchange striction induces a ferroelectric polarization P along $\pm c$ (10). The direction of P is determined by the relative orientation of the two magnetic sublattices so that

$$F_{\text{DTFO}} \propto -MLP \quad (1)$$

yields a trilinear contribution to the free energy (11). In field poling experiments on DTFO and the related compound GdFeO_3 , it has been shown that a magnetic field can act on P and that an electric field can act on M (10, 11). In the latter case, the temporal profile of the electric field poling pulse is crucial. Poling experiments in electric fields with $E > E_c$ (with E_c as coercive field) have revealed that for a fast electric field pulse with a sufficiently steep leading edge, P reverses jointly with M , whereas for a slow electric field pulse, P reverses without affecting M (10).

This response can be understood in terms of the aforementioned coupling behavior, where the reversal of one of the parameters (here, P) enforces the compensating reversal of one of the remaining two [here, (i) M or (ii) L , leaving M unchanged] to minimize Eq. 1. The dynamical coupling in the electric field would then be associated with the characteristic relaxation time scales of the 3d and 4f spin systems. The strongly anisotropic, Ising-like $\text{Dy}^{3+}/\text{Tb}^{3+}$ spin system (12, 13) exhibits slower reversal dynamics (14) than the isotropic Heisenberg-like Fe^{3+} spin system, so that the latter responds to a fast electric field pulse (10, 11, 15) along with P .

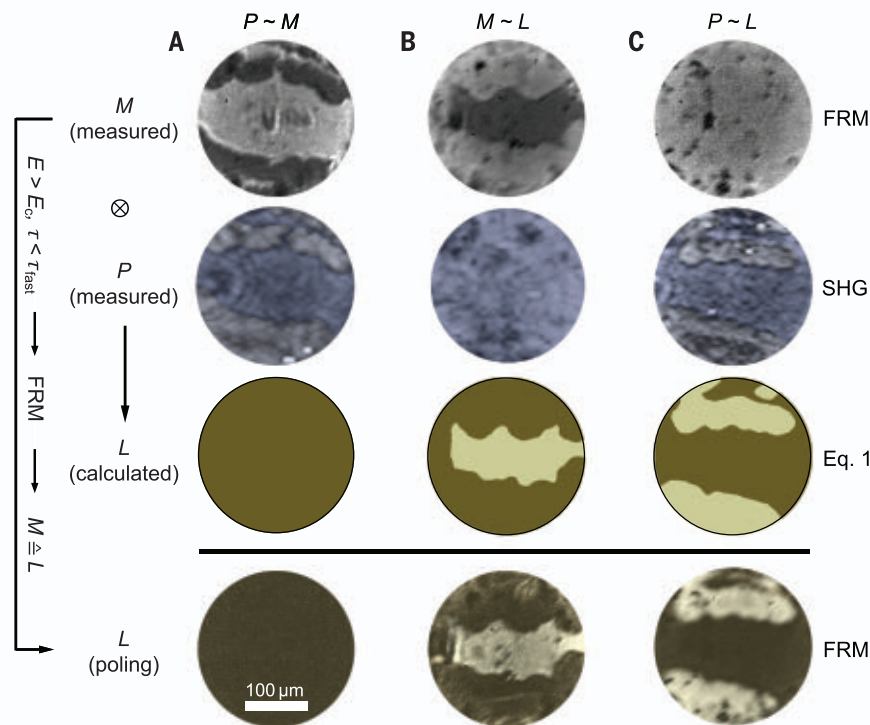


Fig. 2. Verification of the deterministic coupling and of M , L , and P domain configurations. FRM and SHG images of a c -oriented DTFO sample, revealing the distribution of the M (row 1) and P (row 2) domains, respectively. In row 3, we calculate the distribution of L from a poling experiment. We apply an electric field poling pulse ($\tau < 50 \text{ ms} < \tau_{\text{fast}}$, $E = 40.0 \text{ kVcm}^{-1} > E_c$), converting P into a single-domain configuration. With minimization of Eq. 1, the domain configuration in M and L must then become identical so that L can be determined from another FRM measurement of M (row 4). The domain patterns are prepared from an M - L - P single-domain configuration by applying the following fields (Fig. 1, D to F). (A) An electric field pulse ($\tau < 50 \text{ ms} < \tau_{\text{fast}}$, $E = -25.0 \text{ kVcm}^{-1} \sim -E_c$) creates identical M and P multidomain patterns. (B) After (A), an electric field pulse ($\tau = 15 \text{ s} > \tau_{\text{slow}}$, $E = -33.3 \text{ kVcm}^{-1} < -E_c$) switches P together with L , creating a single-domain P configuration and identical multidomain M and L patterns. (C) After (B), a magnetic field $\mu_0 H = 200 \text{ mT} > \mu_0 H_c$ turns M single domain while putting P into the same multidomain pattern as L . A small discrepancy between the field values and Fig. 1, D to F, is caused by laser heating and is discussed in the supplementary materials (18).

However, because the polar displacement P and the antiferromagnetic order L both originate in the rare-earth ions, a slow electric field pulse naturally switches the $\text{Dy}^{3+}/\text{Tb}^{3+}$ spins along with P (10).

Because L had not been measured, this pairwise coupling could not be verified in prior work. In fact, there was evidence that interaction between domain walls guides the poling behavior, which would be in contradiction to the strictly pairwise coupling described above (11).

We examined the coupling of the ordered states in DTFO by the experimental determination of all three parameters, M , L , and P . In doing so, it is not sufficient to consider the single-domain states of a poling process. Because of the proposed influence of domain walls (11), it is possible that a pairwise coupling of M , L , and P applies differently to a single-domain configuration than to a multi-

domain configuration, with its characteristic formation, movement, and crossing of domains and domain walls under the poling fields.

We begin by imaging the spatial distribution of M and P in Faraday rotation microscopy (FRM) and second-harmonic generation (SHG) measurements, respectively. The Faraday effect represents the rotation of the linear polarization of the transmitted light proportional to a longitudinal magnetization M . Hence, the distribution of the ferromagnetic domains is accessible by polarization microscopy. SHG, frequency doubling of a light wave in a material, is sensitive to the breaking of inversion symmetry by P . It produces a light wave with a phase that is proportional to the sign of P . At the domain walls, the sign change of P leads to a sign change of the SHG wave, leading to destructive interference. This highlights the ferroelectric domain walls as dark grooves (16, 17) and enables the mapping of the distribution of

the ferroelectric domains [see section S3 in the supplementary materials (18)].

A single-domain configuration in M and P is prepared by combined electric and magnetic field cooling (18). To this single-domain configuration, now at zero field, we apply field poling pulses. In Fig. 2A, the poling leads to identical multidomain patterns in M and P . In Fig. 2, B and C, only one of M or P becomes multidomain, whereas P or M , respectively, remain single domain. We then determine the complementary distribution of the L domains in two ways (sketched in fig. S1).

First, we calculate this distribution from the known distribution of M and P under the assumption that the free energy in Eq. 1 is always minimized. With normalized values $M, L, P = \pm 1$, we then have $-MLP \equiv -1$ so that $L = 1/MP$ can be reconstructed in a pixel-by-pixel analysis. Second, we determine the configuration of the L domains from a poling experiment. We do this by applying a fast electric field poling pulse, which, as explained before, switches M along with P . With P in its electric field-induced single-domain configuration, we have $P = +1$ so that with $-MLP \equiv -1$, we get $M = L$. This allows us to determine the distribution of the L domains through the measurement of M by FRM.

If the above assumption, that Eq. 1 is always minimized so that M , L , and P are pairwise coupled, holds, then the fast electric field poling affecting P and M leaves L untouched, and the distribution of the L domains derived from the calculation and the poling experiment must look the same. If the above assumption does not hold, a correlation between these two patterns is not expected. Notably, the corresponding domain patterns in rows 3 and 4 of Fig. 2 look very similar in all three cases. This validates the assumption of a pairwise bulk coupling of M , L , and P as a result of the minimization of Eq. 1. Specifically, we detect no interference by the suspected interaction of domain walls (11). The coincidence of the domain walls in Fig. 2 is the result of the bulk order-parameter coupling. Coupled order parameters lead to identical domains, for which the domain walls then necessarily also match.

With our verification of the deterministic MLP coupling, FRM can provide access to all three DTFO domain patterns. The distribution of M is measured directly, and as described above, the fast electric field poling pulse reveals L through M in a second FRM measurement, whereas P is derived from the product of M and L . In sections S1 and S2 of the supplementary materials (18), we provide a sketch of this workflow, and we use it to spatially resolve the most general case with three different domain patterns for M , L , and P , respectively.

In the next step, the dynamical coupling between M , L , and P in response to electric field pulses of different duration τ and field magnitude E is quantified in Fig. 1, D to F.

We begin with a field-cooled M - L - P single-domain configuration (18). Next, the M - L - P domain patterns resulting from subsequent application of an electric field poling pulse were analyzed by FRM as just described. Depending on the length of the poling pulse, the coercive electric field E_c ranges between <20 and 45 kVcm^{-1} . Above E_c , the P - M and P - L reversals occur at $\tau < \tau_{\text{fast}} \approx 1 \text{ s}$ and $\tau > \tau_{\text{slow}} \approx 3 \text{ s}$, respectively. The range around E_c or at $\tau_{\text{fast}} < \tau < \tau_{\text{slow}}$ is nondeterministic in terms of the polarization switching or in terms of the clamping of P to either M or L . In Fig. 1, D to F, we show full control over the coupling of domains in DTFO, which we used to obtain the domain patterns in Fig. 2, A to C.

This finally enables us to demonstrate the magnetoelectric transfer of a domain pattern. For imaging the domain configurations in magnetization and polarization space, we have two options, highlighted in fig. S1. We may access P directly by SHG. Alternatively, we can derive P indirectly, first determining M and L through successive FRM experiments as described for Fig. 2, row 4, and then calculating P by means of $-MLP \equiv -1$.

In Fig. 3, we use the direct approach. As in Fig. 2B, we prepare a ferromagnetic multidomain pattern while retaining the ferroelectric single-domain configuration (Fig. 3A). A magnetic field $H > H_c$ induces a ferromagnetic single-domain configuration and transfers the domain

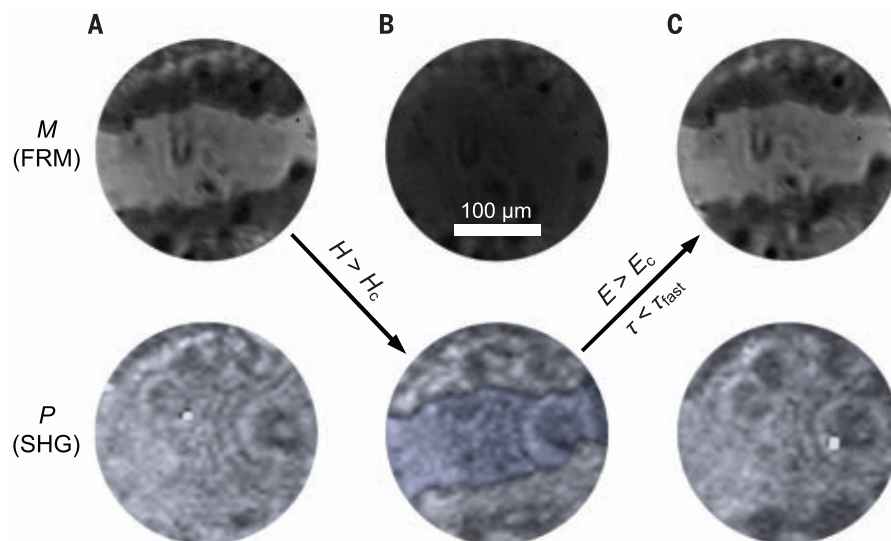


Fig. 3. Magnetoelectric transfer of a domain configuration. Imaging of magnetization and polarization space by FRM and SHG, respectively. (A) Ferromagnetic multidomain and ferroelectric single-domain state in a c -oriented DTFO sample prepared according to the procedure in Fig. 2B. (B) A magnetic field at $\mu_0 H = 200 \text{ mT}$ erases the multidomain configuration in M and recreates it in P . (C) An electric field pulse ($\tau < 50 \text{ ms} < \tau_{\text{fast}}$, $E = -41.6 \text{ kVcm}^{-1} < -E_c$) erases the multidomain configuration in P and recreates it in M , thus completing the transfer cycle between magnetization and polarization space. The presence and absence of the ferroelectric domain walls in (B) and [(A) and (C)], respectively, is corroborated by line scans of the SHG images in fig. S5.

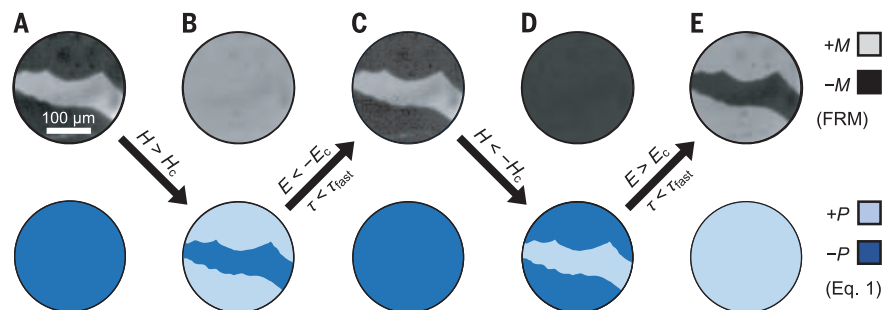


Fig. 4. Repeated magnetoelectric transfer cycles. Imaging of magnetization and polarization, based on FRM and minimization of Eq. 1. (A to C) Replication of the cycle in Fig. 3. (D and E) Repetition of the cycle depicted in (A) to (C) but with the opposite assignment of the $\pm M$ to the $\pm P$ domain states. This is accomplished by reversing the sign of the magnetic and electric fields.

pattern from magnetization to polarization space (Fig. 3B). The magnetically induced nature of the polarization dictates that a reversal of M is accompanied by a reversal of P . Hence, the emergence of the domain pattern in P is inseparably linked to its erasure in M , which distinguishes this transfer process from an ordinary duplication. The transfer of the domain pattern back from polarization to magnetization space in Fig. 3C is accomplished with an electric field pulse at $E > E_c$ and $\tau < \tau_{\text{fast}}$.

The SHG measurements directly detecting P suffer from instability caused by laser heating and long exposure times, so sequential magnetoelectric transfer cycles are hard to accomplish. This is avoided in Fig. 4, where we apply the indirect approach to probe P , based on FRM only. We first reproduce the magnetoelectric transfer cycle of Fig. 3 and add a second cycle, now with the reversed association between the $\pm M$ and $\pm P$ domain states. This is achieved by reversing the sign of the magnetic field in the first transfer. Note that throughout the transitions between magnetization and polarization space in Figs. 3 and 4, the domain pattern is preserved in the spatial distribution of the antiferromagnetic order parameter L .

We have reversibly transferred a domain pattern in multiferroic DTFO between magnetization and polarization space. The creation of the domain pattern in the target space depends on its simultaneous erasure in the space of origin. The basis of the magnetoelectric transfer is minimization of the free-energy contribution from the coupling of the three order parameters describing the multiferroic order of DTFO. Given that multiferroics are often described by three or more order parameters, it is likely that more examples for the magnetoelectric transfer of a domain pattern will be discovered.

The main objective of our work was to provide evidence that, in multiferroics, not only the coupling between magnetic and electric order matters, but that fundamental correlations can also emerge from the spatial distribution of this coupling. In terms of applications, the magnetoelectric transfer of a domain pattern may allow for the creation of a distribution of domains in one space and hide or protect this information against stray fields or unwanted access in the other.

REFERENCES AND NOTES

1. T. H. E. Lahtinen, J. O. Tuomi, S. van Dijken, *Adv. Mater.* **23**, 3187–3191 (2011).
2. F. Nolting *et al.*, *Nature* **405**, 767–769 (2000).
3. S. Brück *et al.*, *Adv. Mater.* **17**, 2978–2983 (2005).
4. M. Fiebig, T. Lottermoser, D. Meier, M. Trassin, *Nat. Rev. Mater.* **1**, 16046 (2016).
5. T. Birol *et al.*, *Curr. Opin. Solid State Mater. Sci.* **16**, 227–242 (2012).
6. J. A. Mundy *et al.*, *Nature* **537**, 523–527 (2016).
7. J.-Y. Chaudhary, E. Haltz, C. Carrétero, S. Fusil, M. Viret, *Nat. Mater.* **16**, 803–807 (2017).
8. I. E. Chupis, *Ferroelectromagnets*. Fifty years after discovery. arXiv:1012.2024 [cond-mat.mtrl-sci] (2010).
9. J. T. Heron *et al.*, *Phys. Rev. Lett.* **107**, 217202 (2011).
10. Y. Tokunaga, Y. Taguchi, T.-H. Arima, Y. Tokura, *Nat. Phys.* **8**, 838–844 (2012).
11. Y. Tokunaga *et al.*, *Nat. Mater.* **8**, 558–562 (2009).
12. L. S. Wu *et al.*, *Phys. Rev. B* **96**, 144407 (2017).
13. K. Křížek, Z. Jiráček, P. Novák, C. de la Cruz, *Solid State Sci.* **28**, 26–30 (2014).
14. N. Ishikawa, M. Sugita, T. Ishikawa, S.-Y. Koshihara, Y. Kaizu, *J. Am. Chem. Soc.* **125**, 8694–8695 (2003).
15. L. A. Prelorenzo, C. E. Johnson, M. F. Thomas, B. M. Wanklyn, *J. Phys. C Solid State Phys.* **13**, 2567–2578 (1980).
16. S. Denev, T. Lummen, E. Barnes, A. Kumar, V. Gopalan, *J. Am. Ceram. Soc.* **94**, 2699–2727 (2011).
17. M. Fiebig, D. Fröhlich, T. Lottermoser, M. Maat, *Phys. Rev. B* **66**, 144102 (2002).
18. The supplementary materials are available online.
19. E. Hassanpour *et al.*, Data and analysis repository for: Magnetoelectric transfer of a domain pattern, ETH Research Collection (ETH Zurich, 2022); <https://doi.org/10.3929/ethz-b-000555414>.

ACKNOWLEDGMENTS

Funding: This work was financially supported by SNSF (grant no. 200021_178825/1) and the European Research Council (advanced grant 694955-INSEETO). Y. Tokun. was supported by JSPS Grant-in-Aids for Young Scientists (A) (no. 25707032). Y. Tokun., Y. Ta., and Y. Tokur. were supported by the Japan Society for the Promotion of Science (JSPS) through its “Funding Program for World-Leading

Innovative R&D on Science and Technology” (FIRST Program). M.F. thanks CEMS at RIKEN and ETH for supporting his research sabbatical. **Author contributions:** All authors contributed to the discussion and interpretation of the experiment and to the completion of the manuscript. E.H. designed, performed, and analyzed the FRM measurements; characterized the electric field response; and discovered the domain-pattern transfer. Y.Z. designed; performed; and, together with M.C.W., evaluated the combined SHG and FRM measurements. T.L. and M.C.W. coordinated the experiments. Y. Tokun. and Y. Ta. synthesized the DTFO samples, coordinated by Y. Tokur. M.C.W., T.L., and M.F. supervised the work. **Competing interests:** The authors declare that they have no competing interests. **Data and materials availability:** All raw data and analysis scripts used in this work are available online (19). **License information:** Copyright © 2022 the authors, some rights reserved; exclusive licensee American Association for the Advancement of Science. No claim to original US government works. <https://www.science.org/about/science-licenses-journal-article-reuse>

SUPPLEMENTARY MATERIALS

science.org/doi/10.1126/science.abm3058
Materials and Methods
Supplementary Text
Figs. S1 to S5
References (20–22)

Submitted 10 September 2021; accepted 28 July 2022
10.1126/science.abm3058

NANOMATERIALS

3D nanoprinting of semiconductor quantum dots by photoexcitation-induced chemical bonding

Shao-Feng Liu^{1†}, Zheng-Wei Hou^{2†}, Linhan Lin^{1*}, Fu Li³, Yao Zhao¹, Xiao-Ze Li¹, Hao Zhang³, Hong-Hua Fang¹, Zhengcao Li², Hong-Bo Sun^{1,4*}

Three-dimensional (3D) laser nanoprinting allows maskless manufacturing of diverse nanostructures with nanoscale resolution. However, 3D manufacturing of inorganic nanostructures typically requires nanomaterial-polymer composites and is limited by a photopolymerization mechanism, resulting in a reduction of material purity and degradation of intrinsic properties. We developed a polymerization-independent, laser direct writing technique called photoexcitation-induced chemical bonding. Without any additives, the holes excited inside semiconductor quantum dots are transferred to the nanocrystal surface and improve their chemical reactivity, leading to interparticle chemical bonding. As a proof of concept, we printed arbitrary 3D quantum dot architectures at a resolution beyond the diffraction limit. Our strategy will enable the manufacturing of free-form quantum dot optoelectronic devices such as light-emitting devices or photodetectors.

Laser-based nanoprinting features high resolution down to nanometer scale (1–3), but it generally relies on photopolymerization and is limited to photocurable resin. Three-dimensional (3D) manufacturing of functional nanomaterials beyond polymers remains challenging. One strategy

is to use a 3D polymer skeleton as a mask for conformal deposition of inorganic materials, producing organic-inorganic nanohybrids (4–6). However, the existence of unwanted polymer skeletons reduces the material's purity and impedes their intrinsic mechanical or physical properties. Although the polymer template can be etched off, only hollow inorganic structures can be obtained. Another strategy is to mix photocurable monomers with inorganic nanomaterials, i.e., photocurable nanocomposites, for direct laser printing (7–9). The cured polymer can be removed by postsintering, but this leads to structural shrinkage and defect generation (10–12).

The key to resolving these problems is to develop a printing mechanism beyond photopolymerization. Talapin *et al.* designed

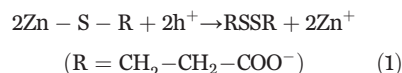
¹State Key Laboratory of Precision Measurement Technology and Instruments, Department of Precision Instrument, Tsinghua University, Haidian, Beijing 100084, China. ²Key Laboratory of Advanced Materials (MOE), School of Materials Science and Engineering, Tsinghua University, Haidian, Beijing 100084, China. ³Department of Chemistry, Tsinghua University, Haidian, Beijing 100084, China. ⁴State Key Laboratory of Integrated Optoelectronics, College of Electronic Science and Engineering, Jilin University, Changchun 130012, China.

*Corresponding author. Email: linh2019@mails.tsinghua.edu.cn (L.L.); hbsun@tsinghua.edu.cn (H.-B.S.)

†These authors contributed equally to this work.

photoactive ligands that decompose under light irradiation for direct optical lithography (13). However, this method requires the sophisticated design of surface ligands that are selective to specific nanocrystals. In the present work, taking semiconductor quantum dots (QDs) as an example, we propose a strategy that uses electron-hole pairs generated by photoexcitation to modify the surface chemistry of QDs to induce interparticle chemical bonding, which we call photoexcitation-induced chemical bonding (PEB). Figure 1A illustrates the design concept. Semiconductor QDs were used because they are able to generate electron-hole pairs under excitation. Such high-energy carriers, once captured or trapped, can modify the local electronic states and tune the chemical reactivity for interparticle bonding.

To demonstrate this concept, we chose water-phase colloidal CdSe/ZnS core/shell QDs capped with 3-mercaptopropionic acid (MPA) as an example (figs. S1 to S3). The MPA molecules are connected to the ZnS shell through Zn-S bonds, with the carboxyl groups exposed to environmental water. Under laser excitation, the excitons generated inside the CdSe core have three decay channels: radiative recombination, nonradiative recombination, and electron-hole pair dissociation to form separated electrons and holes (14), the latter of which plays a substantial role in PEB. Because the highest occupied molecular orbital (HOMO) of MPA molecules is located above the valance band maximum (VBM) of CdSe (Fig. 1B), the generated holes will tunnel through the outer potential barrier and transfer to the nanocrystal surface (see supplementary text S1 for a detailed analysis) (15–17). A thin shell thickness and a small energy difference of core/shell valence bands are preferred to increase the tunneling probability. Specially, the thiol groups on the nanocrystal surface strongly influence the electron and hole wavefunctions and affect the charge-transfer process (18). The surface MPA ligands capture the holes, desorb from the surface, and form dissolved disulfides in the solution (16, 19):



where Zn⁺ refers to the zinc atoms on the nanocrystal surface after ligand desorption. Such exposed zinc atoms are active bonding sites that are connected to the COO[−] group from the nearby QDs for interparticle bonding. In addition to the CdSe/ZnS core/shell QDs, this concept can be extended to other semiconductor nanomaterials such as MPA-capped CdSe and CdS QDs (fig. S4) because the VBM of these QDs is below the HOMO of MPA. By contrast, it cannot work for MPA-capped InP/ZnS QDs because the VBM of InP is higher than the HOMO of MPA (fig. S5 and

table S1). PEB is also applicable to metallic nanoparticles once the generated hot carriers have sufficiently high energy to transfer to the nanocrystal surface and drive ligand desorption (see fig. S6 for the printing of MPA-capped silver nanoparticles).

To understand the PEB process, we conducted Fourier transform infrared (FTIR) spectroscopy on both drop-cast QDs and printed species (Fig. 1C). The peaks between 1300 and 1600 cm^{−1} correspond to the symmetric and asymmetric stretching modes of deprotonated carboxylate COO[−] groups in MPA ligands (20). Although these peaks are observable in both samples, the frequency separations (Δν_{a-s}) between the symmetric and asymmetric stretching modes decrease from 170.5 cm^{−1} (drop-cast QDs) to 140.6 cm^{−1} (printed QDs), revealing that COO[−] groups are bounded to the nanoparticle surface through bidentate bridging (21). Moreover, two new peaks appear at ~800 and 1030 cm^{−1} in the printed sample, corresponding to the weak vibrations of Zn–O bond and stretching vibrations of C–O groups in zinc acetate, respectively, which further confirm the formation of COO–Zn bonds (22, 23). The FTIR results also exclude the possibility of ligand cross-linking or decomposition (see

supplementary text S2). Beyond MPA ligands, PEB can also be applied to QDs capped with other surface ligands composed of thiol, such as cysteamine (fig. S7) and glutathione, if their HOMOs are located above the valance band of QDs. However, the applicability on ligands composed of non-thiol head groups is still unclear.

To further verify the underlying mechanism, we conducted a series of control experiments. Taking a 532-nm continuous-wave laser for excitation, the red QDs are excited and printed, whereas no printing occurs for blue QDs. By comparison, we selected a 780-nm femtosecond laser for two-photon excitation and observed that all the blue, green, and red QDs got printed. Moreover, we ruled out the contribution of optical force (movie S1, fig. S8, and supplementary text S3) and photo-thermal effect (figs. S9 and S10 and supplementary text S4) in initiating the printing process.

PEB is a substrate-independent technique, and we can create suspended QD assembly in the solution, indicating potential 3D nanoprinting capability. As a proof of concept, we sealed the QD dispersions in a homemade chamber ~50 μm in thickness with a cleaned sapphire

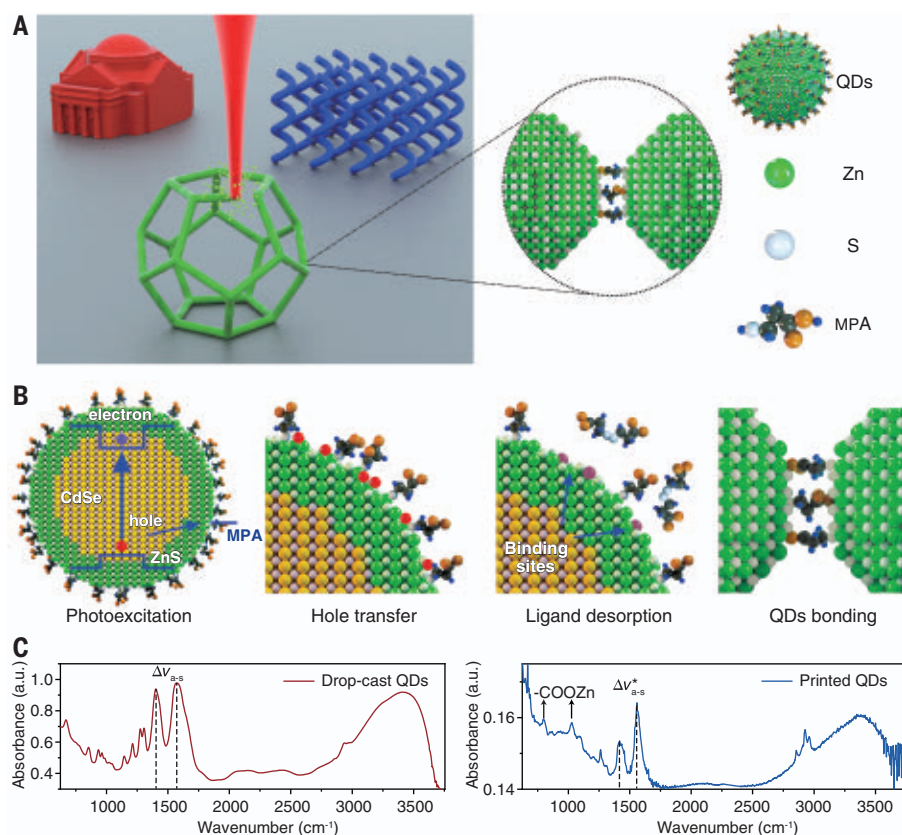


Fig. 1. Working principle of PEB. (A) Schematic illustration showing 3D nanoprinting of MPA-capped CdSe/ZnS QDs using PEB. (B) Schematic illustration showing the underlying mechanism of PEB. (C) FTIR spectra of the drop-cast QDs and printed structure.

substrate on the top. By steering the femto-second laser spot location, we demonstrate the printing of QDs into various nanopillar patterns. As shown in Fig. 2A, we printed hundreds of nanopillars into the Chinese characters of “Tsinghua University,” which exhibit uniform height and fluorescence intensity distribution (fig. S11). The fluorescence intensity of each pixel can be adjusted by controlling the pixel diameter or height (fig. S12). Specifically, the height adjustment allows tuning the fluorescence intensity without variation of printing resolution. As a demonstration, we also printed horse patterns with thousands of nanopixels of different heights (Fig. 2B and fig. S13B). The gap between adjacent nanopillars can be flexibly adjusted to control the integration density (fig. S14). Figure 2C shows the superresolution fluorescence image of the nanopixelated horse pattern with a pixel spacing of ~ 1000 nm and a pixel size of ~ 565 nm [$>2 \times 10^4$ dots per inch; also see the scanning electron microscopy (SEM) images in fig. S15]. From the high-magnification SEM and transmission electron microscopy images (figs. S16 to S18), the printed nanocrystals experience a relatively dense distribution. At a low dose, the QDs are bridged with surface ligands and no aggregation is observed. However, at a high dose (e.g., ≥ 49.1 mJ μm^{-2}), aggregation of QDs is observed because of the large number of desorbed ligands and the induced dispersion instability (see the supplementary text S5 and figs. S19 and S20). The fluorescence lifetime also scales down with the printing dose because of the increased density or formation of large aggregation (fig. S21). Moreover, we measured the photocurrent of the printed materials and obtained a value of ~ 0.5 nA at an applied voltage of 10 V under illumination of the 385-nm light (optical power density: 18 W/m 2 ; see supplementary text S6 and fig. S22). The PEB technique paves the way for the fabrication of highly integrated optoelectronic devices such as photodetectors and QD light-emitting diodes.

We further demonstrated the printing of blue, green, and red QDs to represent three primary colors using the badge of Tsinghua University as a model (Fig. 2D and fig. S23). We also compared the photoluminescence (PL) spectra and radiative recombination lifetimes of QD dispersion, drop-cast QDs, and printed QDs. According to the normalized PL spectra, the emission wavelengths between drop-cast and printed QDs are almost the same, whereas both exhibit a slight redshift in comparison with the QD solution (fig. S24). This redshift may arise from the Förster resonant energy transfer between neighboring QDs (24). From the PL lifetimes, we find that the excitons in printed structure first experience a rapid decay caused by ligand-binding-induced trap states and then decay slowly, similar to dispersed QDs in solution (Fig. 2E).

The longer lifetime observed in the printed samples indicate that they have a lower density than the drop-cast ones.

As a nanoprinting approach, one of the key parameters is the printing resolution. We investigated the printing linewidths as functions of laser power and scanning speed (Fig. 2F). The linewidth increases rapidly, whereas it levels off above a power threshold of ~ 15 mW. This can be explained by power-dependent two-photon absorption as the effective absorption area on the focus plane grows rapidly with the laser power and then slows down. By contrast, the printing linewidth scales down with scanning speed because of the reduction of absorbed power. With parameter optimization, the minimum printing linewidth obtained in our experiments is 81 ± 4 nm, with a line edge roughness of 12 ± 2 nm

(see the inset of Fig. 2F and fig. S25), which is far beyond the optical diffraction limit. The line edge roughness scales down with the increasing height because more QDs are printed and the irregularity at the edge is smoothed out (fig. S26).

To demonstrate the 3D nanoprinting capability, we programmed the laser beam to scan in 3D space and built a wide range of complex structures across from linear and curved to volumetric 3D structures. Figure 3A shows the schematics, SEM images, and cathodoluminescence images of a dodecahedron lattice and a C60 lattice. The identical cathodoluminescence intensity from the 3D structures reveals the structural uniformity. We also built a triangular lattice and a cubic lattice, which are mainly composed of slope line components (Fig. 3B). As shown in Fig. 3C, we built

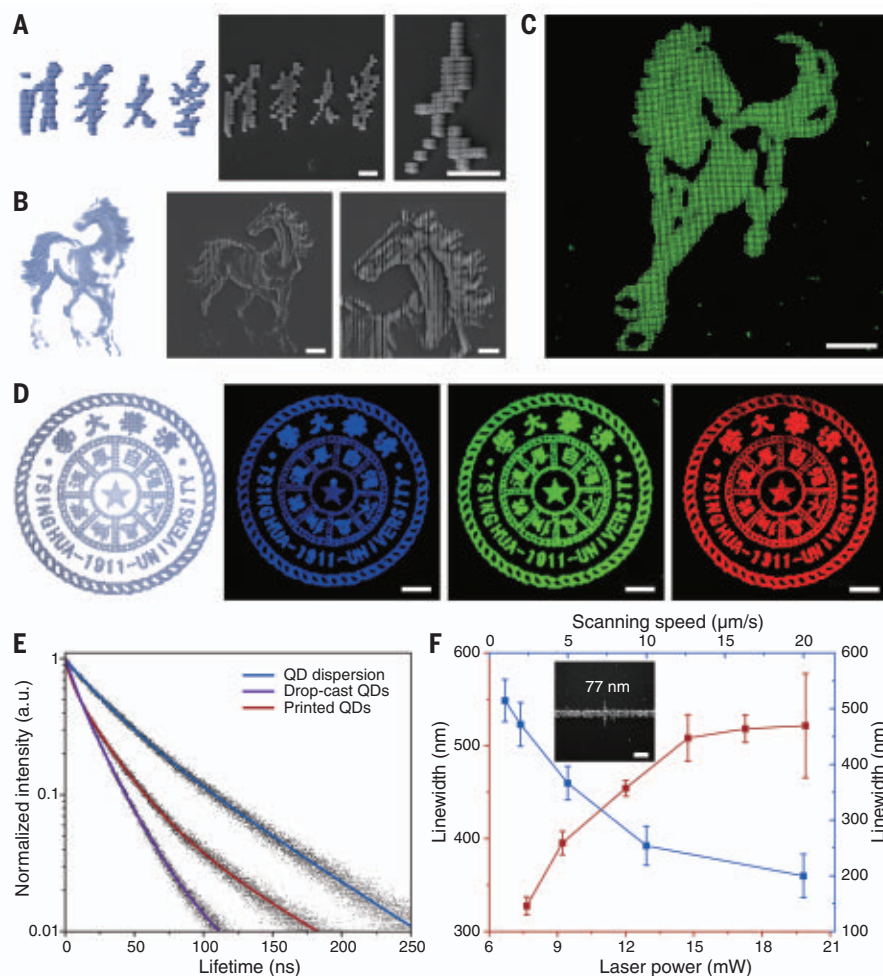


Fig. 2. Nano-pixel printing and QD characterization. (A) Model and tilt-view SEM images of the Chinese characters of “Tsinghua University.” (B) Model and tilt-view SEM images of a horse printed with nanopixels of different heights. (C) Superresolution PL image of the nanopixelated horse. (D) Model and PL images of the badge of Tsinghua University consisted of QDs emitting blue, green, and red light, respectively. (E) PL lifetimes of QD dispersion, drop-cast QDs, and printed QDs. (F) Printing linewidths as functions of laser power and scanning speed. Error bars indicate means \pm SEM. Scale bars: (A) and (B), right panel, 5 μm ; (B), middle panel, 10 μm ; (C) and (D), 20 μm ; and (F), 200 nm.

3D woodpile structures with the length of the bottom straight lines at 20 μm and the length-to-width ratio >40 . This provides the possibility of fabricating 3D active photonic crystal devices without postprocessing treatment such as pyrolysis or calcination (also see fig. S27).

In addition to the linear 3D structures, we also fabricated various curved 3D structures in freeform. As shown in Fig. 3D, we built helical structures with both equal and ever-changing diameters in each circle. The structures are vertically elongated because of laser intensity distribution above and below the focus plane. Such elongation can be reduced by optimizing the incident light field. We also fabricated a lay-flat helical structure by two single, continuous laser scans (Fig. 3E) and more sophisticated curved 3D nanostructures such as nest-like structures and dome structures (Fig. 3, F and G). The PEB approach also exhibits excellent reproducibility. As shown in

Fig. 3G and fig. S28, all of the architectures in the nanoarrays show excellent consistency with each other (also see movie S2). Moreover, we demonstrated the fabrication of volumetric 3D structures, including the auditorium and the old gate of Tsinghua University, using layer-by-layer scanning (Fig. 3, H and I).

Finally, we demonstrated the heterogeneous printing of different QDs into 3D nanostructures. Specifically, the mixing of QDs allows the tuning of emission color. For instance, we mixed the green and red QDs as feedstock and printed the Chinese characters of Tsinghua University with yellow light emitting. For comparison, we printed green QDs around the yellow characters as the background. Each pixel in the fluorescence images contains three sloped nanopillars with a height of 1 μm . Figure 4A shows the fluorescence images of different parts to depict the printing process, and Fig. 4B shows the 3D reconstructed fluorescence image. The excellent overlap

between design and fluorescence image further reveals the high printing accuracy (Fig. 4C). Finally, we demonstrated the printing of a 3D heterogeneous structure composed of four yellow “feet” and a green linker, with the intersection at the top (Fig. 4D). Heterogeneous 3D nanoprinting is very important in the fabrication of multifunctional optoelectronic devices such as full-color 3D nanodisplays in free space.

In summary, taking advantage of the photoexcitation-induced surface chemistry modification and the formation of chemical bonds, we developed a laser nanoprinting technique to directly assemble dispersed QDs into 3D architectures at high accuracy and high resolution. Without any additives or postprocessing treatment, the PEB technique allows us to maintain the photonic and optoelectronic properties of the QDs during the printing process. Although this concept is demonstrated in semiconductor QDs, it can be potentially

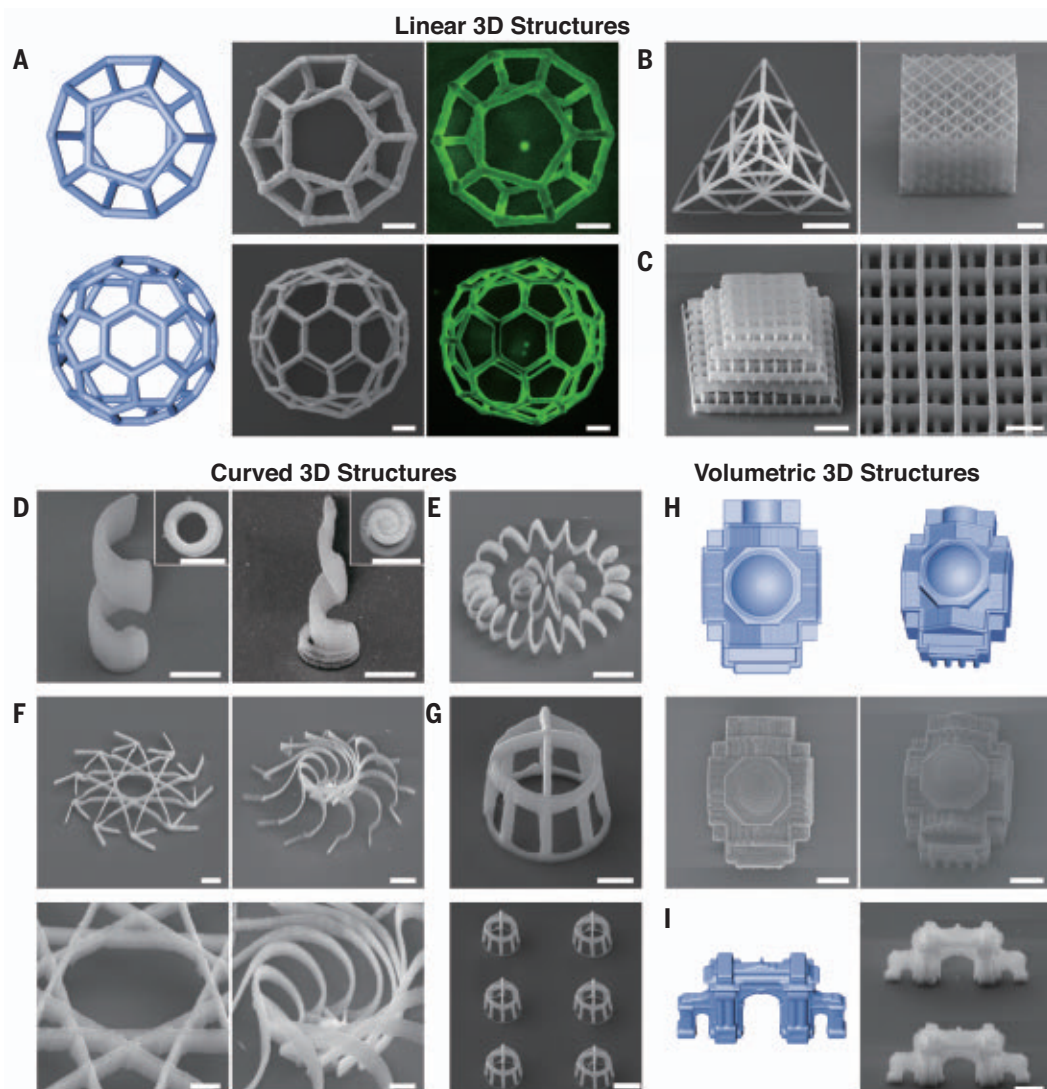


Fig. 3. Linear, curved, and volumetric 3D nanostructures.

(A) Models, SEM, and cathodoluminescence images of dodecahedron and C60 lattice, respectively. (B) SEM images of triangular lattice and cubic lattice structures. (C) SEM images of woodpile structures. (D) Tilt-view SEM images of upright helices (the inset SEM images show the top view). (E) SEM image of a lay-flat helical structure. (F) SEM images of nest-like structures with multiple curved lines. (G) SEM images of dome structures. (H) Models and SEM images of the auditorium at both top view and tilt view. (I) Model and tilt-view SEM image of the old gate. Scale bars: (A) and (C), right panel, (D) and (F), bottom panels, (G), top panel, 2 μm ; (B) and (C), left panel, (E) and (F), top panels, (G), bottom panel, and (I), 5 μm ; and (H), 10 μm .

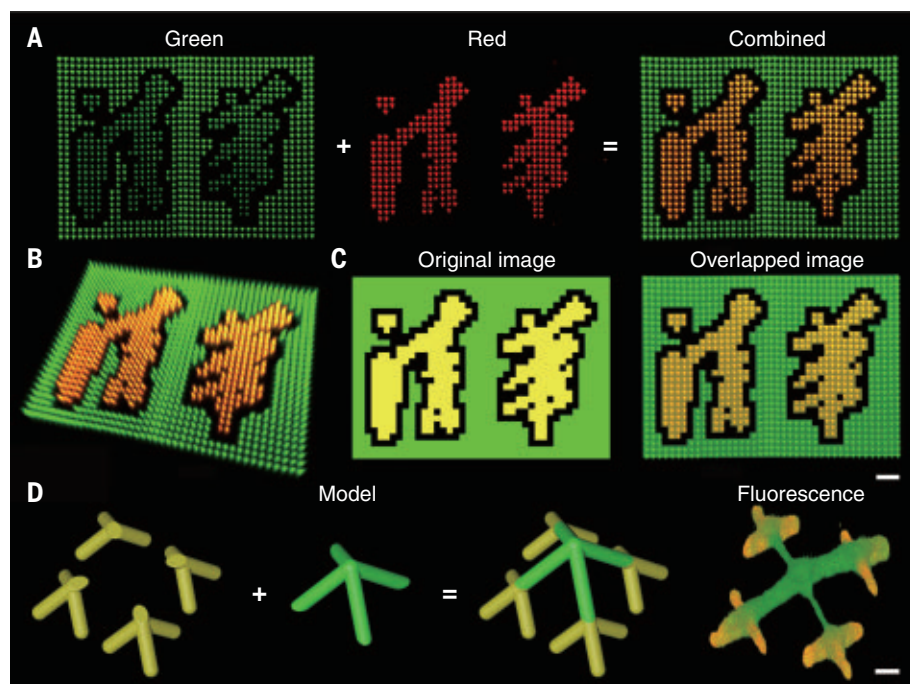


Fig. 4. Multicolor display and heterogeneous printing. (A) Fluorescence images of the printed Chinese characters of “Tsinghua University.” (B) Tilt view of the 3D reconstructed fluorescence image. (C) Designed image and its overlap with printed structure. (D) Heterogeneous printing of a single 3D structure as illustrated by the model and its reconstructed 3D fluorescence image. Scale bars: (A) to (C), 10 μm ; (D), 2 μm .

extended to non-semiconductor nanomaterials once high-energy carriers can be generated to modify the surface chemistry of the nanoparticles.

REFERENCES AND NOTES

- S. Kawata, H.-B. Sun, T. Tanaka, K. Takada, *Nature* **412**, 697–698 (2001).
- V. Hahn et al., *Nat. Photonics* **15**, 932–938 (2021).
- L. Li, R. R. Gattass, E. Gershgoren, H. Hwang, J. T. Fourkas, *Science* **324**, 910–913 (2009).
- L. R. Meza, S. Das, J. R. Greer, *Science* **345**, 1322–1326 (2014).
- A. Issa et al., *ACS Appl. Mater. Interfaces* **13**, 41846–41856 (2021).
- T. A. Schaedler et al., *Science* **334**, 962–965 (2011).
- X. Wen et al., *Nat. Mater.* **20**, 1506–1511 (2021).
- Y. Peng et al., *Adv. Mater. Technol.* **4**, 1800522 (2019).
- F. Kotz et al., *Adv. Mater.* **33**, e2006341 (2021).
- A. Desponds et al., *Small* **17**, e2102486 (2021).
- A. Vyatskikh, R. C. Ng, B. Edwards, R. M. Briggs, J. R. Greer, *Nano Lett.* **20**, 3513–3520 (2020).
- D. W. Yee, M. L. Lifson, B. W. Edwards, J. R. Greer, *Adv. Mater.* **31**, e1901345 (2019).
- Y. Wang, I. Fedin, H. Zhang, D. V. Talapin, *Science* **357**, 385–388 (2017).
- J. Gao, J. Zhang, J. van de Lagemaat, J. C. Johnson, M. C. Beard, *ACS Nano* **8**, 12814–12825 (2014).
- P. Singhal et al., *Nanoscale* **8**, 1823–1833 (2016).
- J. Aldana, Y. A. Wang, X. Peng, *J. Am. Chem. Soc.* **123**, 8844–8850 (2001).
- S. F. Wuister, C. de Mello Donegá, A. Meijerink, *J. Phys. Chem. B* **108**, 17393–17397 (2004).
- D. A. Hines, P. V. Kamat, *J. Phys. Chem. C* **117**, 14418–14426 (2013).
- M. J. Natan, J. W. Thackeray, M. S. Wrighton, *J. Phys. Chem.* **90**, 4089–4098 (1986).
- C. D. Dieleman et al., *Nanoscale* **12**, 11306–11316 (2020).
- E. R. Kennehan et al., *J. Am. Chem. Soc.* **143**, 13824–13834 (2021).
- G. Hitkari, S. Singh, G. Pandey, *Nano-Structures & Nano-Objects* **12**, 1–9 (2017).
- M. Gaidi et al., *J. Solid State Electrochem.* **22**, 3631–3637 (2018).
- L. Wang et al., *ACS Appl. Mater. Interfaces* **13**, 17861–17868 (2021).

ACKNOWLEDGMENTS

S.-F.L. thanks X. Chen and G. Huang for constructive comments and fruitful discussions about the experimental results. S.-F.L. thanks R. Zong for performing high-angle annular dark-field scanning transmission electron microscope (HAADF-STEM) characterization. S.-F.L. thanks D. Zhang for performing the photoluminescence quantum yield characterization. Z.-W.H. thanks X. Wang for providing professional help in cathodoluminescence characterization. S.-F.L. and Z.-W.H. thank B. Liu for help in performing superresolution photoluminescence characterization. S.-F.L. and Z.-W.H. also thank P. Li and Y. Zou for providing professional help in photocurrent characterization. We acknowledge support from Nano-optics laboratory at Tsinghua University as well as other characterization platforms. **Funding:** L.L. acknowledges support from the National Key Research and Development Program of China (grant 2020YFA0715000), the National Natural Science Foundation of China (grant 62075111), and L.L. acknowledges the Tsinghua-Foshan Innovation Special Fund (grant 2021THFS0206). H.-B.S. acknowledges support from the National Natural Science Foundation of China (grant 61960206003). L.L. and H.-B.S. acknowledge support from the State Key Laboratory of Precision Measurement Technology and Instruments. **Author contributions:** Conceptualization: S.-F.L., L.L.; Funding acquisition: L.L., H.-B.S.; Investigation: S.-F.L., Z.-W.H., F.L., Y.Z., X.-Z.L.; Methodology: S.-F.L., Z.-W.H.; Project administration: L.L., H.-B.S.; Supervision: L.L., H.-B.S., Z.L.; Visualization: S.-F.L., Z.-W.H.; Writing – original draft: S.-F.L., L.L.; Writing – review and editing: S.-F.L., Z.-W.H., L.L., H.-B.S., Z.L., F.L., Y.Z., X.-Z.L., H.Z., H.-H.F. **Competing interests:** L.L., S.-F.L., and H.-B.S. are inventors on patent applications CN202210286599.4 and PCT/CN2022/099871 submitted by Tsinghua University that covers QD printing mechanisms and methods. The remaining authors declare no competing interests. **Data and materials availability:** All data are available in the main text or the supplementary materials. **License information:** Copyright © 2022 the authors, some rights reserved; exclusive licensee American Association for the Advancement of Science. No claim to original US government works. <https://www.science.org/about/science-licenses-journal-article-reuse>

SUPPLEMENTARY MATERIALS

science.org/doi/10.1126/science.abo5345

Materials and Methods

Supplementary Text

Figs. S1 to S29

Tables S1 and S2

References (25–37)

Movies S1 and S2

Submitted 9 February 2022; accepted 12 July 2022
10.1126/science.abo5345



Molecular Pathology Workstation

Mxmatrix Infinity is a fully automated molecular pathology workstation designed to accelerate life sciences research, drug discovery, and development. It is an open system that allows simultaneous optimization of 40 assay parameters in a single run. The 40 independently thermal-cyclable slide

blocks enable any slide-based staining assays, including IHC, IF, ISH, CISH, FISH, multiplexed codetection, and microRNA ISH. The Infinity system adapts and completely automates any manual protocols such as denaturation, hybridization, stringency washes, counter stain, and final coverslip to maximize testing capacity, minimize hands-on time, and ensure consistent results every time.

BioGenex

For info: 1-800-421-4149

biogenex.com/xmatrix-infinity

Real-Time PCR Detection System

The CFX Opus Deepwell System is the latest addition to the Bio-Rad portfolio of CFX Opus Real-Time PCR instruments. With a 96-well block and the largest reaction volume available in the CFX Opus range—up to 125 μ L—the Deepwell System offers accurate, precise, and reliable quantification to support assay development. The deeper sample wells of the system are designed for workflows that require larger reaction volumes for pooling, certain sample prep procedures, or other specialized protocols such as those for food and industrial testing, and human and veterinary pathogen detection. The Deepwell System can multiplex up to five targets simultaneously and supports fluorescence resonance energy transfer (FRET) applications.

Bio-Rad Laboratories

For info: 1-800-424-6723

bio-rad.com/cfxopusdeepwell

Microarray Printers

Arrayjet introduces Mercury, a new core range of five instruments for ultralow-volume liquid dispensing. These print dispensers offer radically improved functionality and reliability with enhanced speed and precision. Available in a range of output capacities from 25 to 1,000 slides, Mercury instruments can be used for a wide assortment of microarray and microfluidics applications within pharmaceutical, diagnostic, and life science workflows. Arrayjet's high-speed microarray printers harness patented, noncontact inkjet technology for printing multiplex array-based assays onto slides, point-of-care devices, biochips, and microplates. The technology has the versatility to print any biological sample onto any substrate at a speed up to 100 times faster than traditional pin-spotting or tip-dispensing systems.

Arrayjet

For info: +44-(0)-131-440-5220

www.arrayjet.co.uk

Tube Selector and Picker

The Mohawk tube selector and picker from Ziath employs a linear rack reader and 96 pins that allow a frozen or thawed sample

tube to be raised when a rack is scanned according to a picklist. The use of this innovative technology avoids the need for slow, expensive robotics that can take minutes to process racks. Using the Mohawk, a rack is scanned and tubes are selected and picked in just seconds. Designed to work out of the box, Mohawk needs no setup or calibration. For extra sample tracking and security, the Mohawk can be connected directly to a 2D-barcode scanner for tube confirmation. In this mode it can also generate picklists directly from the tube barcodes. For further traceability, a 1D scanner for reading the rack barcode is included as standard. Its compact size, intuitive software, and ability to integrate with tube barcode readers/scanners make the Mohawk an asset in sample management applications with thawed or frozen tubes in SLAS standard format racks.

Ziath

For info: 1-858-880-6920

ziath.com/index.php/products/tube-devices/mohawk

Pipetting Robot

INTEGRA has developed the ASSIST PLUS pipetting robot to streamline routine pipetting tasks at an affordable price. Using INTEGRA electronic multichannel pipettes or the D-ONE single channel pipetting module, this system automates repetitive tasks while eliminating physical strain, providing superior reproducibility, and ensuring error-free processing. Simply mount an INTEGRA VIAFLO or VOYAGER electronic multichannel pipette or D-ONE single channel pipetting module onto the ASSIST PLUS pipette holder, choose a pipetting protocol, add a tip rack and your labware, and press "run." The pipette adapter of ASSIST PLUS allows the use of all VIAFLO and VOYAGER multichannel pipettes, and for unlimited flexibility, the D-ONE single channel pipetting module. Pipette from one to 16 channels and cover a volume range of 0.5 μ L–1,250 μ L, for many different applications.

INTEGRA Biosciences

For info: 1-603-578-5800

www.integra-biosciences.com/united-states/en

Modular High-Content Screening Station

The scanR modular microscope-based imaging platform from Olympus provides fully automated image acquisition and data analysis of biological samples through deep-learning technology. The system's flexible design enables it to meet the requirements for quantitative imaging and image analysis in modern cell biology, molecular biology, systems biology, and medical research. The scanR system excels in drug discovery applications, including showing the biochemical effects of compounds on the cellular level and drug-induced changes at gene expression levels. The solution can measure apoptosis, micronuclei, or DNA fragmentation (comet assays) and covers a variety of screening applications. The scanR solution not only satisfies the specific speed, endurance, and reliability requirements of a fully automated high-content screening system but also provides unmatched flexibility and adaptability with extensive expansion capabilities.

Olympus

For info: 1-800-225-8330

www.olympus-lifescience.com/en/microscopes/inverted/scanr

Electronically submit your new product description or product literature information! Go to www.science.org/about/new-products-section for more information.

Newly offered instrumentation, apparatus, and laboratory materials of interest to researchers in all disciplines in academic, industrial, and governmental organizations are featured in this space. Emphasis is given to purpose, chief characteristics, and availability of products and materials. Endorsement by *Science* or AAAS of any products or materials mentioned is not implied. Additional information may be obtained from the manufacturer or supplier.



CHANGE YOUR JOB AND YOU JUST MIGHT CHANGE THE WORLD.



Find your next job at ScienceCareers.org

The relevance of science is at an all-time high these days. For anyone who's looking to get ahead in—or just plain get into—science, there's no better, more trusted resource or authority on the subject than *Science Careers*. Here you'll find opportunities and savvy advice across all disciplines and levels. There's no shortage of global problems today that science can't solve. Be part of the solution.

ScienceCareers

FROM THE JOURNAL SCIENCE





**Shenzhen Institute of
Advanced Technology**
Chinese Academy of Sciences



Established in partnership between the Chinese Academy of Sciences and the Shenzhen Municipal Government, the Shenzhen Institute of Advanced Technology (SIAT) is a newly-created university with an objective to become the world's preeminent institute for emerging science and engineering programs. SIAT is equipped with state-of-art teaching and research facilities and is dedicated to cultivating international, visionary, and interdisciplinary talents while delivering research support to pursue innovation-driven development.

SIAT is located in Shenzhen, also known as the "Silicon Valley of China," a modern, clean, and green city, well-known for its stunning architecture, vibrant economy, and its status as a leading global technology hub. SIAT is seeking applications for faculty positions of all ranks in the following academic programs: Computer Science and Engineering, Bioinformatics, Robotics, Life Sciences, Material Science and Engineering, Biomedical Engineering, Pharmaceutical Sciences, Synthetic Biology, Neurosciences, etc. SIAT seeks individuals with a strong record of scholarship who possess the ability to develop and lead high-quality teaching and research programs. SIAT offers a comprehensive benefits package and is committed to faculty success throughout the academic career trajectory, providing support for ambitious and world-class research projects and innovative, interactive teaching methods.

Further information:

<https://www.siat-sz.edu.cn/>



Science Careers helps you advance your career. Learn how !

- Register for a free online account on [ScienceCareers.org](https://www.sciencecareers.org).
- Search hundreds of job postings and find your perfect job.
- Sign up to receive e-mail alerts about job postings that match your criteria.
- Upload your resume into our database and connect with employers.
- Watch one of our many webinars on different career topics such as job searching, networking, and more.

Visit [ScienceCareers.org](https://www.sciencecareers.org)
today — all resources are free

ScienceCareers
FROM THE JOURNAL SCIENCE



SCIENCECAREERS.ORG

ETH zürich

Assistant Professor (Tenure Track) of Organic Chemistry

→ The Department of Chemistry and Applied Biosciences (www.chab.ethz.ch) at ETH Zurich invites applications for the above-mentioned position at the Laboratory of Organic Chemistry.

→ Successful candidates are expected to establish a successful, internationally recognized and externally funded research program. A focus on organic chemistry in the broadest sense is desirable. Areas of interest include analytical chemistry, methods and/or target-oriented synthesis, prebiotic (origin of life) chemistry, chemical biology, and physical-organic chemistry. At the assistant professor level, commitment to teaching and the ability to lead a research group are expected. Collaborations with colleagues within and outside the ETH are encouraged. Generous annual support for students and supplies will be provided by the Laboratory of Organic Chemistry to supplement external support obtained for her / his research program.

→ Assistant professorships have been established to promote the careers of younger scientists. ETH Zurich implements a tenure track system equivalent to other top international universities.

→ **Please apply online:**
www.facultyaffairs.ethz.ch

→ Applications should include a curriculum vitae, a list of publications, a statement of future research and teaching interests, a description of the leadership philosophy, and a description of the three most important achievements. The letter of application should be addressed **to the President of ETH Zurich, Prof. Dr. Joël Mesot. The closing date for applications is 31 October 2022.** ETH Zurich is an equal opportunity and family-friendly employer, values diversity, and is responsive to the needs of dual-career couples.

Who's the top employer for 2021?



Science Careers' annual survey reveals the top companies in biotech & pharma voted on by *Science* readers.

Read the article and employer profiles at sciencecareers.org/topemployers

myIDP:
A career plan customized
for you, by you.



For your career in science, there's only one **Science**

Features in myIDP include:

- Exercises to help you examine your skills, interests, and values.
- A list of 20 scientific career paths with a prediction of which ones best fit your skills and interests.
- A tool for setting strategic goals for the coming year, with optional reminders to keep you on track.
- Articles and resources to guide you through the process.
- Options to save materials online and print them for further review and discussion.
- Ability to select which portion of your IDP you wish to share with advisors, mentors, or others.
- A certificate of completion for users that finish myIDP.



Visit the website and start
planning today!
myIDP.sciencecareers.org

**Science
Careers**
MAAAS

In partnership with:



BURROUGHS
WELLCOME
FUND



**UNIVERSITÉ
DE GENÈVE**

The Faculty of Medicine of the University of Geneva is seeking to fill a position of:

**FULL or ASSOCIATE PROFESSOR
in the fields of human genetics and/or genomics**

Genetics and/or genomics is one of the excellence strategic fields of the Faculty of Medicine. The incumbent will undertake research in this area at the highest national and international levels and secure external funding. He/She will have to develop strong links with clinicians based at the medical genetics service at the University Hospitals of Geneva, as well as with other researchers from Geneva lake area and particularly those located at the Genome Center at Campus Biotech.

CHARGE: This full-time position will involve undergraduate and postgraduate teaching in human genetics and/or genomics, as well as supervising Masters' and doctoral theses.

The incumbent will also take up administrative and organizational duties within the Department of Genetic Medicine and Development and the Faculty of Medicine.

REQUIREMENTS:

Doctorate of Medicine (MD) or equivalent degree or PhD
Full postgraduate training in human genetics and/or genomics is required.

Previous teaching and independent research experience.
Publications in leading international journals.
Good knowledge of French is an advantage.

STARTING DATE: October 1st 2023, or according to agreement.

Mandatory online registration until October 15th 2022 at:
<http://www.unige.ch/academ>

Additional information may be obtained from:
viviane.burghardt@unige.ch

*From a gender perspective, the University encourages
applications from women*

By Oliver Symes

Looking for a change

The alarm blared in my ear. After silencing it, I remained in bed, staring at the ceiling for another 30 minutes. My motivation to push ahead with my Ph.D. was waning, making it harder and harder to rise and face each new exhausting day. Continuing with the struggle for the remaining 2 years of my program would risk total burnout and breakdown, I realized. I needed a change. So, with great apprehension, I decided to hit the pause button on my Ph.D. and take a 9-month position at a health care charity, hoping I would return to my Ph.D. with new motivation—and new clarity.

Back when I was looking for Ph.D. positions, I only had a vague idea of what I wanted to study. I viewed the degree mostly as a means to an end—a way to secure more interesting and higher paid positions in the private sector than my master's degree would unlock. So I wasn't picky about the research I pursued. I reasoned that a variety of projects within my field of synthetic organic chemistry would provide the training and degree I wanted.

In hindsight, I should have been more selective. I ended up working on a project I was technically capable of completing and that was intellectually interesting, but over time became disillusioned with because I struggled to see how it would make an impact on the wider world.

Pandemic-induced challenges amplified my problems. I started my program in 2020, when meetings were virtual and in-person contact was actively discouraged, so I had few opportunities to meet and form personal connections with colleagues. Research became my sole focus, and when my interest in that started to falter, my project felt suffocating. It got harder and harder every day to get myself to the lab, where I endured the bench work—much of it tedious and frustrating—in a state of deep unhappiness.

I wondered whether I should have expected this level of despair, given that doing a Ph.D. is hard, even in the best of times. However, 11 months into my program, I struggled to find a single thing I was enjoying about grad school. It was clear I needed to pause and re-evaluate.

After seeking advice from a university adviser and talking with my supervisor, I decided to take a break from my program. I searched online for internships and other short-term positions in science-related roles, including those that involved science policy, intellectual property, and science writing. Ultimately, I signed a contract with the Multiple Sclerosis Society to provide support for its research team.



“It was clear I needed to pause and re-evaluate.”

At first, I worried I was wasting time I could have spent finishing my Ph.D. But after only 1 month in my new role, it became clear I'd made the right decision. I was able to decompress and spend my days doing a variety of tasks that were new to me. For instance, I helped the grants management team find suitable peer reviewers for funding applications, built a survey to better understand the diversity and inclusion of the society's funded research, and supported the communications team by writing blog posts. My mental health improved noticeably and I found it easier to come into work each day, buoyed by the sense that I was supporting the organization's mission to help people. The work I did could matter

after all—if I chose wisely.

After that realization, I decided I wanted to return to my Ph.D. program once my contract expired—as long as I could make some changes. I told my Ph.D. supervisor I wasn't interested in working on purely academic research. To my relief, he was supportive, and over the next few months we designed a project that better fit my interests and long-term goals.

I returned to my program last month, optimistic that this time around my experience will be different. But if it doesn't go as I hope, my charity experience has given me confidence that I'll be able to find a satisfying job elsewhere, with or without a Ph.D.

I encourage any Ph.D. student who is struggling to consider taking a break. Try something different, gain new skills, and thoroughly scrutinize whether your graduate program is working for you—because this is *your* Ph.D. and you do have the power to change it. ■

Oliver Symes is a Ph.D. student at Imperial College London. Do you have an interesting career story to share? Send it to SciCareerEditor@aaas.org.


What's Your Next Career Move?

From networking to mentoring to evaluating
your skills, find answers to your career questions
on *Science Careers*

To view the complete collection, visit
ScienceCareers.org/booklets



Science Careers

FROM THE JOURNAL SCIENCE  AAAS



PRIZE FOR IMMUNOLOGY

REWARDING HIGH-RISK RESEARCH.
SUPPORTING EARLY-CAREER SCIENTISTS.
HELPING TO FIND CURES FASTER.
APPLY TODAY

**Now accepting applications for the Michelson
Philanthropies & Science Prize for Immunology.**

The Michelson Philanthropies and Science Prize for Immunology focuses on transformative research in human immunology, with trans-disease applications to accelerate vaccine and immunotherapeutic discovery. This international prize supports investigators 35 and younger, who apply their expertise to research that has a lasting impact on vaccine development and immunotherapy. It is open to researchers from a wide range of disciplines including computer science, artificial intelligence/machine learning, protein engineering, nanotechnology, genomics, parasitology and tropical medicine, neurodegenerative diseases, and gene editing.

Application deadline: Oct. 1, 2022.

For more information visit:
www.michelsonmedicalresearch.org

#MichelsonPrizes



"The Michelson Philanthropies & Science Prize for Immunology will greatly impact my future work. As I am just starting my scientific career, it will illuminate my work, spark interest and support me to continue my research in this field."

Paul Bastard, MD, PhD,
Laboratory of Human Genetics
of Infectious Diseases, Imagine
Institute (INSERM, University of
Paris), Paris, France; and The
Rockefeller University, New York.

Dr. Bastard received the inaugural
Grand Prize for his essay: "Why
do people die from COVID-19:
Autoantibodies neutralizing type
I interferons increase with age."

GRAND PRIZE:
\$30,000

FINALIST PRIZE:
\$10,000